



Article

Differential Antioxidant Response to Supplemental UV-B Irradiation and Sunlight in Three Basil Varieties

Sonja Milić Komić ^{1,†}, Bojana Živanović ^{1,†}, Jelena Dumanović ² , Predrag Kolarž ³, Ana Sedlarević Zorić ¹, Filis Morina ⁴, Marija Vidović ⁵ and Sonja Veljović Jovanović ^{1,*}

¹ Institute for Multidisciplinary Research, Department of Life Science, University of Belgrade, Kneza Višeslava 1, 11030 Belgrade, Serbia; sonjamilic@imsi.bg.ac.rs (S.M.K.); bojana.zivanovic@imsi.bg.ac.rs (B.Ž.); ana.sedlarevic@imsi.bg.ac.rs (A.S.Z.)

² Department of Analytical Chemistry, Faculty of Chemistry, University of Belgrade, 11158 Belgrade, Serbia; dumanovicjelena@gmail.com

³ Institute of Physics Belgrade, University of Belgrade, 11080 Belgrade, Serbia; kolarz@ipb.ac.rs

⁴ Biology Center of the Czech Academy of Sciences, Institute of Plant Molecular Biology, Department of Plant Biophysics and Biochemistry, Branišovska 31/1160, 370 05 Ceske Budejovice, Czech Republic; morina@umbr.cas.cz

⁵ Institute of Molecular Genetics and Genetic Engineering, Laboratory for Plant Molecular Biology, University of Belgrade, Vojvode Stepe 444a, 11042 Belgrade, Serbia; mvidovic@imgge.bg.ac.rs

* Correspondence: sonjavel@imsi.rs or sonjavel@imsi.bg.ac.rs

† These authors contributed equally to this work.

Abstract: Three basil plant varieties (*Ocimum basilicum* var. Genovese, *Ocimum × citriodorum*, and *Ocimum basilicum* var. *purpurascens*) were grown under moderate light (about 300 $\mu\text{mol photons m}^{-2} \text{s}^{-1}$) in a glasshouse or growth chamber and then either transferred to an open field (average daily dose: 29.2 $\text{kJ m}^{-2} \text{d}^{-1}$) or additionally exposed to UV-B irradiation in a growth chamber (29.16 $\text{kJ m}^{-2} \text{d}^{-1}$), to reveal the variety-specific and light-specific acclimation responses. Total antioxidant capacity (TAC), phenolic profile, ascorbate content, and class III peroxidase (POD) activity were used to determine the antioxidant status of leaves under all four light regimes. Exposure to high solar irradiation at the open field resulted in an increase in TAC, total hydroxycinnamic acids (HCAs, especially caffeic acid), flavonoids, and epidermal UV-absorbing substances in all three varieties, as well as a two-fold increase in the leaf dry/fresh weight ratio. The supplemental UV-B irradiation induced preferential accumulation of HCAs (rosmarinic acid) over flavonoids, increased TAC and POD activity, but decreased the ascorbate content in the leaves, and inhibited the accumulation of epidermal flavonoids in all basil varieties. Furthermore, characteristic leaf curling and UV-B-induced inhibition of plant growth were observed in all basil varieties, while a pro-oxidant effect of UV-B was indicated with H_2O_2 accumulation in the leaves and spotty leaf browning. The extent of these morphological changes, and oxidative damage depended on the basil cultivar, implies a genotype-specific tolerance mechanism to high doses of UV-B irradiation.

Keywords: ascorbate; epidermal flavonoids; hydrogen peroxide; *Ocimum basilicum* var. Genovese; *Ocimum × citriodorum*; *Ocimum basilicum* var. *purpurascens*; polyphenols; supplemented and ecologically relevant UV-B irradiation; total leaf antioxidant capacity



Citation: Milić Komić, S.; Živanović, B.; Dumanović, J.; Kolarž, P.; Sedlarević Zorić, A.; Morina, F.; Vidović, M.; Veljović Jovanović, S. Differential Antioxidant Response to Supplemental UV-B Irradiation and Sunlight in Three Basil Varieties. *Int. J. Mol. Sci.* **2023**, *24*, 15350. <https://doi.org/10.3390/ijms242015350>

Academic Editors: Byoung Ryong Jeong and Iftikhar Ali

Received: 22 September 2023

Revised: 9 October 2023

Accepted: 17 October 2023

Published: 19 October 2023



Copyright: © 2023 by the authors. Licensee MDPI, Basel, Switzerland. This article is an open access article distributed under the terms and conditions of the Creative Commons Attribution (CC BY) license (<https://creativecommons.org/licenses/by/4.0/>).

1. Introduction

Plants are inevitably exposed to seasonal and diurnal variations in light intensity and quality as a result of variations in the ratio of UV-A/UV-B/photosynthetically active radiation (PAR, 400–700 nm) [1,2]. Ultraviolet (UV) irradiation accounts for only a small fraction of total solar radiation, about 6% UV-A (315–400 nm) and 0.5% UV-B (290–315 nm); nevertheless, it can induce a variety of responses in plants. Since the 1980s, the depletion of the stratospheric ozone layer has led to an increase of up to 14% in UV-B radiation

reaching the Earth's surface [3]. The Montreal Protocol and its amendments were remarkably effective in saving the Earth's stratospheric ozone layer and led to its restoration. Nevertheless, there is a strong link between ozone depletion and climate changes caused by increasing greenhouse gases. Recent studies predict a 3–8% increase in the UV index over the tropics or mid-latitudes by 2100, depending on the greenhouse gas scenario, cloud cover, and aerosol concentration used for modelling [4–6]. The predicted decrease in mean cloud cover over the Mediterranean region, due to climate change, could also lead to an increase in the intensity of UV radiation over the Mediterranean region in the near future [7]. The meteorological data for this study were collected in Belgrade (Serbia), situated at the 45th parallel of northern latitude humid subtropical and humid continental climate, exhibiting four distinct seasons and precipitation evenly distributed throughout the year. Malinović-Milićević and co-authors showed that the average daily UV-B dose ranged from 2.062 kJ m^{-2} (December) to 58.773 kJ m^{-2} (June) and estimated a 3.7% increase in UV-B radiation intensity per decade in the territory of Vojvodina (northern region of Serbia) [8]. Similar UV-B doses have been measured in Cyprus, where radiation doses vary from 70 kJ m^{-2} in Larnaca to 55 kJ m^{-2} in Athalassa, depending on the climate regime of the island [9]. High UV-B radiation can cause DNA damage and/or induce the generation of reactive oxygen species (ROS), which can oxidize proteins and membranes, and inhibit photosynthesis and growth [10]. However, plants rarely show signs of damage even though they are constantly exposed to natural UV-B irradiation [11]. There are numerous studies with conflicting results on the effect of UV-B irradiation on plants, which can be explained with different ratios of UV-B/UV-A/PAR, and unnaturally high UV-B doses applied in the experiments, as well as species/genotype-specific sensitivity to UV-B radiation, different experimental conditions, and previous acclimation periods [12]. Moreover, high PAR, combined with other limiting environmental factors such as water and/or nutrient deficiencies, can overcome the capacity of photosynthetic assimilation and energy dissipation processes and provoke the generation of ROS, resulting in photo-oxidative damage to the photosynthetic apparatus [13,14].

Plants respond to light by developing numerous photoprotective mechanisms against the deleterious effects of excess PAR and UV-B, of which the antioxidant network and redox signaling pathways play an important role in maintaining cellular redox homeostasis [15,16]. The most efficient and rapid photoprotective process of the photosynthetic apparatus is the dissipation of excess excitation energy in photosystem II (PSII) with heat, which is controlled with the trans-thylakoid proton gradient and zeaxanthin formation [17,18]. As part of the acclimation mechanisms to PAR and UV radiation, the enhanced biosynthesis of phenolics can also be considered a photosynthetic energy escape valve, with 20% of the fixed carbon in photosynthesis being directed into the phenylpropanoid pathway [19]. The accumulation of phenolics, particularly flavonoids, is considered a hallmark of the UV-B response in plants [2]. Polyphenols are the largest and most diverse group of secondary metabolites that play a crucial role in the dynamic interactions between plants and the environment. Under full sunlight, plants tend to accumulate UV-absorbing phenolics, especially flavonols, in the epidermal layer of exposed leaves, providing them with an effective protective shield against potentially harmful UV radiation [20]. In addition to their protective role in attenuating UV radiation and PAR, flavonoids and anthocyanidins are potent antioxidants, whose efficiency in ROS scavenging is mainly determined with their structure [21]. Flavonoids and anthocyanidins with *ortho*-dihydroxyl substitution in the B ring have almost four times higher antioxidant activity than the other polyphenols. Anthocyanins exhibit multiple functional roles in plants that have to cope with a variety of abiotic and biotic stress factors [22,23]. In addition to their absorption in the blue and green regions of the spectrum, they are extremely effective antioxidants that can scavenge ROS *in vitro* and act as substrates for PODs and participate in H_2O_2 scavenging [24]. Anthocyanins are commonly induced with high light intensity, low nitrogen content, and low temperatures. On the other hand, both UV-B and high PAR intensities induce

phenylpropanoid accumulation in the epidermal layers, such as quercetin and catechin, which also exhibit a strong antioxidant potential through direct interaction with ROS [25].

In contrast to the deleterious effects of high UV-B irradiation, low UV-B levels trigger a UV-B-specific signaling pathway that mediates photomorphogenic responses and the development of the so-called “UV-acclimated phenotype” with shorter petioles and shorter, narrower, and/or thicker leaf blades, as well as leaf curling [26]. The photomorphogenic UV-B signaling pathway is mediated with the UV-B-specific component UV RESISTANCE LOCUS8 (UVR8). Both UVR8 and CONSTITUTIVE PHOTOMORPHOGENESIS 1 (COP1) are required for UV-B-induced expression of the ELONGATED HYPOCOTYL5 (HY5) transcription factor, which plays a central role in regulating genes involved in photomorphogenic UV-B responses [2].

Basil (*Ocimum basilicum* L.) is a widely used aromatic herbaceous plant in nutrition, as well as in traditional medicine, pharmaceuticals, perfumes, and cosmetics [27,28]. Traditionally, basil was grown in an open field. However, in response to increasing market demand, and unpredictable weather conditions, basil cultivation has strongly shifted to controlled environment agriculture, such as glasshouses, high tunnels, and vertical indoor farms for herb production [29,30]. Light intensity and quality have a significant impact on the basil growth rate, morphology, and anatomical characteristics [31–33]. Considering the increased demand for high-quality basil (particularly fresh leaf material), special attention is paid to the cultivation treatment, especially the beneficial effects of low UV radiation on the functional properties, antioxidant value, and content of secondary metabolites [34,35]. In different basil varieties (purple and green), competition in the induction of either flavonoid or anthocyanin metabolic pathways depending on light quality and intensity has been shown [36]. In addition, purple basil varieties have attracted increasing interest in the last decade due to their much higher content of health-promoting substances compared to green varieties, especially when the plants are grown under limited light intensity [37]. A comparison of green and red basil leaves developed at full sunlight showed higher photosynthetic performance and higher stomatal conductance in red leaves than in green ones at a given time point [36]. However, to our knowledge, dynamics of the accumulation of UV screening compounds in basil have not been investigated. Moreover, varieties of *O. basilicum* with constitutively different contents of anthocyanins and phenolics represent a suitable system to investigate the acclimation response to different UV/PAR ratios. Comparative analyses of green vs. purple leaf response of the same age within the same species to light treatments can reveal the functional role of anthocyanins, which is still debatable as discussed by Landi and co-authors [38]. In addition, lemon basil differs from other varieties not only by its characteristic aroma and high content of biologically active polyphenolic compounds, but also by its particular morphology, characterized by a small stature, early flowering, and narrow leaves [39].

In this study, we aimed to distinguish between UV-B and high PAR effects on their pro-oxidant effects as well as on ascorbate and polyphenol contents, total and epidermal, in the leaves of three commonly consumed basil varieties: “Genovese” (*Ocimum basilicum* Genovese, GB), “Lemon” (*Ocimum × citriodorum*, CB), and “Purple” (*Ocimum basilicum* purpurascens, PB). We compared two green-leaf varieties and one purple-leaf cultivar, to investigate the functional role of anthocyanins in photoprotection (including excessive PAR and UV-B radiation). Based on the physicochemical properties of anthocyanins and other abundant phenylpropanoids in the leaves of three basil varieties, we hypothesized that the purple-leaf cultivar would be more tolerant to high solar radiation, and show fewer symptoms of oxidative stress damage. Furthermore, we aimed to find out whether the varieties differ in their dynamics of acclimation response to different UV/PAR ratios (supplemental UV-B irradiation, and full sun irradiance). To achieve this, the analyses of phenolic profiles, dynamics of accumulation of epidermal UV-absorbing compounds, and redox status were performed.

2. Results

2.1. Effects of Light Regimes on Growth

After 1 month of growth in the glasshouse (GH) with complete attenuation of UV irradiation and 84% of solar PAR, half of the basil plants were transferred to an open field (OF). Upon transferring the basil plants from the glasshouse to full sun for 15 days in the open field (the average daily UV-B dose was 29.20 kJ m^{-2}), all three varieties showed differences in the fresh/dry weight ratio (FW/DW) compared to glasshouse plants (experiment I; Table 1). The FW/DW ratios were lower in plants grown in the open field compared to the glasshouse plants regardless of variety, with the most pronounced difference in *Ocimum basilicum* var. *purpurascens* (PB). However, only “lemon” basil (CB), DW, and, to a lesser extent, FW increased in the open field compared to the glasshouse, while growth inhibition (evidenced in FW) was only observed in “Genovese” basil (GB) (Table 1). In addition, 1 week after full sun exposure, leaf thickening was observed in “lemon” basil (CB).

Table 1. Experiment I. Leaf fresh weight (FW) and dry weight (DW) (g) and their ratio after 15 days of treatment in the open field exposed to full sunlight (OF) and continuous treatment in the glasshouse (GH). Values represent the sum of the masses of all leaves from individual plant; means \pm SE ($n \geq 4$). Significant differences between GH and OF plants according to *t*-test are indicated (* $p \leq 0.05$, ** $p < 0.01$, *** $p < 0.001$). *Ocimum basilicum* var. Genovese (GB), *Ocimum* \times *citriodorum* (CB), and *Ocimum basilicum* var. *purpurascens* (PB).

	GB		CB		PB	
	GH	OP	GH	OP	GH	OP
FW (g)	19.00 \pm 1.78	12.33 \pm 0.62 *	8.67 \pm 0.94	12.00 \pm 1.47	9.00 \pm 0.82	8.67 \pm 0.94
DW (g)	1.56 \pm 0.13	1.80 \pm 0.08	0.86 \pm 0.05	1.65 \pm 0.21 *	0.53 \pm 0.02	0.91 \pm 0.06
FW/DW	12.18 \pm 0.17	6.88 \pm 0.36 ***	10.16 \pm 0.39	7.27 \pm 0.06 **	16.88 \pm 0.97	9.47 \pm 0.47 **

In experiment II, 1-month-old plants were grown in a growth chamber (GC) under controlled conditions (PAR, $300 \pm 50 \mu\text{mol m}^{-2} \text{ s}^{-1}$), and half of the plants of all three varieties were exposed to supplemental UV-B irradiation (1.35 W m^{-2} , i.e., 29.16 kJ m^{-2}) for 6 h per day (UV-B). After only 3 days, the first small brown blotches/spots, characteristic of UV-induced damage, were noticed on the directly exposed leaves. Over the next 5 days, the damaged leaf areas increased in size and became necrotic and the young leaves began to curl, especially in the Genovese variety, which appeared to be the most sensitive variety (Figure 1). Moreover, chlorophyll content was measured with Dualex and no significant changes were observed in both experiments (Supplementary Figure S1, Supplementary Table S1).

2.2. Light-Induced Accumulation of UV-Absorbing Substances

In the glasshouse, the basal concentration of epidermal flavonoids (EpFlav, DA₃₇₅) in the leaves of all three basil varieties ranged from 0.2 to 0.4 (AU). Nevertheless, an initial increase in EpFlav accumulation was detected 24 h after transferring the plants to the open field, and it continued to increase in all varieties, but the increase rate was the slowest in *Ocimum basilicum* var. *purpurascens* (Figure 2A). On the other hand, EpFlav content in leaves of plants grown continuously in the glasshouse remained constant. After 15 days, the content of epidermal UV-absorbing compounds was seven-fold higher in *Ocimum basilicum* var. Genovese and *Ocimum* \times *citriodorum* and five-fold higher in *Ocimum basilicum* var. *purpurascens* grown in the open field compared to the respective varieties grown in the glasshouse.



Figure 1. Representative images of three basil varieties (five plants for each variety) grown at constant PAK and artificial UV-B radiation (1.35 W m^{-2}) 6 h per day after 8 days of treatment. **Figure 2.** The dynamics of epidermal flavonoid (EpFlav) accumulation, in the leaves of three basil varieties (*Ocimum basilicum* var. Genovese—GB, *Ocimum x citriodorum*—CB, and *Ocimum basilicum* var. purpurascens—PB) grown in (A) glasshouse (GH) and open field (OF) during 15 days; (B) growth chamber (GC) and growth chamber with additional UV-B supplementation (UV-B—red line) during 8 days. Values are given as means \pm SE. Significant differences in EpFlav between plants grown in GH and OF, as well as between plants grown in GC and UV-B are indicated for all varieties according to the Mann–Whitney U-test ($p \leq 0.05$). Significant differences in EpFlav between plants grown in GH and OF, as well as between plants grown in GC and UV-B are indicated for all varieties according to the Mann–Whitney U-test ($p \leq 0.05$).

Int. J. Mol. Sci. 2023, 24, x FOR PEER REVIEW

Ocimum basilicum var. purpurascens (PB) (bottom).
 2.2. Light-Induced Accumulation of UV-Absorbing Substances

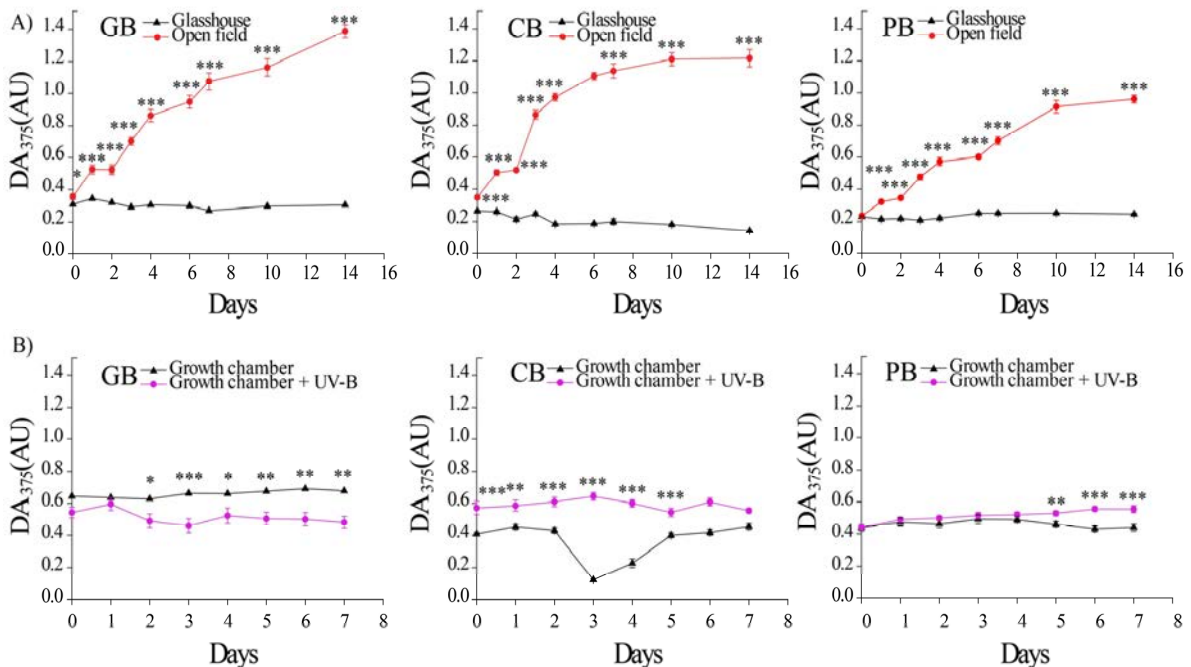


Figure 2. The dynamics of epidermal flavonoid (EpFlav) accumulation, in the leaves of three basil varieties (*Ocimum basilicum* var. Genovese—GB, $n = 20$; *Ocimum x citriodorum*—CB, $n = 20$; and *Ocimum basilicum* var. purpurascens—PB, $n = 20$) grown in (A) glasshouse (GH) and open field (OF) during 15 days; (B) growth chamber (GC) and growth chamber with additional UV-B supplementation (UV-B—red line) during 8 days. Values are given as means \pm SE. Significant differences in EpFlav between plants grown in GH and OF, as well as between plants grown in GC and UV-B are indicated for all varieties according to the Mann–Whitney U-test ($p \leq 0.05$). Significant differences in EpFlav between plants grown in GH and OF, as well as between plants grown in GC and UV-B are indicated for all varieties according to the Mann–Whitney U-test ($p \leq 0.05$).

2.3. Phenolic Profile of Basil Leaves under Different Light Regimes

Significantly higher basal levels of syringic acid (SyA), *p*-coumaric acid (*p*CA), and cyanidin (Cy) were found in the *Ocimum basilicum* var. purpurascens variety. Furthermore, anthocyanins were only detected in *Ocimum basilicum* var. purpurascens. *Ocimum basilicum* var. Genovese had significantly higher basal levels of hydroxycinnamic acids (HCAs), and the lowest basal levels of quercetin (Q), while *Ocimum x citriodorum* had the highest basal

Exposure to supplemental UV-B irradiation at constant PAR, comparable to the intensity of solar UV-B irradiation, resulted in only a slight increase in EpFlav accumulation in all three basil varieties, far less dramatic than in the open field conditions, where the EpFlav content increase was four–nine times higher in comparison to the glasshouse (Figure 2B, significant “light” effects, Supplementary Table S2).

2.3. Phenolic Profile of Basil Leaves under Different Light Regimes

Significantly higher basal levels of syringic acid (SyA), *p*-coumaric acid (*p*CA), and cyanidin (Cy) were found in the *Ocimum basilicum* var. *purpurascens* variety. Furthermore, anthocyanins were only detected in *Ocimum basilicum* var. *purpurascens*. *Ocimum basilicum* var. Genovese had significantly higher basal levels of hydroxycinnamic acids (HCAs), and the lowest basal levels of quercetin (Q), while *Ocimum × citriodorum* had the highest basal levels of protocatechuic acid (PrcA).

Generally, the most abundant hydroxybenzoic acids (HBAs) in all three varieties under all light regimes were protocatechuic acid (PrcA) and unidentified HBA, followed by *p*-HBA, and gallic acid (GA) (Figure 3). The HBA and GA contents were not affected by full sunlight exposure or UV-B supplementation (Figure 3), while significant differences in the levels of PrcA and *p*-HBA induced with sunlight were observed between the three basil cultivars (Supplementary Table S3, ANOVA, $p \leq 0.05$). The accumulation of *p*-HBA was slightly higher with full sunlight compared to the glasshouse for all three cultivars, while the highest accumulation of this compound was noted in the leaves of *Ocimum basilicum* var. *purpurascens* from the growth chamber. The content of syringic acid (SyA) (variety-specific for PB) was significantly higher in the growth chamber and the open field than in the glasshouse and under UV-B (Figure 3).

Int. J. Mol. Sci. 2023, 24, x FOR PEER REVIEW

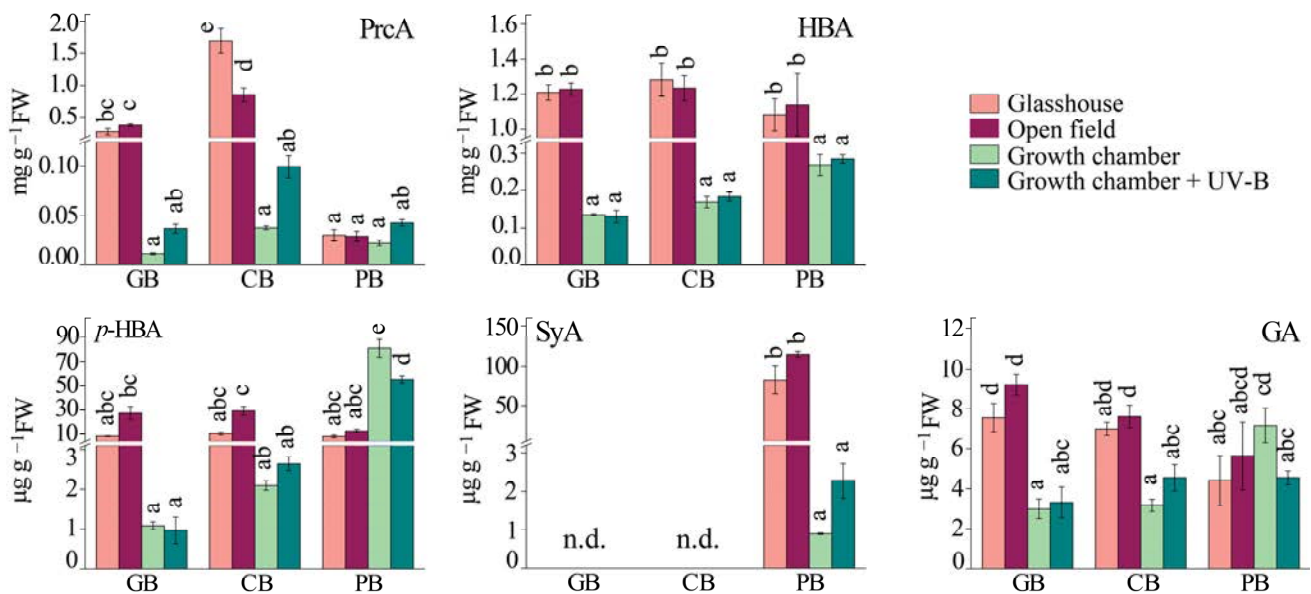


Figure 3. The content of hydroxybenzoic acids (HBAs) in the leaves of three basil varieties (*Ocimum basilicum* var. Genovese, GB, $n = 7-9$; *Ocimum × citriodorum*, CB, $n = 7-9$; and *Ocimum basilicum* var. *purpurascens*, PB, $n = 7-9$) grown under different conditions: glasshouse (light purple), open field (dark purple), growth chamber (light green), and growth chamber + UV-B (dark green). PrcA, protocatechuic acid; HBA, unidentified hydroxybenzoic acid; *p*-HBA, *p*-hydroxybenzoic acid; SyA, syringic acid; GA, gallic acid. Values are given as means \pm SE. Different letters denote significant differences between the different treatments and basil varieties (n.d.—not detected, $p \leq 0.05$), according to Tukey’s post hoc test.

The dominant hydroxycinnamic acids (HCA) in all three varieties were rosmarinic acid (RA), caffeic acid (CA), and *p*-coumaric acid (*p*CA). Sunlight exposure (open field) and UV-B supplementation had the most remarkable effects on the accumulation of RA in all three varieties, but to a greater extent with UV-B supplementation. Nevertheless, the content of RA within the same treatment was relatively similar among basil varieties (Figure 4, Supplementary Table S4, ANOVA, $p \leq 0.05$).

and UV-B supplementation had the most remarkable effects on the accumulation of RA in all three varieties, but to a greater extent with UV-B supplementation. Nevertheless, the content of RA within the same treatment was relatively similar among basil varieties (Figure 4, Supplementary Table S4, ANOVA, $p \leq 0.05$).

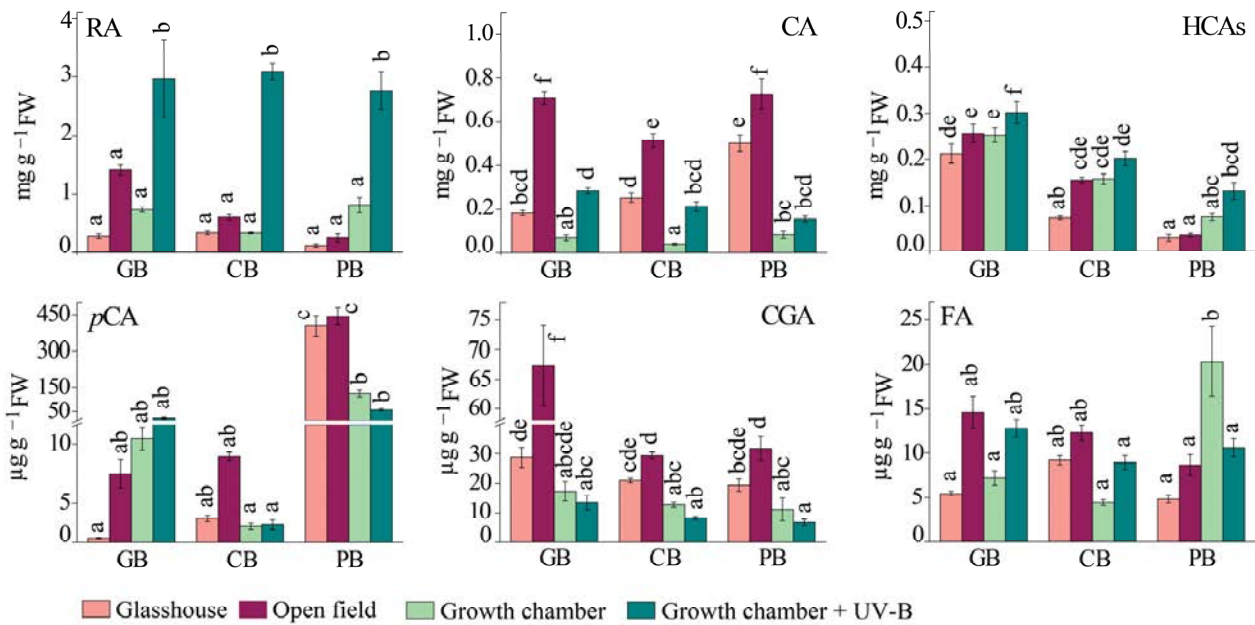


Figure 4. The content of hydroxycinnamic acids (HCA) in leaves of three basil varieties (*Ocimum basilicum* var. Genovese, GB, $n = 7-9$; *Ocimum × citriodorum*, CB, $n = 7-9$; and *Ocimum basilicum* var. purpurascens, PB, $n = 7-9$) grown under different conditions: glasshouse—GH (light purple), open field—OF (dark purple), growth chamber—GC (light green), and growth chamber + UV-B (dark green). RA—rosmarinic acid, CA—caffeic acid, HCAs—other unidentified hydroxycinnamic acids, pCA—p-coumaroyl chlorogenic acid, CGA—chlorogenic acid, FA—ferulic acid. Values are given as mean \pm SE. Different letters denote significant differences between the different treatments and basil varieties ($p \leq 0.05$), according to Tukey's post hoc test.

Common responses to sunlight (OF) and UV-B supplementation were increased levels of caffeic acid (CA) and other unidentified hydroxycinnamic acids in all three cultivars. While full sunlight resulted in higher accumulation of CA in all three varieties (although the increase was the lowest in purple basil), UV-B supplementation had a much greater impact on total HCA content (the increase with UV-B treatment was from 5 to 9 $\mu\text{mol g}^{-1}$ FW in *Ocimum basilicum* var. Genovese, 2.6 to 9.7 $\mu\text{mol g}^{-1}$ FW in *Ocimum citriodorum*, and 0.94 to 9 $\mu\text{mol g}^{-1}$ FW in *Ocimum basilicum* var. purpurascens). Opposite were the effects of open field treatment compared to UV-B supplementation that were observed for chlorogenic acid (CGA) accumulation (Supplementary Table S4, Supplementary Figure S2). On the other hand, the content of ferulic acid (FA) was not significantly affected by the different treatments, although an increasing trend was observed in *Ocimum basilicum* var. Genovese in the open field (Figure 4, Supplementary Table S4, ANOVA, $p \leq 0.05$).

Genovese in the open field (Figure 4, Supplementary Table S4, ANOVA, $p \leq 0.05$) was opposite to the accumulation and flavan-3-ol-bis(catechin) (Flav) and epicatechin (ECat) to the glasshouse and open field (Figure 5, Supplementary Table S5). Epicatechin was increased in the glasshouse and open field (Figure 5, Supplementary Table S5). ECat levels were higher in *Ocimum basilicum* var. Genovese in the glasshouse and open field. In all three basil varieties, more UV-B supplementation induced ECat accumulation. In all three basil varieties, moreover, UV-B supplementation without UV-B (GC) accumulation in all three basil varieties compared with a respective treatment without UV-B (GC).

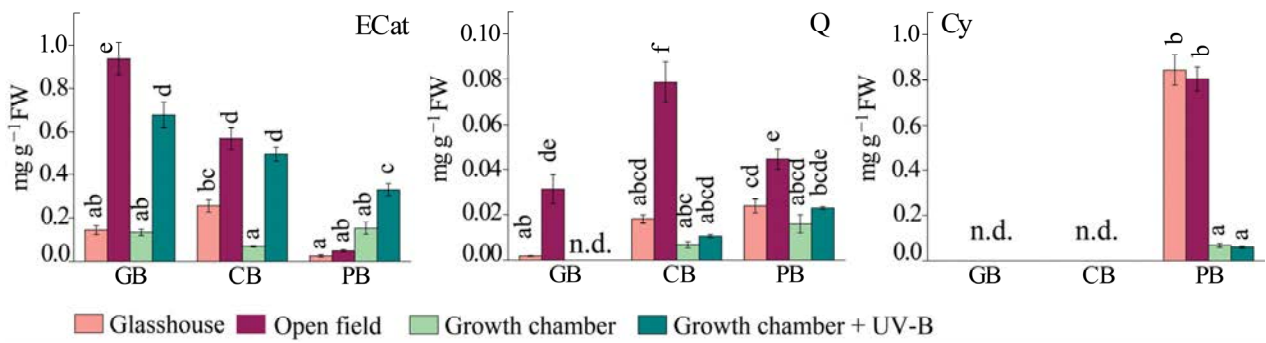


Figure 5. The content of epicatechin (ECat), quercetin (Q), and cyanidin (Cy) in the leaves of three basil varieties (*Ocimum basilicum* var. Genovese, GB, $n = 7-9$; *Ocimum × citriodorum*, CB, $n = 7-9$; and *Ocimum basilicum* var. *purpurascens*, PB, $n = 7-9$) grown under different conditions: glasshouse—GH (light purple), open field—OF (dark purple), growth chamber—GC (light green), and growth chamber + UV-B—GC+UV-B (dark green). Under different treatments and basil varieties (letters) denote significant differences between the different treatments and basil varieties ($p \leq 0.05$), according to Tukey's post hoc test. n.d.—not detected.

Furthermore, the induction of quercetin (Q) accumulation was a common response of all three varieties at full sunlight (OF), but to different extents: it increased almost 20-fold in *Ocimum basilicum* var. Genovese plants compared with the glasshouse plants, and 4-fold and 2-fold in *Ocimum × citriodorum* and *Ocimum basilicum* var. *purpurascens*, respectively (Figure 5, Supplementary Table S5). However, Q content in *Ocimum × citriodorum* and *Ocimum basilicum* var. *purpurascens* did not change significantly after UV-B exposure compared to the growth chamber in any other variety. As expected, the anthocyanin cyanidin (Cy) was only detected in *Ocimum basilicum* var. *purpurascens* leaves compared to the growth chamber in any other variety. As expected, the anthocyanin cyanidin (Cy) was only detected in *Ocimum basilicum* var. *purpurascens* leaves. Plants grown in the glasshouse and the open field had more than 10 times higher Cy content than plants grown in the growth chamber and under UV-B (Figure 5).

2.4. Antioxidant Response
 Total antioxidant capacity (TAC), as determined with the ABTS assay, was highest in the leaves of *Ocimum basilicum* var. *purpurascens* plants under glasshouse and growth chamber light conditions (Figure 6). When plants were exposed to full sunlight for 15 days (open field), TAC increased in all three basil varieties compared to plants grown in the glasshouse. The highest increase was measured in *Ocimum basilicum* var. Genovese (about 16-fold higher TAC values compared with the glasshouse), followed by *Ocimum × citriodorum* and *Ocimum basilicum* var. *purpurascens* (about 2.5-fold higher values) (Figure 6). In contrast, exposure to artificial UV-B irradiation induced only a slight increase in TAC in *Ocimum basilicum* var. Genovese and *Ocimum basilicum* var. *purpurascens*, whereas a three-fold increase was observed in *Ocimum × citriodorum* (Supplementary Table S6, ANOVA, $p \leq 0.05$).

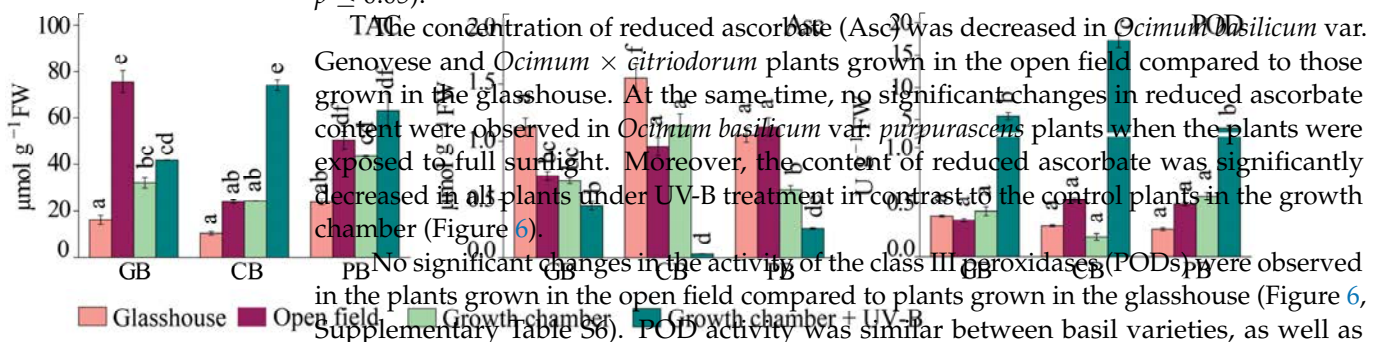


Figure 6. Total antioxidant capacity (TAC) and ascorbic acid (Asc) content in the leaves of three basil varieties (*Ocimum basilicum* var. Genovese, GB, $n = 7-9$; *Ocimum × citriodorum*, CB, $n = 7-9$; and *Ocimum basilicum* var. *purpurascens*, PB, $n = 7-9$) grown under different conditions: glasshouse—GH (light purple), open field—OF (dark purple), growth chamber—GC (light green), and growth chamber + UV-B—GC+UV-B (dark green). Under different treatments and basil varieties (letters) denote significant differences between the different treatments and basil varieties ($p \leq 0.05$), according to ANOVA.

No significant changes in the activity of the class III peroxidases (PODs) were observed in the plants grown in the open field compared to plants grown in the glasshouse (Figure 6, Supplementary Table S6). POD activity was similar between basil varieties, as well as between the different treatments. On the other hand, the POD activity drastically increased in response to UV-B supplementation in all three varieties compared to the growth chamber.

4.6-fold higher TAC values compared with the glasshouse, as well as by *Ocimum × citriodorum* and *Ocimum basilicum* var. *purpurascens* (about 2-fold higher values) (Figure 6). In contrast, exposure to artificial UV-B irradiation induced only a slight increase in TAC in *Ocimum basilicum* var. *Genovese* and *Ocimum basilicum* var. *purpurascens*, while a three-fold increase was observed in *Ocimum × citriodorum* (Supplementary Table S6, ANOVA, $p \leq 0.05$).

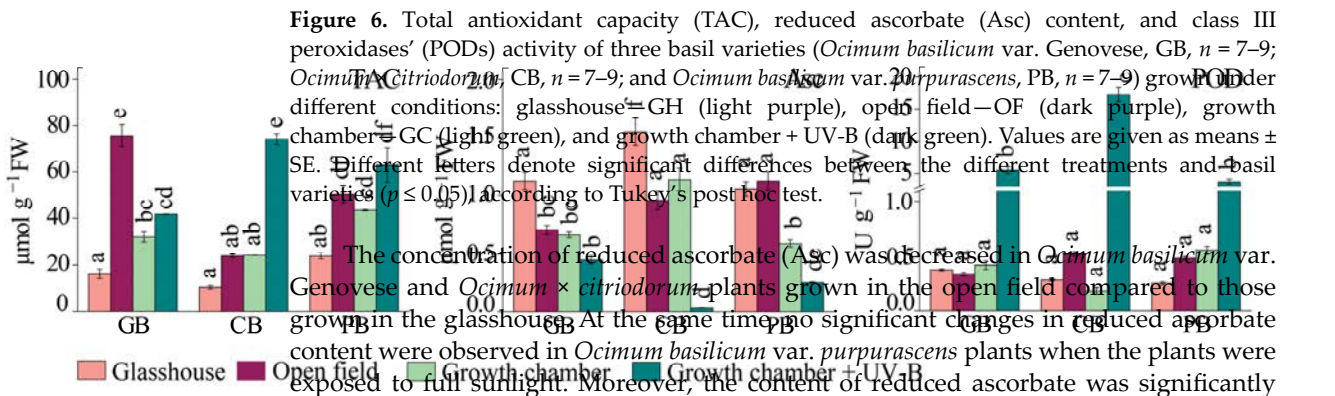


Figure 6. Total antioxidant capacity (TAC), reduced ascorbate (Asc) content, and class III peroxidases' (PODs) activity of three basil varieties (*Ocimum basilicum* var. *Genovese*, GB, $n = 7-9$; *Ocimum × citriodorum*, CB, $n = 7-9$; and *Ocimum basilicum* var. *purpurascens*, PB, $n = 7-9$) grown under different conditions: glasshouse—GH (light purple), open field—OF (dark purple), growth chamber—GC (light green), and growth chamber + UV-B (dark green). Values are given as means \pm SE. Different letters denote significant differences between the different treatments and basil varieties ($p \leq 0.05$) according to Tukey's post hoc test.

2.5. H₂O₂ Accumulation in Leaves

Visible signs of damage in response to changing light conditions were observed only in experiment II, following exposure to UV-B irradiation at constant PAR. To elucidate whether UV-B irradiation provoked oxidative injury in leaves, 8 days after the start of treatment, H₂O₂ accumulation was visualized with the DAB uptake method. Indeed, in all three basil varieties, an increased H₂O₂ accumulation was observed both in the veins and in mesophyll cells compared to leaves of non-UV-B treated plants (Figure 7).

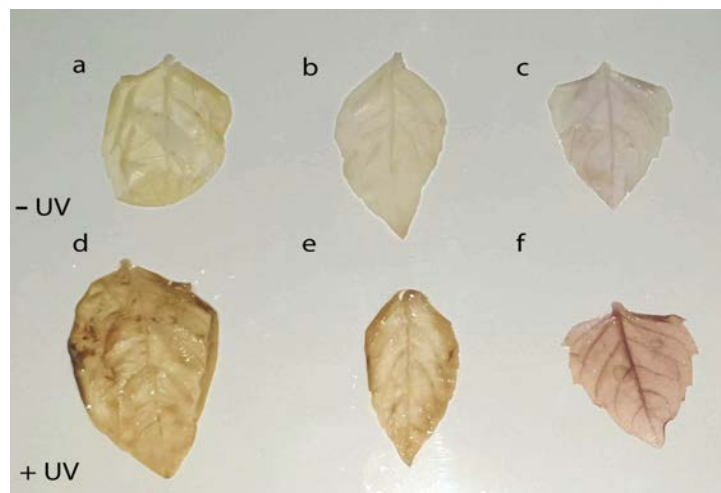


Figure 7. Representative images of H₂O₂ accumulation using the DAB uptake method in the leaves of three basil varieties grown at constant PAR (a–c) and constant PAR with artificial UV-B irradiation (d–f) after 8 days of treatment. *Ocimum basilicum* var. *Genovese* (GB) (a,d), *Ocimum × citriodorum* (CB) (b,e), and *Ocimum basilicum* var. *purpurascens* (PB) (c,f).

3. Discussion

3.1. Contrasting Effects of Sunlight and UV-B/Moderate Light

The three varieties of basil used in the study showed specific, as well as general, responses to changing light conditions—full sunlight or UV-B supplementation under moderate PAR. While high sunlight including natural UV-B irradiation developed no visible signs of photo-oxidative damage in any variety, it induced a strong antioxidant response with a significant increase in TAC and total HCAs and both total flavonoid leaf content and epidermal flavonoids indicated ROS signaling in antioxidant defense [40]. In

contrast, a supplemental UV-B irradiation (daily dose: $29.16 \text{ kJ m}^{-2} \text{ d}^{-1}$, comparable to the intensities of ambient UV-B) combined with moderate background PAR induced oxidative stress within 8 days, which may imply a deficient mechanism of antioxidative defense under the given condition [11]. This was demonstrated with the accumulation of H_2O_2 and the appearance of brown lesions on the upper surface of mature leaves. Moreover, under supplemental UV-B irradiation, the formation of the UV-absorbing shield failed, which was accompanied by the absence of quercetin accumulation, indicating its important role in UV-B protection and the possible role of UV-A or high PAR in its formation. The results are not in agreement with numerous reports highlighting the central role of UV-B radiation in induction of the epidermal UV shield in a variety of plant species [2,41–43]. Interestingly, the high efficiency of UV-B radiation in promoting flavonoid biosynthesis has been demonstrated even at very low UV-B fluence rates [44–46]. The failure of UV-B/moderate light to induce epidermal flavonoids' accumulation could be explained with the lack of interaction with COP1, which can be triggered with an excess of PAR or blue light that upregulates chalcone synthase, a key enzyme for flavonoid biosynthesis, via the COP1/HY5 pathway [44,47]. Preferential accumulation of phenolics under high light over UV was observed in *Pelargonium zonale* leaves [48]. In addition, supplemental UV-B induced a change in the morphology of developing leaves similar to stress-induced morphogenic responses (SIMRs) commonly induced with high UV-B radiation and ROS accumulation [26,49]. UV-B-induced oxidative stress has been characterized as a non-specific response to ROS generated with high UV-B radiation [50]. The simultaneous drastic increase in PODs' activity and decrease in reduced Asc content in leaves under supplemental UV-B indicated the predominant pro-oxidative effect of UV-B irradiation (indicated with H_2O_2 accumulation in the leaf) and the strong antioxidant response of plants [51]. Instead, acclimation to sunlight resulted in leaf thickening, indicating a possible important role of the induced formation of a secondary cell wall, which led to an almost two-fold decrease in the FW/DW biomass ratio, in addition to the known protective formation of an epidermal UV shield of UV-absorbing substances. Similar effects of low UV-B radiation have been reported by other authors [26,52]. However, in addition to the fluence rate of UV-B; the ratio between the UV-B and background PAR intensity, blue light, and UV-A radiation; as well as other climate factors may determine the contradictory UV-B effects on plants, i.e., stress response or regulation [41,43,44]. Therefore, there is a possibility that UV-A radiation could have beneficial effects on plant acclimation with a shifted ratio of UV-B/PAR; however, this remains to be explored. In our study, the stimulation of phenylpropanoid metabolism, but different classes of phenolics, in relation to different UV-B/PAR ratios, suggests the importance of HCAs and flavonoids in antioxidative defense against photo-oxidation.

3.2. The Epidermal UV-Attenuation Capacity in Green vs. Purple Leaves

The most striking difference between the varieties was visible in the dynamics of accumulation of epidermal UV-attenuating compounds upon exposure to the open field conditions. The maximum levels of EpFlav were reached after 11 days, with a delay of 2 to 3 days before the first significant increase. Previously, we observed that the induction period to reach maximal EpFlav levels upon exposure to full sunlight is species-specific and is reached earlier in *Solanum lycopersicum*, *Salvia officinalis*, and *Eruca sativa* compared to basil plants in this study, after 4 days [53].

Similar dynamics in the formation of the protective sun-screening shield have also been reported for other plant species [42,54]. However, the mechanism underlying the delay in EpFlav accumulation has not yet been elucidated. Bidel and co-authors (2015) suggested that the observed kinetics of plant response to a new light regime might depend on the combination of environmental factors, as well as on the previous plant's history [42]. In their comprehensive study of UV-B-induced dynamics of EpFlav accumulation in *Centella asiatica*, the authors suggested that the screening effect may contribute to a slower accumulation of flavonoids as a result of negative feedback regulation of flavonol

biosynthesis due to exponential attenuation of UV-B radiation through the epidermis [42]. The discrepancy between the high sensitivity and rapid activation of the UVR8 signaling pathway [55,56] on the one hand and the slow attainment of maximal EpFlav on the other hand could be explained with an interplay between UV-B radiation and other specific phenylpropanoid inducers such as UV-A, blue light, or high PAR fluxes in general [57]. The higher basal accumulation of anthocyanins, syringic acid, *p*-coumaric acid, and caffeic acid in *Ocimum basilicum* var. *purpurascens* may be the reason for the slower response to full light exposure. The anthocyanins in red basil leaves are primarily located in the abaxial and adaxial epidermises of basil leaves [58]. Thus, they can preferentially serve as partial absorbers of incident light energy, slowing the generation of ROS with the excess light-exposed chloroplasts. On the other hand, it had the highest chlorophyll concentration in the open field towards the later acclimation phase compared to the other two varieties, as observed previously [36]. Comparative study of full sunlight acclimation of green and purple basil leaves showed that purple leaves have shade avoidance characteristics and that high-light-responsive genes are downregulated [36].

3.3. Accumulation of Asc, HCAs, and Flavonoids Is Affected by the Different UV-B/PAR Ratio

Under both sunlight and supplemental UV-B irradiation, TAC was enhanced in the leaf extract of all three varieties; strikingly, the highest TAC increase occurred in *Ocimum* × *citriodorum* under both light regimes. On the other hand, UV-B decreased the level of reduced ascorbate compared with sunlight. Although the leaf constitutive molar content of ascorbate exceeded that of total phenolics by more than 500-fold, the accumulated HCAs and flavonoids contributed more to TAC under stress conditions [21]. Among the HCAs, RA was most abundant in *Ocimum basilicum* var. *purpurascens* (74% and 90% of all HCAs under open field conditions, and UV-B, respectively) and least abundant in *Ocimum basilicum* var. *Genovese* (64% and 82% of all HCAs at open field, and UV-B, respectively). We measured the antioxidant capacity of each compound present in basil leaves. Their activity decreased in descending order, RA > Cat > Ecat > CGA > Q > Cy > FA > CA > Eriodictyol > Asc (Supplementary Table S7), and this is in accordance with Rice-Evans et al. (1997) [21]. Full sunlight exposure (a combination of UV radiation and high PAR intensity) can lead to increased oxidative stress. In our study, it led to a decrease in the ratio of Asc/HCAs (flavonoids), indicating carbon allocation from primary to secondary metabolism, towards the biosynthesis of phenolics and growth inhibition (Supplementary Figure S3).

We propose that induced hydroxycinnamic acids (HCAs), flavonoids, and cyanidin may play a role in H₂O₂ scavenging via PODs. The resulting phenoxyl radical can be reduced by ascorbate in the so-called phenolics/peroxidase/ascorbate cycle (PPA), which is localized in the apoplast and vacuole, as proposed by Takahama and Oniki (1997) [51]. However, the ratio between HCAs and flavonoids was also changed: in comparison to sunlight (open field including ambient UV-B and UV-A), UV-B radiation supplemented to PAR increased the HCAs/flavonoids ratio in all three basil varieties. The role of HCAs in response mechanisms to excess UV radiation has been underestimated in previous studies [59]. Tattini and co-authors (2004) reported differential spatial accumulation of these two polyphenol groups (flavonoids and HCAs) under excess light and drought [60]. They proposed that flavonoids play a preferential screening role in the epidermis, while HCAs act as important antioxidants in palisade leaf tissue. However, HCAs' absorbance characteristics imply even greater protection than flavonoids against UV-B-induced damage [61]. Thus, HCAs might be crucial components in the acclimation mechanisms to full solar radiation under field conditions [59,62].

3.4. Differential Photomorphogenic and Antioxidative Response of Three Basil Varieties

The obtained results indicate that UV-B radiation under moderate PAR does not cause significant accumulation of flavonoids in the epidermis, but instead induces morphogenic changes, especially in younger leaves. The most sensitive variety, GB with visible lesions, browning, and vitrification of the upper exposed leaf surface, had the lowest TAC and no

epidermal flavonoid accumulation under artificial UV-B irradiation, accompanied by no significant increase in quercetin.

In *Ocimum basilicum* var. *purpurascens* and *Ocimum* × *citriodorum*, DW increased almost two-fold at OF, which may indicate enhanced content of cell wall compounds (e.g., lignin). Increased lignification in response to UV-B radiation has been observed elsewhere [26,63]. HCAs are structural components of the cell wall and provide mechanical reinforcement of the cell wall through the formation of covalent cross-links with lignin and polysaccharides.

The extent of the antioxidant responses described above depended on the basil variety, in descending order: *Ocimum* × *citriodorum* > *Ocimum basilicum* var. Genovese > *Ocimum basilicum* var. *purpurascens*. Furthermore, full sunlight had no effect on both the reduced ascorbate level and POD activity of *Ocimum basilicum* var. *purpurascens*, which is consistent with the higher constitutive antioxidative capacity of anthocyanins [64]. A common response in all three basil varieties was the induction of rosmarinic acid (RA) and caffeic acid, under supplementary UV-B irradiation and open field conditions, upon transferring plants, though the induction was smaller in open field conditions. Based on the scavenging capacity of the ABTS radicals, RA was the most potent antioxidant among the phenolics found in basil leaves. Cyanic leaves of *Ocimum basilicum* var. *purpurascens* had the lowest content of RA, and the light effect on the biosynthesis of RA was the least pronounced, suggesting that this compound was not the main component of acclimation in this variety. Cyanidin, on the other hand, remained unchanged in the *Ocimum basilicum* var. *purpurascens* variety regardless of light conditions. In addition, the slower accumulation of epidermal flavonoids in sunlight in this variety compared to *Ocimum* × *citriodorum* and *Ocimum basilicum* var. Genovese may be attributed to a higher shielding effect of the cyanic leaves [65].

The variety-specific differences not only in the dynamics of epidermal flavonoid induction, but also in the level of reduced ascorbate (reduced in green but not in purple leaves) upon open field acclimation, and in the profile of total phenolics, are important for the selection of the best variety for growers in relation to regional conditions and for the choice of the optimal harvest time to achieve the best functional quality of basil.

4. Materials and Methods

4.1. Plant Material and Growth Conditions

Seeds of *Ocimum basilicum* var. Genovese (GB), *Ocimum* × *citriodorum* (hybrid of *Ocimum basilicum* and *Ocimum americanum*, CB), and *Ocimum basilicum* var. *purpurascens* ('Red Rubrum', PB) were obtained commercially and sown in the substrate Klasman-Potgrond H (Klasmann-Deilmann, Geeste, Germany). Plants were grown in different systems: in a glasshouse (GH), in the open field (OF), and in a growth chamber without UV-B supplementation (GC) and with UV-B supplementation (UV-B).

The first part of the experiments started in spring, when basil was grown in the GH. Two-week-old uniform plants were randomly divided and planted in 8 × 8 cm plastic pots. The seedlings were grown for another 2 weeks in the GH without additional lighting or heating until they reached a height of about 4–5 cm. Then, they were repotted into larger pots and grown for the next 3 weeks until they reached the stage of 4 fully developed leaves and a height of about 15–20 cm.

The basil plants obtained were divided into two groups: the control group, which remained in the GH, and group OF, which was exposed to full sunlight for the rest of the treatment (15 days in total). Radiation conditions (PAR, UV-A, and UV-B) were measured daily in both growing systems. The intensity of PAR was measured with the PAR Quantum Sensor CE (SKP 215 42474; Skye Instruments, Llandrindod Wells, Powys LD1 6DF, UK), whereas intensity of UV-A radiation was measured with the PMA 2100 radiometer (Solar Light Company Inc., Glenside, PA, USA), equipped with UV-A (PMA 2110, 320–400 nm). A UV-B detector for biologically active radiation (Solar Light's Model 501 Series Biometer-Radiometers), which has continuously measured the UV index over Belgrade since 2009 [66], was used to assess UV-B radiation using the McKenzie and co-authors' [67] relationship between erythemally weighted UV-B and UV-B_{280–315 nm}. The average daily temperature

in the GH and field was 22.0 ± 0.8 °C and 25.2 ± 4.1 °C, respectively, while the relative humidity was 30–40% in the glasshouse and 40–50% in the OF.

For the second part of the experiment, the plants were grown in GC under controlled conditions with a photoperiod of 14/10 h (day/night), a temperature of 26 °C, and a relative humidity of 40–50%. The plants were grown as described for the first part of the experiment. Half of the plantlets were exposed to supplemental UV-B irradiation (1.35 W m^{-2}) for 6 h daily, for 8 days ($29.16 \text{ kJ m}^{-2} \text{ d}^{-1}$). For UV-B supplementation, a UV lamp with a visible light philter (Carl Roth GmbH, Karlsruhe, Germany; product number: H469.1) and tubes with maximum emission at 312 nm (G15T8E, Sankyo Denki, Tokyo, Japan) were used. Lamp radiation intensity was characterized using the Vilber Lourmat instrument with the CX-312 sensor (312 nm medium-wave UV, bandwidth: 280 to 320 nm). The intensity of irradiation with the UV-B lamp was determined with the distance from the surface of the plant leaves (approx. 0.45 m), while the daily energy of UV-B radiation was chosen to correspond with the previously performed OF measurements.

The content of chlorophyll (Chl), leaf epidermal flavonoids (EpFlav), and the nitrogen balance index (NBI), based on the Chl/flavonoids ratio, were measured daily using the Dualex 4 (FORCE-A, Orsay, France; Cerović et al., 2012) [68]. All measurements were performed on healthy, fully developed, and light-exposed leaves.

Four to five biological replicates of all three genotypes were used for each light treatment (GH, OF, GC, and UV-B). For biochemical measurements, light exposed, fully developed leaves were harvested (three to four leaves per plant, 4–5 plants per treatment). Leaf material was immediately frozen in liquid nitrogen and stored at -80 °C for further analyses. The remaining plants from GH and OF were used to determine fresh weight and dry weight of leaves ($n = 4-5$). To obtain the dry weight, samples were dried at 70 °C for 48 h.

4.2. Phenolics Determination with HPLC-DAD

Frozen leaves were rapidly homogenized in liquid nitrogen and extracted in methanol containing 0.1% HCl, followed by acid hydrolysis to obtain aglycones. All extracts were purged with nitrogen and stored at -80 °C until a further analysis [43].

The phenolic compounds were identified and quantified with HPLC-PDA (LC-20AB Prominence liquid chromatography, Shimadzu, Kyoto, Japan) with an SPD-M20A diode array Prominence detector using a reversed-phase C18 column (5.0 μm , 250×4.6 mm Luna C18 (2); Phenomenex Ltd., Torrance, CA, USA). The elution procedure was 0–5 min, 100% solution B (isocratic step); 5–25 min, 100–80% solution B (linear gradient); 25–35 min, 80–60% solution B (linear gradient); 35–40 min, 60–100% solution B (linear gradient). Chromatograms were recorded at different wavelengths, depending on the characteristic absorption maximum of the selected phenolics: 320 nm for hydroxycinnamic acids and their derivatives, 280 nm for catechins, hydroxybenzoic acids, and their derivatives, and 520 nm for anthocyanins. The individual phenolics were identified by comparing the absorption spectra with authentic standards and quantified with peak area using Shimadzu LC Solution software (LCsolution Version1.25 SP2, Shimadzu, Kyoto, Japan) [43].

4.3. Measurement of Reduced Ascorbate

For the determination of reduced ascorbate content, frozen leaf samples were rapidly homogenized in liquid nitrogen, extracted in 1.5% meta-phosphoric acid containing 1 mM EDTA, and centrifuged for 5 min at $16,000 \times g$ and 4 °C, according to Morina et al. (2010) [69]. The reduced form of ascorbate was analyzed with the decrease in absorbance at 265 nm after the addition of one unit of ascorbate oxidase (Sigma Aldrich, Steinheim am Albuch, Germany) in reaction mixtures consisting of 950 μL of a 50 mM sodium phosphate buffer (pH 6.5) containing 2.5 mM EDTA and 50 μL of a plant extract ($\epsilon = 14.3 \text{ mM}^{-1} \text{ cm}^{-1}$) [69].

4.4. Determination of POD Activity

For soluble class III peroxidases (PODs, EC 1.11.1.7), frozen leaf material was homogenized in liquid nitrogen and extracted in a 100 mM sodium phosphate buffer (pH 6.5) with 2 mM EDTA, 2 mM PMSF (phenylmethanesulfonyl fluoride), and 5% (*w/v*) insoluble polyvinylpyrrolidone (PVP). The homogenate was centrifuged at $10,000\times g$ for 10 min at 4 °C. The peroxidase activity of POD was measured spectrophotometrically in a reaction mixture of a 100 mM K-phosphate buffer (pH 6.5), 20 mM guaiacol, and aliquots of the plant extract [43]. The reaction was started by adding 5 mM H₂O₂, and the increase in absorbance at 470 nm was followed. Peroxidase activity was calculated using the extinction coefficient for guaiacol ($\epsilon = 26.6 \text{ mM}^{-1} \text{ cm}^{-1}$).

4.5. Antioxidant Capacity

The methanol leaf extracts described in Section 4.3. were used for the determination of total antioxidative capacity (TAC). The reaction mixture contained 2 mM 2,2'-azino-bis(3-ethylbenzothiazoline-6-sulfonic acid) (ABTS), 0.015 mM H₂O₂, and horseradish peroxidase (HRP) in a 50 mM potassium phosphate buffer (pH 7.5) and 20 μL of the extract. The absorbance was measured at 730 nm. The ascorbic acid standard curve was used to determine the relative antioxidant capacity of the samples [70].

4.6. Determination (Visualization) of H₂O₂ in Basil Leaves

To detect H₂O₂ accumulation, three sun-exposed, fully developed leaves per plant (three plants per group) were cut from GC and UV-B treatments and incubated with 3,3'-diaminobenzidine (DAB) [71]. Leaves were placed in 1 mg mL⁻¹ (DAB-HCl) in a 100 mM sodium acetate buffer (pH 3.8), infiltrated for 15 s at low vacuum, and incubated for 2 h with shaking. Leaves were cleared in boiling 70% (*v/v*) ethanol (for 10 min) with 10% glycerol.

4.7. Statistical Analysis

A one-way repeated-measures ANOVA was conducted to determine differences in EpFlav and Chl content during the experiment (within-subject factor) in plants exposed to different treatments (between-subject factors). To test for significant differences in FW, DW, FW/DW, EpFlav, and Chl, content between the different treatments, the Mann–Whitney *U*-test was used, and the significance threshold was set at 0.05. Two-way ANOVA was used to show the effects of variety type, treatment, and their interaction on the content of phenolic compounds, TAC, reduced ascorbate content, and POD activity. The homogeneity of variance was checked with Levene's test. The experimental data were analyzed using the software package Statistica 8.0.

5. Conclusions

In this study, we demonstrated a contrasting effect of UV-B radiation on the leaves of three basil varieties depending on the quality and intensity of background light. Different UV-B/UV-A/PAR ratios affected (1) epidermal UV shielding capacity; (2) Asc/HCAs/flavonoids ratio; and (3) antioxidant response in three basil varieties, which may imply the variety-specific tolerance to high PAR and UV-B irradiation. We have shown here that full sunlight overcomes the limitations of supplemental artificial UV-B radiation in combination with moderate PAR to induce the formation of a UV-absorbing shield in the basil leaf based on the accumulation of flavonoids, particularly quercetin. Under full sunlight, the potential risk of UV-B-induced photo-oxidative stress in the leaves of three basil varieties was suppressed. While the response to UV-B-induced photo-oxidation differed among varieties in terms of magnitude and defense strategy, the response to full sunlight was more general, similar among all selected varieties and involved the increase in epidermal flavonoid accumulation. The most striking difference in the responses of the three basil varieties to UV-B is the POD induction and the possible involvement of the PPA cycle, which is greatest in CB and lowest in PB with constitutively high cyanidin content. Thus, the results of our study provided further evidence for the effects of epidermal anthocyanins and flavonoids,

as potent antioxidants and philters of PAR and UV-B radiation on the morphological and antioxidant protection responsible for the different acclimation mechanisms to high solar irradiance and UV-B irradiation in red and green leaves. We have shown that purple-leaf basil directs lower assimilated carbon flux to other non-red phenylpropanoids (quercetin, epicatechin) compared to green basil varieties at full sunlight. This indicates competition between flavonol and anthocyanin biosynthesis, possibly leading to two defense strategies in green and purple varieties. We suggest that the role of the philter and sink for reduced carbon in the purple-leaf variety is more responsible for the specific tolerance mechanism in this variety, implying a lower excitation pressure in its leaves. On the other hand, hydroxycinnamates and PODs were found to be the main protective mechanism against UV-B, particularly in the green cultivar CB.

Supplementary Materials: The supporting information can be downloaded at: <https://www.mdpi.com/article/10.3390/ijms242015350/s1>.

Author Contributions: Conceptualization, S.V.J.; methodology, S.M.K., B.Ž., J.D., M.V., F.M. and P.K.; validation, P.K., S.M.K., M.V. and F.M.; formal analysis, S.M.K., B.Ž., J.D., M.V. and A.S.Z.; investigation, S.M.K., A.S.Z., B.Ž., J.D., M.V., P.K. and F.M.; resources, S.V.J.; data curation, S.V.J. and S.M.K.; writing—original draft preparation, S.V.J., B.Ž., M.V., S.M.K. and A.S.Z.; writing—review and editing, S.V.J., M.V. and F.M.; visualization, B.Ž., A.S.Z. and J.D.; supervision, S.V.J., S.M.K. and M.V.; project administration, S.V.J.; funding acquisition, S.V.J. All authors have read and agreed to the published version of the manuscript.

Funding: This research was funded by the Ministry of Science, Technological Development and Innovation, the Republic of Serbia (Contract Nos.: 451-03-47/2023-011200053; 451-03-47/2023-01/200042), by the Centre for Green Technologies, University of Belgrade, and by Science Fund of the Republic of Serbia, Green Program of Cooperation between Science and Industry, grant no. 5661. The views expressed herein are those of the authors and do not represent the opinion of the Science Fund. FM was funded with grant “KOROLID”, CZ.02.1.01/0.0/0.0/15_003/0000336 (MEYS, CZ with co-funding from EU). The APC was funded by the Ministry of Science, Technological Development and Innovation, and by the Centre for Green Technologies (Contract No. 451-03-47/2023-011200053, and by the Institute of Physics Belgrade).

Institutional Review Board Statement: Not applicable.

Informed Consent Statement: Not applicable.

Data Availability Statement: Not applicable.

Conflicts of Interest: The authors declare no conflict of interest.

References

1. Favory, J.J.; Stec, A.; Gruber, H.; Rizzini, L.; Oravec, A.; Funk, M.; Albert, A.; Cloix, C.; Jenkins, G.I.; Oakeley, E.J.; et al. Interaction of COP1 and UVR8 regulates UV-B-induced photomorphogenesis and stress acclimation in Arabidopsis. *EMBO J.* **2009**, *28*, 591–601. [[CrossRef](#)]
2. Vidović, M.; Morina, F.; Veljović Jovanović, S. Stimulation of various phenolics in plants under ambient UV-B radiation. In *UV-B Radiation: From Environmental Stressor to Regulator of Plant Growth*; Singh, V.P., Singh, S., Prasad, S.M., Parihar, P., Eds.; Wiley-Blackwell: Hoboken, NJ, USA, 2017; pp. 9–56.
3. Kataria, S.; Jajoo, A.; Guruprasad, K.N. Impact of increasing Ultraviolet-B (UV-B) radiation on photosynthetic processes. *J. Photochem. Photobiol. B Biol.* **2014**, *137*, 55–66. [[CrossRef](#)]
4. Barnes, P.W.; Robson, T.M.; Zepp, R.G.; Bornman, J.F.; Jansen, M.A.K.; Ossola, R.; Wang, Q.W.; Robinson, S.A.; Foereid, B.; Klekociuk, A.R.; et al. Interactive effects of changes in UV radiation and climate on terrestrial ecosystems, biogeochemical cycles, and feedbacks to the climate system. *Photochem. Photobiol. Sci.* **2023**, *22*, 1049–1091. [[CrossRef](#)]
5. Bernhard, G.H.; Bais, A.F.; Aucamp, P.J.; Klekociuk, A.R.; Liley, J.B.; McKenzie, R.L. Stratospheric ozone, UV radiation, and climate interactions. *Photochem. Photobiol. Sci.* **2023**, *22*, 937–989. [[CrossRef](#)] [[PubMed](#)]
6. Lamy, K.; Portafaix, T.; Josse, B.; Brogniez, C.; Godin-Beekmann, S.; Bencherif, H.; Revell, L.; Akiyoshi, H.; Bekki, S.; Hegglin, M.I.; et al. Clear-sky ultraviolet radiation modelling using output from the Chemistry Climate Model Initiative. *Atmos. Chem. Phys.* **2019**, *19*, 10087–10110. [[CrossRef](#)]
7. Sanchez-Lorenzo, A.; Enriquez-Alonso, A.; Calbó, J.; González, J.A.; Wild, M.; Folini, D.; Norris, J.R.; Vicente-Serrano, S.M. Fewer clouds in the Mediterranean: Consistency of observations and climate simulations. *Sci. Rep.* **2017**, *7*, 41475. [[CrossRef](#)] [[PubMed](#)]

8. Malinovic-Milicevic, S.; Mihailovic, D.T.; Lalic, B.; Dreskovic, N. Thermal environment and UV-B radiation indices in the Vojvodina region, Serbia. *Clim. Res.* **2013**, *57*, 111–121. [[CrossRef](#)]
9. Pashiardis, S.; Kalogirou, S.A.; Pelengaris, A. Statistical Analysis and Inter-Comparison of Solar UVB and Global Radiation for Athalassa and Larnaca, Cyprus. *SM J. Biometr. Biostat.* **2017**, *2*, 1006.
10. Podolec, R.; Demarsy, E.; Ulm, R. Perception and signaling of ultraviolet-B radiation in plants. *Annu. Rev. Plant Biol.* **2021**, *72*, 793–822. [[CrossRef](#)]
11. Hideg, É.; Jansen, M.A.; Strid, Å. UV-B exposure, ROS, and stress: Inseparable companions or loosely linked associates? *Trends Plant Sci.* **2013**, *18*, 107–115. [[CrossRef](#)]
12. Yadav, A.; Singh, D.; Lingwan, M.; Yadukrishnan, P.; Masakapalli, S.K.; Datta, S. Light signaling and UV-B-mediated plant growth regulation. *J. Integr. Plant Biol.* **2020**, *62*, 1270–1292. [[CrossRef](#)]
13. Asada, K. Production and scavenging of reactive oxygen species in chloroplasts and their functions. *Plant Physiol.* **2006**, *141*, 391–396. [[CrossRef](#)] [[PubMed](#)]
14. Fischer, B.B.; Hideg, É.; Krieger-Liszkay, A. Production, detection, and signaling of singlet oxygen in photosynthetic organisms. *Antioxid. Redox Signal.* **2013**, *18*, 2145–2162. [[CrossRef](#)] [[PubMed](#)]
15. Foyer, C.H.; Shigeoka, S. Understanding oxidative stress and antioxidant functions to enhance photosynthesis. *Plant Physiol.* **2011**, *155*, 93–100. [[CrossRef](#)] [[PubMed](#)]
16. Vidović, M.; Morina, F.; Prokić, L.; Milić Komić, S.; Živanović, B.; Veljović Jovanović, S. Antioxidative response in variegated *Pelargonium zonale* leaves and generation of extracellular H₂O₂ in (peri) vascular tissue induced by sunlight and paraquat. *J. Plant Physiol.* **2016**, *206*, 25–39. [[CrossRef](#)]
17. Krause, G.H. The high-energy state of the thylakoid system as indicated by chlorophyll fluorescence and chloroplast shrinkage. *Biochim. Biophys. Acta Bioenerg.* **1973**, *292*, 715–728. [[CrossRef](#)] [[PubMed](#)]
18. Briantais, J.M.; Verrotte, C.; Picaud, M.; Krause, G.H. Chlorophyll fluorescence as a probe for the determination of the photo-induced proton gradient in isolated chloroplasts. *Biochim. Biophys. Acta Bioenerg.* **1980**, *591*, 198–202. [[CrossRef](#)]
19. Hernández, I.; Van Breusegem, F. Opinion on the possible role of flavonoids as energy escape valves: Novel tools for nature's Swiss army knife? *Plant Sci.* **2010**, *179*, 297–301. [[CrossRef](#)]
20. Golovatskaya, I.F.; Laptev, N.I. Effect of UV-B radiation on plants growth, active constituents, and productivity. In *Plants and Their Interaction to Environmental Pollution*; Elsevier: Amsterdam, The Netherlands, 2023; pp. 25–60.
21. Rice-Evans, C.; Miller, N.; Paganga, G. Antioxidant properties of phenolic compounds. *Trends Plant Sci.* **1997**, *2*, 152–159. [[CrossRef](#)]
22. Neill, S.O.; Gould, K.S. Anthocyanins in leaves: Light attenuators or antioxidants? *Funct. Plant Biol.* **2003**, *30*, 865–873. [[CrossRef](#)]
23. Gould, K.S. Nature's Swiss army knife: The diverse protective roles of anthocyanins in leaves. *J. Biotechnol. Biomed.* **2004**, *2004*, 314. [[CrossRef](#)] [[PubMed](#)]
24. Ferreres, F.; Figueiredo, R.; Bettencourt, S.; Carqueijeiro, I.; Oliveira, J.; Gil-Izquierdo, A.; Pereira, D.M.; Valentão, P.; Andrade, P.B.; Duarte, P.; et al. Identification of phenolic compounds in isolated vacuoles of the medicinal plant *Catharanthus roseus* and their interaction with vacuolar class III peroxidase: An H₂O₂ affair? *J. Exp. Bot.* **2011**, *62*, 2841–2854. [[CrossRef](#)] [[PubMed](#)]
25. Agati, G.; Matteini, P.; Goti, A.; Tattini, M. Chloroplast-located flavonoids can scavenge singlet oxygen. *New Phytol.* **2007**, *174*, 77–89. [[CrossRef](#)]
26. Jansen, M.A.; Coffey, A.M.; Prinsen, E. UV-B induced morphogenesis: Four players or a quartet? *Plant Signal. Behav.* **2012**, *7*, 1185–1187. [[CrossRef](#)]
27. Castronuovo, D.; Russo, D.; Libonati, R.; Faraone, I.; Candido, V.; Picuno, P.; Andrade, P.; Milella, L. Influence of shading treatment on yield, morphological traits and phenolic profile of sweet basil (*Ocimum basilicum* L.). *Sci. Hortic.* **2019**, *254*, 91–98. [[CrossRef](#)]
28. Aldarkazali, M.; Rihan, H.Z.; Carne, D.; Fuller, M.P. The growth and development of sweet basil (*Ocimum basilicum*) and bush basil (*Ocimum minimum*) grown under three light regimes in a controlled environment. *Agronomy* **2019**, *9*, 743. [[CrossRef](#)]
29. Dou, H.; Niu, G.; Gu, M.; Masabni, J.G. Effects of light quality on growth and phytonutrient accumulation of herbs under controlled Environments. *Horticulturae* **2017**, *3*, 36. [[CrossRef](#)]
30. Sipos, L.; Balázs, L.; Székely, G.; Jung, A.; Sárosi, S.; Radácsi, P.; Csambalik, L. Optimization of basil (*Ocimum basilicum* L.) production in LED light environments—A review. *Sci. Hortic.* **2021**, *289*, 110486. [[CrossRef](#)]
31. Taulavuori, K.; Pyysalo, A.; Taulavuori, E.; Julkunen-Tiitto, R. Responses of phenolic acid and flavonoid synthesis to blue and blue-violet light depends on plant species. *Environ. Exp. Bot.* **2018**, *150*, 183–187. [[CrossRef](#)]
32. Stagnari, F.; Di Mattia, C.; Galieni, A.; Santarelli, V.; D'Egidio, S.; Pagnani, G.; Pisante, M. Light quantity and quality supplies sharply affect growth, morphological, physiological and quality traits of basil. *Ind. Crops Prod.* **2018**, *122*, 277–289. [[CrossRef](#)]
33. Pennisi, G.; Pistillo, A.; Orsini, F.; Cellini, A.; Spinelli, F.; Nicola, S.; Fernandez, J.A.; Crepaldi, A.; Gianquinto, G.; Marcelis, L.F. Optimal light intensity for sustainable water and energy use in indoor cultivation of lettuce and basil under red and blue LEDs. *Sci. Hortic.* **2020**, *272*, 109508. [[CrossRef](#)]
34. Sakalauskaite, J.; Viškelis, P.; Duchovskis, P.; Dambrauskiene, E.; Sakalauskiene, S.; Samuoliene, G.; Brazaityte, A. Supplementary UV-B irradiation effects on basil (*Ocimum basilicum* L.) growth and phytochemical properties. *J. Food Agric. Environ.* **2012**, *10*, 342–346.

35. Semenova, N.A.; Smirnov, A.A.; Ivanitskikh, A.S.; Izmailov, A.Y.; Dorokhov, A.S.; Proshkin, Y.A.; Yanykin, D.V.; Sarimov, R.R.; Gudkov, S.V.; Chilingaryan, N.O. Impact of Ultraviolet Radiation on the Pigment Content and Essential Oil Accumulation in Sweet Basil (*Ocimum basilicum* L.). *Appl. Sci.* **2022**, *12*, 7190. [[CrossRef](#)]
36. Tattini, M.; Sebastiani, F.; Brunetti, C.; Fini, A.; Torre, S.; Gori, A.; Centritto, M.; Ferrini, F.; Landi, M.; Guidi, L. Dissecting molecular and physiological response mechanisms to high solar radiation in cyanic and acyanic leaves: A case study on red and green basil. *J. Exp. Bot.* **2017**, *68*, 2425–2437. [[CrossRef](#)]
37. Torre, S.; Tattini, M.; Brunetti, C.; Guidi, L.; Gori, A.; Marzano, C.; Landi, M.; Sebastiani, F. De novo assembly and comparative transcriptome analyses of red and green morphs of sweet basil grown in full sunlight. *PLoS ONE* **2016**, *11*, e0160370. [[CrossRef](#)] [[PubMed](#)]
38. Landi, M.; Agati, G.; Fini, A.; Guidi, L.; Sebastiani, F.; Tattini, M. Unveiling the shade nature of cyanic leaves: A view from the “blue absorbing side” of anthocyanins. *Plant Cell Environ.* **2021**, *44*, 1119–1129. [[CrossRef](#)] [[PubMed](#)]
39. Jakovljević, D.; Topuzović, M.; Stanković, M. Nutrient limitation as a tool for the induction of secondary metabolites with antioxidant activity in basil cultivars. *Ind. Crops Prod.* **2019**, *138*, 111462. [[CrossRef](#)]
40. Foyer, C.H.; Noctor, G. Redox homeostasis and antioxidant signaling: A metabolic interface between stress perception and physiological responses. *Plant Cell* **2005**, *17*, 1866–1875. [[CrossRef](#)] [[PubMed](#)]
41. Caldwell, M.M.; Bornman, J.F.; Ballaré, C.L.; Flint, S.D.; Kulandaivelu, G. Terrestrial ecosystems, increased solar ultraviolet radiation, and interactions with other climate change factors. *Photochem. Photobiol. Sci.* **2007**, *6*, 252–266. [[CrossRef](#)]
42. Bidel, L.P.; Chomicki, G.; Bonini, F.; Mondolot, L.; Soulé, J.; Coumans, M.; La Fisca, P.; Baissac, Y.; Petit, V.; Loiseau, A.; et al. Dynamics of flavonol accumulation in leaf tissues under different UV-B regimes in *Centella asiatica* (Apiaceae). *Planta* **2015**, *242*, 545–559. [[CrossRef](#)]
43. Vidović, M.; Morina, F.; Milić, S.; Zechmann, B.; Albert, A.; Winkler, J.B.; Veljović Jovanović, S. Ultraviolet-B component of sunlight stimulates photosynthesis and flavonoid accumulation in variegated *Plectranthus coleoides* leaves depending on background light. *Plant Cell Environ.* **2015**, *38*, 968–979. [[CrossRef](#)]
44. Jenkins, G.I.; Long, J.C.; Wade, H.K.; Shenton, M.R.; Bibikova, T.N. UV and blue light signalling: Pathways regulating chalcone synthase gene expression in Arabidopsis. *New Phytol.* **2001**, *151*, 121–131. [[CrossRef](#)]
45. Jenkins, G.I. Signal transduction in responses to UV-B radiation. *Annu. Rev. Plant Biol.* **2009**, *60*, 407–431. [[CrossRef](#)]
46. Ulm, R.; Baumann, A.; Oravec, A.; Máté, Z.; Ádám, É.; Oakeley, E.J.; Schäfer, E.; Nagy, F. Genome-wide analysis of gene expression reveals function of the bZIP transcription factor HY5 in the UV-B response of Arabidopsis. *Proc. Natl. Acad. Sci. USA* **2004**, *101*, 1397–1402. [[CrossRef](#)]
47. Brown, B.A.; Cloix, C.; Jiang, G.H.; Kaiserli, E.; Herzyk, P.; Kliebenstein, D.J.; Jenkins, G.I. A UV-B-specific signaling component orchestrates plant UV protection. *Proc. Natl. Acad. Sci. USA* **2005**, *102*, 18225–18230. [[CrossRef](#)]
48. Vidović, M.; Morina, F.; Milić, S.; Albert, A.; Zechmann, B.; Tosti, T.; Winkler, J.B.; Veljović Jovanović, S. Carbon allocation from source to sink leaf tissue in relation to flavonoid biosynthesis in variegated *Pelargonium zonale* under UV-B radiation and high PAR intensity. *Plant Physiol. Biochem.* **2015**, *93*, 44–55. [[CrossRef](#)]
49. Potters, G.; Pasternak, T.P.; Guisez, Y.; Palme, K.J.; Jansen, M.A. Stress-induced morphogenic responses: Growing out of trouble? *Trends Plant Sci.* **2007**, *12*, 98–105. [[CrossRef](#)] [[PubMed](#)]
50. Hideg, É.; Vass, I. UV-B induced free radical production in plant leaves and isolated thylakoid membranes. *Plant Sci.* **1996**, *115*, 251–260. [[CrossRef](#)]
51. Takahama, U.; Oniki, T. A peroxidase/phenolics/ascorbate system can scavenge hydrogen peroxide in plant cells. *Physiol. Plant.* **1997**, *101*, 845–852. [[CrossRef](#)]
52. Smith, J.L.; Burritt, D.J.; Bannister, P. Shoot dry weight, chlorophyll and UV-B-absorbing compounds as indicators of a plant’s sensitivity to UV-B radiation. *Ann. Bot.* **2000**, *86*, 1057–1063. [[CrossRef](#)]
53. Živanović, B.; Sedlarević, A.; Vidović, M.; Morina, F.; Veljović Jovanović, S. Differential dynamics of flavonoid biosynthesis and accumulation in five medicinal herbs under full sunlight exposure. In Proceedings of the UV 4Plants, 1st Network Conference, Pecs, Hungary, 30–31 May 2016; In Book of abstracts, p. 64.
54. Kolb, C.A.; Kopecký, J.; Riederer, M.; Pfündel, E.E. UV screening by phenolics in berries of grapevine (*Vitis vinifera*). *Funct. Plant Biol.* **2003**, *30*, 1177–1186. [[CrossRef](#)] [[PubMed](#)]
55. Hectors, K.; Prinsen, E.; De Coen, W.; Jansen, M.A.; Guisez, Y. *Arabidopsis thaliana* plants acclimated to low dose rates of ultraviolet B radiation show specific changes in morphology and gene expression in the absence of stress symptoms. *New Phytol.* **2007**, *175*, 255–270. [[CrossRef](#)] [[PubMed](#)]
56. Singh, S.; Agrawal, S.B.; Agrawal, M. UVR8 mediated plant protective responses under low UV-B radiation leading to photosynthetic acclimation. *J. Photochem. Photobiol. B* **2014**, *137*, 67–76. [[CrossRef](#)] [[PubMed](#)]
57. Jenkins, G.I. Regulation of phenylpropanoid and flavonoid biosynthesis genes by UV-B in Arabidopsis. In *Plant Responses to Environmental Stress*; Bios Scientific Publishers Ltd.: Oxford, UK, 1999; pp. 9–15.
58. Makri, O.; Kintzios, S. *Ocimum* sp.(basil): Botany, cultivation, pharmaceutical properties, and biotechnology. *J. Herbs Spices Med. Plants* **2008**, *13*, 123–150. [[CrossRef](#)]
59. Kolb, C.A.; Kaser, M.A.; Kopecký, J.; Zotz, G.; Riederer, M.; Pfundel, E.E. Effects of natural intensities of visible and ultraviolet radiation on epidermal ultraviolet screening and photosynthesis in grape leaves. *Plant Physiol.* **2001**, *127*, 863–875. [[CrossRef](#)]

60. Tattini, M.; Galardi, C.; Pinelli, P.; Massai, R.; Remorini, D.; Agati, G. Differential accumulation of flavonoids and hydroxycinnamates in leaves of *Ligustrum vulgare* under excess light and drought stress. *New Phytol.* **2004**, *163*, 547–561. [[CrossRef](#)]
61. Li, J.; Ou-Lee, T.M.; Raba, R.; Amundson, R.G.; Last, R.L. Arabidopsis flavonoid mutants are hypersensitive to UV-B irradiation. *Plant Cell.* **1993**, *5*, 171–179. [[CrossRef](#)]
62. Grace, S.C.; Logan, B.A.; Adams, W.W. Seasonal differences in foliar content of chlorogenic acid, a phenylpropanoid antioxidant, in *Mahonia repens*. *Plant Cell Environ.* **1998**, *21*, 513–521. [[CrossRef](#)]
63. Clarke, L.J.; Robinson, S.A. Cell wall-bound ultraviolet-screening compounds explain the high ultraviolet tolerance of the Antarctic moss, *Ceratodon purpureus*. *New Phytol.* **2008**, *179*, 776–783. [[CrossRef](#)]
64. Zhang, K.M.; Yu, H.J.; Shi, K.; Zhou, Y.H.; Yu, J.Q.; Xia, X.J. Photoprotective roles of anthocyanins in *Begonia semperflorens*. *Plant Sci.* **2010**, *179*, 202–208. [[CrossRef](#)]
65. Larsen, D.H.; Li, H.; Shrestha, S.; Verdonk, J.C.; Nicole, C.; Marcelis, L.F.; Woltering, E.J. Lack of blue light regulation of antioxidants and chilling tolerance in Basil. *Front. Plant Sci.* **2022**, *13*, 852654. [[CrossRef](#)]
66. Schmalwieser, A.W.; Gröbner, J.; Blumthaler, M.; Klotz, B.; De Backer, H.; Bolsée, D.; Werner, R.; Tomsic, D.; Metelka, L.; Eriksen, P.; et al. UV Index monitoring in Europe. *Photochem. Photobiol. Sci.* **2017**, *16*, 1349–1370. [[CrossRef](#)]
67. McKenzie, R.; Smale, D.; Kotkamp, M. Relationship between UVB and erythemally weighted radiation. *Photochem. Photobiol. Sci.* **2004**, *3*, 252–256. [[CrossRef](#)] [[PubMed](#)]
68. Cerović, Z.G.; Masdoumier, G.; Ghozlen, N.B.; Latouche, G. A new optical leaf-clip meter for simultaneous non-destructive assessment of leaf chlorophyll and epidermal flavonoids. *Physiol Plant.* **2012**, *146*, 251–260. [[CrossRef](#)]
69. Morina, F.; Jovanović, L.; Mojović, M.; Vidović, M.; Panković, D.; Veljović Jovanović, S. Zinc-induced oxidative stress in *Verbascum thapsus* is caused by an accumulation of reactive oxygen species and quinhydrone in the cell wall. *Physiol. Plant.* **2010**, *140*, 209–224. [[CrossRef](#)] [[PubMed](#)]
70. Cano, A.; Hernández-Ruiz, J.; García-Cánovas, F.; Acosta, M.; Arnao, M.B. An end-point method for estimation of the total antioxidant activity in plant material. *Phytochem. Anal.* **1998**, *9*, 196–202. [[CrossRef](#)]
71. Thordal-Christensen, H.; Zhang, Z.; Wei, Y.; Collinge, D.B. Subcellular localization of H₂O₂ in plants. H₂O₂ accumulation in papillae and hypersensitive response during the barley powdery mildew interaction. *Plant J.* **1997**, *11*, 1187–1194. [[CrossRef](#)]

Disclaimer/Publisher’s Note: The statements, opinions and data contained in all publications are solely those of the individual author(s) and contributor(s) and not of MDPI and/or the editor(s). MDPI and/or the editor(s) disclaim responsibility for any injury to people or property resulting from any ideas, methods, instructions or products referred to in the content.



Estimating aerosol particle removal in indoor air by ion-enhanced deposition

P. Kolarž^{a,*,1}, A.Ž. Ilić^{a,*,1}, M. Janković^b, A. Janićijević^c, A.M. Trbovich^d

^a Institute of Physics Belgrade, University of Belgrade, Belgrade, 11080, Serbia

^b Department of Virology, Faculty of Medicine, University of Belgrade, Belgrade, 11000, Serbia

^c Faculty of Technology and Metallurgy, University of Belgrade, Belgrade, 11000, Serbia

^d Department of Pathological Physiology, Faculty of Medicine, University of Belgrade, Belgrade, 11000, Serbia

ARTICLE INFO

Handling Editor: Chris Hogan

Keywords:

Small air ions
Bioaerosol pathogens
Breathing zone
Indoor air
Airborne viruses and SARS-CoV-2
Removal

ABSTRACT

Small air ions have the ability to charge airborne particles, thereby increasing their accumulation on surfaces. Indoor air purification by applying ionization uses electrostatic particle deposition. Respiratory pathogens, including viruses and respiratory droplets carrying viruses or other pathogens, represent bioaerosols, whose particle size distributions contain increasingly larger proportion of fine and ultrafine particles, as the evaporation process proceeds. We have generated two model aerosols: the nebulized NaCl solution, resembling human saliva, and the cigarette smoke, having relatively low water content. We have conducted real life experiments of such surrogate aerosol particle deposition without ionization, using bipolar ionization, as well as using unipolar negative air ions. Particle number concentrations have been measured in the 10 nm–10 μm particle size range. The calculated deposition rates and aerosol particle half-life times were correlated with bioaerosol pathogens based on the core pathogen sizes. Bipolar ionizers emitting equal concentrations of positive and negative ions had low impact to the particle concentration decrease. Intense negative air ionization resulted in pronounced deposition rate increases, particularly in the particle size range of viruses including the SARS-CoV-2. The impact of negative air ionization was most pronounced in the same size range where the deposition rates without ionization were the lowest. Therefore, the results are very promising from the standpoint of air purification and bioaerosol pathogen removal, bearing in mind that the effect of ions will be most pronounced if the unipolar ion rich air stream is directed towards the breathing zone.

1. Introduction

Over the past three years, the pandemic of coronavirus disease has disrupted public health systems, transportation and logistics, and economy worldwide; throwing a focus of the public on airborne pathogens causing respiratory diseases (Shang et al., 2021; Shankar et al., 2022; Zhou et al., 2021). Amongst other solutions for suppressing the pandemic, studies on air purification and pathogen removal have received the increased attention. Namely, it is necessary to remove pathogenic particles from the respiratory

* Corresponding author. Institute of Physics Belgrade, Pregrevica 118, 11080, Belgrade, Serbia.

** Corresponding author. Institute of Physics Belgrade, Pregrevica 118, 11080, Belgrade, Serbia.

E-mail addresses: kolarz@ipb.ac.rs (P. Kolarž), andjelijailic@ieee.org (A.Ž. Ilić), marko.jankovic@med.bg.ac.rs (M. Janković), janicaco@tmf.bg.ac.rs (A. Janićijević), alexander.m.trbovich@gmail.com (A.M. Trbovich).

¹ These authors contributed equally to this work and, thus, share the first authorship.

<https://doi.org/10.1016/j.jaerosci.2023.106199>

Received 16 January 2023; Received in revised form 27 April 2023; Accepted 30 April 2023

Available online 11 May 2023

0021-8502/© 2023 Elsevier Ltd. All rights reserved.

zone, in order to prevent human inhalation of pathogens, especially viruses. There are only a few ways to accomplish that goal.

Exposure to ozone has been shown to affect the internal structure of viruses and cause damage to the nucleic acids, taking several minutes to show some effects (Cao et al., 2021; Criscuolo et al., 2021). However, ozone is harmful to humans and, therefore, needs to be used in the absence of people. Meanwhile, viral particles can accumulate again in previously treated indoor spaces. A number of studies have demonstrated the effectiveness of the ultraviolet germicidal irradiation (UVGI) in eliminating viruses indoors including the SARS-CoV-2 (Heilingloh et al., 2020; Sellera et al., 2021). A disadvantage of using UVGI is again the harmfulness to humans; however, the UVGI has been recognized as an efficient solution when installed in the upper-room zone, taking precautions to avoid human exposures (Escombe et al., 2009; Mphahlele et al., 2015; Nardell et al., 2013; Sung & Kato, 2011). UV energy directed or reflected into the occupied space has the potential to cause temporary eye or skin damage; therefore, assistance from a qualified HVAC professional or a reputable UV system manufacturer is required to ensure that the system is installed properly, i.e., the UV energy is directed above the occupied space and the system is operating safely. With good air mixing, the upper-room UVGI can reliably add the equivalent of 10–20 room air changes per hour to the existing natural or mechanical ventilation (Nardell et al., 2013). In particular, the vertical air mixing is integral to the efficacy of upper-room UVGI systems. Upper-room UVGI could also be combined with other particle removal methods, e.g. air ionization.

The intense air filtration using HEPA (High Efficiency Particulate Air) filters is safe for humans. HEPA type of air filter can collect more than 99.97% of airborne particles with the most penetrating particle size of 300 nm, whereas the filtration efficiency is even higher for larger as well as smaller particles (Pawar et al., 2021). However, lower grade filters are also often being used due to the higher price and higher power consumption which are linked with the high density HEPA filters.

Another method of indoor air cleaning safe in the presence of people, is by employing intense air ionization to continuously inactivate airborne pathogens in the breathing zone of indoor spaces (Hyun et al., 2017; Kolarž et al., 2016; Yu et al., 2008). It is an active air purification technique which could be employed separately or in combination with the air filtration, to remove particles and pathogens by directing relatively high ion concentrations (10^3 – 10^5 cm⁻³) along the horizontal plane at the height of the breathing zone. It has been previously demonstrated, that ionization can even bring additional health benefits to humans (Chu et al., 2019; Gaisberger et al., 2012; Jiang et al., 2018; Liu et al., 2022).

High energy source is required to induce ionization and separation of charge, which is derived from nuclear, thermal, electrical, or chemical processes (Daniels, 2002). Natural ways of global small ion generation in the atmosphere are radioactive decay (mostly by gas radon and ⁴⁰K) and cosmic radiation. Local sources of ion generation are lightning, waterfall Lenard effect (Kolarž et al., 2012), fire etc. Concerning artificial indoor ion sources, nowadays, corona discharge on carbon fibre brushes (instead of metal needles), is the most common ion source due to the highly desired zero ozone emissions. After the ionization occurs, primary ions evolve by the process of hydration in less than microseconds, forming small cluster ions (known as small air ions) with sizes up to 0.9 nm and mobility ≥ 3.2 cm²V⁻¹s⁻¹. Further evolution of air ions leads to big cluster ions (0.9–1.6 nm), intermediate (1.6–4.8 nm), light large (4.8–22.0 nm) and heavy large (22.0–79.0 nm) ions (Hörrak et al., 2000). However, their mobility somewhat decreases with the size increase (Hörrak et al., 2000).

Air purification based on ionization works on the principle of electrostatic charging of airborne particulate matter, mainly through the diffusion charging mechanism (Zheng et al., 2016). Unipolarly charged particles will repel each other, filling the surrounding space and charging the surrounding surfaces in accordance with the surface materials and distances to the surfaces. In addition to the air drag forces due to air resistance and friction forces on surfaces, enhanced particle deposition on nearby surfaces results from image charges, dielectric polarization, or static electricity (triboelectricity) (Berry et al., 2007; Sawant et al., 2012). The resulting contamination of indoor surfaces is disadvantageous and should be managed periodically. The major advantage of ionization is in the possibility to direct air ions towards the breathing zone, to most effectively remove airborne respiratory pathogens. Additionally, many studies have shown effective inactivation of a large number of viruses and bacteria by an exposure to air ions (Fletcher et al., 2007; Grinshpun et al., 2005; Hagbom et al., 2015; Kerr et al., 2006; Kettleson et al., 2009). In that sense, air ions are biologically active (Jiang et al., 2018; Krueger & Reed, 1976).

Ionizers typically use one of the three ways of ion generation: corona discharge, dielectric barrier discharge (DBD), or radioactive decay of alpha emitters. Until recently, air ionization was not entirely predictable, as a certain quantity of ozone could be present as by-product of ionization (first two cases). In the third case, a radioactive decay is involved, which could pose problems due to the uncertain safety levels of the sources. The permitted ozone concentrations for human exposure are relatively low (United States Environmental Protection Agency (US EPA) in The National Ambient Air Quality Standards (NAAQS) has set official exposure limits for ozone at no more than 0.07 ppm average over an 8-h period). Ozone accumulates due to the relatively long half-life of 7–10 min (Weschler, 2000). The ozone concentration in indoor spaces is always the sum of background ozone concentration and any additionally produced ozone concentration, such as produced by ionization device. Stronger ionizers reach the above value rapidly, limiting the intensity of ionization they can produce. Fortunately, air ionization with a negligible ozone production has been demonstrated by applying corona discharge, i.e., a few thousand volts, on a carbon fibre instead of a metal needle (Han et al., 2008). Namely, a carbon fibre brush used with voltages that do not exceed 5 kV still provided high rates of ion production. As a result, during the last two decades, indoor air ionization is again in the centre of interest in the field of indoor air purification. Many studies have been carried out concerning air ion behaviour and distributions in indoor spaces, and their air purifying ability (Fletcher et al., 2008; Grinshpun et al., 2001; Lee et al., 2004; Shiue, 2011; Wu et al., 2006a, 2006b, 2015; Zeng et al., 2022). Considering the current need for more efficient particle removal from the air breathing zone, we have decided to reevaluate the utility of air ionization with negligible ozone production, which was not always the case in early investigations. Moderately high ion concentrations were used; however, to make the most benefit out of the short-lived small air ions, we have directed the ion stream towards the air breathing zone. Such an approach, in our opinion, would be of key significance for truly efficient air purification in practical applications, concerning the short half-life time

of small air ions. The focus of this work was on the precise calculation of particle deposition coefficients and linked particle half-life times, covering a very wide range of particle sizes commensurate with different airborne pathogens (10.0 nm–10.0 μm). Effects of the unipolar and bipolar ionization were critically compared. To ensure the reliability and repeatability of experiments, this first investigation was performed under very controlled conditions using two surrogate particle aerosols. In that way, we expect to be able to consistently appraise size-specific relative merits of the applied ionization.

2. Materials and methods

2.1. Experimental setup description

In real life experiment, we studied the removal of surrogate aerosols (including the SARS-CoV-2 size range of 80–200 nm) from indoor air by static deposition and agglomeration under different ion polarities. All of the experiments were repeated in two similar moderately sized indoor places. The first one was an office (5 m \times 3 m) with 4 plastic coated desks and wooden parquet. The other one was a small room (4 m \times 3 m) equipped with a bed, study desk, two cabinets, and a small carpet in the middle. Room ventilation in these two indoor places was not available apart from the doors and windows; to avoid inconsistencies due to imprecise control of ventilation conditions, experiments were conducted with all windows and doors kept closed for the entire duration of experiments. Thus, a zero air exchange rate is assumed. The particle concentration decrease without and with ionization was measured and attributed to particle deposition. Fig. 1 presents an overview of the experimental setup described in detail in the following paragraphs.

All experiments were performed under standard atmospheric conditions ($T \sim 20\text{--}25$ $^{\circ}\text{C}$, $p \sim 998\text{--}1010$ hPa, $RH \sim 40\text{--}60\%$). Experiments were performed in summer and early autumn; as a result, there were no significant temperature differences inside/outside. Any air inflow through the uPVC window and door isolation thus had to be extremely low and it was considered negligible, given that the relatively high aerosol concentrations, significantly higher than background levels, were used at the beginning of each measurement. It has been previously demonstrated that, under such conditions, the outdoor source contribution could be ignored (He et al. 2005). In the absence of indoor particle sources, ventilation, i.e., air exchange rate simply adds to the static deposition rate to increase the overall

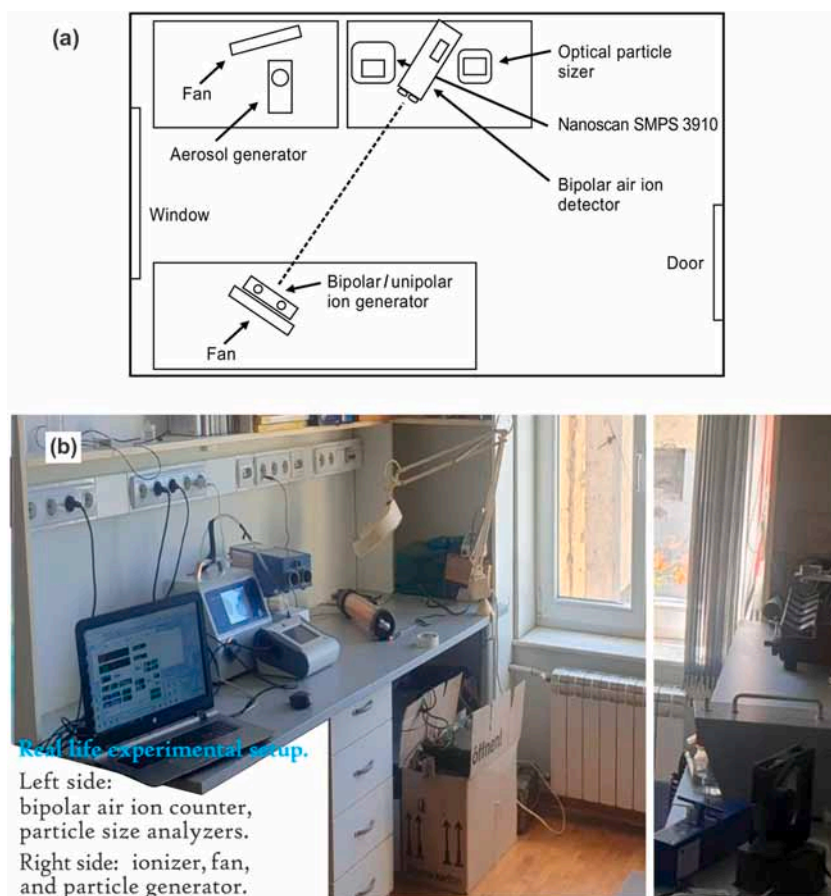


Fig. 1. Real life office experimental setup: (a) schematic, (b) photograph. There was about 2.5 m straight line distance between the aerosol and ion stream generating equipment and the measuring equipment. Particle number concentrations without and with air ionization were measured in the particle size range 10 nm–10 μm .

particle removal as explained in [subsection 2.5](#). (He et al. 2005). In our experiments, upon the high enough particle concentrations were established, particle generation was turned off and the ion generation was turned on after a minute or two, or not turned on at all. Experiments were of a short duration and were performed over several daytime hours. Aerosol concentration was measured once in a minute and ion concentration every 20 s. Thirty to fifty consecutive samples taken at high aerosol concentrations were typically used to determine particle deposition rates, so that the impact of the measurement equipment errors to the calculated deposition rate accuracy was minimized. The idea behind this work was to obtain, as accurately as possible, the deposition rate coefficients of particles in a wide size range in real space environment where each surface (tables, floor, carpets, ceiling, furniture, etc.) has a different conductivity, which also affects deposition rates, and then to correlate the results with common airborne pathogens. By conducting our experiments in a realistically sized and furnished closed space, we allowed particles to distribute in a more natural way throughout the room as opposed to very homogeneous distributions within the smaller experimental chambers. The gravitational settling also affects the deposition processes for particles larger than a micrometer. In a chamber, settling could occur sooner than in an open space due to aerosol being more closely positioned to the chamber walls. Small air ions, while being directed by a fan, showed certain concentration gradients in a larger space, which could have also affected particle deposition. The influx of new particles from indoor or outdoor sources is typically intermittent; thus, the calculated deposition rates correspond to a number of cases and also provide a good starting point for possible modelling of more complex cases.

2.2. Generation of small air ions and measurement of their concentration

Nowadays, corona discharge on carbon fibre brushes (instead of metal needles), is the most common ion source due to the highly desired zero ozone emissions. Corona generated small air ions result from applying potential differences of several kilovolts at small distances (using wires, needles, or carbon fibre brushes), thereby giving rise to high electric fields. The corona plasma region occurs only in the small volume, i.e., in the immediate locality of the active point electrode. The ions with the same polarity as the electrode drift away from it, transferring momentum to the surrounding neutral molecules. The induced particle movement is called the ionic wind, leading to further propagation of ions (Zhang et al., 2019). According to (Han et al., 2008), ozone is being generated during the corona discharge on carbon-fibre brushes when the voltage applied on the electrodes exceeds 5 kV, whereas the ozone quantity reaches a threshold of 4 ppb at about 7.0 kV. Although 4 ppb seems almost negligible, ozone can accumulate in indoor spaces; thus, carbon-fibre brushes should be used up to 5 kV to avoid generating ozone.

We used the bipolar ion generator GPS-FC48™-AC (GPS Ltd., USA), UL 2998 certified, employing carbon fibre brushes for ozone-free bipolar and unipolar (negative) ion production. It is important to mention the two ways of assessing ozone production: measuring the ozone concentration or determining the ozone generation rate. In the previous UL standard, the ozone concentration after 24 h of continuous operation in a stainless steel chamber, of 31.1 m³, was tested at a distance of 50 mm from the outlet. However, the ozone production rate, sizing and furnishing of the rooms can differ; thus, more ozone could accumulate. The UL 2998 test requires measured concentrations to be 10 times lower than the actual regulatory requirements for ozone, an order of magnitude stricter requirement which should help to stay below the limits regardless of practical differences in the spaces of application. The ion generator was placed 2.5 m away from the aerosol measuring instruments inlets, in both rooms. Additionally, ozone levels were monitored at all times using Aeroqual series 500 with O₃ Low Sensor Head (0.0–0.5 ppm). Our measurements showed that the ozone concentrations were below the detection limit of this sensor which is 0.001 ppm (1 ppb); therefore, ozone concentration during all experiments was below 5 ppb which is considered the UL 2998 threshold for zero ozone emissions. In all experiments, 12 cm diameter fans were used for two purposes. Firstly, it was used to homogeneously distribute the aerosols during their emission; subsequently, it was put directly behind the ion source with an aim of directing ion-rich air in the desired direction. The air velocity generated by the fan was 1 ms⁻¹ at a distance of 60 cm. During the negative ion generation, positive electrodes were covered. Initial total ultrafine particle concentration (11.5–365.2 nm) for all experiments was measured (please see [subsection 2.3](#).) to be above $\sim 1 \times 10^5$ cm⁻³. After the end of each measurement and before the following one, the room was purged with fresh air.

The air ion concentration was measured using a bipolar cylindrical measuring instrument named BCDI (Bipolar Cylindrical Ion Detector), which was designed and assembled in the Institute of Physics (Belgrade, Serbia). It is the third generation of ion concentration measuring instruments developed for this purpose (Kolarž et al., 2011; Kolarž & Čurguz, 2015). The BCDI works on the principle of an aspirated Gerdien condenser (Gerdien, 1905) and it measures simultaneously the concentration of positive and negative ions, temperature, humidity and pressure. It has an autonomous power supply, internal data acquisition and data transfer to PC via Bluetooth. The instrument performs self-zeroing at defined intervals, and calibration is performed via a picoampere source. Sensitivity of ion measurements is ± 5 ions/cm³ of both polarities. This instrument was positioned at a 2.5 m distance away from the ionizer. During the experiments with unipolar ions, the ion detector must be grounded. Only the negative ions were used because they performed well with unipolar charging principle of the Nanoscan SMPS 3910. Namely, a built-in unipolar charger uses positive ions to charge the air, which is then mixed with the sampled aerosol particles. Charging of the aerosol particles is needed to size them accordingly to their electrical mobility. Positive pre-charge and internal positive charging of the NanoScan SMPS lead to highly multiply charged aerosol, which seems not to work well with the NanoScan SMPS data retrieval algorithm. Measurement accuracy and reliability of the Nanoscan SMPS is not given for the case of highly positively charged particle measurement.

2.3. Aerosol particle generation and concentration measurements

Two different sources of surrogate particles were used: the nebulized NaCl solution aerosol and the cigarette smoke aerosol. Portable Test Aerosol Generator Model 3073 (TSI Inc., St. Paul, MN, USA) was used as an atomizer to generate the nebulized NaCl

aerosol from an aqueous 10% NaCl solution. In experiments, the atomized stream was blown by a fan to disperse it relatively homogeneously throughout the interaction volume. The filling of the space with NaCl particles was relatively slow (taking cca 45 min), allowing precise control of the achieved particle number concentrations, presented in Fig. 2. Generation of cigarette smoke particles was much faster (cca 4 min) but less precise in terms of particle number control.

Cigarette smoke is a complex mixture of gaseous compounds and particulates. In our experiments, it was generated by the burning end of cigarette, i.e., not through a cigarette filter. Such side-stream smoke was directed and blown by a fan (for the majority of experiments) to obtain a more homogeneous distribution in space and direct the ions towards the inlets of the measuring equipment. Particulate matter generated by the burning end of a cigarette can be considered relatively dry in comparison with the NaCl aerosol,

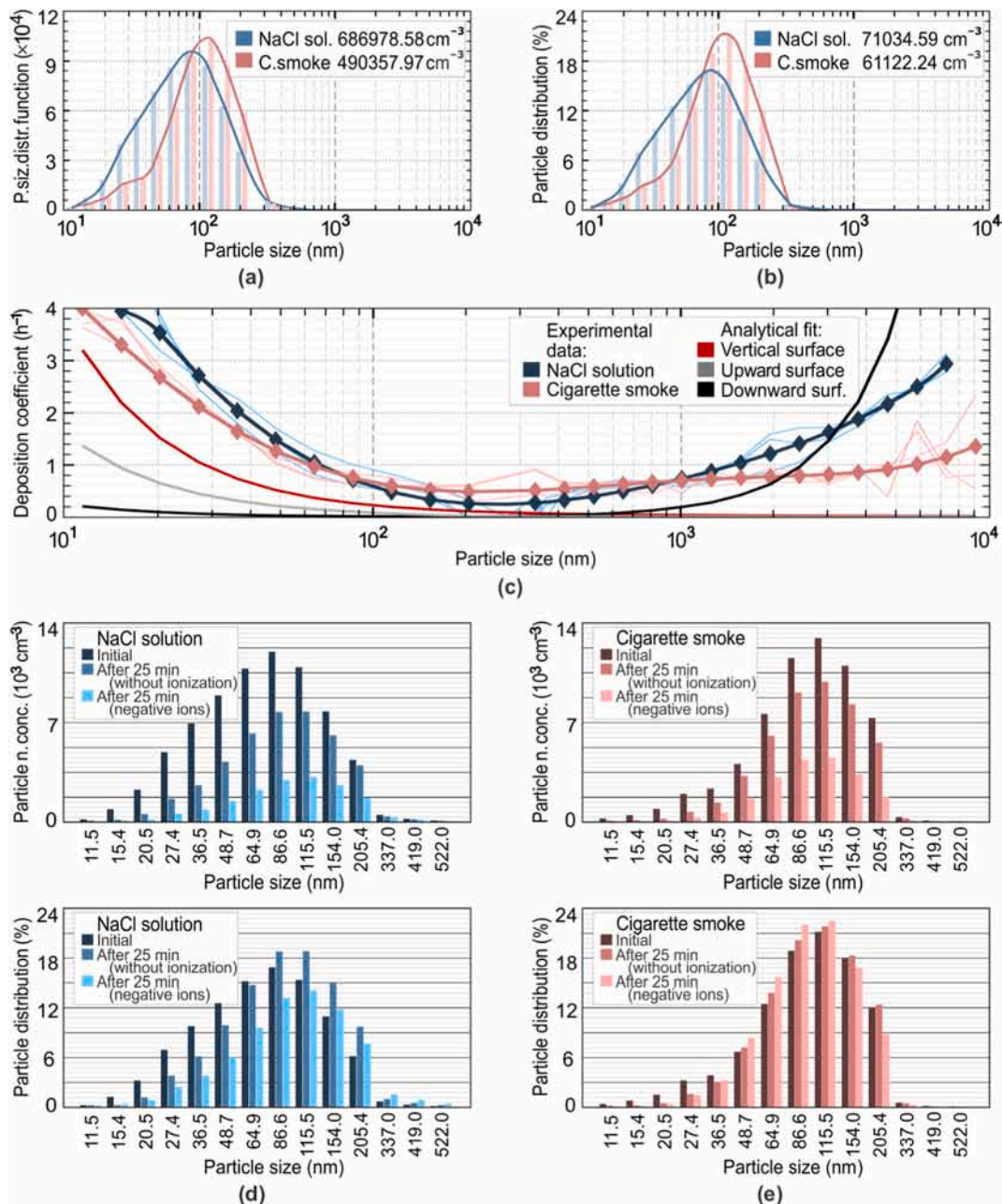


Fig. 2. Aerosol particle size distributions. (a) Particle size distribution functions, $dN/d \ln D_p$. (b) Normalized initial particle size distributions in percents with respect to the total concentrations (71034.59 cm^{-3} for NaCl solution, 61122.24 cm^{-3} for cigarette smoke). (c) Different deposition coefficients for two aerosols (without ionization). Comparison with the theoretically calculated deposition rates (Lai & Nazaroff, 2000) is given. Particle concentrations after 25 min, without and with air ionization, for the (d) NaCl solution and (e) cigarette smoke, shown in the top two plots. Bottom plots depict the normalized size distributions.

which, on the other side, very well mimics human saliva droplets. Saliva comprises of about 99.5% water but also contains salt, proteins, peptides, mucins, enzymes, etc, which remain to form the droplet nuclei upon the evaporation of water (Pourfattah et al., 2021; Rezaei & Netz, 2021). However, cigarette smoke particles could represent well the solid core of the pathogens after evaporation, and are a suitable model for particle transport in predominantly dry environments. The geometric mean diameter of the primary particles from side-stream cigarette smoke has been shown to range from 160 to 400 nm (Wang et al., 2018). In this work, cigarette smoke particles sized 80–400 nm comprised 70% of all particles in the initial size distributions. These particle sizes correspond well with many viruses including the SARS-CoV-2. Moreover, the large span of monitored particle sizes also allows some estimates of the effectiveness of small air ions for the removal of other bioaerosol pathogens (bacteria and fungi).

Initial particle size distributions for our experiments are listed in Table S1 of the Supplementary information for the NaCl solution and in Table S2 for the cigarette smoke aerosol. Total initial particle size distributions for the two cases are listed in bottom rows of the tables. Additionally, particle diameter distribution data is presented graphically in Fig. 2. When plotted, all three sets of data for the cigarette smoke aerosol showed almost an order of magnitude lower concentration of particles larger than 0.8 μm in comparison with the NaCl solution aerosol. Due to mutually very similar distributions when considering a single aerosol, we have shown one example per group in Fig. 2(a) and (b), namely the NaCl solution measurement presented in the first column of Table S1 and the cigarette smoke measurement in the third column of Table S2. Data shown in Fig. 2(b) is normalized with respect to the total particle number concentration for each of the two examples. We observe the differences in the initial fine particle distributions for the two considered aerosols. For the cigarette smoke, particles sized 80–205 nm comprised 70% of all particles, as compared to the 49% for the same size range, for the NaCl aerosol. In both cases, 99% of generated particles were of diameters smaller than 340 nm.

First part of the performed experiments consisted of measuring aerosol concentration changes in a room without airstream which could be guiding ions towards the measuring equipment. Ionizer was about 2.5 m away from the measuring equipment during all measurements. Experiments were performed using none, negative and positive/negative ionization. During all three measurements, no difference was observed in the rate of decrease in the concentration of aerosols of any diameter. This, like all other experiments, was repeated three times.

We measured the particle sizes and number concentrations of both ultrafine and coarser particles about 1 m above the room floors, with all of the equipment for particle generation, ion generation, and measurements of concentrations of both kept at approximately the same height and distanced about 2.5 m from the sources. The Optical Particle Sizer (OPS) Model 3330 (TSI Inc., St. Paul, MN, USA) was used to measure particle number concentrations from 0.3 μm to 10.0 μm . The NanoScan SMPSTM Nanoparticle Sizer 3910 spectrometer (TSI Inc., St. Paul, MN, USA) was used to measure concentrations in the particle size range from 10 nm to 0.3 μm . The OPS and SMPS inlets were joined together to perform the sampling for each of them from the same spot. The particle concentration decrease without and with ionization was measured once per minute.

The charging rate of aerosol particles, R_i , resulting from the interaction with ions, is proportional with both the aerosol particle number concentration, n_p , and ion number concentration, n_i . The proportionality coefficient corresponds to the ion attachment probability, α_i :

$$R_i = \alpha_i n_p n_i. \quad (1)$$

In (1), the symbol α_i is used instead of the more usual symbol β_i , to denote the attachment coefficient, in order to avoid any possible confusion with the particle deposition rate, to room surfaces, also denoted by β . The attachment coefficient is also known as the particle-ion collision kernel, or collision rate coefficient, or ion flux coefficient (Li et al., 2020; Li & Gopalakrishnan, 2021). Recently, a quite general model of particle charging in collisions between unlike charged particle-ion (bipolar charging) and like charged particle-ion (unipolar charging) has been validated by extensive comparisons against the published experimental data, including the arbitrary aerosol particle shapes and charging ions presented by polydisperse ion distributions of variable masses and mobilities with known relative abundance of each type of \pm ion (Li & Gopalakrishnan, 2021). The model is based on Langevin dynamics simulations

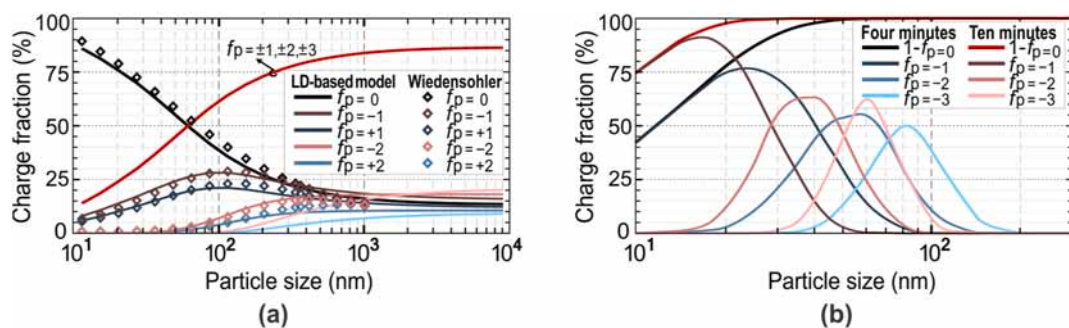


Fig. 3. Particle charge fractions as a function of the particle diameter, for the NaCl solution aerosol. Charge fractions were determined by the Langevin dynamics based model (Li & Gopalakrishnan, 2021). (a) Bipolar charge distributions, assuming that the steady-state has been reached. The results are additionally compared with the Wiedensohler's regression expression (Wiedensohler, 1988). (b) Negative unipolar charge distributions, assuming the charging duration of four or 10 min, when the aerosol particles are exposed to the nominal ion number concentration $n_i = 2.10^4 \text{ cm}^{-3}$. (f_p – fraction of particles carrying p charges, $p \in \{-3, -2, -1, 0, +1, +2, +3\}$).

along with some additional data fitting in order to obtain equations applicable for a wide range of model parameters of interest; it is based on a decade of previous research by the same group of authors. It is valid for perfectly conducting particles and in the absence of external electric fields. Here, we have employed it to assess the charge fractions primarily for the NaCl aerosol, which can be well modelled as the perfectly conducting spherical particles. Singly charged bipolar, or negative ions in the second case, were modelled in air using data from Tables S3–A (supplementary information). Results for the bipolar charging case, obtained under an assumption that the steady-state was achieved given relatively long exposures to ions in our case, are shown in Fig. 3(a). The black line corresponds to the fraction of particles left uncharged. The red line shows summed fractions for the singly, doubly, or triply charged particles (both polarities). The lightest blue and lightest pink lines correspond to the triply charged particles, positively and negatively, respectively. It is interesting to note, that for particles smaller in diameter than 50–60 nm, the majority of fine and ultrafine particles will remain uncharged. For particles larger than 300 nm, summed charge fractions up to $p = \pm 3$ amount to more than 80% of particles being charged. Yet, as the subsequent data shows, the effectiveness of particle charging for particle removal by deposition also depends on the particle size. The observed effects seem to be more pronounced for smaller particle diameters. There is also an excellent agreement of results with the (Wiedensohler, 1988) model, as shown in Fig. 3(a), where the charge fractions based on Wiedensohler’s regression fit are depicted by diamonds. While the steady-state can only be attained with bipolar ions, though not necessarily of equal concentrations (positive/negative ions), we have used the calculated collision kernels α_i with the charging equations as described in (Li et al., 2020). In such a case, the particle–ion exposure parameter is assumed, governing the charge fraction dynamics with time. Although the experiments were done outside the chamber, continuous exposure to the nominal ion number concentration $n_i = 2 \cdot 10^4 \text{ cm}^{-3}$ was considered for two time durations. The results are shown in Fig. 3(b). In practice, due to the open space, charge fractions might be somewhat smaller than the ones shown in Fig. 3(b). Still, they are significantly higher than those attained with bipolar ions. Additionally, the larger particles easily become multiply charged. Along with the decrease of aerosol particle concentrations, there is a continual rise in small air ion concentrations, as illustrated in Fig. 4 by the measured particle and ion concentration data.

2.4. Estimation of particle deposition rates

It is well known that several factors dominantly influence the process of exponential decrease of indoor particle concentrations with respect to time: the ventilation rate (air exchange rate), the particle generation, the indoor and outdoor concentrations (Hussein et al., 2009; Kanaani et al., 2008). In most cases, the indoor air can be considered well-mixed, under the low ventilation conditions coagulation can be considered negligible, and the evaporation occurs rapidly leaving the aerosol residue. Therefore, it is sufficient to account for the deposition and ventilation processes, in which case the exponential concentration decay equation simplifies to

$$\ln\left(\frac{C_i(t)}{C_{0,i}}\right) = - (\kappa + \beta_i)t \tag{2}$$

In (1), $C_i(t)$ denotes the decreasing concentration for the i -th particle size, $C_{0,i}$ the initial peak concentration for the i -th particle size, κ the ventilation rate, and β_i the particle-size-dependent deposition rate coefficient (abbreviated in figure labels as ‘Deposition

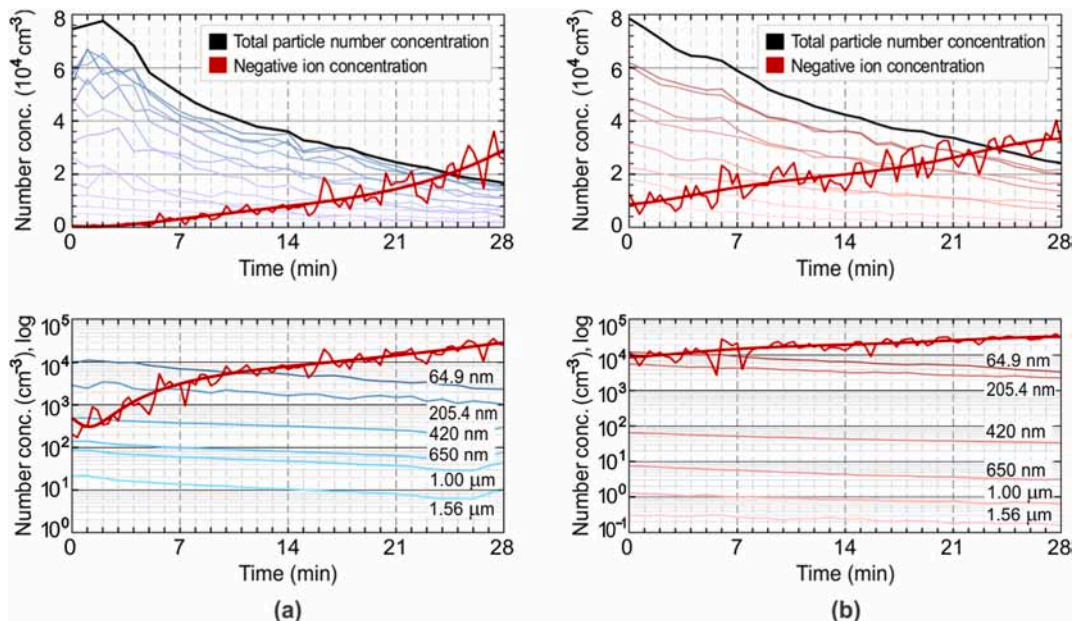


Fig. 4. Gradual increase of negative ion concentrations and the corresponding decrease of particle number concentrations. (a) NaCl solution aerosol. (b) Cigarette smoke aerosol.

coefficient'). In our experiments, the ventilation rate of $\kappa = 0$ was assumed; therefore, the particle-size-dependent deposition rate coefficient, β_i , can be determined simply as a best linear fit to the data to minimize the root mean square variations. In all cases, the aerosol particle concentration measurements were conducted for a sufficient time to reach the lower asymptotic values of the exponential decay. However, when the concentrations are very low, relative errors of the measurement tend to be more pronounced. For that reason we used a sufficient number of data samples close to the initial peak and at the beginning of the decrease process, typically 30–50 samples (30–50 min of measurement). Particle half-life, τ_i , for each considered particle size, was calculated as

$$\tau_i = \frac{60 \ln(2)}{\beta_i} \tag{3}$$

In (2), β_i should be expressed as the deposition rate coefficient per hour, in order to obtain τ_i in minutes.

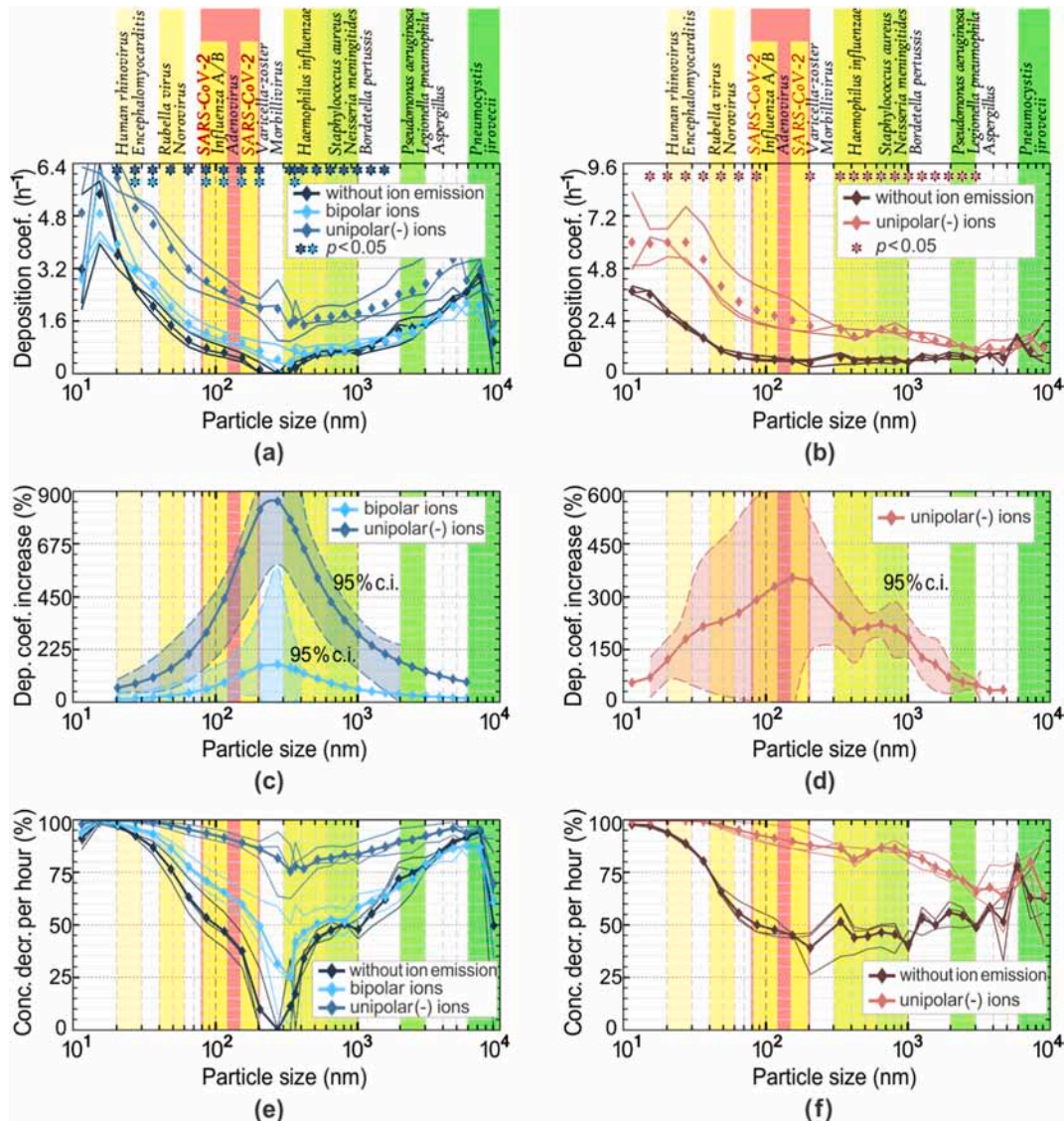


Fig. 5. Deposition coefficients, without and with air ionization. Different airborne pathogen sizes are depicted by different shades of green/yellow. (a) Deposition coefficients for NaCl solution aerosol. (b) Deposition coefficients for cigarette smoke. Percentage increase of deposition coefficients with air ionization and the corresponding 95% confidence intervals are shown in (c) for NaCl solution and in (d) for cigarette smoke. Particle number concentration decrease per hour is shown in (e) for NaCl solution and (f) for cigarette smoke. (For interpretation of the references to colour in this figure legend, the reader is referred to the Web version of this article.)

2.5. Statistical data analysis

We have performed three independent measurements for each case, i.e., each of the two aerosols as well as the case without ionization, with bipolar or unipolar ionization. We have previously observed that the β_i , deposition rate coefficients, for each particle size taken separately, tend to be normally distributed when the measurements are carried out with the similar initial particle and ion concentrations. The two-sample t -test, not assuming equal variances of the samples, was therefore used to compare the data and check out on the statistical significance of the differences between the size-dependent β_i coefficients obtained from the measurements with different ionization type (without, with bipolar, with unipolar). Alternatively, the Mann-Whitney U Test could be used as a non-parametric alternative to a two sample t -test. When assuming that the two data samples do not belong to populations with equal variances, the test statistic has an approximate Student's t distribution and it is known as the Welch's t -test. The 5% significance level, $p < 0.05$, was used, and the statistical significance of the differences is denoted in Figs. 5 and 6 by asterisks (please see the legend). We have calculated the 95% confidence intervals of the differences of population means and the 95% confidence intervals of the inferred deposition rate enhancements with ionization. The confidence intervals are given as a basic assessment of the ionization impact, since they are based on only three sets of measurements.

3. Results and discussion

3.1. Correlating the pathogen sizes with experiments on surrogate aerosols

Surrogate particles were used in this study, to precisely obtain deposition coefficients for a wide range of particle sizes under the same conditions. However, one of the aims of the study was to correlate the obtained results with the assumed respiratory droplet sizes or droplet residue sizes of different airborne pathogens. It proved remarkably difficult to determine with certainty the final droplet residue sizes for different pathogens. In the existing literature, respiratory droplet sizes were often determined relatively close to the mouth opening and focusing on particle sizes above 1 μm . In (Fennelly, 2020), studies of cough aerosols and of exhaled breath from patients with various respiratory infections have shown striking similarities in aerosol size distributions, with a predominance of pathogens in small particles $< 4.7 \mu\text{m}$. Studied pathogens included *Mycobacterium tuberculosis*, *Pseudomonas aeruginosa*, Influenza A/B. In (Chao et al., 2009), the most frequent droplet size range close (60 mm) to the mouth opening was 4–8 μm , which was more pronounced for coughing than for breathing. In (Johnson et al., 2011), three distinct droplet size distribution modes were identified, which originated from lower respiratory tract, 1.6 μm , larynx, about 2 μm , and upper respiratory tract, about 120–150 μm in size. In (Nazaroff, 2016), in the measurement of airborne viruses indoors, a substantial proportion of the detected virus was associated with fine particles ($< 2.5 \mu\text{m}$) that can remain airborne for extended periods and that can also deposit deeply in the respiratory tract. In (Alsvéd et al., 2023), virus carrying droplets were partially dried during the collection. The majority of the SARS-CoV-2 RNA has been found in droplets sized 1.0–2.8 μm ; however, significant SARS-CoV-2 RNA has also been found in the droplets as small as 340–550 nm.

It is well known that evaporation plays an important role in the respiratory droplet transport; however, it also depends on many factors which are not quite straightforward to account for. The main parameters of interest for accurate theoretical and numerical analysis of respiratory droplets transport, as well as credible interpretation of experimental data, include the exhaled particle size distributions, the time-dependent velocity and flow rate profiles, and the evaporation rates depending on temperature and humidity (Pourfattah et al., 2021). Higher humidity prolongs evaporation times, whereas a higher supply rate of ventilation air increases the rate of particle evaporation and influences the particle deposition rates. It has been calculated that the evaporation occurs in less than 1 s for 10 μm particles, and less than 1 min for 100 μm , even in the high humidity (Morawska, 2006; Pourfattah et al., 2021; Xie et al., 2007). However, these results assumed pure water droplets in idealized conditions. One of the major shortcomings of such a model was in neglecting the presence of solutes, which lowers the chemical potential of water and lowers the rate of evaporation (Božić & Kanduć, 2021; Rezaei & Netz, 2021). It is estimated that saliva comprises of about 99% water but also contains salt, proteins, peptides, mucins, enzymes, and possibly pathogens, which remain to form the droplet nuclei upon the evaporation of water (Pourfattah et al., 2021; Rezaei & Netz, 2021). The typical volume proportion of non-water content in a small droplet can be around 1%–10%. Then, a completely dried-out droplet could have a radius which is from 22% to 46% of the initial droplet radius. However, humidity plays an important role; for example, at RH = 50%, the dried-out droplet shrinks down to 27%–58% of its initial radius. In the RH = 50% case, an estimate of droplet sedimentation implies that 99% of the initially exhaled droplet volume settles within 30 s (Božić & Kanduć, 2021). The rest of evaporated droplet residues could be suspended in the air for prolonged time. Nevertheless, two points can be noticed. Firstly, if the majority of virus laden droplets is $< 2.5 \mu\text{m}$, upon evaporation these could contain up to several virions; on the other side, if *Mycobacterium tuberculosis* particle is 1–2 μm in size, the evaporated 4.7 μm droplet (to 27%–58% of its initial radius) could contain one or two bacteria. Large droplets will be settled due to gravity in a couple of seconds. Secondly, the measured deposition rates without and with ions correspond to much longer half-life times in comparison with the time needed for a droplet to evaporate, making the aerosol residue sizes most important for this study. Given that there are up to date only approximate estimates of the aerosol residue sizes which are on the order of magnitude of core pathogen sizes (multiplied by a factor of about two to five), we have decided to present the size-specific relative merits of the applied ionization in terms of the accurately known core pathogen sizes, as the lowest size limit.

3.2. Changes in particle size distributions for the two aerosols

First part of all experiments comprised of measuring aerosol concentration changes in the room without airstream which would be

guiding ions towards the measuring equipment. For that purpose, we generated large amounts of negative ions, which were directed from the floor to the ceiling (similar to what commercial ionizers with filter air purifiers typically perform). Unfortunately, no visible effects on particle concentration decrease within 1 h of measurements were obtained. In our opinion, the most probable explanation lies in the short lifetimes of air ions, which tend to be even shorter than usual when the high aerosol concentrations are present. Also, the insufficient air mixing, due to the low fan power, could not appreciably reduce the particle concentration. We focused our attention further exclusively onto the distributions of air ions which were directed and made more homogeneous by an air stream of initial velocity 1.4 m/s (produced by the fan). Since it is very difficult to distribute the air stream evenly all over the room, we focused on providing relatively homogeneous distributions of aerosols as well as ions within the interaction volume in the middle of each room. In practical implementation of ionizers in buildings, additional attention must be paid on the distribution of ions in parts of the indoor spaces where it is of highest importance. In occupied rooms, that would be the air breathing zone. The air flow velocity on an order of 1 m/s through the breathing zone could be considered pleasant enough for the occupants of indoor spaces.

As we already mentioned in subsection 2.2., the initial particle size distributions for the NaCl aerosol (denoted in figures as the ‘NaCl solution’) and for the cigarette smoke differed (please see Fig. 2(a)). Moreover, we determined the averaged particle deposition rates without ionization, from the three measurements of the NaCl solution and cigarette smoke, and revealed significant differences between the two (please see Fig. 2(b)). Both deposition rate curves are U-shaped, which is characteristic for the considered interval of particle diameters (He et al. 2005). To better illustrate this, we also compared the deposition rates in the absence of ions with a theoretical solution based on the mathematical model proposed and developed in (Lai & Nazaroff, 2000), assuming the air pressure of 1 atm, temperature 293 K, and friction velocity of 2.6 cm/s. Particle density of 1000 kg/m³ was used for the NaCl. The resulting curves, corresponding to the vertical, upward, and downward horizontal surfaces are shown in Fig. 2(b), denoted as ‘Analytical fit’. The deposition of cigarette smoke particles is mostly lower than that for NaCl solution particles, which could probably be attributed to the higher content of water in the NaCl solution. As a result of initial differences, as well as different deposition rates, particle diameter distributions remain different for the two aerosols. Particle number concentration and size distribution at two time points is shown in Fig. 2(c) for the NaCl solution and in Fig. 2(d) for the cigarette smoke. Top plots correspond to actual particle concentrations and give an illustration of concentration decrease processes. Bottom plots show distributions, normalized with respect to total particle concentration at a given time instant. More accurate information on concentration decrease can be obtained from Figs. 5 and 6, where the changes in particle size distributions during the exponential decrease were accounted for.

Main conclusion from Fig. 2 is that particles in the size range of most interest to us currently (on the order of 200 nm) are also the most difficult ones to remove from the breathing zone. Due to larger deposition, there are less and less particles outside of the above mentioned size range, making the particles in the virus-size range dominant in distributions, as the time passes by. Still, overall particle numbers are decreasing, which is quite pronounced when air ionization is used, as can be better seen from the data in Figs. 5 and 6.

Ion number concentrations were on the order of 2·10⁴ cm⁻³. We would turn on the small air ion generation upon the establishment of high enough initial particle concentrations. Fig. 4 shows the typical increase of ion concentrations along with the decrease in total particle number concentrations. Rate of increase of ion concentrations influenced the particle deposition efficiencies. Upper plots show, purely for illustration purposes, also the exponential decrease of actual concentrations for individual particle sizes, scaled by a factor of 6 for particles up to 300 nm and by 16 for larger particles in (a), and scaled by a factor of 4 for particles up to 300 nm in (b).

Table 1

Particle deposition rates (per hour), with the 95% confidence intervals, for particle sizes where the measured deposition rate differences were statistically significant ($p < 0.05$).

Particle size (nm)	NaCl solution aerosol			Cigarette smoke aerosol				
	Without ionization	Bipolar ionization	95% Confid. interval	Negative ionization	95% Confid. interval	Without ionization	Negative ionization	95% Confid. interval
20.5	3.61			5.98	[4.96, 7.00]	2.77	5.98	[4.45, 7.52]
27.4	2.60	3.18	[2.80, 3.55]	5.03	[3.78, 6.29]	2.18	6.00	[2.53, 9.48]
36.5	2.05	2.69	[2.17, 3.21]	4.55	[2.89, 6.20]	1.63	5.21	[1.79, 8.64]
48.7	1.46			3.80	[2.28, 5.32]	1.07	3.99	[1.10, 6.90]
64.9	1.02			3.18	[1.95, 4.42]	0.82	3.28	[0.85, 5.71]
86.6	0.78	1.25	[0.78, 1.72]	2.81	[1.85, 3.77]	0.70	2.90	[0.70, 5.10]
115.5	0.64	1.08	[0.69, 1.47]	2.52	[1.75, 3.29]	0.65	2.65	[0.43, 4.87]
154.0	0.48	0.92	[0.57, 1.27]	2.24	[1.69, 2.79]	0.60	2.44	[0.48, 4.40]
205.4	0.12	0.70	[0.19, 1.20]	1.99	[1.39, 2.60]	0.51	2.18	[1.10, 3.26]
337.0	0.14			1.51	[0.28, 2.73]	0.75	2.01	[1.39, 2.62]
365.2	0.20	0.69	[0.23, 1.14]	1.62	[0.32, 2.93]			
419.0	0.42			1.48	[0.88, 2.07]	0.58	1.70	[1.10, 2.30]
522.0	0.58			1.69	[0.98, 2.40]	0.59	1.85	[1.60, 2.10]
650.0	0.64			1.73	[1.03, 2.44]	0.63	2.02	[1.77, 2.28]
809.0	0.70			1.81	[1.23, 2.40]	0.61	2.01	[1.46, 2.57]
1007.0	0.65			1.84	[1.07, 2.61]	0.53	1.81	[1.41, 2.20]
1254.0	0.81			1.99	[1.09, 2.88]	0.76	1.70	[1.23, 2.17]
1562.0	0.99			2.13	[1.08, 3.18]	0.69	1.51	[0.91, 2.11]
1944.0	1.32					0.83	1.37	[0.98, 1.77]
2421.0	1.39					0.79	1.25	[1.02, 1.48]
3014.0	1.56					0.67	1.08	[0.92, 1.23]

Table 2

Deposition rates for the NaCl solution aerosol for typical particle sizes of bioaerosol pathogens, if pathogens persisted in an aerosol bare, and not incorporated into larger particles.

Estimated deposition rate coefficients per hour without and with air ionization						
Pathogen size (nm)	Pathogen name	Without ionization	Bipolar ionization	Percent increase (%)	Negative ionization	Percent increase (%)
24.0	<i>Human rhinovirus ref.</i> (t1)	3.08	3.53	14.84	5.49	78.22
	<i>Torquetenovirus ref.</i> (t2)					
30.0	<i>Human rhinovirus ref.</i> (t1)	2.49	3.00	20.73	4.84	94.56
	<i>Encephalomyocarditis virus</i> (t3)					
	<i>Polio virus ref.</i> (t4)					
38.0	<i>Norovirus ref.</i> (t5)	1.96	2.51	28.29	4.28	118.88
60.0	<i>Rubella virus ref.</i> (t6)	1.16	1.73	49.69	3.42	195.87
80.0	<i>SARS-CoV-2 ref.</i> (t7)	0.80	1.36	70.02	2.99	274.63
	<i>Influenza A/B ref.</i> (t8)					
	<i>Rotavirus ref.</i> (t9)					
	<i>Adenovirus ref.</i> (t10)					
	<i>SARS-CoV-2 ref.</i> (t7)					
120.0	<i>SARS-CoV-2 ref.</i> (t7)	0.46	0.96	110.98	2.48	441.06
	<i>Influenza A/B ref.</i> (t8)					
	<i>Cytomegalovirus ref.</i> (t11)					
	<i>Adenovirus ref.</i> (t10)					
150.0	<i>SARS-CoV-2 ref.</i> (t7)	0.34	0.82	136.81	2.24	551.59
	<i>Cytomegalovirus ref.</i> (t11)					
	<i>Respiratory syncytial virus</i> (t12)					
	<i>Varicella-zoster virus ref.</i> (t13)					
	<i>Morbillivirus ref.</i> (t4)					
	<i>Epstein-Barr virus ref.</i> (t14)					
200.0	<i>SARS-CoV-2 ref.</i> (t7)	0.26	0.68	157.90	1.99	654.02
	<i>Cytomegalovirus ref.</i> (t11)					
	<i>Varicella-zoster virus ref.</i> (t13)					
300.0	<i>Haemophilus influenzae ref.</i> (t15)	0.26	0.59	129.80	1.74	574.45
	<i>Staphylococcus aureus ref.</i> (t16)					
	<i>Haemophilus influenzae ref.</i> (t15)					
	<i>Neisseria meningitidis ref.</i> (t17)					
600.0	<i>Bordetella pertussis ref.</i> (t18)	0.46	0.65	41.84	1.62	252.03
	<i>Staphylococcus aureus ref.</i> (t16)					
	<i>Haemophilus influenzae ref.</i> (t15)					
	<i>Neisseria meningitidis ref.</i> (t17)					
	<i>Mycoplasma pneumoniae</i> (t19)					
	<i>Bordetella pertussis ref.</i> (t18)					
	<i>Stenotrophomonas maltophilia</i> (t20)					
<i>Escherichia coli ref.</i> (t21)						
1000.0	<i>Haemophilus influenzae ref.</i> (t15)	0.73	0.83	13.56	1.84	149.98
	<i>Neisseria meningitidis ref.</i> (t17)					
	<i>Mycoplasma pneumoniae</i> (t19)					
	<i>Bordetella pertussis ref.</i> (t18)					
	<i>Stenotrophomonas maltophilia</i> (t20)					
2000.0	<i>Escherichia coli ref.</i> (t21)	1.24	1.22	0.00	2.44	96.99
	<i>Mycoplasma pneumoniae</i> (t19)					
	<i>Streptococcus A group ref.</i> (t22)					
	<i>Pseudomonas aeruginosa</i> (t23)					
	<i>Aspergillus ref.</i> (t24)					
<i>Penicillium ref.</i> (t25)						

(t1) (Rankl et al., 2008); available at <https://basicmedicalkey.com/6-viruses-basic-concepts/>, accessed at Dec 14th, 2022.

(t2) (Dimitrov, 2004).

(t3) (Nikitin et al., 2015).

(t4) (Van Regenmortel, 1999).

(t5) (Yang et al., 2009).

(t6) (Bardeletti et al., 1975).

(t7) (Chen et al., 2020); (Tai et al., 2021).

(t8) (Mosley & Wyckoff, 1946).

(t9) (Long & McDonald, 2017).

(t10) (Kramberger, Ciringir, Štrancar, & Peterka, 2012).

(t11) (Schottstedt et al., 2010).

(t12) (Utley et al., 2008).

(t13) (Mueller et al., 2008).

(t14) (Henson et al., 2009).

(t15) (Khattak & Anjum, 2022).

(t16) (Sitjar et al., 2021).

(t17) At: <https://www.britannica.com/science/meningitis>.

(t18) (Loeffelholz & Sanden, 2007).

(t19) (Taylor-Robinson, 2007).

(t20) (Palleroni & Bradbury, 1993).

- (t21) (El-Hajj & Newman, 2015).
 (t22) (Kilian, 1998).
 (t23) (Diggle & Whiteley, 2020).
 (t24) (Kwon-Chung & Sugui, 2013).
 (t25) (Meklin et al., 2002).

Bottom plots use the log scale in order to represent actual particle concentration decaying for different particle sizes, along with the increase of ion concentrations.

3.3. Deposition rate coefficients

In Fig. 5, the deposition rate coefficients in indoor air ('Deposition coef. ') were determined for each particle size. Experimental data, three measurements per case, is shown by the thin solid lines, whereas markers are used to present the means for the three measurements. Particle sizes where the differences in deposition were statistically significant are denoted by asterisks in the top parts of Fig. 5(a) and (b). Particle deposition rates, with the 95% confidence intervals, are also presented in Table 1 for particle sizes where the measured deposition rate differences were statistically significant ($p < 0.05$).

Plots in (c) and (d) show calculated increases of the deposition rates (in percents) when negative ionization is applied, along with the 95% confidence intervals, for the (c) NaCl solution aerosol and (d) cigarette smoke. Plots in (e) and (f) show the concentration decrease per hour (percents) for NaCl solution and cigarette smoke, respectively. We notice again the U-shape of the deposition rate curves in cases without and with air ionization. We also notice, however, relatively low effects of ionization for particles sized 5–10 μm . Fortunately, air ionization proves very effective for the size ranges corresponding to most respiratory viruses and bacteria, and even for some fungal species (as seen from Table 2, Fig. 5). In the size range 200 nm–5 μm , the smaller the particles, the larger the ionization effects due to the deposition rates. Maximal relative improvement in particle deposition is observed for particle sizes, where the deposition without ionization is low but the deposition with applied ionization already significantly increased, i.e., 100 nm–1 μm . Although the SARS-CoV-2 pathogen is probably carried by somewhat larger droplets (~0.5–1 μm), a significant increase in particle deposition rates should be expected, based on the experimental data obtained with two distinctly different particle aerosol types.

The obtained results show an excellent agreement with some of the previous similar investigations and the conclusions therein. It is interesting to compare our findings with the previous research focusing on wearable ionizers (Grinshpun et al., 2001), producing the ion jet in front of the device of maximum velocity about 400 cm/s. The study also utilized the polydisperse NaCl particles ranging from 0.3 to 3.0 μm , as well as bacteria sized 0.8 μm . It was interesting that the particle removal efficiency did not significantly depend on the particle size (within the size range tested), and did not notably depend on the particle type (biological versus non-biological) (Grinshpun et al., 2001). The particle removal efficiency was defined in the mentioned work as the relative concentration decrease when using ionizers in comparison with the case when the ionizers were turned off. Based on Fig. 5(e) we can assess the so defined particle removal efficiency for the exposure duration of 1 h. For the particle diameter 1 μm , an improvement of 35% over a concentration decrease of 50% without ionizer gives an efficiency of 0.7, i.e., 70% after 1 h. For the particle diameter of 7 μm , there is practically no effect of ionizer use. In between, the change in particle removal efficiency is approximately inversely proportional to the logarithm of particle size. For the size range 0.3–1 μm , the removal efficiency did not significantly depend on the particle size in our study either. However, our results were most interesting for particles sized 10 nm–300 nm.

Namely, the concentration decrease without the applied ionization is very slow for 200–300 nm particle sizes; therefore, the ionization effects are very pronounced. Moreover, the particle removal efficiency is higher than 30% for fine particles larger than 50 nm. Except for the size range tested, which in our case also included fine particles, our investigation differed from the study in (Grinshpun et al., 2001) in the applied ion concentrations, which were higher in (Grinshpun et al., 2001). Measurements in that study were also conducted closer to the point electrodes producing ionization, as it was a study of wearable ionizers.

The measured deposition rates in Fig. 5 and Table 2, without and with ions, correspond to much longer half-life times in comparison with the time needed for a droplet to evaporate (please see subsection 3.1). Therefore, Table 2 as well as Table 3 (half-life times) correlate the obtained results from the experiments with surrogate particles with typical sizes of single pathogen particles, noting that a bioaerosol droplet, i.e., the evaporated bioaerosol residue could be larger than listed in tables, also containing multiple pathogens. The listed pathogen sizes therefore represent lower limits of the infectious bioaerosols. Fig. 6 shows particle half-life times corresponding to the deposition rate coefficients from Fig. 5. As an illustration of negative ions efficiency in the removal of pathogens from the breathing zone, plots (c) and (d) show the percentages of particles left (per each particle size) after 15 min, 25 min, and 35 min of continuously applying negative ions. Table 2 lists the particle half-life times for the NaCl aerosol and remaining concentrations (C/C_0), after 20 min of ionization. Half-life times serve as estimates of bioaerosol pathogen half-life times without and with ionization.

4. Conclusions

In conclusion, ionization employing unipolar (in case of this study negative) air ions showed great potential for increased deposition of particles with sizes corresponding to various airborne pathogens from the breathing zone. The half-life times were successfully reduced at or below 25 min, resulting from a significant increase in the deposition rate coefficients. Since the time periods required by negative air ions to produce a sufficient decrease of particle concentrations in the breathing zone equal tens of minutes, whereas respiratory droplets take seconds to evaporate, we assumed potential bioaerosol pathogens to be sized on an order of a single pathogen particle to several times larger than that (in the sense of order of magnitude of interest). Consequently, the aerosol particle sizes of most

Table 3

Estimated bioaerosol pathogen half-life times based on the NaCl surrogate particle deposition, if pathogens persisted in an aerosol bare, and not incorporated into larger particles.

Estimated pathogen half-life (min) without and with air ionization						
Pathogen size (nm)	Pathogen name	Without ionization	Bipolar ionization	C/C ₀ after 20 min (%)	Negative ionization	C/C ₀ after 20 min (%)
24.0	<i>Human rhinovirus ref.</i> (t1)	13.53	11.78	30.78	7.59	16.06
	<i>Torquetenovirus ref.</i> (t2)					
30.0	<i>Human rhinovirus ref.</i> (t1)	16.70	13.84	36.75	8.59	19.92
	<i>Encephalomyocarditis virus</i> (t3)					
	<i>Polio virus ref.</i> (t4)					
38.0	<i>Norovirus ref.</i> (t5)	21.26	16.57	43.31	9.71	23.99
60.0	<i>Rubella virus ref.</i> (t6)	35.95	24.02	56.16	12.15	31.97
80.0	<i>SARS-CoV-2 ref.</i> (t7)	52.13	30.67	63.64	13.92	36.94
	<i>Influenza A/B ref.</i> (t8)					
	<i>Rotavirus ref.</i> (t9)					
	<i>Adenovirus ref.</i> (t10)					
120.0	<i>SARS-CoV-2 ref.</i> (t7)	90.80	43.04	72.46	16.78	43.78
	<i>Influenza A/B ref.</i> (t8)					
	<i>Cytomegalovirus ref.</i> (t11)					
	<i>Adenovirus ref.</i> (t10)					
150.0	<i>SARS-CoV-2 ref.</i> (t7)	120.81	51.01	76.21	18.54	47.35
	<i>Cytomegalovirus ref.</i> (t11)					
	<i>Respiratory syncytial virus</i> (t12)					
	<i>Varicella-zoster virus ref.</i> (t13)					
	<i>Morbillivirus ref.</i> (t4)					
200.0	<i>Epstein-Barr virus ref.</i> (t14)	157.67	61.15	79.72	20.92	51.55
	<i>SARS-CoV-2 ref.</i> (t7)					
	<i>Cytomegalovirus ref.</i> (t11)					
	<i>Varicella-zoster virus ref.</i> (t13)					
300.0	<i>Haemophilus influenzae ref.</i> (t15)	162.17	70.53	82.16	24.03	56.16
	<i>Staphylococcus aureus ref.</i> (t16)					
600.0	<i>Haemophilus influenzae ref.</i> (t15)	90.37	63.72	80.45	25.68	58.28
	<i>Neisseria meningitidis ref.</i> (t17)					
	<i>Bordetella pertussis ref.</i> (t18)					
	<i>Staphylococcus aureus ref.</i> (t16)					
1000.0	<i>Haemophilus influenzae ref.</i> (t15)	56.71	49.94	75.76	22.69	54.28
	<i>Neisseria meningitidis ref.</i> (t17)					
	<i>Mycoplasma pneumoniae</i> (t19)					
	<i>Bordetella pertussis ref.</i> (t18)					
	<i>Stenotrophomonas maltophilia</i> (t20)					
	<i>Escherichia coli ref.</i> (t21)					
2000.0	<i>Mycoplasma pneumoniae</i> (t19)	33.53	34.04	66.55	17.02	44.29
	<i>Streptococcus A group ref.</i> (t22)					
	<i>Pseudomonas aeruginosa</i> (t23)					
	<i>Aspergillus ref.</i> (t24)					
	<i>Penicillium ref.</i> (t25)					

(t1) (Rankl et al., 2008); available at <https://basicmedicalkey.com/6-viruses-basic-concepts/>, accessed at Dec 14th, 2022.

(t2) (Dimitrov, 2004).

(t3) (Nikitin et al., 2015).

(t4) (Van Regenmortel, 1999).

(t5) (Yang et al., 2009).

(t6) (Bardeletti et al., 1975).

(t7) (Chen et al., 2020); (Tai et al., 2021).

(t8) (Mosley & Wyckoff, 1946).

(t9) (Long & McDonald, 2017).

(t10) (Kramberger et al., 2012).

(t11) (Schottstedt et al., 2010).

(t12) (Utley et al., 2008).

(t13) (Mueller et al., 2008).

(t14) (Henson et al., 2009).

(t15) (Khattak & Anjum, 2022).

(t16) (Sitjar et al., 2021).

(t17) At: <https://www.britannica.com/science/meningitis>.

(t18) (Loeffelholz & Sanden, 2007).

(t19) (Taylor-Robinson, 2007).

(t20) (Palleroni & Bradbury, 1993).

- (t21) (El-Hajj & Newman, 2015).
- (t22) (Kilian, 1998).
- (t23) (Diggle & Whiteley, 2020).
- (t24) (Kwon-Chung & Sugui, 2013).
- (t25) (Meklin et al., 2002).

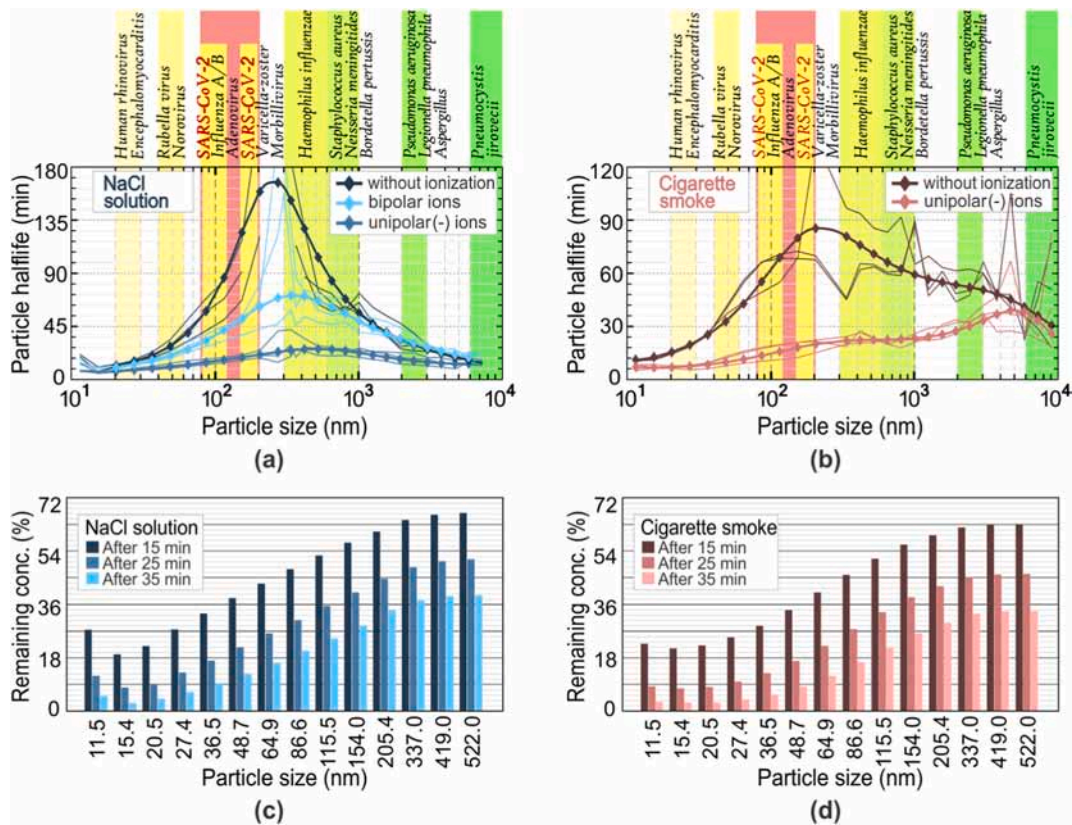


Fig. 6. Particle half-life times, without and with air ionization. Different airborne pathogen sizes are depicted by different shades of green/yellow. (a) Particle half-life times for NaCl solution. (b) Particle half-life times for cigarette smoke. Percentages of remaining concentrations with air ionization (negative ions), per particle size, are shown for (c) NaCl solution and (d) cigarette smoke. (For interpretation of the references to colour in this figure legend, the reader is referred to the Web version of this article.)

interest for viral transmission control would be up to 1 μm (0.1 μm –1 μm). For bacteria, the aerosol particle sizes up to 5 μm could be of most interest. Our investigation covered relatively wide size interval, 10 nm–10 μm . SARS-CoV-2, sized 80 nm–200 nm, falls into the size range where deposition rates are the lowest. On the other side, in this range of sizes and up to 1 μm , negative air ions are most influential to the increase of deposition rates. We also concluded that continuous exposure to directed ionization would be required. A limitation of the study is that a specific ion concentration was used throughout the study, and the results apply to this specific ion concentration. Increasing or decreasing ion concentration will affect the particle–ion attachment probability and could therefore impact the effectiveness of particle removal by ionization. The particle half-life and deposition rate coefficients would then differ from those presented here. For higher ion concentrations, the deposition rates should be increased, at least up to some point, and the particle half-lives should be even shorter. Our future investigations will address bipolar ionization with variable polarity ratios, i.e., with a pronounced excess of positive or negative small air ions, as well as the effects of lower and higher ion concentrations.

Another question opened by this investigation is related to the actual volumes of indoor spaces which could be exposed to ionization. As mentioned, in the first sets of experiments concentration changes were measured without an airstream guiding ions towards the interaction volume. No visible effects on particle concentration decrease within 1 h of measurements were obtained, most probably due to short ion lifetimes and low horizontal air mixing ratio. Practical applications based on this research could include specifically designed tabletop applicators for offices or cafes, which would include ionizers as well as proper ion guiding towards the breathing zone and air mixing designed for achieving the desired particle removal effects. Also, ionizers designed in particular for implementation in combination with HVAC systems would be of interest. Any such applications require detailed investigations of ion-enhanced deposition, to guide the future designs. In practical implementations, ions would have to be guided by air streams in certain directions, as was done in this work. To provide sufficient air mixing, while still being pleasant enough for the occupants of

indoor spaces, it seems most reasonable to use moderate fans to direct ions horizontally. For some indoor spaces it might be necessary to use multiple ionizers, optimize their positioning, and air streams, with a final purpose of covering the most part of the air breathing zone.

CRedit authorship contribution statement

P. Kolarž: Conceptualization, Methodology, Investigation, Validation, Resources, Funding acquisition, Project administration, Writing – original draft, Writing – review & editing. **A.Ž. Ilić:** Conceptualization, Methodology, Formal analysis, Software, Data Curation, Visualization, Writing – original draft, Writing – review & editing. **M. Janković:** Investigation, Validation. **A. Jančićević:** Investigation, Writing – review & editing. **A.M. Trbovič:** Conceptualization, Funding acquisition, Project administration.

Role of funding source

No funding body had any involvement in the preparation or content of this article or in the decision to submit it for publication.

Declaration of competing interest

The authors declare that they have no known competing financial interests or personal relationships that could have appeared to influence the work reported in this paper.

Data availability

Data will be made available on request.

Acknowledgements

The authors acknowledge funding provided by the Institute of Physics Belgrade and the Faculty of Medicine, University of Belgrade, through the grants by the Ministry of Science, Technological Development, and Innovation, of the Republic of Serbia. This work was financially supported by the Science Fund of the Republic of Serbia through the Special Research Program on COVID-19 by the grant No #7552286. The views expressed herein are those of the authors and do not represent the opinion of the Science Fund.

Appendix A. Supplementary data

Supplementary data to this article can be found online at <https://doi.org/10.1016/j.jaerosci.2023.106199>.

References

- Alsved, M., Nygren, D., Thuresson, S., Fraenkel, C.-J., Medstrand, P., & Löndahl, J. (2023). Size distribution of exhaled aerosol particles containing SARS-CoV-2 RNA. *Infectious Diseases*, 55(2), 158–163. <https://doi.org/10.1080/23744235.2022.2140822>
- Bardeletti, G., Kessler, N., & Aymard-Henry, M. (1975). Morphology, biochemical analysis and neuraminidase activity of rubella virus. *Archives of Virology*, 49, 175–186. <https://doi.org/10.1007/BF01317536>
- Berry, D., Mainelis, G., & Fennell, D. (2007). Effect of an ionic air cleaner on indoor/outdoor particle ratios in a residential environment. *Aerosol Science and Technology*, 41(3), 315–328. <https://doi.org/10.1080/02786820701199702>
- Božić, A., & Kanduć, M. (2021). Relative humidity in droplet and airborne transmission of disease. *Journal of Biological Physics*, 47, 1–29. <https://doi.org/10.1007/s10867-020-09562-5>
- Cao, J., Zhang, Y., Chen, Q., Yao, M., Pei, R., Wang, Y., Yue, Y., Huang, Y., Wang, J., & Guan, W. (2021). Ozone gas inhibits SARS-CoV-2 transmission and provides possible control measures. *Aerosol Science and Engineering*, 5, 516–523. <https://doi.org/10.1007/s41810-021-00118-1>
- Chao, C. Y. H., Wan, M. P., Morawska, L., Johnson, G. R., Ristovski, Z. D., Hargreaves, M., Mengersen, K., Corbett, S., Li, Y., Xie, X., & Katoshevski, D. (2009). Characterization of expiration air jets and droplet size distributions immediately at the mouth opening. *Journal of Aerosol Science*, 40, 122–133.
- Chen, N., Zhou, M., Dong, X., Qu, J., Gong, F., Han, Y., ... Zhang, L. (2020). Epidemiological and clinical characteristics of 99 cases of 2019 novel coronavirus pneumonia in Wuhan, China: A descriptive study. *Lancet*, 395, 507–513.
- Chu, C.-H., Chen, S.-R., Wu, C.-H., Cheng, Y.-C., Cho, Y.-M., & Chang, Y.-K. (2019). The effects of negative air ions on cognitive function: An event-related potential (ERP) study. *International Journal of Biometeorology*, 63, 1309–1317. <https://doi.org/10.1007/s00484-019-01745-7>
- Crisuolo, E., Diotti, R. A., Ferrarese, R., Alippi, C., Viscardi, G., Signorelli, C., Mancini, N., Clementi, M., & Clementi, N. (2021). Fast inactivation of SARS-CoV-2 by UV-C and ozone exposure on different materials. *Emerging Microbes & Infections*, 10(1), 206–209. <https://doi.org/10.1080/22221751.2021.1872354>
- Daniels, S. L. (2002). Air ionization of indoor environments for control of volatile and particulate contaminants with nonthermal plasmas. *IEEE Transactions on Plasma Science*, 30(4), 1471–1481. <https://doi.org/10.1109/TPS.2002.804211>
- Diggle, S. P., & Whiteley, M. (2020). Microbe profile: *Pseudomonas aeruginosa*: Opportunistic pathogen and lab rat. *Microbiology (Reading)*, 166(1), 30–33. <https://doi.org/10.1099/mic.0.000860>. Erratum in: *Microbiology (Reading)* 167(8).
- Dimitrov, D. S. (2004). Virus entry: Molecular mechanisms and biomedical applications. *Nature Reviews Microbiology*, 2(2), 109–122. <https://doi.org/10.1038/nrmicro817>
- El-Hajj, Z. W., & Newman, E. B. (2015). How much territory can a single *E. coli* cell control? *Frontiers in Microbiology*, 6, 309. <https://doi.org/10.3389/fmicb.2015.00309>

- Escombe, A. R., Moore, D. A. J., Gilman, R. H., Navincopa, M., Ticona, E., Mitchell, B., Noakes, C., Martinez, C., Sheen, P., Rameriz, R., Quino, W., Gonzalez, A., Friedland, J. S., & Evans, C. A. (2009). Upper-room ultraviolet light and negative air ionization to prevent tuberculosis transmission. *PLoS Medicine*, 6(3), Article e1000043. <https://doi.org/10.1371/journal.pmed.1000043>
- Fennelly, K. P. (2020). Particle sizes of infectious aerosols: Implications for infection control. *Lancet Respiratory Medicine*, 8(9), 914–924. [https://doi.org/10.1016/S2213-2600\(20\)30323-4](https://doi.org/10.1016/S2213-2600(20)30323-4)
- Fletcher, L. A., Gaunt, L. F., Beggs, C. B., Shepherd, S. J., Sleigh, P. A., Noakes, C. J., & Kerr, K. G. (2007). Bactericidal action of positive and negative ions in air. *BMC Microbiology*, 7, 32. <https://doi.org/10.1186/1471-2180-7-32>
- Fletcher, L. A., Noakes, C. J., Sleigh, P. A., Beggs, C. B., & Shepherd, S. J. (2008). Air ion behavior in ventilated rooms. *Indoor and Built Environment*, 17(2), 173–182. <https://doi.org/10.1177/1420326X08089622>
- Gaisberger, M., Šanović, R., Dobias, H., Kolarž, P., Moder, A., Thalhamer, J., Selimović, A., Huttegger, I., Ritter, M., & Hartl, A. (2012). Effects of ionized waterfall aerosol on pediatric allergic asthma. *Journal of Asthma*, 49(8), 830–838. <https://doi.org/10.3109/02770903.2012.705408>
- Gerdien, H. (1905). Demonstration eines Apparates zur absoluten Messung der elektrischen Leitfähigkeit der Luft. *Phys. Zeitung*, 6, 800–801.
- Grinshpun, S. A., Mainelis, G., Reponen, T., Willeke, K., Trunov, M., & Adhikari, A. (2001). Effect of wearable ionizers on the concentration of respirable airborne particles and microorganisms. *Journal of Aerosol Science*, 32(suppl.1), 335–336. [https://doi.org/10.1016/S0021-8502\(21\)00157-9](https://doi.org/10.1016/S0021-8502(21)00157-9)
- Grinshpun, S. A., Mainelis, G., Trunov, M., Adhikari, A., Reponen, T., & Willeke, K. (2005). Evaluation of ionic air purifiers for reducing aerosol exposure in confined indoor spaces. *Indoor Air*, 15(4), 235–245.
- Hagbom, M., Nordgren, J., Nybom, R., Hedlund, K.-O., Wigzell, H., & Svensson, L. (2015). Ionizing air affects influenza virus infectivity and prevents airborne transmission. *Scientific Reports*, 5, Article 11431. <https://doi.org/10.1038/srep11431>
- Han, B., Kim, H.-J., Kim, Y.-J., & Sioutas, C. (2008). Unipolar charging of fine and ultra-fine particles using carbon fiber ionizers. *Aerosol Science and Technology*, 42(10), 793–800. <https://doi.org/10.1080/02786820802339553>
- Heilingloh, C. S., Aufderhorst, U. W., Schipper, L., Dittmer, U., Witzke, O., Yang, D., Zheng, X., Sutter, K., Trilling, M., Alt, M., Steinmann, E., & Krawczyk, A. (2020). Susceptibility of SARS-CoV-2 to UV irradiation. *American Journal of Infection Control*, 48, 1273–1275. <https://doi.org/10.1016/j.ajic.2020.07.031>
- He, C., Morawska, L., & Gilbert, D. L. (2005). Particle deposition rates in residential houses. *Atmospheric Environment*, 39(21), 3891–3899. <https://doi.org/10.1016/j.atmosenv.2005.03.016>
- Henson, B. W., Perkins, E. M., Cothran, J. E., & Desai, P. (2009). Self-assembly of Epstein-Barr virus capsids. *Journal of Virology*, 83(8), 3877–3890. <https://doi.org/10.1128/JVI.01733-08>
- Hörrak, U., Salm, J., & Tammet, H. (2000). Statistical characterization of air ion mobility spectra at Tahkuse Observatory: Classification of air ions. *Journal of Geophysical Research*, 105(D7), 9291–9302. <https://doi.org/10.1029/1999JD901197>
- Hussein, T., Hruška, A., Dohányosová, P., Džumbová, L., Hemerka, J., Kulmala, M., & Smolík, J. (2009). Deposition rates on smooth surfaces and coagulation of aerosol particles inside a test chamber. *Atmospheric Environment*, 43(4), 905–914. <https://doi.org/10.1016/j.atmosenv.2008.05.059>
- Hyun, J., Lee, S.-G., & Hwang, J. (2017). Application of corona discharge-generated air ions for filtration of aerosolized virus and inactivation of filtered virus. *Journal of Aerosol Science*, 107, 31–40. <https://doi.org/10.1016/j.jaerosci.2017.02.004>
- Jiang, S.-Y., Ma, A., & Ramachandran, S. (2018). Negative air ions and their effects on human health and air quality improvement. *International Journal of Molecular Sciences*, 19(10), 2966. <https://doi.org/10.3390/ijms19102966>
- Johnson, G. R., Morawska, L., Ristovski, Z. D., Hargreaves, M., Mengersen, K., Chao, C. Y. H., Wan, M. P., Li, Y., Xie, X., Katoshevski, D., & Corbett, S. (2011). Modality of human expired aerosol size distributions. *Journal of Aerosol Science*, 42(12), 839–851. <https://doi.org/10.1016/j.jaerosci.2011.07.009>
- Kanaani, H., Hargreaves, M., Ristovski, Z., & Morawska, L. (2008). Deposition rates of fungal spores in indoor environments, factors effecting them and comparison with non-biological aerosols. *Atmospheric Environment*, 42(30), 7141–7154. <https://doi.org/10.1016/j.atmosenv.2008.05.059>
- Kerr, K. G., Beggs, C. B., Dean, S., Thornton, J., Donnelly, J. K., Todd, N. J., Sleigh, P. A., Qureshi, A., & Taylor, C. C. (2006). Negative air ionisation and colonisation/infection with methicillin-resistant *Staphylococcus aureus* and *acinetobacter* species in an intensive care unit: A pilot study. *Intensive Care Medicine*, 32, 315–317.
- Kettleson, E. M., Ramaswami, B., Hogan, C. J., Lee, M.-H., Statyukha, G. A., Biswas, P., & Angenent, L. T. (2009). Airborne virus capture and inactivation by an electrostatic particle collector. *Environmental Science and Technology*, 43(15), 5940–5946. <https://doi.org/10.1021/es803289w>
- Khattak, Z. E., & Anjum, F. (2022). *Haemophilus influenzae*. [Updated 2022 Sep 12]. In: StatPearls [internet]. Treasure island (FL). StatPearls Publishing. Available from: <https://www.ncbi.nlm.nih.gov/books/NBK562176/>. (Accessed 14 December 2022).
- Kilian, M. (1998). *Streptococcus and lactobacillus*. In A. Balows, & B. I. Duerden (Eds.), *Topley & Wilson's microbiology and microbial infections* (9th ed., pp. 633–668). London: Arnold.
- Kolarž, P., & Čurguz, Z. (2015). Air ions as indicators of short-term indoor radon variations. *Applied Radiation and Isotopes*, 99, 179–185.
- Kolarž, P., Gaisberger, M., Madl, P., Hofmann, W., Ritter, M., & Hartl, A. (2012). Characterization of ions at Alpine waterfalls. *Atmospheric Chemistry and Physics*, 12, 3687–3697. <https://doi.org/10.5194/acp-12-3687-2012>
- Kolarž, P., Miljković, B., & Čurguz, Z. (2011). Air-ion counter and mobility spectrometer. *Nuclear Instruments and Methods in Physics Research B*, 279, 219–222.
- Kolarž, P., Vaupotić, J., Kobal, I., Ujić, P., & Žunić, Z. S. (2016). Air ion and aerosol study in rural dwellings. *Journal of Aerosol Science*, 95, 118–134. <https://doi.org/10.1016/j.jaerosci.2016.02.002>
- Kramberger, P., Ciringir, M., Štrancar, A., & Peterka, M. (2012). Evaluation of nanoparticle tracking analysis for total virus particle determination. *Virology Journal*, 9, 265. <https://doi.org/10.1186/1743-422X-9-265>
- Krueger, A. P., & Reed, E. J. (1976). Biological impact of small air ions. *Science*, 193, 1209–1213.
- Kwon-Chung, K. J., & Sugui, J. A. (2013). *Aspergillus fumigatus*—what makes the species a ubiquitous human fungal pathogen? *PLoS Pathogens*, 9(12), Article e1003743.
- Lai, A. C. K., & Nazaroff, W. W. (2000). Modeling indoor particle deposition from turbulent flow onto smooth surfaces. *Journal of Aerosol Science*, 31(4), 463–476. [https://doi.org/10.1016/S0021-8502\(99\)00536-4](https://doi.org/10.1016/S0021-8502(99)00536-4)
- Lee, B. U., Yermakov, M., & Grinshpun, S. A. (2004). Removal of fine and ultrafine particles from indoor air environments by the unipolar ion emission. *Atmospheric Environment*, 38(29), 4815–4823. <https://doi.org/10.1016/j.atmosenv.2004.06.010>
- Li, L., Chahl, H. S., & Gopalakrishnan, R. (2020). Comparison of the predictions of Langevin Dynamics-based diffusion charging collision kernel models with canonical experiments. *Journal of Aerosol Science*, 140, Article 105481. <https://doi.org/10.1016/j.jaerosci.2019.105481>
- Li, L., & Gopalakrishnan, R. (2021). An experimentally validated model of diffusion charging of arbitrary shaped aerosol particles. *Journal of Aerosol Science*, 151, Article 105678. <https://doi.org/10.1016/j.jaerosci.2020.105678>
- Liu, S., Li, C., Chu, M., Zhang, W., Wang, Y., Guo, X., & Deng, F. (2022). Associations of forest negative air ions exposure with cardiac autonomic nervous function and the related metabolic linkages: A repeated-measure panel study. *Science of the Total Environment*, 850, Article 158019. <https://doi.org/10.1016/j.scitotenv.2022.158019>
- Loeffelholz, M. J., & Sanden, G. N. (2007). *Bordetella*. In P. R. Murray, E. J. Baron, J. H. Tenover, & M. A. Tenover (Eds.), *Manual of clinical microbiology* (9th ed., pp. 803–814). Washington D.C.: ASM Press.
- Long, C. P., & McDonald, S. M. (2017). Rotavirus genome replication: Some assembly required. *PLoS Pathogens*, 13(4), Article e1006242. <https://doi.org/10.1371/journal.ppat.1006242>
- Meklin, T., Reponen, T., Toivola, M., Koponen, V., Husman, T., Hyvärinen, A., & Nevalainen, A. (2002). Size distributions of airborne microbes in moisture-damaged and reference school buildings of two construction types. *Atmospheric Environment*, 36(39–40), 6031–6039.
- Morawska, L. (2006). Droplet fate in indoor environments, or can we prevent the spread of infection? *Indoor Air*, 16, 335–347.
- Mosley, V., & Wyckoff, R. (1946). Electron micrography of the virus of influenza. *Nature*, 263, 3983.
- Mphahlele, M., Dharmadhikari, A. S., Jensen, P. A., Rudnick, S. N., van Reenen, T. H., Pagano, M. A., Leuschner, W., Sears, T. A., Milonova, S. P., van der Walt, M., Stoltz, A. C., Weyer, K., & Nardell, E. A. (2015). Institutional tuberculosis transmission. Controlled trial of upper room ultraviolet air disinfection: A basis for new dosing guidelines. *American Journal of Respiratory and Critical Care Medicine*, 192(4), 477–484. <https://doi.org/10.1164/rccm.201501-00600C>

- Mueller, N. H., Gilden, D. H., Cohrs, R. J., Mahalingam, R., & Nagel, M. A. (2008). Varicella zoster virus infection: Clinical features, molecular pathogenesis of disease, and latency. *Neurologic Clinics*, 26(3), 675–697. <https://doi.org/10.1016/j.ncl.2008.03.011>
- Nardell, E., Vincent, R., & Sliney, D. H. (2013). Special Issue: Symposium in Print on upper-room ultraviolet germicidal irradiation for air disinfection. *Photochemistry and Photobiology*, 89(4), 764–769. <https://doi.org/10.1111/php.12098>
- Nazaroff, W. W. (2016). Indoor bioaerosol dynamics. *Indoor Air*, 26, 61–78. <https://doi.org/10.1111/ina.12174>
- Nikitin, N., Trifonova, E., Evtushenko, E., Kirpichnikov, M., Atabekov, J., & Karpova, O. (2015). Comparative study of non-enveloped icosahedral viruses size. *PLoS One*, 10(11), Article e0142415. <https://doi.org/10.1371/journal.pone.0142415>
- Palleroni, N. J., & Bradbury, J. F. (1993). *Stenotrophomonas*, a new bacterial genus for *Xanthomonas maltophilia* (Hugh 1980) Swings et al. 1983. *International Journal of Systematic and Evolutionary Microbiology*, 43(3), 606–609.
- Pawar, S. D., Khare, A. B., Keng, S. S., Kode, S. S., Tare, D. S., Singh, D. K., More, R. L., & Mullick, J. (2021). Selection and application of biological safety cabinets in diagnostic and research laboratories with special emphasis on COVID-19. *Review of Scientific Instruments*, 92, Article 081401. <https://doi.org/10.1063/5.0047716>
- Pourfattah, F., Wang, L.-P., Deng, W., Ma, Y.-F., Hu, L., & Yang, B. (2021). Challenges in simulating and modeling the airborne virus transmission: A state-of-the-art review. *Physics of Fluids*, 33, Article 101302. <https://doi.org/10.1063/5.0061469>
- Rankl, C., Kienberger, F., Wildling, L., Wruss, J., Gruber, H. J., Blaas, D., & Hinterdorfer, P. (2008). Multiple receptors involved in human rhinovirus attachment to live cells. *Proceedings of the National Academy of Sciences*, 105, 46. <https://doi.org/10.1073/pnas.0806451105>
- Rezaei, M., & Netz, R. R. (2021). Airborne virus transmission via respiratory droplets: Effects of droplet evaporation and sedimentation. *Current Opinion in Colloid & Interface Science*, 55, Article 101471.
- Sawant, V. S., Meena, G. S., & Jadhav, D. B. (2012). Effect of negative air ions on fog and smoke. *Aerosol and Air Quality Research*, 12, 1007–1015. <https://doi.org/10.4209/aaqr.2011.11.0214>
- Schottstedt, V., Blümel, J., Burger, R., Drosten, C., Gröner, A., Gürtler, L., Heiden, M., Hildebrandt, M., Jansen, B., Montag-Lessing, T., Offergeld, R., Pauli, G., Seitz, R., Schlenkrich, U., Strobel, J., Willkommen, H., & Wirsing von König, C.-H. (2010). Human cytomegalovirus (HCMV) – revised. *Transfusion Medicine and Hemotherapy*, 37(6), 365–375. <https://doi.org/10.1159/000322141>
- Sellera, F. P., Sabino, C. P., Cabral, F. V., & Ribeiro, M. S. (2021). A systematic scoping review of ultraviolet C (UVC) light systems for SARS-CoV-2 inactivation. *Journal of Photochemistry and Photobiology A*, 8, Article 100068. <https://doi.org/10.1016/j.jpap.2021.100068>
- Shang, Y., Tao, Y., Dong, J., He, F., & Tu, J. (2021). Deposition features of inhaled viral droplets may lead to rapid secondary transmission of COVID-19. *Journal of Aerosol Science*, 154, Article 105745. <https://doi.org/10.1016/j.jaerosci.2021.105745>
- Shankar, S. N., Witanachchi, C. T., Morea, A. F., Lednický, J. A., Loeb, J. C., Alam, M. M., Fan, Z. H., Eiguren-Fernandez, A., & Wu, C.-Y. (2022). SARS-CoV-2 in residential rooms of two self-isolating persons with COVID-19. *Journal of Aerosol Science*, 159, Article 105870. <https://doi.org/10.1016/j.jaerosci.2021.105870>
- Shiue, A. (2011). Particles removal by negative ionic air purifier in cleanroom. *Aerosol and Air Quality Research*, 11, 179–186. <https://doi.org/10.4209/aaqr.2010.06.0048>
- Sitjar, J., Liao, J. D., Lee, H., Tsai, H. P., Wang, J. R., & Liu, P. Y. (2021). Challenges of SERS technology as a non-nucleic acid or-antigen detection method for SARS-CoV-2 virus and its variants. *Biosensors and Bioelectronics*, 181, Article 113153.
- Sung, M., & Kato, S. (2011). Estimating the germicidal effect of upper-room UVGI system on exhaled air of patients based on ventilation efficiency. *Building and Environment*, 46, 2326e2332. <https://doi.org/10.1016/j.buildenv.2011.05.015>
- Tai, L., Zhu, G., Yang, M., Cao, L., Xing, X., Yin, G., Chan, C., Qin, C., Rao, Z., Wang, X., Sun, F., & Zhu, Y. (2021). Nanometer-resolution in situ structure of the SARS-CoV-2 postfusion spike protein. *Proceedings of the National Academy of Sciences*, 118(48), Article e2112703118. <https://doi.org/10.1016/j.pnas.2112703118>
- Taylor-Robinson, D. (2007). The role of mycoplasmas in pregnancy outcome. *Best Practice & Research Clinical Obstetrics & Gynaecology*, 21(3), 425–438. <https://doi.org/10.1016/j.bpobgyn.2007.01.011>
- Utley, T. J., Ducharme, N. A., Varthakavi, V., Shepherd, B. E., Santangelo, P. J., Lindquist, M. E., Goldenring, J. R., & Crowe, J. E., Jr. (2008). Respiratory syncytial virus uses a Vps4-independent budding mechanism controlled by Rab11-FIP2. *Proceedings of the National Academy of Sciences*, 105(29), 10209–10214. <https://doi.org/10.1073/pnas.0712144105>
- Van Regenmortel, M. H. V. (1999). Chapter 8 - synthetic peptides as vaccines. In M. H. V. Van Regenmortel, & S. Muller (Eds.), *Laboratory techniques in biochemistry and molecular biology* (Vol. 28, pp. 281–317). [https://doi.org/10.1016/S0075-7535\(08\)70453-4](https://doi.org/10.1016/S0075-7535(08)70453-4)
- Wang, C., Collins, D. B., Hems, R. F., Borduas, N., Antiñolo, M., & Abbott, P. D. (2018). Exploring conditions for ultrafine particle formation from oxidation of cigarette smoke in indoor environments. *Environmental Science and Technology*, 52(8), 4623–4631. <https://doi.org/10.1021/acs.est.7b06608>
- Weschler, C. J. (2000). Ozone in indoor environments: Concentration and chemistry. *Indoor Air*, 10, 269–288.
- Wiedensohler, A. (1988). An approximation of the bipolar charge distribution for particles in the submicron size range. *Journal of Aerosol Science*, 19(3), 387–389. [https://doi.org/10.1016/0021-8502\(88\)90278-9](https://doi.org/10.1016/0021-8502(88)90278-9)
- Wu, Y.-Y., Chen, Y.-C., Yu, K.-P., Chen, Y.-P., & Shih, H.-C. (2015). Deposition removal of monodisperse and polydisperse submicron particles by a negative air ionizer. *Aerosol and Air Quality Research*, 15, 994–1007.
- Wu, C. C., Lee, G. W. M., Cheng, P., Yang, S., & Yu, K.-P. (2006). Effect of wall surface materials on deposition of particles with the aid of negative air ions. *Journal of Aerosol Science*, 37(5), 616–630. <https://doi.org/10.1016/j.jaerosci.2005.05.018>
- Wu, C. C., Lee, G. W. M., Yang, S., Yu, K.-P., & Lou, C. L. (2006). Influence of air humidity and distance from the source on negative air ion concentration in indoor air. *Science of the Total Environment*, 370, 245–253.
- Xie, X., Li, Y., Chwang, A. T. Y., Ho, P. L., & Seto, W. H. (2007). How far droplets can move in indoor environments – revisiting the Wells evaporation–falling curve. *Indoor Air*, 17, 211–225.
- Yang, S., Zhang, W., Shen, Q., Huang, F., Wang, Y., Zhu, J., Cui, L., Yang, Z., & Hua, X. (2009). Molecular characterization and phylogenetic analysis of the complete genome of a porcine sapovirus from Chinese swine. *Virology Journal*, 6, 216. <https://doi.org/10.1186/1743-422X-6-216>
- Yu, K.-P., Lee, G. W.-M., Lin, S.-Y., & Huang, C. P. (2008). Removal of bioaerosols by the combination of a photocatalytic filter and negative air ions. *Journal of Aerosol Science*, 39, 377–392. <https://doi.org/10.1016/j.jaerosci.2007.12.005>
- Zeng, Y., Heidarinejad, M., & Stephens, B. (2022). Evaluation of an in-duct bipolar ionization device on particulate matter and gas-phase constituents in a large test chamber. *Building and Environment*, 213, Article 108858, 2022.
- Zhang, T., Zhang, Y., Ji, Q., Li, B., & Ouyang, J. (2019). Characteristics and underlying physics of ionic wind in dc corona discharge under different polarities. *Chinese Physics B*, 28(7), Article 075202. <https://doi.org/10.1088/1674-1056/28/7/075202>
- Zheng, C., Chang, Q., Lu, Q., Yang, Z., Gao, X., & Cen, K. (2016). Developments in unipolar charging of airborne particles: Theories, simulations and measurements. *Aerosol and Air Quality Research*, 16, 3037–3054.
- Zhou, L., Yao, M., Zhang, X., Hu, B., Li, X., Chen, H., ... Zhang, Y. (2021). Breath-, air- and surface-borne SARS-CoV-2 in hospitals. *Journal of Aerosol Science*, 152, 105693. <https://doi.org/10.1016/j.jaerosci.2020.105693>

Dear Author,

Please, note that changes made to the HTML content will be added to the article before publication, but are not reflected in this PDF.

Note also that this file should not be used for submitting corrections.



Contents lists available at ScienceDirect

Journal of Aerosol Science

journal homepage: www.elsevier.com/locate/jaerosci

Q2 Air ion and aerosol study in rural dwellings

Q1 Predrag Kolarž^a, Janja Vaupotič^b, Ivan Kobal^b, Predrag Ujić^c, Zora S. Žunić^c

^a Institute of Physics, University of Belgrade, Belgrade, Serbia

^b Jožef Stefan Institute, Ljubljana, Slovenia

^c Institute of Nuclear Sciences "Vinča", University of Belgrade, Belgrade, Serbia

ARTICLE INFO

Article history:

Received 15 April 2015

Received in revised form

18 November 2015

Accepted 3 February 2016

Keywords:

Particles

Cluster ions

Attachment rate

Indoor air

Radon

ABSTRACT

Concentration and size distribution of airborne particles (size range 10–1100 nm), using a SMPS+C Scanning Mobility Particle Sizer, and concentrations of positive and negative cluster ions (size range 0.36–1.6 nm), using several CDI-06 Gerdien-type integral air ion detectors, have been monitored in three rooms in rural dwellings of Serbia and Slovenia, during periods when nobody was present in the room and while smoking and heating were taking place. The highest particle generation rate was $2.4 \times 10^{11} \text{ min}^{-1}$ while cigarette smoking was taking place and was $1.5 \times 10^{11} \text{ min}^{-1}$ during heating with a cast iron stove with wood burning at 150 °C, and $1.1 \times 10^{10} \text{ min}^{-1}$, during heating with an Alpine-type oven at 40–50 °C. The related particle loss rate constants were 0.0603 min^{-1} , 0.0442 min^{-1} , and 0.0067 min^{-1} . The estimated mean values of the effective ion attachment rate β_{eff} vary between $(2.2\text{--}5.4)10^{-6} \text{ cm}^3 \text{ s}^{-1}$. A correlation between ions concentration and particles concentration and their sizes has been sought, and findings are discussed and shown.

© 2016 Published by Elsevier Ltd.

1. Introduction

Particulate matter is classified by size (Morawska, Moore & Ristovski, 2004; Tammet & Kulmala, 2005) as: coarse particles with an aerodynamic diameter between 2.5 μm and 10 μm, and fine particles between 0.1 μm and 2.5 μm. Ultrafine particles include all particles with aerodynamic diameter of under 0.1 μm. Parts of ultrafine particles size range are defined as Aitken nuclei (20–90 nm), nano-particles (under 50 nm) and particles in the range from 3 to 20 nm referred as the “nucleation mode”, also called the ultrafine mode (Tammet & Kulmala, 2005).

Many studies have been carried out on aerosol growth and generation dynamics in urban environments due to a growing concern about human health (Oberdörster, Oberdörster & Oberdörster, 2005; Heal, Kumar & Harrison, 2012; Kumar et al., 2014; WHO, 2013). Epidemiologic studies suggest that toxicity of inhaled particles is not related due only to their mass, but mostly to their number concentration and surface area (Wichmann & Peters, 2000; Oberdörster et al., 2005; Nel, Xia, Mädler & Li, 2006; Murr & Garza, 2009). With regard to indoor air, the extent of change in number concentration and size distribution of particles is strongly dependent on the type of house heating. In a rural or suburban indoor environment, where almost no traffic or industry is present, the main source of artificially created ultrafine particles are human activities such as fossil fuel burning, cooking (mainly from heating of hot plate) and cigarette smoke (Wallace, 2000; Afshari, Matson & Ekberg, 2005; Morawska, He, Hitchins, Mengersen & Gilbert, 2003; Hussein, Hameri, Heikkinen & Kulmala, 2005; Wallace, 2006).

As has been mentioned, indoor activities such as the use of wood and coal for heating and cooking, candle burning and smoking create great amounts of ultrafine particles. If the combustion of carbon is complete then the only products are CO₂

<http://dx.doi.org/10.1016/j.jaerosci.2016.02.002>

0021-8502/© 2016 Published by Elsevier Ltd.

1 and water. Incomplete combustion produces particulate matter and different gasses. Most combustion particles in terms of
 3 number concentration and size are in the ultrafine range, while mass concentration is in the sub-micrometre range. Other
 5 sources of ultrafine particles are gas-to-particle conversion, nucleation and a photochemical process emitted directly from
 7 source (primary emission) or a secondary aerosol formation from gaseous precursors (nucleation mode).

11 It has been shown (Matson, 2005; Hussein et al., 2005, 2006) that when there is no particle source indoors, most indoor
 13 particles are of outdoor origin, brought in by air penetration, the indoor/outdoor concentration ratio being 0.5–0.8 and
 15 rarely exceeding 1. Indoor concentration is a result of three main contributions: penetration of outdoor particles, indoor
 17 production by human activity, and deposition. These processes are described by the equation (Koutrakis, Briggs & Leaderer,
 19 1992; Chen, Yuanhui & Barber, 2000; He, Morawska, Hitchins & Gilbert, 2004; Wallace, Emmerich & Howard-Reed, 2004,
 21 Hussein et al., 2005).

$$\frac{dN_{\text{tot}}^{\text{in}}}{dt} = P\lambda_v N_{\text{tot}}^{\text{out}} - (\lambda_v + \lambda_d)N_{\text{tot}}^{\text{in}} + \frac{Q_s}{V} \quad (1)$$

with:

$N_{\text{tot}}^{\text{in}}, N_{\text{tot}}^{\text{out}}$ – indoor and outdoor total particle number concentrations, cm^{-3}

P – outdoor → indoor particle penetration coefficient

λ_v – rate constant of air-exchange, h^{-1}

λ_d – rate constant of particle deposition, h^{-1}

Q_s – rate constant of particle generation of an indoor source, h^{-1}

V – room volume, cm^3 .

Its solution (Wallace et al., 2004)

$$N_{\text{tot}}^{\text{in}} = \frac{P\lambda_v N_{\text{tot}}^{\text{out}}}{\lambda_v + \lambda_d} + \frac{Q_s}{V(\lambda_v + \lambda_d)} (1 - e^{-(\lambda_v + \lambda_d)t}) \quad (2)$$

27 shows particle number concentration indoors at any time, as a result of the processes mentioned above. Coagulation and
 29 condensation are not comprised. Because P (Hussein et al., 2005; Wallace, 2006), λ_v (Matson, 2005; Hussein et al., 2005,
 31 2006) and λ_d (Hussein et al., 2006) are size-specific, their values in the above general form of Eq. (2) are considered as
 33 averages for all particles sizes.

35 Before the human activity starts to produce indoor particle at time $t=0$ (and $Q_s=0$), $N_{\text{tot}}^{\text{in}}(0)$ was equal to the first term on
 37 the right side of Eq. (2), and is considered as the baseline or background level of N_{tot} prior to an event caused by human
 39 activity. Because the outdoor particle concentration do not appear in the expressions hereafter, upper indices 'in' and 'out' at
 41 N_{tot} are omitted. With particle generation started, $\Delta N_{\text{tot}}(t) = N_{\text{tot}}(t) - N_{\text{tot}}(0)$ begins to grow and reaches its maximum value
 43 $\Delta N_{\text{tot}}(t_M)$ at time $t=t_M$, after the indoor particle source is stopped. $\Delta N_{\text{tot}}(t)$ decay follows. Thus, $\Delta N_{\text{tot}}(t_M)$ shows the
 45 maximum increase in particle number concentration during an event caused by human activity. Assuming that $N_{\text{tot}}(0)$ is
 47 constant during a short human activity event, Eq. (2) can be used to calculate the source generation rate:

$$Q_s = \Delta N_{\text{tot}}(t) \frac{V(\lambda_v + \lambda_d)}{1 - e^{-(\lambda_v + \lambda_d)t}} \quad (3)$$

49 Result for $\Delta N_{\text{tot}}(t_M)$ at $t=t_M$ gives the average particle generation rate Q_s . If Q_s is multiplied by t_M (duration of particle
 51 generation), total number of particles emitted during an activated source is obtained.

53 The $(\lambda_v + \lambda_d)$ sum can be obtained from the exponential decay of $N_{\text{tot}}(t)$ with time, starting soon after $\Delta N_{\text{tot}}(t_M)$ (Wallace
 55 et al., 2004; Hussein et al., 2005), by using the relation:

$$\ln \Delta N_{\text{tot}}(t) = \ln \Delta N_{\text{tot}}(t_{M+}) - (\lambda_v + \lambda_d)t, t > t_M, \quad (4)$$

47 in which $\Delta N_{\text{tot}}(t_{M+})$ is a value at a point after the maximum, where exponential form of the $\Delta N_{\text{tot}}(t)$ curve decay appears.

49 Cluster air ion generation depends primarily on indoor radon concentration which is related to local geology and floor
 51 insulation (United Nations Scientific Committee on the Effects of Atomic Radiation, 2000). He and Hopke (1996) showed
 53 that nucleation rates increase substantially with increasing radon at low activity concentrations. Unlike homogenous
 55 nucleation, ion-induced nucleation involves additional electrostatic interactions between vapour phase molecules and ions.
 57 The negative electrostatic energy helps to form stable ion clusters (pre-nucleation embryos) and lower the free energy
 59 barrier for nucleation. Both radon (^{222}Rn) and thoron (^{220}Rn) are α emitters with similar energies 5.49 MeV (Rn) and
 61 6.29 MeV (Tn) and the majority (almost 50%) of their radioactive descendants are also α emitters. Alpha particles, originated
 from radon and aerosol-carried radon progenies, are powerful air ionizers (average ionization energy of air is 34 eV/ion pair)
 and thus being the main source of air ion pair production in troposphere. The near-ground ionization rate caused by
 background ionization (cosmic radiation, natural radioactivity of soil and gasses) of 10 ion pairs $\text{cm}^{-3} \text{s}^{-1}$ is considered as a
 standard reference in continental areas (Chalmers, 1967).

Ions in the air are divided by size into small (cluster), intermediate and large ions. From atmospheric electricity point,
 most important class are small ions with size diameter $< 1.6 \text{ nm}$ with peak concentration $< 1 \text{ nm}$. The small ions are
 typically charged clusters with electric mobilities of $1\text{--}2 \text{ cm}^2 \text{ V}^{-1} \text{ s}^{-1}$ and size of $0.6\text{--}1 \text{ nm}$ (Tamm et al., 2005), and

are also called cluster ions. Concentration of cluster air ions (n^\pm) is determined by the balance equation:

$$\frac{dn^\pm}{dt} = q - \alpha n^\pm n^\mp - n^\pm \beta N \quad (5)$$

where q is the volumetric production rate, N is the aerosol number concentration, α coefficient of ion-to-ion recombination, and β_{eff} is the effective ion-to-aerosol particle attachment coefficient, which is the integral over the size distribution of aerosol particles. Typical ratio of positive and negative small air ion concentrations (n^+/n^-) in clean air is near to 1.12 (Hörrak, 2001). Concentration of cluster air ions is inversely proportional to the aerosol concentration. The solution of the differential Eq. (5) is given by the following equation:

$$n(t) = \frac{-\beta_{\text{eff}} + \sqrt{-\beta_{\text{eff}}^2 N^2 - 4\alpha q} \tan \left[\frac{1}{2} \left(k \sqrt{-\beta_{\text{eff}}^2 N^2 - 4\alpha q} - t \sqrt{-\beta_{\text{eff}}^2 N^2 - 4\alpha q} \right) \right]}{2\alpha} \quad (6)$$

or in equilibrium $dn/dt=0$:

$$q - \alpha n^2 - \beta_{\text{eff}} N_{\text{tot}} n = 0 \quad (7)$$

where k is a constant defined by the Cauchy boundary condition, and it was assumed that $n^+ \approx n^-$ which does not change the qualitative conclusion about the ion's behaviour.

The solution of the Eq. (5), when the usual intervals of values of parameters are used, shows direct reciprocity to the coefficient of the attachment rate. If the Eq. (5) is valid for the description of the ion's behaviour, then the only parameter of this equation which could make difference between the concentrations of the positive and the negative ions is the coefficient of the attachment rate (β_{eff}). Thus, the ratio of the positive and the negative ion concentration is directly proportional to the ratio between attachment rate of the positive and the negative ions ($n^+/n^- \sim \beta^+/\beta^-$) $\beta_{\text{eff}}^+/\beta_{\text{eff}}^-$. In fact, the attachment rate coefficient depends on the aerosol size and it is different for different polarity of the ions, if they are physically different (Hoppel & Frick, 1986), which is, in principle, a correct assumption. If the air ion concentration of both polarities is completely described by Eq. (5), all the other parameters are identical to this. The response of the Eq. (6) is very quick, so the local equilibrium is established in several seconds.

In highly polluted indoor air, cluster ions play important role in aerosol growth, but also sink due to deposition on electrostatic surfaces. Also, cluster ions evolve into nano-particles and accumulate in the ultrafine size range (Yu & Turco, 2000).

In this work, studies of the behaviour of aerosol particles and small positive and negative cluster ions in a rural dwelling have been carried out under different conditions: (i) when nobody was present in the room and (ii) during smoking and heating, human activities producing significant amounts of nanoparticles (Hussein et al., 2006; Wallace & Ott, 2011; Hosgood et al., 2012; Kumar et al., 2013). Concentrations of particles and ions were monitored and particle size distribution measured. One of our aims was also to evaluate interrelations of the measured quantities. Both particle generation and loss rates were determined, in order to quantify indoor particle sources and assess the exposure of residents during these activities.

Table 1
Characteristics of the selected experimental rooms.

Characteristic/room	Dwelling 1 Trubarevac Serbia Room-1	Dwelling 2 Resnik Serbia Room-2	Dwelling 3 Rakitna Slovenia Room-3
Room type	Guest room	Living room	Living room
Room size/m × m × m	4 × 5 × 2.7	4 × 3 × 2.6	5 × 5 × 2.6
Building material, walls	Brick, concrete	Brick, concrete	Stone, brick, concrete
Building material, floor	Parquet on concrete	Linoleum on concrete	Parquet on concrete
Basement underneath	No	No	No
Construction year/renewed	1980	1974	1910/1980
Regular heating	Water radiator of central system	Iron stove burning wood	Water radiator of central system
$C_{Rn}/\text{Bq m}^{-3}$	19 ^a	117 ^a	4600 ^b
$C_{Tn}/\text{Bq m}^{-3}$	211 ^a	220 ^a	< 20 ^b

^a Annual average (Mishra et al., 2014).

^b Weekly average (Vaupotič et al., 2013).

2. Experimental

2.1. Experimental rooms

The experiments were carried out in three rooms (Table 1) of the dwellings included in the national radon surveys in Slovenia (Vaupotič et al., 2013) and Serbia (Mishra et al., 2014). The rooms were selected on the basis of their radon and thoron levels. Thus, in guest Room-1 and living Room-2 (Trubarevac, and Resnik, respectively, Southern Serbia), both levels were low, with Tn level exceeding that of Rn (Table 1). In guest Room-3 (Rakitna, Slovenia), Rn levels were among the highest found in dwellings in the country, and substantially higher than Tn levels (Table 1). In contrast to a living room, which is the most occupied place in the house, a guest room is used only occasionally when relatives and friends gather to celebrate family festivals. All the dwellings were located in rural areas of a very low traffic, with only several cars and light agricultural equipment passing by a day.

2.2. Measuring instruments

An SMPS+C Scanning Mobility Particle Sizer was used, comprising a Condensation Particle Counter and a medium DMA unit (denoted as SMPS) (Grimm, Germany), to measure the number concentration and number size distribution of the aerosol particles in the size range of 10–1100 nm; analysis scanning frequency was once every 7 min. The following output data are presented and discussed: total number concentration of aerosol particles (N_{tot}), geometric mean of their electric mobility-equivalent diameter (d_{GM}), particle number size distributions ($dN(d)/d\ln d$, with d – electric mobility-equivalent diameter), and number concentrations of particles within selected size channels, i.e., 0–11.1 nm channel (N_{11}), 46.8–51.3 nm channel (N_{50}), 91.5–101.1 nm channel (N_{100}), 171.1–191.3 nm channel (N_{200}), and 271.8–307.4 nm channel (N_{300}).

Four CDI-06 Gerdien-type integral air ion detectors (Hirsikko et al., 2011) manufactured at the Institute of Physics, Beograd, Serbia, were used to continuously measure concentrations of positive and negative cluster ions in the air in the size range 0.36–1.6 nm ($3.15\text{--}0.5\text{ cm}^2\text{ V}^{-1}\text{ s}^{-1}$); air is pumped through the detectors at a flow rate of $5\text{ dm}^3\text{ s}^{-1}$ and acquisition frequency was set to 2 min (Kolarž, Filipović & Marinković, 2009; Kolarž, Miljković & Ćurguz, 2011).

Radon (^{222}Rn) and thoron (^{220}Rn) activity concentrations in air were measured with a RTM 1688-2 Radon/Thoron Monitor (Sarad, Germany). Air is pumped continuously through the detector at a flow rate of $3\text{ dm}^3\text{ min}^{-1}$ and analysis frequency was set to once an hour.

The owners of dwellings were asked to keep the experimental room closed and unattended at least a day prior to our measurements. The instruments were placed on tables, at a height of 80 cm above the floor, more than 0.5 m away from any wall, more than 3 m away from the door, and more than 3 m away from the heater. At each location, measurements lasted about a day, including overnights. There were long periods of measurement without human presence or activity (indicated as non-events) and several short periods affected by humans, such as checking instruments, lighting the fire, smoking cigarettes, etc. (indicated as events).

2.3. Calibration of instruments

Manufacturers of the SMSP system and RTM device regularly calibrate these instruments every two years. Air ion detectors were calibrated at the Institute of Physics, Beograd, Serbia. In addition, an inter-comparison experiment was carried out before our study. Detectors were placed side by side 1 m above the ground in a basement room with average radon and thoron activity concentrations during the experiment of $482 \pm 186\text{ Bq m}^{-3}$ and $761 \pm 265\text{ Bq m}^{-3}$. Results for negative ions are shown in Fig. 1. They show a standard deviation among detectors of less than 5%, which is satisfactory,

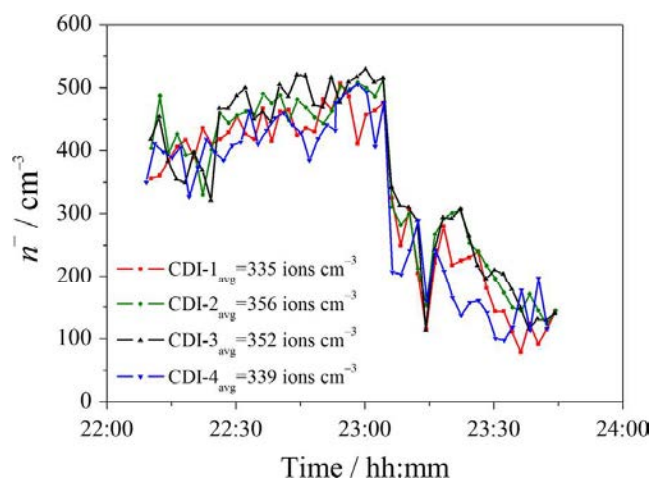


Fig. 1. Time variations of concentration of negative (n^-) ions, obtained with four ion detectors in the inter-comparison experiment.

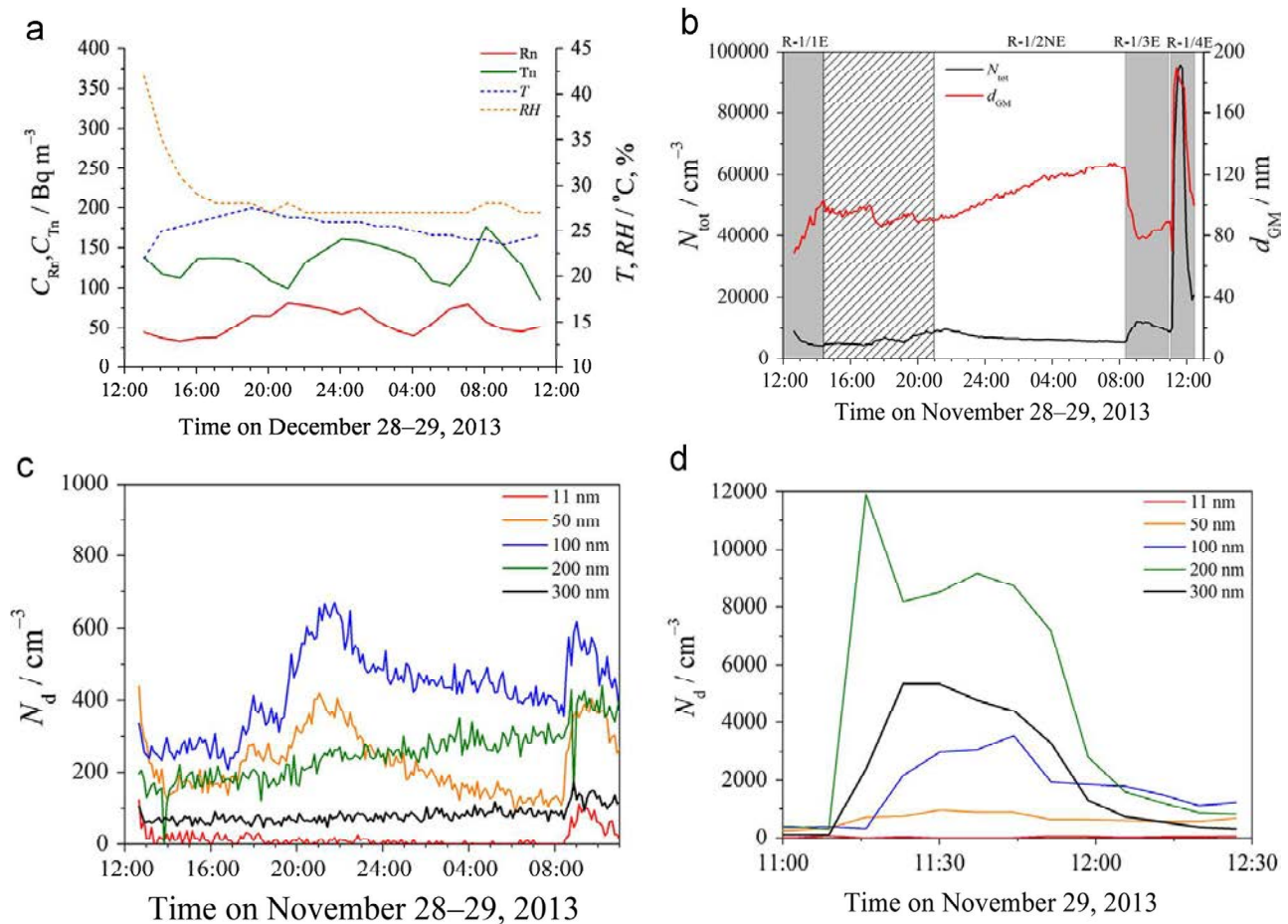


Fig. 2. (a) Time variations of activity concentrations of radon (C_{Rn}) and thoron (C_{Tn}), air temperature (T) and relative air humidity (RH) in Room-1. (b) Time variations of total number concentration of aerosol particles (N_{tot}) and geometric mean of their diameter (d_{GM}) in Room-1. (c) Time variations of number concentrations of particles within selected size channels (N_{11} , N_{50} , N_{100} , N_{200} and N_{300}), from the beginning to the R-1/4E smoking event in Room-1. (d) Time variations of number concentrations of particles within selected size channels (N_{11} , N_{50} , N_{100} , N_{200} and N_{300}) during R-1/4E smoking event in Room-1.

taking into account the non-ideal measuring conditions, micro-climatic influence on positions of detectors and overall uncertainty of air ion measurements.

3. Results and discussion

Results are presented and commented on for every experimental room separately. The average particle generation rate (Q_s) was calculated using Eq. (3), and rate constant of total particle loss ($\lambda_v + \lambda_d$), Eq. (4).

3.1. Room-1

After entering the room, about 60 min were needed for four persons to install the instruments and put them into operation. At that time, water radiators also connected to the central system were opened to keep the room warm. Then, the room was left and kept closed till 8:00 the next day when two persons entered the room for 10 min to check the instruments. At 11:00, three persons entered, one of them smoking a cigarette. Thus, the entire experiment is considered to show results of the following periods: the R-1/1E event of installation of instruments, the R-1/2NE non-event during the period when the room was unattended, the R-1/3E event of checking the instruments, and the R-1/4E event of cigarette smoking (Fig. 2a, Table 2).

Time variations of C_{Rn} , C_{Tn} , T and RH are shown in Fig. 2a. The temperature increased from its initial value of 22 °C to its maximum of 27 °C in the evening and then slowly decreased till the next morning. By heating, the initial RH value of 43% decreased in first several hours and then remained constant around 27% till next morning. Neither Rn nor Tn demonstrated their usual overnight maxima. Because of their low concentration, relative measurement errors were high and therefore time variations are not clearly seen.

Table 2

Description of events during measurements in Room-1, Room-2 and Room-3, with: $\Delta N_{\text{tot}}(t_M)$ – an increase of the total number particle concentration from the baseline to its maximum value, t_M – time needed for N_{tot} to reach its $\Delta N_{\text{tot}}(t_M)$ value, Q_s – average particle generation rate, and $(\lambda_v + \lambda_d)$ – rate constant of total particle loss.

Place event	Duration	Description	$\Delta N_{\text{tot}}(t_M)$ [cm^{-3}]	t_M [min]	Q_s [min^{-1}]	$\lambda_v + \lambda_d$ [min^{-1}]
Room-1						
R-1/1E	12:46–14:24	Starting measurements, 4 persons, 60 min				
R-1/2NE	20:56–08:15	No human activity				
R-1/3E	08:15–11:01	Checking measurements				
R-1/4E	11:01–12:26	Smoking, 3 persons present, 13 min, 1 smoking	8.7×10^4	36	2.4×10^{11}	0.0603
Room-2						
R-2/1E	10:26–12:47	Starting measurements and lighting wood in a stove, 4 persons, 90 min	7.6×10^4	28	1.5×10^{11}	0.0442
R-2/2E	13:02–00:59	5 Times adding wooden logs, 1 person, 1–2 min				
	08:40–10:34	3 Times adding wooden logs, 1 person, 1–2 min				
R-2/3NE	00:59–06:54	No human activity				
R-2/4E	06:54–08:19	Lighting wood in an iron stove, 1 person, 5 min	3.0×10^4	14	8.5×10^{10}	0.0291
Room-3						
R-3/1E	15:36–20:06	Starting measurements, 3 persons, 60 min				
R-3/2NE	20:06–06:52	No human activity				
R-3/3E	06:52–15:16	Alpine oven heating, without entering room	1.3×10^4	107	1.1×10^{10}	0.0067

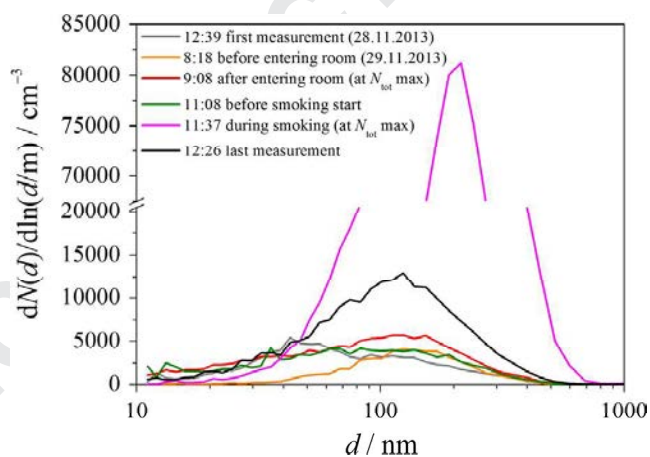


Fig. 3. Size distributions of aerosol particles ($dN(d)/d\ln d$) at selected times during measurement in Room-1, indicated in inset.

The initial values of N_{tot} and d_{GM} , obtained 10 min after our entry the room in the beginning of the R-1/1E event, were $8.9 \times 10^3 \text{ cm}^{-3}$ and 69 nm (Fig. 2b), respectively, with a bimodal size distribution of broad and not well pronounced maxima, higher at 40 nm and lower at 100 nm (Fig. 3). Then, N_{tot} was decreasing and d_{GM} , increasing for the next few hours. This trend points out that N_{tot} was even higher and d_{GM} , lower before our entry than shown by the first SMPS measurement. The N_{tot} maximum and d_{GM} minimum at 14:24 may be considered as the time when the R-1/1E event ended. Afterwards, N_{tot} and d_{GM} started to fluctuate around 5000 cm^{-3} and 95 nm (Fig. 2b), respectively, presumably because of entries to the room (see later in the text), although the residents denied this. Average values of n^+ and n^- for this event were 538 cm^{-3} and 259 ions cm^{-3} while the ratio $n^+/n^- = 2.1$. After the room air was disturbed as a result of people entering the room to read the instruments, the ion concentration started to rise as a consequence of radon accumulation. A few rapid drops of ion concentration visible in Fig. 4a are caused by opening the door and air perturbation inside the room.

Thus, as an R-1/2NE non-event may be represented by the period between 20:56 and 8.18 the next morning, when the aerosol was not affected by human activity, as confirmed by smooth runs of both curves in Fig. 2b: N_{tot} was steadily decreasing and d_{GM} , increasing, presumably because of particle coagulation; the highest values of N_{50} and N_{100} started to

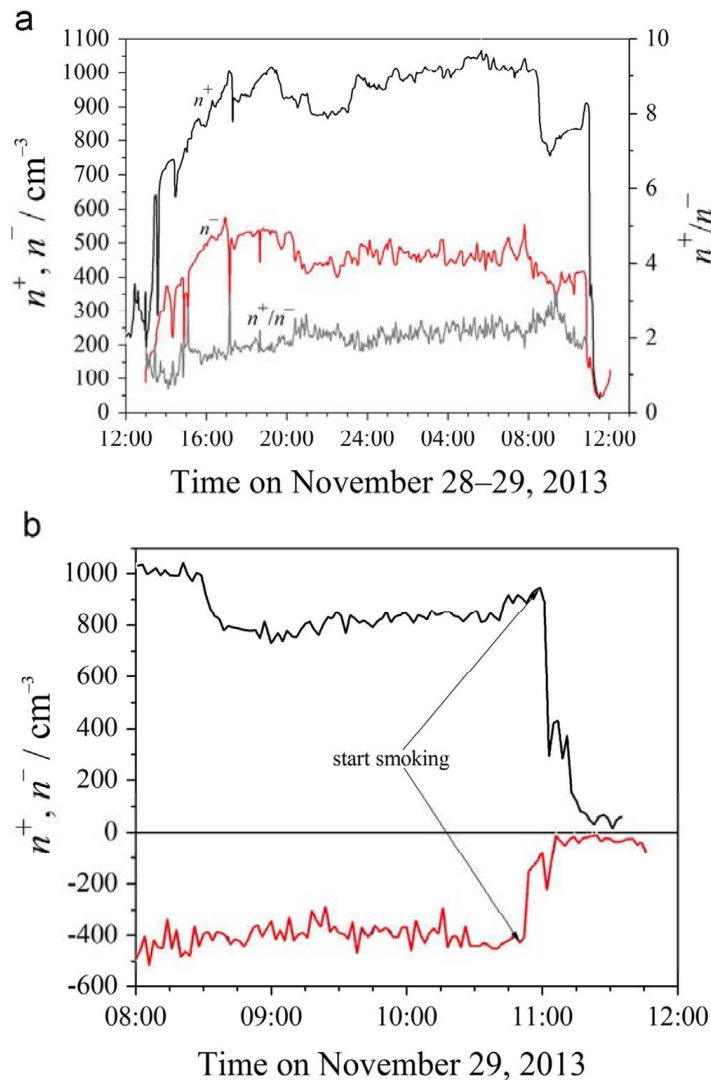


Fig. 4. (a) Time variation of positive (n^+) and negative (n^-) ion concentrations and ratio of positive to negative ions concentration (n^+/n^-) in Room-1. (b) Magnified time section of (a) between 8:00 and 11:45 in Room-1.

decrease after 21:00, while N_{200} and N_{300} steadily increased (Fig. 2c). The average positive ion concentration for this event was 981 ions cm^{-3} with tendency to slowly rise. At the same negative ion concentration remained constant with average of 460 ions cm^{-3} with ratio $n^+/n^- = 2.1$.

The R-1/3E event started at 8:15 when two persons entered the room for 10 min to survey measurements. N_{tot} increased from $5.8 \times 10^3 \text{ cm}^{-3}$ to $12.2 \times 10^3 \text{ cm}^{-3}$ and d_{GM} , decreased from 125 nm to 78 nm, mainly due to an increase of N_{100} and to a lesser extent of N_{50} and N_{200} (Fig. 2c), either brought in by persons, or resuspended by the movement of disturbed air. As a result, size distribution (Fig. 3, at 8:18) was extended towards smaller sizes (Fig. 3, at 9:08). It is not understood why this time N_{tot} and d_{GM} changes are opposite to those in the R-1/1E event. After they left the room, N_{tot} and d_{GM} resumed their trend from before their entry, i.e., of decreasing and increasing, respectively. Nevertheless, they did not reach their values of 8:18 and the R-1/3E event did not terminate, but is considered having continued until the smoking event started at 11:01 (R-1/4E). In this period $n^+ = 841 \text{ ions cm}^{-3}$ and $n^- = 385 \text{ ions cm}^{-3}$, ratio $n^+/n^- = 2.2$.

Average values for all 3 events of n^+ and n^- were 768 cm^{-3} and 368 ions cm^{-3} , respectively. Similarly as d_{GM} , n^+/n^- was increasing till the room was entered (Fig. 4a), due to increase of positive ions concentration and uniform concentration of negative ions. Typical cluster ion concentration peak at dawn (Kolarž et al., 2009), due to temperature inversion (Blauboer & Smetsers, 1996), was absent, probably due to good house insulation. Average positive to negative ion ratio was $n^+/n^- = 2.1$, showing relatively high ion to aerosol attachment coefficient or presence of electrostatic surfaces that was lowering n^- .

At 11:01 the R-1/4E event of smoking started. Three persons entered the room and one was asked to smoke a cigarette at a distance of 2 m from the instrument inlets. As seen in Fig. 2d, smoking produced a significant amount of the 100–300 nm particles (with 200 nm particles prevailing), thus causing a substantial increase of both N_{tot} from $8.7 \times 10^3 \text{ cm}^{-3}$ to $9.6 \times 10^4 \text{ cm}^{-3}$ and d_{GM} from 90 nm to 190 nm (Fig. 2b). This resulted in shifting the size distribution maximum to 220 nm (Fig. 3, at 11:37) and eliminating almost all cluster ions (Fig. 4a). At the same time, a rapid cluster ion sink was observed

(Fig. 4a and b). At the last reading, 40 min after the smoking stopped, size distribution gained a similar pattern as before smoking, with a maximum at about 110 nm (Fig. 3 at 12:26). Nevertheless, number of particles still remained high, pointing out that the consequence of the R-1/4E event had not been terminated and could last for longer periods (Afshari et al., 2005; Hussein et al., 2006).

The highest particle concentration of $8.5 \times 10^4 \text{ cm}^{-3}$ above the baseline reached during the R-1/4E event (Table 2) is markedly lower than that observed by Morawska et al., (2003) between $2.0 \times 10^5 \text{ cm}^{-3}$ and $3.6 \times 10^6 \text{ cm}^{-3}$ and by Afshari et al. (2005) of $2.2 \times 10^5 \text{ cm}^{-3}$, but higher than that reported by He et al. (2004) of $2.7 \times 10^4 \text{ cm}^{-3}$ and Hussein et al. (2006) of $3.6 \times 10^4 \text{ cm}^{-3}$. Our particle size of 100–300 nm is ranked between the reported values of 400–500 nm (Afshari et al., 2005) and 6–50 nm (Van Dijk, 2011). The difference may be explained by measurement conditions. Van Dijk (2011) used a smoking machine with an analysis frequency higher than 1 s^{-1} , and were thus able to detect particles in their nascent state, before any growth. On the other hand, our cigarette was (i) smoked by a person, (ii) 2 m away from the instrument inlet, (iii) two other persons were present, and (iv) the first reading was 7 min after the smoking started. Thus, particles had time to grow (Kulmala et al., 2004; Hussein et al., 2005; Hu et al., 2010).

Average particle generation rate during the R-1/4E of $2.4 \times 10^{11} \text{ min}^{-1}$ (Table 2) was about five times higher than that found by Hussein et al. (2006) of $4.9 \times 10^{10} \text{ min}^{-1}$, and about 1.5 times lower than $3.8 \times 10^{11} \text{ min}^{-1}$ of Afshari et al. (2005) – possibly because of our higher $\lambda_v + \lambda_d$ value of 0.0603 min^{-1} (Table 2) than theirs of 0.011 min^{-1} . The total number of particles emitted was 8.7×10^{12} .

Over the past decade, exposure to particles produced by smoking has been reduced noticeably in public places, because the number of countries which prohibit smoking at these places has been growing. There have been a few humble trials to also ban smoking indoors in private places, but these have not resulted in more than recommendations, and the decision is left to residents themselves.

3.2. Room-2

At 9:00, five persons entered the room for 90 min to install the instruments, along with the owner, who lit a fire of wood in a small cast iron stove. During his procedure, the stove top lid was open and hot air with smoke could easily expand into the room. Everybody then left, and the owner entered the room for several min at 12:00, 15:05, 16:30, 18:30 and 23:00 to

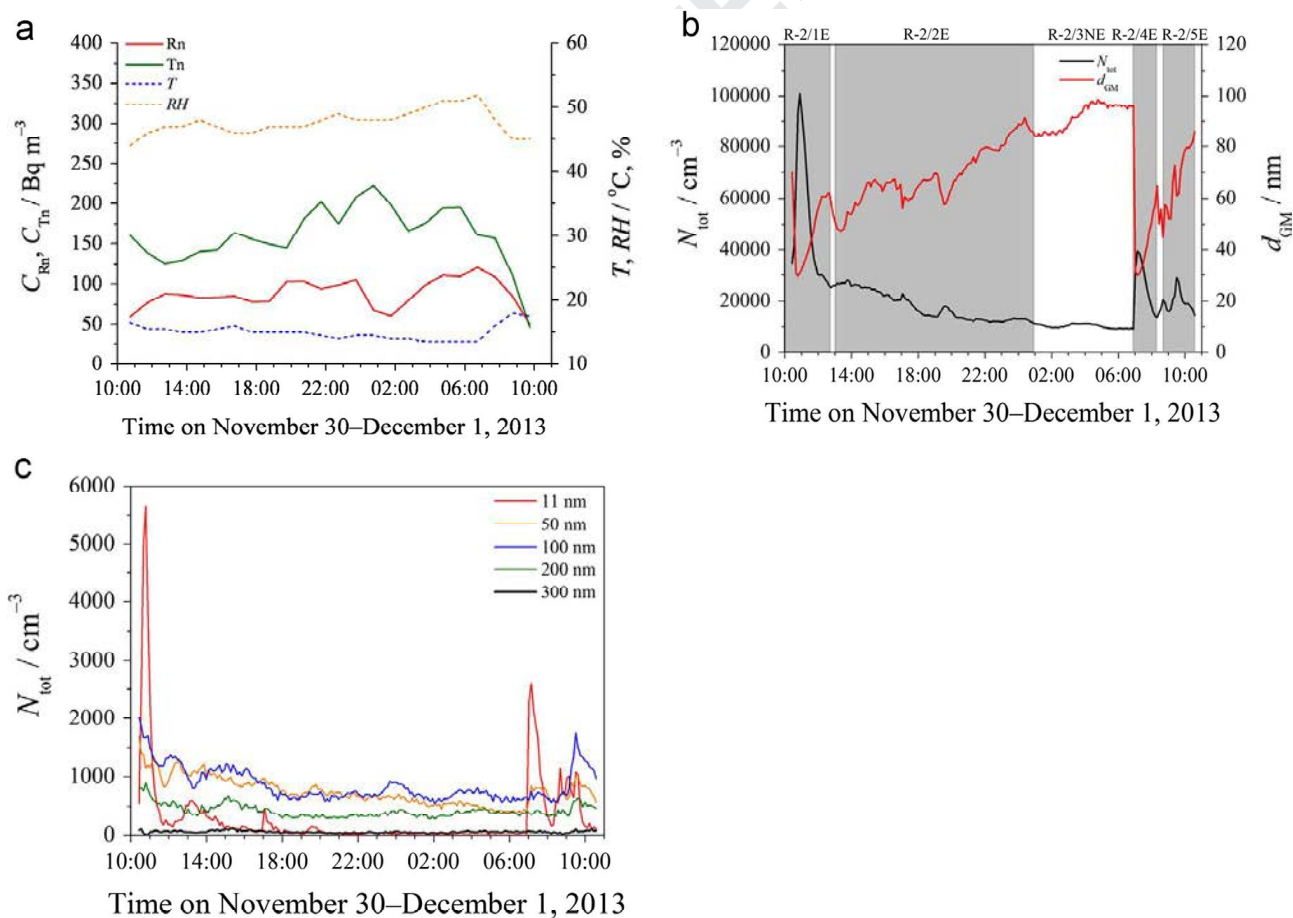


Fig. 5. (a) Time variations of activity concentrations of radon (C_{Rn}) and thoron (C_{Tn}), air temperature (T) and relative air humidity (RH) in Room-2. (b) Time variations of total number concentration of aerosol particles (N_{tot}) and geometric mean of their diameter (d_{GM}) in Room-2. (c) Time variations of number concentrations of particles within selected size channels (N_{11} , N_{50} , N_{100} , N_{200} and N_{300}), in Room-2.

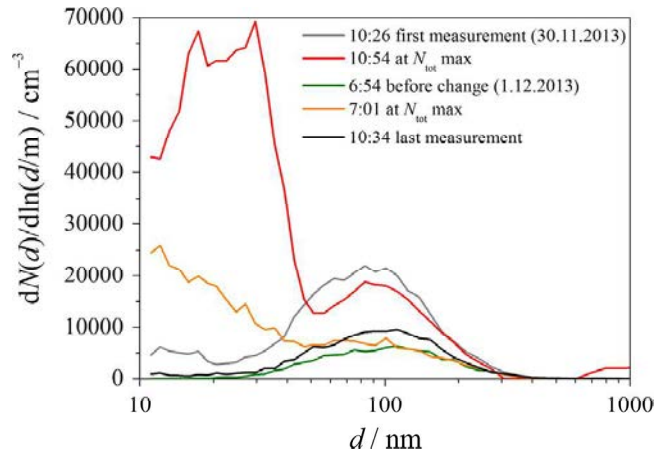


Fig. 6. Size distributions of aerosol particles ($dN(d)/d\ln(d)$) at selected times during measurement in Room-2, indicated in inset.

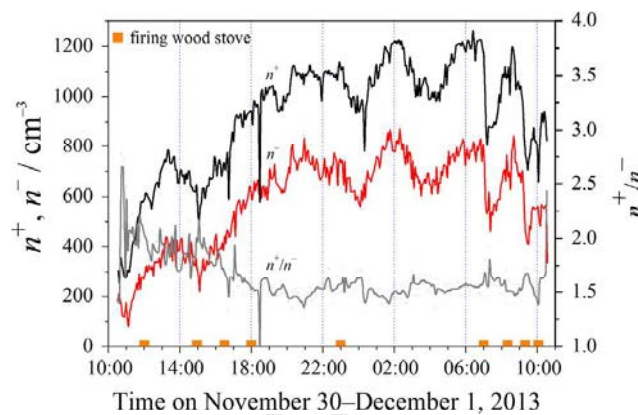


Fig. 7. Time variation of positive (n^+) and negative (n^-) ion concentrations and ratio of positive to negative ions concentration (n^+/n^-) in Room-2.

add wood logs to the stove and keep the room warm. At 7:00 the next morning, the owner entered the room for 5 min to light the fire; he entered for several minutes again at 8:21, 9:20, and 10:05, to add fuel to the fire. As the fire burned the stove heating surface area of about 0.5 m^2 was about $150 \text{ }^\circ\text{C}$.

Thus, the entire measurement comprised: a of installing instruments and lighting fire in the beginning, followed by five similar $R-2/2E$ events of adding wood logs, a $R-2/3NE$ non-event during the period when the room was closed and unattended, the $R-2/4E$ event of lighting fire in the morning, followed by three $R-2/2E$ events of adding wood logs (Fig. 5b, Table 2).

During the measurement (Fig. 5a), R_n and T_n levels were similarly low as in Room-1, while air temperature was lower and relative air humidity higher than in Room-1 (Fig. 2a). While T was almost constant at about $15 \text{ }^\circ\text{C}$, until next morning at 7:00 when it was slightly increased, RH was steadily increasing and decreased toward the end of measurement.

The first SMPS measurement in the $R-2/1E$ event 10 min after our entry showed (Fig. 5b) $N_{\text{tot}} = 3.5 \times 10^4 \text{ cm}^{-3}$ and $d_{\text{GM}} = 70 \text{ nm}$, the former being much higher and the latter similar to the value in Room-1 (Fig. 2b). The initial particle size distribution (Fig. 6 at 10:26) was bimodal, with a not well expressed maximum at 10–20 nm and a broad population between 40 and 200 nm, maximised at about 80 nm. Bimodal distributions were observed also by Hussein et al. (2005) and Zhang et al. (2012), though not with maxima at the same sizes. Our presence and activities in the room (above all lighting the fire) caused a drastic increase of N_{tot} to its maximum of $1.0 \times 10^5 \text{ cm}^{-3}$ and decrease of d_{GM} to its minimum of 30 nm (Fig. 5b), mainly due to a sharp increase of concentrations of the 11 nm particles, while concentrations of the 50–200 nm particles had been decreasing since the very beginning (Fig. 5c). As a result, at the N_{tot} maximum, size distribution (Fig. 6 at 10:54) was composed of a lower maximum at about 80 nm (as initially) and higher, not well separated maxima at 15 nm and 30 nm, thus differing from distribution by Zhang et al. (2012) with a single maximum in the latter size range. Particles in the size region of around 100 nm have been reported in a number of works (EPA, 2000; Hedberg et al., 2002; Weichenthal, Dufresne, Infante-Rivard & Joseph, 2007; Burtscher, 2010; Commodo, Sgro, D'Anna & Minutolo, 2012). Differences in results most probably originate from different burning conditions, first of all material, construction and temperature of the stove, as well as kind of wood (EPA, 2000). In our size distribution, a noticeable contribution of secondary particles of unknown size is also expected, as dirt and dust is lifted from the hot oven surface (Pedersen, Bjørseth, Syversen & Mathiesen, 2001).

During the $R-2/1E$ event, N_{tot} increase of $7.6 \times 10^4 \text{ cm}^{-3}$ above the baseline (Table 2) was bigger than $1.5 \times 10^4 \text{ cm}^{-3}$ by Weichenthal et al. (2007). Average particle generation rate was $1.5 \times 10^{11} \text{ min}^{-1}$, and total number of released particles,

1 4.3×10^{12} , with loss rate constant, $\lambda_v + \lambda_d = 0.044 \text{ min}^{-1}$ (Table 2). The average generation rate of 11 nm particles was
 2 $2.2 \times 10^{10} \text{ min}^{-1}$ and reached its maximum concentration above the baseline 5.2×10^3 and total amount of released particles of 4.7×10^{11} . Their $\lambda_v + \lambda_d = 0.122 \text{ min}^{-1}$ was higher than 0.044 min^{-1} for all particles (comprising bigger ones), as
 3 expected (Hussein et al., 2006).

4 As N_{tot} , also concentration of cluster ions started to increase after we entered the room (Fig. 7). Although the frequency of
 5 Rn monitoring of 1 h^{-1} was too low to show Rn concentration in real time with the changes in ion concentration, one
 6 should not assume that Rn level is increased after entering the room – rather the opposite can be true. Therefore, Rn could
 7 not enhance the ion concentration. At the beginning, the increase of positive air ions was higher than of negative ones. This
 8 can be explained by higher particle concentration and accordingly higher attachment rate of negative air ions, resulting in
 9 their lower concentration. Average values, during the R-2/1E event, of n^+ , n^- and n^+/n^- were 470 ions cm^{-3} , 237 ions
 10 cm^{-3} , and positive to negative ion ratio 2.0, respectively (Fig. 7).

11 After this intense emission of smallest particles, N_{tot} and d_{GM} started to rapidly decrease and increase, respectively
 12 (Fig. 5b), due to a faster deposition (Hussein et al., 2006) of smallest particles; in less than an hour, N_{tot} and d_{GM} almost
 13 approached their initial levels. Thus, the R-2/1E event was understood as terminated at 12:00, when N_{11} reached its
 14 minimum (Fig. 5c).

15 This period was followed by five R-2/2E events in which the owner entered the room for 1–2 min, opened the stove and
 16 added logs of wood. His activity caused temporary fluctuations of N_{tot} and d_{GM} (Fig. 5b), and appearances of N_{11} peaks
 17 (Fig. 5c), although not as distinctive as when lighting the fire. During this period, the bimodal size distribution converts into
 18 a unimodal (Fig. 6 at 6:54), as observed also during wood burning by Zhang et al. (2012). Ion concentration was almost
 19 constantly increasing with a clearly visible sharp but short decrease of concentration caused by opening the door. At the
 20 same time ratio n^+/n^- increased, which is clearly related with lowering N_{tot} (Eqs. (5) and (6)).

21 During the R-2/3NE non-event in the period from 00:59 to 6:54 the next morning, when the room was left unattended,
 22 N_{tot} decreased further and d_{GM} , which increased because of particle coagulation, to reach their lowest and highest values,
 23 respectively (Fig. 5b), with size distribution shown in Fig. 7 (at 6:54). This distribution is slightly shifted to higher sizes with
 24 losing smaller sizes tail when compared to that in the beginning of measurements (Fig. 6 at 10:26).

25 The R-2/4E event commenced after the owner entered the room at 7:00 to light the fire. N_{tot} abruptly increased and d_{GM}
 26 abruptly decreased (Fig. 5b), similar to the R-2/1E event, although not to the same extent because there was only a single
 27 person present for a shorter period. Again, N_{tot} peak was mostly contributed by 11 nm particles and to a lesser extent, by
 28 50 nm and 100 nm particles (Fig. 5c). Size distribution at the N_{tot} peak (Fig. 6 at 7:01) differed from that at the first N_{tot} peak
 29 the previous day (Fig. 6 at 10:54) by a significantly smaller contribution of $< 50 \text{ nm}$ particles. After the owner left the room,
 30 N_{11} started to decrease, resulting in a decrease in N_{tot} and increase in d_{GM} (Fig. 5b), similar to after initially lighting fire the
 31 previous day. The time when N_{11} reached its minimum was considered of the end of the R-2/4E event.

32 During the R-2/4E event, particle generation rate was $8.5 \times 10^{10} \text{ min}^{-1}$, their total number released, 1.2×10^{12} , maximum
 33 concentration increase $3.0 \times 10^4 \text{ cm}^{-3}$ above the baseline, and $\lambda_v + \lambda_d = 0.029 \text{ min}^{-1}$ (Table 2). And for the 11 nm particles:
 34 $Q_s = 8.4 \times 10^9 \text{ min}^{-1}$, $\Delta N_{11}(t_M) = 2.4 \times 10^3 \text{ cm}^{-3}$, $\lambda_v + \lambda_d = 0.060 \text{ min}^{-1}$, and total number of released particles was 1.2×10^{11} .
 35 It is not clear at the moment why this $\Delta N_{11}(t_M)$ increase was for an order of magnitude lower than in the experiment of
 36 Zhang et al. (2012), with $2.0 \times 10^5 \text{ cm}^{-3}$ increase of 10–20 nm particles and $1.0 \times 10^5 \text{ cm}^{-3}$ increase of 40–50 nm particles.

37 Because heating cannot be stopped, the owner would substantially reduce exposure to nano-particles by choosing a
 38 suitable heater and fuel (EPA, 2000) with a lower temperature of the heating body and by maintaining clean and dust-free
 39 hot surfaces (Pedersen et al., 2001).

40 The origin of the 11 nm particles during the R-2/1E and R-2/4E events (Fig. 5c) has not been clarified. They can hardly be
 41 ascribed to dirt and dust lifted from the hot stove surface (Pedersen et al., 2001; Afshari et al., 2005), because these were not
 42 emitted during the entire period of burning, but only during the time of lighting the fire when several (one in the second
 43 morning) persons were in the room and the stove lid was open, enabling hot air and smoke to expand into the room. Did
 44 they originate from the persons' breathing and skin evaporation or were they produced by volatile organic compounds
 45 (VOC; He & Hopke, 1996; O'Dowd, Aalto, Hmeri & Kulmala, 2002; Wang, Ang & Tade, 2007) released from fire? (Hedberg
 46 et al., 2002; Cerqueira, Gomes, Tarelho & Pio, 2013; Evtuyugina et al., 2014).

47 This period was followed by three R-2/2E events with the owner's entries to the room to fuel the fire. Similarly as in the
 48 previous afternoon, these caused fluctuations in d_{GM} increase and N_{tot} decrease (Fig. 5b).

49 Based on the N_{tot} and d_{GM} situation at 6:54 and soon afterwards (Fig. 5b), one may speculate that N_{tot} might have been
 50 lower and d_{GM} , higher than found by the first SMPS measurement.

51 Unlike in Room-1, a cluster ion concentration peak at dawn (Fig. 7 at 6:00) was visible here. Ion concentration minima at
 52 about 04:00 that coincided with C_{Rn} maxima is difficult to explain and is probably a consequence of artefact. An increase of
 53 d_{GM} and a decrease of N_{tot} resulted in an increase of air ion concentrations of both polarities (Fig. 7). Obviously, n^+ and n^-
 54 changes coincide with the firing of wood stove. Changes were caused by opening the room door, entry of air from outside,
 55 and also by opening the stove when a lot of smoke particles entered the room and attracted the cluster ions. Thus, ions
 56 became larger and could not be detected by the system. Increase of n^+ and n^- was accompanied by d_{GM} increase and N_{tot}
 57 decrease (Fig. 5b).

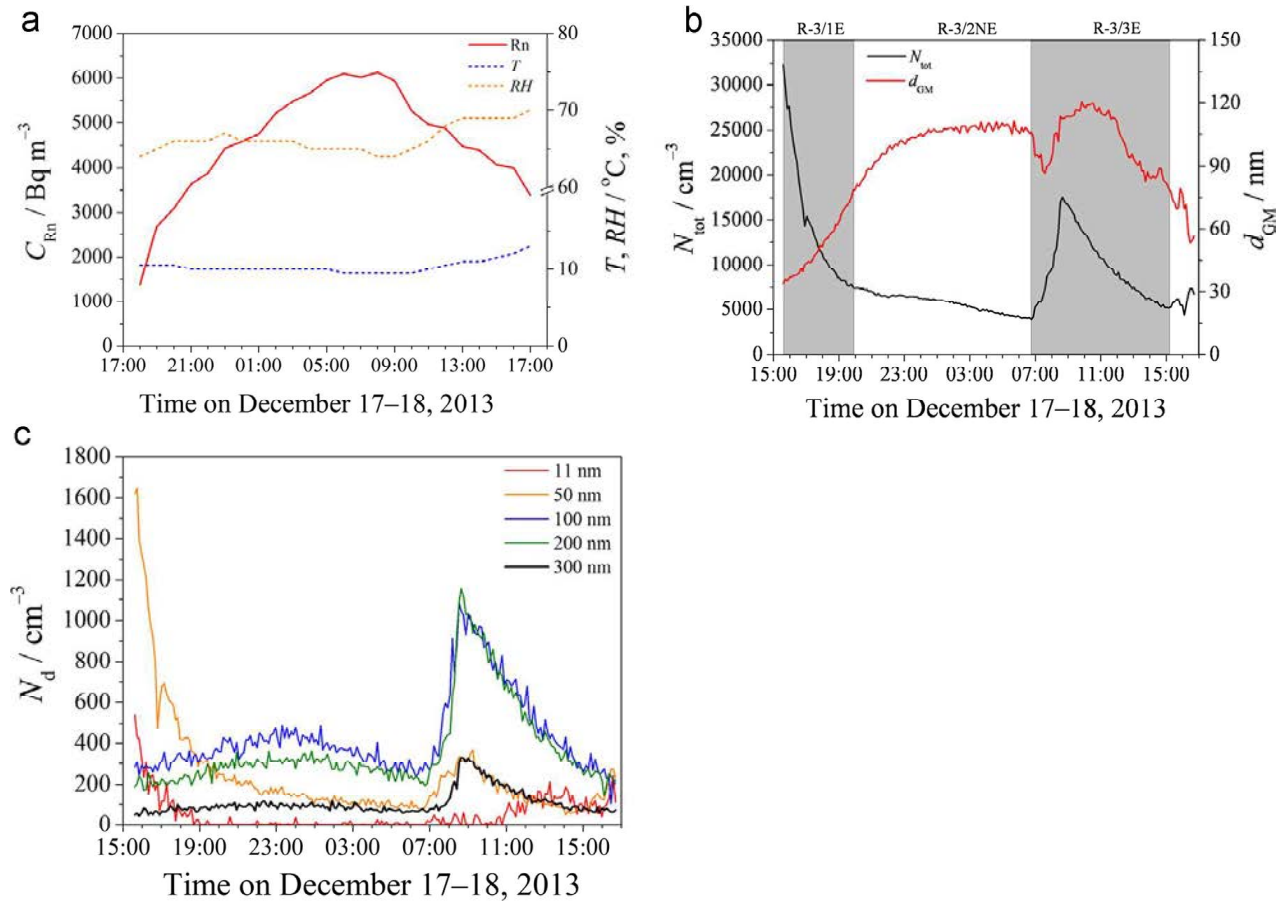


Fig. 8. (a) Time variations of activity concentrations of radon (C_{Rn}), air temperature (T) and relative air humidity (RH) in Room-3 (Tn levels were too low to be shown). (b) Time variations of total number concentration of aerosol particles (N_{tot}) and geometric mean of their diameter (d_{GM}) in Room-3. (c) Time variations of number concentrations of particles within selected size channels (N_{11} , N_{50} , N_{100} , N_{200} and N_{300}) in Room-3.

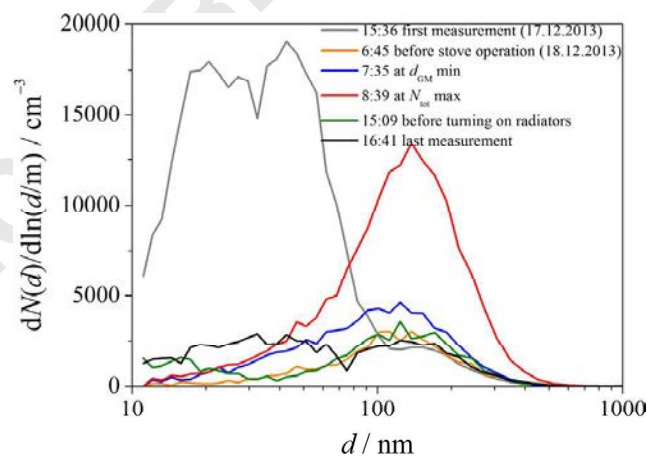


Fig. 9. Size distributions of aerosol particles ($dN(d)/d\ln(d)/dm$) at selected times during measurement in Room-3.

3.3. Room-3

The experimental room is mostly heated with water radiators connected to the central heating system, and temporarily with an Alpine-type oven; its heating body (about 6 m² surface area), made of special clay brick and covered with ceramic tiles, is in the guest room (experimental room) and the door to add wooden logs and place dough to bake bread is located in the kitchen. The room had been closed for five days prior to our measurement. After the measurements were started, the room was left unattended till the next afternoon when the radiator was turned on at 15:52. At 6:45 the next day, the fire in the oven was lit, without entering the room. Thus, the entire measurement may be divided into the following event: the R3/

1E event of installing instruments, followed by the R3/2NE non-event till next morning when the R3/3E event started to cover the period of the oven heating (Fig. 8b, Table 2).

In contrast to the previous rooms, in Room-3, Tn level was mostly below the detection level and Rn concentration was substantially higher, showing a typical diurnal variation, with a broad maximum overnight (Fig. 8a). Air temperature was almost constant around 10 °C, while relative humidity varied from 65% in the beginning to 70% in the end of measurement.

During the R-3/1E event, three persons were present for 60 min to install the instrument. The first SMPS reading 10 min after our entry showed $N_{\text{tot}} = 3.2 \times 10^4 \text{ cm}^{-3}$ and $d_{\text{GM}} = 34 \text{ nm}$ (Fig. 8b), presented by a size distribution with two high but not well separated peaks at around 20 nm and 50 nm, and a small, not well pronounced maximum at about 105 nm (Fig. 9 at 15:36). Because of a rapid N_{tot} decrease, one may speculate that particle concentration ought to be markedly higher prior to our entry and presence. As observed in our previous study in a rural environment (Smerajec & Vaupotič, 2013), N_{tot} in outdoor air reached $(20\text{--}40) \times 10^4 \text{ cm}^{-3}$ levels in the early afternoon, often 30% populated by the $< 10 \text{ nm}$ particles, and then decreased towards 1000 cm^{-3} or even lower, with only several percent of the $< 10 \text{ nm}$ particles. Our initial indoor N_{tot} value in the R-3/1E event resembled that observed outdoors, thus showing that indoor particles prior to our entry were mostly of outside origin; the smaller contribution of the $< 10 \text{ nm}$ particles (538 cm^{-3} , Fig. 8c) was simply due to smaller outdoor \rightarrow indoor penetration coefficient P for this particle size (Hussein et al., 2005; Wallace, 2006).

In first hours, N_{11} and N_{50} rapidly decreased (Fig. 8c), presumably because our entry and presence caused air movement and as a consequence a preferential deposition of the smallest particles (Hussein et al., 2006), or simply because of diurnal change in the outdoor air aerosol concentration. On the other hand, N_{100} and N_{200} were slowly but steadily increasing and reached maximum at about midnight, while N_{300} was permanently low and almost unchanged (Fig. 8c). These changes are reflected in a steady N_{tot} decrease and d_{GM} increase. The border between the R-3/1E event and the R-3/2NE non-event is argued because the time at which consequences of our presence in the room ceased, is to fix; it was probably around 22:00, when N_{tot} and d_{GM} changes became slower.

The average positive ion concentration in this period was $15,570 \text{ ions cm}^{-3}$ while negative was $12,467 \text{ ions cm}^{-3}$ with a ratio of $n^+/n^- = 1.2$. The lower ratio of positive and negative ions than in Room-1 and in Room-2 was due to a higher concentration of ions than of aerosols which limits the attachment rate of ions.

During the R-3/2NE after 22:00, N_{tot} and d_{GM} continued to decrease and increase steadily, respectively, though more slowly than before. Their final values the next morning before oven heating started were $3.9 \times 10^3 \text{ cm}^{-3}$ and $d_{\text{GM}} 106 \text{ nm}$, respectively. At that time, 11 nm and 50 nm particles almost disappeared (Fig. 8c) and size distribution showed a broad maximum at 100–110 nm (Fig. 9 at 6:45). Ion concentrations were in constant increase with averages $n^+ = 23,391 \text{ ions cm}^{-3}$ and $n^- = 21,140 \text{ ions cm}^{-3}$ and their ratio of 1.1.

The R-3/3E event started at 7:00, when the fire was lit in the oven from the kitchen side, without entering the room. As the oven grew warmer, a large amount of secondary particles appeared in air, mainly as dirt and dust lifted from the hot ($40\text{--}50 \text{ °C}$) oven surface (Pedersen et al., 2001; Afshari et al., 2005), and also resuspended from the floor, by thermal air movement, caused by the rising temperature of the heating body and the room air in general. The contribution of 100 nm particles was highest, followed by 200 nm, 50 nm and 300 nm particles (Fig. 8c). In first half-hour, the increase in N_{50} was higher than that of N_{200} , resulting first in a d_{GM} decrease at concomitant N_{tot} rising. Thus, size distribution at minimum d_{GM} was largely extended to smaller sizes (Fig. 9 at 7:35). After that, N_{tot} and d_{GM} increased simultaneously because of the large amount of 100 nm and 200 nm particles emitted (Fig. 8c), to show a sharp symmetrical peak at about 105 nm at maximum N_{tot} of $1.7 \times 10^4 \text{ cm}^{-3}$ (Fig. 9 at 8:39). Because of the different origin of particles in this event, this distribution is completely different from that shown in Fig. 6 at 10:54 for particles emitted during heating with an iron stove in Room-2.

At 8:39, the fire in the oven was extinguished and the heating surface of the oven started to slowly grow colder. After this peak, N_{tot} started to decrease, while d_{GM} increased further for an hour or so, thus demonstrating particle growth by coagulation (Kulmala et al., 2004; Hussein et al., 2005; Hu et al., 2010). Then d_{GM} also started to decrease, approaching the value in the beginning of measurement (Fig. 8b). On the other hand, final N_{tot} was quite different from the value in the beginning

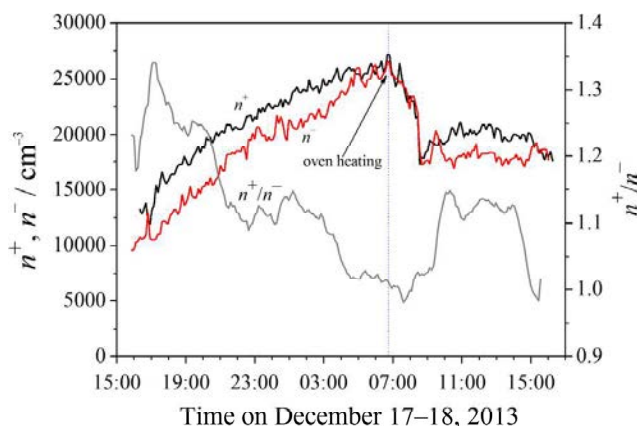


Fig. 10. Time variation of positive (n^+) and negative (n^-) ion concentrations and ratio of positive to negative ions concentration (n^+/n^-) in Room-3.

of measurements, but close to that before the R-3/3E started. Towards the end of measurement, the contribution of < 80 nm particles to the size distribution increased, thus emerging in two broad maxima in the 20–70 nm and 80–110 nm size regions (Fig. 9 at 16:41). This slightly resembled the shape in the first measurement (Fig. 9 at 15:36), though of much lower contribution of smaller particles.

The average particle generation rate during the stove heating was $1.1 \times 10^{10} \text{ min}^{-1}$ and the maximum increase in aerosol concentration above the baseline, $1.3 \times 10^4 \text{ cm}^{-3}$ (Table 2), substantially lower than the related values for the hot surface of an electric radiator of $8.8 \times 10^{11} \text{ min}^{-1}$ and $2.2 \times 10^5 \text{ cm}^{-3}$, respectively (Afshari et al., 2005), presumably because of higher radiator temperature. The total number of emitted particles was 1.2×10^{12} . Our $\lambda_v + \lambda_d$ value of 0.007 min^{-1} is only a half of theirs: 0.012 min^{-1} .

Because the room is used only occasionally for family gatherings and celebrations, the exposure to nano-particles is of no great concern. Nonetheless, the owner may diminish it by thoroughly cleaning the oven heating surfaces (Pedersen et al., 2001).

A person's entry for 1 min at 15:52 to turn on the water radiator caused only a small and short N_{tot} decrease and d_{GM} increase (Fig. 8b).

Lighting the fire in the stove caused a reduction of $n^+ = 20,342 \text{ ions cm}^{-3}$ and $n^- = 19,054 \text{ ions cm}^{-3}$ starting at 7:00. After three hours (11:00), cluster ion concentration started to slowly decrease as a result of radon concentration decrease.

Because of high radon levels (average 4600 Bq m^{-3}), radon and its short-lived products in this place are considered as a significant source of ionization and ion generation. This is manifested by much higher air ion concentrations than in Room-1 and Room-2. Time variations of n^+ and n^- are shown in Fig. 10. Increase of cluster ion concentration is followed by a reduction of the total number of aerosol particles, but also with the rise of their mean diameter. Similarly as in Room-2, the n^+/n^- ratio increased with an attachment coefficient, i.e., the number of particles.

3.4. Correlations

The correlation between the concentrations of the positive and the negative ions is relatively high: 0.84, 0.98 and 0.94 for Room-1, Room-2 and Room-3, respectively. As the perturbation of air ion concentration induced by the stove heating (R-3/3E) in Room-3 was significant, these data were treated as two groups: one before and the other during the R-3/3E event. In that case the correlation between n^+ and n^- are 0.97 and 0.83, before and during the R-3/3E event, respectively.

Although the correlations between n^+ and n^- are relatively high, the Mann–Whitney test shows that the normalized distribution of the positive and the negative ions are not significantly different (with 0.05 level of confidence) except in the case of Room-2. This implies that the involvement of all influences on the ion concentration is not included in the Eq. (1). *F*-test of variances difference between n^+ and n^- shows that the variances of the two distributions are significantly different (0.05 level of confidence) only during the R-3/3E event in Room-3, during the heating.

Coefficients of correlation (*R*) between n^+ , n^- , their ratio n^+/n^- on one side and N_{tot} , d_{GM} , and concentration of aerosols smaller than 50 nm ($N_{<50}$) and concentration of aerosol particles bigger than 50 nm ($N_{>50}$) on the other in Room-1 (Trubarevac), Room-2 (Resnik) and Room-3 (Rakitna) are presented in Table 3.

Table 3

Coefficients of correlation (*R*) between concentrations of positive ions (n^+) and negative ions (n^-) and their ratio (n^+/n^-), total number concentration of aerosol particles (N_{tot}), geometric means of particle diameter (d_{GM}), concentration of particles smaller than 50 nm ($N_{<50}$) and concentration of particles bigger than 50 nm ($N_{>50}$) in Room-1, Room-2 and Room-3 during different events.

		N_{tot} [cm^{-3}]	d_{GM} [nm]	$N_{<50}$ [cm^{-3}]	$N_{>50}$ [cm^{-3}]
Room-3, before R-3/3E	n^+ [cm^{-3}]	−0.88	0.95	−0.86	−0.58
	n^- [cm^{-3}]	−0.80	0.92	−0.78	−0.59
	n^+/n^-	0.38	−0.64	0.37	0.31
Room-3, during R-3/3E	n^+ [cm^{-3}]	−0.14	0.07	−0.05	−0.15
	n^- [cm^{-3}]	−0.04	−0.08	−0.04	−0.07
	n^+/n^-	−0.15	0.17	−0.64	−0.09
Room-2, during R-2/1E	n^+ [cm^{-3}]	−0.77	0.50	−0.67	−0.62
	n^- [cm^{-3}]	−0.73	0.49	−0.62	−0.89
	n^+/n^-	0.69	−0.44	0.64	0.64
Room-2, during R-2/3NE	n^+ [cm^{-3}]	−0.87	−0.04	−0.23	−0.92
	n^- [cm^{-3}]	0.79	0.16	0.11	0.87
	n^+/n^-	0.13	0.23	−0.16	0.193
Room-1, during R-1/1E	n^+ [cm^{-3}]	0.06	−0.08	−0.15	−0.14
	n^- [cm^{-3}]	−0.08	0.26	−0.22	0.01
	n^+/n^-	0.07	−0.02	0.10	0.02
Room-1, during R-1/2E	n^+ [cm^{-3}]	−0.88	0.82	−0.88	−0.87
	n^- [cm^{-3}]	−0.20	0.10	−0.16	−0.21
	n^+/n^-	−0.42	0.46	−0.45	−0.40
Room-1, during R-1/3E	n^+ [cm^{-3}]	−0.88	−0.81	−0.69	−0.88
	n^- [cm^{-3}]	−0.71	−0.66	−0.74	−0.70
	n^+/n^-	−0.56	−0.44	0.36	−0.57

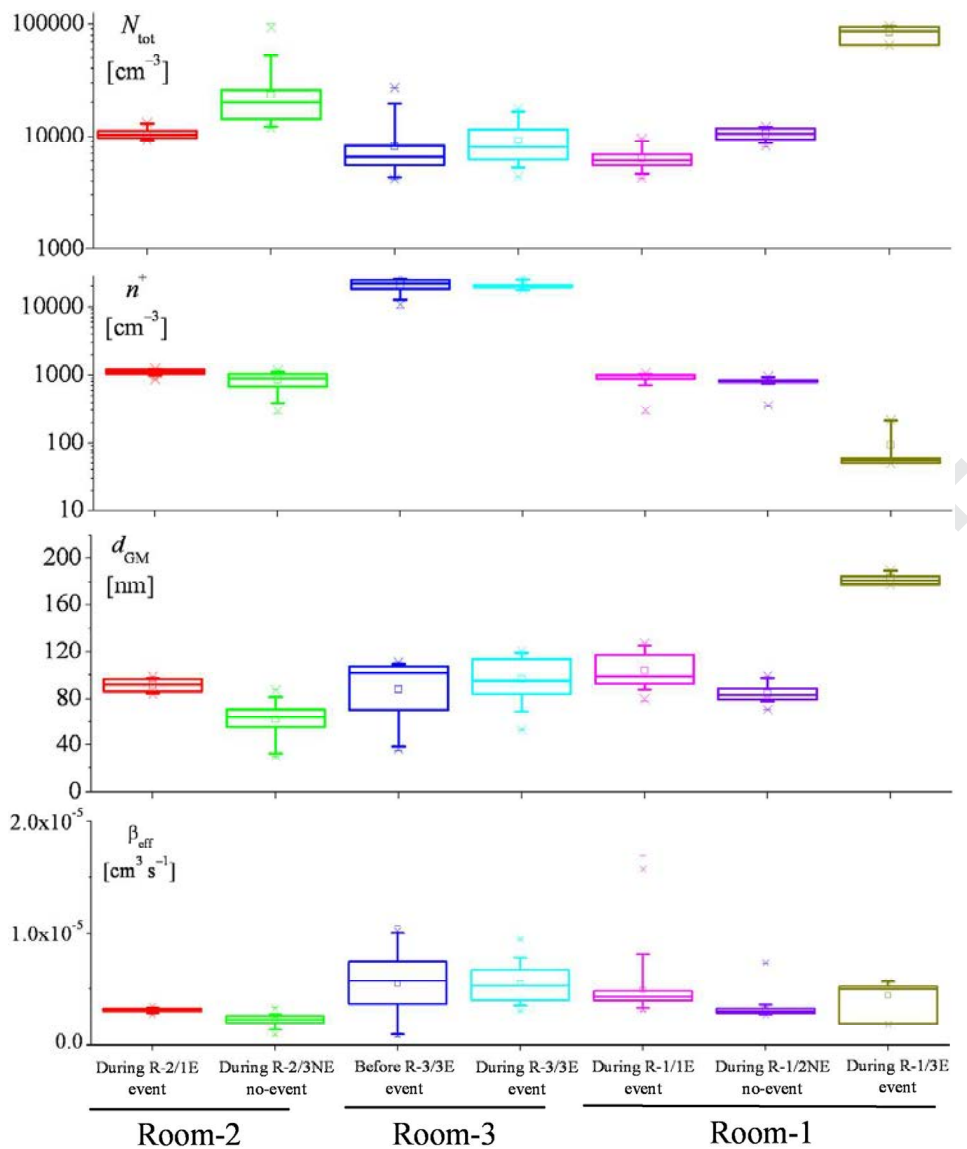


Fig. 11. The box chart of the total aerosol concentration (N_{tot}), the positive ions concentration (n^+), the geometric mean of the diameter of aerosols (d_{GM}) and the effective ion-aerosol attachment coefficient (β_{eff}). The charts are divided according to events. The box with inner line shows 1st quartile, median and 3rd quartile. The whiskers shows 5th and 95th percentile, the empty square shows an average, the cross shows 1st and 99th percentile and the minus sign shows minimum and maximum value.

As in the cases of Room-2 and Room-3, sudden increases of different fractions of particle sizes appeared during the measurement, thus their correlation with the ion concentration were investigated separately.

In the case of Room-3, during the R-3/3E event all correlations between ion and aerosol concentrations were lost. The exception is the slight negative correlation between the n^+/n^- ratio and the concentration of the aerosol fraction of 10–50 nm, although the positive correlation should be expected. This should be considered as a coincidence. Before the R-3/3E event, the correlations were more pronounced especially for the positive and negative ions, while for their ratio n^+/n^- , the correlations are weak, with exception of the correlation with the geometric mean of aerosol diameter which was moderate (0.64). This indicates that the simple theoretical model given by the Eq. (1) cannot explain the dynamics conditioned by the burning wood in a stove – at least the case of Room-3.

The correlations of measurements in Room-2 during the R-2/1E event are relatively high and they behave as it would be expected according to the Eq. (1), which is indicated by the abovementioned Mann–Whitney test. Without the wood firing (R-2/3NE) the correlations between ion concentrations and the d_{GM} and aerosols smaller than 50 nm were broken.

The ion concentrations and ratio n^+/n^- in Room-1 during the period when short entrances occurred (R-1/3E) show no correlations with the aerosol particles. During the R-1/2NE non-event, the strong correlation between positive ions and other parameters was re-established, while the negative ion concentration remained uncorrelated. The R-1/4E event established the correlations between the both ion concentrations and other parameters. However, in this case, the correlations between the ion concentrations and the parameters related to the size of the aerosol particles have to be considered

1 in light of the two facts: 1) the cigarette smoking did not influence the aerosol particles concentration of fraction smaller
2 than 50 nm, and 2) there were only seven measurements during the smoking which does not assure good statistics.

3 The effective ion–aerosol attachment coefficient $-\beta_{\text{eff}}$ is calculated using the Eq. (2) under the assumption of equilibrium
4 ($dn/dt=0$; Fig. 11). The ion-to-ion recombination coefficient is taken to be $1.5 \times 10^{-6} \text{ cm}^3 \text{ s}^{-1}$ (Hörrak et al., 2008), while the
5 volumetric ion production rate is calculated using the radon, thoron and their progenies concentrations with equilibrium
6 factors of 0.4 and 0.1 for radon and thoron, respectively. As the main origin of the creation of the ion pairs in sites inves-
7 tigated is radon and thoron, the escape fraction correction is applied (Mayya & Holländer, 1995) for an aerosol concentration
8 of $\sim 10,000 \text{ cm}^{-3}$ and source strength $< 1000 \text{ cm}^{-3} \text{ s}^{-1}$.

9 In Room-1 and Room-2 the radon and the thoron concentrations were practically constant. The average thoron and
10 radon concentration in Room-1 were 131 Bq m^{-3} and 57 Bq m^{-3} (Fig. 2a) and in Room-2, 161 Bq m^{-3} and 88 Bq m^{-3}
11 (Fig. 5a), respectively. In Room-3, the radon concentration gradually increased from $\sim 2000 \text{ Bq m}^{-3}$ to $\sim 6000 \text{ Bq m}^{-3}$ and
12 then decreased to $\sim 3000 \text{ Bq m}^{-3}$ (Fig. 8a), which was accounted for in the estimation of the ion production rate. The thoron
13 concentration was $\sim 20 \text{ Bq m}^{-3}$.

14 The mean values of the parameter β_{eff} vary between $(2.2\text{--}5.4) \times 10^{-6} \text{ cm}^3 \text{ s}^{-1}$ (Fig. 11), which is higher than the values
15 measured in the boreal forests in Finland $(1\text{--}2) \times 10^{-6} \text{ cm}^3 \text{ s}^{-1}$ (Hörrak et al., 2008). According to Flanagan (1966), and
16 Hoppel & Frick, 1986, the effective attachment rate increases with the aerosol radius. This behaviour was noticed in Room-2,
17 where the correlation between β_{eff} and d_{GM} was 0.86 during the R-2/1E event (entry and lighting fire) and 0.70 during the R-
18 2/3NE no-event (no human activity) from 12:59 to 6:54 In Room-3, this correlation was 0.91 during no human activity (R-3/
19 2NE non-event), while when the wood in the stove was lit (start of the R-3/3E event) this correlation turned to be negative
20 -0.86 . In comparison with the Table 3, it should be noted that when the correlation between ion concentrations and the
21 aerosol parameters is broken, the correlation between β_{eff} and d_{GM} is broken as well.

27 4. Conclusion

28 Our results show the highest average particle generation rate of $2.4 \times 10^{11} \text{ min}^{-1}$ during cigarette smoking, followed by
29 $1.5 \times 10^{11} \text{ min}^{-1}$ during heating with a cast iron stove at $150 \text{ }^\circ\text{C}$ burning wood, and $1.1 \times 10^{10} \text{ min}^{-1}$ during heating with an
30 Alpine-type oven at $40\text{--}50 \text{ }^\circ\text{C}$. The same sequence was observed for the rate constant of the total particle loss ($\lambda_v + \lambda_d$), being
31 0.0603 min^{-1} during smoking, 0.0442 min^{-1} during heating with the stove, and 0.0067 min^{-1} during heating with the
32 Alpine-type oven. The total number of particles released was 8.7×10^{12} during smoking, 1.2×10^{12} during heating with the
33 Alpine-type oven, and 4.2×10^{12} during heating with the stove.

34 Exposure to nano-particles due to smoking (strongest particle source) in public places has recently decreased quickly,
35 because of steadily increasing prohibition rules of smoking indoors. To ban smoking indoors is also highly advisable for
36 private places, but decision is left to residents themselves. Although heating cannot be stopped, exposure to the generated
37 nano-particles can be diminished markedly by choosing a suitable heater and fuel with lower temperature of the heating
38 body and by maintaining clean and dust-free hot surfaces.

39 Differences in correlation coefficients of the same parameters in different houses arise from different way of heating. The
40 heating body of the stove in Room-2 was the source of a permanent inflow of new particles, while in Room-1, the central
41 heating provided an almost constant concentration of particles during measurements. In Room-3, there was no heating
42 before 7:00, and correlation was higher. Introduction of new particles with maximum size distribution peak at 100 nm
43 reduced the number of cluster ions by processes of ion-to-aerosol particles attachment. Nevertheless, correlation coefficient
44 between average air ion and radon concentrations during all four measurements remained high.

45 High concentrations of nano-particles and particles in nucleation mode observed in Room-2 and Room-3 only in the
46 presence of several persons lead to a conclusion that they are the consequence of strong VOC evaporation from the skin
47 during measurements. One of the possible explanations, especially in the case of Room-3 where ion concentration was high,
48 is that gas-to-particle conversion of VOCs and particles in the phase of growth are assisted by ion-induced nucleation. But in
49 Room-2, nano-particle concentration was 40 times higher than concentration of cluster ions of both polarities.

50 During the measurements, there were certain external influences which induced unexpected air ions behaviour. The
51 strongest influence came from the heating, however other influences (such as temperature gradient, thus convective air
52 current, air draft, presence of electrostatic surfaces, human presence, micro-climatic influence etc.) were certainly present.
53 Human activities, especially a presence of people in the room, perturb the common correlation between the ion con-
54 centrations and the aerosol parameters, sometimes completely breaking all correlations. The correlations between the
55 positive ions and the airborne particle parameters were in principal higher than between the negative ions and the same
56 parameters. The mean values of the effective ion attachment rate β_{eff} were estimated and they vary between $(2.2\text{--}5.4)$
57 $10^{-6} \text{ cm}^3 \text{ s}^{-1}$.

1 Q6 Uncited references

3 Glasius et al. (2006); Hays, Smith, Kinsey, Dong, & Kariher (2003); Kleeman, Schauer, & Cass (1999); Kolarž & Čurguz
 5 (2015); Rau (1989); Ulevicius et al. (2010); Vaupotič (2011); Vaupotič et al., 2012; Wright, Fewes, Keitch, & Henshow (2007);
 7 Žunić et al. (2010).

7 Acknowledgment

9 The study was funded through the Bilateral Slovenia–Serbia Project of scientific cooperation Nos. 451-03-1251/2012-09/
 11 08, 171020, 45003 and P 41028 in Serbia and BI-RS/12-13-008 and P1-0143 in Slovenia. The authors appreciate the hos-
 13 pitality and technical support of the residents.

15 References

- 17 Afshari, A., Matson, U., & Ekberg, L. E. (2005). Characterization of indoor sources of fine and ultrafine particles: a study conducted in a full-scale chamber.
Indoor Air, 15, 141–150.
- 19 Smerajec, M., & Vaupotič, J. (2013). Nanoaerosols including radon decay products in outdoor and indoor air at a suburban site. *Journal of Toxicology*, 13,
 823–831.
- 21 Blaauboer, R. O., & Smetsers, R. C. G. M. (1996). Outdoor concentrations of the equilibrium-equivalent decay products of ²²²Rn in the Netherlands and the
 effect of meteorological variables. *Radiation Protection Dosimetry*, 69, 7–18.
- 23 Burtcher, H. (2010). The origin and production of nanoparticles in environment and industry. In J. C. M. Marijnissen, & L. Gradon (Eds.), *Nanoparticles in
 medicine and environment, inhalation and health effects*. Berlin, Germany: Springer Science+Business Media B. V.
- 25 Chalmers, J. A. (1967). *Atmospheric electricity*. Oxford, London: Pergamon Press.
- 27 Chen, Y.-C., Yuanhui, Z., & Barber, E. M. (2000). A dynamic method to estimate indoor dust sink and source. *Building and Environment*, 35, 215–221.
- 29 Cerqueira, M., Gomes, L., Terelho, L., & Pio, C. (2013). Formaldehyde and acetaldehyde emissions from residential wood combustion in Portugal. *Atmospheric
 Environment*, 72, 171–176.
- 31 Commodo, M., Sgro, L. A., D'Anna, A., & Minutolo, P. (2012). Size distribution of nanoparticles generated by a heating stove burning wood. *EQA – Inter-
 national Journal of Environmental Quality*, 8, 21–26.
- 33 Evtugina, M., Alves, C., Calvo, A., Nunes, T., Terelho, L., Duarte, M., Prozil, S. O., Evtuguin, D. V., & Pio, C. (2014). VOC emissions from residential combustion
 of Southern and mid-European woods. *Atmospheric Environment*, 83, 90–98.
- 35 EPA (2000). United states environmental protection agency, research and development – wood stove emissions: particle size and chemical composition.
 EPA-600/R-00-050, June 2000.
- 37 Glasius, M., Ketzel, M., Wählin, P., Jensen, M., Mønster, M., Berkowicz, R., & Palmgren, F. (2006). Impact of wood combustion on particle levels in residential
 area in Denmark. *Atmospheric Environment*, 40, 7115–7124.
- 39 Hays, M. D., Smith, D. N., Kinsey, J., Dong, Y., & Kariher, P. (2003). Polycyclic aromatic hydrocarbon size distribution in aerosol from appliances of residential
 wood combustion as determined by direct thermal deposition – GC/MS. *Journal of Aerosol Science*, 34, 1061–1084.
- 41 He, C., Morawska, L., Hitchins, J., & Gilbert, D. (2004). Contribution from indoor sources to particle number and mass concentrations in residential houses.
Atmospheric Environment, 38, 3405–3415.
- 43 He, F., & Hopke, P. K. (1996). Experimental study of ion-induced nucleation of volatile organic compounds by radon decay. In M. Kulmala, & P. E. Wagner
 (Eds.), *Nucleation and atmospheric aerosols* (pp. 50–53). Oxford, U. K.: Elsevier Science Ltd.
- 45 Heal, M. R., Kumar, P., & Harrison, R. M. (2012). Particles, air quality, policy and health. *Chemical Society Reviews*, 41, 6606–6630.
- 47 Hedberg, E., Kristensson, A., Ohlsson, M., Johansson, C., Johansson, P.A., Swietlicki, E., Vesely, V., Widequist, U., & Westerholm, R. (2002). Chemical and
 physical characterization of emissions from birch wood combustion in a wood stove. *Atmospheric Environment*, 36, 4823–4837.
- 49 Hirsikko, A., Nieminen, T., Gagné, S., Lehtipalo, K., Manninen, H. E., Ehn, M., Hörrak, U., Kerminen, V.-M., Laakso, L., McMurry, P. H., Mirme, A., Mirme, S.,
 Petäjä, M., Tammet, H., Vakkari, V., Vana, M., & Kulmala, M. (2011). Atmospheric ions and nucleation: a review of observations. *Atmospheric Chemistry,
 11*, 767–798.
- 51 Hoppel, William A., & Frick, Glendon M. (1986). Ion–aerosol attachment coefficients and the steady-state charge distribution on aerosols in a bipolar ion
 environment. *Journal of Aerosol Science Technology*, 5, 1–21.
- 53 Hörrak, U. (2001). *Air ion mobility spectrum at a rural area (Ph.D thesis)*. Estonia: University of Tartu.
- 55 Hörrak, U., Aalto, P. P., Salm, J., Komsaare, K., Tammet, H. J., Mäkelä, M., Laakso, L., & Kulmala, M. (2008). Variation and balance of positive air ion con-
 centrations in a boreal forest. *Atmospheric Chemistry and Physics*, 8, 655–675.
- 57 Hu, D., Qiao, L., Chen, J., Ye, X., Yang, X., & Cheng, T. (2010). Hygroscopicity of inorganic aerosols: size and relative humidity effects in the growth factor.
Aerosol and Air Quality Research, 10, 255–264.
- 59 Hussein, T., Hameri, K., Heikkinen, M., & Kulmala, M. (2005). Indoor and outdoor particle size characterization at a family house in Espoo–Finland.
Atmospheric Environment, 39, 3697–3709.
- 61 Hussein, T., Glytsos, T., Ondráček, J., Dohányosová, P., Ždímal, V., Hämeri, K., Lazaridis, M., Smolík, J., & Kulmala, M. (2006). Particle size characterization and
 emission rates during indoor activities in a house. *Atmospheric Environment*, 40, 4285–4307.
- Kleeman, M. J., Schauer, J. J., & Cass, G. R. (1999). Size distribution of fine particulate matter emitted from wood burning, meat charbroiling, and cigarettes.
Environmental Science and Technology, 33, 3516–3523.
- Kolarž, P. M., Filipović, D. M., & Marinković, B. P. (2009). Daily variations of indoor air ion and radon concentrations. *Applied Radiation and Isotopes*, 67,
 2062–2067.
- Kolarž, P., Miljković, B., & Čurguz, Z. (2011). Air-ion counter and mobility spectrometer. *Nuclear Instruments and Methods in Physics Research B*, 279, 219–222.
- Kolarž, P., & Čurguz, Z. (2015). Air ions as indicators of short term indoor radon variations. *Applied Radiation and Isotopes*, 99, 179–185.
- Koutrakis, P., Briggs, S. L. K., & Leaderer, B. P. (1992). Source apportionment of indoor aerosols in Suffolk and Onondaga counties, New York. *Environmental
 Science and Technology*, 26, 521–527.
- Kulmala, M., Vehkamäki, H., Petäjä, T., Dal Maso, M., Lauri, A. M., Kerminen, V., Birmili, W., & McMurry, P. H. (2004). Formation and growth rates of ultrafine
 atmospheric particles: a review of observations. *Journal of Aerosol Science*, 35, 143–176.
- Kumar, P., Morawska, L., Birmili, W., Paasonen, P., Hu, M., Kulmala, M., Harrison, R. M., Norford, L., & Britter, R. (2014). Ultrafine particles in cities. *Envir-
 onment International*, 66, 1–10.
- Mayya, Y. S., & Holländer, W. (1995). Ion densities and particle charges for alpha ionization in an aerosol atmosphere: columnar recombination corrections.
Aerosol Science and Technology, 23(4), 628–640.
- Matson, U. (2005). Indoor and outdoor concentrations of ultrafine particles in some Scandinavian rural and urban areas. *Science of the Total Environment*,
 343169–176.

- 1 Mishra, R., Zunic, Z. S., Venoso, G., Bochicchio, F., Stojanovska, Z., Carpentieri, C., Prajith, R., Sapra, B. K., Mayya, Y. S., Ishikawa, T., Omori, Y., Veselinovic, N.,
Tollefsen, T., Ujić, P., & Bossew, P. (2014). An evaluation of thoron (and radon) equilibrium factor close to walls based on long-term measurements in
3 dwellings. *Radiation Protection Dosimetry*, *160*(1–3), 164–168.
- Morawska, L., Moore, M.R., & Ristovski, Z.D. (2004). Desktop literature review and analysis: health impacts of ultrafine particles. For the Australian
5 department of the environment and heritage, ISBN 0 642 550557 (pp. 1–207).
- Morawska, L., He, C., Hitchins, J., Mengersen, K., & Gilbert, D. (2003). Characteristics of particle number and mass concentrations in residential houses in
7 Brisbane, Australia. *Atmospheric Environment*, *37*, 4195–4203.
- Murr, L. E., & Garza, K. M. (2009). Natural and anthropogenic environmental nanoparticulates: Their microstructural characterization and respiratory health
9 implications. *Atmospheric Environment*, *43*, 2683–2692.
- Nel, A., Xia, T., Mädler, L., & Li, N. (2006). Toxic potential of materials at the nano level. *Science*, *331*, 622–627.
- Oberdörster, G., Oberdörster, E., & Oberdörster, J. (2005). Nanotoxicology: an emerging discipline evolving from studies of ultrafine particles. *Environmental
11 Health Perspectives*, *113*, 823–839.
- O'Dowd, C. D., Aalto, P., Hmeri, I., & Kulmala, M. (2002). Aerosol formation: atmospheric particles from organic evaporation. *Nature*, *416*, 497–498.
- Pedersen, E. K., Bjørseth, O., Syversen, T., & Mathiesen, M. (2001). Physical changes of indoor dust caused by hot surface contact. *Atmospheric Environment*,
13 *35*, 4149–4157.
- Rau, J. A. (1989). Composition and size distribution of residential wood smoke particles. *Aerosol Science and Technology*, *10*, 181–192.
- Tammet, H., & Kulmala, M. (2005). Simulation tool for atmospheric aerosol nucleation bursts. *Aerosol Science*, *36*, 173–196.
- Ulevičius, V., Byčėnkiėnė, S., Remeikis, V., Garbaras, A., Kecorius, S., Andriejauskienė, J., Jasinevičienė, D., & Močnik, G. (2010). Characterization of pollution
15 events in the east Baltic region affected by biomass fire emissions. *Atmospheric Research*, *98*, 190–200.
- United Nations Scientific Committee on the Effects of Atomic Radiation (2000). Sources and effects of ionizing radiation. In: UNSCEAR 2000, report to the
17 general assembly, with scientific annexes, Vol. 1.
- Van Dijk, W. D. (2011). Nanoparticles in cigarette smoke; real-time undiluted measurements by scanning mobility particle size. *Analytical and Bioanalytical
19 Chemistry*, *399*, 3573–3578.
- Vaupotič, J. (2011). Nano aerosols including radon decay products in ambient air. In N. A. Mazzeo (Ed.), *Chemistry, emission control, radioactive pollution and
21 indoor air quality* (pp. 153–190). Rijeka, Croatia: InTech.
- Vaupotič, J., Bezek, M., Kávási, N., Ishikawa, T., Yonehara, H., & Tokonami, S. (2012). Radon and thoron doses in kindergartens and elementary schools.
23 *Radiation Protection Dosimetry*, *152*247–252.
- Vaupotič, J., Gregorič, A., Leban, M., Bezek, M., Žvab Rožič, P., Zmazek, B., Kobal, I. (2013). Radon survey within a regular grid in homes in Slovenia. VII.
25 *Hungarian Radon Forum and Radon and Environment Satellite Workshop*. Veszprém: Pannonian University Press (pp. 195–200).
- Wallace, L. (2000). Real-time monitoring of particles, PAH, and CO in an occupied townhouse. *Applied Occupational and Environmental Hygiene*, *15*, 39–47.
- Wallace, L. (2006). Indoor sources of ultrafine and accumulation mode particles: size distribution, size-resolved concentrations, and source strengths.
27 *Aerosol Science and Technology*, *40*, 348–360.
- Wallace, L. A., Emmerich, S. J., & Howard-Reed, C. (2004). Source strengths of ultrafine and fine particles due to cooking with gas stove. *Environmental
29 Science and Technology*, *38*, 2304–2311.
- Wang, S., Ang, H. M., & Tade, M. O. (2007). Volatile organic compound in indoor environment and photocatalytic oxidation; state of the art. *Environment
31 International*, *33*, 694–705.
- Weichenthal, S., Dufresne, A., Infante-Rivard, C., & Joseph, L. (2007). Indoor ultrafine particle exposures and home heating systems: a cross-sectional survey
of Canadian homes during the winter months. *Journal of Exposure Science and Environmental*, *17*, 288–297.
- WHO (2013). Review of evidence on health aspects of air pollution – REVIHAAP: first results. World Health Organisation (WHO) European Centre for
33 Environment and Health. Germany: WHO Regional Office for Europe Bonn.
- Wichmann, H.-E., & Peters, A. (2000). Epidemiological evidence of the effects of ultrafine particle exposure. *Philosophical Transactions of the Royal Society A*,
35 *358*, 2751–2769.
- Wright, M. D., Fewes, A. P., Keitch, P. A., & Henshaw, D. L. (2007). Small-ion and nano-aerosol production during candle burning: size distribution and
concentration profile with time. *Aerosol Science and Technology*, *41*, 475–484.
- Yu, F., & Turco, R. P. (2000). Ultrafine aerosol formation via ion-mediated nucleation. *Geophysical Research Letters*, *27*, 883–886.
- Zhang, H., Wang, S., Hao, J., Wan, L., Jiang, J., Zhang, M., Mestl, H. E. S., Alnes, L. W. H., Aunan, K., & Mellouki, A. W. (2012). Chemical and size characterization
37 of particles emitted from the burning of coal and wood in rural households in Guizhou, China. *Atmospheric Environment*, *51*, 94–99.
- Žunić, Z. S., Čeliković, I., Tokonami, S., Ujić, P., Onischenko, A., Zhukovsky, M., Milić, G., Jakupi, B., Čuknić, O., Veselinović, N., Fujimoto, K., Sahoo, S. K., &
Yarmoshenko, I. (2010). Collaborative investigations on thoron and radon in some rural communities of Balkans. *Radiation Protection Dosimetry*, *141*,
346–350.

Article

Modeling Indoor Particulate Matter and Small Ion Concentration Relationship—A Comparison of a Balance Equation Approach and Data Driven Approach

Miloš Davidović¹, Milena Davidović², Rastko Jovanović¹, Predrag Kolarž³,
Milena Jovašević-Stojanović¹ and Zoran Ristovski^{4,*} 

¹ VINČA Institute of Nuclear Sciences, National Institute of the Republic of Serbia, University of Belgrade, 11351 Belgrade, Serbia; davidovic@vin.bg.ac.rs (M.D.); virrast@vin.bg.ac.rs (R.J.); mjovst@vin.bg.ac.rs (M.J.-S.)

² Faculty of Civil Engineering, University of Belgrade, 11120 Belgrade, Serbia; milena@grf.bg.ac.rs

³ Institute of Physics, University of Belgrade, 11080 Belgrade, Serbia; kolarz@ipb.ac.rs

⁴ School of Earth and Atmospheric Sciences, Queensland University of Technology, 4000 Brisbane, Australia

* Correspondence: z.ristovski@qut.edu.au

Received: 17 July 2020; Accepted: 24 August 2020; Published: 27 August 2020



Featured Application: An ANN model successfully helped in harmonizing inputs from several instruments of different grade (low cost radon and lab grade particulate matter monitors) and enabled predictions of small ions concentration of comparable quality to the lab grade Gerdien type instrument.

Abstract: In this work we explore the relationship between particulate matter (PM) and small ion (SI) concentration in a typical indoor elementary school environment. A range of important air quality parameters (radon, PM, SI, temperature, humidity) were measured in two elementary schools located in urban background and suburban area in Belgrade city, Serbia. We focus on an interplay between concentrations of radon, small ions (SI) and particulate matter (PM) and for this purpose, we utilize two approaches. The first approach is based on a balance equation which is used to derive approximate relation between concentration of small ions and particulate matter. The form of the obtained relation suggests physics based linear regression modelling. The second approach is more data driven and utilizes machine learning techniques, and in this approach, we develop a more complex statistical model. This paper attempts to put together these two methods into a practical statistical modelling approach that would be more useful than either approach alone. The artificial neural network model enabled prediction of small ion concentration based on radon and particulate matter measurements. Models achieved median absolute error of about 40 ions/cm³ and explained variance of about 0.7. This could potentially enable more simple measurement campaigns, where a smaller number of parameters would be measured, but still allowing for similar insights.

Keywords: indoor air quality; small ions; radon; particulate matter; linear regression; artificial neural networks

1. Introduction

Our health and wellbeing is a complex and multifaceted phenomenon, but clean air can be with certainty regarded as one of its most critical components. Not surprisingly, it has been shown that air pollution is the single largest environmental health risk in Europe [1]. While level of concentration of air pollutants can widely vary even locally, the reactions people may have in response to exposure even

to the same level of air pollutants concentration can additionally vary due to the breathing volume (e.g., because of different age and levels of physical fitness and activity) and duration of exposure (e.g., large amount of time spent indoors, as a commuter, etc.). Furthermore, some age groups have behavioral patterns that may affect their exposure in a negative manner, such as elderly or young children, and result in various negative health effects including asthma, allergies, and other [2,3].

Monitoring of outdoor ambient air quality is usually done via networks at national and local level. However, despite having high quality of instrumentation these kinds of networks are usually very sparse, may not monitor all parameters of interest, and give little insight into personal exposure, for which indoor air quality may be of greater importance. This makes additional measuring campaigns necessary, especially for indoor places where sensitive age groups may spend considerable amount of time. The level and composition of air pollutant differs indoors and outdoors, and some air pollutants can be more prominent outdoors (e.g., gaseous pollutants sulfur dioxide or ozone), while others are usually more dominant in the indoor environment (e.g., formaldehyde, carbon monoxide or nitrogen oxides and radon) [4,5]. Even more so than the gas phase pollutants, PM concentration along with its size distribution and chemical composition is also a significant problem. It is well documented that serious health effects may result from long-term exposure to an elevated concentration of particulate matter [6]. Short term air pollution levels were found to correlate with reduced lung function, and remained visible up to 24 h after exposure [7]. In many European cities [6], particulate matter concentration is two to three times higher outdoors than that recommended by the World Health Organization (WHO). Outdoor air also contributes to indoor air quality, since it can diffuse easily into indoor environment. Air quality indoors can be further worsened by non-satisfactory ventilation quality.

In this paper we focus on a smaller subset of indoor air pollution phenomena with a focus on an interplay between primary pollutants radon and particulate matter (PM) [8] and small ions (SI) concentrations. Reasoning and arguments found in scientific literature behind the question why small air ions may have an impact on human health are the following. Small ions can be considered as natural air cleaners and sterilizers, and also biologically active constituents of the environmental air. Additionally, process of ion to aerosol attachment is leading to aggregation of ultrafine particles (UFP) in environmental air and thus reduces their number concentration (at the account of mass gain) and deposition on electrostatic surfaces. Recent scientific research shows that the health hazard possibly increases with the decrease of diameter of the inhaled particles. Peters et al. [9] demonstrated that the number concentration of nanoparticles is more strongly associated with health effects than the mass concentration. Other health impacts of air ions include psychological effects that have been reported in many studies and summarized in Perez et al. [10] and Pino and Ragione [11]. Most of the studies claimed that ionization was significantly associated with lower depression ratings. It is important to note that most of research refers to high levels of ion concentration exposure. Studies of background ion concentration relative to the ion-free state studies were not found but health benefits of rich ion background could be expected. Jiang et al. [12] claim that the reports where the presence of negative ions is credited for increasing psychological health are without reliable evidence in therapeutic practice. The studies showing that negative ions could help people with symptoms of allergies to dust, mold spores, and other allergens need additional confirmations. However, it is encouraging that there are no known negative effects of negative ions, so positive effect should be studied further. On the other hand, adverse health effects of radon [13] and particulate matter [14] are long well known. Since all three quantities (radon, SI and PM concentration) are linked via a balance equation, even though the health effects are only firmly established for radon and PM [8], it is useful to consider all three simultaneously. Understanding the way in which various air quality variables interact can be beneficial for developing predictive models, and also enable obtaining more knowledge about air quality based only on several key predictor measurements. Children spend a large part of their time at school microenvironment. In the last decade several large studies conducted within the framework of European projects BREATHE and SINPHONIE addressed the topics of level

and chemical composition of particulate matter fractions including ultrafine particulate matter and gaseous air pollutants, also addressing differences during teaching and non-teaching hours and periods when there are no occupants in schools [15,16]. In the framework of numerous studies at national and international level radon concentration was measured in school classrooms, usually by utilizing passive samplers.

The objectives of this paper are the following. The first objective was to bring additional insight into indoor air quality by measuring a number of important air quality variables including quantities that are somewhat more rarely measured with higher temporal resolution namely SI concentration and radon concentration in two elementary schools' indoor environments. In addition, we have measured PM concentration and size with high temporal and size resolution. Descriptive statistics of the measured parameters is presented and discussed. We then proceed to studying association between SI, radon and PM concentrations, based on a balance equation. Parameters of the balance equation are estimated from the data in two schools. We investigate the hypothesis that small ion concentration can be predicted based on radon and particulate matter measurements predictors, by using artificial neural network model. If successful, this kind of modelling effort could enable obtaining more knowledge about air quality based only on several key predictor measurements. This could potentially enable more simple measurement campaigns, where a smaller number of parameters would be measured, but still allowing for similar insights. The outline of this paper is as follows. First, we provide a brief explanation of the physical processes involved in creation of small ions, and then utilize balance equation to describe it quantitatively. We then discuss the link between small ion concentration, volumetric production rate and particulate matter concentration. Following this discussion, we describe the method that was used in the indoor measuring campaign, in which a number of relevant parameters appearing in the balance equation are measured either directly or via an important proxy. We study an interplay between concentrations of radon, SI and PM. For this purpose, we utilize two approaches. The first approach is based on a balance equation which is used to derive approximate relation between concentration of small ions and particulate matter. The form of the obtained relation is transformed via Taylor expansion to enable meaningful linear regression modelling with several predictors. The second approach is data driven and utilizes machine learning techniques, namely shallow feed forward neural networks, and in this approach, we develop a more complex statistical model, but utilize predictors that were used in physics based linear regression modelling. Performance and trade-offs of the two approaches are then discussed.

2. Materials and Methods

2.1. Form of the Balance Equation Suitable for Statistical Modelling

The small air ion concentration (n_{\pm}) is determined by the following balance equation:

$$\frac{dn_{\pm}}{dt} = q - \alpha n_{\pm} n_{\mp} - n_{\pm} \beta Z \quad (1)$$

where q is the volumetric production rate, Z is the aerosol number concentration, α coefficient accounts for the losses of ion-to-ion recombination and β represents an effective ion-aerosol attachment coefficient, which is the integral over the size distribution of aerosol particles. The balance equation can include additional terms. If electrostatic deposition (occurring mainly in indoor air) is included in a model, there is an additional right-hand side term $-\delta^{\pm} n_{\pm}$, where δ^{\pm} is an electrostatic deposition rate coefficient of the air ions. Additional details about physics behind changes in SI concentration and relevant terms in balance equations are given in Appendix A.

While Equation (1) seems very intuitive, it is worth noting that it was discovered rather painstakingly, and some terms were added to increase its scope of validity. Namely, in the first half of last century Schweidler [17] showed that the quadratic law of recombination previously held valid (quadratic law is Equation (1) without the last (linear) term on the right-hand side. Since $n_{+} \approx n_{-}$,

equality being only approximate due to the different mobility of positive and negative small ions, the middle term in Equation (1) is a quadratic term) is not valid in ordinary air, but only for clean air (Equation (1) when $Z \approx 0$). As another interesting historical note ion-aerosol attachment coefficient was previously referred to as “diminution coefficient of small ions in the presence of nuclei and large ions” [18].

If we neglect the quadratic term present in (1) we can obtain the following (under the assumption of a quasi-steady state):

$$\frac{dn^-}{dt} \approx 0 \approx q - n^-(\beta Z + \delta^-) \tag{2}$$

(since our campaign was situated indoors, the electrostatic deposition rate coefficient δ^- was also included). After expanding βZ term we obtain:

$$n^- \approx \frac{q}{\sum \beta_i Z_i + \delta^-} \tag{3}$$

or more conveniently

$$\sum \beta_i Z_i + \delta^- \approx \frac{q}{n^-} \tag{4}$$

The form of the above equation suggests linear regression is a justified modelling approach if we want to model the interdependence between the concentration of larger aerosol particles of various diameter and small ion concentration. The physical meaning of the coefficients in linear regression (β_i) are an ion-aerosol attachment coefficient and the intercept term corresponds to the electrostatic deposition rate coefficient of the air ions (δ^-). Note, however, that in a non-laboratory type of campaign, one cannot precisely control the aerosol distribution and there may be a significant correlation between individual channels corresponding to different particle sizes, which makes calculation (and interpretation) of the regression coefficients as attachment coefficients largely approximate.

Taking one more look into (4) brings up an important issue, that is taking a quotient of two noisy variables on the right-hand side of the Equation (4), that may also have values close to zero. The right hand side of (4) therefore may produce a quotient not suitable for further statistical modelling. Instead of using Equation (4) directly, we will do the following. By Taylor expanding expression (3) around some value of volumetric production rate q_0 and some value of particle concentrations Z_{i0} we obtain

$$\begin{aligned} n^- &\approx \frac{q}{\sum \beta_i Z_i + \delta^-} = f(q, Z_i) \approx \\ &\approx f(q_0, Z_{i0}) + \frac{\partial f(q, Z_i)}{\partial q} \Big|_{q_0, Z_{i0}} (q - q_0) + \frac{\partial f(q, Z_i)}{\partial Z_i} \Big|_{q_0, Z_{i0}} (Z_i - Z_{i0}) \end{aligned} \tag{5}$$

The derivatives in (5) are given by

$$\begin{aligned} \frac{\partial f(q, Z_i)}{\partial q} &= \frac{1}{\sum \beta_i Z_i + \delta^-} \Big|_{q_0, Z_{i0}} = \frac{1}{\sum \beta_i Z_{i0} + \delta^-} = \frac{n_0}{q_0} \\ \frac{\partial f(q, Z_i)}{\partial Z_i} &= \frac{-q}{(\sum \beta_i Z_i + \delta^-)^2} \beta_i \Big|_{q_0, Z_{i0}} = \frac{-q_0}{(\sum \beta_i Z_{i0} + \delta^-)^2} \beta_i = \frac{-n_0^2}{q_0} \beta_i \end{aligned}$$

And finally, we arrive at:

$$n^- \approx n_0 + \frac{n_0}{q_0} (q - q_0) - \sum \frac{n_0^2}{q_0} \beta_i (Z_i - Z_{i0}) \tag{6}$$

This equation is more suitable for developing linear regression model, since it doesn't include quotients of the noisy occasionally close-to-zero random variables as does Equation (4). If a linear regression model is developed based on (6) it would allow us to model and predict concentration of small ions based on the knowledge of rate of volumetric production rate (in this paper we use radon concentration as a proxy for volumetric production rate) and knowledge of particulate matter concentration. Additionally, it will allow us to estimate attachment coefficients.

2.2. Description of the Statistical Modeling Methodology

The first modelling approach that we will utilize is linear regression, with several input predictors (radon and aggregated particle channels) and one target variable (small ion concentration). General form of linear regression equation with several input predictors and one target is given by

$$y_i = a_0 + a_1 \cdot x_{i1} + \dots + a_p \cdot x_{ip} + z_i \quad (7)$$

where p is number of predictors, i is number of points we use for fitting model parameters a_0, a_1, \dots, a_p , y_i is sample of target, $x_{i1}, x_{i2} \dots x_{ip}$ are samples of predictors and z_i represents noise in i -th sample. Model parameters are determined by ordinary least squares i.e., by minimizing $\sum z_i^2$ (summed over all samples). Input was transformed by subtracting median, since it is a more robust statistical measure than mean. Thus, the linear model built around Equation (6) can be considered as Taylor expansion around median. Note that particular linear scaling of input has no effect on R^2 score of the linear model, but serves to aid interpretation of coefficients in Equation (6).

Second approach we utilize for statistical modeling is a simple feed-forward artificial neural network (ANN) with one hidden layer. Such shallow feed-forward ANNs were previously used successfully in a number of contexts, and recently for calibration of low-cost sensors [19]. Input was scaled using standard normalization scaling (transforming it to zero mean and unit standard deviation). The hidden layer uses rectified linear unit (ReLU) activation function, which is known to have certain benefits such as non-vanishing gradient compared to commonly used, sigmoid transfer function. Implementation of the network was done via software library scikit-learn [20]. Network optimization procedure is the default 'adam' solver used in multi-layer perceptron (MLP)-regressor in scikit-learn, and further details can be found in [21]. Class MLPRegressor implements a multi-layer perceptron (MLP) with no activation function in the output layer. It uses the squared error as the loss function, and the output is a set of continuous values. Model selection criterion was based on R^2 score, and two requirements: to have as high as possible R^2 score, and also a balanced result on training and test set. These criteria were examined via parametric sweep of number of input PCA components and neurons in the hidden layer. Since it is not generally possible to prescribe physical meaning to model parameters in the ANN models we will only compare the predictive power of the models.

2.3. Description of the Experimental Setup

A wide range of relevant air quality parameters were measured in indoor environments of two elementary schools located far apart 20 km, namely: an elementary School "Aleksa Šantić" in Belgrade suburb Kaluđerica, and in an elementary school "20. oktobar" in a residential background of the New Belgrade municipality, referred to as School 1 and School 2 in further text, respectively. The measurement campaigns in both schools, that have natural ventilation, were conducted during March 2017. Measuring spots in both schools were in classrooms on the ground floor, occupied on workdays. Instruments were arranged rather densely, and we can assume that the sampled air was well-mixed. Area surrounding location of School 1 and 2 is depicted in Figure 1. School 1 is in the near vicinity of a major local road, and also in the neighborhood where there is a significant amount of domestic heating sources. School 1 itself has a coal-based heating system. School 2 on the other hand is located further apart from the major roads, and is situated in a block of buildings connected to the district heating system.



Figure 1: Larger area surrounding location of (a) School 1 (WGS84: 20.556337261, 44.764855909) and (b) School 2 (WGS84: 20.395445055, 44.799510267). Approximate location of indoor school space is marked as a blue dot.

The measurement instrumentation setup included the following. SI concentration was measured using a Gardner-type air ion detector [22]. PM concentrations for diameter of particles going from from 10 to 1000 nm in 10 size channels were detected using TSI NanoScan SMPS Model 3910, and PM concentrations for diameter of particles going from from 0.3 to 10 μm in 6 channels were recorded using TSI OPS-3 particle sizer. In addition, the radon concentration level was measured by using a Radon Scout, along with the in-cha temperature, pressure, and humidity. The Radon Scout consists of a scintillation chamber with high voltage collection and Si detector. Si and samples are by diffusion. Remaining reagents sample air actively either by pump (particle size) or pass (air) on detector. Accuracy of radon and manufacturer info of the used instrument is further described in Appendix B and Table A1 and Table A1.

The collected data describes all relevant processes quantified by a balance equation: 2-minute SI concentration measurements describe steady state; radon concentration gives insight into the rate of volumetric ion pair generation and 1-minute PM measurements give insight into main loss mechanism for SI.

3. Results

Based on the descriptive statistics given in Table 3, some remarkable observations can be made. School 1 and School 2 both had mean and median SI concentration were more than twice as large as School 2. On the other hand, median concentration was similar in both schools, although the mean was higher in School 1. Looking at the particle concentration, we can observe that while 0.3–10 μm diameter particles were similar in concentration in both schools, this is not the case for 10–420 nm particles. This could explain lower SI concentration in School 2, since increased concentration of nanometer sized particles could explain main loss mechanism. While it is desirable to have sensitive indoor environments properly ventilated, this was not the case in the two schools where the experiments were conducted, which have natural ventilation. Due to this, radon and particulate matter concentration exhibited strong diurnal variations in both schools. Temperature had some what extreme values for indoor space (min and max see in Table Table 1) and the standard deviation was as high as 2.0 $^{\circ}\text{C}$. Relative humidity had similar values of mean and median (diagram suggests significant difference) that both schools of about 30%, 30% standard deviation of about 6%. Particulate matter size distribution plots that are not attached to some problems (e.g., low level of working fluid or out of range in low level) these data points were not taken into consideration. Table Table 1 serves as a reference for what is the scope of validity of predictive models associated in quality estimates that will be developed and discussed in further text.

Table 1. Summary statistics (minimum, maximum, mean, median and standard deviation) of air quality variables for the campaign conducted in Schools 1 (S1) and 2 (S2).

	Negative Small Ions [#/cm ³]		Radon [Bq/m ³]		Particle conc. 10–420 nm [#/cm ³]		Particle conc. 0.3–10 µm [#/cm ³]		Pressure (atm)		t [°C]		RH [%]	
	S1	S2	S1	S2	S1	S2	S1	S2	S1	S2	S1	S2	S1	S2
Min	0.0	0.0	0.0	0.0	0.0	776.5	53.2	30.4	0.97	0.98	19.60	20.12	18.97	18.87
Max	871.0	643.0	118.0	234.0	95,023.6	116,127.2	541.9	572.6	1.00	1.01	28.81	32.62	46.14	49.18
Mean	239.9	104.8	36.8	56.5	2512.7	15,198.2	161.1	151.1	0.98	1.00	24.24	26.64	29.77	31.20
Med.	212.0	63.0	39.0	41.0	1577.5	3724.6	142.7	132.8	0.98	1.00	24.27	26.78	29.40	30.81
Std. dev	143.8	113.9	22.2	41.6	4283.2	31,759.4	82.3	81.3	0.01	0.01	1.80	2.00	6.23	5.37

Initial exploratory data analysis shows that there is a correspondence between radon concentration and small ion concentration, shown in Figure 2 for both schools. Note that radon measurements appear to be more noisy compared to the small ion measurements, despite having much larger sampling time of 1h. This could be attributed to sampling mechanism of Radon Scout, since it samples air via diffusion. It also appears that for some periods of time variation in radon and small ions is “matched”, e.g., School 2, last week of March, where there is low concentration of radon and ions during workdays, and a sudden increase during weekend (25 and 26 March 2017). Similar, but less pronounced effect is seen in School 1 in the same week. This is probably due to different regimes of window opening and general use of indoor space during weekends. However, there are also periods where a “mismatch” between radon and SI concentrations seems to happen, probably due to loss mechanisms of attachment of small ions to particulate matter (see for example 9th of March in School 1, with a large spike in radon concentration not matched by ion concentration). In the following text we will see whether simple linear regression suggested by (6) could explain these and similar situations, and to what extent.

But before doing that, let us consider a correlation matrix of the wide array of quantities that we have measured simultaneously in two schools. Correlation plots are given in Figure 3, and include TSI Nanoscan channels (denoted in Figure 3 by channel size 11.5, 15.4, . . . , 273.8 nm, concluding with total concentration), followed by TSI OPS channels (denoted in Figure 2 by 0.337, 0.419, . . . , 9.015 µm, concluding with total concentration), followed by meteorological parameters, and finally small ions and radon. Notice that in both schools SI concentration negatively correlates with all particle channels (Pearson correlation coefficient is -0.36 for total particle concentration measured by TSI Nanoscan and -0.39 for total particle concentration measured by TSI OPS in School 1, and -0.09 and -0.37 in School 2), and that it positively correlates with radon (Pearson correlation coefficient is 0.33 and 0.59 in Schools 1 and Schools 2 respectively). This coincides with the conclusions that can be made from Equations (3), (4) and (6), and therefore it is justified to use these equations as a starting point for development of statistical models.

It is clear looking at TSI Nanoscan and OPS channels in the correlation matrix, that larger groups of channels correlate and thus it wouldn't be useful to consider all channels as independent predictors (signals) in the framework of regression modelling due to multicollinearity effects. We have, therefore, reduced the number of predictors for particulate matter we use in the modelling to the most significant ones.

This can be done in a number of ways, and in statistical modelling this technique is known as feature selection [25]. However, at this stage, in order to keep physical interpretation of predictors possible, we have opted not to use principal component analysis and similar methods for feature selection, and aggregated particle channels into larger size bins, approximately corresponding to groups of correlated channels depicted in Figure 3. Aggregations that were used are shown in Table 2. Aggregations only include consecutive channels, and for that reason in School 2, 11.5 nm channel was excluded from Aggr2, despite the high correlation evident from Figure 3. Note that this kind of aggregation somewhat lacks in terms of desirable properties of predictors (such as low cross correlation) that could be achieved via use of principal component analysis (PCA) [25], however, it still preserves

of 1h. This could be attributed to sampling mechanism of Radon Scout, since it samples air via diffusion. It also appears that for some periods of time variation in radon and small ions is “matched”, e.g., School 2, last week of March, where there is low concentration of radon and ions during workdays, and a sudden increase during weekend (25 and 26 March 2017). Similar, but less pronounced effect is seen in School 1 in the same week. This is probably due to different regimes of window opening and general use of indoor space during weekends. However, there are also periods where a “mismatch” between radon and SI concentrations seems to happen, probably due to loss mechanisms of attachment of small ions to particulate matter (see for example 9th of March in School 1, with a large spike in radon will also explore the possible benefits of PCA for aggregation of particle channels in the context of concentration not matched by ion concentration). In the following text we will see whether simple predictive modeling linear regression suggested by (6) could explain these and similar situations, and to what extent.

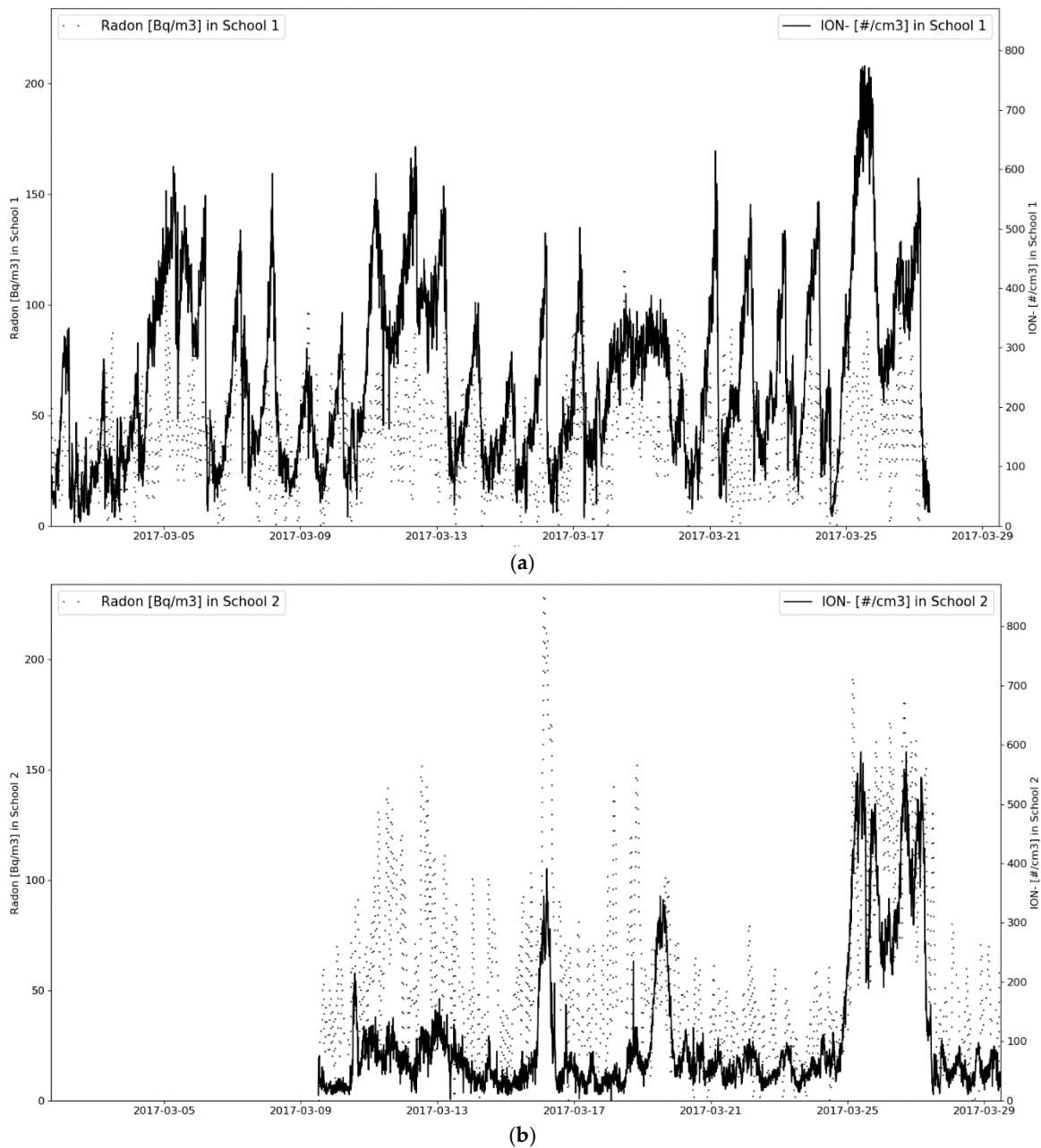


Figure 2. Radon concentration (dotted) vs. small ion concentration (full line) in (a) School 1 and (b) School 2.

(Pearson correlation coefficient is -0.36 for total particle concentration measured by TSI Nanoscan and -0.39 for total particle concentration measured by TSI OPS in School 1, and -0.09 and -0.37 in School 2), and that it positively correlates with radon (Pearson correlation coefficient is 0.33 and 0.59 in Schools 1 and Schools 2 respectively). This coincides with the conclusions that can be made from Equations (3), (4) and (6), and therefore it is justified to use these equations as a starting point for development of statistical models.

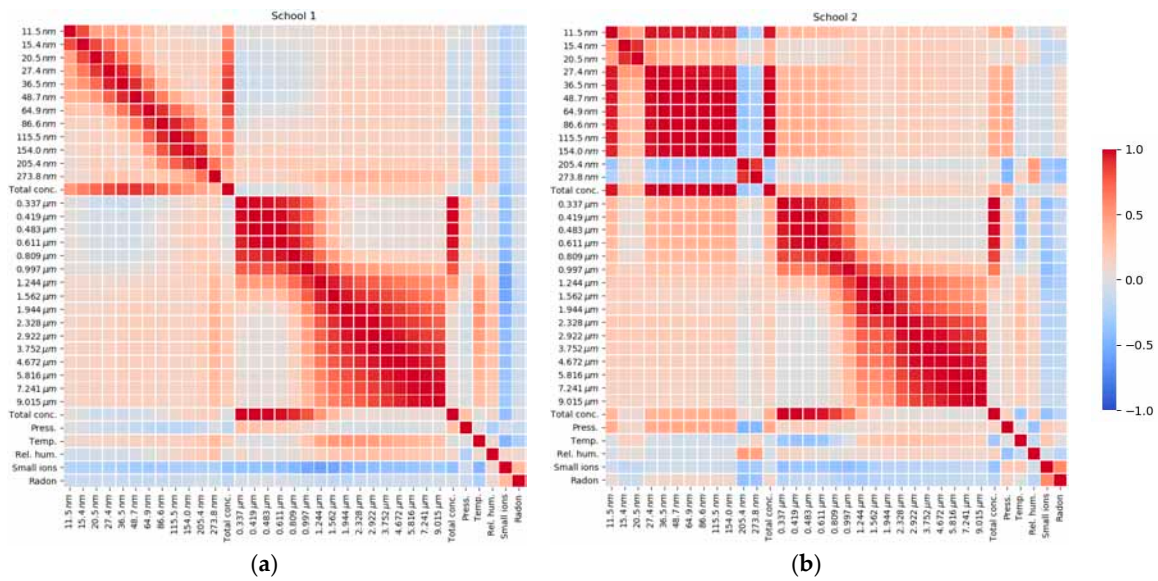


Figure 3. Correlation matrix of quantities measured in (a) School 1 and (b) School 2. Shades of red are used for positive correlations, and shades of blue for negative correlations. (Plots were produced in Python 3.7.4 environment using libraries Seaborn 0.9.0 [23] for visualization and Pandas 0.23.2 [24] for data processing and calculations.)

It is clear looking at TSI Nanoscan and OPS channels in the correlation matrix, that larger groups of channels correlate and thus it wouldn't be useful to consider all channels as independent predictors (signals) in the framework of regression modeling due to multicollinearity effects. We have, therefore, reduced the number of predictors for particulate matter we use in the modelling to the most significant ones.

TSI channel (nm)	Aggr1	Aggr2	Aggr3
11.5	11.5-15.4	15.4-20.5	20.5-27.4
15.4	11.5-15.4	15.4-20.5	20.5-27.4
20.5	11.5-15.4	15.4-20.5	20.5-27.4
27.4	11.5-15.4	15.4-20.5	20.5-27.4
36.5	11.5-15.4	15.4-20.5	20.5-27.4
48.7	11.5-15.4	15.4-20.5	20.5-27.4
64.9	11.5-15.4	15.4-20.5	20.5-27.4
86.6	11.5-15.4	15.4-20.5	20.5-27.4
115.5	11.5-15.4	15.4-20.5	20.5-27.4
154.0	11.5-15.4	15.4-20.5	20.5-27.4
205.4	11.5-15.4	15.4-20.5	20.5-27.4
273.8	11.5-15.4	15.4-20.5	20.5-27.4
Total conc.	0.337 μm	0.419 μm	0.483 μm
Press.	0.611 μm	0.809 μm	0.997 μm
Temp.	1.244 μm	1.562 μm	1.944 μm
Rel. hum.	2.328 μm	2.922 μm	3.752 μm
Small ions	4.672 μm	5.816 μm	7.241 μm
Radon	9.015 μm		

As mentioned earlier we will test the predictive power of the two statistical modeling approaches, which will be inspired, in part, by Equation (6). Let us first consider linear regression model with predictors being radon concentration and aggregated particle channels showed in Table 2. Since we are using radon concentration as a proxy for volumetric production rate we will also need a way of converting radon concentration to volumetric production rate. Since activity of 1 Bq/m^3 produces alpha particle of 5.49 MeV in cubic meter every second, and mean energy to create an ion pair in air is around 35.6 eV [26], one decay per second producing alpha particle will produce on average $A_0 \approx \frac{5.49 \text{ MeV}}{35.6 \text{ eV} \cdot 10^6 \text{ cm}^3} = 0.15 \frac{\text{i.p.}}{\text{cm}^3 \text{s}}$. Using this approximate conversion constant, we can notice using data from Table 1, that in School 1 volumetric production rate has a median of around $6 \text{ i.p./cm}^3 \text{s}$ and maximum of $19 \text{ i.p./cm}^3 \text{s}$, while in School 2 median is similar and maximum is about $37 \text{ i.p./cm}^3 \text{s}$. Going back to linear regression model, which was implemented using software library [20], using whole data sets in Schools 1 and 2 we obtained coefficients given in Table 3. Explained variance of the model is 0.49 in School 1, and 0.52 in School 2. Note that this explained variance should not be interpreted as predictive power of the model, since it was calculated on the whole data set. We will further discuss the issue of data set splitting a bit later.

Looking at the results listed in Table 3, several conclusions can be made. In both schools, the linear model had a similar value of explained variance, despite School 2 having one additional predictor. The intercept (corresponding to n_0 in Equation (6)) of the linear model is larger in School 1, which is in accordance with relative value of descriptive statistics for ions for two schools listed in Table 1. Note that n_0 in Equation (6) is *not* the median of n^- , but rather a value corresponding to the medians of radon and particle concentrations. The radon term is very similar in both schools, indicating similar increase in ion concentration with radon concentration.

In the linear model for both schools, the sign of attachment coefficients is physically justified (positive), despite the fact that we have used ordinary least squares, and did not enforce the sign of predictors a priori. Attachment coefficients become larger for aggregations corresponding to larger particle diameters, in accordance to theoretical expectations [26]. However, the magnitude of the attachment coefficients is larger compared to theoretical expectation, and this effect could be due to non-controlled PM size distribution which is to be expected in non-laboratory conditions, and also differences in number of particles in different size channels that were aggregated.

So as an intermediate conclusion, we can note that the balance equation provided valuable guidance for choice of predictors, and also that due to understanding of underlying physics we could inspect and verify the sign of predictors. On the other hand, despite all these advantages, the explained variance seems low, which makes physical interpretation of model parameters rather approximate. Furthermore, the relatively low explained variance would negatively influence predictive ability of the model. Let us now examine possible predictive power of the statistical models developed around balance equation.

In the further text we will focus on School 1, since during this particular campaign we have collected more data, and furthermore data gaps in particulate predictors were smaller compared to School 2. Having sufficient data for training and testing is paramount for developing models and also for testing them in a meaningful way. Under optimal conditions, stages of model validation, selection, and predictive errors should be calculated using independent i.e., previously unseen data, however this is often not possible. For smaller datasets it can easily happen that data is incomplete, and there could be different ratios of incompleteness for the test and training sets. Best way for doing cross validation is when it resembles and mimics the way in which model is to be practically used. This brings issues of optimal training test split, both in terms of amount of data and also temporal position of the data. Similar issues are encountered in low cost sensor calibration [19,27]. Additionally, since we are dealing with time series analysis test data will always need to be temporally separated and have timestamp later in time compared to training data. Thus, to satisfy these requirements of complete data sets and optimal timestamps of training and test data we opted to use 50-50 training test split. One additional requirement for the predictive models of small ion concentration is that they must produce positive output. A way to ensure positive prediction of the statistical model, is to take logarithm of the concentration when training the model and then to exponentiate the prediction of the model [25], and this was applied here.

Figure 4 shows comparison of a linear model based on radon and particle aggregates for School 1 and a measurement of small ions. The score metric (R^2) on the training set is 0.44 and on test set, it is 0.49. While the model shows similar trend as the measurements it is also evident that it significantly under predicts small ions concentration. Gaps in the figure correspond to periods where data for particles was missing.

Table 3. Linear model based on Equation (6), with radon as a proxy for volumetric rate and aggregated particle channels.

Parameters of The Linear Model	Intercept	Radon Term	Aggr1	Aggr2	Aggr3	Aggr4	
School 1 parameters	291.6	1.61	-5.08×10^{-3}	-8.24×10^{-3}	-5.08×10^{-1}	-4.88×10^1	
School 1 attachment $\beta_i [\text{cm}^3/\text{s}]$			2.87×10^{-7}	4.65×10^{-7}	2.87×10^{-5}	2.75×10^{-3}	
Parameters of The Linear Model	Intercept	Radon Term	Aggr1	Aggr2	Aggr3	Aggr4	Aggr5
School 2 parameters	111.8	1.52	-2.00×10^{-3}	-6.88×10^{-3}	-2.08×10^{-2}	-3.75×10^{-1}	-2.29×10^0
School 2 attachment $\beta_i [\text{cm}^3/\text{s}]$			1.05×10^{-6}	3.61×10^{-6}	1.09×10^{-5}	1.97×10^{-4}	1.20×10^{-3}

this was applied here.

Figure 4 shows comparison of a linear model based on radon and particle aggregates for School 1 and a measurement of small ions. The score metric (R^2) on the training set is 0.44 and on test set, it is 0.49. While the model shows similar trend as the measurements it is also evident that it significantly under-predicts small ions concentration. Gaps in the figure correspond to periods where data for particles was missing.

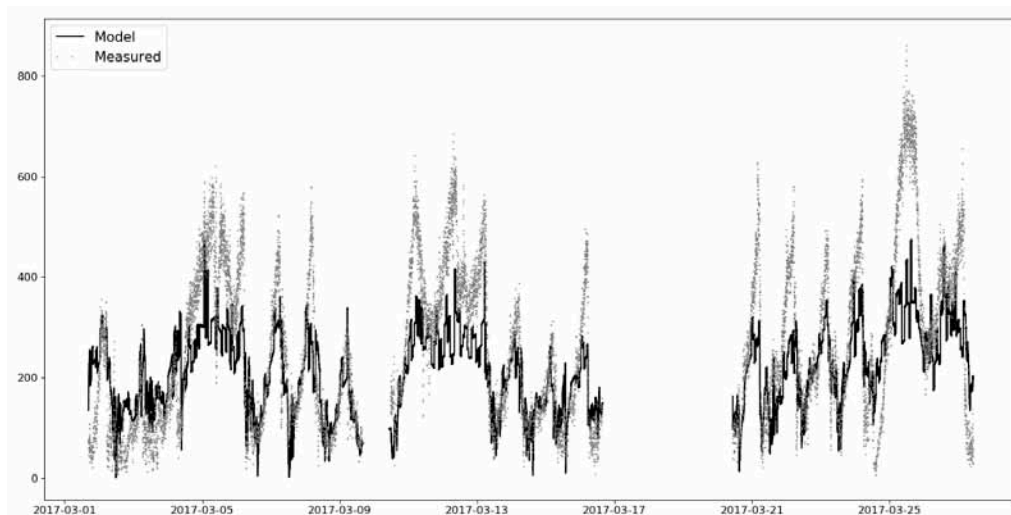


Figure 4. Comparison of a linear model based on radon and particle aggregates for School 1 (solid line) and a measure of small ions (dotted line). R^2 in % on Training/test set is 44/49.

Let us now examine if ANNs can improve the situation compared to the linear model. If we move away from a requirement that parameters of the statistical models have simple and precisely defined physical interpretation, we can bring several improvements to our modeling methodology. Choice of predictor variables can now become less stringent compared to the linear model that was based on a balance equation, so we can actually make statistically more justified aggregations of particle channels, e.g., by using PCA. Since for the linear model aggregation was based on correlation matrices derived from complete dataset, this could introduce so called “knowledge leak” from training to test data, and is thus best to avoid it, e.g., by using PCA. Furthermore, when using PCA it is more clear what amount of variance is left out of the model predictors when reducing the number of particulate matter related features. For example, first two PCA components explain 62% of the particle channels variance. The number of neurons in the hidden layer, and the optimal number of input PCA components was determined in optimization procedure. The most optimal training/test ratio was observed for ANN that has 4 neurons with ReLU activation function in the hidden layer and uses 2 PCA components and radon concentration, a total of 3 signals, as input. The optimal ANN model achieved median absolute error of about 40 ions/cm³ and explained variance of about 0.70. Some additional details about network architecture, hyperparameters and tuning procedures are given in Appendix C.

Predictive power of the optimized ANN model is illustrated in Figure 5. It seems that the model now doesn't significantly under predict small ion concentration, and it improves on the linear model, despite having smaller number of input predictors. Furthermore, the score on test set is significantly improved. It also appears that some of the noise introduced by radon measurements is now less pronounced compared to the linear model output shown in Figure 4. However, it seems that while the overall trend in small ions concentration is well modelled, the shape of the peaks is not always preserved. Since final ANN has rather simple architecture and there are no discrepancies between training and test scores it can be concluded that the model is not overly complex to introduce overfit, and additionally, training and test datasets are sufficiently complete.

improved. It also appears that some of the noise in radon measurements is now less pronounced compared to the linear model output shown in Figure 4. However, it seems that while the overall trend in small ions concentration is well modelled, the shape of the peaks is not always preserved. Since final ANN has rather simple architecture and there are no discrepancies between training and test scores it can be concluded that the model is not overly complex to introduce overfit, and additionally, training and test datasets are sufficiently complete.

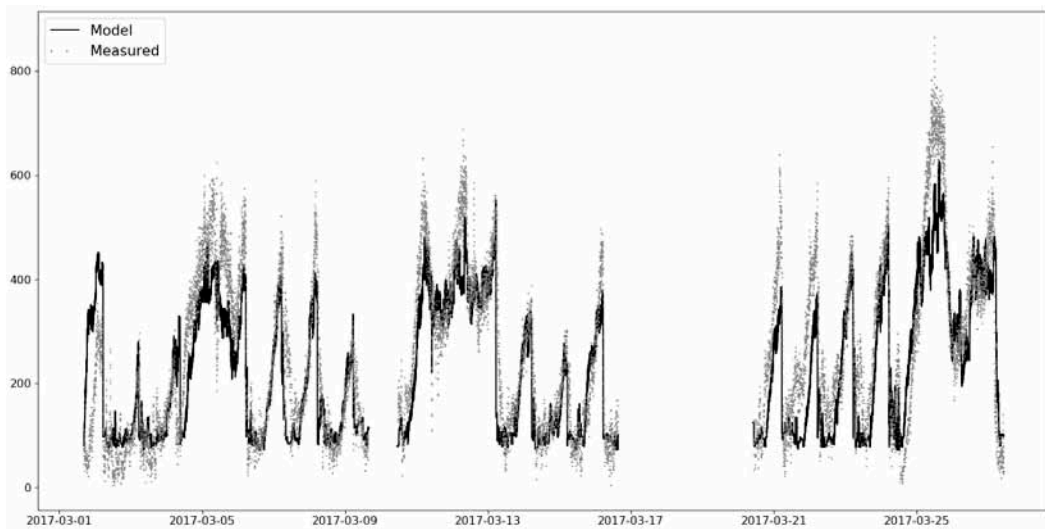


Figure 5. Comparison of an artificial neural network (ANN) model based on radon and 2-PCA particle components for School 11 (solid line) and a measurement of small ions (dotted line). Units is $[\#/cm^3]$. Training test score 0.69/0.69.

4. Conclusions

In this work, we have studied indoor air quality related to important, but more rarely continuously measured parameters: small ion concentration and its association with radon and PM concentration in two elementary schools' indoor environments. We have analyzed the association using two approaches: descriptive statistical analysis coupled with linear modelling and artificial neural network predictive modelling. The following conclusions can be made.

- Descriptive statistics showed that for similar median radon concentrations larger number of nanosized particles corresponds to smaller number of small ions. This observation is coherent with the balance equation.
- The linear model derived directly from balance equation allowed estimation of balance equation parameters. The parameters corresponding to the radon term were similar in both schools, indicating similar increase in small ion concentration with radon concentration in both schools. Regarding particulate matter parameters, it was observed that attachment coefficients become larger for particle aggregations corresponding to larger particle diameters, in accordance to theoretical expectations. However, these parameters were different in two schools, possibly due to different air pollution composition.
- The hypothesis that small ion concentration, which may have certain impact on human health and wellbeing, can be predicted based on radon and particulate matter measurements predictors was successfully tested.
- Explained variance for the linear predictive model was under 0.5, and for the artificial neural network (ANN) predictive model with similar predictors was around 0.7. ANN predictive model has achieved median absolute error of about 40 ions/cm^3 on test data.

These modelling efforts enable several future work directions and applications that may be of wider interest for indoor air quality monitoring. Since small ions can be an important part of air quality consideration, their concentration could be to a certain extent modelled based on several more easily obtained/measured predictors. We have showed that the ANN model successfully helped in harmonizing inputs from several instruments of different grade (low cost radon and lab grade particulate matter monitors) and enabled predictions of small ions concentration of comparable quality to the lab grade Gerdien type instrument. Furthermore, since the particulate matter concentration was one of the important predictors, and having in mind recent uptake of low-cost PM monitors, data

driven solution for estimating small ions concentration based on these sensors as supporting predictors is an interesting future research topic.

Author Contributions: Conceptualization, M.D. (Miloš Davidović); data curation, M.D. (Miloš Davidović) and M.J.-S.; formal analysis, M.D. (Miloš Davidović) and M.D. (Milena Davidović); funding acquisition, M.D. (Miloš Davidović), M.D. (Milena Davidović) and M.J.-S.; investigation, M.D. (Miloš Davidović), P.K. and M.J.-S.; methodology, M.D. (Miloš Davidović), P.K., M.J.-S. and Z.R.; project administration, M.D. (Miloš Davidović); resources, P.K. and M.J.-S.; software, M.D. (Miloš Davidović); supervision, M.J.-S. and Z.R.; validation, M.D. (Miloš Davidović) and M.D. (Milena Davidović); visualization, M.D. (Miloš Davidović); writing—original draft, M.D. (Miloš Davidović), M.D. (Milena Davidović), R.J., P.K., M.J.-S. and Z.R.; writing—review and editing, M.D. (Miloš Davidović), M.D. (Milena Davidović), R.J., P.K., M.J.-S. and Z.R. All authors have read and agreed to the published version of the manuscript.

Funding: The research was funded by the Ministry of Education, Science and Technological Development of the Republic of Serbia.

Acknowledgments: We would like to thank the participating pupils and staff of Elementary School “Aleksa Šantić” in Kaluđerica, Belgrade, and Elementary School “20. oktobar” New Belgrade, Belgrade, for helping with the smooth realization of the experiments. The authors are thankful to the COST Action INDAIRPOLLNET CA17136, supported by COST (European Cooperation in Science and Technology).

Conflicts of Interest: The authors declare no conflict of interest.

Appendix A

There are several main physical processes that are involved in changes in SI concentration. Firstly, SI are constantly created, in pairs, by ionizing radiation that exists in the environment. SI are continuously created when neutral air molecules are irradiated by cosmic rays or radiations from natural radioactive materials in soil and air. Neutral air molecules may be ionized into positive ions and free electrons that are attached to other hydrous or oxygen molecules in air, and in order to become stable these ions are adsorbed to neutral molecules forming cluster ions.

UV radiation is mainly responsible for ionization of molecules and atoms in high atmosphere, but it is exhausted at higher levels and doesn't arrive to lower troposphere [28]. Several natural sources of ionizing radiation are responsible for air-ion production in the lower troposphere, namely radioactive gases (particularly ^{222}Rn and its progenies), radioactive substances at ground level (e.g., natural α and β emitters in the air and soil) and cosmic rays. These three contributions are comparable, approximately 20% of the total surface ionization rate is due to ionization from cosmic rays, and remaining 80% arises from natural α and β emitters in the air and soil.

Air-ion pair generation near the ground varies mostly with the concentration of ^{222}Rn and its progenies. The half-life of ^{222}Rn is approximately 3.8 days and the decay product is an alpha particle with energy 5.49 MeV. The decay of ^{222}Rn generates a large number of nitrogen and oxygen molecular ions (order of magnitude $\sim 10^5$) per each α -particle. As a consequence, the near-ground ionization rate caused by background ionization, is about 10 ion pairs/cm³s in continental areas [28]. Within microseconds of the ionization process, primary ions evolve through the process of hydration to form small cluster ions, also known as small air ions or nano-air ions. This class of air ions can survive much longer, up to 100 s, depending predominantly on air pollution and air density [22].

While small air ions technically are particulate matter belonging to ultrafine particulate fraction (albeit only a few nanometers in diameter), it is worth pointing out the following. Small air ions are electrically charged clusters consisting of several molecules in which ordinarily neutral atmospheric molecules/atoms have gained or lost electrons. While particulate matter can also be charged, it is composed of a much larger number of molecules and is thus up to several orders of magnitude larger in diameter compared to the small ion clusters. Since cluster ions readily attach to particles, it is known that their concentration decreases sharply within few tens of meters from the road [29], this making indoor ion sources most significant, which is important to keep in mind for indoor air monitoring.

SI are also continually being destroyed in a process of recombination, producing neutral molecular clusters. In addition to the process of recombination, SI can attach to PM. Because of this, a change in PM concentration directly results in a change in SI concentration. A significant portion of PM in the

urban environment is a result of human activities, where smaller particles are typically associated with the process of combustion occurring in vehicles, industrial activities, biomass burning, and similar, while larger particles are typically due to construction and demolition activities, entrainment of outdoor dust and similar. The SI balance equation can be used to quantitatively describe the above-mentioned processes.

Appendix B

Table A1. Description of the instruments used in data gathering campaigns conducted in this study.

Instrument	Specification Based on Datasheets, Application Notes and Calibration Certificates	Type of Calibration
TSI NanoScan SMPS Model 3910	Relative standard deviations in total concentration 2.7% Sizing of the particles: standard deviations in median particle diameter 1.1% Discrepancy relative to certified size ranges of 20, 60, 80, 200 and 300 nm less than 8%.	NIST traceable using TSI calibration system, conducted in test atmosphere of polystyrene latex particles
TSI Optical particle sizer 3330	Counting efficiency at 0.5 μm (90–110%) Inlet flow: 0.95–1.05 L/min Sizing of 1 μm particles: 90–100% <i>Allowable range is given in parenthesis, calibration certificate includes traceably measured single value.</i>	NIST traceable using TSI calibration system, conducted in test atmosphere of polystyrene latex particles
Radon Scout	Sampling type: Diffusion Sensitivity: 1.8 count per minute/kBq/m ³ (4 cph/pCi/L) Measurement range: 0 . . . 2 MBq/m ³ Error: $\pm 5\%$ within the whole range or smaller	Factory calibration, instrument class certified by the US-EPA/NRSB
Gerdien-type air ion detector	Sensitivity of the current measurement is limited by AD converter resolution and amounts 1.6 fA. Using Equation (1) in [22], this value equals to 2 ions/cm ³ . Measuring sensitivity is limited by noise induced by various sources (uncertainties of air-flow, calibration, temperature drift, gain error, etc.) and is experimentally obtained to be ± 5 ions/cm ³ .	Calibrated using Equation (1) in [22] and Keithley 261 small current generator (output signal ~ 10 fA). Flow tuning was done via hot-wire anemometer.

Particle sizers were manufactured by TSI Incorporated, 500 Cardigan Road, Shoreview, Minnesota 55126 USA. Radon Scout was manufactured by SARAD GmbH, Wiesbadener Straße 10, DE-01159 Dresden, Germany. Gerdien-type air ion detector was developed by Institute of Physics, University of Belgrade, Belgrade, Serbia. The divide between low-cost and lab grade instruments is not strict, and does not always refer to price of the sensor itself. The line is further blurred by the fact that low cost sensors may require extensive, i.e., costly (re)calibration efforts. While operating principles of both type of instruments can be very similar, lab grade instruments are typically characterized by better implementation of these principles, for example better sampling method, higher quality of the sensors that allow better temporal resolution etc. and consequently better accuracy. In this paper, all of the instruments used, except for the Radon Scout (due to instruments sampling method, time resolution, cost and lack of traceability) could be considered to be lab grade instruments.

Appendix C

There are two classes of parameters of neural networks that can be tuned in order to improve the predictions. The first class consists of model parameters that are calculated during the process of neural network training. This is done by optimizing a loss function, which in our case was squared error (MSE). The second class of parameters are hyperparameters. These parameters define the structure of the model and need to be defined a priori. Hyperparameters used in this study are shown in Table A2. Parameter tuning can easily become an exhaustive task, and it is desirable to use simple models if they can achieve similar accuracy to the more complex ones, in order to keep solution space more manageable.

There are two classes of parameters of neural networks that can be tuned in order to improve the predictions. The first class consists of model parameters that are calculated during the process of neural network training. This is done by optimizing a loss function, which in our case was squared error (MSE). The second class of parameters are hyperparameters. These parameters define the structure of the model and need to be defined a priori. Hyperparameters used in this study are shown in Table A2. Parameter tuning can easily become an exhaustive task, and it is desirable to use simple models if they can achieve similar accuracy to the more complex ones, in order to keep solution space more manageable.

Table A2. Hyperparameters of the artificial neural network model used in this study.

Hyperparameters	Minimum	Maximum	Step Size
Hidden layers	1	2	1
Neurons per hidden layer	1	15	1
Neurons in input layers (Radon + PCA components)	2	5	1
Early stopping	Not used	Not used	Not used
Activation function		'relu'	
Cost function		MSE	
Solver		'adam'	

Figure A1a shows what happens with the R2 score on training and test data sets when number of neurons is increased in the hidden layer. It can be observed that only a small network, with 3–4 neurons results in a balanced training/test score, and that further increase of number of neurons results in increased test set discrepancy, due to an overfit. This was the reason why no additional layers were introduced, since this would certainly lead to an overfit, i.e., an ANN model that behaves excellently on the training data, and very poorly on the test data. Furthermore, similar conclusion can be made by observing MSE observed on a test set, shown in Figure A1b. The network with two hidden layers had a greater MSE compared to the simpler one hidden layer network. The simplest models that have optimal statistics are ANN models with three and four hidden neurons (network architecture and activation function is shown in Figure A2), with more complex model being slightly better in terms of R2 score and MSE. MSE is susceptible to outliers, and a more robust statistical measure of model performance is a median absolute error, which turned out to be around 40 ions/cm³ for optimal ANN models. The explained variance of around 0.70 was from the test set for the optimal ANN models.

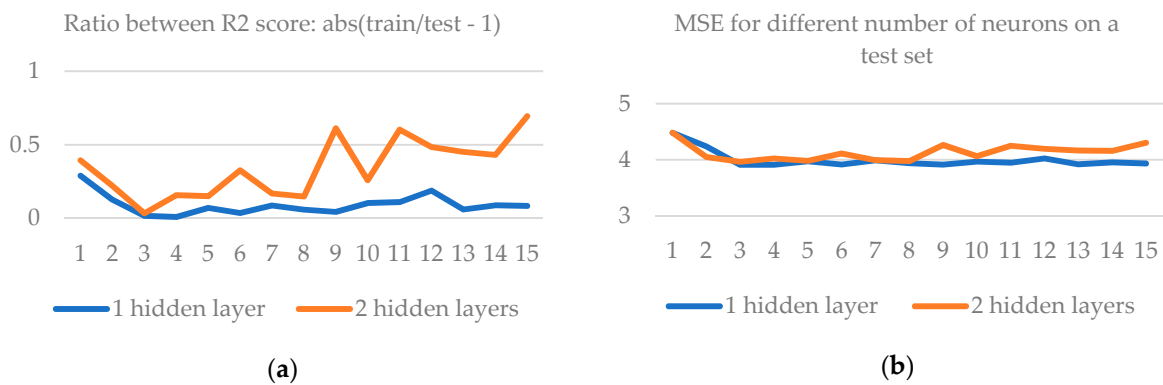


Figure A1. Statistics for different ANN models where several hyperparameters are changed (number of hidden layers and number of neurons per hidden layer). (a) R2 score training test ratio (b) MSE on a test set. All models have radon and 2 particulate matter related PCA components as inputs. Figure A1b uses log10 scale.

17. Schweidler, E. Ueber das Gleichgewicht zwischen ionenerzeugenden und ionenvernichtenden Vorgaengen in der Atmosphaere. *S. B. Akad. Wiss. Wien* **1918**, *128*, 947–955.
18. Donnelly, M.I. *A Study of the Nuclear Content of the Atmosphere and the Lifetime of Small Ions in New York City*; ETD Collection for Fordham University: New York City, NY, USA, 1950.
19. Topalović, D.B.; Davidović, M.D.; Jovanović, M.; Bartonova, A.; Ristovski, Z.; Jovašević-Stojanović, M. In search of an optimal in-field calibration method of low-cost gas sensors for ambient air pollutants: Comparison of linear, multilinear and artificial neural network approaches. *Atmos. Environ.* **2019**, *213*, 640–658. [[CrossRef](#)]
20. Pedregosa, F.; Varoquaux, G.; Gramfort, A.; Michel, V.; Thirion, B.; Grisel, O.; Blondel, M.; Prettenhofer, P.; Weiss, R.; Dubourg, V. Scikit-learn: Machine learning in Python. *J. Mach. Learn. Res.* **2011**, *12*, 2825–2830.
21. Kingma, D.P.; Ba, J. Adam: A method for stochastic optimization. *arXiv* **2014**, arXiv:1412.6980.
22. Kolarž, P.; Miljković, B.; Čurguz, Z. Air-ion counter and mobility spectrometer. *Nucl. Instrum. Methods Phys. Res. Sect. B Beam Interact. Materials At.* **2012**, 219–222. [[CrossRef](#)]
23. Waskom, M.; Botvinnik, O.; O’Kane, D.; Hobson, P.; Ostblom, J.; Lukauskas, S.; Gemperline, D.C.; Augspurger, T.; Halchenko, Y.; Cole, J.B.; et al. mwaskom/seaborn: V0. 9.0 (July 2018). Available online: <https://zenodo.org/record/1313201#.X0dZDSMRWUk> (accessed on 6 July 2020).
24. McKinney, W. Data structures for statistical computing in python. In Proceedings of the 9th Python in Science Conference, Austin, TX, USA, 28 June–3 July 2010; pp. 51–56.
25. Kuhn, M.; Johnson, K. *Applied Predictive Modeling*; Springer: Berlin/Heidelberg, Germany, 2013; Volume 26.
26. University of Arizona, Hydrology & Atmospheric Sciences, Atmospheric Electricity ATMO/ECE 489/589 Spring Term, Lecture Notes. Available online: <http://www.atmo.arizona.edu/students/courselinks/spring13/atmo589/> (accessed on 6 July 2020).
27. De Vito, S.; Di Francia, G.; Esposito, E.; Ferlito, S.; Formisano, F.; Massera, E. Adaptive machine learning strategies for network calibration of IoT smart air quality monitoring devices. *Pattern Recognit. Lett.* **2020**. [[CrossRef](#)]
28. Iribarne, J.; Cho, H.-R. *Atmospheric Physics*; D. Reidel Publishing Company: Dordrecht, The Netherlands, 1980.
29. Jayaratne, E.; Ling, X.; Morawska, L. Observation of ions and particles near busy roads using a neutral cluster and air ion spectrometer (NAIS). *Atmos. Environ.* **2014**, *84*, 198–203. [[CrossRef](#)]



© 2020 by the authors. Licensee MDPI, Basel, Switzerland. This article is an open access article distributed under the terms and conditions of the Creative Commons Attribution (CC BY) license (<http://creativecommons.org/licenses/by/4.0/>).

FACTORS AFFECTING INDOOR RADON VARIATIONS: A CASE STUDY IN SCHOOLS OF EASTERN MACEDONIA

Z. STOJANOVSKA¹, B. BOEV², Z. S. ZUNIC³, K. IVANOVA⁴, S. AJKA⁵, I. BOEV²,
Z. ČURGUZ⁶, P. KOLARŽ⁷

¹ Faculty of Medical Sciences, Goce Delčev University Stip, Republic of Macedonia
E-mail: zdenka.stojanovska@ugd.edu.mk

² Faculty of Natural and Technical Sciences, Goce Delčev University Stip, Republic of Macedonia
E-mails: blazo.boev@ugd.edu.mk, ivan.boev@ugd.edu.mk

³ Vinca Institute of Nuclear Sciences, University of Belgrade, Belgrade, Serbia
E-mail: zzunic@verat.net

⁴ National Centre of Radiobiology and Radiation Protection, Sofia, Bulgaria
E-mail: k.ivanova@ncrrp.org

⁵ Croatian Geological Survey, Zagreb, Croatia
E-mail: ajka.sorsa@hgi-cgs.hr

⁶ Faculty of Transport, University of East Sarajevo
E-mail: curguzoran@yahoo.com

⁷ Institute of Physics, University of Belgrade
E-mail: kolarz@ipb.ac.rs

Received May 13, 2018

Abstract. The subject of this study is the radon concentrations variations, measured with a nuclear track detectors in a total of 58 premises in all 29 primary schools of 4 municipalities in the Eastern part of the Republic of Macedonia. Despite a relatively small territory, the variability of radon concentrations proved to be significant. The geometric means (geometric standard deviations) of radon concentrations in the examined municipalities were in the range from $GM = 71 \text{ Bq/m}^3$ ($GSD = 2.08$) to $GM = 162 \text{ Bq/m}^3$ ($GSD = 2.69$), while for the entire region it was: $GM = 96 \text{ Bq/m}^3$ ($GSD = 2.47$). The influence of the geographical and geological features of the school site as well as the building characteristics on the radon variations were investigated. The analysis showed that type of municipality, building materials, basement and geology have significant effects and respectively describe 6%, 16%, 22%, 39% of the radon total variability.

Key words: geology, building characteristics, radon variations.

1. INTRODUCTION

Radon is a natural radioactive gas present in each indoor environment. Indoor radon concentration (R_n) is subject to large spatial and temporal variations. The main R_n source is radium that is contained in the soil under the building as well as in the building materials. In other words, the amount of radon generated in the terrestrial material depends on the quantity of radium, and how much will exhale from the surface and further accumulate in the indoor atmosphere depends on a series of natural and artificial factors. Apart from the radon geogenic potential and meteorological conditions that affect the radon dynamics, the characteristics of

the building and the living habits of its inhabitants are also factors that significantly affect Rn variations.

Many studies have been concerned with the analysis of Rn variations as a function of a given factor, using different manner for their quantification. These are usually expressed by the: *coefficient of variation (CV)* [1, 2] defined as ratio of the Rn standard deviation to the Rn mean value; *geometric standard deviation (GSD)* [3] which describes how spread out are a set of Rn values whose average is presented by the geometric mean; Pearson's correlation coefficient (R), as a measure of the linear relationship between two Rn variables; Spearman's rank correlation coefficient (ρ), as measure of how well the relationship between two Rn variables can be described by a monotonic function [4] or by the correlation ratio (η) [5] which is a measure of the relationship between the Rn dispersion within individual categories and the dispersion across the whole sample.

A recent study of the GSD values of 81 national and regional Rn surveys has revealed that the main factors influencing the Rn variations over a territory are: area of territory, sample size, characteristics of measurements technique, radon geogenic potential, building construction characteristics and living habits [3]. Furthermore, the factors associated with building construction and livings habits have a regional character. In a study carried out in 3 different regions of Bulgaria, is reported that factors effects are in function of geology and geographical position of the measuring location [4].

Motivated by this, we decided to conduct a survey to examine the factors that influence radon variations in a relatively small area with a limited number of measurements. This paper presents the results of that research and compares them with the ones reported in the literature.

2. MATERIALS AND METHODS

The geographical position of study area is shown in Figure 1. It covering: one urban (M3) and three rural municipalities (M1, M2, M4) in Eastern part of Macedonia.

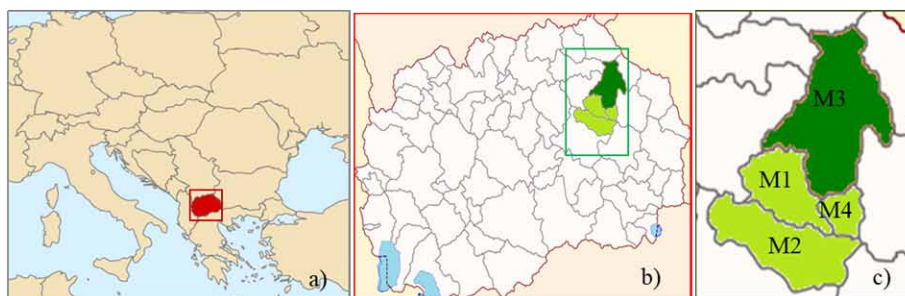


Fig 1 – a) Geographical position of Macedonia in Europe; b) municipalities location in the country; c) Cesinovo-Oblesevo (M1), Karbinci (M2), Kocani (M3), Zrnovci (M4).

According to geology, the area belongs to a Geotectonic zone named the Serbo Macedonian Massif bordering with the Kratovo Zletovska volcanic area to the north and with the Vardar geotectonic zone to the west.

Having in mind that the spatial distribution of primary schools is in function with the population density, we supposed that the Rn in the schools could be representative for the whole region [6]. The survey started at the beginning of the summer semester in January 2016. In each school, two nuclear track detectors for Rn measurements were installed: in a classroom and an assembly hall. The criteria for deployment detectors in the classrooms were their location on the ground floor and that the youngest students (first or second class) stay in them. Generally, the assembly hall in the schools is also located on the ground floor, so out the total 58 monitored premises in 29 schools, only two were on the first floor. At the end of the semester (June 2016), the detectors were collected and sent for analysis.

The Rn concentration was measured by commercial Gamma 1 detectors provided and analyzed by Landauer Company, Sweden. This type of detector has been used in some earlier studies [7–9].

During this field survey, information about the measuring locations was collected. It included: GPS coordinates, altitude, type of municipality. We also considered some characteristics of the buildings such as: presence of basement, total number of the floors, room type and window type. The litho-stratigraphy for the locations were extracted from the detailed geological map of the country [10].

2.1. DATA ANALYSIS

Characteristics of the measuring locations (further named factors) along with the measured Rn were analyzed. The Rn data are well fitted with a log normal function and log transformed values met the criterion for normal distribution. In the cases where the variance of $\ln Rn$ among certain categorical factors was the same, the parametric ANOVA and Fisher LSD tests were applied to test the differences between the mean values. In addition, when the requirement of homogeneity was not satisfied, the corresponding non-parametric: Kruskal-Wallis and Mann-Whitney tests were applied. As a measure of the level of association between $\ln Rn$ and categorical factors the squared correlation ratio (η^2) was used, which was calculated as a decimal number in range between 0 and 1 or as a percentage.

3. RESULTS AND DISCUSSION

Descriptive statistics of the measured Rn in schools premises of the entire region and for each municipality separately are given in Table 1.

Table 1

Descriptive statistic of Rn measured in 58 schools premises of the four municipalities

Statistic	Rn				
	All	M1	M2	M3	M4
N	58	18	16	20	4
Minimum (Bq/m ³)	10	10	16	15	57
Maximum (Bq/m ³)	508	508	339	201	137
AM (Bq/m ³)	136	223	106	90	104
SD (Bq/m ³)	115	148	84	60	36
GM (Bq/m ³)	96	162	78	71	98
GSD	2.47	2.69	2.41	2.08	1.49

AM: arithmetic mean; SD: standard deviation; GM: geometric mean; GSD: geometric standard deviation.

The GM value for Rn that refers to the whole region was slightly higher than the national value of GM=84Bq/m³ (GSD = 1.9) [11], but it was lower than the GM = 131Bq/m³ (GSD = 2.34) published for the Northern and Western neighboring municipalities [12]. Although the chosen region is in a relatively small territory belonging to a geotectonic zone, the Rn variations between municipalities and within them were significant (ANOVA, $p = 0.02$). Rn in the M1 municipality was higher than in M2 and M3 (LSD, $p < 0.05$). The Rn in the M4 municipality did not differ in comparison to the other three municipalities.

The first step in our analysis was to examine the impact of the geographical characteristics of the measuring locations on Rn variations. The correlations between: the longitude, the latitude, the altitude and the Rn were not significant. In addition, Rn were grouped according to the type of municipality. The higher Rn are related to the rural municipalities and the lower to the urban ones (Table 2). In Figure 2, the relatively small value of $\eta^2 = 0.06$, indicated the low degree of association between this factor and Rn. We assumed that its effects are practically related to the type of school buildings that in our case were bigger and newer in urban areas than in rural ones. In other words, this factor itself is not independent and can be overlapping with another factor as has been reported in literature it is sometimes significant [13] and sometimes not [12].

Table 2

Rn measured in rural and urban municipalities

Type of municipality	N ¹	Rn (Bq/m ³)			
		Min ²	Max ³	GM ⁴	GSD ⁵
Rural	38	10	508	113	2.59
Urban	20	15	201	71	2.08

¹Number of measurements, ²Minimum, ³Maximum, ⁴Geometric mean, ⁵Geometric standard deviation (dimensionless).

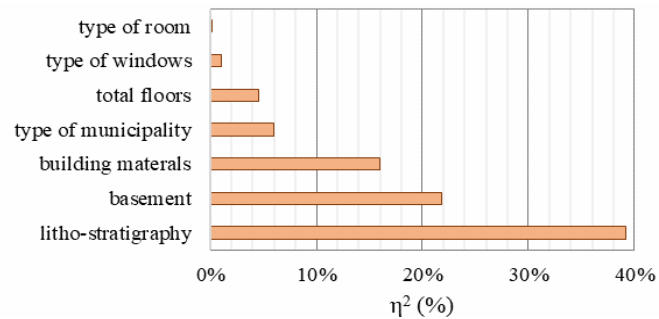


Fig. 2 – η^2 (%) for each categorical factor.

In order to investigate the influence of the geology on the Rn, the measured data were assigned to litho-stratigraphic units. Rn variations between them (Table 3) were significant (KW, $p = 0.014$). The analysis of the multiple pairwise Rn differences between litho-stratigraphic units did not show a strong differentiation in groups. For example, Rn in the andesite-breccia unit was higher only in comparison to units of lower river terrace (MW, $p = 0.02$), proluvial deposits (MW, $p = 0.01$) and schistous granite (MW, $p = 0.04$) while differences with other units were not significant. Similarly, Rn in the schistous granite was significantly lower only in relation to andesitic tuff and andesite-breccia and so on. The highest value of $\eta^2 = 39\%$ in Figure 2 is for the litho-stratigraphic units, indicating the Rn strongest relation with this factor in comparison to all others. This result was expected, bearing in mind that the main source of Rn is radon in the soil gas and that its generation and transport through it are closely related to geology. Different levels of association between Rn and geology, appeared in the literature. For example, regression based on grouping by geological units explains $R^2 = 33\%$ of the variation in Switzerland [14] while in research from the Techa River region (Russia), for association between Rn and geological factors the value of $\eta = 0.32$ has been reported [5].

Table 3

Statistic of Rn ascribe to litho-stratigraphic units

Litho-stratigraphic units	N ¹	Rn (Bq/m ³)			
		Min ²	Max ³	GM ⁴	GSD ⁵
Amphibole-chlorite schist and metadiabase	2	15	66	31	2.85
Andesite-breccia	8	43	508	236	2.40
Andesitic tuff	2	200	201	200	1.00
Deluvial deposits	2	105	177	136	1.45
Lower river terrace	20	21	361	99	1.83
Mica-schist and lepttionolite	4	41	101	69	1.55
Proluvial deposits	12	10	243	70	2.60
Schistous granite	2	16	18	17	1.09

¹Number of measurements, ²Minimum, ³Maximum, ⁴Geometric mean, ⁵Geometric standard deviation (dimensionless).

In our study, stone used as a building material was appeared to be another significant source of Rn. Those buildings made of stone had higher concentrations in comparison to buildings built of bricks (Table 4). A similar trend has been obtained in our previous studies [15]. The value for η^2 presented in Figure 3 shows that construction materials describe 16% of the total Rn variability. Detailed examination of the Rn variability as a function of building characteristics was done in three regions of Bulgaria where building material was significant only in two regions ($\rho^2 \approx 20\%$).

Table 4

Statistic of Rn measurements in buildings grouped by building materials and presence of basement

Factor		N ¹	Rn (Bq/m ³)			
			Min ²	Max ³	GM ⁴	GSD ⁵
Building materials	brick	30	16	236	68	2.02
	stone	28	10	508	139	2.60
Presence of basement in the building	no	44	15	508	122	2.19
	yes	14	10	137	46	2.38

¹Number of measurements, ²Minimum, ³Maximum, ⁴Geometric mean, ⁵Geometric standard deviation (dimensionless).

The next factor that significantly affected Rn variations was the presence or absence of a basement in the building [16, 17]. From Table 4 it is clearly seen that the buildings with basement have lower concentrations compared to those without basement (LSD, $p = 0.0002$).

It should be noted that the effect of a basement on the Rn in a building is two-fold: although the Rn on a ground floor above a basement can be comparatively low (as the room has no ground contact) the Rn in basements themselves are generally high. Despite the fact that the factor *basement* is well known and confirmed in many studies, the level of its contribution in Rn variability is not everywhere the same. For example in our case, this factor describes 22% of the Rn variability, while in the previously mentioned Bulgarian study in the continental region of volcanic geology the contribution was similar to our $\rho^2 \approx 23\%$, while in continental with sedimentary geology it was about $\rho^2 \approx 6\%$.

The effects of the factors: *window type*, *total number of floors*, *room type* on Rn variations were also investigated. Their influence proved to be not significant, although theoretically it was expected. For example, more building floors reduce the pressure gradient, which further reduces the radon emanation from the soil into indoors, further the new type of windows hermetically sealed the room, making the natural ventilation much lower compared to the rooms with old wooden windows. Yet, it is our assumption that other factors prevail over the impact of these factors. An explanation for the absence of differences between classrooms and assembly hall is assumed due to their similar usage.

4. CONCLUSION

The subject of this study was factors affecting Rn variations in schools premises of 4 municipalities located in Eastern part of Republic of Macedonia.

The geographical position (*longitude, latitude, altitude, type of municipality*), geology of the site (*lithostratigraphic units*) and building characteristics (*building materials, presence of basement, window type, total number of floors, room type*) influence on Rn variation was investigated. The analysis has been showed that the factors which appeared to have significant contribution in Rn variations are:

- (1) *lithostratigraphic units* which was proved to have the most dominant influence describing 39% of the Rn variability in the examined region;
- (2) *basement* affected 22% of Rn variation;
- (3) *building materials* allow explanations of 16% Rn variation;
- (4) *type of municipality* that explained 6 % of the Rn variability.

In general, comparison of the results obtained in this study with those published in the literature confirms that the factors effects on Rn variations are subject of spatial variability and they should be carefully considered.

Acknowledgements. The authors highly appreciate the collaboration of the mayors and schools directors in Cesinovo-Oblesevo, Karbinci, Kocani, Zrnovci municipalities during this survey. A special acknowledgment to Dr Ilia V. Yarmoshenko and Dr Georgy Malinovski from IIE UB RAS, Ekaterinburg, Russia, for their careful reading of the manuscript and helpful comments.

The Gamma 1 detectors were provided within the Project P- 41028 of the Ministry of Education, Science and Technological Development of the Republic of Serbia.

REFERENCES

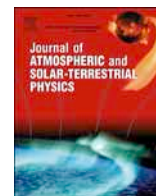
1. F. Bochicchio, Z. Žunić, C. Carpentieri, S. Antignani, G. Venoso, V. Carelli, C. Cordedda, N. Veselinović, T. Tollefsen, P. Bossew *Indoor Air*. **24**(3), 315–326 (2013).
2. Z. Stojanovska, Z. Zunic, P. Bossew, F. Bochicchio, C. Carpentieri, G. Venoso, R. Mishra, R. Rout, B. Sapra, B. Burghel, A. Cucos Dinu, B. Boev, C. Cosma, *Radiat Prot Dosim*. **162**(1–2), 152–156 (2014).
3. I. Yarmoshenko, A. Vasilyev, G. Malinovsky, P. Bossew, Z.S. Žunić, A. Onischenko, M. Zhukovsky, *Sci Total Environ*. **541**, 155–160 (2016).
4. K. Ivanova, Z. Stojanovska, M. Tsenova, B. Kunovska, *Air Qual Atmos Health* (2017) <https://doi.org/10.1007/s11869-017-0501-0>
5. I. Yarmoshenko, G. Malinovsky, A. Vasilyev, A. Onischenko, A. Seleznev, *Sci Total Environ*. **571**, 1298–1303 (2016).
6. Z.S. Žunić, P. Bossew, F. Bochicchio, N. Veselinovic, C. Carpentieri, G. Venoso, S. Antignani, R. Simovic, Z. Čurguz, V. Udovicic, Z. Stojanovska, T. Tollefsen, *J. Environ. Radioact*. **167**(1), 188–200 (2017).
7. Z. Čurguz, Z. Stojanovska, Z.S. Žunić, P. Kolarž, T. Ischikawa, Y. Omori, R. Mishra, B.K. Sapra, J. Vaupotič, P. Ujčić, P. Bossew, *J Environ Radioact*. **148**, 163–169 (2015).
8. Z. Stojanovska, B. Boev, Z. Zunic, P. Bossew, S. Jovevska, *Nukleonika* **61**(3), 385–389 (2016).
9. Z. Čurguz, Z.S. Zunic, T. Tollefsen, P. Jovanovic, D. Nikezic, P. Kolarz, *Rom. J. Phys*. **58**, S90–S98 (2013).

10. T. Rakicevic, N. Dumurzhanov, P. Petkovski, *Interpreter of the Basic Geological Map of SFRY, I: 100 000, sheet Shtip*. Geological Survey, Skopje, 1–70 (1976).
11. Z. Stojanovska, J. Januseski, B. Boev, M. Ristova, *Radiat. Prot. Dosim.* **148**,162–167 (2012).
12. Z. Stojanovska, B. Boev, Z. S. Zunic, K. Ivanova, M. Ristova, M. Tsenova, S. Ajka, E. Janevik, V. Taleski, P. Bossew, *Radiat Environ Biophys.* **55** (2), 171–183 (2016).
13. K. Ivanova, Z. Stojanovska, V. Badulin, B. Kunovska, *Radiat. Prot. Dosim.* **157**, 594–599 (2013).
14. G. Kropat, F. Bochud, M. Jaboyedoff, J.P. Laedermann, C. Murith, M. Palacios Gruson, S. Baechler, *J. Environ. Radioact.* **147**, 51–62 (2015).
15. Z. Stojanovska, K. Ivanova, P. Bossew, B. Boev, Z. Zunic, M. Tsenova, Z. Curguz, P. Kolarz, M. Zdravkovska, M. Ristova, *Nucl. Technol. Radiat.* **32**(1), 77-84 (2017).
16. K. Ivanova, Z. Stojanovska, M. Tsenova, V. Badulin, B. Kunovska, *Radiat. Prot. Dosim.* **162**(1–2), 163–166 (2014).
17. Z.S. Zunic, C. Carpentieri, Z. Stojanovska, S. Antignani, N. Veselinovic, T. Tollefsen, V. Carelli, C. Cordedda, O. Cuknic, J. Filipovic, *Rom. J. Phys.* **58**, S320–S327 (2013).



Contents lists available at ScienceDirect

Journal of Atmospheric and Solar-Terrestrial Physics

journal homepage: www.elsevier.com/locate/jastp

Changes of atmospheric properties over Belgrade, observed using remote sensing and in situ methods during the partial solar eclipse of 20 March 2015

L. Ilić^{a,*}, M. Kuzmanoski^a, P. Kolarž^a, A. Nina^a, V. Srećković^a, Z. Mijić^a, J. Bajčetić^b, M. Andrić^b

^a Institute of Physics Belgrade, University of Belgrade, Pregrevica 118, 11080, Belgrade, Serbia

^b University of Defence, Military Academy, Generala Pavla Jurisića Šturma 33, 11000, Belgrade, Serbia

ARTICLE INFO

Keywords:

Solar eclipse

Lidar

Planetary boundary layer

Ground based observations

ABSTRACT

Measurements of atmospheric parameters were carried out during the partial solar eclipse (51% coverage of solar disc) observed in Belgrade on 20 March 2015. The measured parameters included height of the planetary boundary layer (PBL), meteorological parameters, solar radiation, surface ozone and air ions, as well as Very Low Frequency (VLF, 3–30 kHz) and Low Frequency (LF, 30–300 kHz) signals to detect low-ionospheric plasma perturbations. The observed decrease of global solar and UV-B radiation was 48%, similar to the solar disc coverage. Meteorological parameters showed similar behavior at two measurement sites, with different elevations and different measurement heights. Air temperature change due to solar eclipse was more pronounced at the lower measurement height, showing a decrease of 2.6 °C, with 15-min time delay relative to the eclipse maximum. However, at the other site temperature did not decrease; its morning increase ceased with the start of the eclipse, and continued after the eclipse maximum. Relative humidity at both sites remained almost constant until the eclipse maximum and then decreased as the temperature increased. The wind speed decreased and reached minimum 35 min after the last contact. The eclipse-induced decrease of PBL height was about 200 m, with minimum reached 20 min after the eclipse maximum. Although dependent on UV radiation, surface ozone concentration did not show the expected decrease, possibly due to less significant influence of photochemical reactions at the measurement site and decline of PBL height. Air-ion concentration decreased during the solar eclipse, with minimum almost coinciding with the eclipse maximum. Additionally, the referential Line-of-Sight (LOS) radio link was set in the area of Belgrade, using the carrier frequency of 3 GHz. Perturbation of the receiving signal level (RSL) was observed on March 20, probably induced by the solar eclipse. Eclipse-related perturbations in ionospheric D-region were detected based on the VLF/LF signal variations, as a consequence of Ly α radiation decrease.

1. Introduction

Abrupt change in the incoming solar radiation flux during solar eclipse induces disturbances in different atmospheric layers (Geropoulos et al., 2008; Aplin et al., 2016). These disturbances are not necessarily similar to those during sunset/sunrise, because of different time scales and initial conditions. They depend on a number of factors, including the percentage of sun obscuration, latitude, season, time of the day, synoptic conditions, terrain complexity and surface properties. Since solar energy impacts the atmosphere primarily by convection of heat from the ground, lower atmospheric layers are more influenced by

changes in solar radiation. The layer of the atmosphere in direct interaction with the surface, thus directly influenced by the Earth's surface forcing, is called the planetary boundary layer (PBL). Since surface is also a source of humidity and pollutants, turbulence within the PBL is responsible for mixing and dispersion of pollutants, while air pollution concentrations in the PBL are generally higher than those in the free troposphere (Stull, 1988).

A number of studies have focused on the effect of solar eclipse on various atmospheric properties, mainly in PBL. Changes in meteorological parameters near the ground level were most extensively investigated, for several eclipse events (Anderson, 1999; Ahrens et al., 2001; Kolarž

* Corresponding author.

E-mail address: luka@ipb.ac.rs (L. Ilić).

<https://doi.org/10.1016/j.jastp.2017.10.001>

Received 31 March 2017; Received in revised form 16 August 2017; Accepted 3 October 2017

Available online xxx

1364-6826/© 2017 Elsevier Ltd. All rights reserved.

et al., 2005; Founda et al., 2007; Nymphas et al., 2009). The studies reported decrease in temperature and wind speed, changes in wind direction and increase in relative humidity, as a result of solar eclipse. The magnitude of these changes varied in different studies. Decrease in height of the PBL during solar eclipse was also observed (Kolev et al., 2005; Amiridis et al., 2007). The PBL quickly responds to surface forcing and its height can range from as low as a few hundred meters to a few kilometers. Diurnal cycle of the PBL height starts with the sunrise by heating of the surface and development of a convective boundary layer (CBL), reaching a steady state in the afternoon. The CBL remains as a residual layer until the development of a new mixing layer on the following day. A region of statically stable layer – the entrainment zone forms at the top of the PBL. It closely follows the PBL development, being shallow in the morning and thickening during the day due to intense turbulence and vigorous convection (Stull, 1988). During a solar eclipse, the change in the incoming radiation is more abrupt and affects the evolution of the PBL (Amiridis et al., 2007; Kolev et al., 2005), thus providing opportunity for investigating mechanisms involved in PBL evolution.

Some studies investigated eclipse-related changes in ozone concentration (Zerefos et al., 2001; Kolev et al., 2005; Zanis et al., 2001, 2007), due to its strong dependence upon the magnitude of UV flux (Bian et al., 2007). Tropospheric ozone (O_3) is the result of chemical reactions, mostly between nitrogen oxides (NO_x), carbon monoxide (CO) and volatile organic compounds (VOCs), helped with UV radiation via process of photo-dissociation of O_3 . Surface ozone concentrations were reported in literature to decrease during solar eclipse, with exception of unpolluted sites (Zanis et al., 2001, 2007).

Reported observations suggest increase in air ion (Kolarž et al., 2005; Aplin and Harrison, 2003 and references therein) and air radon concentrations (Gasó et al., 1994 and references therein) during solar eclipse, mainly attributed to PBL height decrease. Air ions are natural constituents of the atmosphere produced mostly by cosmic rays (20% of overall ionization) and natural radioactivity from soil (gamma decay of ^{40}K) and the air (^{222}Rn). The first two ionization sources mentioned above are nearly constant in time, and consequently changes of air ion generation are primarily related to changes in Rn concentration. The background concentration of cluster air ions in lower troposphere vary from a few hundred to a few thousand ions cm^{-1} , with an average near-ground ionization rate of 10 ion pairs $cm^{-3}s^{-1}$. Air ions are neutralized mostly by ion-to-ion recombination and ion-aerosol attachment (Dolezalek, 1974). Their concentration changes diurnally: during the night, when the boundary layer conditions are stable concentrations are high, with maximum at dawn. During the day, with the development of convective boundary layer, air ion concentration decreases with minimum in the afternoon (Blaauboer and Smetsers, 1996). Radon and aerosol-carried Rn progenies are powerful air ionizers (energy of α particle decay is more than 5 MeV, while average ionization energy of air is 34 eV/ion pair) and thus the main source of cluster air ion pair production in the troposphere. Radon exhalation from the ground is determined by concentration of uranium, diffusion coefficients and porosity of soil layers on the way to surface (Ishimori et al., 2013). Average Rn concentration over the continents is 10 Bq m^{-3} (UNSCEAR, 1993).

The solar eclipse also influences ionosphere. In the upper part of this area variations in plasma frequencies are detected (Verhulst et al., 2016). Also, there are detected plasma variations in the lower ionosphere (see e.g. Guha et al., 2010; Maurya et al., 2014). One of the ways to register the variations of solar radiation impact within upper atmosphere is based on technology of radio waves which are reflected in ionosphere during propagation between emitters and receivers. Namely, the signal reflection height in the ionosphere and, consequently, parameters describing signal characteristics (propagation geometry, altitude distributions of refractive index and attenuation) depend on local plasma properties (primarily on electron density) (Bajčetić et al., 2015). Electron density declines during solar eclipse, similarly to sunset, resulting in increase of the reflection height of radio signals reflected on relevant atmospheric

layer (Guha et al., 2010), as well as the occurrence of hydrodynamic waves (Nina and Čadež, 2013; Maurya et al., 2014). Because of that, the registered wave variations reflect the non-stationary physical and chemical conditions in the medium, along the considered wave trajectories, in real time. In addition to plasma parameters related to low ionosphere, several parameters describing signal propagation, like distance between transmitter and receiver, influence temporal changes in recorded signal characteristics. Because of that, the electron density decrease (or increase) can result in either increase and decrease of recorded amplitude (Grubor et al., 2008). Thus, only variation from the expected values is important for detection of influences of an event on low ionosphere.

The aim of this paper is to study atmospheric disturbances detected in Belgrade, induced by partial solar eclipse (51% coverage of solar disc) on March 20, 2015. Focusing on troposphere (mainly PBL) and ionosphere (D-region). For that purpose, four experimental setups were used to collect data, including lidar (Light Detection and Ranging) for measurement of PBL height and heights of elevated layers, AWESOME (Atmospheric Weather Electromagnetic System for Observation Modelling and Education) VLF/LF receiver (Cohen et al., 2010) and instruments for measurements solar radiation, meteorological parameters, concentrations of ozone, air ions and radon, and propagation of radio signals in troposphere.

The paper is organized as follows. In Section 2 we describe measurements and methods used in the study, and give overview of background conditions. The results are described in Section 3, and a conclusion of this study is given in Section 4.

2. Measurements and methods

2.1. UV radiation, ozone and air-ion measurements

UV-B erythemal radiation was measured using 501 biometer made by Solar light company, USA. Instrument was set on the roof of the Institute of Physics Belgrade (IPB), so that no obstacles entered the field of view. During the eclipse, data acquisition was set to 10 min. Global Sun radiation was measured by Republic Hydro-meteorological Service in Belgrade using Kipp&Zonen CMP6 pyranometer (<http://www.kippzonen.com/Product/12/CMP6-Pyranometer>), with 1-min data acquisition. Surface ozone measurements were conducted using Aeroqual monitor, series 500 (<http://aeroqual.com/product/series-500-portable-air-pollution-monitor>), made in New Zealand. The instrument was placed near UV 501 biometer and acquisition was set to 6 min. Air ions, temperature, pressure and relative humidity were measured using a Cylindrical Detector and Ion Spectrometer CDIS (Kolarž et al., 2011), made at IPB. The CDIS was placed 1 m above grassy surface (where the soil allows the radon exhalation), at IPB (44.86° N, 20.39° E, 89 m a.s.l.). Only positive air ion concentrations were measured since they have lower mobility than negative ions and consequently lower ion-to-aerosol attachment coefficient. Thus, they are less sensitive to air pollution and provide better picture of atmosphere processes. Radon was measured using continual radon measuring instrument RAD7, DurrIDGE company, USA. Quality of continual Rn measurements is related to level of radon concentration and measuring period, i.e. counting events. The instrument was placed next to CDIS at the same level.

2.2. Measurements of meteorological parameters

The meteorological measurements were obtained at two semi-urban sites in Belgrade. One measurement site was located at IPB. At the site, temperature, relative humidity and atmospheric pressure at altitude 1 m above ground were measured. The meteorological measurements were also available from an automatic weather station collocated with a SYNOP station at Košutnjak, Belgrade (WMO no. 13275, 203 m a.s.l.), about 10 km away from the IPB site.

2.3. Detection of PBL height

A variety of methods can be used to quantify the PBL height, depending on available measurements (Emeis et al., 2008). Differences between PBL and free troposphere can be observed using vertical profiles of thermodynamic quantities and wind from radiosounding measurements. Lidar observations, using atmospheric aerosol as a tracer, can be used to determine heights of both PBL and elevated aerosol layers if present in the atmosphere.

In this study radiosounding and lidar measurements were used to determine PBL height. While radiosoundings are regularly available at 00UTC and 12UTC at the WMO station, providing meteorological data on mandatory and significant pressure levels, the advantage of lidar measurements is that they can be performed continuously with high vertical and temporal resolutions. Data derived from lidar measurements can be used for detection and characterization of aerosols and PBL evolution, and allow for the detection of abrupt and smaller scale changes in the layer structure.

The lidar system at IPB, is a bi-axial system with combined elastic and Raman detection designed to perform continuous measurements of suspended aerosol particles in the PBL and the lower free troposphere. It is based on the third harmonic frequency of a compact, pulsed Nd:YAG laser, emitting pulses of 65 mJ output energy at 355 nm with a 20 Hz repetition rate. The optical receiver is a Cassegrain reflecting telescope with a primary mirror of 250 mm diameter and a focal length of 1,250 mm. Photomultiplier tubes are used to detect elastic backscatter lidar signal at 355 nm and Raman signal at 387 nm. The detectors are operated both in the analog and photon-counting mode and the spatial raw resolution of the detected signals is 7.5 m. Averaging time of the lidar profiles during the March 2015 solar eclipse case was 1 min corresponding to 1,200 laser shots.

Lidar measurements can be used to estimate PBL height using different approaches (Sicard et al., 2006; Baars et al., 2008). In this study, the gradient method was used to determine the position of the strongest gradient of the aerosol vertical distribution, associated with the PBL height (Flamant et al., 1997). The height of a strong negative peak which can be identified as the absolute minimum of the range corrected signal's (RCS) derivative, determines the PBL top height. A strong negative gradient in lidar RCS is a result of decrease in aerosol backscatter due to decrease in aerosol concentration and humidity (Matthias et al., 2004). Our estimate of PBL height is based on lidar measurements at 355 nm. However, when available, measurements at larger wavelengths (i.e. 532 nm and 1,064 nm) are more appropriate for analysis of PBL height due to smaller relative contribution of molecular backscatter compared to 355 nm. Other local minima in the signal derivative, with absolute values above a specified threshold and with transition intervals including a minimum of five points, are associated with elevated aerosol layer top heights in the free troposphere (Flamant et al., 1997).

The Richardson number is used for PBL height estimation from radiosounding measurements. Radiosoundings are performed two times each day, at 00 and 12 UTC, at a weather station (Belgrade Košutnjak, WMO number 13275), 10 km away from the lidar measurement site at 203 m altitude. The Richardson number is defined as (Stull, 1988):

$$R_{ib} = \frac{g[z - z_0][\theta(z) - \theta(z_0)]}{\theta(z)[u(z)^2 + v(z)^2]} \quad (1)$$

where g is acceleration due to gravity, z_0 is the altitude of the weather station, $\theta(z)$ is the potential temperature and $u(z)$ and $v(z)$ are zonal and meridional components of the wind. The layers in which R_{ib} is above a critical value of 0.21 (Vogelezang and Holtslag, 1996; Menut et al., 1999) are considered to be above the PBL.

Since the data are available at discrete heights, at standard and

significant pressure levels, the bulk Richardson number is used (Stull, 1988). Successful estimation of the PBL height from radiosounding measurements from stations in the WMO network, has been previously reported (Jeričević and Grisogono, 2006; Amiridis et al., 2007). Average uncertainty of the PBL height was estimated for March for a 10-year period from 2006 to 2015, from radiosounding profiles retrieved at 12 UTC. Typical resolutions varied from 100 m to 1,000 m, and the uncertainty of PBL height H was estimated using the following formula:

$$H = H_{estimated} \pm \frac{\Delta z}{2} \quad (2)$$

where Δz is the measurement resolution (Jeričević and Grisogono, 2006). It was calculated to be 180 m corresponding to the average vertical resolution of 350 m. On the eclipse day, the resolution and the uncertainty were estimated to be 150 m and 80 m, respectively.

2.4. Terrestrial line-of-sight radio communication measurement setup

The referential Line-of-Sight (LOS) radio link was set in the area of Belgrade, using the carrier frequency of 3 GHz, with the purpose of investigating solar eclipse contribution to receiving signal level (RSL) instability.

The transmitter was emitting non-modulated carrier, having the radio frequency (RF) output power level of 0 dBm. LOS link was established at the distance of 70 m. The signal was transmitted using the signal generator with the frequency stability of TCXO $\leq \pm 0.5$ ppm and signal level stability $\leq \pm 0.7$ dB which was housed at constant temperature. Antenna emitted horizontally polarized electromagnetic (EM) wave. The receiving system (Rx) was formed with Tektronix SA2600 spectrum analyser that was programmed to perform 1 kHz width spectral recording into 500 points. In this way, the generated signal spectrum at the receiving side could be reconstructed with an accuracy of 2 Hz, which made it possible to monitor temporal changes in the level of the received signal peak.

The measuring samples of the received signal level were recorded every 45 s equidistantly during continuous operation of the LOS link. On 20 March 2015, we made 480 recordings through 6 h, including the solar eclipse period.

2.5. Ionospheric observations

Global experimental setup for the low ionospheric observation is based on continuously emitting and receiving the VLF/LF signals by numerous worldwide-distributed VLF/LF transmitters and receivers, respectively. In this study, we based our analysis on D-region monitoring using the 37.5 kHz LF signal emitted by the NRK transmitter located in Grindavik (Iceland) and received at IPB by the AWE-SOMEVLF/LF receiver. This transmitter was chosen because the path of this signal passes through an area that was affected by a total eclipse.

2.6. Background conditions

The eclipse on March 20, 2015 started at 8:40 UTC, ended at 10:58 UTC, reaching maximum coverage of 51% at 9:48 UTC. In the days prior to the eclipse, the synoptic conditions were influenced by a cyclone moving to the east, over Balkans, followed by an increase in geopotential. Wind field was characterized by northwesterly flow shifting to northerly. On the day of the eclipse surface conditions were influenced by weak-gradient anticyclonic field. On the previous day, overcast skies with light rain in the evening were reported. From the morning of the March 20 and during the day, the sky was clear. The calm meteorological conditions provided good opportunity to observe possible eclipse-related changes in meteorological parameters near surface.

3. Results

3.1. Global and UV radiation

Primary effect of solar eclipse is reduction of solar radiation reaching the surface. In Fig. 1 diurnal variation of global sun radiation and UV-B erythemal radiation are shown for the day of the solar eclipse, and for three clear days after the eclipse. Solar eclipse on March 20 occurred during morning increase of both global and UV-B radiation due to sun elevation. Their attenuation was 48%, slightly smaller than the obscuration of the solar disc (51%). This difference could be due to diffuse solar irradiance knowing that UV-B radiation is the shortest wavelength reaching the surface and thus most prone to scattering. While the direct solar irradiance is reduced proportionally to the obscuration of solar disc during the eclipse, the diffuse irradiance is less affected due to contribution of multiple scattering from less shadowed part of the sky (Zerefos et al., 2001). They reported that the difference in reduction of diffuse and direct irradiance was more pronounced at shorter wavelengths.

3.2. Meteorological parameters

Meteorological measurements were analyzed to investigate the response of the air temperature, relative humidity and pressure at near-surface level to the eclipse. As mentioned in the previous section, the meteorological measurements were conducted at two locations: at IPB lidar measurement site and at Košutnjak station, about 10 km away. Diurnal cycle of the temperature was interrupted by the eclipse at both measurement sites (Fig. 2). Change in temperature increase rate was observed at both sites, with similar delay after the first contact. Higher temperatures were measured, and temperature decrease was more pronounced at IPB station, probably due to lower altitude and as a result of lower measurement height above ground. At this station, the temperature decreased during the eclipse, by 2.6 °C, at the rate of 0.043 °Cmin⁻¹, reaching minimum about 15 min after the maximum of the eclipse. At Košutnjak station the temperature was almost constant after the first

contact until the maximum of the eclipse, with an increase rate of 0.003 °Cmin⁻¹. After the eclipse maximum, it started increasing with increased downward radiation, at a higher rate of 0.03 °C/min. To further investigate the effect of the eclipse on temperature, measurements available from Košutnjak station on days following the eclipse were used. The rate of temperature change during the eclipse was compared to the rates recorded during the same period of day on three cloud-free days after the eclipse – March 21, 23 and 24. Increasing trend of maximum daily temperature was measured in this period. On the eclipse day, the increase rate from the first contact to the eclipse maximum (0.003 °Cmin⁻¹) was very low in comparison to the rates of 0.016 °Cmin⁻¹, 0.025 °Cmin⁻¹ and 0.032 °Cmin⁻¹ for the same period on March 21, 23 and 24, respectively. After the eclipse maximum until the end of the eclipse, temperature increase rate of 0.025 °Cmin⁻¹ was comparable to the corresponding rates on the three following days. Total increase in temperature during the eclipse was 2.0 °C, while the corresponding measured increase on March 21, 23 and 24, was 2.3 °C, 3.3 °C and 4.0 °C, respectively.

Relative humidity showed decreasing trend, typical for the beginning of the day and morning increase of temperature. During the eclipse, humidity was almost constant until the maximal obscuration of solar disc, and then it decreased by 10% at both locations (IPB and Košutnjak), in consistency with temperature increase. Until the maximal obscuration, at IPB, the temperature was decreasing while the relative humidity was almost constant. It remains unclear whether its behaviour is an effect of eclipse.

The wind speed measured at the Košutnjak station followed atypical diurnal cycle, until the maximum of the eclipse, when both wind speed and gustiness dropped, and started increasing after the event (Fig. 3). Wind speed decreased from a maximum of 2.7 ms⁻¹ to about 1.1 ms⁻¹ at the end of the eclipse. The absolute minimum of wind speed and gusts was reached about 35 min after the last contact. Wind direction changed from northerly to northeasterly for the duration of the eclipse.

Pressure drop during the eclipse at Košutnjak station was 0.9 hPa (not shown here), which is most probably the consequence of the temperature

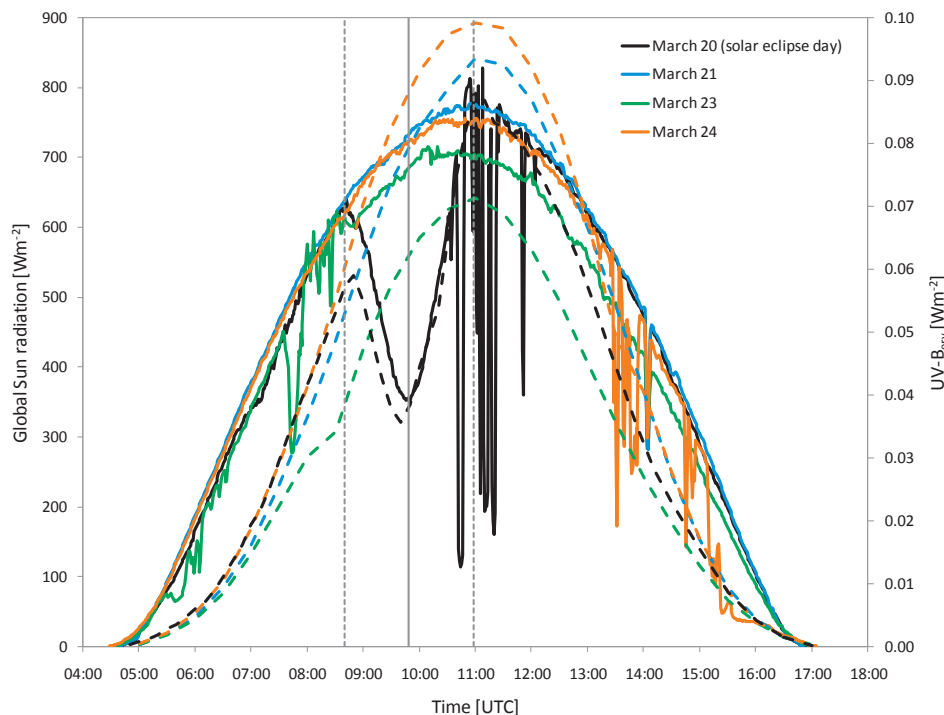


Fig. 1. Global Sun radiation (solid lines) and UV-B erythemal radiation (dashed lines) during partial Solar eclipse (March 20, 2015) and three clear days after the eclipse. Dotted vertical lines indicate beginning, maximum and end of the eclipse.

drop (Fig. 2). The pressure minimum was reached about 30 min after the eclipse maximum. Additional data, from radiosounding, provided information on vertical profiles of meteorological variables 1 h after the event. Up to the top of the PBL, the northerly wind speeds were relatively low, from 2 to 3.5 ms^{-1} . Air in the PBL was not very humid, with relative humidity of 35–60%.

These observed changes are generally in agreement with those reported in previous studies, related to eclipse events with larger obscuration of solar disc. The exception is relative humidity, which was almost constant until the eclipse maximum in this work, while it was reported to increase in previous studies. Anderson (1999) compiled data on near-surface temperature during selected total eclipse events, given in literature. These data showed temperature decrease of 2.0–3.6 °C, with minimal value coinciding with mid-eclipse (in one case), or reached with the time lag of 7–17 min. Founda et al. (2007) presented observations at several sites in Greece, with different degrees of sun obscuration (74–100%) during solar eclipse in March 2007. Their results showed that temperature (measured at altitudes varying from 1.5 m to 17 m at different sites) decreased by 1.6–2.7 °C (3.9 °C at a site affected by low clouds), reaching minimal value 12–14 min after the mid-eclipse. Following the temperature response, the relative humidity was reported to increase by about 20% (Founda et al., 2007; Kolev et al., 2005). A decline in wind speed, after mid-eclipse, as a result of cooling the boundary layer and reduction of turbulent transport (Girard-Arduin et al., 2003) was also reported in literature (Anderson, 1999; Founda et al., 2007).

3.3. PBL evolution assessment from meteorological and lidar measurements

The presence of the residual layer, evolution of the PBL and aerosol layers in the free troposphere during the solar eclipse were observed using lidar measurements in Belgrade. For that purpose, the vertical profiles of the range-corrected analog signal at 355 nm, obtained from 10:15 UTC until 15:25 UTC with temporal resolution of 1 min, were analyzed, using the gradient method. The time series of range corrected signal (RCS) vertical profiles, along with heights of PBL and elevated aerosol layers are presented in Fig. 4.

The eclipse occurred before local noon, during the development of the mixing layer. In the morning, with surface heating, PBL started increasing from 600 m height to about 800 m above ground during the time period of about 2 h until the start of the eclipse at 8:40 UTC. The increase of the PBL height before the eclipse was steady and gradual. During this period, a layer was identified at height of about 1 km. This layer can be identified as the residual layer. With the beginning of the eclipse, the amount of solar radiation reaching the surface started

decreasing (Fig. 1). This affected the change in surface temperature (Fig. 2), and therefore convective motion, with the effects diminishing with height. The PBL height decreased by about 200 m during the solar eclipse, reaching minimum 20 min after the maximum of the eclipse. This decrease in PBL height is similar to those reported in previous research (Amiridis et al., 2007; Kolev et al., 2005), for solar eclipse with larger solar disc obscuration. With passing of the eclipse, the PBL started gaining height until reaching the height of about 1700 m around 13 UTC. Stronger variations of PBL height observed after the eclipse can be attributed to stronger convective motions. In first minutes after the eclipse, shallow cumulus clouds formed with their base at the top of the PBL. A peak in PBL height, coinciding with peaks in temperature and wind speed measurements was observed during the later phase of the event. Depth of the entrainment zone followed the development of the PBL. It showed gradual increase before the eclipse, from low values of about 30 m, to variations in height of several tens of meters after the eclipse as a result of strong convective motions.

The PBL height value calculated as an hourly average around 12 UTC (soon after the end of the eclipse), was $1\,500 \pm 100$ m, in agreement with the one estimated from radiosounding: $1\,600 \pm 80$ m. Small differences of results obtained from radiosounding and lidar measurements can be due to local effects at two measurement sites and differences in the methods used. The gradient method uses gradient in lidar RCS due to decrease in aerosol backscatter while the bulk Richardson number approach relies on thermodynamic properties. Different surface properties and elevations of measurement sites influence the heat and momentum fluxes contributing to the PBL development. Lidar is operated on a fixed location during the whole measurement period, providing information on vertical column of air directly above the instrument. Radiosounding profiles are affected by the horizontal drift of the instrument caused by wind and depend on whether the ascent is made in a thermal or between thermals (Stull, 1988). To further estimate impact of eclipse on PBL height we compared these values with the PBL heights calculated for March for a 10-year period from 2006 to 2015 from the radiosounding profiles taken at 12 UTC (excluding the profile on the day of the eclipse). The values estimated both from lidar (around 12 UTC) and radiosounding measurements made on the day of the eclipse fall within the inter-quartile range of the values for the 10-year reference period (Fig. 4).

The lidar measurements during solar eclipse also showed presence of aerosol layers in free troposphere, at altitudes up to 4 km.

3.4. Ozone and air-ion concentrations

Surface ozone measurements showed no significant decrease, as opposed to most other measured parameters, possibly indicating less significant influence of photochemical reactions at the IPB semi-urban measurement site (see Fig. 5). While a decrease of surface ozone concentration during solar eclipse is expected, this effect could be missing in less polluted areas, or it could be masked by air transport or decline of PBL height (Zanis et al., 2001, 2007). For an urban station in Thessaloniki, Zanis et al. (2001) reported that surface ozone concentration decreased by 10–15 ppbv during the solar eclipse in August 1999 (maximum sun obscuration 90%), with a half-hour delay in starting time of the decrease after the first contact. However, they did not observe any effect on surface ozone in an elevated rural station at Hohenpeissenberg (99.4% sun coverage). Measurements during the solar eclipse in March 2006, conducted in Greece, showed decrease of 5–10 ppb surface ozone in an urban site in Thessaloniki (about 70% sun obscuration), while no effect was observed in relatively unpolluted sites in Finokalia and Kastelozizo, with 82% and 86% solar obscuration, respectively (Zanis et al., 2007). In our study, the measurements were taken at semi-urban site, during solar eclipse event with 51% sun obscuration. It is also noteworthy that measurements conducted for few other days, after the solar eclipse, in the present study showed high time lag of ozone concentration peaks compared to UV radiation peak. This was also reported in Tie et al. (2007) and Bian et al. (2007).

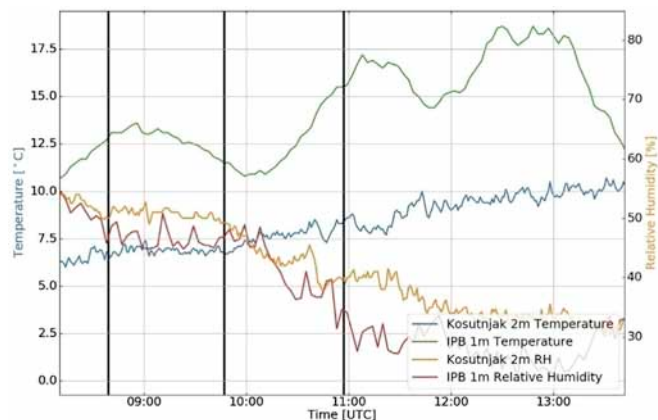


Fig. 2. Temperature and relative humidity. Vertical lines indicate beginning, maximum and end of the eclipse.

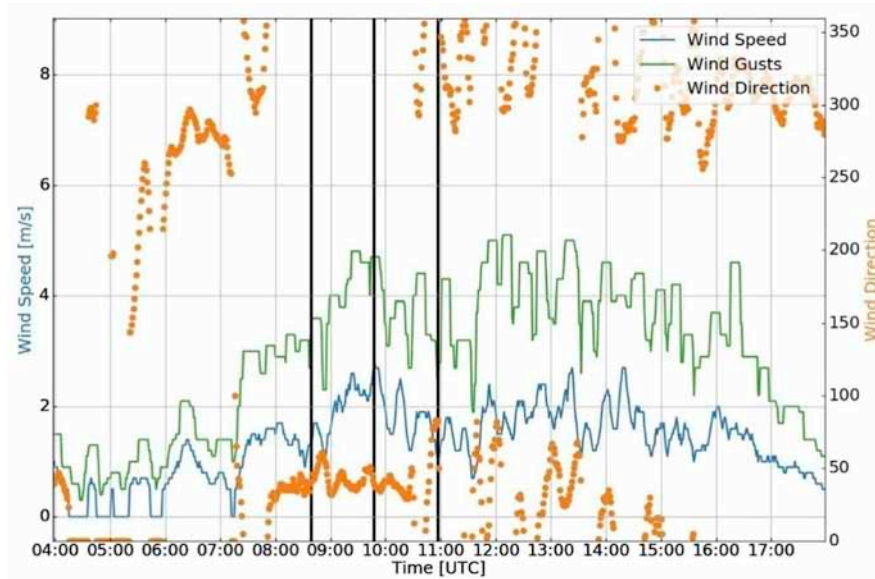


Fig. 3. Wind speed, gusts and direction. Vertical lines indicate beginning, maximum and end of the eclipse.

Radon concentrations measured during the eclipse (not shown here) were in the range between 0 and 15 Bq m^{-3} which is typical background for this part of the day. As shown in Fig. 6, air ion concentration decreased during the course of the day. The decrease was more intensive during the eclipse. After the eclipse, air ion concentration returned to its usual diurnal path to afternoon minimum. This could be explained by decrease of diffusion processes that are responsible for radon exhalation from the soil, as a result of cease of heating the surface during the eclipse. Differences were noted in air ion change during the eclipse in 1999 (97.7% sun obscuration), described in Kolarz et al. (2005) and that described in this study (51% sun obscuration).

3.5. Line-of-Sight radio communication receiving signal change

The observed RSL change during the time of solar eclipse was

compared with the RSL change in few following days. The usual change of RSL in morning hours presented in Bajčetić et al. (2013) was confirmed during regular days, while, the pattern of signal level variation was quite different during the solar eclipse (Fig. 7, left panel).

Additionally, the observed meteorological variables were used to calculate the value of the air refractivity parameter (R) using (3), with the aim of the correlation between variation of that parameter and microwave RSL change (Fig. 7, right panel).

$$R = 77,6 \frac{P}{T} + 3,73 \cdot 10^5 \frac{P_{vp}}{T^2}. \quad (3)$$

R is the value which describes the overall influence of the tropospheric medium on the radio wave propagation and depends on relative air pressure P , absolute temperature T and partially on water vapour pressure P_{vp} (Debye, 1957; Falodun and Ajewole, 2006).

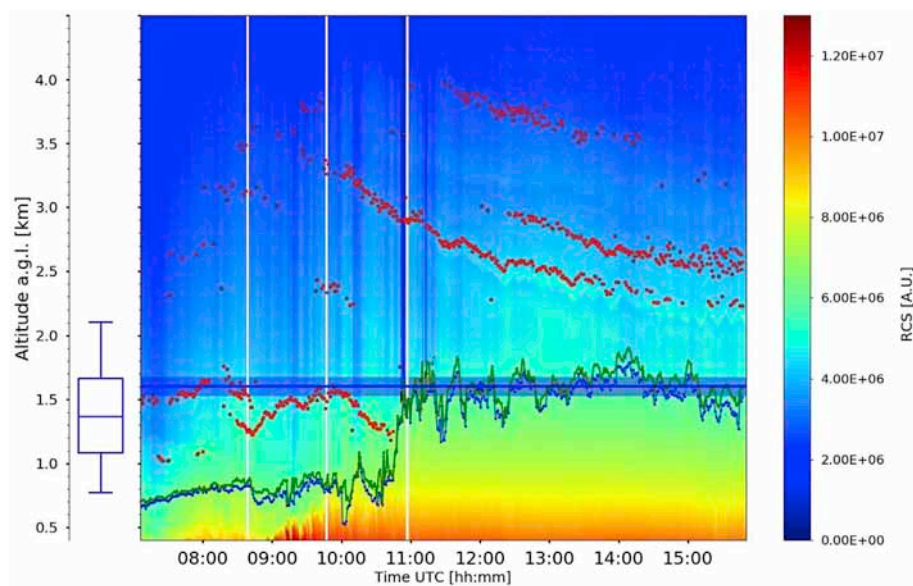


Fig. 4. Temporal evolution of PBL (blue line) and elevated aerosol layers (red dots). Colormaps represent the lidar RCS at 355 nm on March 20, 2015. White vertical lines indicate beginning, maximum and end of the eclipse. Box plot shows the median, first and third quartiles and 5th and 95th percentiles of PBL heights in March for period 2006–2015. (For interpretation of the references to colour in this figure legend, the reader is referred to the web version of this article.)

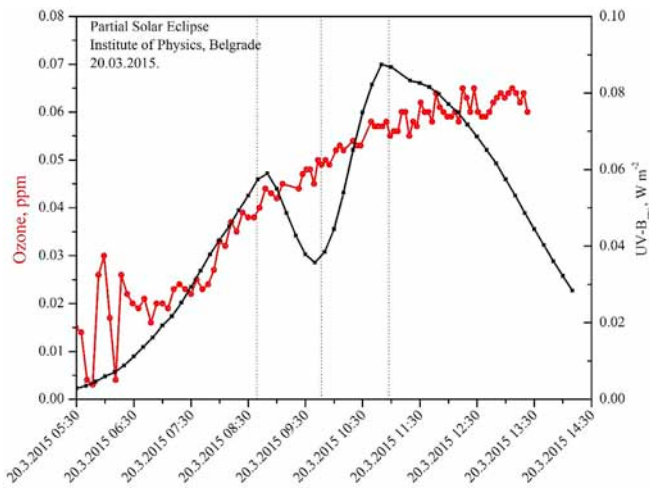


Fig. 5. Ozone and UV-B erythemal radiation during partial solar eclipse. Dotted vertical lines indicate beginning, maximum and end of the eclipse.

We normalized the measured values R_{xi} ($i = 1, \dots, 480$) of the air refractivity parameter to its mean value during the related day (\bar{R}_x), using Eq.2 measured values R_{xi} of the air refractivity parameter, in order to emphasize the level of variation.

$$RSL = 100 \cdot \frac{R_{xi} - \bar{R}_x}{|\bar{R}_x|} \quad (4)$$

Following the presented data in Fig. 8, it can be seen that there was meaningful correlation between RSL and R during the days after the solar eclipse, while their values change fairly independently on the day of the solar eclipse.

Analysing data presented in Fig. 8, it can be seen that before the period of solar eclipse, the disturbance manifested through the unusual R constant value until 08:40 is well correlated with the constant value of RSL. At the moment of solar eclipse maximum, the considerable R

disturbance can be noticed, while this phenomenon does not reflect to the RSL. From 10:00, until the end of the solar eclipse, value of R varied within expected usual values, however RSL changed unusually.

This unusual RSL variation was possibly triggered by the solar eclipse event. In ordinary periods of measurements, the relative air pressure, absolute temperature and partially the pressure of the water vapour directly influence the permittivity of the air, causing the refraction of the electromagnetic wave, so the effects are noticeable as the RSL variation. However, during a solar eclipse event, it is not possible to consequently relate RSL and R. Considering the absolute amplitude variation of RSL, which was in the domain of 2,5 dB for the presented time periods, the sudden not so intense air permittivity perturbation within the area where LOS link was established did not have direct influence on the radio propagation at 3 GHz frequency. While RSL was evidently slightly perturbed during solar eclipse, there is not clear evidence that this perturbation is related to solar eclipse. The observed phenomena are not well presented in the literature for this particular scenario, and will be a subject of future analyses.

3.6. Effects on the ionosphere and LF radio signal propagation

The ionospheric perturbations were detected as variations of recorded NRK signal from Iceland. Generally, the temporal evolution of recorded signal can be used for detection of low ionospheric plasma perturbations; these changes in medium through which signal propagates affect wave reflection height, and consequently, propagation geometry and attenuation, resulting in variations of recorded signal characteristics.

The shapes of the temporal change depend on numerous parameters. Namely, in addition to periodic and sudden variations in the ionospheric plasma conditions, characteristics of signals like mutual locations of transmitter and receiver, power of transmitted signal, and geographical area through which the signal propagates, affect the recorded signal properties. For these reasons the dependencies between the ionospheric changes of electron density induced by radiation increase and VLF/LF signal amplitude are not monotonous, e.g. growth in the electron density does not necessarily cause amplification of recorded signal amplitudes (for detailed explanation see Nina et al., 2017). Thus, for detection of some sudden perturbation it is sufficient to observe changes in temporal

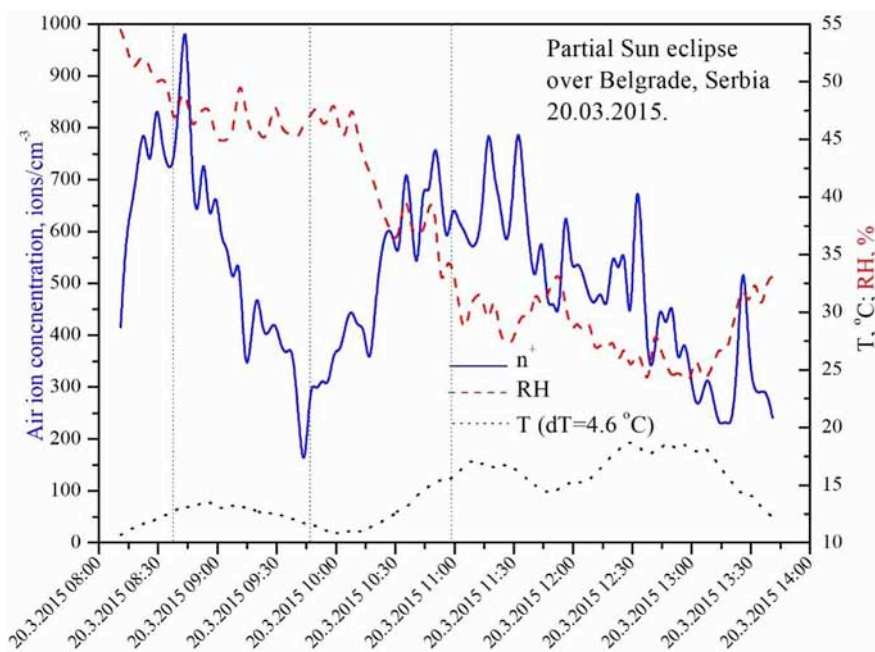


Fig. 6. Air ion concentration, temperature and relative humidity during partial solar eclipse. Dotted vertical lines indicate beginning, maximum and end of the eclipse.

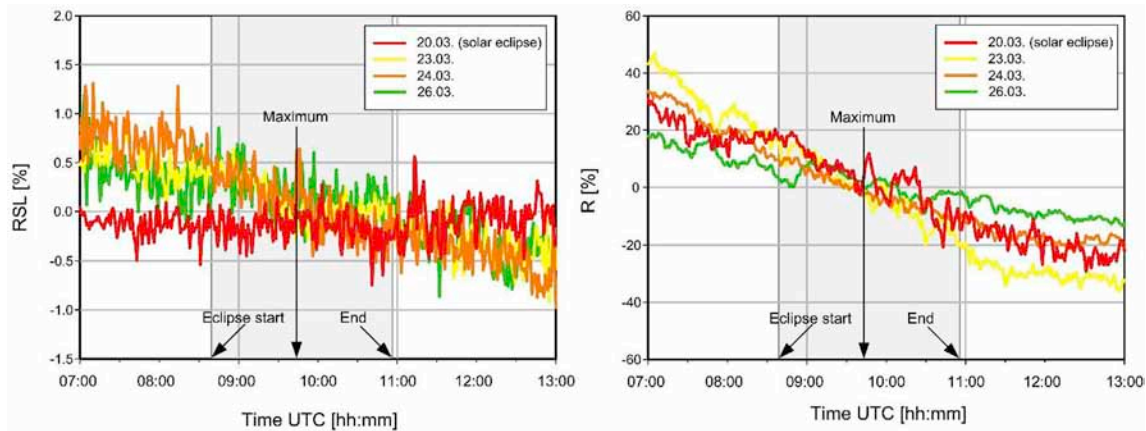


Fig. 7. Receiving signal level (RSL) and refractivity (R) variation. Shaded domains represent the time period when eclipse occurred.

evolution of signal characteristics.

Fig. 9 shows temporal variations of amplitude difference from its initial considered values, recorded by the AWESOME system at the Belgrade station on March 20, 2015 when solar eclipse occurred, and three days after that. The additional days are shown to visualize amplitude variation in solar eclipse period with respect to its shapes in other relevant periods without influence of the eclipse. The reason for choosing these particular days was relatively quiet conditions without significant traveling ionospheric disturbance resulting from atmospheric lightnings, and solar flares among other events. While amplitude variations are pronounced during the solar eclipse, they are practically within noise domains on the other three days. In the first period, a decrease in amplitude was observed, with the minimum occurring before the eclipse maximum. Further, the amplitude increased, exceeded the amplitude values during the first contact and reached the larger value approximately coincidentally with the eclipse maximum time (indicated by a vertical line). Finally, it returned to the expected values, which are around initial values (this can be concluded from the three referent signals).

As explained in Section 1, electron density variation is most important for changes of plasma parameters which influence signal propagation. Its time variations depend on different electron gain and loss processes. The constituents of the low ionosphere can be ionized by γ , X and a part of UV photons. The most important solar influences on the ionization processes in the D-region in absence of large radiation increase, primarily as consequence of solar X-flares (Nina et al., 2012a,b) is coming from the

solar Ly α line (121.6 nm) radiation (Swamy, 1991) whose presence is periodically intensified during the day. Bearing in mind that satellites did not register significant increase of intensity of X radiation, we can conclude that the signal variations are a consequence of Ly α radiation decrease. http://en.wikipedia.org/wiki/Solar_eclipse.

4. Conclusions

Changes in atmospheric properties were observed during a partial solar eclipse (51%) on March 20, 2015 in Belgrade. For that purpose, four experimental setups were used to collect data, including lidar to derive PBL height and heights of elevated layers, AWESOME VLF/LF receiver (Cohen et al., 2010) and instruments for measurements of solar radiation, meteorological parameters, concentrations of ozone, air ions and radon and propagation of radio signals in troposphere. Although the solar eclipse was only partial, its influence on atmospheric properties in troposphere and ionosphere was noticeable. The detected changes in atmospheric parameters were generally similar, but weaker in intensity, to those reported in literature for solar eclipse events with larger obscuration of solar disc.

In troposphere, the influence of the eclipse was observed in meteorological surface parameters, and it was evident up to the top of the PBL. Eclipse-induced decrease in PBL height was 200 m, comparable to that reported in literature, with minimal value occurring 20 min after the eclipse maximum. The PBL height determined from 12 UTC radio-sounding measurements (soon after the eclipse), showed that it was within the usual values for this location at that time of year. The meteorological parameters showed similar behavior at two measurement sites Košutnjak and IPB, respectively. The temperature change was more pronounced and abrupt at the -IPB station, probably due to lower measurement height, where it decreased by 2.6 °C, reaching minimum 15 min after the eclipse maximum. This temperature change is similar to those reported in literature for solar eclipse with larger obscuration of solar disc. At the Košutnjakstation the temperature was almost constant, until the eclipse maximum. Relative humidity was almost constant at both sites from the first contact until the eclipse maximum, as opposed to the increase reported in literature. The diurnal cycle then continued, with the increase in temperature and decrease in relative humidity at both sites. The 10-m wind speed and gusts decreased, reaching a minimum about 30 min after the eclipse. The wind direction changed from northerly to northeasterly for the duration of the event. Decrease of PBL height and the entrainment zone thickness were also observed during the eclipse, as a result of diminished surface heating. Ozone concentrations showed no decrease, as opposed to most results reported in literature, except for those reported for rural measurement sites. The possible reasons are less significant influence of photochemical reactions, decrease in PBL height or advection by changing wind during the event. Measured

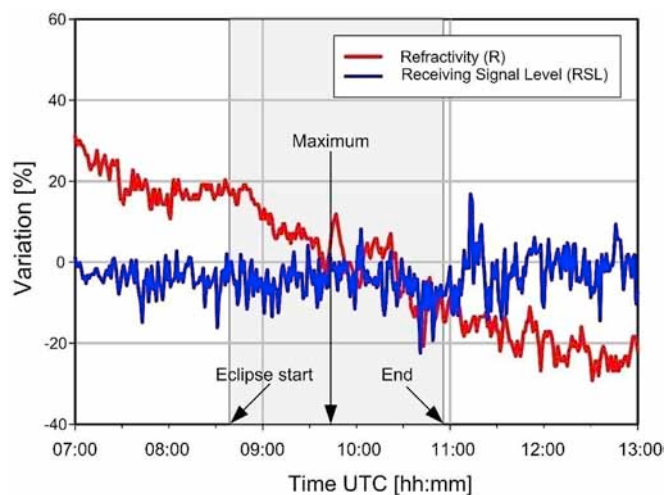


Fig. 8. RSL and R variation during solar eclipse. Shaded domains represent the time period when eclipse occurred.

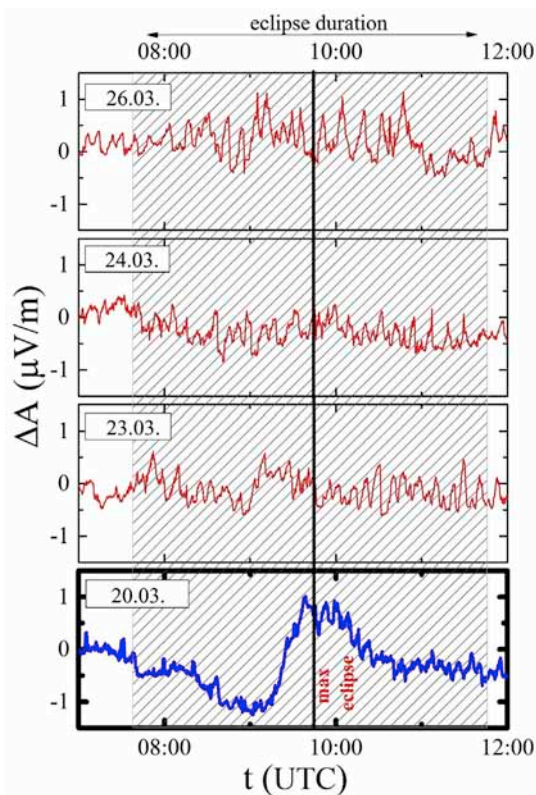


Fig. 9. The variations of amplitude difference from its initial considered values against the universal time (UT), recorded by the AWESOME system at the Belgrade station on March 20, 2015 when solar eclipse occurred (lower panel) and three days after that (top panels). Shaded domains represent the time period when eclipse occurred (here we consider a whole period of eclipse because of long signal propagation path from Iceland to Serbia).

radon concentrations were typically low for this time of the day, while the air ion concentration sharply decreased.

The referential Line-of-Sight (LOS) radio link was set in the area of Belgrade, in order to investigate influence of the event on RSL instability. During the solar eclipse, an unusual pattern of the signal level variation was observed and different relationship between the RSL and the air refractivity parameter (R). Further analysis is needed to clearly relate the perturbation with solar eclipse which affected the atmospheric variables and therefore R.

Impact of the solar eclipse on the ionosphere was registered through changes of characteristics of radio waves which are reflected in ionosphere. The amplitude variations, were pronounced during the solar eclipse, and were at the expected values on the days after the event. Since satellite measurements did not show significant increase of intensity of X radiation, it was concluded that the signal variations are consequence of $Ly\alpha$ radiation decrease.

Acknowledgements

This research was realized as a part of projects no. III43007, no. III41011, no. III44002, no. 176002, no. P171020, no. III45003 financed by the Ministry of Education, Science and Technological Development of the Republic of Serbia within the framework of integrated and interdisciplinary research for the period 2011–2017. Also, this study is made within the COST project TD1403 and VarSITY project.

References

Ahrens, D., Moses, G.I., Lutz, J., Andreas, M., Helmut, M., 2001. Impacts of the solar eclipse of 11 August, 1999 on routinely recorded meteorological and air quality data in South-West Germany. *Meteorol. Z.* 10 (3), 215–223.

- Amiridis, V., Melas, D., Balis, D.S., Papayannis, A., Founda, D., Katragkou, E., Giannakaki, E., Mamouri, R.E., Gerasopoulos, E., Zerefos, C., 2007. Aerosol Lidar observations and model calculations of the planetary boundary layer evolution over Greece, during the March 2006 total solar eclipse. *Atmos. Chem. Phys.* 7, 6181–6189. <https://doi.org/10.5194/acp-7-6181-2007>.
- Anderson, J., 1999. Meteorological changes during a solar eclipse. *Weather* 54 (7), 207–215.
- Aplin, K.L., Harrison, R.G., 2003. Meteorological effects of the eclipse of 11 August 1999 in cloudy and clear conditions. *Proc. R. Soc. Lond. A* 459, 353–371.
- Aplin, K.L., Scott, C.J., Gray, S.L., 2016. Atmospheric changes from solar eclipses. *Philosophical Trans. R. Soc. A* 374, 20150217.
- Baars, H., Ansmann, A., Engelmann, R., Althausen, D., 2008. Continuous monitoring of the boundary-layer top with lidar. *Atmos. Chem. Phys.* 8, 7281–7296. <https://doi.org/10.5194/acp-8-7281-2008>.
- Bajčetić, J., Andrić, M., Todorović, B., Pavlović, B., Suša, V., 2013. The correlation of geomagnetic component disturbances and 5 GHz LOS received signal daily variation. *Microw. Rev.* 19 (1).
- Bajčetić, J.B., Nina, A., Čadež, V., Todorović, B.M., 2015. Ionospheric D-region temperature relaxation and its influences on radio signal propagation after solar X-flares occurrence. *Therm. Sci.* 19 (Suppl. 2), S299–S309.
- Bian, H., Han, S., Tie, X., Sun, M., Liu, A., 2007. Evidence of impact of aerosols on surface ozone concentration in Tianjin, China. *Atmos. Environ.* 41, 4672–4681.
- Blauboer, R.O., Smeters, R.C.G.M., 1996. Outdoor concentrations of the equilibrium-equivalent decay products of ^{222}Rn in The Netherlands and the effect of meteorological variables. *Radiat. Prot. Dosim.* 69, 7–18.
- Cohen, M.B., Inan, U.S., Paschal, E.W., 2010. Sensitive broadband ELF/VLF radio reception with the AWESOME instrument. *IEEE Trans. Geosci. Remote.* 48, 3–17.
- Debye, P., 1957. *Polar Molecules*. Dover Publications, New York.
- Dolezalek, H., 1974. *Electrical Processes in Atmospheres*, Springer Verlag, Electrical Processes in Atmospheres. Springer Verlag.
- Emeis, S., Schafer, K., Munkel, C., 2008. Surface-based remote sensing of the mixing-layer height – A review. *Meteorol. Z.* 17 (5), 621–630.
- Falodun, S.E., Ajewole, M.O., 2006. Radio refractive index in the lowest 100-m layer of the troposphere in Akure, South Western Nigeria. *J. Atmos. Sol.-Terr. Phys.* 236–243.
- Flamant, C., Pelon, J., Flamant, P.H., Durand, P., 1997. Lidar determination of the entrainment zone thickness at the top of the unstable marine atmospheric boundary-layer. *Boundary-Layer Meteorol.* 83, 247–284.
- Founda, D., Melas, D., Lykoudis, S., Lisaridis, I., Gerasopoulos, E., Kouvarakis, G., Petrakis, M., Zerefos, C., 2007. The effect of the total solar eclipse of 29 March 2006 on meteorological variables in Greece. *Atmos. Chem. Phys.* 7, 5543–5553. <https://doi.org/10.5194/acp-7-5543-2007>.
- Gasó, M.I., Cervantes, M.L., Segovia, N., Espindola, V.H., 1994. Atmospheric radon concentration levels. *Radiat. Meas.* 23, 225–230.
- Gerasopoulos, E., Zerefos, C.S., Tsagouri, I., Founda, D., Amiridis, V., Bais, A.F., Belehaki, A., Christou, N., Economou, G., Kanakidou, M., Karamanos, A., Petrakis, M., Zanis, P., 2008. The total solar eclipse of March 2006: overview. *Atmos. Chem. Phys.* 8, 5205–5220.
- Girard-Ardhuin, F., Bénech, B., Campistron, B., Dessens, J., Jacoby-Koaly, S., 2003. Remote sensing and surface observations of the response of the atmospheric boundary layer to a solar eclipse. *Boundary-Layer Meteorol.* 106, 93–115.
- Grubar, D.P., Sulić, D.M., Zigman, V., 2008. Classification of X-ray solar flares regarding their effects on the lower ionosphere electron density profile. *Ann. Geophys.* 26 (7), 1731–1740.
- Guha, A., De, B.K., Roy, R., Choudhury, A., 2010. Response of the equatorial lower ionosphere to the total solar eclipse of 22 July 2009 during sunrise transition period studied using VLF signal. *J. Geophys. Res.* 115, A11302. <https://doi.org/10.1029/2009JA015101>.
- Ishimori, Y., Lange, K., Martin, P., Mayya, Y.S., Phaneuf, M., 2013. Measurement and Calculation of Radon Releases from NORM Residues. *International Atomic Energy Agency*, Vienna.
- Jeričević, A., Grisocono, B., 2006. The critical bulk richardson number in urban areas: verification and application in a numerical weather prediction model. *Tellus A* 58, 19–27. <https://doi.org/10.1111/j.1600-0870.2006.00153.x>.
- Kolarž, P., Šekarić, J., Marinković, B.P., Filipović, D.M., 2005. Correlation between some of the meteorological parameters measured during the partial solar eclipse, 11 August, 1999. *J. Atmos. Sol. Terr. Phys.* 67, 1357–1364.
- Kolarž, P., Miljković, B., Čurguz, Z., 2011. Air-ion counter and mobility spectrometer. *Nucl. Instrum. Methods Phys. Res. B* 279, 219–222.
- Kolev, N., Tatarov, B., Grigorieva, V., Donev, E., Simenonov, P., Umlensky, V., Kaprielov, B., Kolev, I., 2005. Aerosol Lidar and in situ ozone observations of the planetary boundary layer over Bulgaria during the solar eclipse of 11 August 1999. *Int. J. Remote Sens.* 26, 3567–3584.
- Matthias, V., Balis, D., Bosenberg, J., Eixmann, R., Iarlori, M., Komguem, L., Mattis, I., Papayannis, A., Pappalardo, G., Perrone, M.R., Wang, X., 2004. Vertical aerosol distribution over Europe: statistical analysis of Raman lidar data from 10 European aerosol research lidar network (EARLINET) stations. *J. Geophys. Res.* 109, D18201. <https://doi.org/10.1029/2004JD004638>.
- Maurya, Ajeet K., Phanikumar, D.V., Rajesh, Singh, Sushil, Kumar, Veenadhari, B., Kwak, Y.-S., Abhikesh, Kumar, Singh Abhay, K., Niranjan, Kumar K., 2014. Low-mid latitude D region ionospheric perturbations associated with 22 July 2009 total solar eclipse: wave-like signatures inferred from VLF observations. *J. Geophys. Res. Space Phys.* 119 (10), 8512–8523.
- Menut, L., Flamant, C., Pelon, J., Flamant, P.H., 1999. Evidence of interaction between synoptic and local scales in the surface layer over the Paris area. *Bound. Layer Meteorol.* 93, 269–286. <https://doi.org/10.1023/A:1002013631786>.
- Nina, A., Čadež, V.M., 2013. Detection of acoustic-gravity waves in lower ionosphere by VLF radio waves. *Geophys. Res. Lett.* 4018, 4803–4807.

- Nina, A., Čadež, V., Srečković, V., Šulić, D., 2012a. Altitude distribution of electron concentration in ionospheric D-region in presence of time-varying solar radiation flux. *Nucl. Instrum. Methods. B* 279, 110–113.
- Nina, A., Čadež, V., Šulić, D., Srečković, V., Žigman, V., 2012b. Effective electron recombination coefficient in ionospheric D-region during the relaxation regime after solar flare from February 18, 2011. *Nucl. Instrum. Methods. B* 279, 106–109.
- Nina, A., Čadež, V.M., Popović, Č.L., Srečković, A.V., 2017. Diagnostics of plasma in the ionospheric D-region: detection and study of different ionospheric disturbance types. *Eur. Phys. J. D* 71 (7). <https://doi.org/10.1140/epjd/e2017-70747-0>, 189, 1–12.
- Nymphas, E.F., Adeniyi, M.O., Ayoola, M.A., Oladiran, E.O., 2009. Micrometeorological measurements in Nigeria during the total solar eclipse of 29 March, 2006. *J. Atmos. Sol. Terr. Phys.* 71 (12), 1245–1253.
- Sicard, M., Pérez, C., Rocadenbosch, F., Baldasano, J.M., García-Vizcaino, D., 2006. Mixed-layer depth determination in the Barcelona Coastal area from regular lidar measurements: methods, results and limitations. *Bound. Layer Meteorol.* 119 (1), 135–157. <https://doi.org/10.1007/s10546-005-9005-9>.
- Stull, R.B., 1988. *An Introduction to Boundary Layer Meteorology*. Kluwer Acad., Dordrecht, The Netherlands.
- Swamy, A.B., 1991. A new technique for estimating D-region effective recombination coefficients under different solar flare conditions. *Astrophys. Space Sci.* 185 (1), 153–164.
- Tie, X., Madronich, S., Li, G.H., Ying, Z.M., Zhang, R., Garcia, A., Lee-Taylor, J., Liu, Y., 2007. Characterizations of chemical oxidants in Mexico City: a regional chemical/dynamical model (WRF-Chem) study. *Atmos. Environ.* 41, 1989–2008.
- United Nations Scientific Committee on the Effects of Atomic Radiation (UNSCEAR), 1993. *Report to the General Assembly, with Scientific Annexes*. New York.
- Verhulst, T.G.W., Sapundjiev, D., Stankov, S.M., 2016. High-resolution ionospheric observations and modeling over Belgium during the solar eclipse of 20 March 2015 including first results of ionospheric tilt and plasma drift measurements. *Adv. Space Res.* 57 (No.11), 2407–2419. <https://doi.org/10.1016/j.asr.2016.03.009>.
- Vogelezang, D.H.P., Holtslag, A.A.M., 1996. Evolution and model impacts of alternative boundary layer formulations. *Bound. Layer. Meteorol.* 81, 245–269. <https://doi.org/10.1007/BF02430331>.
- Zanis, P., Zerefos, C.S., Gilge, S., Melas, D., Balis, D., Ziomas, I., Gerasopoulos, E., Tzoumaka, P., Kaminski, U., Fricke, W., 2001. Comparison of measured and modeled surface ozone concentrations at two different sites in Europe during the solar eclipse on August 11, 1999. *Atmos. Environ.* 35, 4663–4673.
- Zanis, P., Katragkou, E., Kanakidou, M., Psiloglou, B., Karathanasis, S., Vrekoussis, M., Gerasopoulos, E., Lysaridis, I., Markakis, K., Poupkou, A., Amiridis, V., Melas, D., Mihalopoulos, N., Zerefos, C., 2007. Effects on surface atmospheric photo-oxidants over Greece during the total solar eclipse event of 29 March 2006. *Atmos. Chem. Phys. Discuss.* 7, 11399–11428.
- Zerefos, C.S., Balis, D.S., Zanis, P., Meleti, C., Bais, A.F., Tourpali, K., Melas, D., Ziomas, I., Galani, E., Kourtidis, K., Papayannis, A., Gogosheva, Z., 2001. Changes in surface UV solar irradiance and ozone over the Balkans during the eclipse of 11 August 1999. *Adv. Space Res.* 27 (12), 1955–1963.

Contents of phenolics and carotenoids in tomato grown under polytunnels with different UV-transmission rates

Bojana ŽIVANOVIĆ¹, Marija VIDOVIĆ^{1*}, Sonja MILIĆ KOMIĆ¹, Ljubinko JOVANOVIĆ²,
Predrag KOLARŽ³, Filis MORINA¹, Sonja VELJOVIĆ JOVANOVIĆ¹

¹Institute for Multidisciplinary Research, University of Belgrade, Belgrade, Serbia

²Faculty of Ecological Agriculture, Educons University, Sremska Kamenica, Serbia

³Institute of Physics, University of Belgrade, Belgrade, Serbia

Received: 16.12.2016 • Accepted/Published Online: 15.03.2017 • Final Version: 03.05.2017

Abstract: Tomato (*Solanum lycopersicum* L.) is among the economically most important vegetables in Europe, valued for its bioactive properties due to significant contents of vitamins, carotenoids, and phenolic compounds. In this study, the tomato cultivar Big Beef F1 was grown in the open field (OF) and under polytunnels in central Serbia during 3 years. Poly tunnels were covered with two foils (both with 57% reduced photosynthetic active radiation, PAR) differing in UV-A and UV-B transmittance. The aim of our work was to determine the influence of light conditions on accumulation of phytonutrients (carotenoids and phenolics) in the peel and flesh of ripe tomato fruits. The amount of effective antioxidants, caffeic acid, and quercetin (phenolics with *ortho*-dihydroxy substitution) in the peel was the highest in tomato fruits grown in the OF (maximal PAR and UV-A and UV-B radiation). Moreover, the content of leaf epidermal flavonoids was the highest in the OF. The content of lycopene and β -carotene in the flesh of tomato fruit was higher under the polytunnel with higher UV-transmittance. Our results showed that selection of the right light conditions (quality and intensity) for tomato production has a significant effect on the accumulation of beneficial phenolics and carotenoids.

Key words: Phytonutrients, flavonoids, solar radiation, protected cultivation, *Solanum lycopersicum* L., UV radiation

1. Introduction

Numerous reports on the beneficial effects of natural antioxidants for human health have drawn attention to food sources (fruits and vegetables) and means of improving their nutritional value. Tomato (*Solanum lycopersicum* L.) is a high-value crop and one of the most widely grown vegetables (Sabir and Singh, 2013). According to the Food and Agriculture Organization (<http://faostat.fao.org>), in the period from 2013 to 2014 tomato production in four Mediterranean countries (Turkey, Egypt, Italy, and Spain) ranked second in the world, after China. Moreover, tomato was among the top three vegetables in EU in terms of the level of production (17.6×10^6 t in 2015; Eurostat, 2016). The geographical location of Serbia, with a predominantly moderate continental (north) and Mediterranean (south, southeast) climate, has proved to be suitable for tomato production; in 2012 and 2013 Serbia was in the fourth place in tomato production (135,000–155,000 t/year) in Southeast Europe, after Greece, Romania, and Albania (<http://faostat.fao.org>).

During the last decade, protected cultivation under polytunnels increased and became a major production system for supplying tomato all year round throughout the world (Peet and Welles, 2005; Boulard et al., 2011; Sabir and Singh, 2013). However, under glasshouses and polytunnels photosynthetically active radiation (PAR, 400–700 nm) intensity is attenuated and most of the UV radiation is excluded (Jansen et al., 2008; Lamnatou and Chemisana, 2013).

Red tomatoes are a rich source of bioactive compounds, such as carotenoids and phenolics. The beneficial effects of carotenoids (lycopene and β -carotene) have been reported with respect to a wide range of diseases and health conditions and have been attributed to their antioxidative and provitamin A activities (Rao and Rao, 2007; Kotíková et al., 2011). In addition, polyphenolics, a large group of secondary metabolites in plants, are the subject of increasing scientific interest due to their importance for human health (Del Rio et al., 2013; Zhang and Tsao, 2016), mostly based on their antioxidative functions (Rice-Evans et al., 1997). In plants, phenolic compounds are involved

* Correspondence: marija@imsi.rs

in many processes, from growth and development to flowering, reproduction, and seed dispersion, and in protection against abiotic stress and pests (Gould and Lister, 2005; Lattanzio et al., 2006). For example, depending on their chemical structure and localization at tissue level (dermal tissues, mesophyll, etc.), phenylpropanoids and flavonoids can act either as ultraviolet (UV) and/or visible light attenuators (screeners), or as efficient antioxidants (Agati et al., 2013).

Although accumulation of secondary metabolites and especially flavonoids and terpenoids in fruits may be determined by internal factors (e.g., genetic variation), it can be triggered by ecologically relevant doses of UV-A (320–400 nm) and UV-B (280–320 nm) radiation (Jansen et al., 2008; Becatti et al., 2009; Schreiner et al., 2014). The final effect of UV radiation on accumulation of phytonutrients depends on the biologically effective dose applied and/or the spectral quality (Giuntini et al., 2005; Avena-Bustillos et al., 2012), as well as on interactions with other environmental factors, such as background PAR intensity (Neugart et al., 2012). Moreover, the synergistic effect of UV-A, UV-B, red, and blue light on the accumulation of phenolics and carotenoids in leaves and fruits has been observed (Ilić et al., 2015; Vidović et al., 2015). Therefore, manipulation of light quality and quantity has opened new possibilities in crop production for increasing the yield, antioxidative, nutritional, organoleptic, and pharmacological value of vegetables, e.g., by increasing the content of carotenoids and phenolics (Luthria et al., 2006; Olle and Viršilic, 2013; Bian et al., 2015).

The aim of our study was to determine how tomato production in the open field and under polytunnels differing in PAR, UV-A, and UV-B transmittance influences the accumulation of lycopene (Ly), β -carotene (β -Car), hydroxybenzoic and hydroxycinnamic acids (HBAs and HCAs), and flavonoids in the flesh and peel of tomato fruits. We hypothesized that different light conditions would alter the amounts and distribution of specific phenolics and carotenoids in red tomato fruits of the cultivar Big Beef F1.

2. Materials and methods

2.1. Experimental site and design

The field experiments were conducted in Svilajnac (44°13'28"N, 21°11'30"E), in central Serbia, on an organic vegetable farm during 2013, 2014, and 2015. Tomato was grown in three different adjacent cropping systems: an open field (OF), and two typical 2-year-old polytunnels. The material, orientation, shape, and dimensions of the polytunnels were the same: 20 m length, 4.5 m width, and 2.5 m maximal height, but covered with two different commonly used polyethylene foils in Serbia: F1 (Tim d.o.o., Banatski Karlovac, Serbia) and F2 (C605, Suncover white, Ginegar Ltd., Kibbutz Ginegar, Israel). Both foils transmitted about 43% of PAR, while UV-A (320–400 nm) and UV-B (280–320 nm) radiation penetration levels were different; UV-B was almost completely excluded by F2 (Table 1). No supplementary lighting or heating was provided under the polytunnels. UV transparency of the covering materials was measured using a PMA 2100 radiometer (Solar Light Company Inc., Glenside, PA, USA) equipped with a UV-A detector (PMA 2110) and UV-B biologically effective radiation detector (PMA 2101). Intensity of PAR was measured using a PAR Quantum Sensor CE (SKP 215 42474; Skye Instruments, Llandrindod Wells, UK). During the 3 years of the experiment we monitored PAR, UV-A, and UV-B transmission properties under the F1 and F2 polytunnels, and no significant changes were observed for F1 or F2.

Each cropping system had two plots with the same size (10 × 4.5 m). The experiment was conducted in a randomized block design with two replicates. All three cropping systems had the same cultivation history and soil properties and were placed on a field that had been under cultivation for at least 50 years before being converted to organic production of vegetables in 2010. The growing substrate in all plots was composed of 70% soil and 30% compost manure, composed of sheep (60%, w/w), pig (30%, w/w), and chicken (10%, w/w) manure. The soil composition (upper layer: 0–30 cm) was CaCO₃ (2%–4%), organic matter content (2.84%), and total N content in organic matter (0.14%), while both total P and K contents

Table 1. PAR, UV-A, and UV-B irradiance in three cropping systems (F1, F2, and OF) and transmittance rates (%) of two plastic cover materials (F1 and F2) used in the experiments.

	PAR, UV-A, and UV-B irradiance			Transmittance rate, %	
	OF	F1	F2	F1	F2
PAR ($\mu\text{mol m}^{-2} \text{s}^{-1}$)	1816.0 \pm 12.9	782.5 \pm 19.3	771.5 \pm 65.7	43.1 \pm 1.1	42.6 \pm 3.6
UV-A irradiance, (W m^{-2})	45.2 \pm 1.8	14.5 \pm 0.1	3.7 \pm 0.3	32.1 \pm 0.3	8.1 \pm 0.7
BE UV-B irradiance, (mW m^{-2}) _{BE}	163.9 \pm 7.8	38.2 \pm 2.2	0.3 \pm 0.0	23.3 \pm 1.4	0.2 \pm 0.0

BE, biologically effective.

were higher than 40 mg/100 g. The soil pH value in H₂O was 7.95 and in 1 M KCl 6.84.

Irrigation was done daily, by the drip system, during 1 h in the afternoon, equally for all plots. According to organic cropping management, plants in all plots received only copper sulfate as pesticide, once prior to flowering and the second time prior to fruit formation. Weeds were removed manually when required. The average monthly weather conditions (precipitation; insolation; minimal, maximal, and mean temperature; cloudiness; and relative humidity) from February to July 2013–2015 are presented in Table A1 in Appendix A.

2.2. Plant material and growth conditions

In this study we used the indeterminate Big Beef F1 tomato cultivar, popular among Serbian farmers. Tomato seeds (Seminis, Monsanto Holland BV, Enkhuizen, the Netherlands) were sown in plug trays with a peat/perlite (3:1, v/v) medium in February. Twenty days later, the uniform seedlings were separated and planted in plastic pots for another 30 days. In the first half of April, plants (about 20 cm high) were replanted with uniform spacing (100 cm within the row and 50 cm between rows) to all plots in all three cropping systems within the same day. Six uniform plants per plot, all equally exposed to light, were randomly chosen for the experiments. At the end of June, four to seven healthy, fully light-exposed, red-ripe fruits (RR stage according to Grierson and Kader, 1986) of uniform size per plant were carefully collected by hand at around 1400–1500 hours. Shaded leaves and fruits were carefully excluded from the analyses. Although the average fruit weight varied among the experimental years, fruits from the OF were always about 30% lighter than F1 and F2, while no significant changes were observed between them (data not shown). Temperature at the fruit and leaf surface during sampling was similar in all cropping systems (average: 31.6 ± 1.0 °C). Fruits were washed and wiped, and the flesh and peel (exocarp, approximately 2 mm thick) were excised by razor and separated and samples that originated from the same plant were pooled together. The samples of peel and previously homogenized flesh were freeze-dried and stored at –80 °C for carotenoid and phenolics analysis.

2.3. Epidermal flavonoids and total chlorophyll measurements

Immediately prior to harvest, total chlorophyll content (Chl), content of leaf epidermal flavonoids (EpFlav), and their ratio, the nitrogen balance index (NBI), of the same plants used for fruit collection were measured *in vivo* with the Dualex FLAV (FORCE-A, Orsay, France; see Cerović et al., 2012 for more details). About ten uniform, fully developed, and fully daily sun-exposed leaves per plant in each plot were analyzed.

2.4. Carotenoid determination

Following homogenization in liquid nitrogen, carotenoids from approximately 0.2 g of dry weight (DW) were extracted according to a modified method described by Davuluri et al. (2005). All samples were extracted in duplicates. The main carotenoids, Ly and β-Car, in pooled extracts (three reextractions) were separated and quantified by HPLC-PDA (LC-20AB Prominence liquid chromatograph, Shimadzu, Kyoto, Japan) using a reversed-phase C18 column (5.0 μm, 250 × 4.6 mm Luna C18 (2); Phenomenex Ltd., Torrance, CA, USA) and isocratic elution gradient composed of 90% methanol and 10% acetonitrile at 25 °C, according to Olives Barba et al. (2006). Ly and β-Car were identified using standards (Sigma Chemical Co., St Louis, MO, USA) and quantified by peak area using Shimadzu LC Solution software (Shimadzu, Kyoto, Japan).

2.5. Phenolics determination

Phenolic compounds were extracted in methanol containing 0.1% HCl and hydrolyzed in 2 M HCl for aglycone determination according to Vidović et al. (2015). All samples were extracted in duplicates. Phenolic compounds were identified and quantified from pooled extracts (three reextractions) using the same HPLC apparatus as for determination of carotenoids. For quantification of flavonoids (chalconaringenin and kaempferol), quercetin was used as standard.

2.6. Statistical analysis

Two-way ANOVA was used to reveal the effects of light conditions (cropping system, CS) and year (Y) and their interactions on the carotenoid and phenolics contents in the peel and flesh of tomato fruits and on the EpFlav, Chl, and NBI. Tukey's post hoc test was used to test for significant differences in the outlined parameters among cropping systems for both tissue types. Both tests were conducted with IBM SPSS statistics software (Version 20.0, IBM Corp., Armonk, NY, USA). The significance threshold value was set at 0.05.

3. Results and discussion

3.1. Chlorophyll and epidermal flavonoid content in the leaves

In order to monitor the fitness of tomato plants, we measured total Chl and EpFlav contents and their ratio, NBI, which is an indicator of C/N allocation changes due to stimulation of flavonoid metabolism under different ambient light conditions (Tremblay et al., 2012). Leaf Chl content was higher in the plants grown in the OF compared with F1 and F2 in 2013 and 2015, while the opposite was observed in 2014 (Table 2; significant effects of CS and Y and their interactions are given in Table B1 in Appendix B).

Table 2. Total chlorophyll (Chl) content, epidermal flavonoid (EpFlav) content, and NBI index in the leaves of tomato grown in OF and under two polytunnels (F1 and F2) during 2013, 2014, and 2015.

Year and cropping system	Chl, mg cm ⁻²	EpFlav, g cm ⁻²	NBI
2013			
OF	36.3 ± 0.4 ^b	0.93 ± 0.02 ^c	39.2 ± 1.0 ^a
F1	29.4 ± 0.3 ^a	0.68 ± 0.02 ^b	45.4 ± 1.3 ^b
F2	28.7 ± 0.3 ^a	0.54 ± 0.01 ^a	53.8 ± 1.8 ^c
2014			
OF	22.4 ± 0.8 ^a	0.72 ± 0.02 ^c	34.9 ± 1.3 ^a
F1	36.2 ± 0.9 ^c	0.50 ± 0.01 ^b	74.8 ± 2.8 ^b
F2	32.0 ± 0.7 ^b	0.41 ± 0.01 ^a	75.0 ± 2.9 ^b
2015			
OF	31.1 ± 1.1 ^b	0.87 ± 0.05 ^c	40.8 ± 2.9 ^a
F1	24.1 ± 0.5 ^a	0.53 ± 0.03 ^b	49.5 ± 2.7 ^a
F2	23.6 ± 0.8 ^a	0.26 ± 0.01 ^a	95.9 ± 6.1 ^b

Values represent mean ± SE (n = 21–30); different letters denote statistically significant differences between different cropping systems for each year (P < 0.05).

In all 3 years, the highest accumulation of EpFlav was in the leaves of OF grown plants, compared to polytunnels with reduced PAR and UV radiation (Table 2). Moreover, the content of EpFlav was higher in the leaves of plants from F1 compared to those grown in F2, which received four times lower UV-A and almost no UV-B radiation. This is in line with numerous reports on induction of phenylpropanoids and flavonoids in the leaf epidermis by UV radiation (Schreiner et al., 2014; Vidović et al., 2017). Stimulated accumulation of flavonoids in the leaves can contribute to increased tolerance to strong sunlight and resistance to pathogens (Lattanzio et al., 2006; Agati et al., 2013). Moreover, lower NBI in the leaves of plants grown in the OF, compared with F1 and F2, corresponded to intraleaf allocation of resources towards flavonoid metabolism (Meyer et al., 2006).

3.2. Carotenoid accumulation in tomato fruits

Distribution of Ly in the tomato fruit was not uniform: its content was several times higher in the dried peel compared with the dried flesh, irrespective of radiation regimes (Figure 1). This is in line with results reported by Toor and Savage (2005) for three tomato cultivars. Lycopene was the major carotenoid in tomato and contributed about 80%–95% to total carotenoids in the peel and 70%–85% in the flesh, similarly to previously reported results (Dorais et al., 2008; Kotíková et al., 2011). Only in 2014 was β-Car lower in the peel compared to the flesh, and the portion of Ly in the flesh was about 62%, which can be attributed to

extremely high precipitation and lower insolation in this year.

The content of Ly in the peel of tomato fruits showed more variation between the years than among the CSs (for significant effects see Table B2, Appendix B). On the other hand, higher accumulation of β-Car in the peel was observed in the fruits grown under polytunnels compared to the OF. In 2013 and 2015 (sunnier years than 2014) Ly and β-Car contents in the flesh were higher in fruits from the F1 polytunnel than F2, which transmitted 4 times lower UV-A and almost completely excluded UV-B radiation. It was shown that the effects of UV radiation on Ly and β-Car accumulation (stimulative or inhibiting) depend on intensity, duration, and quality of light (Giuntini et al., 2005; Dorais et al., 2008; Bian et al., 2015; Ilić et al., 2015). For example, Guintini et al. (2005) reported a positive effect of UV-B radiation on total Ly content in one tomato hybrid, while there was no effect in the other. Furthermore, Kläring and Krumbein (2013) reported a positive correlation of β-Car content and PAR in the whole tomato fruit, without affecting Ly content. On the contrary, in cherry tomato cultivar Alina, Ly content in the fruit was higher in the greenhouse, which had 30%–55% reduced PAR compared to OF, while β-Car content was unaffected (Leyva et al., 2014).

3.3. Phenolic compounds in tomato fruits

The main HBAs in tomato fruits were protocatechuic acid (PA), syringic acid (SA), and an unidentified HBA

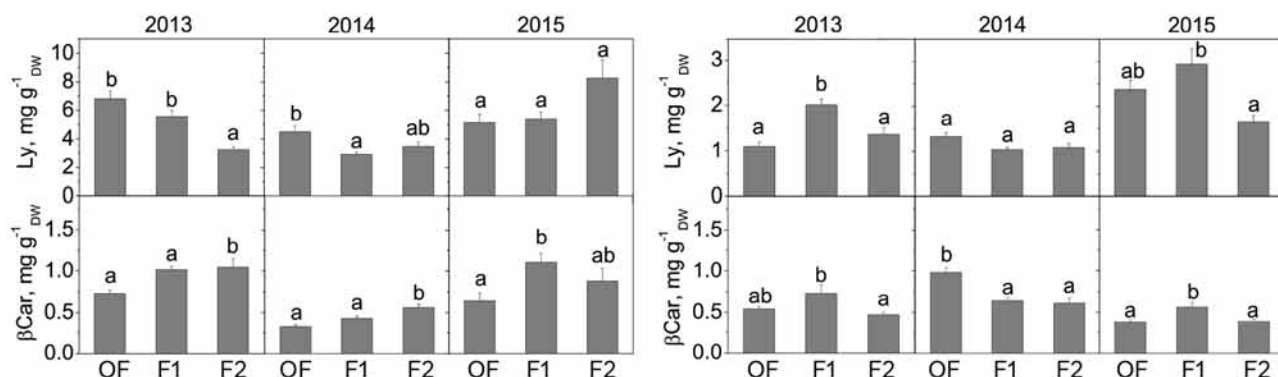


Figure 1. Content of lycopene (Ly) and β -carotene (β -Car) in the peel (left) and flesh (right) of tomato fruits grown in the OF and under two polytunnels (F1 and F2) during 2013, 2014, and 2015. Values represent mean \pm SE ($n = 4-5$); different letters denote statistically significant differences between different CSs for each year for peel and flesh ($P < 0.05$).

derivative (spectral characteristics: peak at 264 nm, shoulder at 290 nm). The contents of the three HBAs in tomato peel and flesh were not affected by different CSs in 2013 and 2014 (Figure 2; significant Y and CS effects are given in Table B2 in Appendix B). However, in 2015 the peel content of PA and the unknown HBA derivative was higher in the OF than in the fruits grown in F1 and F2.

Derivatives of caffeic acid (CA), *p*-coumaric acid (*p*-CA), and ferulic acid (FA) were the most abundant HCAs in the fruits. Similar HCA composition was reported for other tomato cultivars (Luthria et al., 2006; Anton et al., 2014). In tomato peel the decrease in CA and FA content was in correlation with PAR reduction for all 3 years, since no significant changes were observed between F1 and F2 (Figure 3; for significant CS effects see Table B2 in

Appendix B). No consistent trend in CA, *p*-CA, and FA content in the flesh of tomatoes regarding light conditions was found between the years. These results may suggest that preferential accumulation of CA and FA in the peel is a part of acclimation response to direct exposure to solar radiation, while in the flesh other factors may influence the composition of HCAs. Similarly to our results for 2013 and 2014, Calvenzani et al. (2015) reported that total concentration of HCAs in fully ripe tomato fruits was higher under ambient UV-B than in UV-B shielded fruits.

The main flavonoid aglycones in the Big Beef F1 cultivar were quercetin (Q), kaempferol (K), and chalconaringenin (ChN), which was consistent with the flavonoid composition of other tomato cultivars (Slimestad et al., 2008; Anton et al., 2014). Independently of the year and

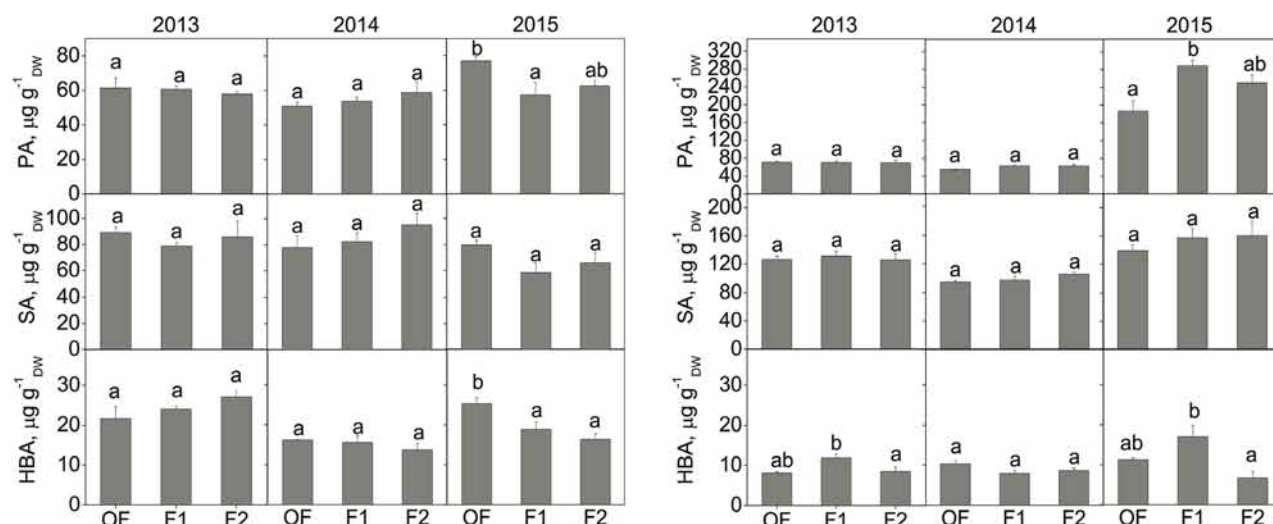


Figure 2. Contents of protocatechuic acid, syringic acid, and unidentified hydroxybenzoic acid derivative (PA, SA, and HBA) in the peel (left) and flesh (right) of tomato fruits grown in the OF and under two polytunnels (F1 and F2) during 2013, 2014, and 2015. Values represent mean \pm SE ($n = 4-5$); different letters denote statistically significant differences between different CSs for each year for peel and flesh ($P < 0.05$).

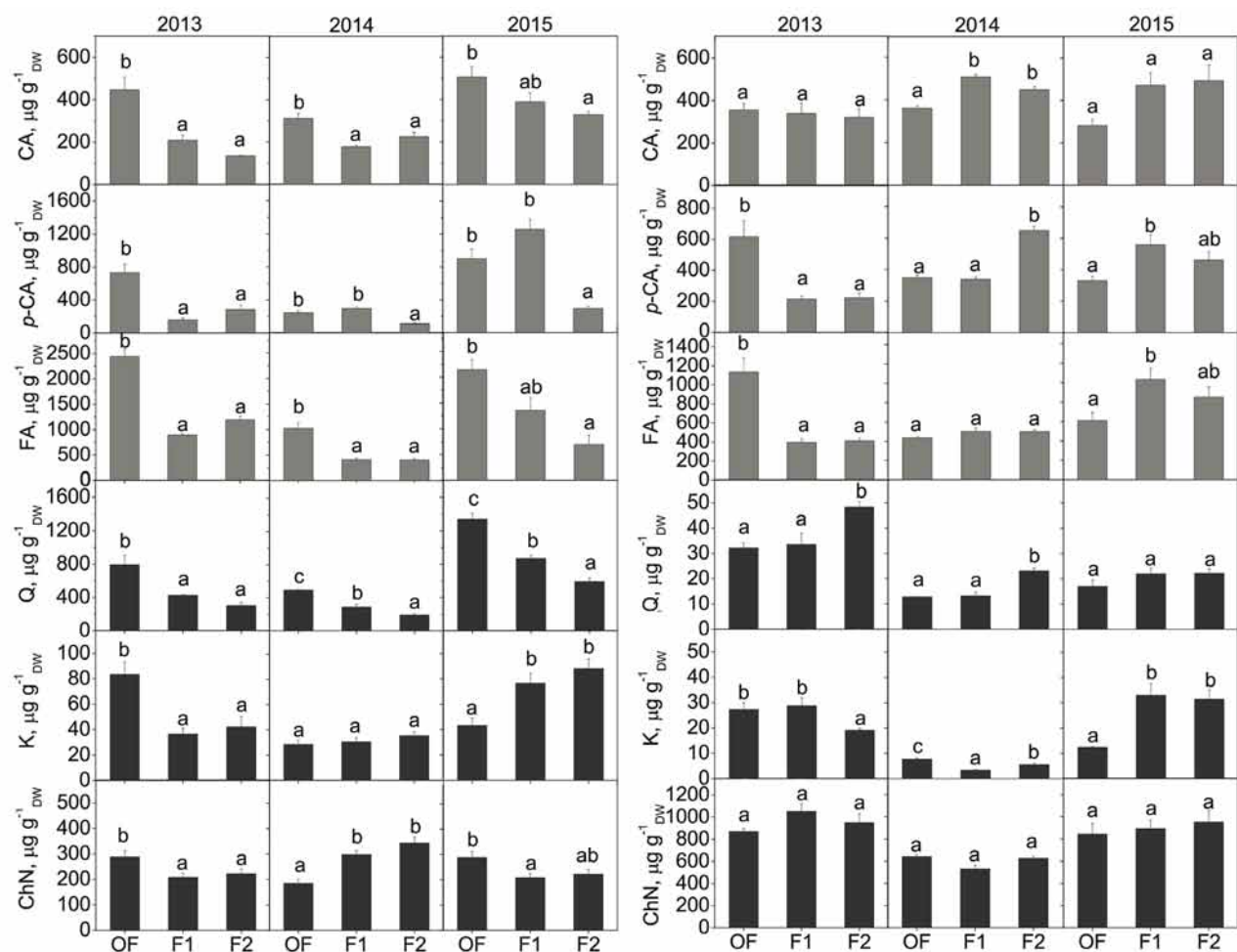


Figure 3. Contents of caffeic, *p*-coumaric, and ferulic acids (CA, *p*-CA, and FA) and quercetin, kaempferol, and chalconaringenin (Q, K, and ChN) in the peel (left) and flesh (right) of tomato fruits grown in the OF and under two polytunnels (F1 and F2) during 2013, 2014, and 2015. Values represent mean ± SE (n = 4–5); different letters denote statistically significant differences between different CSs for each year for peel and flesh (P < 0.05).

CS, both Q and K contents were higher in the peel than in the flesh, while the content of their biosynthetic precursor, ChN, was almost two times higher in the flesh in all 3 years (Figure 3). Moreover, in all 3 years, the content of Q was the highest in the peel of fruits grown in the OF and lowest in F2, implicating the role of PAR and UV-B radiation in stimulation of Q biosynthesis. This is in line with higher content of Q and its glycosides in the peel compared to the flesh of tomato grown under full solar radiation (Giuntini et al., 2008).

The HCAs and flavonoids with *ortho*-dihydroxyl substitution on the B-ring (e.g., Q, CA) are more efficient antioxidants than those with one hydroxyl group (K, *p*-CA) (Rice-Evans et al., 1997). During all 3 years, peel content of Q and CA was the highest in the fruits from the OF, while K and *p*-CA differentially varied with changes in PAR and

UV radiation (significant CS effects are given in Table B2 in Appendix B). These results indicate enhancement of antioxidative capacity of the fruits. Increased HCA and flavonol accumulation (mostly Q glycosides) by full sun exposure was observed not only in tomato (Giuntini et al., 2008; Leyva et al., 2014), but also in the skins of other fruits, such as apples (Merzlyak et al., 2002) and grape berries (Martinez-Lüscher et al., 2014).

Cultivar-specific and annual variability in polyphenolic content (HCAs, flavonoids) in tomato fruits grown both in open fields and under polytunnels and greenhouses was reported (Chassy et al., 2006; Anton et al., 2014). The interaction of temperature and light quality, quantity, and duration is the most important factor affecting the nutritional value (phenolic and carotenoid content) of tomato (Dumas et al. 2003; Dorais et al., 2008).

3.4. Conclusions

According to our results, stimulation of beneficial phytonutrients in tomato fruits is determined not only by the intensity of solar radiation components, but by other variable weather conditions as well. In all 3 years of the study, PAR and UV radiation (both UV-A and UV-B) had a synergistic effect on the accumulation of dihydroxylated polyphenols such as CA and Q in the tomato peel. Furthermore, significant accumulation of EpFlav in the leaves of plants from the OF and in F1 (compared to F2) enhanced the overall plant resilience to environmental conditions during the ripening period. Finally, when comparing the two polytunnels, we showed that tomato

fruits grown under the foil with higher UV transmittance (F1) had higher contents of *p*-CA and Q in the peel and Ly and β -Car in the flesh. Therefore, by choosing covering materials with higher UV-transmittance in tomato production, the antioxidative capacity of fruits can be improved without influencing fruit weight.

Acknowledgments

This work was supported by the Ministry of Education, Science, and Technological Development of the Republic of Serbia (Project No. III 43010). The authors would like to thank Zorica Milošević for growing the tomatoes (Organic Food Produces, household Milošević Svilajnac).

References

- Agati G, Brunetti C, Di Ferdinando M, Ferrini F, Pollastri S, Tattini M (2013). Functional roles of flavonoids in photoprotection: new evidence, lessons from the past. *Plant Physiol Biochem* 72: 35-45.
- Anton D, Matt D, Pedastsaar P, Bender I, Kazimierczak R, Roasto M, Kaart T, Luik A, Püssa T (2014). Three-year comparative study of polyphenol contents and antioxidant capacities in fruits of tomato (*Lycopersicon esculentum* Mill.) cultivars grown under organic and conventional conditions. *J Agric Food Chem* 62: 5173-5180.
- Avena-Bustillos RJ, Du WX, Woods R, Olson D, Breksa AP, McHugh TH (2012). Ultraviolet-B light treatment increases antioxidant capacity of carrot products. *J Sci Food Agr* 92: 2341-2348.
- Becatti E, Petroni K, Giuntini D, Castagna A, Calvenzani V, Serra G, Mensuali-Sodi A, Tonelli C, Ranieri A (2009). Solar UV-B radiation influences carotenoid accumulation of tomato fruit through both ethylene-dependent and -independent mechanisms. *J Agric Food Chem* 57: 10979-10989.
- Bian ZH, Yang QC, Liu WK (2015). Effects of light quality on the accumulation of phytochemicals in vegetables produced in controlled environments: a review. *J Sci Food Agric* 95: 869-877.
- Boulard T, Raepel C, Brun R, Lecompte F, Hayer F, Carmassi G, Gailard G (2011). Environmental impact of greenhouse tomato production in France. *Agron Sustain Dev* 31: 757-777.
- Calvenzani V, Castagna A, Ranieri A, Tonelli C, Petroni K (2015). Hydroxycinnamic acids and UV-B depletion: profiling and biosynthetic gene expression in flesh and peel of wild-type and hp-1. *J Plant Physiol* 181: 75-82.
- Cerović ZG, Masdoumier G, Ghozlen NB, Latouche G (2012). A new optical leaf-clip meter for simultaneous non-destructive assessment of leaf chlorophyll and epidermal flavonoids. *Physiol Plant* 146: 251-260.
- Chassy AW, Bui L, Renaud EN, Van Horn M, Mitchell AE (2006). Three-year comparison of the content of antioxidant microconstituents and several quality characteristics in organic and conventionally managed tomatoes and bell peppers. *J Agric Food Chem* 54: 8244-8252.
- Davuluri GR, Van Tuinen A, Eraser PD, Manfredonia A, Newman R, Burgess D, Brummell DA, King SR., Palys J, Uhlig J et al. (2005). Fruit-specific RNAi-mediated suppression of DET1 enhances carotenoid and flavonoid content in tomatoes. *Nat Biotechnol* 23: 890-895.
- Del Rio D, Rodriguez-Mateos A, Spencer JP, Tognolini M, Borges G, Crozier A (2013). Dietary (poly)phenolics in human health: structures bioavailability and evidence of protective effects against chronic diseases. *Antioxid Redox Signal* 18: 1818-1892.
- Dorais M, Ehret DL, Papadopoulos AP (2008). Tomato (*Solanum lycopersicum*) health components: from the seed to the consumer. *Phytochem Rev* 7: 231-250.
- Dumas Y, Dadomo M, Di Lucca G, Grolier P (2003). Effects of environmental factors and agricultural techniques on antioxidant content of tomatoes. *J Sci Food Agric* 83: 369-382.
- Eurostat (2016). Europe in Figures: EUROSTAT Yearbook 2016. Luxembourg City, Luxembourg: European Commission.
- Giuntini D, Graziani G, Lercari B, Fogliano V, Soldatini GF, Ranieri A (2005). Changes in carotenoid and ascorbic acid contents in fruits of different tomato genotypes related to the depletion of UV-B radiation. *J Agric Food Chem* 53: 3174-3181.
- Giuntini D, Lazzeri V, Calvenzani V, Dall'Asta C, Galaverna G, Tonelli C, Petroni K, Ranieri A (2008). Flavonoid profiling and biosynthetic gene expression in flesh and peel of two tomato genotypes grown under UV-B-depleted conditions during ripening. *J Agric Food Chem* 56: 5905-5915.
- Gould KS, Lister C (2005). Flavonoid functions in plants. In: Andersen ØM, Markham KR, editors. *Flavonoids: Chemistry Biochemistry and Applications*. 1st ed. Boca Raton, FL, USA: CRC Press, pp. 397-441.
- Grierson D, Kader A (1986). Fruit ripening and quality. In: Atherton J, Rudich G, editors. *The Tomato Crop*. 1st ed. London, UK: Chapman and Hall, pp. 241-280.
- Ilić ZS, Milenković L, Šunić Lj, Fallik E (2015). Effect of coloured shade-nets on plant leaf parameters and tomato fruit quality. *J Sci Food Agric* 95: 2660-2667.

- Jansen MAK, Hectors K, O'Brien NM, Guisez Y, Potters G (2008). Plant stress and human health: do human consumers benefit from UV-B acclimated crops? *Plant Sci* 175: 449-458.
- Kläring HP, Krumbein A (2013). The effect of constraining the intensity of solar radiation on the photosynthesis, growth, yield and product quality of tomato. *J Agron Crop Sci* 199: 351-359.
- Kotíková Z, Lachman J, Hejtmánková A, Hejtmánková K (2011). Determination of antioxidant activity and antioxidant content in tomato varieties and evaluation of mutual interactions between antioxidants. *Lebenswiss Technol* 44: 1703-1710.
- Lamnatou C, Chemisana D (2013). Solar radiation manipulations and their role in greenhouse claddings: Fresnel lenses, NIR-and UV-blocking materials. *Renew Sust Energ Rev* 18: 271-287.
- Lattanzio V, Lattanzio VM, Cardinali A (2006). Role of phenolics in the resistance mechanisms of plants against fungal pathogens and insects. In: Imperato F, editors. *Phytochemistry: Advances in Research*. 1st ed. Trivandrum, India: Research Signpost, pp. 23-67.
- Leyva R, Constan-Aguilar C, Blasco B, Sánchez-Rodríguez E, Romero L, Soriano T, Ruiz JM (2014) Effects of climatic control on tomato yield and nutritional quality in Mediterranean screenhouse. *J Sci Food Agric* 94: 63-70.
- Luthria DL, Mukhopadhyay S, Krizek DT (2006). Content of total phenolics and phenolic acids in tomato (*Lycopersicon esculentum* Mill.) fruits as influenced by cultivar and solar UV radiation. *J Food Compos Anal* 19: 771-777.
- Martínez-Lüscher J, Torres N, Hilbert G, Richard T, Sánchez-Díaz M, Delrot S, Aguirreolea J, Pascual I, Gomès E (2014). Ultraviolet-B radiation modifies the quantitative and qualitative profile of flavonoids and amino acids in grape berries. *Phytochemistry* 102: 106-114.
- Meyer S, Cerović ZG, Goulas Y, Montpied P, Demotes-Mainard S, Bidet LPR, Moya I, Dreyer E (2006). Relationships between optically assessed polyphenols and chlorophyll contents, and leaf mass per area ratio in woody plants: a signature of the carbon-nitrogen balance within leaves? *Plant Cell Environ* 29: 1338-1348.
- Merzlyak MN, Solovchenko AE, Chivkunova OB (2002). Patterns of pigment changes in apple fruits during adaptation to high sunlight and sunscald development. *Plant Physiol Biochem* 40: 679-684.
- Neugart S, Zietz M, Schreiner M, Rohn S, Kroh LW, Krumbein A (2012). Structurally different flavonol glycosides and hydroxycinnamic acid derivatives respond differently to moderate UV-B radiation exposure. *Physiol Plant* 145: 582-593.
- Olives Barba AI, Cámara Hurtado M, Sánchez Mata MC, Fernández Ruiz V, López Sáenz de Tejada M (2006). Application of a UV-Vis detection-HPLC method for a rapid determination of lycopene and β -carotene in vegetables. *Food Chem* 95: 328-336.
- Olle M, Viršilė A (2013). The effects of light-emitting diode lighting on greenhouse plant growth and quality. *Agric Food Sci* 22: 223-234.
- Peet MM, Welles GWH (2005). Greenhouse tomato production. In: Heuvelink E, editor. *Tomatoes - Crop Production Science in Horticulture*, Vol. 13. 1st ed. Wallingford, UK: CABI Publishing, pp. 257-304.
- Rao AV, Rao LG (2007). Carotenoids and human health. *Pharmacol Res* 55: 207-216.
- Rice-Evans CA, Miller NJ, Papanga G (1997). Antioxidant properties of phenolic compounds. *Trends Plant Sci* 2: 152-159.
- Sabir N, Singh B (2013). Protected cultivation of vegetables in global arena: a review. *Indian J Agr Sci* 83: 123-135.
- Schreiner M, Martínez-Abaigar J, Glaab J, Jansen MAK (2014). UV-B induced secondary plant metabolites. *Optik Photonik* 9: 34-37.
- Slimestad R, Fossen T, Verheul MJ (2008). The flavonoids of tomatoes. *J Agric Food Chem* 56: 2436-2441.
- Toor RK, Savage GP (2005). Antioxidant activity in different fractions of tomatoes. *Food Res Int* 38: 487-494.
- Tremblay N, Wang Z, Cerović ZG (2012). Sensing crop nitrogen status with fluorescence indicators. A review. *Agron Sustain Dev* 32: 451-464.
- Vidović M, Morina F, Milić S, Zechmann B, Albert A, Winkler JB, Veljović Jovanović S (2015). UV-B component of sunlight stimulates photosynthesis and flavonoid accumulation in variegated *Plectranthus coleoides* leaves depending on background light. *Plant Cell Environ* 38: 968-979.
- Vidović M, Morina F, Veljović Jovanović S (2017). Stimulation of various phenolics in plants under ambient UV-B radiation. In: Singh VP, Singh S, Prasad SM, Parihar P, editors. *UV-B Radiation: From Environmental Stressor to Regulator of Plant Growth*. 1st ed. Chichester, UK: Wiley-Blackwell, pp. 9-56.
- Zhang H, Tsao R (2016). Dietary polyphenols, oxidative stress and antioxidant and anti-inflammatory effects. *Curr Opi Food Sci* 8: 33-42.

Appendix A.

Average monthly weather conditions during the experiments in 2013, 2014, and 2015.

Table A1. Average monthly weather conditions during the experiments in 2013, 2014 and 2015.

	Insolation, h	Precipitation, mm	Minimal temperature, °C	Maximal temperature, °C	Average daily temperature, °C	Relative humidity, %	Cloudiness
2013							
Feb	38.5	87.4	1.4	7.4	3.8	82	8.1
Mar	117.3	38.1	2.7	11.3	5.7	73	6.6
Apr	206.9	64.3	7.2	20.8	12.7	69	4.5
May	226.5	78.0	10.0	25.1	18.1	68	5.6
Jun	227.0	20.8	13.4	26.2	19.8	75	5.0
Jul	311.0	25.3	15.9	30.3	21.7	66	3.1
2014							
Feb	111.9	15.9	0.6	8.1	6.1	73	5.4
Mar	181.9	111.3	1.0	12.0	8.8	75	5.2
Apr	141.5	185.2	5.2	18.7	12.1	78	6.7
May	212.1	85.4	11.3	24.4	15.6	78	6.2
Jun	240.5	124.6	13.8	26.7	19.4	76	5.0
Jul	243.6	56.0	13.2	32.7	21.6	76	5.0
2015							
Feb	110.1	41.1	-1.3	12.6	2.6	78	5.4
Mar	119.9	46.3	2.0	16.0	6.5	76	6.6
Apr	224.1	115.1	4.0	18.2	11.2	65	5.1
May	213.3	80.3	11.4	22.2	17.6	73	5.1
Jun	244.0	21.5	13.2	26.4	19.7	73	4.7
Jul	333.1	26.7	15.7	28.8	24.4	60	2.3

Appendix B

Statistical analysis (two-way ANOVA) for the effects of cropping system (CS) and year (Y), and their interactions on NBI, and on the contents of Chl, EpFlav, carotenoids, and phenolics in the leaves of tomato grown in the open field (OF) and under two polytunnels (F1 and F2) during 2013, 2014, and 2015 are shown in Tables B1 and B2.

Table B1. Two-way ANOVA results for the effects of CS and Y and their interactions on the contents of Chl and EpFlav, and NBI, in the leaves of tomato plants.

Trait	CS	Y	CS × Y
Chl	<0.001	<0.001	<0.001
EpFlav	<0.001	<0.001	<0.001
NBI	<0.001	<0.001	<0.001

Table B2. Two-way ANOVA results for the effects of CS and Y and their interactions on the contents of phenolics compounds in the peel and flesh of tomato fruits.

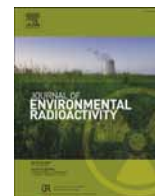
Trait	Peel			Flesh		
	CS	Y	CS × Y	CS	Y	CS × Y
Ly	0.3085	<0.0010	<0.001	<0.0010	<0.0010	<0.0010
β-Car	<0.0010	<0.0010	0.0928	<0.0010	<0.0010	<0.0010
PA	0.2295	0.0033	0.0265	0.0015	<0.0010	<0.0010
SA	0.6383	0.0063	0.1131	0.3470	<0.0010	0.7814
HBA	0.1414	<0.0010	0.0031	<0.0010	0.0311	<0.0010
CA	<0.0010	<0.0010	0.0167	0.0046	0.0106	0.0303
p-CA	<0.0010	<0.0010	<0.001	0.0051	0.0242	<0.0010
FA	<0.0010	<0.0010	0.0033	0.1045	<0.0010	<0.0010
Q	<0.0010	<0.0010	<0.001	<0.0010	<0.0010	<0.0010
K	0.7946	<0.0010	<0.001	0.0259	<0.0010	<0.0010
ChN	0.0013	0.1069	<0.001	0.4057	<0.0010	0.2835

Ly, Lycopene; β-Car, β-carotene; PA, protocatechuic acid; SA, syringic acid; HBA, hydroxybenzoic acid; CA, caffeic acid; p-CA, p-coumaric acid; FA, ferulic acid; Q, quercetin; K, kaempferol; ChN, chalconaringenin.



Contents lists available at ScienceDirect

Journal of Environmental Radioactivity

journal homepage: www.elsevier.com/locate/jenvrad

Thoron, radon and air ions spatial distribution in indoor air

Predrag Kolarž^{a,*}, Janja Vaupotič^b, Ivan Kobal^b, Predrag Ujić^c, Zdenka Stojanovska^d, Zora S. Žunić^c^a Institute of Physics, 11080, Belgrade, Serbia^b Jožef Stefan Institute, 1000, Ljubljana, Slovenia^c Institute of Nuclear Sciences Vinča, University of Belgrade, 11000, Belgrade, Serbia^d Faculty of Medical Sciences, Goce Delcev University, 2000, Stip, Macedonia

ARTICLE INFO

Article history:

Received 8 August 2016

Received in revised form

5 November 2016

Accepted 8 November 2016

Available online xxx

Keywords:

Radon

Thoron

Thoron diffusion length

Thoron diffusion constant

Air ion concentrations

ABSTRACT

Spatial distribution of radioactive gasses thoron (Tn) and radon (Rn) in indoor air of 9 houses mostly during winter period of 2013 has been studied. According to properties of alpha decay of both elements, air ionization was also measured. Simultaneous continual measurements using three Rn/Tn and three air-ion active instruments deployed on to three different distances from the wall surface have shown various outcomes. It has turned out that Tn and air ions concentrations decrease with the distance increase, while Rn remained uniformly distributed. Exponential fittings function for Tn variation with distance was used for the diffusion length and constant as well as the exhalation rate determination. The obtained values were similar with experimental data reported in the literature. Concentrations of air ions were found to be in relation with Rn and obvious, but to a lesser extent, with Tn.

© 2016 Elsevier Ltd. All rights reserved.

1. Introduction

In recent years in several countries of Balkan region i.e., Serbia with Kosovo, Slovenia, Republic of Srpska and Macedonia extensive and systematic indoor Rn and Tn surveys have been performed (Žunić et al., 2001, 2010a; Milić et al., 2010; Gulan et al., 2012; Vaupotič et al., 2008, 2013; Čurguz et al., 2015; Stojanovska et al., 2013, 2014). Since 2008, in Serbia in the Sokobanja municipality, a systematic survey on Rn in 26 schools has been started and carried out until 2010 (Žunić et al., 2010b, 2013; Carpentieri et al., 2011; Žunić et al., 2013; Boichichio et al., 2014; Bossew et al., 2014). From 2011 to 2012 this survey has continued and extended to houses which surrounded schools in the villages of the Sokobanja municipality, as well as in the Sokobanja town itself (Mishra et al., 2014). In most of the houses, Tn levels were higher than those of Rn, as already observed in traditional Japanese houses (Doi et al., 1994), in Italian buildings made of volcanic material (Boichichio et al., 1996) and in cave dwellings in China (Tokonami et al., 2004; Zhang et al., 2005). Because in such cases the contribution of Tn to Rn doses may not be simply ignored (Akiba et al., 2010;

Tokonami, 2010; Vaupotič et al., 2013), we decided to pay additional attention to Tn and its spatial distribution, particularly due to the high indoor Tn concentrations and low Rn concentration in the dwellings in villages of southern Serbia and Slovenia.

The sources of Rn and Tn are radium and thorium, respectively in the soil and building materials. Their transport by diffusion and advection through the porous environment is driven by the concentration and pressure gradient, respectively. The relatively short Tn half-life of 55.6 s compared to the Rn long life of 3.8 days resulting in different distribution within the indoor environment. In absence of pressure driven flow, the diffusion process is expressed with equation (UNSCEAR, 1982):

$$C(x) = C_0 e^{-x/L} \quad (1)$$

where $C(x)$ is the Rn or Tn concentration at distance x from the exhalation surface expressed in m; C_0 represents the Rn or Tn concentration at the surface, L is Rn or Tn diffusion length in m. Furthermore, the C_0 can be expressed due to Tn or Rn exhalation rate E from the source, D diffusion coefficient (m^2s^{-1}); and decay constant $\lambda(\text{s}^{-1})$ using the relation:

$$C_0 = \frac{E}{\sqrt{\lambda D}} \quad (2)$$

* Corresponding author.

E-mail address: kolarz@ipb.ac.rs (P. Kolarž).

Air ions in indoor air are generated mostly by MeV-energy α -particles produced in radioactive transformations of Rn and Tn and its short-lived descendants. Since the intensity of all other air ionizing sources is significantly lower and mostly constant in time, air ions may serve as confident indicator for spatial and temporal distribution of ^{222}Rn and ^{220}Rn concentrations indoors. The near-ground ionization rate caused by background ionization of 10 ion pairs $\text{cm}^{-3}\text{s}^{-1}$ is considered as a standard in continental areas (Chalmers, 1967). Ratio of positive and negative small air ion concentrations is called coefficient of unipolarity and in clean air is equal to $n^+/n^- = 1.12$ (Hörrak, 2001).

In this study we present the experimental results of Rn, Tn and air ions spatial distribution measurements in indoor environment. Mentioned values were measured simultaneously at three different distances from walls in 9 houses during the winter period.

2. Material and methods

For our study nine houses have been selected, 7 in Serbia and 2 in Slovenia (Table 1). The measurements were performed in December 2014 in closed indoor conditions. In the villages of Serbia (SRB-#1-5 and SRB-V), Tn concentrations nearby walls and floors were higher than Rn while in one village in Serbia (SRB-#6) and two villages in Slovenia (SLO-#1-2), Rn concentrations measured nearby walls and floor were much higher than Tn. Following equipment was used for the measurements: two Rad7 (DurrIDGE, USA) and one RTM 1688-2 (Sarad, Germany) Rn/Tn monitors, and three Gerdién-type air-ion CDI-06 detectors (Kolarž et al., 2009). Typical set-up is shown in Fig. 1.

During the measurements, inlets of measuring devices were fixed at different distances from the walls (from 0.5 to 40 cm) and about 1 m above the floor. All measurements were in total 24 h long except in house (marked as: SRB-#3) where measurements lasted 2 h. The measurements were divided in time series of several minutes.

For quality assurance purpose, the inter-comparison of air ion and Rn/Tn measuring instruments were performed day before measurements. The measuring procedure and results are presented in Kolarž et al. (2016). Standard deviations of the means of measured Rn concentrations were below to 5%. Also, inter-comparison of 4 ion counters showed relatively small standard deviation within 5% which is very satisfactory concerning non ideal measuring conditions, micro-climatic influence on position of each



Fig. 1. Typical experimental setup.

counter and overall uncertainty of air ion measurements, which assures a reliability of the measurements.

3. Results and discussion

3.1. Tn and Rn measurements

The scatter plots of Tn and Rn concentrations measured in all houses on three distances is presented in Fig. 2. Houses in Serbia are marked as SRB (SRB-#1 to SRB-#6), while houses in Slovenia are marked as SLO (SLO-#1 and SLO-#2). Vertical gradient measurements are marked with SRB-V. Because of wide range of measured concentrations as well in some cases small differences in concentrations between the houses for better perception, the results for Rn and Tn are presented in separate graphs for separated houses.

From this graph, it is obvious that there is no relation between Rn concentration and distance. This assumption was also confirmed by statistical test. The calculated correlation coefficient was not statistically significant at 95% confidence interval. Practically the Rn mean values at different distance were in the range of measured Rn fluctuations.

Although measurements were performed in indoor conditions, the results indicate that the Rn diffusion flow is affected by outdoor

Table 1

Name, date of measurements and description of measuring places.

House ID	Village and date of measurements	Building material	Year of construction	Type of heating, average temperature
SRB-#1	Bogdinac 25.11.2013.	Fired bricks of clay from Moravica river, concrete floor;	1970	Quartz heater switched on upon our arrival, T = 15 °C;
SRB-#2	Čitluk 26.11.2013.	Fired bricks of clay from Moravica river, concrete floor covered with a parquet;	1962	Wood – burning stove, fired on upon our arrival; T = 14.5 °C;
SRB-#3	Trubarevac (long) 29.11.2013.	Fired bricks of clay from Moravica river, concrete floor covered with a parquet;	1974	Wood – burning stove, T = 20 °C - 14.6 °C (during the night);
SRB-#4	Trubarevac (short) 27.11.2013.	Wood, straw, mud of red clay “crvenica”, concrete floor with a parquet and a carpet;	1951	Wood – burning stove, T = 14.5 °C;
SRB-#5	Resnik 30.11.2013.	Fired bricks of clay from Moravica river, concrete floor covered with a parquet;	1980	Central heating with radiators, T = 22.8 °C;
SRB-#6	Niška Banja 13.05.2014.	Blocks and concrete, concrete floor covered with a parquet;	2006	No heating, T = 22.5 °C;
SRB-V	Sokobanja 24.11.2013.	Concrete basement walls, rammed earth floor;	2002	No heating, T = 17.2 °C;
SLO-#1	Rakitna 18.12.2013.	Brick and concrete, concrete floor covered with a parquet and carpet;	1980	Alpine-type oven, T = 18.5 °C;
SLO-#2	Gorišnica 16.12.2013.	Brick and concrete, concrete floor covered with a parquet and carpet;	1977	Central heating, T = 17.2 °C.

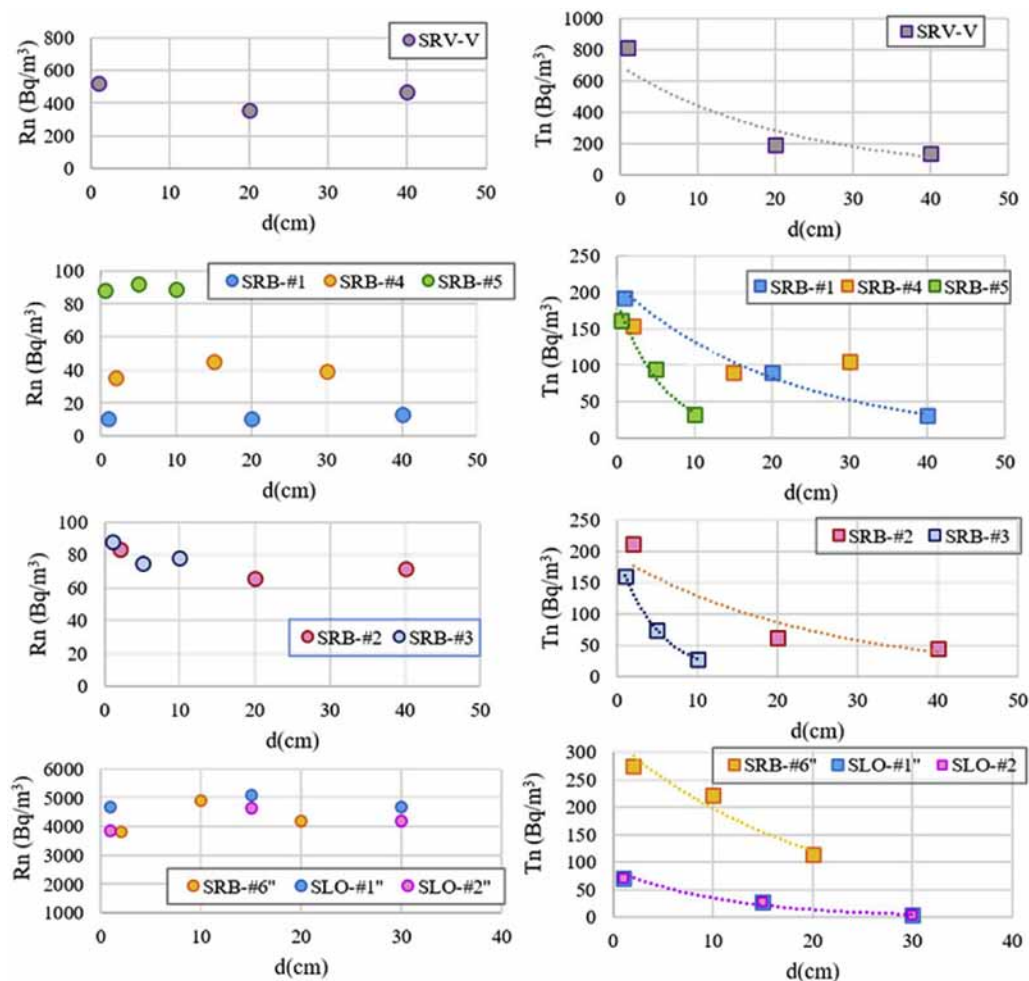


Fig. 2. Scatter plots of Rn (left graphs) and Tn (right graphs) concentrations measured on different distances in 9 houses. The Tn concentrations area fitted by exponential function $f(x)=ae^{-bx}$.

air. For example, high temperature and pressure difference between indoor and outdoor environment cause air movement indoors. Also, convection of outer air through the cracks in the walls and windows is causing the air turbulence inside the room. Due to relatively long half-life of Rn, all process affected by the air movement contribute to a homogeneous distribution of Rn in the room.

Opposite to this, the correlation between Tn and distance appeared to be significant ($p = 0.013$). Indoor air dynamic affects Rn and Tn in the same way but much shorter half-life of Tn resulting its high concentration gradient with distance (Fig. 1-right graphs). The Chi square tests of goodness of fit confirmed that the measured Tn distribution can be described by the exponential function $f(x)=ae^{-bx}$ with an interval of confidence of 95%. The exception is the case of SRB#4 where the Chi square test did not confirm the exponential distribution. On the same graph the dependence between Tn and distance was fitted with exponential function.

Thus with combination of Equations (1) and (2) for Tn gradient can be written:

$$Tn(x) = \frac{E}{\sqrt{\lambda D}} e^{-\frac{x}{L}} \quad (3)$$

where E is expressed in $Bq\ m^{-2}s^{-1}$, D in (m^2s^{-1}) and $\lambda = 0.0125\ s^{-1}$.

Comparing the fitting model with Equation (3) as well as using the relation $L = \sqrt{\frac{D}{\lambda}}$ we obtained the values for L , D and E for all

houses. The results together with fitting parameters are given in Table 2. Some Tn concentration measurements deviate from the exponential fit curve (SRB-#4) due to their measurement uncertainty (which was of order of 30%).

In case of these 4 houses given in Fig. 2 and Table 2, the values of R^2 were in range from 0.8676 to 0.9947, which means that the model applied for example in house SLO-#1 explained 99.47% of Th variation with distance. It can be seen from the graphs that function decreasing in the specific condition is equal (the functions are almost overlapped) but they differ from one another.

In absence of air motion in indoor space, Tn diffusion length is ~ 3 cm. Tn has a short half-life and corresponding decay constant $\lambda = 0.0125s^{-1} = 4.62\ h^{-1}$ which is higher than typical indoor air exchange rate ($v = 1\ h^{-1}$). As a consequence, air movement within the room slightly contributes to Tn distribution over the room, contrary to Rn. Thus the effective Tn diffusion length could be used to describe the Tn gradient, but in real conditions it is always longer than 3 cm as it is in our case.

The effective Tn diffusion length measured in different dwellings given in Table 1 is in the range from 5 to 25 cm (without SRB#4). The values for L and D obtained in this study were in the range from experimentally obtained result reported in other studies. For example, the effective diffusion Tn length reported by Doi et al. (1994) was 21 cm (corresponds to diffusion coefficient $D_{Tn} = 5.4 \times 10^{-4}\ ms^{-1}$). Nevertheless, the reason that the Tn values

Table 2
Ranges of measured Rn and Tn concentrations together with Tn exponential fitting and calculated diffusion parameters where E - exhalation rate, L - diffusion length, D - diffusion coefficient.

House ID	Mean concentrations at different distances (Bq m^{-3})		Tn: fitting parameters				Tn: Calculated parameters	
	Rn range	Tn range	R^2	a (Bq)	b (m^{-1})	L (cm)	$D \cdot 10^{-3}$ ($\text{m}^2 \text{s}^{-1}$)	E ($\text{Bqm}^2 \text{s}^{-1}$)
SRV-V	353–520	138–812	0.87	694	4.5	22	0.62	1.93
SRB-#1	11–13	32–192	0.99	210	4.6	22	0.59	0.57
SRB-#2	66–83	46–213	0.87	193	4.0	25	0.78	0.60
SRB-#3	75–88	28–161	0.99	197	19	5	0.03	0.13
SRB-#4	35–45	91–154						
SRB-#5	88–92	33–161	0.98	189	17	6	0.04	0.14
SRB-#6	3830–4901	115–275	0.94	308	4.6	22	0.59	0.84
SLO-#1	4668–5088	6–85	0.99	88	9.0	11	0.15	0.12
SLO-#2	3849–4625	5–70	0.98	87	9.2	11	0.15	0.12

in SRB#4 did not satisfy criteria for exponential modeling can be explained by inverted temperature gradient since heating was switched on after our arrival, so that walls were cold and air was hot causing the forced convection of indoor air. Due to relatively short time measurements (2 h) in this house temperature of the walls and air did not equalized.

The test of goodness of fit proves that this model can be used for the estimation of effective Tn exhalation rate E for each house. The values obtained for E shown in Table 2, are similar as the values that usually occur in the literature. The Tn exhalation rates E values in one of the houses of our study were higher than the typical E for soil $1 \text{ Bq m}^2 \text{ s}^{-1}$ given in UNSCEAR 1982 (Annex D). Also, these values were higher than the values obtained for building materials examined in laboratory conditions, for instance De With et al. (2014) reported E values in range from 0.01 to $0.43 \text{ Bq m}^2 \text{ s}^{-1}$. On the other hand, the results of E values obtained from Indian houses were higher than ours, whereby Ramachandran and Sathish, 2014 reported E in range from 4.19 to $10.68 \text{ Bq m}^2 \text{ s}^{-1}$. Therefore, it can be concluded that the differences in results originating from the content of Th and porosity of building materials rather than measurement methodology.

3.2. Air ion measurements

Air ion measurements were conducted on every measuring site but some of them were unsuccessful. Unfortunately, walls are mostly made of electrostatic materials and coatings. As a consequence they are not electrostatically neutral and thus deflecting or attracting the air ions and corrupting near-wall air ion measurements. From that reason, only a few air ion gradient measurements were successful. The most interesting was vertical air ion gradient performed in house with high Tn concentration in the soil, marked as SRB-V. During the measurements, we switched instrument places in order to confirm regularity of the measurements (Fig. 3).

Air ion concentration gradients were obviously the consequence of Tn gradients. Air ion concentration at the height of 85 cm was 37% lower than at 10 cm while in the case of Tn reduction was 75% after 40 cm. This kind of results was expected due to additional ionization of Rn which was uniformly distributed.

In Fig. 4, the horizontal decreasing of air ion concentrations with distance until 30 cm is presented. Since the ions are produced both by Tn and Rn (gamma as well), the exponential function with offset $f(x) = ae^{-bx} + c$ is used to fit the measurements. We assume that c is responsible for the ionization that comes from Rn and is homogeneously distributed throughout the room, while the ionization d originating from Tn and decreases exponentially in the same way as it decreases the concentration of Tn. Due to the fact that only three distances were measured, the number of degrees of freedom is zero. Consequently, no test of goodness of fit could be performed.

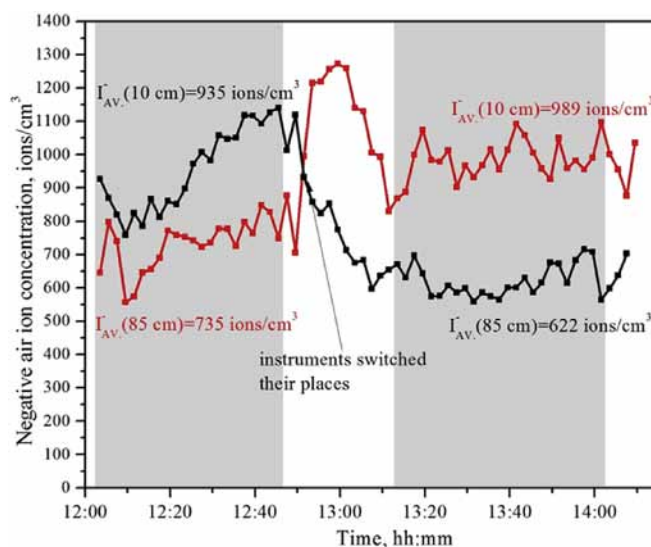


Fig. 3. Vertical gradient of air ion concentrations at 10 and 85 cm above the earthen floor.

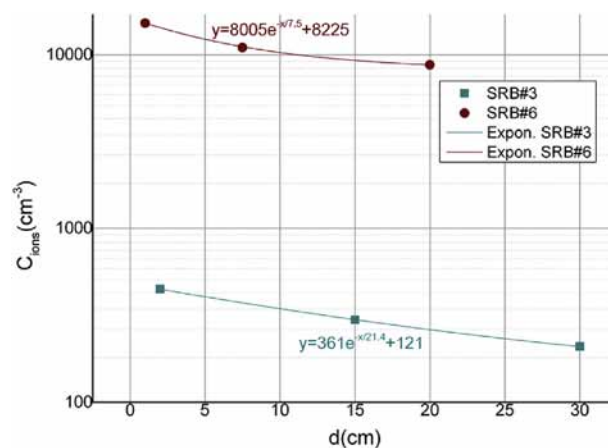


Fig. 4. Horizontal decreasing of air ion concentrations measured in SRB#3,6.

However the fit residuals are smaller than the measurement uncertainties and the coefficients of determination are very high $R^2 > 0.99$, which indicates that the exponential function with offset can describe the ions concentration. Comparing the results obtained from these three houses SRB-V, SRB-#3 and SRB-#6 dominant ionization closer distances to the wall originates from Tn while

going toward to the center of the room dominance assumes Rn alpha particles.

4. Conclusion

During the survey, measurements of the Tn, Rn and air ion spatial distribution were carried out at different measuring sites and distances from walls and have shown exponential pattern for Tn and ions. The effective Tn diffusion length measured in different dwellings were in the range from 5 to 25 cm. The values for the effective Tn diffusion lengths and exhalation rates were in the range of experimentally obtained results reported in other studies.

Air ions concentration gradient from the floor to the center of the room, as a consequence of Tn decay, was clearly present during the measurements above Tn rich earthen floor in SRB-V. Similar results were obtained during the measurements of horizontal gradients in SRB-#3 and SRB-#6. In a few cases gradients were absent due to existence of electrostatic forces of insulating surfaces of the walls.

Acknowledgment

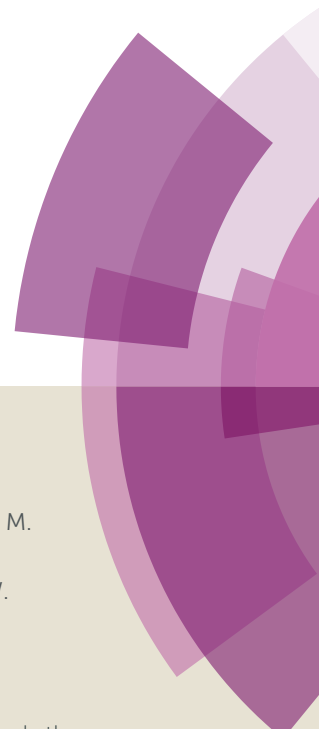
The study was funded through the bilateral Slovenia – Serbia project of scientific cooperation nos. 451-03-1251/2012-09/08 and P41028, 171020 in Serbia and BI-RS/12-13-008 in Slovenia. The authors appreciate the hospitality and technical support of the residents.

References

- Akiba, S., Tokonami, S., Bochicchio, F., McLaughlin, J., Tommasino, L., Harley, N., 2010. Thoron: its metrology, health effects and implications for radon epidemiology: a summary of roundtable discussions. *Radiat. Prot. Dosim.* 141, 477–481.
- Bochicchio, F., Campos, Venuti, G., Nuccetelli, C., Risica, S., Tancredi, F., 1996. Indoor measurements of ^{220}Rn and ^{222}Rn and their decay products in a Mediterranean climate area. *Environ. Int.* 22 (1), S633–S639.
- Bochicchio, F., Žunić, Z.S., Carpentieri, C., Antignani, S., Venoso, G., Carelli, V., Cordedda, C., Veselinović, N., Tollefsen, T., Bossew, P., 2014. Rn in indoor air of primary schools: a systematic survey to evaluate factors affecting Rn concentration levels and their variability. *Indoor Air* 24 (3), 315–326.
- Bossew, P., Žunić, S.Z., Stojanovska, Z., Tollefsen, T., Carpentieri, C., Veselinović, N., Komatina, S., Vaupotić, J., Simović, D., Antignanie, S., Bochicchio, F., 2014. Geographical distribution of the annual mean Rn concentrations, in primary schools of Southern Serbia –application of geostatistical methods. *J. Environ. Radioact.* 127, 141–148.
- Carpentieri, C., Žunić, S.Z., Carelli, V., Cordedda, C., Ferrigno, G., Veselinović, N., Bossew, P., Tollefsen, T., Čuknić, O., Vojinović, Z., Bochicchio, F., 2011. Assessment of long-term Rn concentration measurement precision in field conditions (Serbian schools) for a survey carried out by an international collaboration. *Radiat. Prot. Dosim.* 145 (2–3), 305–311.
- Chalmers, J.A., 1967. *Atmospheric Electricity*. Pergamon Press, Oxford, London, UK.
- Čurguz, Z., Stojanovska, Z., Žunić, Z.S., Kolarž, P., Ischikawa, T., Omori, Y., Mishra, R., Sapra, B.K., Vaupotić, J., Ujić, P., Bossew, P., 2015. Long-term measurements of radon, thoron and their airborne progeny in 25 schools in Republic of Srpska. *J. Environ. Radioact.* 148, 163–169.
- De With, G., de Jong, P., Röttger, A., 2014. Measurement of Tn exhalation rates from building materials. *Health Phys.* 107 (3), 206–212.
- Doi, M., Fujimoto, K., Kobayashi, S., Yonehara, H., 1994. Spatial distribution of Tn and Rn concentrations in the indoor air of a traditional Japanese wooden house. *Health Phys.* 66 (1), 43–49.
- Gulan, L., Milić, G., Bossew, P., Omori, Y., Ishikawa, T., Mishra, R., Mayya, Y.S., Stojanovska, Z., Vučković, B., Žunić, Z.S., 2012. Field experience on indoor radon, thoron and their progenies with solid state detectors in a survey of Kosovo and Metohija. *Radiat. Prot. Dosim.* 152, 189–197.
- Hörrak, U., 2001. *Air Ion Mobility Spectrum at a Rural Area* (Ph.D. thesis), Tartu, Estonia.
- Kolarž, P., Vaupotić, J., Kobal, I., Ujić, P., Žunić, Z.S., 2016. Air ion and aerosol study in rural dwellings. *J. Aerosol Sci.* 95, 118–134.
- Kolarž, P.M., Filipović, D.M., Marinković, B.P., 2009. Daily variations of indoor air-ion and radon concentrations. *Appl. Radiat. Isot.* 67 (11), 2062–2067.
- Milić, G., Jakupi, B., Tokonami, S., Trajković, R., Ishikawa, T., Čeliković, I., Ujić, P., Čuknić, O., Yarmoshenko, I., Kosanović, K., Adrović, F., Sahoo, S.K., Veselinović, N., Žunić, Z.S., 2010. The concentrations and exposure doses of radon and thoron in residences of the rural areas of Kosovo and Metohija. *Radiat. Meas.* 45, 118–121.
- Mishra, R., Žunić, S.Z., Venoso, G., Bochicchio, F., Stojanovska, Z., Carpentieri, C., Prajith, R., Sapra, B.K., Mayya, Y.S., Ishikawa, T., Omori, Y., Veselinović, N., Tollefsen, T., Ujić, P., Bossew, P., 2014. An evaluation of Tn (and Rn) equilibrium factor close to walls based on long-term measurements in dwellings. *Radiat. Prot. Dosim.* 160 (1–3), 164–168.
- Ramachandran, T.V., Sathish, L.A., 2014. Environmental Tn (^{220}Rn), a review. *Res. J. Chem. Environ. Sci.* 2 (2), 5–31.
- Stojanovska, Z., Bossew, P., Tokonami, S., Žunić, Z.S., Bochicchio, F., Boev, B., Ristova, M., Januseski, J., 2013. National survey of indoor thoron concentration in FYR of Macedonia (continental Europe–Balkan region). *Radiat. Meas.* 49, 57–66.
- Stojanovska, Z., Žunić, Z., Bossew, P., Bochicchio, F., Carpentieri, C., Gennaro, V., Mishra, R., Rout, R.P., Sapra, B.K., Burghelle Bety, D., Cucos-Dinu A Boev, B., Cosma, C., 2014. Results from time integrated measurements of indoor Rn, Tn and their decay product concentrations in schools in the Republic of Macedonia. *Radiat. Prot. Dosim.* 162 (1–2), 152–156.
- Tokonami, S., Sun, Q., Akiba, S., Zhuo, W., Furukawa, M., Ishikawa, T., Hou, C., Zhang, S., Narazaki, Y., Ohji, B., Yonehara, H., Yamada, Y., 2004. Radon and thoron exposure for cave residents in Sahnxi and Shaanxi Province. *Radiat. Res.* 162, 390–396.
- Tokonami, S., 2010. Why is ^{220}Rn (thoron) measurement important? *Radiat. Prot. Dosim.* 141, 335–339.
- United Nations Scientific Committee on the Effects of Atomic Radiation (UNSCEAR), 1982. *Sources and Effects of Ionizing Radiation*. Report to the General Assembly with Scientific Annexes (Annex D). NY: UN.
- Vaupotić, J., Čeliković, I., Smrekar, N., Žunić, Z.S., Kobal, I., 2008. Concentrations of ^{222}Rn and ^{220}Rn in indoor air. *Acta Chim. Slov.* 55, 160–165.
- Vaupotić, J., Streil, T., Tokonami, S., Žunić, Z.S., 2013. Diurnal variations of radon and thoron activity concentrations and effective doses in dwellings in Niška Banja, Serbia. *Radiat. Prot. Dosim.* 157, 375–382.
- Zhang, B., Chen, B., Gao, Y., Wang, Y., Cui, H., Li, Z., 2005. Thoron levels in traditional Chinese residential dwellings. *Radiat. Environ. Biophys.* 44, 193–199.
- Žunić, Z.S., McLaughlin, J.P., Walsh, C., Birovljev, A., Simopoulos, S.E., Jakupi, B., Gordanic, V., Demajo, M., Trotti, F., Falk, R., Vanmarcke, H., Paridaens, J., Fujimoto, K., 2001. Integrated natural radiation exposure studies in stable Yugoslav rural communities. *Sci. Total Environ.* 272, 253–259.
- Žunić, Z.S., Čeliković, I., Tokonami, S., Ujić, P., Onischenko, A., Zhukovsky, M., Milić, G., Jakupi, B., Čuknić, O., Veselinović, N., Fujimoto, K., Sahoo, S.K., Yarmoshenko, I., 2010a. Collaborative investigations on thoron and radon in some rural communities of Balkans. *Radiat. Prot. Dosim.* 141, 346–350.
- Žunić, Z.S., Veselinović, N., Bochicchio, F., Carelli, V., Vaupotić, J., Čuknić, O., Simović, R., Vojinović, Z., Kisić, D., Tollefsen, T., 2010b. The indoor radon survey in Serbian schools: can it also reflect the general population exposure? *Nukleonika* 55 (4), 419–427.
- Žunić, Z.S., Carpentieri, C., Stojanovska, Z., Antignani, S., Veselinović, N., Tollefsen, T., Carelli, V., Cordedda, C., Čuknić, O., Filipović, J., Bossew, P., Bochicchio, F., 2013. Some results of a Rn survey in 207 Serbian schools. *Rom. J. Phys.* 58, S320–S327.

Photochemical & Photobiological Sciences

Accepted Manuscript



This article can be cited before page numbers have been issued, to do this please use: A. W. Schmalwieser, J. Gröbner, B. Klotz, M. Blumthaler, H. De Backer, D. Bolsee, R. Werner, D. Tomsic, L. Metelka, P. Eriksen, N. Jepsen, M. Aun, A. Heikkilä, T. Duprat, H. Sandmann, T. Weiss, A. Bais, Z. Toth, A. M. Siani, L. Vaccaro, H. Diemoz, G. Lorenzetto, D. Grifoni, G. Zipoli, B. Petkov, A. G. di Sarra, F. Massen, C. Yousif, A. Aculinin, P. den Outer, T. Svendby, A. Dahlback, B. J. Johnsen, J. Biszczuk-Jakubowska, J. W. Krzyscin, D. Henriques, N. Chubarova, P. Kolarž, Z. Mijatovic, A. Pribulova, D. Grosej, J. Bilbao, J. R. Moreta González, J. M. Vilaplana Guerrero, A. Serrano, S. Andersson, L. Vuilleumier, A. Webb and J. B. O'Hagan, *Photochem. Photobiol. Sci.*, 2017, DOI: 10.1039/C7PP00178A.



This is an Accepted Manuscript, which has been through the Royal Society of Chemistry peer review process and has been accepted for publication.

Accepted Manuscripts are published online shortly after acceptance, before technical editing, formatting and proof reading. Using this free service, authors can make their results available to the community, in citable form, before we publish the edited article. We will replace this Accepted Manuscript with the edited and formatted Advance Article as soon as it is available.

You can find more information about Accepted Manuscripts in the [author guidelines](#).

Please note that technical editing may introduce minor changes to the text and/or graphics, which may alter content. The journal's standard [Terms & Conditions](#) and the ethical guidelines, outlined in our [author and reviewer resource centre](#), still apply. In no event shall the Royal Society of Chemistry be held responsible for any errors or omissions in this Accepted Manuscript or any consequences arising from the use of any information it contains.

Svendby, Tove; NILU – Norwegian Institute for Air Research
Dahlback, Arne; University of Oslo, Institute of Physics
Johnsen, Bjørn; Statens stralevern, monitoring and research
Biszcuk-Jakubowska, Julita; Institute of Meteorology and Water
Management
Krzyscin, Janusz; Institute of Geophysics, Polish Academy of Sciences,
Henriques, Diamatino; Instituto Português do Mar e da Atmosfera,
Observatório Afonso Chaves
Chubarova, Natasha; Moscow State University
Kolarž, Predrag; University of Belgrade
Mijatovic, Zoran; University of Novi Sad
Pribulova, Anna; Slovakian Academy of Sciences
Groselj, Drago; Slovenian Environment Agency
Bilbao, Julia; University of Valladolid
Moreta González, Juan Ramón; Spanish Meteorological Agency, Area of
Atmospheric Observation Networks
Vilaplana Guerrero, José; National Institute for Aerospace Technology
Serrano, Antonia; University of Extremadura, Department of Physics
Andersson, Sandra; SMHI
Vuilleumier, Laurent; MeteoSwiss
Webb, Ann; University of Manchester,
O'Hagan, John; Public Health England Centre for Radiation Chemical and
Environmental Hazards, Radiation Dosimetry

SCHOLARONE™
Manuscripts

UV Index monitoring in Europe

Alois W. Schmalwieser, Julian Gröbner, Mario Blumthaler, Barbara Klotz, Hugo De Backer, David Bolsée, Rolf Werner, Davor Tomsic, Ladislav Metelka, Paul Eriksen, Nis Jepsen, Margit Aun, Anu Heikkilä, Thierry Duprat, Henner Sandmann, Tilman Weiss, Alkis Bais, Zoltan Toth, Anna-Maria Siani, Luisa Vaccaro, Henri Diémoz, Daniele Grifoni, Gaetano Zipoli, Giuseppe Lorenzetto, Boyan H. Petkov, Alcide Giorgio di Sarra, Francis Massen, Charles Yousif, Alexandr A. Aculinin, Peter den Outer, Tove Svendby, Arne Dahlback, Bjørn Johnsen, Julita Biszczuk-Jakubowska, Janusz Krzyscin, Diamantino Henriques, Natalia Chubarova, Predrag Kolarž, Zoran Mijatovic, Drago Groselj, Anna Pribulova, Juan Ramon Moreta Gonzales, Julia Bilbao, José Manuel Vilaplana Guerrero, Antonio Serrano, Sandra Andersson, Laurent Vuilleumier, Ann Webb, John O'Hagan

Abstract

The UV Index was established more than 20 years ago as a tool for sun protection and health care. Shortly after its introduction, UV Index monitoring started in several countries either by newly acquired instruments or by converting measurements from existing instruments into the UV Index. The number of stations and networks has increased over the years. Currently, 160 stations in 25 European countries deliver online values to the public via the Internet. In this paper an overview of these UV Index monitoring sites in Europe is given. The overview includes instruments as well as quality assurance and quality control procedures. Furthermore, some examples are given about how UV Index values are presented to the public. Through these efforts, 57% of the European population is supplied with high quality information, enabling them to adapt behaviour. Although health care, including skin cancer prevention, is cost-effective, a proportion of the European population still doesn't have access to UV Index information.

1. Introduction

The potential of natural solar UV radiation to cause detriment has been a matter of concern for many decades. With respect to sunburn, it was the German physicist Karl Hausser, about 100 years ago, who started investigations to quantify the erythral efficiency of UV radiation. During heliotherapy in the Alps to treat tuberculosis, he observed differences in the efficiency of UV in causing erythema, as a function of wavelength. In 1918 he started, together with his colleague Wilhelm Vahle, detailed investigations and succeeded a few years later in deriving the wavelength dependence of human erythema¹. Henceforward it was possible to determine the erythral efficiency of the sun and any other source of UV radiation.

For many years, measurements of solar UV radiation were done by spectroradiometers only – like the pioneering work of P. Bener at Davos² - and erythemally effective irradiance was calculated from these measurements. These sophisticated instruments need experienced operators and intensive care.

The need for all-day continuous measurements under all weather conditions at several, often remote, locations provoked the development of a less expensive, easy to use but accurate, instrument that can work unattended. The development of the first instrument delivering the erythemally effective irradiance was started about 1958 by Robertson.³ Based on experience Berger⁴ improved this instrument and several of these so called Robertson-Berger-Meters were installed from 1973 onward in the USA, Australia and later in Europe.⁵ The spectral sensitivity was similar to that of human erythema as derived by Coblenz and Stair.⁶ At this time the output was given in “sun burn units” which correspond to 250 J/m² to 350 J/m² of erythemally weighted dose⁽⁷⁾ and is close to the minimal erythema dose for skin type II⁽⁸⁾. A later output unit was also the Minimal Erythema Dose per hour⁽⁹⁾ equivalent to 210 J/m².⁽¹⁰⁾

The evidence for the increasing number of skin cancer cases^{e.g. 11} made it necessary to inform the public about about the risk from solar radiation. In order to provide easy understandable and useful information for sun protection and health care, a dimensionless index for the erythemally effective irradiance was devised¹². Different UV indices were established in several countries. A joint definition for the UV Index (UVI) was internationally agreed in 1995 under the umbrella of WHO, WMO and ICNIRP¹³ using the action spectrum as specified by McKinlay and Diffey¹⁴ for weighting: The UVI is calculated by weighting the measured solar spectrum of global irradiance (in W/(m² nm)) with the standardised erythema action spectrum, integrating from 250 to 400 nm and then dividing by 0.025 W/m². This results in a unit-less quantity. For most conditions in Europe the UVI is less than 10. By now a slightly corrected action spectrum was published in CIE S 007/E-1998 and subsequently ISO 17166:1999¹⁵, which may lead to slight differences (e.g., less than 2%).¹⁶ In 2002 the WHO distributed a colour scheme for visualisation of the UVI.¹⁷ Since its definition, several promotion campaigns were undertaken (e.g. Intersun by WHO) to make people familiar with the UVI. Necessary parts of such a campaign are recent UVI values that are easily accessible for the public.¹⁸ Health authorities and people that care about sun protection are often knowledgeable about the conditions at home. However many people receive a noticeable part of the annual exposure during holidays.¹⁹ With the availability of UVI values at a holiday destination, appropriate advice can be made available. For almost 20 years such online measurements have been available on the Internet. The financial efforts for this do not only help to avoid illness and suffering but also to avoid costs for medical treatment. In the meanwhile it could be shown that skin cancer prevention initiatives are highly cost effective and cost-saving.²⁰ The changes in the ozone layer, climate change and those complex interaction in respect to UV radiation^{e.g.21}, have caused seasonal and local changes (e.g. ²²). Therefore up-to-date information is more important than ever.

In this paper we will provide an overview of UVI measurements in Europe, focusing on those stations and networks that do online monitoring on the Internet. As the UVI values have to be reliable, we will also consider the instruments used and the corresponding quality assurance and quality control procedures. Service radius is used to provide an estimate of the coverage provided by individual measurement sites. The area of the country or region is divided by the number of measurement sites. Assuming a circular area, the service radius is the radius of that area.

2. UV Index monitoring sites

In the following chapter a short summary of UVI monitoring in the European countries (in alphabetical order) is given. The stations which deliver online UV-Index values to the Internet are listed in Table 1, together with additional information such as location, instruments and year of start. Figure 1 shows the locations of these stations. Table 2 summarizes the networks.

Austria: The monitoring network was established in 1996 on behalf of the Federal Department of Environment. The locations have been selected by an objective method²³ and quality assurance was well defined from the beginning.²⁴ Austria possesses a high alternating topography and is within 4 climatic zones (Oceanic European, Alpine, Pannonian continental, Mediterranean). At the present time the network consists of 13 stations. At 3 stations a second device is equipped with a shadow band to measure diffuse irradiance. By taking into account the area of the country (83.879 km²) each station covers approximately 6450 km² on average, denoting a service radius of 45 km for each station. The altitude of stations ranges from 150 m to 3105 m above sea level (asl). Online-publication of measurements includes two stations from Germany (Munich and Zugspitze) and two stations from Switzerland (Davos and Weissfluhjoch). A special feature of the website is a map which shows the spatial distribution of the UVI over Austria. This map is produced by combining measurements from all stations, clear sky model calculations, digital elevation information, and cloud attenuation factors derived from high resolution Meteosat pictures every 15 minutes.²⁵ Highest UVI values at the stations span a relatively wide range although the difference in latitude is only 1.6°. At Vienna (156 m asl) the UVI may reach values between 7 and 8 while at Sonnblick (3105 m asl) it may go up to 11.

Belgium: In contrast to Austria, altitude does not significantly influence the UVI over Belgium. Two institutions monitor the UVI there. The Royal Meteorological Institute of Belgium (RMI) has been measuring the UV radiation since 1989 at Uccle in the south of Brussels with a Brewer spectroradiometer.²⁶ Presently, several instruments run there in parallel. The second institution is the Royal Belgian Institute for Space Aeronomy (BIRA-IASB) at Brussels which operates another five stations and is responsible for publication. The website also includes the UVI from Luxemburg (see below). Each of the Belgian stations is equipped with a multichannel instrument and a broadband meter which provide one measurement per minute. The stations are relatively homogeneously distributed over the country. The highest station is Mont Rigi (680 m asl), a skiing and hiking resort in the vicinity of Mt. Botrange (694 m asl), and the highest Mountain of Belgium. The six Belgian stations are responsible for an area of 30528 km², denoting a service radius of 40 km each. There are no large differences in the UVI on a clear-sky day in summer. For low altitude stations, the highest UVI values observed during recent years were between 8 and 9. For Mont Rigi, the highest UVI was up to 9.8.²⁷ Both institutes measure the UVI also in Antarctica at the Princess Elisabeth Station with a broadband meter (BIRA-IASB) and a Brewer (RMI) where the UVI may reach a value between 10 and 11 in December. The maximum UVI was 12.3, measured in 2015.

Bulgaria: In February 2015 a multichannel instrument was installed at Stara Zagora²⁸, in the centre of the country, just south of the Balkan Mountains and near to the famous tourist attraction, Rose Valley. Since this time regular measurements of the UV irradiance have been carried out and the total ozone column is retrieved. The Space Research and Technology Institute plans to start the determination of the UVI during 2017.

Croatia: Croatia is a very popular holiday destination, especially famous for its beaches and the hundreds of islands. About 10 million tourists are welcomed each year. The UVI network consists of 11 stations, equipped with broadband meters, with 6 of them providing UVI values online. The stations are spread over the whole country including locations close to the beaches and on some islands (Krk and Solta). Another station, important for tourists, is located in the national park Plitvicka Jezera, which is well known for its lakes and waterfalls. The highest station (Parg, 863 m asl) is located in the woodlands north of Rijeka, and the largest city and capital Zagreb has an instrument. Bringing all 11 stations online would reduce the service radius from 111 km to 81 km.

Cyprus: The island of Cyprus itself belongs geographically to Asia, but culture and economy are strongly connected to Europe and the Republic of Cyprus is a member of the European Union. An important branch of economy in Cyprus is tourism. The island is well known for summer vacation but also for its pleasant climate during winter. Beside the beaches, attractions for visitors are the historical places but also the high mountain areas up to Mt. Olympus (1952 m asl). These result in about 14 million guest-nights per year. Apart from short term stays, many Europeans, especially from the UK, have chosen Cyprus as their secondary residence. One UVI station is located in Akrotiri (a British air base) and participates in the UVI network of Public Health England (see below). During summer UVI up to 10 can be measured. This value differs significantly from the highest values experienced on the British Isles and justifies the efforts of online monitoring.

Czech Republic: Measurements at the solar and ozone observatory in Hradec Kralove by the Czech Hydrometeorological Institute (CHMI) have a long tradition dating back to the 1960s. UVI monitoring using a broadband meter started there, and at another station, in 1996. In 2009 a third station was added. At all locations global and diffuse irradiance is measured. Main attractions for visitors from all over the world are the capital Prague, cities possessing a core from the middle age as well as the long traditional spa resorts like Carlsbad. Skiing resorts can be found in the north, west and south-west and are visited mainly by natives. The stations span a triangle centred to the middle of the country and provide new data every 10 minutes. Another broadband meter is operated by the Masaryk University in Brno in the south of the country but it is not yet included in the network. In the near future the network will be expanded by a station at Krkonose Mountain (Giant Mountains - about 1400 m asl) in North Bohemia. The establishment of this station will reduce the service radius from 183 km to 159 km. The highest UVI is usually 8, and on rare days 9.

Denmark: In Denmark the UVI is made available online for Copenhagen by the Danish Meteorological Institute (DMI). Copenhagen is located on the eastern shore of the island of Zealand and partly on the island of Amager. Measurements at Copenhagen have been made with a broadband meter since 1992. Values are updated every 30 minutes. Beside this instrument there is a Brewer MK IV (since 1992), MK III (since 2014) and another broadband meter (UVS-B-T, since 2016) in operation which ensures high quality data. While the UVI from Copenhagen may be representative for a large part of the Danish archipelago, which consists of more than 440 islands, the peninsula of Jutland may remain uncovered depending on meteorological conditions. To overcome this, the online values are connected to model calculations that use cloud cover information. With that, the UVI distribution over Denmark is estimated. Altitude is not an issue as the highest hills are around 170 m asl. There are also other instruments running, e.g. in Greenland, but not online. The highest UVI value in Copenhagen is of the order of 7.²⁹

Estonia: In Estonia there are five stations operated by the Estonian Environmental Agency, which deliver online values. Broadband meter measurements started in 2000 at the Tartu-Toravere meteorological station and the network has been expanded over the years. Together with two other stations it builds a measuring chain in the southern part of the country, whereas one of these (Pärnu), lies on the west coast and the other one on the Island of Saaremaa, around 50 km off shore. The fourth station is located in the middle of the country. The most northern station is Tallinn which is also the main region for tourism. The service radius is approximately 107 km. Summer UVI values can exceed 7.

Finland: Measurements of erythemally effective irradiance using broadband meters started in 1991.³⁰ The online network of the Finish Meteorological Institute started with 6 stations in 1997. A seventh station was added in 2014. Data is measured with a resolution of 1 minute, the update frequency being 10 min. The most southerly station on the mainland is located in the metropolitan region of Helsinki and supports approximately 1.5 million people with real-time values. A second urban station was established in central Finland (Jyväskylä Tikkakoski). Another three stations are located in the southern and central part of the country where most of the population lives. The most northerly station is Sodankylä, located just above the northern polar circle where the sun does not rise around the winter solstice. Measurements have been carried out there since 1989 using a Brewer MkII. Another special station is Parainen Utö, located on the island of Utö, which lies half way between Helsinki and Stockholm, and borders an archipelagoes national park. On average the service radius is 248 km on the mainland. UVI values as high as 6 and even 7 are reached in the summertime.

France: Meteo-France started UVI monitoring a couple of years ago with broadband meters at three locations. The devices are located in the southern part of the country. Considering the size of France, 3 stations cannot give an adequate estimate of UVI across the country. Therefore a UVI forecast is provided to the public instead of measurements. UVI data are collected every hour for climatological purposes and for validation of the forecast. The highest UVI values during the past years were around 9 to 10. France also has two NDACC stations which record the UVI, but do not provide data online.

Germany: Since 1993, the Federal Office for Radiation Protection (BfS) together with the German Environment Agency (UBA), the German Weather Service (DWD), and associated institutions operates the German UV monitoring network.³¹ Today, the network consists of ten stations which are located at relevant sites for UV radiation and climate. Significantly, all instruments in the network are spectroradiometers. Two of the stations are located on islands in the North Sea: Sylt³² and Norderney. Both are important holiday destinations with about 10 million guest-nights per year. The most northern station on the mainland is located on the peninsula of Zingst in the Baltic Sea, which is a popular recreational site too. The highest station is Schauinsland (1205 m asl) in the south-west of the country where UVI may be of the order of 9 in summer. The lowest summer maximum values are measured in the densely populated Ruhr-region (Dortmund) with values around 7. The service radius of one station is around 213 km. BfS informs the public by publishing the maximum UVI of the day. In case of extraordinary high UVI values, e.g. at low ozone events³³, BfS issues a press release. In the near future, the varying UVI values throughout a day will be presented. Furthermore it is planned to extend the network with three array radiometers (e.g. one of them at the Zugspitze at about 2660 m asl) and with about 20 broadband meters.

In the capital **Berlin**, a manufacturer of a miniature erythema meter (sg-lux, Berlin, Germany) publishes recent values together with those from a station in Brazil.

Gibraltar: The most southern station on the European continent is located in Gibraltar, on the southern end of the Iberian Peninsula. Public Health England operates the device there, because it is a British Overseas Territory, and more than a quarter of the inhabitants are of British ancestry and therefore light skinned. The south of the Iberian Peninsula is not only popular for summer vacation but also a favoured golf destination in winter. The UVI may reach a value of 9 in summer.

Greece: Greece is one of the most popular holiday destinations for Europeans in summer, where visitors spent a lot of time outdoors either on beaches or on the usually treeless ancient sites. The National Network for monitoring solar UV radiation was established by the Aristotle University of Thessaloniki, Laboratory of Atmospheric Physics in 2004 aimed at providing long-term monitoring over Greece and related services such as the UVI to the local population and visitors.³⁴ Since 2004 a few stations ceased operation due to technical reasons. Presently, 7 stations are in operation distributed at locations with different environmental conditions ranging from rural and coastal to urban. Five stations are located on the mainland and 2 at the islands of Crete and Lesbos. Stations cover a range in altitudes from 60 to 540 m asl. Measurements are conducted with NILU-UV multi-filter radiometers. Online publication takes advantage of the multichannel data and provides also other biologically weighted irradiances. The maximum monthly averaged UVI of about 10 has been measured at Finokalia while in Thessaloniki and Ioannina maximum monthly values are about 8.

Hungary: Solar radiation measurements have a long tradition at the Hungarian Meteorological Service, starting in the 1930s in Budapest and resulting in the longest (homogenized) global radiation data series in Europe. The Hungarian UV network consists of 5 stations and was established under a collaboration between the cooperation of the Ministry of Agriculture and the Hungarian Meteorological Service in 1994.³⁵ Agriculture is an important branch of the economy in Hungary, so that UV-B-radiation is also an important factor for food production.³⁶ The network covers the recreational region of Lake Balaton by a station on the western end and one on the eastern end. The station at Budapest (where a Brewer has run in parallel since 1998) delivers the UVI for the urban region with about 1.7 million inhabitants. One station is also located at a rural site on top of the highest Hungarian mountain (Mt. Kékes, 1012 m asl). The fifth station (Kecskemet) is located in the north of one of the Puszta regions. It is representative of this unique habitat as well as for tourists' activities there. On average each station represents an area of 18600 km² denoting a service radius of 154 km. In summer UVI may reach 7 in most of the cases when sky is clear or partly covered and the ozone content is not extremely high and may exceed 8 in cases of clear sky and very low ozone. It can reach or exceed 9 in very few cases almost every summer.

Iceland: Currently, two stations are operated by the Icelandic Radiation Safety Authority. One station is located in the capital Reykjavik on the west-coast of the island. The second one is located in Egilsstaðir close to Lake Lagarfljot near the east-coast. The highest UVI values of the day are published on a web-page.

Ireland: UVI monitoring is done in Malin Head, on the Inishowen Peninsula, which is the most northerly point of the island of Ireland. This meteorological station provides essential data for shipping traffic. Apart from this site in the Republic of Ireland, another station operates in Belfast in Northern Ireland. Both stations are equipped with broadband meters and are operated by Public Health England (see below). In summer, the maximum UVI is usually 7.

Italy: In Italy UVI monitoring and publishing is done separately by different institutions. In the **Aosta Valley** (3262 km²), an attractive tourism region in the north-west of Italy, a network consisting of three stations was established in 2006 by ARPA (Agenzia Regionale per la Protezione Ambientale) Valle d'Aosta supported by the regional government. The northern border of Valle d'Aosta is formed by the highest mountains in Europe like the Matterhorn and Mont Blanc. A special characteristic of this network is that the stations are geographically close to each other but span a large range in altitude from 570 m to 3500 m asl. This network is able to communicate the UVI to the public, especially to the tourists, for the varying environmental conditions from the bottom of the valley³⁷ up to the glacier ski field of Plateau Rosa where skiing is done also during summer.³⁸ Online values are updated every 5 minutes. The network allows the altitude effect to be studied³⁹, including the annual variation of the snow line. At the bottom of the valley the UVI can be 9 for clear sky (10 for broken-clouds conditions) but it can reach a value of 14 at the Plateau Rosa.

In between Verona and Venetia, the ARPA Veneto has been measuring the UVI in **Vicenza** with a broadband meter since 2011. Values are updated every 5 minutes and may reach 9 in summer. In the near future the ARPA Veneto will install another broadband meter in a mountain place within the Belluno dolomites.

Another station in Italy is operated by the Institute of Atmospheric Sciences and Climate (ISAC) from the National Research Council (CNR) in **Bologna**. An in-house developed narrow-band filter radiometer⁴⁰, which determines the UVI with a temporal resolution of 5 min was installed in 2005. Data are delivered every 30 min. During summer a UVI of 10 was measured.⁴¹ This station may cover the eastern part of the Emilia-Romagna. The UVI for the famous tourist region of Tuscany is provided by the Institute of Biometeorology (CNR-IBIMET) in **Florence**. A broadband meter has been operating since 2003. The station delivers an update every 15 minutes and could cover the region from Siena to the Apennines, and from Pisa to San Marino, at least for lowland locations during days with homogeneous atmospheric conditions. The highest UVI values can be between 8 and 9 during the summer.⁴²

Information about the UVI for the metropolitan region of **Rome**, with around 4 million inhabitants, as well as the nearby popular seaside locations at the Tyrrhenian Sea is provided by the Physics Department of the Sapienza University of Rome. Spectral measurements started in 1992 using a Brewer MkIV spectrophotometer⁴³⁻⁴⁵ and are displayed and updated on the Internet every 30 minutes. A broadband UV radiometer has also been in operation since 2000 located in the same place close to the Brewer. Another broadband device, installed in Rome by the Italian National Institute for Environmental Protection and Research (ISPRA) in 2015, delivers a graphical bulletin of hourly UVI based on erythemally weighted irradiance values measured every 10 minutes. In summer the UVI in Rome (at both locations) at local noon may reach values in the very high category (between 8 and 9) under clear sky conditions due to the combined effect of lower total ozone content and solar zenith angle.⁴⁶

The most southerly station is located on the island of **Lampedusa**, in between Malta and Tunisia. A Brewer has been operated there by ENEA since 1997⁴⁷, together with an UV multi-filter rotating shadowband radiometer (UV-MFRSR⁴⁸). The UVI at Lampedusa may exceed 10 during the summer. A large modulation effect is produced at Lampedusa, in addition to clouds⁴⁹ and ozone, by Saharan dust events⁵⁰, which may produce significant enhancements of the aerosol optical depth. UVI values are derived from these measurements and are available online.

Luxemburg: In 1996, the Lycée Classique de Diekirch (LCD) (a secondary school) built up the meteorological station MeteoLCD. Apart from the usual meteorological parameters, atmospheric gases (e.g. CO₂, NO_x), total ozone column, total solar irradiance and UV-A are measured. UVI measurements are available as an average over the past 30 minutes. Recent and past data are freely available on the web site. In contrast to many other stations, MeteoLCD is not an official government financed station, but an ongoing project of the LCD that provides financing for the day to day operation and equipment, and the Ministry of Education helps in an unofficial manner to pay for maintenance of the sensors. All work is done graciously by volunteers. The UVI values from Diekirch are also displayed on the web-page of the Belgium UVI network. By being responsible for Luxemburg the station has a service radius of 57 km. During summer the UVI may reach a value of 8.

Malta: The Institute for Sustainable Energy of the University of Malta measures solar radiation at its premises in the village of Marsaxlokk situated on the south-east coast of the Island of Malta. In 2014, broadband instruments were added to measure the UVI and other parameters others. One-minute average data are being collected. Although the solar radiation data is online, the UV data is still not displayed on the Internet. The maximum UVI measured was 11 at around solar noon in summer.^{51,52} The service radius of this station is 11 km.

Moldova: Since 2003 the erythemally effective UV radiation has been measured at a station in the urban environment of the capital, Kishinev city. The Atmospheric Research Group of the Institute of Applied Physics operates two broadband meters (global and diffuse). The daily radiant exposure is provided on web-page (but not the UVI). The highest measured value was 12 UVI.

The Netherlands: In the Netherlands, one station delivers online UVI values. The station was established in 1994 and is equipped with two double monochromator spectroradiometers that run in parallel. The station is located at the premises of the National Institute for Public Health and the Environment (RIVM) in Bilthoven, in the centre of The Netherlands, close to Utrecht. The measured UVI, with a frequency of one per 12 minutes, is shown in a graph together with the cloudless sky forecast. During summer the UVI may lie between 6 and 7: values above 8 have been measured over the last 23 years.⁵³ Within a radius of approximately 50 km there is an agglomeration of large cities (Randstad) like Amsterdam and Rotterdam where about 7 million people live.

Norway: Monitoring started in 1994⁵⁴ and was expanded over the years.⁵⁵ Today, the UVI is measured at nine different stations. Data are updated every hour. The measurements are performed by the Norwegian Radiation Protection Authority, the University of Oslo, the Norwegian Institute for Air Research on behalf of the Ministry of Climate and Environment, and the Ministry of Health and Care Services. The distinctiveness of the Norwegian network is the type of devices used: multichannel, moderate bandwidth filter instruments, model GUV (Biospherical Instruments, San Diego, USA). A description of this instrument can be found in Section 3.3. The network covers the southern part of the country (where most of the people live) up to Trondheim, with 7 stations. On a few days the UVI reaches a value of 7. The highest location of the whole network, is Finse (1210 m asl), a small village reachable only by a railway, which is a tourist attraction as well as a starting point for hiking, cross country skiing and glacier hiking. The highest ever measured UVI was 10. In addition, there are two stations north of the Arctic Circle (Andøya and Spitzbergen). The most spectacular station is located at Ny-Ålesund (78.9°N) on the island of Spitzbergen, which is the northernmost UVI monitoring site in Europe and the third northernmost in the world. The highest UVI measured at Ny-

Ålesund was 3. Besides UVI, there are currently nine other irradiance detectors for the UV and visible radiation for each location (e.g. Vitamin-D irradiance) with complementary data sets since 1995.

Poland: In Poland two networks exist. One is operated by the Institute of Meteorology and Water Management - National Research Institute and was established under a project of the State Environmental Monitoring at the request of the Chief Inspector of Environmental Protection, funded by the National Fund for Environmental Protection and Water Management in July 1993. Three broadband meters were placed at selected sites. One station (Leba) is located on the Baltic coast which is an important site for recreational exposure. UVI may reach values between 6 and 7. The device in Legionowo provides UVI values for the urban region of Warsaw (summer: 7). Another monitoring site, representative for outdoor activities like skiing in winter and hiking in summer, is Zakopane (855 m asl) in the Tatra Mountains where UVI values can reach-around 7 to 8. In 2006 these three sites were equipped additionally with a new broadband meter and a fourth station was established in the south of Poland (Katovice). However production of this broadband meter and of spare parts has been stopped so it is uncertain how long the fourth station will continue. The loss of this station would enlarge the service radius for each station from 315 km to 364 km.

The second network, started in 2012, was expanded over the years and today consists of four stations (Warsaw, Lodz, and stations near Lublin and Gdansk). It is carried out by the Institute of Geophysics of the Polish Academy of Sciences. The network uses miniature devices which are part of low cost weather stations. UVI values are available via the web page of the manufacturer. The core of the network is the Central Geophysical Observatory Belsk where various broadband meters (since 1975) and the Brewer No. 64 Mark II (since 1991)⁵⁶ measured in parallel. UVI is published on a web-page every 24 hours. In Warsaw, Brewer No. 207 Mark III started to operate in 2013. UVI can reach a value of 8 for a few days each year in Warsaw and Belsk. One purpose of this network is to support people in antipsoriatic heliotherapy.⁵⁷

Portugal: UVI values are collected on two islands (Funchal, Madeira and Angra do Heroísmo, Terceira, Azores) by the Instituto Português do Mar e da Atmosfera.⁵⁸ Online values are available for the island of Madeira, a year-round holiday destination for around 1 million tourists (mainly from Germany, UK and Scandinavia) per year. The main attraction for tourists is not the coastal region but the flora-rich landscape so tourists spend a lot of time walking and hiking up to the highest Mountain Pico Ruivo (1862 m asl). Because of the location and the resulting climate, UVI and air temperature are not that closely related to other locations. At moderate temperatures UVI may reach values around 11 which are comparable to those in the Saharan dessert. UV measurements started in 1989 with a Brewer and have been accompanied by a broadband instrument since 2004.

Russia: Potentially, there are around 20 stations in Russia with Brewer instruments operated by the Russian Hydrometeorological Service. However no online data are available. Long UVI data series exists from the Meteorological Observatory of the Moscow State University. The devices have been running since 1999⁵⁹ in accordance with WMO standards. The maximum UVI in Moscow during this period reached 7.7 in June.⁶⁰

Serbia: UVI measurements have been made in the two largest cities of the country: Belgrade and Novi Sad⁶¹ since 2009 and 2003, respectively. The station in Belgrade is operated by the Institute of Physics and provides values for around 1.7 million people. The station in Novi Sad is operated by the Department of Physics, University of Novi Sad and provides information for around 350000 people.

Both cities are also the most popular tourism destinations in Serbia. Each station is equipped with a broadband meter. The values on the joint web-page are updated every 30 minutes, but are also available from other web-pages. The UVI may exceed 9 at both locations.

Slovakia: Measurements of solar UV radiation started in the 1970s with broadband UV-A meters at stations of the Geophysical Institute of the Slovakian Academy of Sciences.⁶² In 1993, Brewer spectrophotometer measurements were established and daily information about UV radiation has been provided for mass-media since that time by the Slovak Hydrometeorological Institute (SHMI). UVI monitoring started in 1997 in Bratislava in a cooperation of the Ministry of Environment and the SHMI. Over the years the network was expanded and now consists of 5 stations⁶³ located in the capital (Bratislava), nearby regional centres Košice and Banská Bystrica, at Poprad-Gánovce (close to a mountain tourist resort) and Hurbanovo at the Danubian lowland region, rich with sunshine in the summer. The Institute of the Earth's sciences provides UV radiation measurements at the Tatra mountain station Skalnaté Pleso (1778 m asl). Due to past problems with internal network capacity, measurements are not currently available online. The UVI values exceed 7 from May till August at all stations under clear-sky condition. The mean hourly UVI values exceeded 8 during low total column ozone and under cumiform clouds.

Slovenia: At the present time the Slovenian Environment Agency operates 4 stations equipped with UV-B broadband meters. The network started in 2014 with its first station in the west of the country close to the Mediterranean Sea. In the following year a second device was installed at 2512 m asl, close to the top of Mt. Triglav (2864 m asl) which is the highest mountain in the country. In 2016 another two instruments started operation. One was mounted in the east of the country (Murska Sobota-Rakičan) and one at the ski resort in Rogla (1496 m asl). Measured UVI values are not yet provided to the public but are available on request.

Spain: The UVI network operated by Agencia Estatal de Meteorología (AEMet) has the largest number of stations. It started in 1995 and currently devices are mounted at 26 locations. 22 stations are spread over the mainland. The highest location is Puerto de Navacerrada (1858 m asl), a mountain pass and skiing resort, in the Sierra de Guadarrama close to the capital Madrid where another instrument operates. Most stations are in the vicinity of the larger cities so that many of them are on or close to the coast. The Spanish beaches are attractive holiday destinations for tourists from all over Europe. After France and the USA, Spain is the most visited country in the world. UVI values may come close to a value of 11. Apart from the mainland, stations are also located on the important tourism archipelagos of the Balears in the Mediterranean Sea (Palma de Mallorca) and Canary islands. Each of these archipelagos is visited by more than 12 million tourists per year. At the Canaries there is a station at Maspalomas (Gran Canaria) and two on the island of Tenerife whereas one station is located at sea level (Santa Cruz), while the other is located at the mountain plateau of Mt. Izana (2400 m asl). At Palma de Mallorca the UVI may reach a value of 10. At Maspalomas and Izana, the UVI reaches a value of 11 on 12% and 51% of the days, respectively. The update frequency of the AEMet network is once per day, displaying the highest values as well as the daily graph of the past day.

Additionally, southwestern Spain is covered by the regional **Extremadura-Andalusia** UV network, which started in 2002⁶⁴⁻⁶⁶ and is currently operated in cooperation with the Universidad de Extremadura (UEX) and the Instituto Nacional de Técnica Aeroespacial (INTA). The monitored region covers Extremadura and Western Andalusia with 11 stations equipped with UV broadband

radiometers measuring erythemally-weighted irradiance. A large range of altitudes is sampled, varying from sea level (e.g. El Arenosillo station) to almost 2000 m asl at a ski resort (La Covatilla station). The network reports measured UVI values every 20 minutes via its website, as well as foreseeable cloud-free-sky maximum UVI values for each day. The highest UVI in summer in the area is around 9 to 10, with occasional values of 11.

Beside these networks, the Laboratory for Atmosphere and Energy at University of **Valladolid** has been measuring erythemally effective UV radiation for more than a decade⁶⁷ and has been providing online measurements from a broadband meter since 2014. The highest UVI values in summer are 9 to 10.⁶⁸

Sweden: Several years ago, four stations delivered current UVI values to the public. Today there is only one station running (Norrköping) but data are not available on the web. The Swedish Meteorological and Hydrological Institute (SMHI) provides a forecast instead. In summer, the UVI may be as high as 7.

Switzerland: For Switzerland, UVI values for 5 locations are available. 4 of them are connected to a network operated by MeteoSwiss. One of these and a fifth station participate in the Austrian UVI network. Switzerland is an important holiday destination in winter as well as in summer for visitors from all over the world. Tourism focuses mainly on the alpine region which covers the southern part of the country. Most inhabitants live in the northern plateau and hill lands. There are several large lakes within the foothills of the Alps that are important for recreational activities. The network covers a range of altitude from 366 m (Lago Maggiore) to 3582 m asl (Jungfrauoch) and includes an inner-alpine valley (Davos) and the region around Lake Neuchatel in the north-west. The service radius is 115 km. A special feature of the network is that direct radiation is measured with a separate broadband meter at each station. The broadband meters are equipped with a collimating system and mounted on a sun tracker. Such measurements can be used in conjunction with a 3D-human model to estimate the personal UV exposure.⁶⁹ UVI during summer can reach values up to about 8 in the lowland regions (near Lake Neuchatel or Lago Maggiore), slightly higher than 9 at Davos and up to 12 at Jungfrauoch.

United Kingdom: Broadband monitoring started in Chilton, near Oxford, in 1990. In 1995 six stations were in operation, one of which was in the Republic of Ireland (see above). During the past 4 years another 6 stations were added, giving Public Health England 12 stations today. One of these stations is in London (since 2013). In this metropolitan region more than 13.5 million people live within a radius of 50 km, meaning this station now represents the sun exposure of more people than any other station in Europe. Further instruments operate in Wales, Scotland and Northern Ireland, plus the Republic of Ireland (see above). The most northern station is located in Lerwick on Mainland, the largest of the Shetland Islands. In 2015 the UVI monitoring was expanded to British Overseas Territories to enable proper sun care for tourists from UK but also for the military staff. One station is at Cyprus and one is on Gibraltar, both are described above.

A further two stations provide UVI data to the public through the same Internet interface. The fourteen stations that participate in this network include Reading and Manchester. These are operated on behalf of the Department of Environment Food and Rural Affairs by the University of Manchester and the sites provide a much broader suite of data including ozone and a wide range of meteorological parameters.⁷⁰ While at all other locations broadband meters are in use, the UVI at

Reading (most representative of London from 1993 - 2013) results from a spectroradiometer, while that at Manchester (since 1997) comes from a multifilter radiometer, supported by spectral UV irradiance from a Brewer spectrophotometer. The maximum UVI value for the south of the UK is 8.

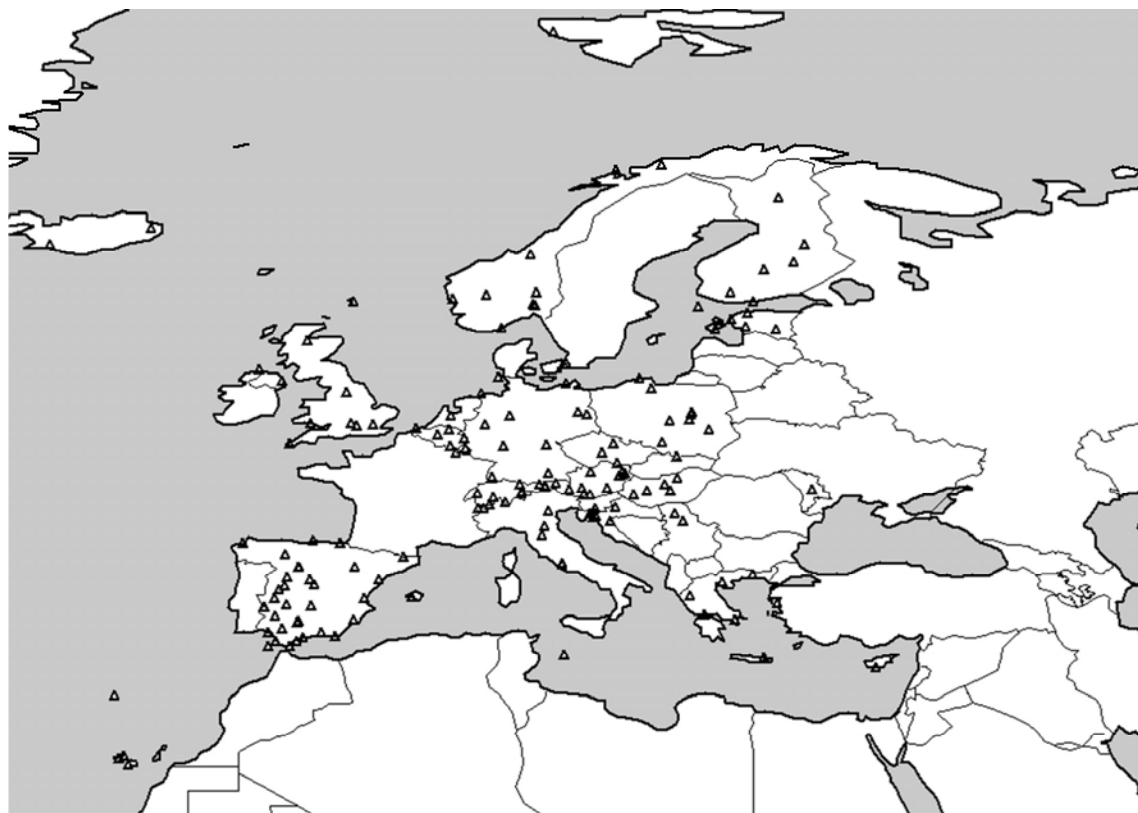


Figure 1: UV Index monitoring sites in Europe which deliver online values.

3. Instruments and quality assurance

The number of stations where erythemally effective UV radiation is measured has increased over time. Figure 2 shows the number of stations as a function of time. By the end of 1995, 32 stations were in operation. With the standardization of the UVI the number increased significantly and is further increasing. Today, online UVI values are available from 160 locations. At several stations different instruments run in parallel so that the number of instruments involved in UVI measurements is higher. The following chapter delivers an overview on the instruments used for UVI monitoring and the quality assurance and control procedures.

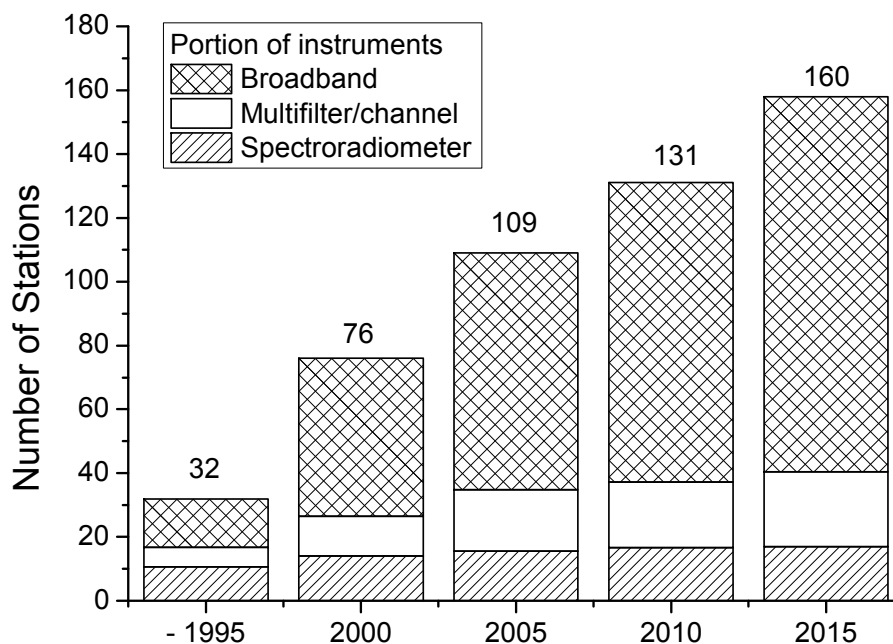


Figure 2: Number of Stations publishing the UVI on the internet. The different patterns indicate the portion of different instruments.

3.1 Broadband meters

Most of the stations are equipped with broadband meters. At present, 125 of these deliver online UVI values. The most common detector is the Model 501 (Solar Light Inc., Philadelphia, USA) followed by the UVB-1 (Yankee Env. Sys. Inc., Turners Falls, USA) and by UV-S-A-E-T, UV-S-E-T and UV-S-E-C (all Kipp&Zonen, Delft, The Netherlands). Beside these, there are a few OPTIX UVEM-6C instruments in use (which are no longer manufactured), a few Thies Clima E1c (Adolf Thies GmbH, Göttingen, Germany), a few MS-212W UVB Meters (EKO Instruments CO. Ltd, Tokyo, Japan) which are restricted to the UV-B range, a miniature meter Model EryCa (sglux GmbH, Berlin, Germany) as standalone instruments and a few miniature erythema meters as part of a weather station (Davis Instruments, Hayward, USA). The UVS-AE-T (Kipp&Zonen, Delft, The Netherlands) is used at 4 stations and measures both UV-A irradiance and erythemally weighted irradiance. It is a dual-band radiometer which has two separate detection systems.

Broadband meters are generally easy to operate. However, there are certain requirements on calibration and maintenance to ensure reliable measurements. Both have been topics of a variety of national and international co-operations^{e.g. 71} but also as European wide initiatives (e.g. COST Action 713⁷², COST Action 726^{73,74}).

3.1.1 Properties and Calibration

A broadband meter measures the total irradiance over a certain wavelength range (broad band) and delivers a single electrical output value S (either voltage or current) which has to be converted into the UVI by a certain factor c_0 . An appropriate broadband meter for measuring the UVI must have the same spectral response as the human skin for erythema.¹⁵ This is realized by the combination of the spectral response of the photodetector and the transmission curve of an optical filter. However it is technically not possible to gain a perfect fit. So, differences remain which vary with wavelength (see Figure 3). With that, the difference between the erythemally effective irradiance and the output value of the device depends on the spectrum of the source, in our case the sun. This denotes F further, this means that the magnitude of the difference changes whenever the spectrum changes. The solar spectrum at the earth's surface is mainly influenced by the solar zenith angle (SZA) and the total ozone content of the atmosphere (O_3). Therefore it changes during the day and during the year. To overcome this, a correction factor $c_1(O_3, SZA)$ is necessary that takes both into account.

Another source of error is the angular response of the instrument which must follow a cosine-function. Deviations need a correction factor $c_2(SZA)$ dependent on solar elevation. Temperature sensitivity $c_3(T)$ could be also matter of concern⁷⁵, but is generally solved by an internal heater that stabilizes the temperature of the device. Humidity ($c_4(rH)$) can also influence measurements.⁷⁶ A silica gel reservoir within the device can absorb ingressing water vapour. This reservoir has to be changed periodically. Deviation from linearity $c_5(S)$ is rarely seen because the dynamic range necessary for the UVI is not that large. Any dark signal S_0 also has to be subtracted first. The following correction formula takes all these factors into account:

$$E_{UVI} = (S - S_0) * c_0 * c_1(O_3, SZA) * c_2(SZA) * c_3(T) * c_4(rH) * c_5(S)$$

For some types of instrument in use (SL501, UV-S-A-E-T, UV-S-E-T and UVB-1) the correction factors $c_3(T)$, $c_4(rH)$, $c_5(S)$ can be neglected⁷⁷, and therefore are respectively equal to one.

The methods to derive all of these calibration factors are described in detail e.g. by WMO/GAW⁷⁸. As shown by several international intercomparisons, all these parameters must be proven for each single instrument separately^{72,79,80}, as there are obvious differences. Each single low cost miniature erythema meter needs the same care (characterisation, calibration factors, mounting, and maintenance) as a research grade broadband meter. Otherwise measurements are not trustworthy, can be incorrect by up to 50%⁸¹ and publication would be even counterproductive to health care.

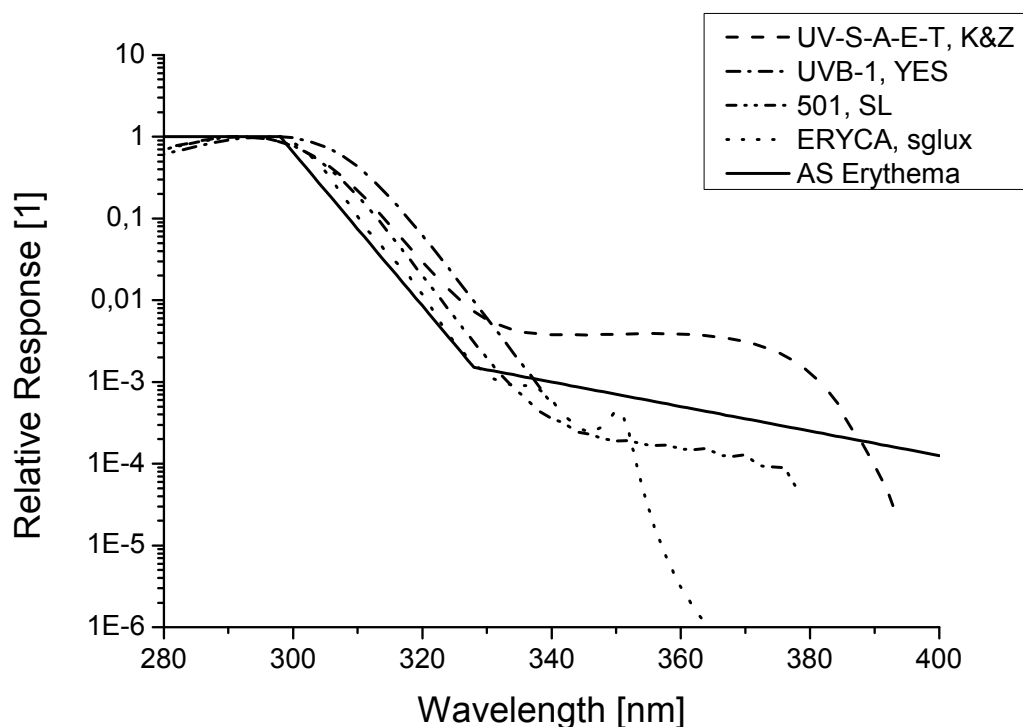


Figure 3: Relative spectral response of broadband instruments and of the human skin for erythema according CIE¹¹.

Other biologically effective irradiances can be measured with these broadband meters only if the corresponding action spectrum is close to the spectral response curve. Otherwise, the calibration matrix c_1 cannot be determined with the necessary accuracy. An appropriate action spectrum for the instruments used is that for Vitamin D photosynthesis.⁸² The same raw data can be used as for UVI monitoring but a calibration function is needed which differs in c_0 and c_1 .⁸³

3.1.2 Quality assurance and control

The performance of a broadband meter alters with time due to aging of the filter or of the photodetector. Therefore a detailed schedule for maintenance has to be implemented. A practical guide for operating was released within the COST Action 726.⁷⁷ This guide also includes mounting and data acquisition. To assure high quality UVI measurements, the most important points are:

- 1) Calibrations should be repeated periodically, typically on a yearly basis.
- 2) Redundant instrumentation should help with detecting drifts in individual instruments.
- 3) Silica gel to keep instrument dry, because filters maybe hydrophilic.

3.2 Spectroradiometers and Spectrophotometers

There are two types of spectral instrument in use for UVI measurements. Common spectroradiometers (e.g. DTM series from Bentham, Reading, UK) adapted for outdoor measurements and spectrophotometers type Brewer Mark II and III (Kipp&Zonen, Delft, The Netherlands). These are the most sophisticated instruments, deliver spectral information and correct operation requires the considerable efforts.

The Brewers spectrophotometers⁸⁴ are especially designed for high quality outdoor measurements of total ozone⁸⁵, NO₂⁸⁶ and UV radiation in a harsh environment. The operators are well organized e.g. by the WMO-Global Atmospheric Watch Brewer Users Group with periodic meetings, or the recent COST Action ES1207, and possess detailed QA/QC and calibration procedures.

A common spectroradiometer needs special adaption to be resistant for all day outdoor measurements e.g. weatherproof input optics⁸⁷ and arrangements to avoid any influences that may affect the stability of the instruments (e.g. temperature). For spectroradiometers, calibration, and QA and QC procedures are well defined.^{e.g. 88} The portable UV European reference spectroradiometer QASUME⁸⁹ has been on duty for more than a decade, improved recently to the QASUME II⁹⁰ and is available from the World Radiation Center (PMOD/WRC), Davos, Switzerland.

These spectroradiometers and the Brewers are often in use as a reference instrument for a broadband meter network. Both instruments can measure any biologically effective irradiance by simple weighting of the measured spectrum with the corresponding action spectrum.

3.3 Multichannel filter radiometers

In between the broadband meters and the spectroradiometers are the multichannel, moderate or narrow bandwidth filter instruments.⁹¹ Those used for UVI monitoring are the GUV541, GUV511 and GUV2511 (all Biospherical Instruments, San Diego, USA), NILU-UV (Norwegian Institute for Air Research, Norway)⁹² and narrowband filter radiometers UV-Rad (ISAC-CNR, Bologna, Italy)⁹³ and UV-MFRSR⁹⁴ (Yankee Env. Sys. Inc., Turners Falls, USA).

This type of instrument consists of a cosine-adapted diffuser element as the front optic and one or multiple sensor elements fitted with stacks of interference- and blocking filters. Instruments are hermetically sealed and temperature stabilized, which helps to keep the front optic free from snow and ice. A special case is the UV-Rad instrument, which instead of individual, stationary filter and sensor elements applies a rotating wheel, which sequentially positions filter stacks above a single sensor element to make a wavelength scan. By definition, a multichannel filter radiometer has several channels, in the UV, and sometimes also in the visual and near-infrared part of the spectrum (e.g. photosynthetically active radiation). Originally, the instrument type was designed to measure not only UV irradiance but also total ozone (utilizing a pair of channels in the UV-B and UV-A) and cloud optical depth (UV-A). The retrieval of these atmospheric parameters, in addition to surface albedo, relies on a characterization of spectral and angular response functions, combined with radiative transfer modelling to generate look-up tables as a function of SZA.^{92,93,95,96} Different irradiance data products, based on e.g. health- or plant-response functions, are based on linear combinations of detector signals and corrections for SZA.^{92,96-99}

International intercomparisons and harmonisations were carried out e.g. ¹⁰⁰ which resulted in documents describing calibration and quality assurance procedures e.g. ⁹¹, that are similar to those dealing with broad band instruments and spectroradiometers. This instrument type is robust and very flexible in offering a large set of data products.

4. Presentation of measurement

The simplest way to publish the UVI is to give a single integer number (or with one decimal). The number can be coloured as proposed by WHO ¹⁷ (e.g. Madeira, Estonia). Some networks use this way of visualisation in conjunction with a symbolised map of the country to indicate locations (Germany, Norway, Extramadura-Spain). The presentation can be accompanied by symbols for sun protection recommendations (e.g. Switzerland).

Another way for visualisation is a plot which shows the daily progress either by providing numbers (e.g. Croatia) or by a line graph together with a legend that rates the values (e.g. Czech Rep). Another possibility is to colour the line according to the WHO scale (e.g. Denmark, Hungary, and Luxembourg). The background of the graph can be WHO-coloured instead (e.g. Tartu-Observatory, UK, Lampedusa) or the area under the line can be filled by the colour which corresponds to the plotted UVI values (e.g. Finland, Poland, and Greece). The Belgian network gives such line graphs for all stations on an underlying map of the country. Bar charts (e.g. Serbia) and WHO coloured bar charts (e.g. ISPRA,) are also in use to indicate the daily progress.

Plots which show the daily course are often accompanied by a second line that provides a forecast for the whole day (e.g. Netherlands, Denmark). Such forecasts can be shown for different cloud coverages (e.g. Hungary). With that it is possible to estimate the further progress of the UVI. Especially before midday such forecasts provide helpful information for sun protection applications.

The most sophisticated way of presentation is to show the spatial distribution over a region or over the whole country. This needs a mathematical model and additional information, at least a near real-time cloud cover distribution and topography.²⁵ An example can be found on the web page of the Austrian monitoring network (see Figure 4). An additional animation visualises the progress from sunrise onwards until the recent status.

There are two different strategies for the update frequency. One is to publish the noon value. The German and the Spanish AEMET-network do it this way for each station. This strategy is based on the original recommendation that the UVI is the average within a 30 minute period about solar noon.¹³

Information technology now enables the provision of real-time values. Therefore the other strategy is to update values a few times per hour whereas most common are mean values over the past 15 minutes. More frequent updates, like every minute, could be critical as values would vary very strongly under broken clouds conditions. Such short term updates may not be presented as a single number but as a line graph or bar chart. Much less frequent updates, like once per hour, lead to underestimations before noon and to overestimations after noon because changes up to 1.5 UVI per hour can be observed in Europe under clear sky.

Most of the networks provide measurements through all the year but several networks restrict the service to the main period of interest (March to September).

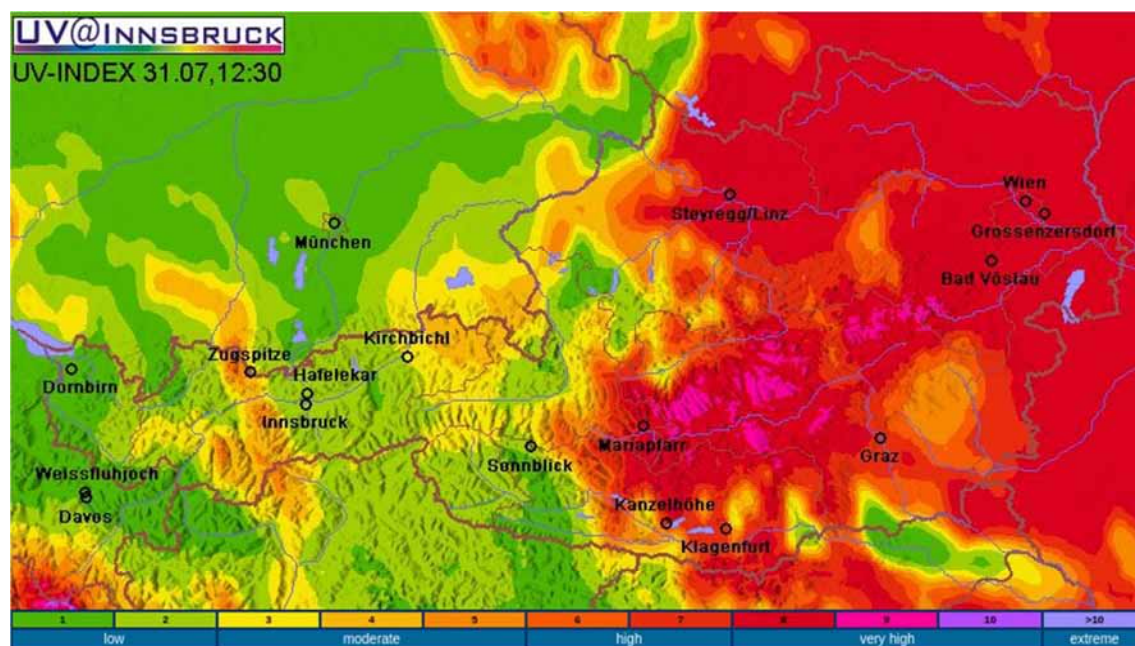


Figure 4: Example for the near real-time distribution of the UV Index gained from measurements at marked locations (black symbols).

5. Summary

Twenty years after the establishment of the UVI, a proportion of the European population still lacks adequate information about the acute risk of health damage from solar UV radiation in their countries. UV overexposure is a creeping epidemic and is manifested by severe diseases with long latency periods. For skin cancer, Gordon and Rowell²⁰ provided an overview of the estimates of the direct health system costs for skin cancer in Europe and the cost-effectiveness of interventions for skin cancer prevention or early detection. It was shown that skin cancer prevention initiatives are highly cost-effective and are cost-saving. Online UVI values and connected sun protection recommendations are an appropriate tool not only for skin cancer prevention but also for avoiding other diseases, such as cataracts, the economic dimensions of which are less well studied. A main problem in finding financial support for UVI monitoring is that the general health improvement and cost-savings are not countable from the first day onwards. However, in many countries the importance was recognized and online information is supported. Currently, in 25 of the 46 European countries online UVI values are available on the Internet. With that, approximately 32% of the area of Europe is covered and 57% of the European population can have access to information. As seen in Figure 1 there are large differences in the spatial coverage. Especially in the east and the south-east, coverage is lacking.

The number of instruments delivering online UVI has increased over time (see Figure 2). Measurements are obtained mainly from broadband meters (75%), partly from multichannel filter instruments (15%) and less from spectroradiometers (10%). The quality of these instruments and of the measurements was well studied in the past (see chapter 3). Appropriate quality assurance and quality control procedures are available and in use to guarantee accurate values.

An important parameter of a network is the distance between the stations. The appropriate service radius depends on climate and topography. Locations can be selected by objective methods and spatial representativeness can be calculated.²³ In countries with a highly alternating topography the distance between stations should be shorter than in flat lands. The shortest service radius found was on the order of 40 km while on average it is around 180 km.

The colour scheme suggested by WHO for the UVI is adopted by most of the institutes as well as the rating and also the WHO recommendations for sun protection are provided by many web pages.

The radiant exposure is the relevant parameter (rarely the irradiance) for quantifying photobiological effects. In the case of the UVI, Saxebøl¹⁰¹ has suggested the usage of “UV Index hours” as the corresponding unit for the erythemally effective exposure. The minimal erythema dose (exposure necessary to cause a noticeable erythema) is usually given in J/m² or in the arbitrary defined SED¹⁵ but can be expressed easily in UV Index hours as 1 UVIh is 90 J/m².¹⁰² In conjunction with the UVI it would provide an easy way to estimate the maximum time that could be spent in the sun or to select the minimum sun protection factor.

All of the instruments used possess the potential to deliver the Vitamin D effective irradiance too. The broadband meters and the multifilter radiometers would need a different calibration factor while the spectroradiometers need the action spectrum only.^{83,92} Today Vitamin D effective irradiance is given in effective $W_{\text{vitD}}/\text{m}^2$ (e.g. as provided by the Norwegian Network). However it is questionable if this unit is appropriate for public information because the levels of Vitamin D circulating in the body cannot be predicted reliably from the effective irradiance. Units similar to those for the erythema are under discussion.¹⁰³ Another perspective for the use of the instruments is supporting people in antipsoriatic heliotherapy as done in Poland.⁵⁷

At present, it is not so easy to find online UV-Index measurements for a certain region or country (e.g. for a holiday destination) by Internet search engines because of several reasons (language, names of stations, etc.). In some countries UVI publishing is done by different institutions on different web-pages. For the future and the further promotion of the UVI and related health care we propose a European Internet portal that guides users to the different networks. A first approach was undertaken on the web-page of the COST Action 726 which ended in 2009 (which is now out of date). For the future consideration should be given to the possibility of increasing the coverage of Europe.

Finally, it should be noted that all web pages provide the UVI values for free.

Acknowledgement

The authors would like to thank all the (unnamed) operators and responsible persons of the stations during the past decades.

The authors would like also to thank all the (unnamed) grant foundations that have enabled the development and operation the stations.

REFERENCES

1. K. W. Hausser and W. Vahle, Die Abhängigkeit des Lichterythems und der Pigmentbildung von der Schwingungszahl (Wellenlänge) der erregenden Strahlung, *Strahlentherapie*, **13**, 1921, 41-71.
2. P. Bener, *Investigation on the spectral intensity of UV sky and sun+ sky radiation (between 297.5 m μ and 370 m μ) under Different Conditions of Cloudless Weather at 1590 m a.s.l.*, Technical Summary Report No.1, PMOD, Davos, Switzerland, 1960.
3. D.F. Robertson, Long-term field measurements of erythemally effective natural ultraviolet radiation. in: *The biological effects of Ultraviolet Radiation*, ed. F. Urbach, Pergamon Press, Oxford, UK, 1969, 433-436.
4. D. Berger, The sunburning ultraviolet meter: design and performance. *Photochem. Photobiol.*, **24**, 1976, 587-593.
5. J. Scotto, G. Cotton, F. Urbach, D. Berger, T. Fears, Biologically Effective Ultraviolet Radiation: Surface Measurements in the United States, 1974 to 1985. *Science*, 1988, **239**, 762-764.
6. W. W. Coblenz and R. Stair, Data on the spectral erythemic reaction of the untanned human skin to ultraviolet radiation, *Bur. Stand. J. Res.*, 1934, **12**, 13.
7. J. DeLuisi and J. Harris (1983) A determination of the absolute radiant energy of a Robertson-Berger meter sunburn unit. *J. Atmos. Environ.* **17**, 751-758.
8. CIE 2014, Sensitivity of Human Skin to Ultraviolet Radiation, Expressed as Minimal Erythema Dose (MED), Technical Report CIE 207:2014, Vienna, Austria.
9. Diffey B.L. (1987) A comparison of dosimeters used for solar ultraviolet radiometry. *Photochem. Photobiol.* **46**, 55-60.
10. SolarLight (1993) UV-Biometer User's Manual. SolarLight, Philadelphia, USA
11. IARC, *IARC monographs on the evaluation of carcinogenic risks to humans: solar and ultraviolet radiation*. IARC Monogr Eval Carcinog Risks Hum. 1992;55: 1-316.
12. WMO, *Report of the WMO-WHO Meeting of Experts on Standardization of UV Indices and their Dissemination to the Public, Les Diablerets, Switzerland, 21-25 July 1997*, WMO TD No. 921, WMO Report No. 127, WMO, Geneva, Switzerland, 1998.
13. ICNIRP, *Global Solar UV Index. A joint recommendation of the World Health Organization, the World Meteorological Organization, the United Nations Environment Programme, and the International Commission on Non-Ionizing Radiation Protection*. ICNIRP, Oberschleißheim, Germany, 1995
14. A.F. McKinlay and B.L. Diffey, A reference action spectrum for ultraviolet induced erythema in human skin. *CIE J.*, 1987, **6**, 17-22.
15. CIE, *Erythema Reference Action Spectrum and Standard Erythema Dose*, CIE S007E-1998, ISO 17166:1999, CIE Central Bureau, Vienna, Austria, 1998.
16. A.R. Webb, H. Slaper, P. Koepke and A.W. Schmalwieser, Know your Standard: Clarifying the CIE Erythema Action Spectrum. *Photochem. Photobiol.*, 2011, **87**, 483-486.

17. WHO, *Global solar UV Index - A Practical Guide*. World Health Organization, World Meteorological Organization, United Nations Environment Program, and International Commission on Non-Ionizing Radiation Protection, Geneva, Switzerland, 2002.
18. K. Vanicek, T. Frej, Z. Litynska, A. Schmalwieser, *UV Index for the Public*, European Communities, Brussels, Belgium, 2000.
19. E. Thieden, M.S. Agren and H.C. Wulf, Solar UVR exposures of indoor workers in a Working and a Holiday Period assessed by personal dosimeters and sun exposure diaries. *Photodermatol. Photoimmunol. Photomed.*, 2001, **17**, 249-255.
20. L.G. Gordon and D. Rowell, Health system costs of skin cancer and cost-effectiveness of skin cancer prevention and screening: A systematic review. *European Journal of Cancer Prevention*, 2015, **24**, 141-149.
21. C.E. Williamson, R.G. Zepp, R.M. Lucas, S. Madronich, A.T. Austin, C. L. Ballaré, M. Norval, B. Sulzberger, A.F. Bais, R.L. McKenzie, S.A. Robinson, D.-P. Häder, N.D. Paul and J. F. Bornman, Solar ultraviolet radiation in a changing climate. *Nature Climate Change*, 2014, **4**, 434-441.
22. H.E. Rieder, F. Holawe, S. Simic, M. Blumthaler, J.W. Krzyscin, J.E. Wagner, A. W. Schmalwieser, and P. Weihs, Reconstruction of erythemal UV-doses for two stations in Austria: a comparison between alpine and urban regions. *Atmos. Chem. Phys.*, 2008, **8**, 6309-6323.
23. A.W. Schmalwieser and G. Schauburger, A monitoring network for erythemally-effective solar ultraviolet radiation in Austria: determination of the measuring sites and visualisation of the spatial distribution. *Theor. Appl. Climatol.*, 2001, **69**, 221-229.
24. M. Blumthaler, Quality assurance and quality control methodologies within the Austrian UV monitoring network. *Rad. Prot. Dos.*, 2004, **111**, 359-362.
25. B. Schallhart, M. Blumthaler, J. Schreder and J. Verdebout, A method to generate near real time UV-Index maps of Austria. *Atmos. Chem. Phys.*, 2008, **8**, 7483-7491.
26. H. de Backer, Time series of daily erythemal UV doses at Uccle, Belgium. *Int. J. of Remote Sensing*, 2009, **30**, 4145-4151.
27. D. Gillotay, P. Pandey and C. Depiesse, Climatology of Ultra Violet (UV) irradiance at the surface of the Earth as measured by the Belgian ground-based UV radiation monitoring network during the time period 1995-2014. *International Journal of Climatology*, 2017, submitted.
28. R. Werner, B. Petkov, D. Valev, A. Atanassov, V. Guineva and A. Kirillov, Ozone Determination by GUV 2511 Ultraviolet Irradiation Measurements at Stara Zagora. *Sun and Geosphere*, 2017, **12**, in press
29. H.C. Wulf and P. Eriksen, UV index and its implications. *Ugeskrift for laeger*, 2010, **72**, 1277-1279.
30. K. Leszczynski, K.T. Jokela, R. Visuri and L. Ylianttila, Calibration of the broadband radiometers of the Finnish Solar UV monitoring network. *Metrologia*, 1995, **32**, 701-704.

31. M. Steinmetz, Continuous solar UV monitoring in Germany. *J. Photochem. Photobiol. B.*, 1997, **41**, 181–187.
32. H. Sandmann and C. Stick, Spectral and Spatial UV Sky Radiance Measurements at a Seaside Resort Under Clear Sky and Slightly Overcast Conditions. *Photochem. Photobiol.*, 2014, **90**, 225–232.
33. C. Stick, K. Krüger, N. Schade, H. Sandmann and A. Macke, Episode of unusual high solar ultraviolet radiation over central Europe due to dynamical reduced total ozone in May 2005. *Atmos. Chem. Phys.*, 2006, **6**, 1771-1776.
34. A. Kazantzidis, A. Bais, C. Topaloglou, K. Garane, M. Zempila, C. Meleti and C. Zerefos, Quality assurance of the Greek UV Network: Preliminary results from the pilot phase operation. *Proceedings of SPIE*, 2006, **6362**, 636229.
35. Z. Tóth, High resolution solar spectrophotometry and narrow spectral range solar radiation measurements at the Hungarian Meteorological Service. *Idojaras*, 2013, **117**, 403-433.
36. S. Hidvégi, F. Rácz, G. Hadi, L. Gesztesi and Z. Tóth, Effect of UV-radiation on the pollen viability of some parental lines of hybrid maize. *Cereal Research Communications*, 2009, **37(SUPPL.1)**, 349-352.
37. H. Diémoz, L. Egli, J. Gröbner and A.M. Siani, Solar ultraviolet measurements in Aosta (Italy): an analysis of short- and middle-term spectral variability, *Radiation Processes in the Atmosphere and Ocean*, 2013, **1531**, 856-859.
38. G.R. Casale, A.M. Siani, H. Diémoz, G. Agnesod, A.V. Parisi and A. Colosimo, Extreme UV index and solar exposures at Plateau Rosà (3500m a.s.l.) in Valle d'Aosta Region, Italy, *Sci. Total Environ.*, 2015, **512-513**, 622-630.
39. H. Diémoz and B. Mayer, UV radiation in a mountaineous terrain: comparison of accurate 3D and fast 1D calculations in terms of UV index. Presented in part at One Century of UV Radiation Research, Davos, Switzerland, September, 2007.
40. B. Petkov, V. Vitale, C. Tomasi, U. Bonafé, S. Scaglione, D. Flori, R. Santaguida, M. Gausa, G. Hansen, and T. Colombo, Narrowband filter radiometer for ground-based measurements of global ultraviolet solar irradiance and total ozone. *Appl. Opt.*, 2006, **45**, 4383-4395.
41. B. Petkov, V. Vitale, C. Tomasi, M. Mazzola, C. Lanconelli, A. Lupi and M. Busetto, Variations in total ozone column and biologically effective solar UV exposure doses in Bologna, Italy during the period 2005–2010. *Int. J. Biometeorol.*, 2014, **58**, 31–39.
42. M. Morabito, D. Grifoni, A. Crisci, L. Fibbi, S. Orlandini, G.F. Gensini and G. Zipoli, Might outdoor heat stress be considered a proxy for the unperceivable effect of the ultraviolet-induced risk of erythema in Florence? *J. Photochem. Photobiol. B.*, 2014, **130**, 338-348.
43. A.M. Siani, N.J. Muthama, E. Piervitali and S. Palmieri, Detailed analysis of solar ultraviolet radiation: a preliminary investigation on data collected at Rome ('La Sapienza' University). *Science of the Total Environment*, 1995, **171**, 143-150.
44. G. R. Casale, D. Meloni, S. Miano, S. Palmieri, A. M. Siani and F. Cappellani, Solar UV-B irradiance and total ozone in Italy: Fluctuations and trends. *J. Geophys. Res.*, 2000, **105**, 4895-4901.

45. I. Ialongo, G.R. Casale, A.M. Siani, Comparison of total ozone and erythemal UV data from OMI with ground-based measurements at Rome station. *Atmos. Chem. Phys.*, 2008, **8**, 3283-3289.
46. A.M. Siani, S. Modesti, G.R. Casale, H. Diemoz and A. Colosimo, Biologically effective surface UV climatology at Rome and Aosta, Italy. *AIP Conference Proceedings*, 2013, **1531**, 903-906.
47. D. Meloni, A. di Sarra, J.R. Herman, F. Monteleone and S. Piacentino, Comparison of ground-based and TOMS erythemal UV doses at the island of Lampedusa in the period 1998-2003: Role of tropospheric aerosols, *J. Geophys. Res.*, 2005, **110**, D01202.
48. A. di Sarra, D. Fuà, M. Cacciani, T. Di Iorio, P. Disterhoft, D. Meloni, F. Monteleone, S. Piacentino and D. Sferlazzo) Determination of ultraviolet cosine corrected irradiances and aerosol optical thickness by combined measurements with a Brewer spectrophotometer and a MultiFilter Rotating Shadowband Radiometer, *Appl. Opt.*, 2008, **47**, 6142-6150.
49. D. Mateos, A. di Sarra, D. Meloni, C. Di Biagio and D.M. Sferlazzo, Experimental determination of cloud influence on the spectral UV radiation and implications for biological effects, *J. Atmos. Solar Terr. Phys.*, 2011, **73**, 1739-1746.
50. A. di Sarra, M. Cacciani, P. Chamard, C. Cornwall, J.J. DeLuisi, T. Di Iorio, P. Disterhoft, G. Fiocco, D. Fuà and F. Monteleone, Effects of desert dust and ozone on the ultraviolet irradiance at the Mediterranean island of Lampedusa during PAUR II, *J. Geophys. Res.*, 2002, **107(D18)**, 8135.
51. J. Bilbao, R. Román, C. Yousif, D. Mateos and A. de Miguel, Total Ozone Column, Water Vapour and Aerosol Effects on Erythemal and Global Solar Irradiance in Marsaxlokk, Malta. *Atmospheric Environment Journal*, 2014, **99**, 508-518.
52. J. Bilbao, Mateos D., Yousif C., R. Roman and A. De Miguel, Influence of Cloudiness on Erythemal Solar Irradiance in Marsaxlokk, Malta: Two Case Studies. *Journal of Solar Energy*, 2016, **136**, 475-486.
53. P.N. den Outer, H. Slaper and R. Tax, UV radiation in the Netherlands: assessing long-term variability and trends in relation to ozone and clouds. *J. Geophys. Res.*, 2005, **110(D2)**, D02203.
54. O. Mikkelborg, G. Saxebol and B. Johnsen, Ultraviolet Monitoring in Norway on the WEB. *Radiat Prot Dosimetry*, 2000, **91**, 165-167.
55. B. Johnsen, L.-T. Nilsen, A. Dahlback, K. Edvardsen and C.L. Myhre, The Norwegian UV-monitoring network: QC and results for the period 1996-2011. *AIP Conference Proceedings*, 2013, **1531**, 784-787.
56. J.W. Krzyscin, P.S. Sobolewski, J. Jaroslowski, J. Podgorski and B. Rajewska-Wiech, Erythemal UV observations at Belsk, Poland, in the period 1976-2008: Data homogenization, climatology, and trends. *Acta Geophysica*, 2012, **59**, 155-182.
57. J.W. Krzyscin, J. Narbutt, A. Lesiak, J. Jaroslowski, P.S. Sobolewski, B. Rajewska-Wiech, A. Szkop, J. Wink, A. Czerwinska, Perspectives of the antipsoriatic heliotherapy in Poland. *J. Photochem. Photobiol. B.*, 2014, **140**, 111-119.
58. D. Henriques, Programa operacional de previsao do indice UV em Portugal. *Radiacao Solar*, 1999, **1**, 47-60.
59. N. Chubarova, Monitoring of Biologically Active UV Radiation in the Moscow Region, *Izvestiya, Atmospheric and Oceanic Physics*, 2002, **38**, 312-322.

- 60 E. Yu Zhdanova, N. Ye Chubarova, and M. Blumthaler, Biologically active UV-radiation and UV-resources in Moscow (1999–2013). *Geography, Environment, Sustainability*, 2014, **2**, 71–85.
- 61 Z. Mijatovic, S. Milicevic, D.V. Kapor, D.T. Mihailovic, I. Arsenic and Z. Podrascanin, Chapter 11: Solar UV Radiation: Monitoring and a new approach in modelling - pioneering work in Serbia, in: *Advances in Environmental Modeling and Measurements*, eds. D.T. Mihailovic and B. Lalic, Nova Science Publisher, New York, 2010, 113-119.
- 62 E. Závodská, Direct ultraviolet solar radiation at Skalnaté Pleso. *Meteorologické zprávy*, 1972, **1**, 3-5.
- 63 A. Pribulova and M. Chmelik, Typical distribution of the solar erythemal UV radiation over Slovakia. *Atmos. Chem. Phys.*, 2008, **8**, 5393–5401.
- 64 A. Serrano, M. Antón, M.L. Cancillo and V.L. Mateos, Daily and annual variations of erythemal ultraviolet radiation in Southwestern Spain. *Annales Geophysicae*, 2006, **24**, 427-441.
- 65 M. Antón, A. Serrano, M.L. Cancillo and J.A. Garcia, Experimental and forecasted values of the ultraviolet index in southwestern Spain. *J. Geophys. Res.*, 2009, **114**, D5.
- 66 M. Antón, A. Serrano, M.L. Cancillo and J.M. Vilaplana, Quality assurance of broadband erythemal radiometers at the Extremadura UV Monitoring Network (Southwestern Spain). *Atmospheric Research*, 2011, **100**, 83-92.
- 67 A. Miguel, J. Bilbao, R. Roman and D. Mateos, Measurements and attenuation of erythemal radiation in Central Spain. *Int. J. Climatol.*, 2012, **32**, 929–940.
- 68 P. Salvador, J. Bilbao, A. De Miguel and A. Pérez-Burgos, UV-B and UVI measured and calculated in Valladolid, Spain. *UV News-Letter*, 2006, **No 8**, 25-28.
- 69 D. Vernez, A. Milon, L. Vuilleumier, J.-L. Bulliard, A. Koechlin, M. Boniol and J. F. Doré, A general model to predict individual exposure to solar UV by using ambient irradiance data. *Journal of Exposure Science and Environmental Epidemiology*, 2015, **25**, 113-118.
- 70 A.R.D. Smedley, J.S. Rimmer, D. Moore, R. Toumi and A.R. Webb, Total ozone and surface UV trends in the United Kingdom: 1979-2008. *International Journal of Climatology*, 2012, **32**, 338-346.
- 71 G. Hülsen, J. Gröbner, A. Bais, M. Blumthaler, P. Disterhoft, B. Johnsen, K. O. Lantz, C. Meleti, J. Schreder, J. M. Vilaplana Guerrero and L. Ylianttila, Intercomparison of erythemal broadband radiometers calibrated by seven UV calibration facilities in Europe and the USA. *Atmos. Chem. Phys.*, 2008, **8**, 4865–4875.
- 72 A. Bais, C. Topaloglou, S. Kazadzis, M. Blumthaler, J. Schreder, A. Schmalwieser, D. Henriques and M. Janouch, *Report of the LAP/COST/WMO intercomparison of erythemal radiometers*. WMO Rep. 141, WMO-GAW, Geneva, Switzerland, 2000.
- 73 G. Hülsen and J. Gröbner, Characterization and calibration of ultraviolet broadband radiometers measuring erythemally weighted irradiance, *Appl. Opt.*, 2007, **46**, 5877-5886.

- 74 J. M. Vilaplana, A. Serrano, M. Antón, M. L. Cancillo, M. Parias, J. Gröbner, G. Hülsen, G. Zablocky, A. Díaz, B. A. de la Moren, *Report of the El Arenosillo/INTA-COST calibration an intercomparison campaign of UVER broadband radiometers*, COST Office, Brussels, Belgium, 2009.
- 75 M. Huber, M. Blumthaler, J. Schreder, A. Bais and C. Topaloglou, Effect of ambient temperature on Robertson-Berger type erythemal dosimeters. *Appl. Opt.*, 2002, **41**, 4273–4277.
- 76 M. Huber, M. Blumthaler and J. Schreder, Solar UV measurements with Robertson-Berger type instruments: influence of the detector's internal humidity status. *Agric. Forest. Meteorol.*, 2003, **120**, 39-43.
- 77 A. Webb, J. Gröbner and M. Blumthaler, *A practical guide to operating broadband instruments measuring erythemally weighed irradiance*. COST Office, Brussels, Belgium, 2006.
- 78 WMO/GAW, *Instruments to measure erythemally weighted solar irradiance. Part 2: Broadband Instruments Measuring Erythemally Weighted Solar Irradiance*. WMO/GAW No. 164, WMO, Geneva, Switzerland, 2006.
- 79 K. Leszczynski, K. Jokela, L. Ylianttila, R. Visuri and M. Blumthaler, Erythemally weighted radiometers in solar UV monitoring: results from WMO/STUK intercomparison. *Photochem. Photobiol.*, 1998, **67**, 212–221.
- 80 J. Gröbner, G. Hülsen, L. Vuilleumier, M. Blumthaler, J.M. Vilaplana, D. Walker and J.E. Gill, *Report of the PMOD/WRC-COST Calibration and Intercomparison of erthemal radiometers*, COST office Brussels, Belgium, 2009.
- 81 M. de Paula Correa, S. Godin-Beekmann, M. Haeffelin, C. Brogniez, F. Verschaeve, P. Saiag, A. Pazmino and E. Mahe, Comparison between UV index measurements performed by research-grade and consumer-products instruments. *Photochem. Photobiol. Sci.*, 2010, **9**, 459–463.
- 82 CIE, *Action Spectrum for the Production of Previtamin D3 in Human Skin*, Publication 174:2006, International Commission on Illumination, Vienna, Austria, 2006.
- 83 A.W. Schmalwieser, G. Schaubeger, W.B. Grant, S. Mackin and S. Pope, A first approach in measuring, modelling and forecasting the vitamin D effective UV radiation, *Proceedings of SPIE*, 2006, **6362**, C1–C9.
- 84 A.W. Brewer, A replacement for the Dobson spectrophotometer? *Pure and Applied Geophysics*, 1973, **106–108**, 919–927.
- 85 A.W. Brewer and J.B. Kerr, Total ozone measurements in cloudy weather. *Pure and Applied Geophysics*, 1973, **106–108**, 928–937.
- 86 A.W. Brewer, C.T. McElroy and J.B. Kerr, Nitrogen dioxide concentrations in the atmosphere. *Nature*, 1973, **246**, 129–133.
- 87 J.G. Schreder, M. Blumthaler, M. Huber, Design of an input optic for solar UV-measurements, in: *Photochemistry and Photobiology Virtual conference: Protection against the hazards of UVR*, 1998. <http://www.photobiology.com/UVR98/schreder/> (accessed July 2017)

- 88 J. Gröbner, Characterisation of Spectrophotometers used for spectral solar ultraviolet radiation measurements, *Rad. Prot. Dos.*, 2001, **97**, 415–418.
- 89 J. Gröbner, J. Schreder, S. Kazadzis, A. F. Bais, M. Blumthaler, P. Görts, R. Tax, T. Koskela, G. Seckmeyer, A. R. Webb, and D. Rembges, Traveling reference spectroradiometer for routine quality assurance of spectral solar ultraviolet irradiance measurements, *Appl. Opt.*, 2005, **44**, 5321–5331.
- 90 G. Hülsen, J. Gröbner, S. Nevas, P. Sperfeld, L. Egli, G. Porrovecchio and M. Smid, Traceability of solar UV measurements using the QASUME reference spectroradiometer, *Appl. Opt.*, 2016, **55**, 7265–7275.
- 91 WMO/GAW, *Instruments to Measure Solar Ultraviolet Radiation Part 3: Multi-channel filter instruments*, GAW report no. 190, WMO/TD-No. 1537, WMO. Geneva, Switzerland, 2010.
- 92 A. Dahlback, Measurements of biologically effective UV doses, total ozone abundances, and cloud effects with multichannel, moderate bandwidth filter instruments. *Appl. Opt.*, 1996, **35**, 6514–6521.
- 93 B. Petkov, V. Vitale, C. Tomasi, U. Bonafè, S. Scaglione, D. Flori, R. Santaguida, M. Gausa, G. Hansen and T. Colombo, Narrow-band filter radiometer for ground-based measurements of global UV solar irradiance and total ozone. *Appl. Opt.*, 2006, **45**, 4383–4395.
- 94 D.S Bigelow and J.R. Slusser, Establishing the stability of multifilter UV rotating shadow-band radiometers, *J. Geophys. Res.*, 2000, **105**, 4833–4840.
- 95 B.A.K. Høiskar, R. Haugen, T. Danielsen, A. Kylling, K. Edvardsen, A. Dahlback, B. Johnsen, M. Blumthaler and J. Schreder, Multichannel moderate-bandwidth filter instrument for measurement of the ozone-column amount, cloud transmittance, and ultraviolet dose rates. *Appl. Opt.*, 2003, **42**, 3472–3479.
- 96 G. Bernhard, C.R. Booth and J.C. Ehamjian, Real-time ultraviolet and column ozone from multichannel ultraviolet radiometers deployed in the National Science Foundation's ultraviolet monitoring network. *Optical Engineering*, 2005, **44**, 1–12.
- 97 B. Johnsen, B. Kjeldstad, T. N. Aalerud, L. T. Nilsen, J. Schreder, M. Blumthaler, G. Bernhard, C. Topaloglou, O. Meinander, A. Bagheri, J.R. Slusser and J. Davis, *Intercomparison of global UV index from multiband filter radiometers: Harmonization of global UVI and spectral irradiance*, Technical Report 179, WMO/TD-No. 1454, WMO, Geneva, Switzerland, 2008.
- 98 B. Johnsen, L.-T. Nilsen, A. Dahlback, K. Edvardsen and C. L. Myhre, The Norwegian UV-monitoring network: QC and results for the period 1996–2011, *AIP Conf. Proc.*, 2013, **1531**, 784–787.
- 99 A. Piedhiero, M. L. Cancillo, A. Serrano, M. Antón and J. M. Vilaplana, Global irradiance calibration of multifilter UV radiometers. *J. of Geophys. Res.*, 2016, **121**, 427–438
- 100 B. Johnsen, B. Kjeldstad, T.N. Aalerud, L.T. Nilsen, J. Schreder, M. Blumthaler, G. Bernhard, C. Topaloglou, O. Meinander, A. Bagheri, J.R. Slusser and J. Davis, Intercomparison and harmonization of UV index measurements from multiband filter radiometers (2008), *J. Geophys Res.*, 2008, **113**, D15206, doi:10.1029/2007JD009731.

101 G. Saxeboel, UVIh—a proposal for a practical unit for biological effective dose for ultraviolet radiation exposure. *Rad. Prot. Dos.*, 2000, **88**, 261-261.

102 A.W. Schmalwieser, G. Schauburger, M. Janouch, M. Nunez, T. Koskela, D. Berger and G. Karamanian, Global Forecast Model to Predict the Daily Dose of the Solar Erythemally Effective UV Radiation, *Photochem. Photobiol.*, **81**, 2005, 154-162.

103 CIE/WMO, *Rationalizing Nomenclature for UV Doses and Effects on Humans*, CIE Technical Report 209, WMO-GAW Report No. 211, CIE Central Bureau, Vienna, Austria, 2014.

Country	Station	Lat	Long	Alt	Device	start
Austria	Bad Vöslau	47.97	16.20	286	501	1997
	Dornbirn	47.43	9.73	410	501	1997
	Gerlitz	46.68	13.91	1526	501	2004
	Graz	47.10	15.42	348	501	1997
	Gross Enzersdorf	48.20	16.57	156	501	2004
	Hafelekar	47.32	11.39	2275	501	2005
	Innsbruck	47.26	11.38	577	501	1998
	Klagenfurt	46.65	14.32	448	501	1997
	Kirchbichl	47.49	12.09	526	501	2016
	Linz/Steyregg	48.29	14.35	335	501	1997
	Mariapfarr	47.15	13.75	1153	501	1998
	Sonnblick	47.05	12.96	3106	501	1998
	Vienna	48.26	16.43	153	501	1998
	München (D)	48.15	11.57	530	UVS-E-T	2004
	Zugspitze (D)	47.42	10.98	2660	UVS-E-T	2004
	Davos (CH)	46.80	9.83	1610	501	2006
	Weissfluhjoch (CH)	46.83	9.82	2540	501	2009
Belgium 1	Uccle	50.80	4.35	10	MkII & MkIII	1989
Belgium 2	Uccle	50.80	4.35	120	UVb	1996
	Mol	51.22	5.08	75	GUV 2511, UVb	2008
	Mont Rigi	50.52	6.08	680	GUV 2511, UVb	2011
	Oostende	51.23	2.93	0	GUV 2511, UVb	2006
	Redu (Ardennes)	50.00	5.15	450	GUV 2511, EKO	2004
	Virton	49.57	5.53	250	GUV 2511, UVb	2007
Croatia	Zagreb Maksimir	45.82	15.97	157	E1c	2004
	Parg	45.69	14.63	863	E1c	2003
	Plitvicka jezera	44.88	15.62	579	E1c	2015
	Opatija	45.34	14.31	5	E1c	1997
	Crikvenica	45.17	14.69	2	E1c	2003
	Malinska /Krk	45.13	14.53	1	E1c	1993
Cyprus	Akrotiri	34.59	32.99	32	501D + 501A	2015
Czech Republic	Hradec Kralove	50.18	15.84	278	501	1996
	Kosetice	49.57	15.08	532	501	1996
	Kucharovice	48.88	16.09	334	501	2009
Denmark	Copenhagen	55.72	12.56	35	UVB-1	1992
Estonia	Toravere	58.26	26.46	70	UVS-E-T	2000
	Haapsalu	58.96	23.53	1.2	UVS-E-T	2007
	Tallinn	59.40	24.60	33	UVS-E-T	2011
	Roomassaare	58.22	22.51	1	UVS-E-T	2009
	Pärnu	58.38	24.48	2.9	UVS-E-T	2012
Finland	Sodankylä Observatory / Arctic Res. Center	67.37	26.63	185	501	1997
	Sotkamo Kuolaniemi	64.11	28.34	171	501	1997
	Kuopio Savilahti	62.89	27.63	107	501	2014
	Jyväskylä Tikkakoski	62.40	25.67	145	501	1997
	Jokioinen Observatory	60.81	23.50	113	501	1997
	Helsinki	60.20	24.96	48	501	1997
	Parainen Utö	59.78	21.37	10	501	1997

Table 1: Networks and stations delivering online UV-Index values to the Internet (Broadband meter; Solar Light 501 (A)nalogue or (D)igital, Kipp&Zonen UVS-E-T, UVS-AE-T, UV-S-B-C, ECO UVb, Yankee UVB-1, Thies Clima E1c, sgflux EryCa, Optix UVEM-6C, Davies Pro2+. Multichannel instruments: Biospherical instruments GUV-511, GUV-541, GUV 2511, NILU NILU-UV, UV-Rad. Spectroradiometer Type Brewer MkII, MkIII, MK IV, Spectroradiometer: Bentham DTM150, DTM 300, DILOR-XY)

Country	Station	Lat	Long	Alt	Device	start
Germany	Westerland/Sylt	54.92	8.32	20	DTM300	1995
	Zingst	54.44	12.72	5	DTM300	1993
	Norderney/Ostfries.Inseln	53.71	7.21	4	DM150	2002
	Lindenberg	52.21	14.11	127	DTM300	1995
	Lüneburg	53,25	10,46	49	DM150	2016
	Dortmund	51.53	7.45	100	DTM300	1995
	Kulmbach	50.11	11.45	310	DM150	1995
	Langen	50.01	8.65	139	DTM300	1993
	München/Neuherberg	48.21	11.58	493	DTM300	1993
	Schauinsland	47.91	7.91	1205	DTM300	1993
	Berlin	52.43	13.54	35	EryCa	2014
Gibraltar	Gibraltar	36.15	-5.35	4	501D + 501A	2015
Greece	Athens	37.99	23.78	180	NILU-UV	2004
	Finokalia/Crete	35.34	25.67	250	NILU-UV	2011
	Ioannina	39.62	20.85	541	NILU-UV	2005
	Mytilene/Lesbos	39.11	26.55	80	NILU-UV	2005
	Patras	38.29	21.79	70	NILU-UV	2005
	Thessaloniki	40.63	22.96	60	NILU-UV	2004
	Xanthi	41.15	24.92	75	NILU-UV	2012
Hungary	Budapest	47.43	19.18	140	UVS-E-T	1994
	Kecskemét	46.97	19.55	127	501	1994
	Kékestető	47.87	20.01	1012	501	1994
	Sármellék	46.69	17.16	120	501	1994
	Siófok	46.91	18.04	108	501	1999
Iceland	Rekjavik	64.14	-21,93	10	Broadband	---
	Egilsstaði	65.27	-14.40	23	broadband	---
Italy 1	Aosta/Saint-Christophe	45.74	7.36	570	DTM300, UVS-AE-T	2006
	La Thuile	45.73	6.97	1640	UVB-1	2006
	Plateau Rosa	45.94	7.71	3500	UVS-AE-T	2007
Italy 2	Vicenza	45.53	11.59	44	501A	2011
Italy 3	Bologna, ISAC-CNR	44.52	11.34	30	UV-Rad	2005
Italy 4	Florence	43.84	11.15	45	501	2003
Italy 5	Rome, ISPRA	41.82	12.47	68	UVS-AE-T	2015
Italy 6	Rome, Sapienza Univ.	41.90	12.50	75	MK IV	1992
Italy 7	Lampedusa	35.52	12.63	45	MK III, UV-MFRSR	1997
Ireland	Malin Head	55.37	-7.34	19	501D + 501A	1995
Luxembourg	MeteoLCD	49.87	6.17	218	501	1996
Moldova	ARG IAP, Kishinev	47.00	28.82	205	UV-S-B-C	2003
Netherlands	Bilthoven	52.12	5.20	20	DILOR-XY	1994
Norway	Blindern	59.93	10.72	95	GUV-511	1994
	Oesteraas	59.95	10.60	135	GUV-541	1999
	Kise	60.77	10.80	130	GUV-541	1996
	Landvik	58.33	8.52	10	GUV-541	1996
	Bergen	60.38	5.33	40	GUV-541	1996
	Finse	60.60	7.52	1210	GUV-541	2003
	Trondheim	63.42	10.40	65	GUV-541	1996
	Andoya	69.28	16.02	380	GUV-541	2000
	Tromsø	69.68	18.97	60	GUV-541	1995
	Ny-Aalesund	78.92	11.92	20	GUV-541	1995

Table 1 (continued): Networks and stations delivering online UV-Index values to the Internet.

Country	Station	Lat	Long	Alt	Device	start
Poland 1	Leba	54.75	17.53	2	501	1993
	Legionowo	52.40	20.97	96	501	1993
	Zakopane	49.30	19.97	855	501	1993
	Katovice	50.27	19.02	266	UVEM-6C	2006
Poland 2	Warsaw	52.25	20.94	113	Pro2+	2012
	Łódź	51.76	19.53	233	Pro2+	2014
	Stary Wiec	54.09	18.32	142	Pro2+	2016
	Kowala Druga	51.22	22.07	185	Pro2+	2015
	Belsk	51.84	20.79	176	UVS-E-T	2005
Portugal	Funchal	32.65	-16.89	56	501, MKII	1989/04
Serbia 1	Novi Sad	45.33	19.85	84	UVB-1	2003
Serbia 2	Belgrade	44.86	20.39	94	501	2009
Spain 1	Valladolid, University	41.66	-4.71	705	UVB-1	2014
Spain 2	Almeria Aeropuerto	36.85	-2.38	29	UVB-1	2007
	Moguer (El Arenosillo)	37.10	-6.73	45	UVB-1	2003
	Badajoz	38.88	-7.02	190	UVB-1	2001
	Barcelona	42.38	2.12	95	UVB-1	1999
	Cáceres	39.47	-6.33	405	UVB-1	2007
	Cádiz - Obs.	36.50	-6.25	2	UVB-1	2005
	Ciudad Real	38.98	-3.92	628	UVB-1	1999
	Córdoba - Aeropuerto	37.83	-4.85	91	UVB-1	2006
	A Coruña	43.37	-8.42	67	UVB-1	1999
	Granada Base Aérea	37.13	-3.28	692	UVB-1	2003
	Izaña	28.30	-16.50	2400	UVB-1	2001
	León Aeropuerto	42.58	-5.65	916	UVB-1	2007
	Madrid, Ciudad Univ.	40.45	-3.72	680	UVB-1	1995
	Málaga	36.72	-4.48	61	UVB-1	1999
	Mas Palomas	27.83	-15.95	25	UVB-1	2001
	Murcia	38.00	-1.17	69	UVB-1	1997
	Puerto de Navacerrada	40.78	-4.02	1894	UVB-1	2012
	Palma de Mallorca	39.55	2.63	6	UVB-1	1999
	Tortosa	40.82	0.48	44	UVB-1	1999
	Salamanca, Mataban	40.95	-5.50	803	UVB-1	2003
Santander	43.48	-3.80	79	UVB-1	1999	
San Sebastián, Igueldo	43.30	-2.03	259	UVB-1	2005	
Sta Cruz de Tenerife	28.47	-16.25	31	UVB-1	2006	
Valencia Aeropuerto	39.48	-0.47	57	UVB-1	1999	
Valladolid	41.65	-4.77	740	UVB-1	1999	
Zaragoza Base Aérea	41.67	-1.07	298	UVB-1	1999	
Spain 3	Arenosillo	37.10	-6.73	52	UVB-1	1996
	Alcalá de Guadaira	37.34	-5.83	72	UVS-E-T	2013
	Algeciras	36.14	-6.73	30	UVS-E-T	2013
	Córdoba	37.90	-4.78	144	UVS-E-T	2013
	Marbella	36.51	-4.87	10	UVS-E-T	2013
	Badajoz	38.88	-7.01	199	UVS-E-T	2001
	Cáceres	39.48	-6.34	397	UVS-E-T	2001
	Covatilla	40.36	-5.69	1965	UVS-E-T	2008
	Fuente de Cantos	38.24	-6.30	582	UVS-E-T	2007
	Orellana	39.00	-5.53	323	UVS-E-T	2007
	Plasencia	40.06	-6.04	372	UVS-E-T	2004

Table 1 (continued): Networks and stations delivering online UV-Index values to the Internet.

Country	Station	Lat	Long	Alt	Device	start
Switzerland	Payerne	46.81	6.94	491	501	1998
	Jungfrauoch	46.55	7.99	3582	501	1996
	Davos	46.81	9.84	1610	501	2003
	Locarno	46.18	8.78	366	501	2000
UK	Chilton	51.58	-1.32	135	501	1990
	Camborne	50.22	-5.33	81	501	1993
	London	51.50	0.12	40	501	2013
	Swansea	51.61	-3.98	24	501	2013
	Leeds	53.85	-1.61	157	501	1992
	Belfast	54.60	-5.83	31	501	2013
	Inverness	57.47	-4.19	34	501	2013
	Lerwick	60.14	-1.18	80	501	1993
	Reading	51.44	-0.94	66	DM150	1993
	Manchester	53.47	-2.23	76	DM150	1997

Table 1 (continued): Networks and stations delivering online UV-Index values to the Internet.

Country	Update	Presentation	Colour system	Archive	Language
Austria	10-30 min	M/G/S	WHO	Y	D/E
P:	Federal Department for Environment				
R:	M. Blumthaler				
O:	Land Niederösterreich; ZAMG, Vienna ; Observatorium Kanzelhöhe, University Graz; Amt der Steiermärkischen Landesregierung; Universität für Bodenkultur, Vienna; Sektion für Biomedizinische Physik, Medical University Innsbruck; CMS Schreder, Kirchbichl; Amt für Natur- und Umweltschutz, Land Oberösterreich; WG Environmental Health, VUW Vienna; Meteorologisches Institut, University Munich; Forschungsstation Schneefernerhaus; WRC-PMO Davos				
web:	www.uv-index.at				
Belgium 1	30 min	G	other	N	NL/F/E/D
P:	Federal service for scientific affairs				
R:	H. De Backer				
O:	Koninklijk meteorologisch Instituut				
web:	http://www.meteo.be/meteo/view/en/522044-UV.html				
Belgium 2	1 min	T	WHO	Y	E
P:	Federal service for scientific affairs				
R:	D. Bolsee				
O:	BIRA-IASB, Brussels				
Web:	http://uvindex.aeronomie.be				
Croatia	10 min	T	WHO	N	E
P:	Meteorological and hydrological institute of Croatia; City of Crikvenica; City of Malinska; National park Plitvicka jezera; City of Opatija				
R:	D. Tomsic				
O:	Meteorological and hydrological institute of Croatia				
web:	http://vrijeme.hr/aktpod.php?id=uvi				
Cyprus	5 min	G	WHO	Y	E
P/O:	Public Health England				
R:	J. B. O'Hagan				
web:	https://uk-air.defra.gov.uk/data/uv-index-graphs				
Czech Republic	10 min	G/S	WHO	Y	CZ
P/O:	Czech Hydrometeorological Institute				
R:	L. Metelka				
Web:	http://portal.chmi.cz/aktualni-situace/aktualni-stav-pocasi/ceska-republika/ozonove-a-uv-zpravodajstvi				
Denmark	30 min	G/S	WHO	N	DK
P/O:	Danish Meteorological Institute				
R:	P. Eriksen, N. Jepsen				
Web:	www.dmi.dk/vejr/sundhedsvejr/uv-indeks				
Estonia	1 min	G/S	WHO	Y	EE/E/RU
P:	Republic of Estonia, Ministry of the Environment				
R:	K. Nurmela				
O:	Estonian Environment Agency, KAUR				
web:	www.ilmateenistus.ee/ilm/ilmavaatlused/uv-indeks/				
Finland	10 min	G	WHO	N	FI / SV / E
P/O:	Finnish Meteorological Institute				
R:	A. Aarva				
web:	http://en.ilmatieteenlaitos.fi/uv-index (EN)				

Table 2: Descriptions of networks and stations delivering online UV-Index values to the websites (Presentation: M: spatial distribution, G: Graph, S: single value, T: table, P: Purchaser/Financer, R: Responsibility, O: Operator).

Country	Update	Presentation	Color system	Archive	Language
Germany 1	1 day	G/S	other / WHO	n	D
P:	Federal Office for Radiation Protection				
R:	H. Sandmann				
O:	Institute for Med. Climatology of Kiel University; German Environment Agency; Trade Supervisory Office Hildesheim; German Weather Service; Federal Institute for Occupational Safety and Health; Bavarian Environment Agency; Federal Office for Radiation Protection;				
web:	www.bfs.de/DE/themen/opt/uv/uv-index/aktuell/aktuell_node.html				
Germany 2	5 min	G	other	N	D/E
P/O:	sglux GmbH				
R:	T. Weiss				
web:	www.sglux.de				
Gibraltar	5 min	G	WHO	Y	E
P/O:	Public Health England				
R:	J. B. O'Hagan				
web:	https://uk-air.defra.gov.uk/data/uv-index-graphs				
Greece	20 min	G	WHO	Y	GR/E
P:	General Secretariat for Research and Technology, Greece				
R:	A. F. Bais				
O:	Laboratory of Atmospheric Physics, AUTH (M. Zempila and K. Garane)				
web:	http://www.uvnet.gr/content/stationDetails.php?id=9&time=0&p=UV_INDEX				
Hungary	1 -10 min	G	other	Y	H/E
P:	Ministry Of Agriculture				
R:	Z. Tóth				
O:	Hungarian Meteorological Service				
web:	http://met.hu/en/idojaras/humanmeteorologia/uv-b/				
Iceland	1 day	S	other	n	Ice
P/R:	----				
O:	Icelandic Radiation Protection Authority				
web:	uv.gr.is				
Italy 1	5-15 min	G	WHO	Y	I
P:	Regional government of Aosta Valley				
R:	H. Diémoz				
O:	ARPA Valle d'Aosta				
web:	www.uv-index.vda.it				
Italy 2:	5min	G/S	WHO	N	I
P/O:	ARPAV (Veneto Regional Agency for environmental protection and prevention)				
R:	G.Lorenzetto, L.M. Belleri				
web:	http://www.arpa.veneto.it/temi-ambientali/agenti-fisici/radiazioni-ionizzanti/radiazioni-uv/dati-in-diretta				
Italy 3:	30 min	G	WHO	N	I/E
P/O:	ISAC-CNR				
R:	Petkov				
web:	http://www.bo.cnr.it/meteo.html				
Italy 4:	15 min	G	WHO	Y	I/E
P:	National Research Council				
R:	G. Zipoli & D. Grifoni				
O:	Institute of Biometeorology				
web:	http://www.lamma.rete.toscana.it/en/weather-stations-data				

Table 2 (continued)

Country	Update	Presentation	Color system	Archive	Language
Italy 5:	10 min	G	WHO	N	I
P/O:	ISPRA, Acoustics Group, Physical Agents Unit				
R:	S. Curcuruto				
web:	http://www.agentifisici.isprambiente.it/radiazioni-ottiche/radiazioni-uv-60/monitoraggio-giornaliero-della-radiazione-ultravioletta/l-indice-uv-orario.html				
Italy 6:	30 min	G	WHO	Y	I
P/O:	Physics Dept., Sapienza University of Rome				
R:	A. M. Siani				
web:	http://www.gmet.eu/				
Italy 7:	20min	G	WHO	N	I/E
P:	ENEA (Lampedusa)				
R:	A. G. di Sarra				
O:	Laboratory for Observations and Analyses of Earth and Climate, ENEA (A. Iaccarino, D. Sferlazzo)				
web:	http://www.lampedusa.enea.it/dati/uvindex/				
Ireland	5 min	G	WHO	Y	E
P/O:	Public Health England				
R:	J. B. O'Hagan				
web:	https://uk-air.defra.gov.uk/data/uv-index-graphs				
Luxembourg	30 min	G/T	other	Y	E
P/O:	Lycée classique Diekirch				
R:	F. Massen				
web:	http://meteo.lcd.lu/today_01.html				
Moldova	1 min	G/T		D	E
P:	Institute of Applied Physics(IAP)				
R:	A. A. Aculinin				
O:	Atmospheric Research Group(ARG), IAP				
web:	http://arg.phys.asm.md/				
Norway	60 min	G/T	WHO	Y	NO/E
P:	Ministry of Climate and Environment Ministry of Health and Care Services				
R:	B. Johnsen, T. Svendby, A. Dahlback				
O:	NILU; Phys. Dept, University of Oslo; Norwegian Radiation Protection Authority (NRPA); Bioforsk Øst, Kise; Geophys Inst, University of Bergen; Finse Res. Center/Univ. Of Oslo; Inst of Phys, Norwegian University of Science and Technology; ALOMAR Observatory; Norwegian Polar Institute				
web:	www.nrpa.no/uvnett				
Netherlands	12 min	G	other	Y	NL
P:	National Fund for Environmental Protection and Water Management				
R:	P.N. den Outer, E. van Putten, H. Slaper				
O:	National Institute for Public Health and the Environment				
web:	http://www.rivm.nl/en/Topics/U/UV_ozone_layer_and_climate/current_UV_level				
Poland 1	5 min	G	WHO	N	PL
P:	National Fund for Environmental Protection and Water Management				
R:	J. Biszczuk-Jakubowska, A. Curyło				
O:	Institute of Meteorology and Water Management - National Research Institute				
web:	http://www.pogodynka.pl/indeksuv				

Table 2 (continued)

Country	Update	Presentation	Color system	Archive	Language
Poland 2	1 min	S	other	N	E/PL
P/O:	Institute of Geophysics PAS				
R:	J. Krzyściński, P. Sobolewski, J. Jarosławski				
web:	www.weatherlink.com/user/igfpan/index.php?view=summary&headers=1 www.weatherlink.com/user/davis3/index.php?view=summary&headers=1 www.weatherlink.com/user/cog2/index.php?view=summary&headers=1 www.weatherlink.com/user/davis4/index.php?view=summary&headers=1 uvb.igf.edu.pl				
Portugal	10 min	S	WHO	N	PT/E
P/O:	Instituto Português do Mar e da Atmosfera				
R:	V. Prior				
web:	ftp://uvb:20bv14@ftpserver.meteo.pt/UVBFUNC/CurrUVB.html				
Serbia 1	10-30 min	G/S	WHO	Y	Serb
P/O:	Department of Physics, Faculty of Sciences, University of Novi Sad				
R:	Z. Mijatovic				
web:	http://cmep-serbia.df.pmf.uns.ac.rs/index.php?option=com_wrapper&Itemid=54 http://uv-srbija.rs/UVIndeks/IzmereneVrednosti/NoviSad				
Serbia 2	30 min	G/S		N	Serb
P/O:	Institute of Physics Belgrade, Serbia				
R:	P. Kolarž				
web:	http://www.weather2umbrella.com/sr/uv-indeks-beograd-danas/eta/9/319 http://uv-srbija.rs/UVIndeks/IzmereneVrednosti/Beograd http://uranus.ipb.ac.rs/~uvif/				
Spain 1	5 min	G	OTHER	Y	Sp/E
P:	Univ. of Valladolid/Spanish Ministry (MINECO), Spanish Research and Economy Ministry				
R:	J. Bilbao, A. De Miguel				
O:	Atmosphere and Energy Laboratory UVA				
web:	www5.uva.es/laten				
Spain 2	1 day	G/T/S	WHO	Y	Sp
P:	AEMET				
R/O:	Area of Atmospheric Observation Networks				
web:	http://www.aemet.es/es/eltiempo/observacion/radiacion/ultravioleta?datos=mapa				
Spain 3	20 min	M/G	WHO	N	Sp
P/O:	Instituto Nacional de Técnica Aeroespacial (INTA) Departamento de Física, Universidad de Extremadura				
R:	J. M. Vilaplana Guerrero, M. Cancillo Fernández				
web:	aire.unex.es/uvi				
Switzerland	15 min	G	WHO	N	D/F/I
P:	Federal Department of Home Affairs				
R:	L. Vuilleumier, J. Gröbner				
O:	Federal Office of Meteorology and Climatology MeteoSwiss, PMOD/WRC Davos				
web:	http://www.bag.admin.ch/uv_strahlung/10652/10683/index.html				
UK	5-30 min	G	WHO	Y	E
P:	Public Health England; Department of Environment Food and Rural Affairs				
R:	J. B. O'Hagan; A. R. Webb				
O:	Public Health England; University of Manchester				
web:	https://uk-air.defra.gov.uk/data/uv-index-graphs				

Table 2 (continued)



Novel method of measurement of radon exhalation from building materials



A. Awhida^a, P. Ujić^{b,*}, I. Vukanac^b, M. Đurašević^b, A. Kandić^b, I. Čeliković^b, B. Lončar^a, P. Kolarž^c

^a Faculty of Technology and Metallurgy, University of Belgrade, 11000 Belgrade, Karnegijeva 4, Serbia

^b Institute of Nuclear Sciences "Vinča", University of Belgrade, P.O. Box 522, 11001 Belgrade, Serbia

^c Institute of Physics Belgrade, University of Belgrade, Pregrevica 118, 11080 Zemun, Serbia

ARTICLE INFO

Article history:

Received 28 April 2016

Received in revised form

6 August 2016

Accepted 6 August 2016

Keywords:

Radon exhalation

Building materials

Radon diffusion length

Radon diffusion coefficient

Radon emanation

ABSTRACT

In the era of the energy saving policy (i.e. more air tight doors and windows), the radon exhaled from building materials tends to increase its concentration in indoor air, which increases the importance of the measurement of radon exhalation from building materials. This manuscript presents a novel method of the radon exhalation measurement using only a HPGe detector or any other gamma spectrometer. Comparing it with the already used methods of radon exhalation measurements, this method provides the measurement of the emanation coefficient, the radon diffusion length and the radon exhalation rate, all within the same measurement, which additionally defines material's radon protective properties. Furthermore it does not necessitate additional equipment for radon or radon exhalation measurement, which simplifies measurement technique, and thus potentially facilitates introduction of legal obligation for radon exhalation determination in building materials.

© 2016 Elsevier Ltd. All rights reserved.

1. Introduction

Radon (further on referring to ^{222}Rn) is the greatest source of the public exposure to radiation. More than 50% of the radiation dose received by the general population is a consequence of the exposure to radon i.e. to its progenies. Namely, the radon itself is a noble gas and the most of the inhaled radon in human lungs is also exhaled. However, the radon progenies are metals by its chemical nature and they attach to the surface of the lungs where its destructive damaging potential due to radioactive decay is the most prominent. As a short-lived and also alpha radioactive, ^{214}Po and ^{218}Po , attached to the lungs, give the epithelial layer of the bronchi a substantial radiation dose (BEIR VI, 1999; Ferlay et al., 2007; WHO, 2009). Ergo, the radon is responsible for between 3% and 14% of lung cancer death, being proved to be the second main cause of the lung cancer after smoking (WHO, 2009).

As a primordial radionuclide ^{238}U is present in the Earth's crust and consequently it is present in the building materials, as well. The ^{238}U is a parent radionuclide of the Uranium decay series which

includes ^{226}Ra which is direct predecessor of ^{222}Rn . The ^{222}Rn can exhale from a building material and increase the indoor radon concentration. By the contribution to the indoor radon concentration the radon exhaling from the building material is at the second place, immediately after the radon originating from the soil or the bedrock where the building is constructed (Denman et al., 2007; Cosma et al., 2013).

In order to quantify and to regulate the exposure to gamma radiation originating from radionuclides in building materials the Activity Concentration Index I_γ (sometimes referenced as "gamma index") has been proposed (EC, 1999):

$$I_\gamma = \frac{C_{\text{Ra}}}{300(\text{Bq kg}^{-1})} + \frac{C_{\text{Th}}}{200(\text{Bq kg}^{-1})} + \frac{C_{\text{K}}}{3000(\text{Bq kg}^{-1})},$$

where C_{Ra} , C_{Th} and C_{K} are the ^{226}Ra , ^{232}Th and ^{40}K specific activities, respectively. The building materials should be restricted in their usage if their gamma index is higher than 1 ($I_\gamma > 1$) which corresponds to an effective annual dose to the inhabitants higher than 1 mSv (EC, 1999).

However, the "alpha index" I_α may be used to regulate the exposure to radon originating from radionuclides in building material (Nordic, 2000):

* Corresponding author.

E-mail address: ujic@vinca.rs (P. Ujić).

$$I_{\alpha} = \frac{C_{Ra}}{200(\text{Bq kg}^{-1})}$$

The alpha index was proposed on the basis of the assumption that if ^{226}Ra concentration exceeds 200 Bq kg^{-1} , it is possible that the indoor radon concentration will exceed 200 Bq m^{-3} (Nordic, 2000).

There are certain indications that the internal dose received from the radon exhaled from building materials can exceed the external dose received from the radium content in the same building material (Petropoulos et al., 2002; Ujčić et al., 2010). Nowadays, this issue becomes more relevant, whereas the energy saving policy (more tight windows and doors) will further decrease the average ventilation rate and increase the radon concentration in indoor air, consequently increasing the dose received from radon (Yarmoshenko et al., 2014). It was shown that the building construction characteristics (like wall materials and period of construction) has significant influence on mean of logarithmic indoor radon concentration (Yarmoshenko et al., 2016) which further implies the necessity to investigate the building materials regarding the radon exhalation issue (exhalation and also the diffusion length).

Due to all the above mentioned reasons the radon exhalation from building materials is still preoccupying interest of many researchers in different countries. Consequently, there are many recent publications dealing with this subject (Topçu et al., 2013; Kumar et al., 2014; Tan and Xiao, 2014; Feng and Lu, 2015; Morelli et al., 2015; Stajic and Nikezic, 2015; Saad et al., 2014), whereby these measurements use exclusively accumulation chamber method.

There are various methods developed for the radon exhalation measurements: the abovementioned accumulation chamber method (sometimes referred as “can” or “sealed can” method), the charcoal method and SSNTD (Solid State Nuclear Track Detector) method (Abu-Jarad et al., 1980; Ingersoll et al., 1983; Iimoto et al., 2008). Some of the methods for radon exhalation measurements are already incorporated into the ISO International Standards i.e. into ISO 11665 Measurement of radioactivity in the environment – Air: Radon-222 as Part 7: Accumulation method for estimating surface exhalation rate (ISO 11665–7:2012) and as Part 9: Test methods for exhalation rate of building materials (ISO 11665–9:2016).

In this manuscript we propose a new method of radon exhalation measurements which does not necessitate any equipment for a radon concentration measurement. Instead, the radon exhalation measurement is performed only by a gamma detector (spectrometer). Moreover, this method provides the values of the radon emanation coefficient, the radon diffusion coefficient and consequently the radon diffusion length, whereby the diffusion coefficient and the diffusion length characterise the building materials regarding their radon protective properties (Tsapalov and Kovler, 2016). Since the gamma spectrometry is the most common tool for radiological analysis of the environmental and other samples, many laboratories would not have to purchase radon equipment in order to estimate radon exhalation. Combined with the fact that only the radionuclide concentration in building materials are regulated, implementation of the proposed method could increase the perspectives to include the radon exhalation in national regulations.

2. Theory and methods

All the mentioned methods of radon exhalation measurement are measuring the exhaled radon directly. Herein described

“gamma” method, the non-exhaled radon in the sample of building material is measured by gamma spectrometry, which then allows to estimate the exhaled radon.

A cylindrical sample with sealed lateral side and one base is considered (see Fig. 1). The sample was left for a period of 10 half-lives of ^{222}Rn (~ 38 days) in order to achieve the equilibrium state. The homogeneity of the sample is assumed. The radon in the building materials exists in two phases: non-emanated (positioned in the mineral phase of the sample) and emanated (positioned in the air phase of the sample) – see Fig. 1. The non-emanated part C_{ne} of the radon has a constant concentration in the sample:

$$C_{ne} = C_{Ra}(1 - \varepsilon) \quad (1)$$

where C_{Ra} is the ^{226}Ra concentration in the sample given in Bq kg^{-1} , ε is the emanation coefficient given in non-dimensional unit. C_{ne} is expressed in Bq kg^{-1} . The emanated radon can diffuse through the air in the sample and its concentration C_e depends on the position on the axis of the sample.

$$D \frac{\partial^2 C_e(x)}{\partial x^2} - \lambda C_e(x) + \frac{C_{Ra} \rho \varepsilon}{p} = 0 \quad (2)$$

where D is the radon diffusion coefficient in the given material ($\text{m}^2 \text{ s}^{-1}$), λ is the decay constant of the radon (s^{-1}), ρ is the density of the material (kg m^{-3}), p is the porosity of the material which defines the percentage of the air in a sample material. As the equilibrium is achieved the radon flux does not change with time,

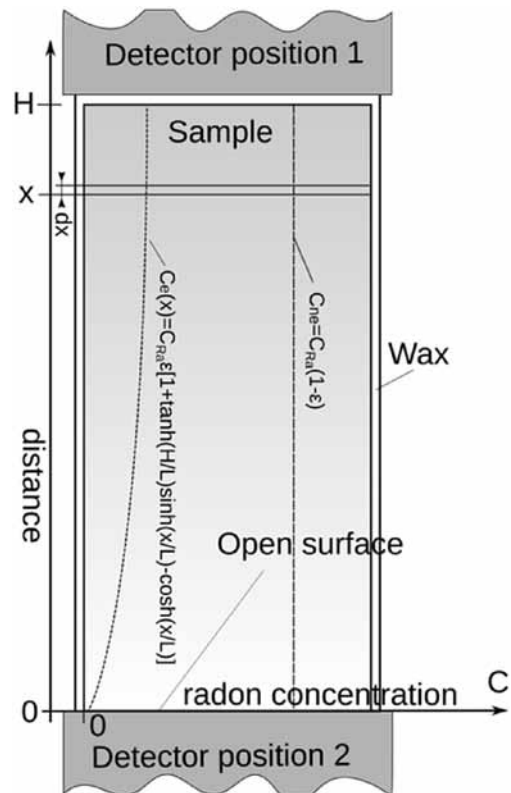


Fig. 1. Scheme of the measurement setup showing the position of the sample and two possible positions of the detector. Radon concentrations (emanated and non-emanated), defined by Eqs. (1) and (4), are also presented. The detector positions are shown as referent to the coordinate system referred to the sample. In reality the detector is at the same position, while the sample is turned upside down between measurements. The wax (beeswax) prevents radon diffusion through sealed sample sides, ensuring the radon exhales only through the open surface.

which means that its concentration at given position does not change with time, as well. It should be noticed that the concentration of emanated radon C_e is in principle expressed by Bq m^{-3} as it is in the air phase of the sample.

The general solution of Eq. (2) is the following (Ujić et al., 2008):

$$C_e(x) = C_{\max} \tanh(H/L)\sinh(x/L) - C_{\max} \cosh(x/L) + C_{\max}, \tag{3}$$

where $L = \sqrt{D/\lambda}$ is the radon diffusion length in given material in m, $C_{\max} = C_{\text{Ra}}\rho\varepsilon/p$ in Bq m^{-3} and H is the height of the sample in m (see Fig. 1). One should take a notice that the axis has a different direction comparing to Ujić et al., 2008 and the signs in Eq. (3) are adjusted accordingly. C_{\max} also presents a theoretical quantity referring to the maximum radon concentration (expressed in Bq m^{-3}) in pore space that can be attained at the bottom of the sample when $H \rightarrow \infty$. In other words, it presents maximum radon concentration in pore space when the emitted radon atoms are completely confined within the sample (by sealing for example).

Eq. (3) is derived for the emanated radon inside the material (sample) expressed in Bq m^{-3} . Nonetheless, it could be easily transformed to concentration expressed in Bq kg^{-1} by multiplying both sides of Eq. (3) by factor p/ρ , obtaining the concentration $C'_e(x)$ expressed in Bq kg^{-1} which is more convenient since this unit is used in the gamma spectrometry:

$$C'_e(x) = C_{\text{Ra}}\varepsilon[\tanh(H/L)\sinh(x/L) - \cosh(x/L) + 1] \tag{4}$$

Therefore the total radon concentration C_{tot} (Bq kg^{-1}) in the sample seen by the detector is:

$$C_{\text{tot}}(x) = C'_e(x) + C_{\text{ne}} = C_{\text{Ra}}[1 + \varepsilon \tanh(H/L)\sinh(x/L) - \varepsilon \cosh(x/L)] \tag{5}$$

Generally, in gamma spectrometry and measurements of radionuclide concentrations in samples, the calibration is performed using radioactive standards of adequate geometry and matrix, whereby the homogeneous distribution of radionuclides within the standard is compulsory (Vukanac et al., 2008). In that case the counting rate of gamma ray i of a radionuclide in given sample is estimated by the following formula:

$$R_i = mI_iC\eta^{(H)}, \tag{6}$$

$$R_i = mI_iC_{\text{Ra}}\eta^{(H)} \frac{\int_0^H [1 + \varepsilon \tanh(H/L)\sinh(x/L) - \varepsilon \cosh(x/L)]\eta_{\Delta x}^{(i)}(H-x)dx}{\int_0^H \eta_{\Delta x}^{(i)}(x)dx} \tag{9}$$

where, m – is the sample mass in kg, I_i – is the relative intensity of the gamma ray i of given radionuclide, C is the radionuclide concentration in the sample in Bq kg^{-1} , $\eta^{(H)}$ is the calibration coefficient, where the superscript H is noting that the sample is in certain geometry i.e. a cylindrical shape with height H presumed.

In the case of open sample where radon exhales at one side of the sample, the homogeneity is obviously not fulfilled (see Fig. 1). Thus, the counting rate estimation using a chosen gamma ray i (i.e. chosen energy) of certain radon progeny is given by the following expression:

$$R_i = mI_i \int_0^H C_{\text{tot}}(x)\eta^{(H)}\eta_i(H-x)dx = mI_iC_{\text{Ra}}\eta^{(H)} \int_0^H [1 + \varepsilon \tanh(H/L)\sinh(x/L) - \varepsilon \cosh(x/L)]\eta_i(H-x)dx \tag{7}$$

where $\eta_i(H-x)$ is a relative contribution to the counting rate of the layer of the sample of thickness dx at distance $(H-x)$ from a detector at the position 1 – see Fig. 1. The other variables are defined as in the previous equations. The assumed sample-detector distance is zero. The sample-detector distance and eventual absorbing material in-between can be corrected within the $\eta_i(x)$.

Thus, the mentioned calibration coefficient $\eta_i(x)$ is needed in order to estimate the contribution of layer dx to the counting rate R_i . However, $\eta_i(x)$ cannot be determined experimentally and to make a calibration exclusively by Monte-Carlo is not recommendable. Thus, the solution is to determine an equivalent of $\eta_i(x)$ by a semi-empirical method, for instance by using the EFFTRAN package (Vidmar, 2005). The EFFTRAN package is used to transfer (recalculate) the calibration coefficient of a standard to a sample which has similar geometry (size and shape) and/or matrix (material). In order to calculate $\eta_i(x)$ as a relative contribution to the counting rate, instead original value of the calibration coefficient, a value 1 was used for the calculation (see Fig. 2). Others simulation packages, like GEANT4 (GEANT4, 2003) could be also used.

In this case, the EFFTRAN package was used to transfer calibration coefficient of a standard (35 mm radius, 35 mm high cylindrical box filled with sand) to layers of finite thickness Δx (instead of infinitesimal dx) at distance x from the detector (see Fig. 1). The relative contributions to gamma ray i of layer dx (i.e. Δx , whereby in this case $\Delta x = 5$ mm) at the distances $x = 0$ mm, 5 mm, 10 mm up to $(H-5)$ mm are interpolated with polynomial function of tenth order – $\eta_{\Delta x}^{(i)}(x)$. As the function $\eta_{\Delta x}^{(i)}(x)$ is a relative contribution, the integral $\int_0^H \eta_{\Delta x}^{(i)}(x)dx$ must be normalized to 1:

$$A \int_0^H \eta_{\Delta x}^{(i)}(x)dx = 1 \Rightarrow A = \frac{1}{\int_0^H \eta_{\Delta x}^{(i)}(x)dx} \tag{8}$$

Therefore, after Eq. (7) is transformed accordingly, the final expression of radon concentration using a chosen radon progeny gamma ray i is:

The non-integral part of the equation is equal to Eq. (6). There are two unknown variables in Eq. (9): the diffusion length – L and the emanation coefficient – ε . The ^{226}Ra concentration – C_{Ra} can be measured directly, while for the estimation of the L and ε , two independent measurements are needed. This could be obtained by a measurement of one sample with two detector positions (see Fig. 1 and Fig. 3). For the measurement at the detector position 2 (Fig. 1) the orientation of x axes is changed and the

3. Results

For the purpose of the simple verification of the method, a concrete sample was prepared in order to confirm the feasibility and to verify the method. The sample has a cylindrical shape of 71 mm diameter with height of 120 mm. The sample is made of 15% silica sand, 45% of travertine (a form of calcium carbonate deposited by mineral springs) and 40% of portland cement (all the weight percentages). The travertine is very porous mineral and it is collected from Niška Banja, Serbia, which is chosen due to the fact that it has high ^{226}Ra content (Žunić et al., 2007), which facilitates the testing of the method. The curing period of the prepared sample was more than 4 weeks, whereby the sample was moistened in the first week of the curing period. After the curing, the sample was covered by beeswax (with one free surface) and it was left for ~40 days to achieve equilibrium between a radon and its daughters.

The measurement was performed with HPGe detector AMETEK-AMT (Ortec) GEM 30–70 (relative efficiency 37%, energy range 50 keV–3 MeV). The detector has a pure lead shielding of outer radius of 26 cm, outer height of 50.5 cm and lead thickness of 10.25 cm. Certified solution of mixed gamma source (^{241}Am , ^{109}Cd , ^{139}Ce , ^{57}Co , ^{60}Co , ^{137}Cs , ^{203}Hg , ^{113}Sn , ^{85}Sr and ^{88}Y), purchased at the Czech Metrological Institute (CMI), was used for preparing a sand multi gamma standard. This standard was used for energy and efficiency calibration of spectrometer. Obtained efficiencies were corrected for coincidence summing effect by using the corrections factors as described by Debertain and Schötzig (1979).

In the estimation of the exhalation the following gamma lines of radon progenies were used: 609 keV, 1120 keV and 1764 keV of ^{214}Bi and 295 keV and 352 keV of ^{214}Pb . It was measured that the radon diffusion length in the sample was $L = 0.31 \pm 0.03$ m (and thus diffusion coefficient $D = (2.0 \pm 0.4)10^{-7} \text{ m}^2 \text{ s}^{-1}$), while the emanation coefficient is $\epsilon = 0.45 \pm 0.02$. The measured ^{226}Ra concentration in the sample was $175 \pm 2 \text{ Bq kg}^{-1}$. The density of our sample is 1750 kg/m^3 . According to Eq. (12) and given values, the radon exhalation rate was calculated to be $0.0326 \pm 0.0014 \text{ Bq s}^{-1} \text{ m}^{-2}$.

The measurement was compared with the standard accumulation chamber method of the measurement of radon exhalation. The same concrete sample, in the same geometry with one free surface was used in this comparison. The radon concentration inside the chamber $C(t)$ is defined by the following expression (Ujić et al., 2008):

$$C(t) = \frac{EA}{V\lambda_{\text{eff}}} (1 - e^{-\lambda_{\text{eff}}t}) \quad (14)$$

where E is the exhalation rate, A is the area of the exhaling surface of the sample (m^2), V is the chamber volume (m^3), λ_{eff} is an effective decay constant of radon $\lambda_{\text{eff}} = \lambda + \lambda_b + \lambda_{\text{leak}}$ (s^{-1}), which includes decay constant, back-diffusion coefficient and chamber leakage coefficient, respectively. The verification measurement was performed using an accumulation chamber of the $0.26 \times 0.275 \times 0.41 \text{ m}^3$ volume and the RAD7 (DurrIDGE Radon Instrumentation).

The result of this measurement is shown on the Fig. 4 and the fit of the measured values on Eq. (14) with two free parameters (E and λ_{eff}) gave the following values $E = 0.0311 \pm 0.0002 \text{ Bq s}^{-1} \text{ m}^{-2}$ and $\lambda_{\text{eff}} = (2.25 \pm 0.03)10^{-6} \text{ s}^{-1}$.

4. Discussion

The comparison of the novel “gamma” method with a standard exhalation measurement with an accumulation chamber showed an excellent agreement. The difference between two

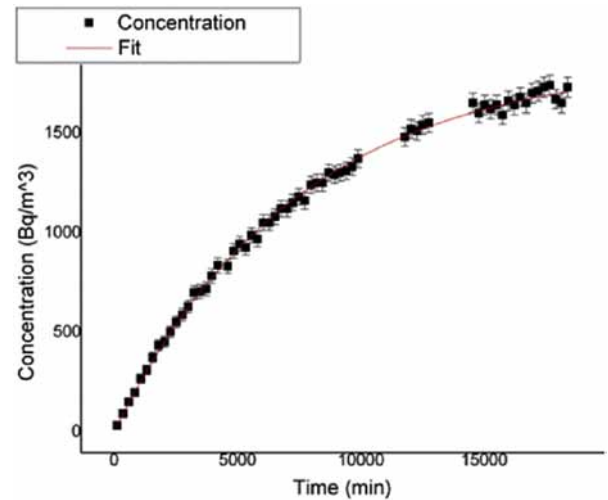


Fig. 4. (Color online) The verification measurement with an accumulation chamber and the RAD7 radon instrument.

measurements of two different methods was 4.6% and it is within the 1 sigma measurement uncertainty which verified the novel method.

Although there is a significant difference between the sample height and the diffusion length, the emanation coefficient is very high and consequently it was possible to obtain a result. The estimated exhalation rate of $0.0326 \text{ Bq s}^{-1} \text{ m}^{-2}$ is very high due to the high radium content in travertine, high emanation coefficient and long radon diffusion length of the sample, which is not surprising since the most of the radium in the sample is actually situated in the travertine which is very porous material with “spongy” structure. In fact, the average concrete density is $2100\text{--}2200 \text{ kg m}^{-3}$, while the density of our sample is 1750 kg m^{-3} .

It is interesting to notice that the building material used for our sample would be allowed to be used in building constructions regarding the ^{226}Ra concentration as its concentration fulfill the restrictions of alpha index mentioned in section 1. According to Eq. (13), a wall of thickness of 12 cm, made of this material will have an exhalation rate $E = 0.0247 \text{ Bq m}^{-2} \text{ s}^{-1}$. Indoor radon concentration originating only from the exhaled radon can be estimated as:

$$C_{\text{Rn}} = \frac{EA_{\text{r}}}{V_{\text{r}}\lambda_{\text{v}}} \quad (15)$$

where A_{r} is the area of the wall surface; V_{r} is the volume of the room and λ_{v} is the room ventilation rate (or room air exchange rate). Ratio A/V is taken to be 1.6 considering a room model with dimensions $(4 \times 5 \times 2.8) \text{ m}^3$ and the ventilation rate lays in the interval $(0.2\text{--}2) \text{ h}^{-1}$ (UNSCEAR, 2000) with the geometric mean of 0.63 h^{-1} . In the case of $\lambda_{\text{v}} = 0.2 \text{ h}^{-1}$ the indoor radon concentration would be very high $C_{\text{Rn}} = 711 \text{ Bq m}^{-3}$ and in case of $\lambda_{\text{v}} = 0.63 \text{ h}^{-1}$, $C_{\text{Rn}} = 226 \text{ Bq m}^{-3}$, which is still above the recommended concentration in many countries. This example illustrates the necessity for the prospection of building materials regarding the radon exhalation. Mustonen, 1984 shows that the normalized radon exhalation rate from 15-cm-thick concrete was $0.38 (\text{Bq m}^{-2} \text{ h}^{-1})/(\text{Bq kg}^{-1})$, which implicates that the building materials with elevated ^{226}Ra concentration can significantly increase indoor radon concentration.

Two purge and trap methods of the measurement of radon exhalation from building materials incorporated into ISO standards (ISO 11665–9, 2016) require a gamma spectrometer and also additional equipment (accumulation chamber, pumps, flowmeters,

etc.). According to the ISO 11665–9, 2016, the sample conditioning should start 8–12 weeks after the curing period of 28 days. In the novel “gamma” method, it is required ~38 days to achieve an equilibrium state between radon and its progenies in a sample, which fits the required ISO standards. The conditioning regarding the temperature and humidity can be achieved in measurement room where gamma spectrometers are placed, as it is usual that the measurement rooms are conditioned.

This novel method has certain restrictions regarding the ratio H/L which is shown on the Fig. 5. These limits depend on the measurement precision of the concentration of radon progenies inside the sample which is chosen to be 0.5% and 1% in the case shown on the Fig. 5. For example if the sample height H is much lower than the radon diffusion length L , there will be too small gradient of radon concentration inside the sample and consequently there will be very small difference between counting rates when the sample is measured from the open and from the sealed side (see Fig. 3). For instance, for the emanation coefficient of 2.5% (which is relatively small emanation coefficient – see Stoulos et al., 2004; Righi and Bruzzi, 2006; Kumar et al., 2015) and the precision of 0.5%, H should be in the interval of 0.9–2.2 of L in given material. If the C_{Ra} is low, the sample should be measured for longer period of time to attain certain precision of the measurement of radon inside the sample.

Effectively, several factors influence a lower detection limit of the “gamma” method: radon emanation coefficient, ^{226}Ra concentration, measurement duration and the H/L ratio. We will consider two of 1-day measurements (one on sealed and one on open surface – Fig. 3) with the best choice of $H/L \sim 1.7$, which would correspond to relatively short measurement in a prospection of building material regarding radon exhalation. The total efficiency of gamma detection for all gamma peaks of radon progenies is taken to be 1% (which was the case for the gamma spectrometer in this experiment). Under these conditions, if the building material has the emanation coefficient of 2.5%, the minimum ^{226}Ra concentration required to estimate the exhalation rate would be 48 Bq kg^{-1} . However, if the emanation coefficient is 5%, the minimum ^{226}Ra concentration would be 12 Bq kg^{-1} . The radium content limit dependence on the emanation coefficient is defined by the gamma ray detection efficiency and will be more favourable in the case of better gamma efficiency.

Nevertheless, in any of these cases (too low emanation coefficient or too low radium content) the radon exhalation would be

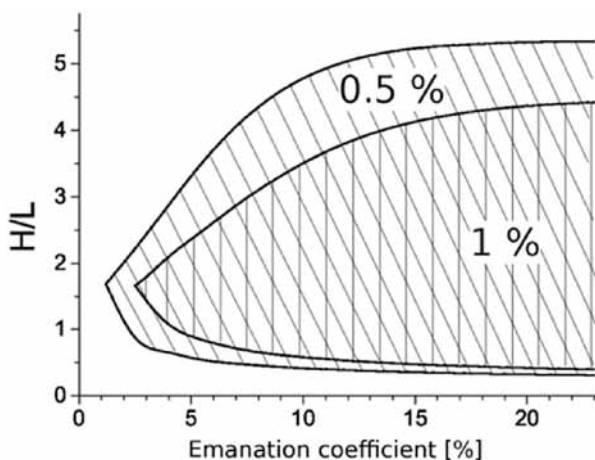


Fig. 5. The shaded areas on the graph are showing for which combination of emanation coefficient and the ratio H/L is possible to estimate the radon exhalation rate, when the precision of the concentration measurement of radon progenies is 0.5% and 1%.

also very low to be measured; the method still retains its applicability as method to make a selection of building materials regarding the radon exhalation. For instance, if the building material would have the emanation coefficient of 2.5% and the radium content of 30 Bq kg^{-1} , it could be determined that the emanation coefficient is $< 3\%$ and the exhalation rate $E < 3 \cdot 10^{-4} \text{ Bq s}^{-1} \text{ m}^{-2}$ (even if L much larger than wall thickness), which would correspond to indoor radon concentration $C_r < 9 \text{ Bq m}^{-3}$ (according to Eq. (15)). The limits can be improved simply by a longer measurement period; however it is a question of the cost-benefit analysis.

5. Conclusion

In the paper a new method of the radon exhalation measurement is presented. The method feasibility is proved and the method is verified by the standard radon exhalation measurement with accumulation chamber.

The advantage of the method is a measurement of the radon exhalation rate without need of the radon measurement equipment, whereas the radon exhalation measurement is performed only by use of a gamma detector (spectrometer) which is already used in the prospection of building materials regarding the radionuclides content. The energy saving policy have a consequence of increasing the average radon concentration in indoor air (even at higher floors) and the average population dose received from radon (Yarmoshenko et al., 2014), which will increase the importance of the measurement of radon exhalation from building materials. This method could be also used to test the mixture design of, for instance, concretes containing fly ash (Taylor-Lange et al., 2014).

In the paper, the test measurement was successfully performed in order to prove the feasibility of the method and the method is verified by the measurement with an accumulation chamber. However, further investigation (as well as an intercomparison of methods) will be continued in order to investigate a margin of applicability in real cases.

Additionally, the measurement by this method will provide the values of the emanation coefficient, the diffusion coefficient and consequently the diffusion length, which requires additional equipment and preparation in standard radon exhalation measurement. This method is very applicable as a prospective method for determining if building materials are exceeding potential limit of radon exhalation. The general necessity for the regulation and measurement of the radon exhalation rate from building materials is illustrated on the example of the sample measurement used in the manuscript.

Acknowledgements

The authors acknowledge the support of the Ministry of Education, Science and Technological Development of the Republic of Serbia [P171018, P171007].

References

- Abu-Jarad, F., Fremlin, J.H., Bull, R., 1980. A study of radon emitted from building materials using plastic α -track detectors. *Phys. Med. Biol.* 25 (4), 683.
- BEIR VI (Committee on Health Risks of Exposure to Radon), 1999. Health Effects of Exposure to Radon: BEIR VI (Free Executive Summary). National Research Council.
- Cosma, C., Cucos-Dinu, A., Papp, B., Begy, R., Sainz, C., 2013. Soil and building material as main sources of indoor radon in Băița-Ștei radon prone area (Romania). *J. Environ. Radioact.* 116, 174–179.
- Debertin, K., Schötzig, U., 1979. Coincidence summing corrections in Ge(Li) -spectrometry at low source-to-detector distances. *Nucl. Instrum. Methods* 158, 471–477.
- Denman, A.R., Groves-Kirkby, N.P., Groves-Kirkby, C.J., Crockett, R.G.M., Phillips, P.S., Woolridge, A.C., 2007. Health implications of radon distribution in living rooms and bedrooms in U.K. dwellings – a case study in Northamptonshire. *Environ.*

- Int. 33 (8), 999–1011.
- EC (European Commission), 1999. Radiation protection 112-Radiological Protection Principles Concerning the Natural Radioactivity of Building Materials. Directorate-General Environment, Nuclear Safety and Civil Protection.
- Feng, T., Lu, X., 2015. Natural radioactivity, radon exhalation rate and radiation dose of fly ash used as building materials in Xiangyang, China. *Indoor Built Environ.* 25 (4), 626–634.
- Ferlay, J., Autier, P., Boniol, M., Heanue, M., Colombet, M., Boyle, P., 2007. Estimates of the cancer incidence and mortality in Europe in 2006. *Ann. Oncol.* 18, 581–592.
- GEANT4 (2003) <https://geant4.web.cern.ch/geant4/>.
- limoto, T., Akasaka, Y., Koike, Y., Kosako, T., 2008. Development of a technique for the measurement of the radon exhalation rate using an activated charcoal collector. *J. Environ. Radioact.* 99 (4), 587–595.
- Ingersoll, J.G., Stitt, B.D., Zapalac, G.H., 1983. A fast and accurate method for measuring radon exhalation rates from building materials. *Health Phys.* 45 (2), 550–552.
- ISO 11665–7:2012, Measurement of Radioactivity in the Environment – Air: Radon-222 – Part 9: Test Methods for Exhalation Rate of Building Materials.
- ISO 11665–9:2016, Measurement of Radioactivity in the Environment – Air: Radon-222 – Part 9: Test Methods for Exhalation Rate of Building Materials.
- Kumar, A., Chauhan, R.P., Joshi, M., Sahoo, B.K., 2014. Modeling of indoor radon concentration from radon exhalation rates of building materials and validation through measurements. *J. Environ. Radioact.* 127, 50–55.
- Kumar, A., Chauhan, R.P., Joshi, M., Prajith, R., Sahoo, B.K., 2015. Estimation of radionuclides content and radon–thoron exhalation from commonly used building materials in India. *Environ. Earth Sci.* 74 (2), 1539–1546.
- Morelli, D., Catalano, R., Filincieri, R., Immè, G., Mangano, G., 2015. Radon exhalation rate in south-east Sicily building materials. *Eur. Phys. J. Spec. Top.* 224 (4), 605–610.
- Mustonen, R., 1984. Natural radioactivity in and radon exhalation from Finnish building materials. *Health Phys.* 46 (6), 1195–1203.
- Nazaroff, W.W., Nero, A.V., 1988. *Radon and Its Decay Products in Indoor Air*. Wiley, New York, NY.
- Nordic, 2000. Naturally Occurring radiation in the Nordic countries—recommendations. In: *The Flag-Book Series. The Radiation Protection Authorities in Denmark, Finland, Iceland, Norway and Sweden*, Reykjavik.
- Petropoulos, N.P., Anagnostakis, M.J., Simopoulos, S.E., 2002. Photon attenuation, natural radioactivity content and radon exhalation rate of building materials. *J. Environ. Radioact.* 61 (3), 257–269.
- Righi, S., Bruzzi, L., 2006. Natural radioactivity and radon exhalation in building materials used in Italian dwellings. *J. Environ. Radioact.* 88 (2), 158–170.
- Saad, A.F., Al-Awami, H.H., Hussein, N.A., 2014. Radon exhalation from building materials used in Libya. *Radiat. Phys. Chem.* 101, 15–19.
- Sahoo, B.K., Sapra, B.K., Gaware, J.J., Kanse, S.D., Mayya, Y.S., 2011. A model to predict radon exhalation from walls to indoor air based on the exhalation from building material samples. *Sci. Total Environ.* 409 (13), 2635–2641.
- Stajic, J.M., Nikezic, D., 2015. Measurement of radon exhalation rates from some building materials used in Serbian construction. *J. Radioanal. Nucl. Chem.* 303 (3), 1943–1947.
- Stoulos, S., Manolopoulou, M., Papastefanou, C., 2004. Measurement of radon emanation factor from granular samples: effects of additives in cement. *Appl. Radiat. Isot.* 60 (1), 49–54.
- Tan, Y., Xiao, D., 2014. A simple model for automatically measuring radon exhalation rate from medium surface. *Radiat. Meas.* 64, 44–47.
- Taylor-Lange, S.C., Juenger, M.C.G., Siegel, J.A., 2014. Radon emanation fractions from concretes containing fly ash and metakaolin. *Sci. Total Environ.* 466–467 (1), 1060–1065.
- Topçu, N., Biçak, D., Çam, S., Ereeş, F.S., 2013. Radon exhalation rate from building materials using CR-39 nuclear track detector. *Indoor Built Environ.* 22 (2), 384–387.
- Tsapalov, A., Kovler, K., 2016. Revisiting the concept for evaluation of radon protective properties of building insulation materials. *Build. Environ.* 95, 182–188.
- Ujić, P., Čeliković, I., Kandić, A., Žunić, Z., 2008. Standardization and difficulties of the thoron exhalation rate measurements using an accumulation chamber. *Radiat. Meas.* 43 (8), 1396–1401.
- Ujić, P., Čeliković, I., Kandić, A., Vukanac, I., Đurašević, M., Dragosavac, D., Žunić, Z.S., 2010. Internal exposure from building materials exhaling ²²²Rn and ²²⁰Rn as compared to external exposure due to their natural radioactivity content. *Appl. Radiat. Isot.* 68 (1), 201–206.
- UNSCEAR, 2000. United Nations Scientific Committee on the Effects of Atomic Radiations Sources, Effects and Risks of Ionizing Radiation, Paragraph 99. United Nations, New York.
- Vidmar, T., 2005. EFFTRAN - a Monte Carlo efficiency transfer code for gamma-ray spectrometry. *Nucl. Instrum. Methods A* 550, 603–608.
- Vukanac, I., Đurašević, M., Kandić, A., Novković, D., Nadder, L., Milošević, Z., 2008. Experimental determination of the HPGe spectrometer efficiency curve. *Appl. Radiat. Isot.* 66, 792–795.
- WHO, 2009. World Health Organization. WHO Handbook on Indoor Radon: a Public Health Perspective. WHO Press, Geneva.
- Yarmoshenko, I.V., Vasilyev, A.V., Onishchenko, A.D., Kiselev, S.M., Zhukovsky, M.V., 2014. Indoor radon problem in energy efficient multi-storey buildings. *Radiat. Prot. Dosim.* 160 (1–3), 53–56.
- Yarmoshenko, I., Vasilyev, A., Malinovsky, G., Bossew, P., Žunić, Z.S., Onishchenko, A., Zhukovsky, M., 2016. Variance of indoor radon concentration: major influencing factors. *Sci. Total Environ.* 541, 155–160.
- Žunić, Z.S., Kozak, K., Ciotoli, G., Ramola, R.C., Kochowska, E., Ujić, P., Čeliković, I., Mazur, J., Janik, M., Demajo, A., Birovljev, A., Bochicchio, F., Yarmoshenko, I.V., Kryeziu, D., Olko, P., 2007. A campaign of discrete radon concentration measurements in soil of Niška Banja town, Serbia. *Radiat. Meas.* 42 (10), 1696–1702.

SPATIAL VARIABILITY OF INDOOR RADON CONCENTRATION IN SCHOOLS: IMPLICATIONS ON RADON MEASUREMENT PROTOCOLS

Z. Curguz¹, G. Venoso^{2,*}, Z. S. Zunic³, D. Mirjanic⁴, M. Ampollini², C. Carpentieri², C. Di Carlo², M. Caprio², D. Alavantic³, P. Kolarz⁵, Z. Stojanovska⁶, S. Antignani² and F. Bochicchio²

¹Faculty of Transport, University of East Sarajevo, Dobo, Republic of Srpska

²Italian National Institute of Health, National Center for Radiation Protection and Computational Physics, Viale Regina Elena, 299-00161 Rome, Italy

³Vinca Institute of Nuclear Sciences, Department of Radiobiology and Molecular Genetics, University of Belgrade, P.O. Box 522, 11000 Belgrade, Serbia

⁴Academy of Sciences and Arts of Republic of Srpska, Banja Luka, Republic of Srpska

⁵Institute of Physics Belgrade, University of Belgrade, Belgrade, Serbia

⁶Faculty of Medical Sciences, Goce Delcev University, 2000 Stip, Republic of North Macedonia

*Corresponding author: gennaro.venoso@iss.it

The requirements about radon measurements in schools and public buildings included in most of the national and international legislations are generally restricted to all the rooms located at the ground floor and basement, assuming the soil beneath the building as the main source of indoor radon. In order to verify such an assumption for small buildings having at maximum two floors, a preliminary study was performed in 50 schools located in 15 municipalities of the Republic of Srpska. Results of this study suggest that a protocol requiring measurements at the ground floor only may be considered adequate. Due to the high radon spatial variability for rooms at the ground floor, it is preferable to require measurements in a high number of rooms (preferably in all of them) in order to assess the compliance with the reference level established by the legislation.

INTRODUCTION

The new requirements included in the recommendations and regulations of international organizations will certainly increase the number of radon concentration measurements in workplaces.^(1–2) Protocols used for workplaces (including schools) are generally different from those used for dwellings, mostly due to fact that radon spatial variability in workplaces is higher than in dwellings.⁽³⁾ For dwellings, it is generally recommended to measure the most inhabited rooms^(4–5); for workplaces, rooms to be measured are generally more numerous.

According to the 2013/59/Euratom Directive, some protocols give priority to measurements in workplaces and schools located in certain areas (i.e. radon priority areas). Assuming that the soil beneath the building is the main source of indoor radon, some protocols recommend to measure all the occupied rooms located at the ground floor and basement only.⁽⁶⁾ Assuming so, it means that measuring radon concentrations in rooms located at the floors in contact with ground allows to fulfill the compliance with reference level (RL) established by national legislations.⁽⁷⁾

For multistory buildings, some of these protocols require measurements to be performed also at

upper floors, but only if at the ground floor (or basement), the radon levels resulted to be higher than the RL.⁽⁶⁾ Measurements at upper floors are generally recommended in case of a possible stack effect from stairwells and/or any ducts such as those for air-conditioning and elevators.⁽⁷⁾

In the framework of an extensive survey in schools conducted in Republic of Srpska (Federation of Bosnia and Herzegovina), a preliminary study on the spatial variability of radon concentration in small buildings (having at maximum two floors) was performed. The aim of this study was to obtain information useful for the optimization of the measurement protocol in this type of building.

MATERIALS AND METHODS

Sample characteristics

Radon concentration measurements were performed in 50 schools: 33 of them have two floors (ground and first floors); the remaining 17 have ground floor only. The buildings are located in 15 municipalities. In each municipality, the number of surveyed buildings ranges between 1 and 25 (in Banja Luka, the main city of Republic of Srpska) with a median number equal to 4.

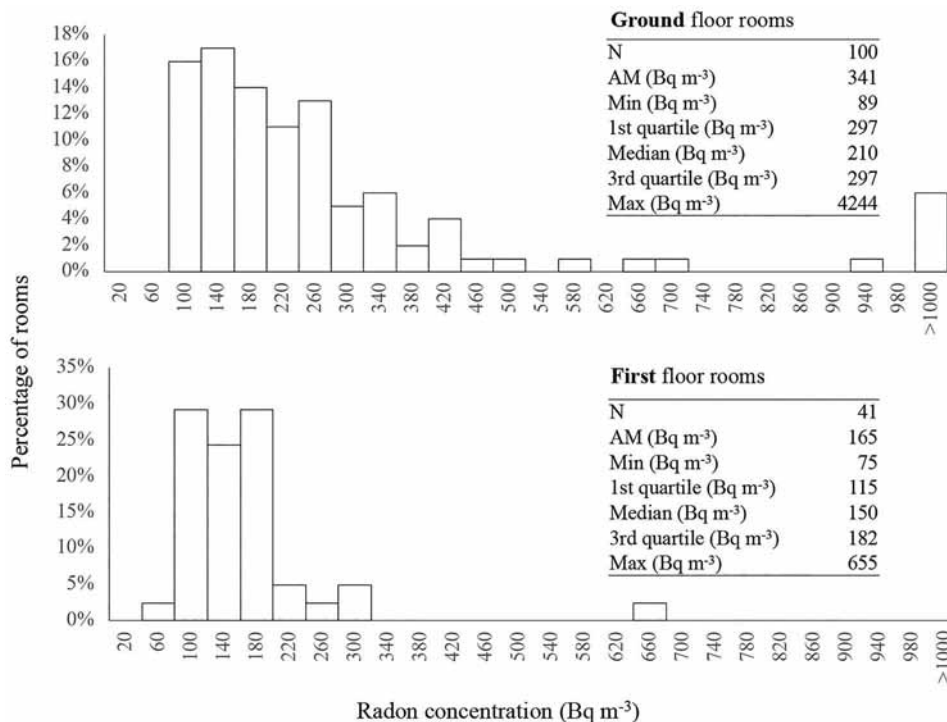


Figure 1: Radon concentration distribution for ground floor rooms (top) and first floor rooms (bottom).

Sampling protocol

A total of 141 rooms were measured. Taking into account the resources and the aim of the survey, a sampling protocol that requires at least two radon detectors for each building was adopted. For buildings having two floors, at least one detector for each floor was deployed. Radon measurements were carried out only in rooms occupied by pupils and staff of the schools, i.e. classrooms and laboratories. However, since all the laboratories are used as classrooms, all the monitored rooms are always occupied during the working hours, and they have approximately the same ventilation regime.

Radon measuring system

Radon measurements were performed using devices based on CR-39 detectors (manufactured by Intercast-Europe srl) enclosed in conductive holders (mi.amradout type). The etching took place in a thermal bath containing a 6.25 M NaOH solution at 98 °C for 60 min. Track counting was carried out with a fully automatic image analysis readout system (*Politrack*). It was chosen a single exposure period of about 1 year considering that these CR-39 detectors (and their measurement techniques) do not show an appreciable sensitivity decrease due to ageing and fading effects.⁽⁸⁾

RESULTS AND DISCUSSION

Radon concentration distributions

For all the monitored rooms, radon concentration distributions in the rooms located at the ground floor and first floor are separately represented in Figure 1.

Radon concentrations at the ground floor are generally higher than at first floor: indeed, they range from about 90 to about 4200 Bq m⁻³, and for more than 25% of these rooms, radon concentrations are higher than 300 Bq m⁻³, the maximum reference level for workplaces established by the 2013/59/Euratom Council Directive.⁽¹⁾

However, as regard to the rooms at first floor, even if the radon concentration was on average lower than that at the ground floor, radon levels were higher than 300 Bq m⁻³ in about 2% of the surveyed rooms.

The impact of floor level on radon concentration is well known due to fact that generally the main entry route for radon indoor is the soil beneath the buildings,⁽⁹⁾ and it was confirmed by several data analyses being conducted in the framework of surveys in dwellings (e.g.^(10,11)) as well as in schools located in the same area.⁽¹²⁾ For a subsample of 33 buildings, described in the next paragraph, the dependence of the average radon concentration on floor level was also estimated using data of the present work.

RADON SPATIAL VARIABILITY IN SCHOOLS

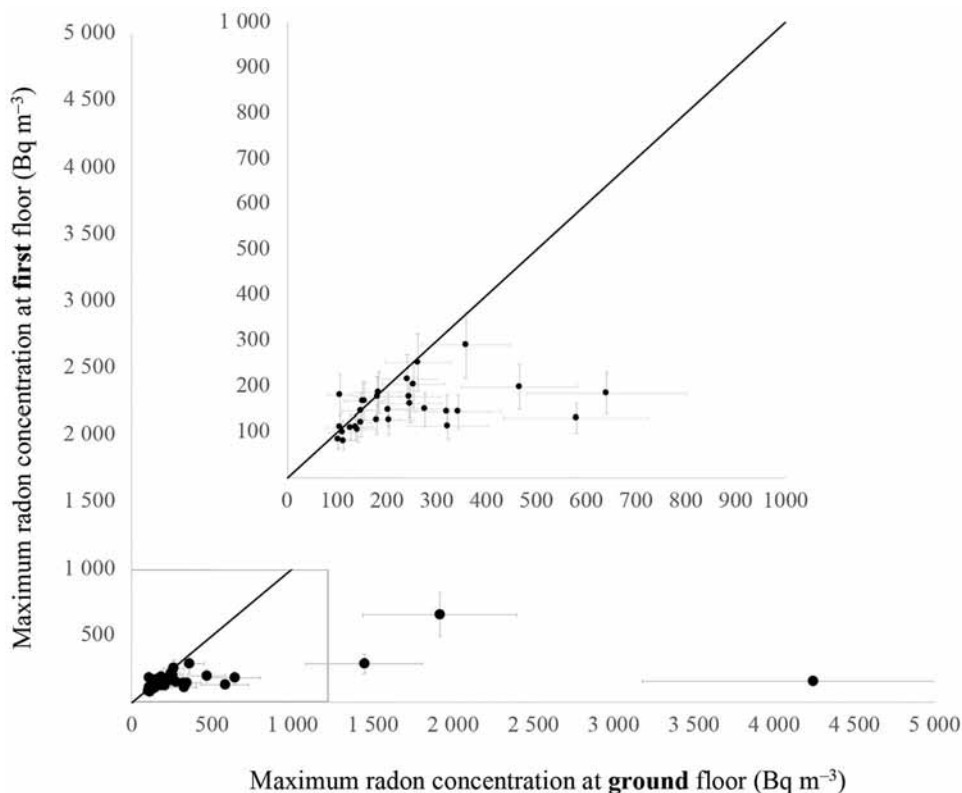


Figure 2: Maximum radon level at ground floor versus that at first floor. The reported uncertainties have a coverage factor $k = 2$. The line represents the bisecting line. The region between 0 and 1000 Bq m^{-3} was zoomed and reported in the box above.

Radon level versus floor level

For each of the 33 buildings having radon concentration measurements both in the rooms at the ground floor and at the first floor, the maximum radon level was calculated for each floor (Figure 2).

As expected, for the same building, radon levels were generally higher at the ground floor than at the first floor. Notably, if rooms with radon levels higher than 300 Bq m^{-3} (or higher than 200 Bq m^{-3}) were found at first floor, they were also found at ground floors. On the contrary, for buildings with the radon concentrations exceeding 300 Bq m^{-3} at the ground floor rooms, this concentration level was exceeded only in 1 of 10 cases at the first floor. If confirmed by further studies, this result suggests that it may be sufficient to perform measurement only in rooms located at the ground floor when verifying the compliance with reference levels for all buildings rooms. In other words, if no exceedance of RL was found in a significant number of rooms monitored at ground floor, it is very unlikely to find radon level exceeding RL at higher floors.

Moreover, it is worth noting that in case of radon surveys aimed to evaluate radon exposure of the pupils and staff of schools, it is necessary to know radon levels at every occupied floor of the buildings. Therefore, protocols used for these surveys have to include also measurements at higher floors. The number of rooms which is preferable to measure at different floors depends on the spatial variability of radon concentration at each floor.

Room-to-room spatial variability

For each building, radon spatial variability has been estimated as the coefficient of variation (CV) of radon concentration between rooms (room-to-room variability), separately for the ground and first floor rooms (Figure 3). For rooms at the ground floor, spatial variability has been estimated in 36 buildings. In 22 of them, radon levels were measured in 2 rooms; in the remaining 14 buildings, in 3 rooms. For rooms at first floor, this kind of variability was estimated in eight buildings, in each of them, measuring was done at two rooms.

RADON SPATIAL VARIABILITY IN SCHOOLS

- of an extensive survey and comparison with radon in homes.* Radiat. Prot. Dosim. **145**(2–3), 202–205 (2011).
4. Bartzis, J. *et al.* Radon Prevention and Remediation: The RADPAR Recommendations. p. 27 (2012). Available on <https://bit.ly/2s69wtC> (accessed 7 January 2020).
 5. IAEA. Design and Conduct of Indoor Radon Surveys. (Safety Report Series 98). (Vienna: IAEA) pp. 1–128 (2019). Available on <https://bit.ly/35sx4X7> (accessed 7 January 2020).
 6. Environmental Protection Agency (EPA Ireland). Protocol for the Measurement of Radon in Homes and workplaces (2016). Available on <https://bit.ly/37KkqV8> (accessed 7 January 2020).
 7. Health Canada. Guide for Radon Measurements in Public Buildings. (Ottawa: Health Canada) (2016).
 8. Caresana, M., Ferrarini, M., Garlati, L. and Paravicini, A. *Further studies on ageing and fading of CR39 PADC track detectors used as air radon concentration measurement devices.* Radiat. Meas. **46**(10), 1160–1167 (2011).
 9. World Health Organization (WHO). WHO Handbook on Indoor Radon: A Public Health Perspective. (Geneva: WHO) (2009).
 10. Demoury, C. *et al.* *A statistical evaluation of the influence of housing characteristics and geogenic radon potential on indoor radon concentrations in France.* J. Environ. Radioact. **126**, 216–225 (2013).
 11. Kropat, G. *et al.* *Major influencing factors of indoor radon concentrations in Switzerland.* J. Environ. Radioact. **129**, 7–22 (2014).
 12. Ćurguz, Z. *et al.* *Long-term measurements of radon, thoron and their airborne progeny in 25 schools in republic of Srpska.* J. Environ. Radioact. **148**, 163–169 (2015).
 13. Bochicchio, F. *et al.* *Radon in indoor air of primary schools: a systematic survey to evaluate factors affecting radon concentration levels and their variability.* Indoor Air **24**(3), 315–326 (2014).

EFFECTIVE DOSES ESTIMATED FROM THE RESULTS OF DIRECT RADON AND THORON PROGENY SENSORS (DRPS/DTPS), EXPOSED IN SELECTED REGIONS OF BALKANS

Zora S. Žunić¹, Rosaline Mishra², Igor Čeliković^{1,*}, Zdenka Stojanovska³, Ilija V. Yarmoshenko⁴, Georgy Malinovsky⁴, Nenad Veselinović¹, Ljiljana Gulan⁵, Zoran Čurguz⁶, Janja Vaupotić⁷, Predrag Ujic¹, Predrag Kolarž⁸, Gordana Milić⁵, Tibor Kovacs⁹, Balvinder K. Saprta², Norbert Kavasi¹⁰ and Sarata K. Sahoo¹⁰

¹Vinča Institute of Nuclear Sciences, University of Belgrade, 11000 Belgrade, Serbia

²Radiological Physics and Advisory Division, Bhabha Atomic Research Centre (BARC), Mumbai 400 085, India

³Faculty of Medical Sciences, Goce Delčev University, 2000 Štip, Republic of Macedonia

⁴Institute of Industrial Ecology Ural Branch of Russian Academy of Science, 620219 Ekaterinburg, Russia

⁵Faculty of Natural Sciences, University of Priština, 38220 Kosovska Mitrovica, Serbia

⁶Faculty of Transport Dobo, University of East Sarajevo, 74000 Dobo, Republic of Srpska

⁷Department of Environmental Sciences, Jožef Stefan Institute, 1000 Ljubljana, Slovenia

⁸Institute of Physics, University of Belgrade, 11080 Belgrade, Serbia

⁹Institute of Radiochemistry and Radioecology, University of Pannonia, 8201 Veszprém, Hungary

¹⁰National Institutes for Quantum and Radiological Science and Technology, National Institute of Radiological Sciences, 263-8555 Chiba, Japan

*Corresponding author: icelikovic@vin.bg.ac.rs

Received 19 December 2018; revised 5 February 2019; editorial decision 6 February 2019; accepted 12 February 2019

The main contribution to population exposure is due to radon and thoron progenies and not radon itself. The aim of this study was therefore to estimate annual effective dose using the results of Direct Radon and Thoron Progeny Sensors were exposed in 69 selected schools and 319 dwellings in several regions of Balkans: in Serbia: regions of Sokobanja and Kosovo and Metohija, Republic of Macedonia, Republic of Srpska and Slovenia. Obtained average total effective doses are in the range from 0.22 mSv a⁻¹ (schools in Republic of Srpska) to 2.5 mSv a⁻¹ (dwellings in Kosovo) and are below the reference level of 10 mSv a⁻¹ recommended by International Commission on Radiological Protection.

INTRODUCTION

Radon and its progeny contribute more than 50% of total dose that population receives from all natural sources⁽¹⁾. Based on the recent epidemiologic studies, conducted in Europe, Asia and North America, WHO has identified radon as the second cause of lung cancer after smoking, being responsible for between 3 and 14% of all lung cancers⁽²⁾.

Based on the pooled studies, a nominal risk coefficient for lung cancer of $5.9 \cdot 10^{-4}$ per WLM was recently proposed by International Commission on Radiological Protection (ICRP), which is almost double from the previous value⁽³⁾. Radon (²²²Rn) and thoron (²²⁰Rn) with half-lives of 3.82 d and 55.3 s are produced in the ²³⁸U and ²³²Th natural radioactive chains. Being a noble gas, and thus chemically inert, with half-life considerably longer than breath rate, most of radon that is inhaled is exhaled as well, rather than decaying in respiratory system. In contrast, radon short-lived progeny are

heavy metals that rapidly attach to surfaces, mainly aerosol particles. When inhaling these particles, together with progeny, they tend to stick to the epithelial tissue, where the energy released by their radioactive transformations causes radiation damage of exposed tissue. Thus, the main contribution to the population exposure is due to radon progeny and not radon itself.

Nevertheless, due to simplicity and cost effectiveness of radon measurement compared with progeny measurement, effective dose is usually estimated on the basis of measured radon concentration and an assumed equilibrium factor between radon and its progeny. The typical value of equilibrium factor for radon in indoor air is 0.4 as recommended by UNSCEAR⁽¹⁾. However, indoor measurements have shown that equilibrium factor may range from 0.1 till 0.9 and is strongly sensitive to aerosol concentration and room parameters, such as ventilation rate, humidity and surface-to-volume ratio⁽⁴⁾.



Figure 1. Regions of the study.

It is estimated by UNSCEAR that thoron in average contributes ~10% to the total exposure of radon⁽⁴⁾. However, there are regions of thoron concentrations higher than that of radon and thoron contribution to the dose should not be neglected⁽⁵⁻⁷⁾. In the case of thoron, an estimation of dose based on thoron measurements and thoron equilibrium factor (recommended value is 0.02)⁽⁴⁾ is even less reliable than the related dose estimation based on radon.

Namely, due to a short half-life of thoron, and consequently a small diffusion length, there is non-uniformity in thoron distribution in a room on one side, and uniform distribution of its ²¹²Po progeny due to its longer half-life on the other side. Therefore, even within a single dwelling there is a non-uniformity in the distribution of thoron equilibrium factor.

Any deviation of recommended radon and thoron equilibrium factors from the real ones could lead to biased estimation of radon and thoron progeny concentrations and consequently to biased estimation of doses received due to exposure to radon, thoron and their progenies. Therefore, in order to have proper estimation of received dose, it is important to measure radon and thoron progeny directly. Such detectors, known as 'Direct Thoron Progeny Sensor' and 'Direct Radon Progeny Sensor' (DTPS/DRPS) have

been developed by Mishra and Mayya^(8, 9) and are designed to measure time-averaged equilibrium equivalent thoron concentration and equilibrium equivalent radon concentration.

The aim of this study is to estimate effective doses due to the exposure to radon and thoron progeny based on the long term measurements using DTPS/DRPS sensors. Measurements were performed in selected dwellings and school in several regions of Balkans, within the framework of a broad international collaboration.

MATERIALS AND METHODS

The investigated area encompassed several regions of Balkans. In total, 388 different locations were analysed using DTPS/DRPS detectors, covering 122 dwellings in the region of Sokobanja, Serbia⁽¹⁰⁾, 48 dwellings in Kosovo and Metohija⁽¹¹⁾, 44 schools in Republic of Macedonia⁽¹²⁾, 37 dwellings and 25 schools in Republic of Srpska⁽¹³⁾ and 112 dwellings in Slovenia⁽¹⁴⁾. A map showing investigated regions is in Figure 1.

Direct measurements of radon and thoron progenies were performed using LR115 Type II solid state nuclear track detectors with thin absorber foil of appropriate thickness. Due to a different energy

Table 1. Range and average of annual effective dose E_{Rn} and E_{Tn} due to exposure to radon and thoron progeny in selected regions of Balkans.

Location number of measurements and place	E_{Rn} (mSv a ⁻¹) range, R average, AV	E_{Tn} (mSv a ⁻¹) range, R average, AV
Serbia, Sokobanja 122 dwellings	R: 0.25–1.0 AV: 0.7	R: 0.04–0.9 AV: 0.28
Republic of Srpska 37 dwellings	R: 0.4–0.9 AV: 0.6	R: 0.03–0.3 AV: 0.13
Kosovo and Metohija 48 dwellings	R: 0.4–6.8 AV: 2.1	R: 0.2–1.1 AV: 0.4
Slovenia 112 dwellings	R: 0.1–9.4 AV: 2.2	R: 0.004–0.7 AV: 0.18
Republic of Srpska 25 schools	R: 0.1–0.27 AV: 0.18	R: 0.006–0.08 AV: 0.036
Republic of Macedonia 44 schools	R: 0.13–0.91 AV: 0.45	R: 0.006–0.43 AV: 0.08

emitted by α -radioactive decay of ^{212}Po (8.78 MeV) and ^{214}Po (7.69 MeV), a 50- μm thick absorber foil (aluminium Mylar) was chosen to detect separately α -particles emitted by ^{212}Po decay on the first LR115 detector. On the other LR115 detector, a thinner, 25- μm aluminium Mylar foil was mounted, enabling detection of α -particles from decay of both, ^{212}Po and ^{214}Po . Based on the track density on both detectors, it is possible to distinguish between the radon and thoron progeny concentrations. The procedure has been elaborated in detail by Mishra and Mayya^(8, 9).

Radon and thoron detectors at all locations were placed far away from windows and doors, but at variable distances from the wall: in Republic of Macedonia and Kosovo and Metohija detectors were placed in the middle of the room, in Republic of Srpska and in Slovenia around 20 cm from the wall, while in Sokobanja, Serbia detectors were placed directly on the wall. For radon and thoron progeny, it is assumed uniform distribution in a room.

Detectors were deployed from 3 months up to 1 y in the period from 2011 to 2013. In some dwellings detectors were deployed two times for 6 months, covering therefore a whole year, and in cases where some of the measurements were missing, seasonal corrections were applied. Due to large variations of progeny concentration in time, averaging equilibrium equivalent radon or thoron concentrations over the year is important for the proper estimation of received dose.

The annual effective dose due to exposure to radon progeny is estimated using the following expression given by UNSCEAR⁽¹⁾:

$$E_{Rn} (\text{mSv a}^{-1}) = \text{EERC} \cdot \text{OF} \cdot \text{DCF}_{Rn} \cdot 10^{-6} \quad (1)$$

where E_{Rn} is the annual effective dose (mSv a⁻¹), EERC is the equilibrium equivalent radon concentration (Bq m⁻³), OF is the occupancy factor (for inhabitants recommended value is 7000 h a⁻¹, while for pupils occupancy was assumed to be 1750 h a⁻¹), and DCF_{Rn} is radon dose conversion factor 9 (nSv h⁻¹ per Bq m⁻³). Additional factor of 10⁻⁶ is necessary to convert nSv to mSv.

Similarly, the annual effective dose due to exposure to thoron progenies (E_{Tn}) is⁽⁴⁾:

$$E_{Tn} (\text{mSv a}^{-1}) = \text{EETC} \cdot \text{OF} \cdot \text{DCF}_{Tn} \cdot 10^{-6} \quad (2)$$

where EETC is the equilibrium equivalent thoron concentration (Bq m⁻³), and DCF_{Tn} is thoron dose conversion factor 40 (nSv h⁻¹ per Bq m⁻³).

RESULTS

For each measurement location, a total number of measuring points for either dwellings or schools, together with the range and average annual effective dose, due to exposure to radon and thoron progeny, is given in Table 1.

Average annual effective doses range from 0.18 mSv a⁻¹ (Republic of Srpska, schools) to 2.2 mSv a⁻¹ (Slovenia, dwellings) for radon and from 0.036 mSv a⁻¹ (Republic of Srpska, schools) to 0.4 mSv a⁻¹ (Kosovo and Metohija, dwellings) for thoron.

Average total effective doses in these regions, due to exposure to indoor radon and thoron, estimated using direct measurements of radon and thoron progeny concentrations, are in the range from 0.22 mSv a⁻¹ (schools in Republic of Srpska) to 2.5 mSv a⁻¹ (dwellings in Kosovo I Metohija).

CONCLUSION

The data show a broad distribution of results obtained with DRPS and DTPS detectors deployed in the regions of investigation, within the framework of an extensive international collaboration. Average effective doses are below the ICRP 103⁽¹⁵⁾ reference level of 10 mSv a⁻¹ for the indoor radon exposure. Although the estimated doses are not extremely high, indoor radon may be considered as the most significant single source of radiation exposure to the population in the region.

ACKNOWLEDGEMENTS

Authors would like to acknowledge financial support of Ministry of Education, Science and Technological

Development of the Republic of Serbia under the projects: 171019 and 41028, and from the Slovenian Research Agency (research core funding No. P1-0143).

REFERENCES

1. UNSCEAR (United Nation Scientific Committee on the Effects of Atomic Radiation Report). *Annex B: Exposure due to Natural Radiation Sources*. Vol. 1, (New York: United Nation) (2000).
2. Health Organisation. *WHO Handbook on Indoor Radon* (Geneva: WHO) (2009).
3. Tirmarche, M., Harrison, J. D., Laurier, D., Paquet, F., Blanchardon, E. and Marsh, J. W., ICRP (International Commission on Radiological Protection). *ICRP Publication 115. Lung cancer risk from radon and progeny and statement on radon*. Ann. ICRP **40**(1), 1–64 (2010). doi:10.1016/j.icrp.2011.08.011.
4. UNSCEAR (United Nation Scientific Committee on the Effects of Atomic Radiation Report). *Vol. II: Sources-to-Effects Assessment for Radon in Homes and Workplaces* (New York: United Nation Scientific Committee on the Effects of Atomic Radiation) (2006).
5. Ramola, R. C. et al. *Levels of thoron and progeny in high background radiation area of southeastern coast of Odisha, India*. Radiat. Prot. Dosim. **152**, 62–65 (2012). doi:10.1093/rpd/ncs188.
6. Kudo, H. et al. *Comparative dosimetry for radon and thoron in high background radiation areas in China*. Radiat. Prot. Dosim. **167**, 155–159 (2015). doi:10.1093/rpd/ncv235.
7. Zunic, Z. S. et al. *Collaborative investigations on thoron and radon in some rural communities of Balkans*. Radiat. Prot. Dosim. **141**(4), 346–350 (2010). doi:10.1093/rpd/ncq258.
8. Mishra, R. and Mayya, Y. S. *Study of a deposition-based direct thoron progeny sensor (DTPS) technique for estimating equilibrium equivalent thoron concentration (EETC) in indoor environment*. Radiat. Meas. **43**, 1408–1416 (2008). doi:10.1016/j.radmeas.2008.03.002.
9. Mishra, R., Mayya, Y. S. and Kushwaha, H. S. *Measurement of $^{220}\text{Rn}/^{222}\text{Rn}$ progeny deposition velocities on surfaces and their comparison with theoretical models*. J. Aerosol Sci. **40**, 1–15 (2009). doi:10.1016/j.jaerosci.2008.08.001.
10. Zunic, Z. S. et al. *Indoor radon, thoron and their progeny concentrations in high thoron rural serbia environments*. Radiat. Prot. Dosim. **177**(1,2), 36–39 (2017). doi:10.1093/rpd/ncx167.
11. Gulan, L. et al. *Field experience on indoor radon, thoron and their progenies with solid-state detectors in a survey of Kosovo and Metohija (Balkan region)*. Radiat. Prot. Dosim. **152**(1–3), 189–197 (2012). doi:10.1093/rpd/ncs221.
12. Stojanovska, Z. et al. *Results from time integrated measurements of indoor radon, thoron and their decay product concentrations in schools in the Republic of Macedonia*. Radiat. Prot. Dosim. **162**(1–2), 152–156 (2014). doi:10.1093/rpd/ncu249.
13. Curguz, Z. et al. *Long-term measurements of radon, thoron and their airborne progeny in 25 schools in Republic of Srpska*. J. Environ. Radioact. **148**, 163–169 (2015). doi:10.1016/j.jenvrad.2015.06.026.
14. Vaupotič, J., Gregorič, A., Leban, M., Bezek, M., Žvab Rožič, P., Zmazek, B. and Kobal, I. *Radon survey within a regular grid in homes in Slovenia. VII. Hungarian Radon Forum and Radon and Environment Satellite Workshop (Veszprém, Hungary: Pannonian University Press) pp. 195–200* (2013).
15. ICRP (International Commission on Radiological Protection). *The 2007 Recommendations of the International Commission on Radiological Protection ICRP Publication 103*. Ann. ICRP **37**, 1–332 (2007).

AD-HOC INTERCOMPARISON OF FOUR DIFFERENT RADON EXHALATION MEASUREMENT METHODS

A. Awhida¹, P. Ujic^{2,*}, G. Pantelić², P. Kolarž³, I. Čeliković², M. Živanović², A. Jančićević¹ and B. Lončar¹

¹Faculty of Technology and Metallurgy, University of Belgrade, 11000 Belgrade, Karnegijeva 4, Serbia

²Institute of Nuclear Sciences ‘Vinča’, University of Belgrade, PO Box 522, 11001 Belgrade, Serbia

³Institute of Physics Belgrade, University of Belgrade, Pregrevica 118, 11080 Zemun, Serbia

*Corresponding author: ujic@vin.bg.ac.rs

Received 24 April 2017; revised 28 June 2017; editorial decision 29 June 2017; accepted 4 July 2017

It is indicated that the exposure to radon originating from the building materials is not negligible and the radon exhalation measurement should get more attention in the future. The experience with four different methods of the exhalation measurement, established in our laboratory for the purpose of the intercomparison is reported. Additionally, a comparison of advantages and disadvantages of used methods is discussed.

INTRODUCTION

Radon is the greatest source of the public exposure to radiation, as more than 50% of the radiation dose received by the general population is due to the exposure to radon. According to World Health Organisation (WHO)⁽¹⁾ radon is responsible for between 3 and 14% of the lung cancer incidences. The main contributor to the indoor radon concentration is the soil and the second important contributor is the building material⁽²⁾.

External radiation exposure of inhabitants to the radionuclides in building materials is regulated in the most of countries. The internal exposure to the radon originating from the building materials is regulated indirectly. In principle it was assumed that the radon exhalation is proportional to the radium content. This approach is very crude and basically misguided, since the exhalation rate strongly depends on the emanation coefficient and somewhat less strongly on the radon diffusion length in the material. It is indicated that the internal dose due to the exposure to radon exhaled from the building material could be higher than the external dose due to the radium content in the building material⁽³⁾. Furthermore, due to the energy saving policy and more tight windows and doors the average ventilation rate of indoor air decreases, increasing the radon concentration even in multi-storey buildings⁽⁴⁾, which indicates importance of the radon exhalation measurement, since the radon in multi-storey buildings originates almost exclusively from the building materials.

Within the ERRICCA framework⁽⁵⁾ a comparison of radon exhalation measurements was performed between 20 participants from 13 countries. In this publication the experience with four different methods is reported. All the methods were established ad-hoc,

within the same laboratory in order to directly compare their advantages and disadvantages.

METHODS

In this section, a brief review of the methods used in this intercomparison is presented. One cylindrically shaped sample of 7.1 cm diameter and 12 cm height was used as the reference sample for the measurement methods performed for this publication. The sample was prepared by ‘mixing’ the travertine in Niška Banja, known for a high radium concentration, with the cement and sand. The accumulation chamber method is performed with the Solid State Nuclear Track Detector (SSNTD) and the active instrument simultaneously. Dimensions of the accumulation chamber are $0.263 \times 0.263 \times 0.424 \text{ m}^3$.

Accumulation chamber with an active instrument method

This method is widely used radon exhalation method and probably the most convenient one. When a sample is put in the sealed accumulation chamber, radon will exhale from the sample and it will accumulate in the chamber where it will eventually decay or escape if the chamber is not sufficiently tight. If the sample volume is not significantly smaller than the chamber volume (at least 10%), there is a significant probability that the radon atom, due to the diffusion, will return back into the sample. This is called the back diffusion.

The exhalation measurements using accumulation chamber with an active instrument and the SSNTD (see [Accumulation chamber with SSNTD method](#)) were performed partially simultaneously. The measurements started at the same time and lasted for

7 days, in the case of the measurement with the active instrument. This measurement was conducted using the RAD7 of DurrIDGE Radon Instrumentation, calibrated in 2015, in National Institute for NBC Protection, Czech Republic.

The radon concentration $C(t)$ (Bq m^{-3}) inside an accumulation chamber is described by the following expression⁽⁶⁾:

$$C(t) = \frac{EA}{V\lambda_{\text{eff}}}(1 - e^{-\lambda_{\text{eff}}t}) + C_0 e^{-\lambda_{\text{eff}}t} \quad (1)$$

where E ($\text{Bq m}^{-2} \text{s}^{-1}$) is the radon exhalation rate of the sample, A (m^2) is the surface area of the sample, V (m^3) is the volume of the accumulation chamber; t (s) is the time of exposure, C_0 is the initial radon concentration in the chamber and λ_{eff} (s^{-1}) is the effective radon removal probability defined as follows:

$$\lambda_{\text{eff}} = \lambda + \lambda_l + \lambda_b \quad (2)$$

where λ is the decay constant of ^{222}Rn , λ_l is the leakage probability and λ_b is the back diffusion probability. Since the sample volume is significantly smaller than the volume of the accumulation chamber the back diffusion can be neglected. C_0 is not considered since it was negligible. Diffusion of the radon from the outside air into the accumulation chamber is also neglected since the radon concentration in the outside air is two orders of magnitude smaller than the concentration inside the chamber.

Sometimes the exhalation measurement is performed only using the linear part of the accumulating radon concentration when the exhalation rate can be approximated as follows:

$$E = \frac{bV}{A} \quad (3)$$

where b ($\text{Bq m}^{-3} \text{s}^{-1}$) is the fitted slope of the first part of the concentration curve, up to 1800 min of measurement for which the linear approximation of the exponential function is applicable.

Accumulation chamber with SSNTD method

The exhalation rate of radon, measured by the accumulation chamber with the SSNTD is basically an integral measurement of the accumulation chamber, could be estimated by the following equation⁽³⁾:

$$E = \frac{\rho_s V \lambda_{\text{eff}}}{kA} \frac{1}{t - \frac{1}{\lambda_{\text{eff}}}(1 - e^{-\lambda_{\text{eff}}t})} \quad (4)$$

If the initial radon concentration C_0 is present exhalation is estimated as follows:

$$E = \frac{V\lambda_{\text{eff}}}{A} \frac{1}{t - \frac{1}{\lambda_{\text{eff}}}(1 - e^{-\lambda_{\text{eff}}t})} \left[\frac{\rho_s}{k} - \frac{C_0}{\lambda_{\text{eff}}}(1 - e^{-\lambda_{\text{eff}}t}) \right] \quad (5)$$

where ρ_s (m^{-2}) is the track density on the SSNTD; k ($(\text{m}^{-2})/(\text{Bq s m}^{-3})$) is the calibration coefficient for the detector. The factor ρ_s/k presents the exposure (sometimes referred as a dose) of the SSNTD. Since the C_0 cannot be determined in the SSNTD method, it is necessary to eliminate the radon in the moment when the accumulation chamber is sealed. The measurement used for intercomparison was performed with the Landauer Radtrack²[®] SSNTD and it lasted for 37 days.

Gamma method

This is the most recently proposed radon exhalation measurement method. It is described in details by Awhida *et al.*⁽⁷⁾ The mathematical procedure of this method is rather complicated to be shortly described in this section, thus only the principles are given. When a cylindrical sample is open on either top or bottom side the radon concentration will have a gradient with lower concentration towards the open surface (Figure 1). The gradient depends on the radon diffusion length and the radon emanation coefficient in the given material. Nevertheless, with two measurements: first from the open side of the sample and

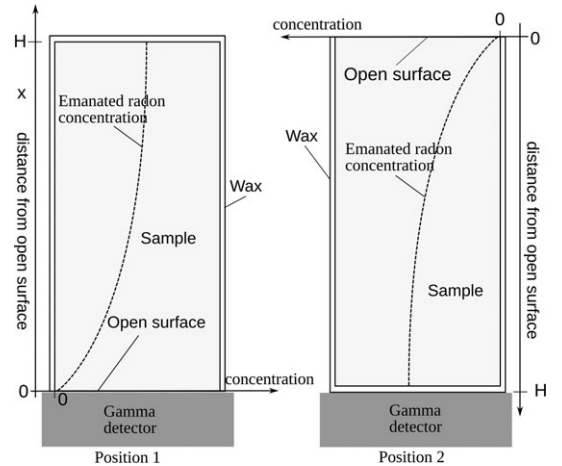


Figure 1. The principles of the gamma method (Awhida *et al.*, 2016). The detector will measure different concentrations depending on whether it measures from the open or the sealed side of the sample. The difference depends on the emanation coefficient and the diffusion length, which could be estimated from these two measurements.

second from the sealed side of the sample, it is possible to determine both radon diffusion length, L (m), the radon emanation coefficient ε and the ^{226}Ra content C_{Ra} (Bq kg^{-1}) which allows to estimate the exhalation rate:

$$E = \lambda L C_{Ra} \rho \varepsilon \tanh(H/L) \quad (6)$$

where λ is the decay constant of the radon, ρ (kg m^{-3}) is the density of the sample and H (m) is its height.

The gamma method measurement was performed with HPGe detector AMETEK-AMT (Ortec) GEM 30–70 with relative efficiency of 37% and the energy range between 50 keV and 3 MeV. The energy and efficiency calibration of the spectrometer was conducted using a certified mixed gamma source.

Charcoal canister method

Radon concentration measurements by charcoal canisters are often performed according to EPA 520/5-87-005, David J. Grey, Sam T. Windham, 1987, EERF Standard Operating Procedures for Radon-222 Measurement Using Charcoal Canisters. The following gamma lines of radon progeny are used for the measurements: 295 KeV (^{214}Pb), 352 keV (^{214}Pb) and 609 keV (^{214}Bi). In the standard indoor radon measurement, the canister is exposed during 2–6 days and then measured on the gamma detector, where the quantity of the adsorbed radon is measured. The details of this method are given elsewhere^(8, 9). This method is also used for the measurement of the radon exhalation rate from soil⁽¹⁰⁾.

The radon concentration C_r (Bq m^{-3}) is estimated using the following expression:

$$C_r = \frac{G - B}{t E_f C_f D_f}, \quad (7)$$

where G is the total area of the three previously mentioned peaks, B is the total area of the background of the three mentioned peaks, t is the detector exposure time, E_f is the detector efficiency and C_f is the calibration factor of the radon adsorption rate on the charcoal. C_f strongly depends on the humidity. The correction factor of the radon decay during the exposure, D_f is approximated as follows:

$$D_f = e^{-\frac{0.693 t_s}{T_{1/2}}} \quad (8)$$

where t_s (s) is the mid-time of between the start of the detector exposure and the start of the measurement and $T_{1/2}$ (s) is the radon half-life.

E_f is obtained from the efficiency calibration of spectrometry system. The product $C_r \cdot C_f$ is effectively a radon adsorption flux or in other words the flux of radon which is going to be adsorbed by the charcoal.

The method of the radon exhalation measurement with charcoal canisters is based on the fact that the activated coal in the charcoal canister absorbs virtually all the radon atoms which enter into the canister. In that case the radon adsorption flux $C_r \cdot C_f$ is equal to the total exhalation rate E_r .

Thus, there is not much sense to put a charcoal canister in the accumulation chamber. Instead, the charcoal canister can be attached directly to the surface of the sample whose radon exhalation rate is measured. It should be attached tightly in order to prevent radon to escape.

$$E_t = \frac{G - B}{t E_f D_f} \quad (9)$$

However, in order to obtain surface exhalation rate E_r , E_t has to be divided by the exhaling surface area A of the sample:

$$E = \frac{G - B}{t E_f D_f A} \quad (10)$$

RESULTS AND INTERCOMPARISON OF METHODS

The comparison of the measurements is shown in Table 1 and Figure 2. It could be noticed that, although the results are in relatively good agreement, there is a certain discrepancy of the results, higher than expected regarding the measurement uncertainties. This implies that there exists a variation of the exhalation rate and/or the uncertainty of the measurement is underestimated. It is certain that two parameters, which were not controlled, could influence the exhalation: the humidity and the atmospheric pressure variation.

The charcoal canisters used in this method have a relatively high MDA of $\sim 12 \text{ Bq m}^{-3}$, which corresponds to an exhalation rate of $\sim 0.002 \text{ Bq s}^{-1} \text{ m}^{-2}$, however, this could be improved for at least one

Table 1. The results of the exhalation rate measurement from the same sample.

	Exhalation ($\text{Bq s}^{-1} \text{ m}^{-2}$)	Uncertainty ($\text{Bq s}^{-1} \text{ m}^{-2}$)
Charcoal	0.028	0.004 ^a
SSNTD	0.035	0.002
Active long	0.0320	0.0003
Active short	0.0293	0.0003
Gamma	0.0326	0.0014

^aThe measurement duration was short (few thousand seconds).

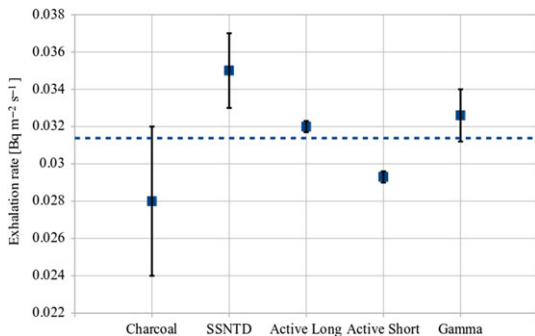


Figure 2. Graphical presentation of the results of the exhalation rate measurement of the same sample. The dashed line presents a mean value (not weighted).

order of magnitude, by longer exposure period and longer gamma spectrometric measurement. It could be noticed that the measurement uncertainty is the highest for the charcoal method, however, the duration of this measurement was far shorter than for the other methods, thus this uncertainty could be lowered by at least five times. Nevertheless, this method has a potential to be used for *in situ* measurements, i.e. the charcoal canister may be attached directly to the inside wall of a building. Compared to the active method, it offers much more comfort to the inhabitants due to the fact that it is less cumbersome and it does not produce noise. In principle, *in situ* measurements could be made more sensitive by an adjustment which would allow to collect the exhaling radon from wider area of the wall.

Essentially, measurements with active instruments are very convenient and simple. In comparison with the SSNTD method, it is also possible to make corrections regarding the leakage of the accumulation chamber. The flaw of this method is in the fact that use of some of these instruments cannot be applied in the moisture controlled regime since these instruments (like RAD7) are constantly drying the air using a silica gel. The fit curve of radon concentration is shown in Figure 3.

An advantage of the SSNTD method is the higher sensitivity or lower minimum detectable exhalation rate (MDER), since this detector is measuring integral dose which allows to measure lower radon concentrations. This also depends on the type of the diffusion chamber for the SSNTD which can significantly lower the MDER. In comparison to the measurement with the active instrument, the measurement with the SSNTD cannot be corrected regarding the accumulation chamber leakage and the leakage of the accumulation chamber was measured prior to the radon exhalation measurement and it was found that the leakage coefficient can vary for $\sim 50\%$. The estimated

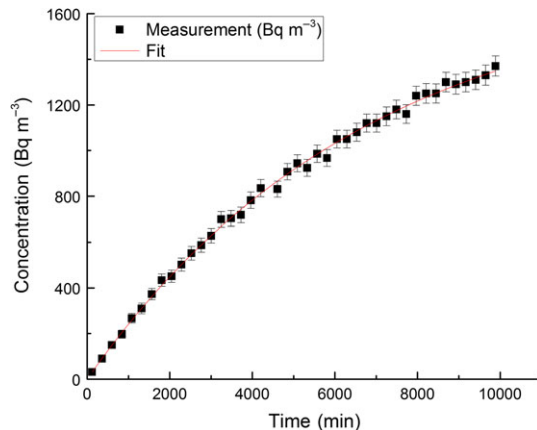


Figure 3. Radon concentration in the accumulation chamber measured by the RAD7.

exposure was $1540 \pm 100 \text{ kBq h m}^{-3}$ and the exhalation rate was $E = 0.035 \pm 0.002 \text{ Bq s}^{-1} \text{ m}^{-2}$ with the previously estimated $\lambda_l = 2.4 \times 10^{-7} \text{ s}^{-1}$. Effectively, when the λ_l is significantly smaller than the decay constant its instability does not influence significantly the exhalation rate estimation and in this measurement it just slightly increased the uncertainty of the measurement. However, for the SSNTD method, the leakage is still uncontrollable, in a sense that it could be much more significant and the laboratory personnel would not be aware of this problem.

Thus, this method is effectively applicable only if the radon leakage from the accumulation chamber is not significant. For the presented result the leakage coefficient estimated during the simultaneous measurement by the SSNTD and the RAD7 is used. Furthermore, SSNTD method cannot show if the measurement started with a certain background radon concentration in the accumulation chamber. Both methods with the accumulation chamber, active and SSNTD method, require a longer measurement, although, the sample preparation is in principle very short.

The gamma method is a unique radon exhalation measurement method since it provides the measurement of the radon diffusion length and the emanation coefficient, which is a main advantage of this method. The estimated radon exhalation rate by the gamma method was $0.0326 \pm 0.0014 \text{ Bq s}^{-1} \text{ m}^{-2}$, while the radon diffusion length was $0.31 \pm 0.03 \text{ m}$ and the emanation coefficient 0.45 ± 0.02 . The disadvantage of this method is a more complicated calculus and a longer sample preparation, since the equilibrium between the radon and its progeny must be attained.

Both the gamma and the charcoal methods do not need radon measurement equipment for the radon

Table 2. Tabular comparison of advantages and disadvantages of the exhalation measurement performed in this intercomparison.

	<i>In situ</i>	MDER	Meas. duration	Measures L, ϵ	Price	Precision	Chamber leakage	Moisture control	Background radon correction
Charcoal	+	– ^a	+	–	+ ^b	–	NR	+	–
SSNTD	–	+	–	–	–	–	–	+	–
Active	+	+	+	–	–	+	+	–/+	+
Gamma	–	–	– ^c	+	+ ^b	–	NR	+	+

NR, not relevant; L , radon diffusion length; ϵ , emanation coefficient; MDER, minimum detectable exhalation rate.

^aIt is possible to improve it, principally for *in situ* measurement.

^bUnder the assumption that a laboratory already has a gamma detector.

^cThe sample preparation included, otherwise the measurement is short.

exhalation measurements and they are convenient for the laboratories which already have a gamma detector.

CONCLUSION

A simplified comparison of four exhalation measurement methods is given in Table 2. The plus sign is marking an advantage. For instance, the plus sign for the price means that it has a lower price.

The choice of a method depends on different factors. For establishing a new method in a laboratory, it seems that the accumulation chamber with an active instrument is the most convenient. The charcoal canister method is simple, not expensive and offers a possibility of *in situ* measurements. The SSNTD method seems to be the least advantageous; however, it is a quite robust and reliable method. Gamma method is probably the most complicated method, however, it is the only one which provides the emanation coefficient and the radon diffusion length which is also important regarding the protective attributes of a building material regarding radon.

ACKNOWLEDGEMENTS

This work was supported by the Ministry of Education, Science and Technological Development of the Republic of Serbia [P171018, P171007, III43009].

REFERENCES

1. World Health Organisation. WHO Handbook on Indoor Radon: A Public Health (Geneva: Perspective WHO Press) (2009).
2. Cosma, C., Cucuș-Dinu, A., Papp, B., Begy, R. and Sainz, C. *Soil and building material as main sources of indoor radon in Băița-Ștei radon prone area (Romania)*. J. Environ. Radioact. **116**, 174–179 (2013).
3. Ujić, P., Čeliković, I., Kandić, A., Vukanac, I., Đurašević, M., Dragosavac, D. and Žunić, Z. *S. Internal exposure from building materials exhaling ²²²Rn and ²²⁰Rn as compared to external exposure due to their natural radioactivity content*. Appl. Radiat. Isot. **68**, 201–206 (2010).
4. Yarmoshenko, I. V., Vasilyev, A. V., Onishchenko, A. D., Kiselev, S. M. and Zhukovsky, M. V. *Indoor radon problem in energy efficient multi-storey buildings*. Radiat. Prot. Dosim. **160**, 53–56 (2014).
5. Petropoulos, N. P., Anagnostakis, M. J. and Simopoulos, S. E. *Building materials radon exhalation rate: ERRICCA intercomparison exercise results*. Sci. Total Environ. **272**, 109–118 (2001).
6. Ujić, P., Čeliković, I., Kandić, A. and Žunić, Z. *Standardization and difficulties of the thoron exhalation rate measurements using an accumulation chamber*. Radiat. Meas. **43**, 1396–1401 (2008).
7. Awhida, A., Ujić, P., Vukanac, I., Đurašević, M., Kandić, A., Čeliković, I., Lončar, B. and Kolarž, P. *Novel method of measurement of radon exhalation from building materials*. J. Environ. Radioact. **164**, 337–343 (2016).
8. Pantelić, G., Eremić-Savković, M., Živanović, M., Nikolić, J., Rajačić, M. and Todorović, D. *Uncertainty evaluation in radon concentration measurement using charcoal canister*. Appl. Radiat. Isot. **87**, 452–455 (2014).
9. Živanović, M. Z., Pantelić, G. K., Krneta Nikolić, J. D., Rajačić, M. M. and Todorović, D. J. *Radon measurements with charcoal canisters: temperature and humidity considerations*. Nucl. Technol. Radiat. Prot. **31**, 65–72 (2016).
10. Iimoto, T., Akasaka, Y., Koike, Y. and Kosako, T. *Development of a technique for the measurement of the radon exhalation rate using an activated charcoal collector*. J. Environ. Radioact. **99**, 587–595 (2008).

ORIGINAL ARTICLE

Open Access



Does waterfall aerosol influence mucosal immunity and chronic stress? A randomized controlled clinical trial

Carina Grafetstätter^{1†}, Martin Gaisberger^{2,3,4†}, Johanna Prosegger¹, Markus Ritter^{2,3,4}, Predrag Kolarž⁵, Christina Pichler¹, Josef Thalhammer⁶ and Arnulf Hartl^{1*} 

Abstract

Background: The specific microclimate of alpine waterfalls with high levels of ionized water aerosols has been suggested to trigger beneficial immunological and psychological effects. In the present three-armed randomized controlled clinical study, we focused on effects on (i) immunological reactivity, on (ii) physiological stress responses, and on (iii) stress-related psychological parameters.

Methods: People with moderate to high stress levels ($n = 65$) spent an active sojourn with daily hiking tours in the National Park Hohe Tauern (Großkirchheim, Austria). Half of the group was exposed to water aerosol of an alpine waterfall for 1 h/day (first arm, $n = 33$), whereas the other half spent the same time at a distant site (second arm, $n = 32$). A third arm (control, $n = 26$) had no intervention (except vaccination) and stayed at home, maintaining their usual lifestyle. The effect of the interventions on the immune system was tested by oral vaccination with an approved cholera vaccine and measuring specific salivary IgA antibody titers. Lung function was determined by peak expiratory flow measurement. Electric skin conductance, heart rate, and adaptation of respiration rate were assessed as physiological stress parameters. Psychological stress-related parameters were analyzed by questionnaires and scales.

Results: Compared to the control group, both intervention groups showed improvement of the lung function and of most physiological stress test parameters. Analysis of the mucosal immune response revealed a waterfall-specific beneficial effect with elevated IgA titers in the waterfall group. In line with these results, exposure to waterfall revealed an additional benefit concerning psychological parameters such as subjective stress perception (measured via visual analog scale), the Global Severity Index (GSI), and the Positive Symptom Total (PST).

Conclusions: Our study provides new data, which strongly support an “added value” of exposure to waterfall microclimate when combined with a therapeutic sojourn at high altitude including regular physical activity.

Keywords: Ionized water aerosol, Waterfall, High-altitude climate therapy, Chronic stress, Green exercise, Burnout prevention, Mucosal immune response, Mountain hiking, Alpine space

* Correspondence: arnulf.hartl@pmu.ac.at

†Equal contributors

¹Institute of Ecomedicine, Paracelsus Medical University, Strubergasse 22, 5020 Salzburg, Austria

Full list of author information is available at the end of the article



Introduction

Therapies at high altitude and green exercise are known to affect a variety of physiological and immunological parameters. These include neurovegetative, cardiovascular or thermoregulation mechanisms [1, 2], and also the reduction of inflammatory diseases, and the induction of balancing immunomodulatory effects [3–5].

High-altitude climate therapy is also characterized as a successful alternative medical treatment for respiratory and allergic diseases such as bronchial asthma, atopic dermatitis, psoriasis, or eczema [6–8].

In addition to high altitude, European alpine regions host numerous waterfalls, which produce inhalable, negatively charged nano-water particles known as “Lenard ions” or ballo-electric ions. Negative air ions nearby waterfalls (hereinafter we call them “ionosols”) are generated by aerosolization of water droplets at an obstacle, aqueous surface, or by aerodynamic break-up during free fall, undergoing charge redistribution forming “water bags” with negatively charged surfaces and fracturing into micro-bubbles due to water shearing. After breaking up, smaller fragments carry negative charge and remain in the air for some time carried by air stream. Their diameter is between 1.5 and 10 nm, whereby 2-nm-sized negative ions were the most abundant. Lifetime of ionosols is long enough so that they can be inhaled. The remaining bigger fragments are positive and precipitate to the ground [9, 10].

“Negative air ions” are positively correlated with relative humidity and their concentration is higher in natural environments compared in urban environment [11–14]. Waterfalls not only produce high levels of negative air ions, they also create a specific microbiological atmosphere by spreading of microbes in the impact zone of a waterfall, which may influence immunological and physiological parameters. Negative air ions also interact with phytoncides released from trees which in turn can interact with microbes, altogether influencing the environmental atmosphere [14]. Phytoncides may also act directly on the innate immune system, as they have been shown to increase the level of natural killer cells [15].

Positive immunomodulating effects of the microclimate in close proximity to the impact zone of alpine waterfalls have already proven beneficial effects for the treatment of allergic asthma [16]. In this previous study, half of a group of asthmatic allergic children ($n = 54$) was exposed to water aerosol of an alpine waterfall for 1 h/day over 3 weeks, whereas the other half spent this hour at a water aerosol free control site. The exposure to water aerosol had a long-lasting beneficial effect on asthma symptoms and lung function, accompanied by a decreased inflammatory immune status as indicated by elevated levels of IL-10 and regulatory T cells.

Mechanisms underlying the immunomodulatory effect of high altitude include the normalization of eosinophil levels, balancing of the TH2/Treg cell ratio, increase of regulatory cytokines (e.g., IL-10), and even alteration of immunoglobulin class switching [3, 4, 16, 17]. Furthermore, alterations of adrenocorticotrophic hormone (ACTH) and glucocorticoid secretion indicate that high altitude affects both neuronal as well as immune circuits [1]. Negative air ions are also associated with psychological well-being, e.g., due to an increased serotonin level [18]. Considering, it is conceivable that high-altitude climate may also affect stress and its pathologic immunological, physiological, and psychical consequences. Stress is known to induce endocrine changes via mediators such as glucocorticoid hormones and catecholamines and thus also to influence humoral and cellular immunity [19]. In a well-balanced but fragile molecular and cellular network, the immune, endocrine, and nervous system affect cognitive performance, well-being, and behavior, and, in general, also maintain health [20, 21]. For example, people with high occupational stress, like caregivers, show impaired specific and unspecific immune responses, both concerning humoral and cellular immunity [22, 23], and chronic stress is associated with a shift from a TH1 to a more TH2-type immune response cytokine pattern [24]. Similar T cell response types are also observed in the development of asthma, which is not only influenced by stress, anxiety, and depression but also affected by the microbiome [25]. Also, mucosal immune responses show a clear correlation with stress. As a consequence of chronic stress, the abundance of salivary IgA is decreased [26–29], and even more subtle psychological parameters (like disgruntlement) seem to influence salivary IgA levels [30–32]. As secretory IgA is present in all mucosal surfaces, it is of crucial importance for the first line of defense of the immune system [33, 34]. Therefore, monitoring specific antibodies in a workload situation, e.g., during a vaccine-induced immune response, represents a suitable model to estimate the immune status of an individual. Several studies demonstrate the strong impact of psychological stress on a developing humoral response, e.g., chronic burden (like nursing care of a sick member of the family) interferes with the humoral immune response to an influenza vaccination [33, 35–39].

Typical and useful physiological parameters indicative for stress and emotional strain are peripheral physiological signals such as electric skin conductance (SC), respiration rate (RSP), and heart rate (HR), all being measurable in response to an artificial stressor [40–42]. The conductance of the skin is dependent of the quantity of sweat, which is controlled by the sympathetic nervous system and positively correlates with stress. Also, respiration reflects the psychological and emotional state, e.g., in relaxed situations, respiration is slow and

regular, whereas fast and irregular rhythms of breath are ascribed to stress emotions [43]. Similarly, the heart rate and its variability correlate with comforting impacts and defensive reactions. Stress and increased sympathetic activity normally lead to an increase of heart rate, whereas parasympathetic activity has the opposite effect [44, 45]; thus, effective stress adaption is known to increase general well-being [46].

Based on the data showing an immunomodulatory effect of the waterfall aerosols, we hypothesized that the waterfall microclimate may exert a positive effect on different stress parameters.

Therefore, the present randomized controlled clinical study investigated whether in combination with a high-altitude climate therapy, waterfall-generated ions would provide an effective and cost-efficient therapy to mitigate various stress-related symptoms and strengthening immunity.

As a trigger of many secondary diseases such as neuropsychiatric, cardiovascular, or metabolic disorders, stress induces enormous economic costs [47, 48]. Interestingly, nature itself may preserve a sustainable health resource to counteract this trigger.

Methods

Subjects

Ninety-one persons working in care professions (19–61 years old; 44 men, 47 women) were enrolled in the study. People working in care professions are known as high-risk occupational groups concerning psychological and immunological consequences of stress [19, 24]. Requirement for study inclusion was moderate to high stress levels as defined by the *Trier Inventory for the Assessment of Chronic Stress (TICS)* questionnaire, assessed 7 days before beginning of the study (Fig. 1), and no previous cholera vaccination. Exclusion criteria were fever, chronic or severe diseases, including immune dysfunctions, and treatment with antibiotics or immunosuppressants. The

study was approved by the ethical committee of Salzburg (E1066/29042009).

Study design/intervention

The study was set up as a randomized controlled clinical trial with three arms.

Except for the non-intervention (control) group (CO, $n = 26$), all participants spent 1 week at the village of Großkirchheim (Carinthia, Austria) located 1024 m above sea level, hosted in hotels and receiving the same meals. For 1 h each day, the groups were separated for intervention into a waterfall- (WF+, $n = 33$) and a “non-waterfall” group (WF-, $n = 32$); group separation was kept identical throughout the study. Individuals of the control group stayed at home (without any intervention, except vaccination), following their usual daily life.

The probands of the WF+ group were exposed for 1 h to the Gartl Waterfall at 1000 m a.s.l., whereas the WF- group spent this hour at a site about 1000 m away from the waterfall, but at the same altitude. The average concentration of ions at this “control” site was 840 ions/cm³ (mean air humidity 72.3% ±23.1, mean temperature 15.3 °C ±2.5), compared to the average 42660 ions/cm³ with maxima up to 57510 ions/cm³ at the waterfall exposed site (mean air humidity 84.6% ±9.9, mean temperature 16.9 °C ±4.1) [9]. In order to exclude effects based on different trainings, this location was selected at the same altitude as the waterfall, with identical cumulative elevation gain and distance from the starting point.

Except for this 1-h intervention, participants of the WF+ and WF- group had the same daily routine, and both groups went through a daily hiking program at an altitude between 1400 and 2900 m, with structured hikes of at least 600 meters of cumulative elevation gain.

All participants received an oral cholera vaccine on day 0 and day 6 of the study (Fig. 1).

The study took place from July to August 2009; follow-up examinations were performed after 2 months

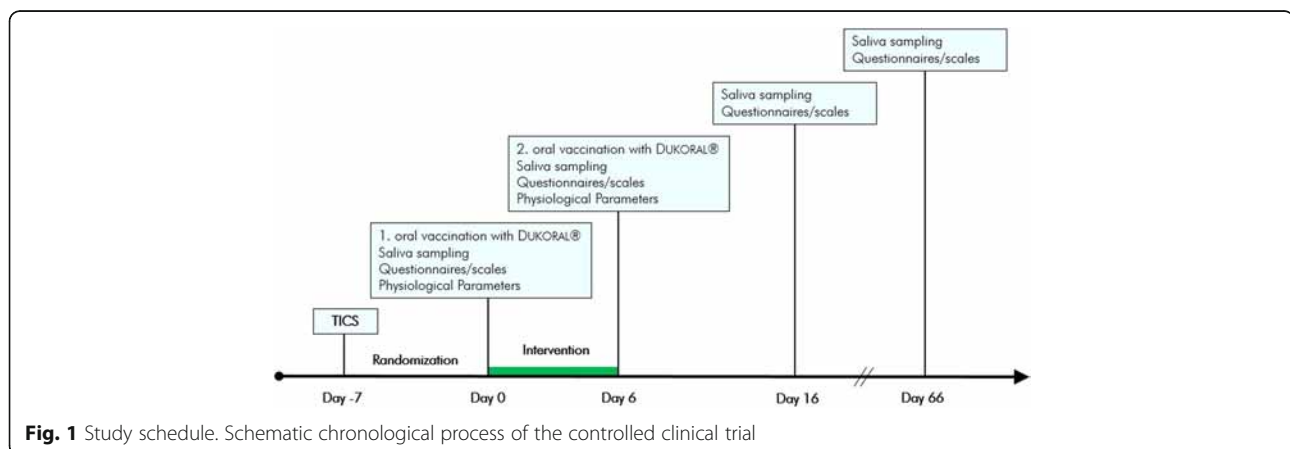


(Fig. 1). Physiological and psychological data from day 0 and day 6 were evaluated on site in a medical field laboratory in Großkirchheim, Carinthia. Follow-up examinations on day 16 and day 66 were held in the Paracelsus Medical University Salzburg. Randomization was performed with “Random allocation software” program [49].

Environmental parameters of the Gartl Waterfall

The waterfall is located in the heart of the National Park Hohe Tauern in Carinthia (Austria), situated in the community Großkirchheim in the upper Möll Valley. It is easily accessible via a gently rising 1.5-km walk from the village center and well established for waterfall exposition. Its approximate drop height is 50 m in two cascades and the average water flow is 0.6 m³/s (max 0.9 m³/s). Despite the moderate drop height, the waterfall features very high concentrations of ionsols (mean 42660 ions/cm³, max 57510 ions/cm³) floating the whole valley beneath the impact zone. Air humidity near the impact zone is 60–90%, consisting of respirable small water drops, whereas ozone levels are virtually zero.

Vaccination

Mucosal immunity was tested by oral vaccination with DUKORAL® from SBL Vaccines, which was given on days 0 and 6 (Fig. 1). Dosage and mode of application were according to the package information leaflet [50, 51].

Collecting and analysis of saliva

Saliva (2–3 ml) was collected from all subjects in sterile 15-ml plastic tubes on days 1, 6, 16, and 66 in the morning (Fig. 1), immediately after waking up (thus containing the matutinal IgA concentration peak) [52]. The tubes were stored at –80 °C until preparation and analysis. To determine DUKORAL® vaccine specific salivary IgA concentrations, 96-well high-bind, flat-bottomed immunoplates (FluoroNunc, Roskilde, Denmark) were coated overnight at 4 °C with DUKORAL® vaccine antigens (1 mg recombinant cholera toxin B subunit (rCTB)) diluted 1:100 with PBS (1×), corresponding to 0.01 mg per well. After blocking for 1 h at room temperature with 200 µl/well PTB (PBS/0.1% Tween 20/0.5% bovine serum albumin (BSA)), the plates were washed with PBS/0.1% Tween 20, and saliva was added at a dilution of 1:100 in 100 µl/well PTB for specific IgA and incubated for 1 h at RT. The plates were washed with PBS/0.1% Tween 20 and incubated with 100 µl/well horseradish peroxidase (HRPO)-conjugated goat anti-human IgA (BioRad, Austria), diluted 1:1000 in PTB for 1 h at RT. Again, the plates were washed (with PBS) and the reaction was detected by adding luminol (Boehringer Mannheim, Germany) (5 ml solution A (100 mM glycine

pH 10 (NaOH)/0.4 mM luminol/8 mM iodophenol), 5 mL solution B (0.12% H₂O₂ in dH₂O), and 10 ml dH₂O). Chemiluminescence was measured by a Promega ELISA-plate luminometer (Promega, Mannheim, Germany). Luminescence was calculated as photon counts per second.

Lung function and physiological stress test

The respiratory parameter analyzed was peak expiratory flow (PEF) by means of a forced ex-in maneuver. All tests were performed with EasyOne™ Plus Diagnostic from ndd Medical Technologies by aid of two trained scientists.

A computer-guided physiological stress test was performed to measure heart rate (three-point ECG), respiration rate (respiration sensor), and skin conductance (finger clip) during a 3-min baseline phase, a 1-min stressor phase (optical and acoustical stressors on the computer screen), and a 4-min post-stress recovery phase using a NeXus 10 multimodal device from Mind Media (Mind Media BV, Netherlands). The arithmetic mean of the respective physiological signal during the stressor phase was set to 100%. The arithmetic mean of the post-stress recovery phase was compared to the 100% line and used to measure the stress adaptation of the peripheral signals heart rate, respiration rate, and skin conductance.

Questionnaires and scales

Trier Inventory for the Assessment of Chronic Stress

This questionnaire was used to differentiate between various facets of chronic stress, measured by the retrospective rate of stress events in six areas (worries, work overload, work discontent, lack of social recognition, social stress, and intrusive memories) on a five-point rating scale [53].

Visual analog scale

VAS was performed as a measurement tool for subjective stress perception. On basis of a linear scale, participants can state their current stress level by indicating a position along a continuous line between the two endpoints “no stress at all” and “unbearable stress”. The analog aspect of linear scales creates preferably metrical characteristics instead of discrete scales [54].

Symptom Check List–SCL 90

The SCL 90 questionnaire enables to analyze treatment or progress of a variety of symptom dimensions, such as somatization, obsessive-compulsive, interpersonal sensitivity, depression, anxiety, hostility, phobic anxiety, aggression, paranoid ideation, and psychoticism. The test provides an overview and displays intensity of symptoms at the moment and in progress, including three global indices, i.e., Global Severity Index (GSI) (describing

overall psychological distress), Positive Symptom Distress Index (PSDI) (describing intensity of symptoms) and Positive Symptom Total (PST) (describing the number of self-reported symptoms) [55].

Maslach Burnout Inventory (MBI-D®)

The original Maslach Burnout Inventory was developed to measure intensity and incidence of perceived burnout in care professions. The authorized German version MBI-D, closely aligned with the original, surveys three components of burnout syndrome based on several specific items: emotional exhaustion, depersonalization, and personal accomplishment [56].

List of complaints (KSb-S BL)

This questionnaire is an independent part of the test-battery KSb-S (the German abbreviation KSb-S stands for “clinical self-assessment-scales”, BL for “list of complaints”, PSYCHIS Munic), which captures the degree of subjective impairment due to physical, e.g., joint pains and general complaints (e.g., faintness). Combination of quantity and levels of manifestations (heavy-moderate-little-not at all) result in a total interference of complaints, reflecting a constitutional change over time [57].

Mental state scale (KSb-S Bf-S)

Like the BL, the Bf-S is also an autonomous part of the test-battery KSb-S which is arranged to reflect the change of the present, psychical, and subjective mental state in an aggregate value, figuring the whole range of normal and pathologic changes of well-being [58].

Recovery-Stress Questionnaire-EBF

This questionnaire figures an individual's current recovery-stress state using retrospective (last 3 days) information of stressful situations, reactions, and recovery activities in a self-assessment test. Answers are queried in a seven-point scale, ranging from never to always [59].

Statistical analysis

All analyses were performed using the IBM SPSS statistics version 22 (IBM, NY, USA, <http://www.spss.com/>). Different linear mixed models, three-armed (LMM1, WF+, and WF- group compared to CO group) and two-armed (LMM2, WF+ group compared to WF- group) were used for statistical analysis of all variables with more than two time points and high individual variations. Unlike a linear regression analysis, a linear mixed model is able to detect changes despite high individual variations in the IgA levels and questionnaires. Time, treatment, and interaction of treatment and time were set as fixed factors. To take individual differences into account, the patient IDs were included in the models as random effect. A third linear mixed model (LMM3) was

used to detect changes over time for the main outcome variable of secretory IgA (sIgA) levels, excluding the interaction of time and treatment, with only time and treatment as fixed factors of each. Linear regressions were performed to detect intervention effects in all physiologic parameters and the visual analog scale, lacking of high-individual variations and inset at two time points. To identify significant differences of the baselines between the three study groups, comparison of means was done with ANOVA including Bonferroni correction for parametric data; Wilcoxon signed-rank test or Mann-Whitney *U* test was applied to non-parametric data.

Figures are shown as means \pm standard deviation (SD). Statistical significance was expressed as $p \leq 0.05$ (*) or as $p \leq 0.01$ (**).

Furthermore, all study data were subjected to Kolmogorov-Smirnov (with Lilliefors correction of significance) and Shapiro-Wilk normality tests—70% of the data generated passed the tests.

Results

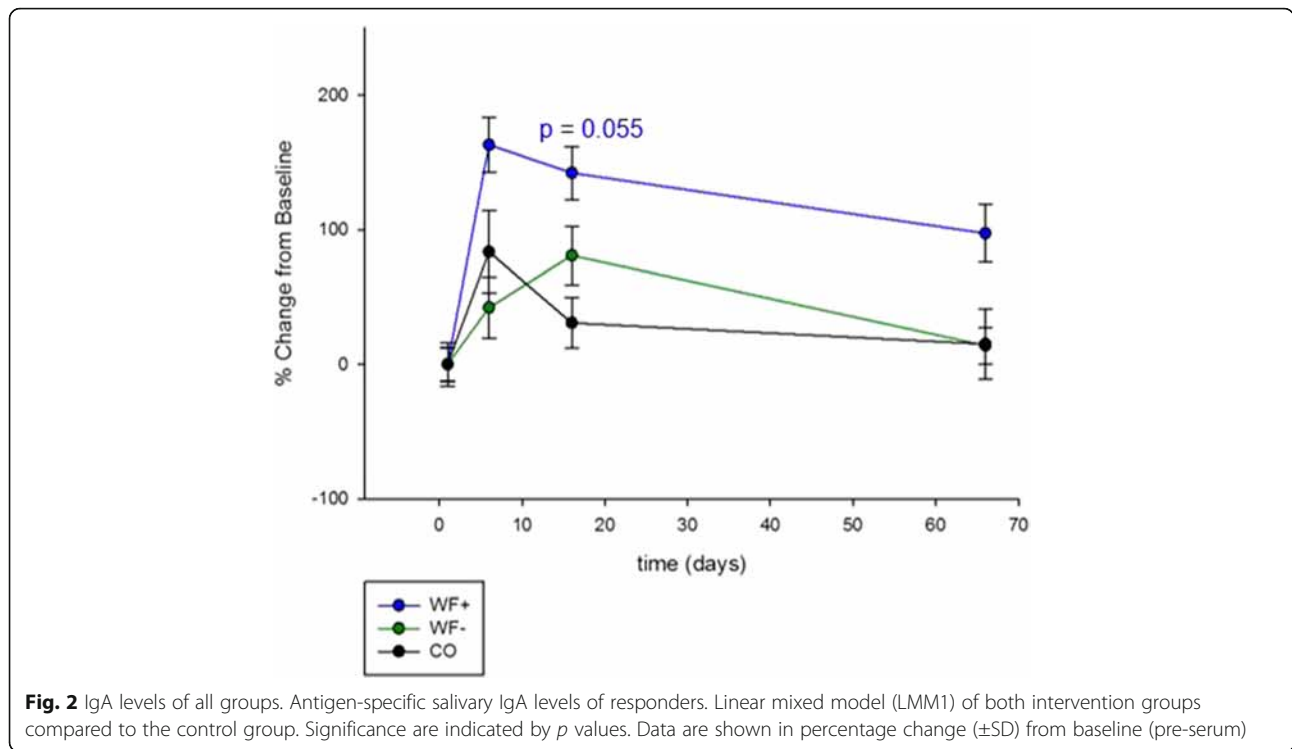
Patient characteristics

The randomized, controlled clinical study comprised 91 participants working in care professions consisting of 47 females (mean BMI 22.50 ± 3.51 SD) and 44 males (mean BMI 24.33 ± 3.16 SD), ranging from 19–61 (30.93 mean ± 10.39 SD) years of age. No significant differences were found between baseline values of both intervention groups (WF+ and WF- group). The control group (CO) had a bias in age and was slightly younger compared to both other groups.

Response to mucosal vaccination

The vaccination protocol led to a detectable antigen-specific mucosal immune response in approximately one half of the immunized subjects. Responders and non-responders were defined by measuring vaccine-specific salivary sIgA titers. A value of three standard deviations above the IgA titer of the serum taken prior to immunization (pre-serum) served as baseline. Participants with values above baseline were determined as responders ($\Sigma n = 48$ (n (WF+) = 16; n (WF-) = 18; n (CO) = 14)). Data of non-responders ($\Sigma n = 43$, equates ~47%) got excluded from statistical analysis of specific IgA levels.

A comparison of IgA titers of both intervention groups (WF+ and WF-) with the non-intervention control group with a linear mixed model (LMM1) shows no significant difference but a statistical trend ($p = 0.055$) on day 16 of the WF+ group, compared to that of the CO group (Fig. 2). The strongest percentage increase at all time points can be found in the WF+ group (Table 1).



The specific impact of the waterfall ionosols was evaluated with a linear mixed model (LMM2) of the two intervention groups WF+ and WF-. The result indicates a significant increase of salivary IgA titers in the WF+ group on day 6 and day 66 (Fig. 3).

A linear mixed model excluding interaction of time and treatment (LMM3) showed significant changes over time in both intervention groups at all time points (day 6 *p* = 0.000, day 16 *p* = 0.000, day 66 *p* = 0.001).

Subjective stress perception

The visual analog scale assessing the subjective stress perception was applied on day 1 and day 6. A significantly lower stress level could be measured in the WF+

group after the intervention week on day 6, compared in the control group (lin. regression, *p* = 0.000, *R*² = 0.615), and a clear trend to a waterfall-specific beneficial influence when compared to the WF- group (lin. regression, *p* = 0.054, *R*² = 0.179) (Fig. 4).

Psychological stress parameters and burnout symptoms

Linear mixed model (LMM1) analysis of the SCL-90 questionnaire revealed improvement in six of the ten symptom dimensions in both intervention groups after 6 days (compared in the control group): aggression, day 6: WF+ *p* = 0.000; WF- *p* = 0.006, day 66: WF+ *p* = 0.058; obsessive-compulsive, day 6: WF+ *p* = 0.005; WF- *p* = 0.023; depression, day 6: WF+ *p* = 0.006; WF- *p* = 0.036; paranoid ideation, day 6: WF+ *p* = 0.006, day 66: WF+ *p* = 0.023; phobic anxiety, day 6: WF+ *p* = 0.005; WF- *p* = 0.042, day 66: WF+ *p* = 0.002; interpersonal sensitivity, day 6: WF+ *p* = 0.034 (Fig. 5). No differences could be detected with respect to the parameters somatization, anxiety, hostility, and psychoticism (data not shown) [55]. Significant long-lasting effects (day 66) could be measured in the waterfall group for two parameters (phobic anxiety and paranoid ideation). Again, the data indicate a clear trend of a beneficial effect of the waterfall environment.

Furthermore, on day 6, both the Global Severity Index assessing overall psychological distress, as well as the Positive Symptom Total, which displays the number of

Table 1 Antigen-specific salivary IgA-levels

		Day 6	Day 16	Day 66
WF+	Photon counts	498 583.8	458 859	374 034.3
	% change	163.1	142.1	97.4
WF-	Photon counts	365 445.3	465 156.6	293 012.7
	% change	42.2	80.9	14
CO	Photon counts	615 312.5	438 061.5	385 653.7
	% change	83.6	30.7	15.1

Data of the intervention groups (WF+ and WF-) and the control group are given in photon counts. % change indicates the increase of IgA titers after immunization compared to the baseline (pre-serum)

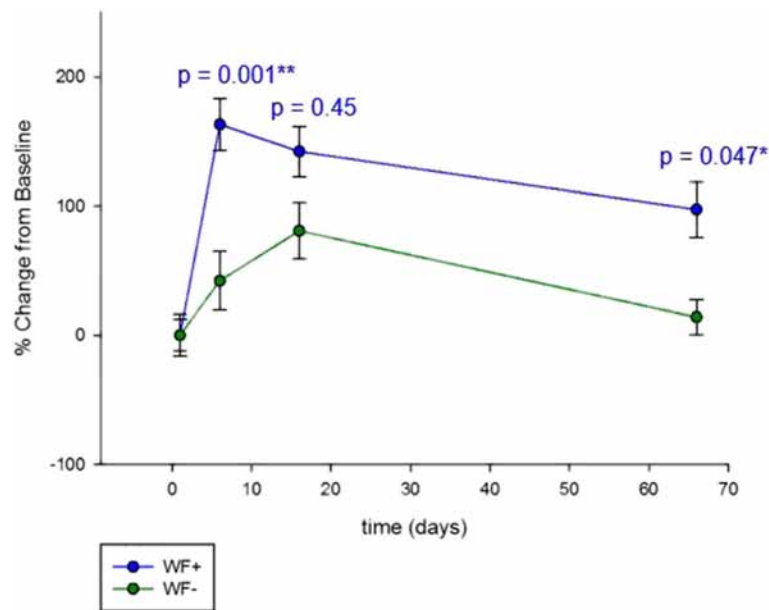


Fig. 3 IgA levels of the two intervention groups. Antigen-specific salivary IgA levels of responders. Linear mixed model (LMM2) of the waterfall group (WF+) compared to the non-waterfall group (WF-). Significances are indicated by *p* values. Data are shown in percentage change (\pm SD) from baseline (pre-serum)

self-reported symptoms, were significantly decreased in the waterfall group only ($p = 0.009$ for GSI and $p = 0.03$ for PST), again indicating a waterfall-specific effect (Fig. 6). The Positive Symptom Distress Index, which describes the intensity of symptoms, elicited no differences

over time between the three study groups (data not shown).

Measuring incidence and severity of burnout by means of the *Maslach Burnout Inventory* (MBI-D) elicited a significant improvement in the WF+ group in the

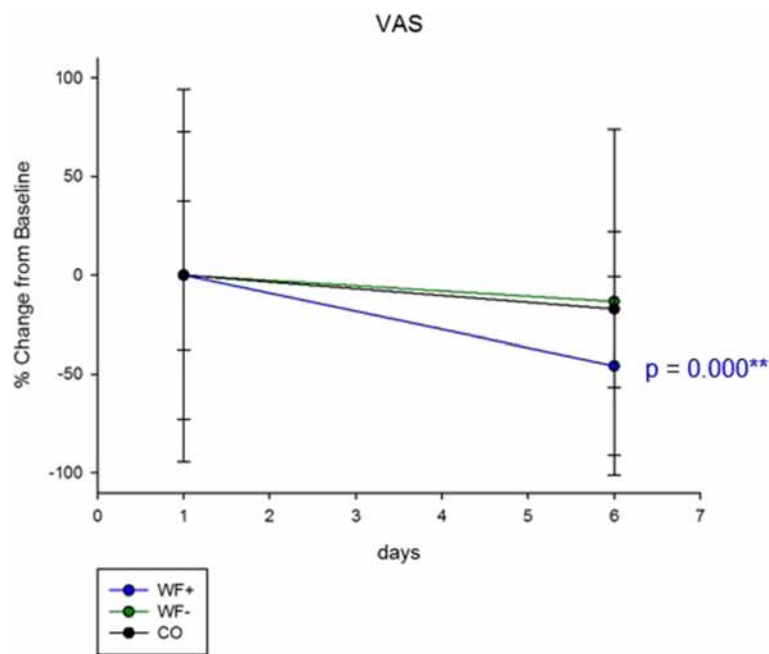


Fig. 4 Subjective stress perception. Visual analog scale of subjective stress perception. Stress levels in the WF+ group were significantly decreased (compared to control) and shown a trend to a specific waterfall effect (WF+ to CO $p = 0.000$, $R^2 = 0.615$; WF+ to WF-: $p = 0.054$, $R^2 = 0.179$; WF- to CO $p = 0.066$, $R^2 = 0.496$). Data shown in means (\pm SD). Statistical analysis calculated with linear regression

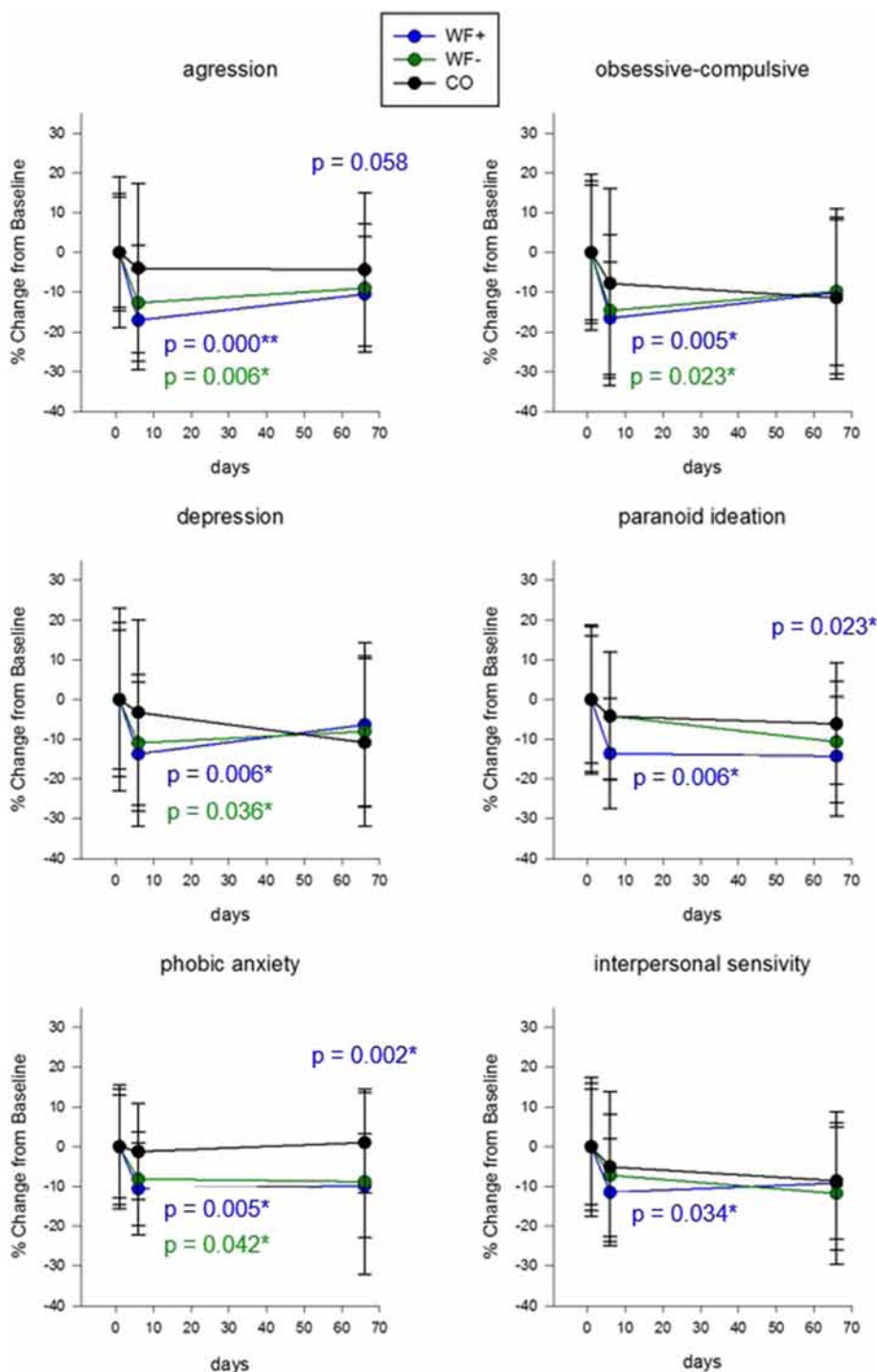
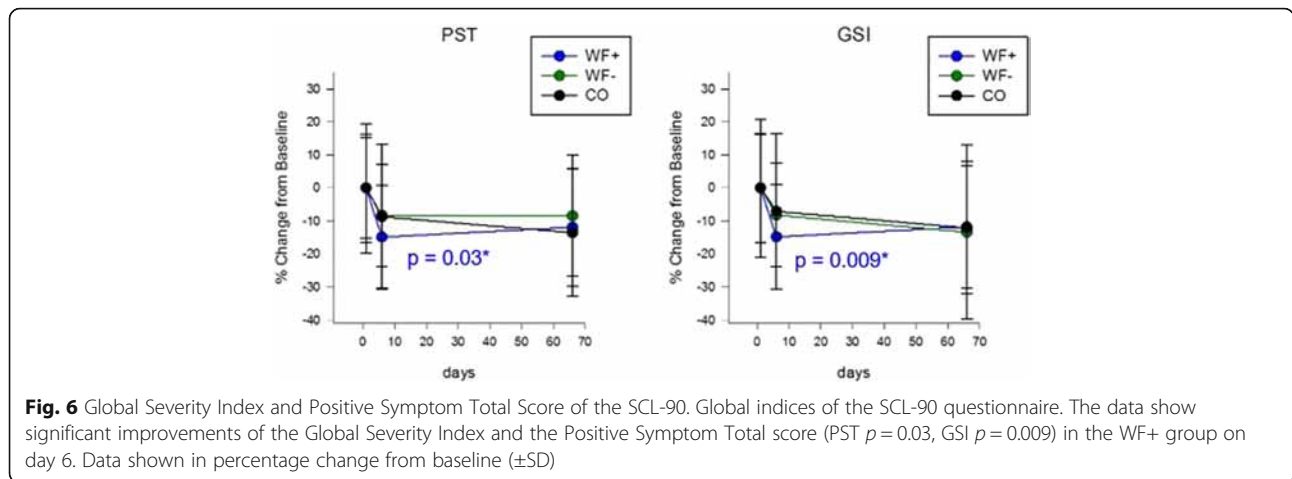


Fig. 5 SCL-90 questionnaire. Results of the SCL-90 questionnaire shown in percentage change from baseline. The data indicate beneficial effects of both interventions, with stronger significances for the waterfall group. Linear mixed models of the three study groups over time. Data shown in means (\pm SD)

category *depersonalization*, compared in the control group on day 66 (day 6 $p = 0.064$, day 66 $p = 0.002$). No differences could be measured concerning the other two components, i.e., *emotional exhaustion* and *personal accomplishment* over time in all groups. With respect to

the list of complaints (BL), reflecting constitutional changes during the trial, the WF+ group showed a significant positive long-term effect on day 66 ($p = 0.011$). Both intervention groups show a decrease of complaints on day 16 (WF+ $p = 0.086$, WF- $p = 0.057$), and the



mental state scale (Bf-S) clearly indicates enhanced well-being short-term effects on day 6 (WF+ $p = 0.051$, WF- $p = 0.06$). The recovery and stress questionnaire (EBF) revealed less stress (day 6, $p = 0.068$) and improved recovery only in the waterfall group (day 6 $p = 0.07$, day 66 $p = 0.036$). All statistical analyses were done with LMM1 (data not shown).

Lung function and stress-associated peripheral physiological parameters

No significant differences between the groups regarding all determined physiological parameters and peripheral signals could be detected at the beginning of the study. Exposure to the waterfall had a significant positive effect on lung function as measured via peak expiratory flow (PEF) on day 6 (WF+ to CO $p = 0.023$, $R^2 = 0.346$). No significant effect could be detected in the WF- group (WF- to CO $p = 0.136$, $R^2 = 0.047$) or between the two intervention groups after 1 week of intervention (WF+ to WF- $p = 0.359$, $R^2 = 0.079$) (Table 2, Fig. 7).

All peripheral signals of the physiological stress test decreased in the W+ and W- group after 1 week. The

results show the arithmetic mean in percentage of the 4-min post-stress recovery phase, compared to a 100% reference line, which reflects the arithmetic mean of the 1-min stressor phase in percentage. Results below 100% indicate the ability to reconstitute a parasympathetic physiological state, to calm down, and to relax after a stressor within the 4-min post-stress recovery phase. Compared to the control group, the respiration rate was decreased significantly in both intervention groups (WF+ to CO $p = 0.016$, $R^2 = 0.164$; WF- to CO $p = 0.004$, $R^2 = 0.169$). Similarly, skin conductance indicating sympathetic activity and sweat production was reduced after 1 week of waterfall exposition (WF+ to CO $p = 0.017$, $R^2 = 0.151$), with a trend to a waterfall-specific additional effect (WF+ to WF- $p = 0.056$, $R^2 = 0.187$). The heart rate was significantly lowered in both intervention groups (WF+ to CO $p = 0.011$, $R^2 = 0.421$; WF- to CO $p = 0.000$, $R^2 = 0.492$) (Table 2, Fig. 7).

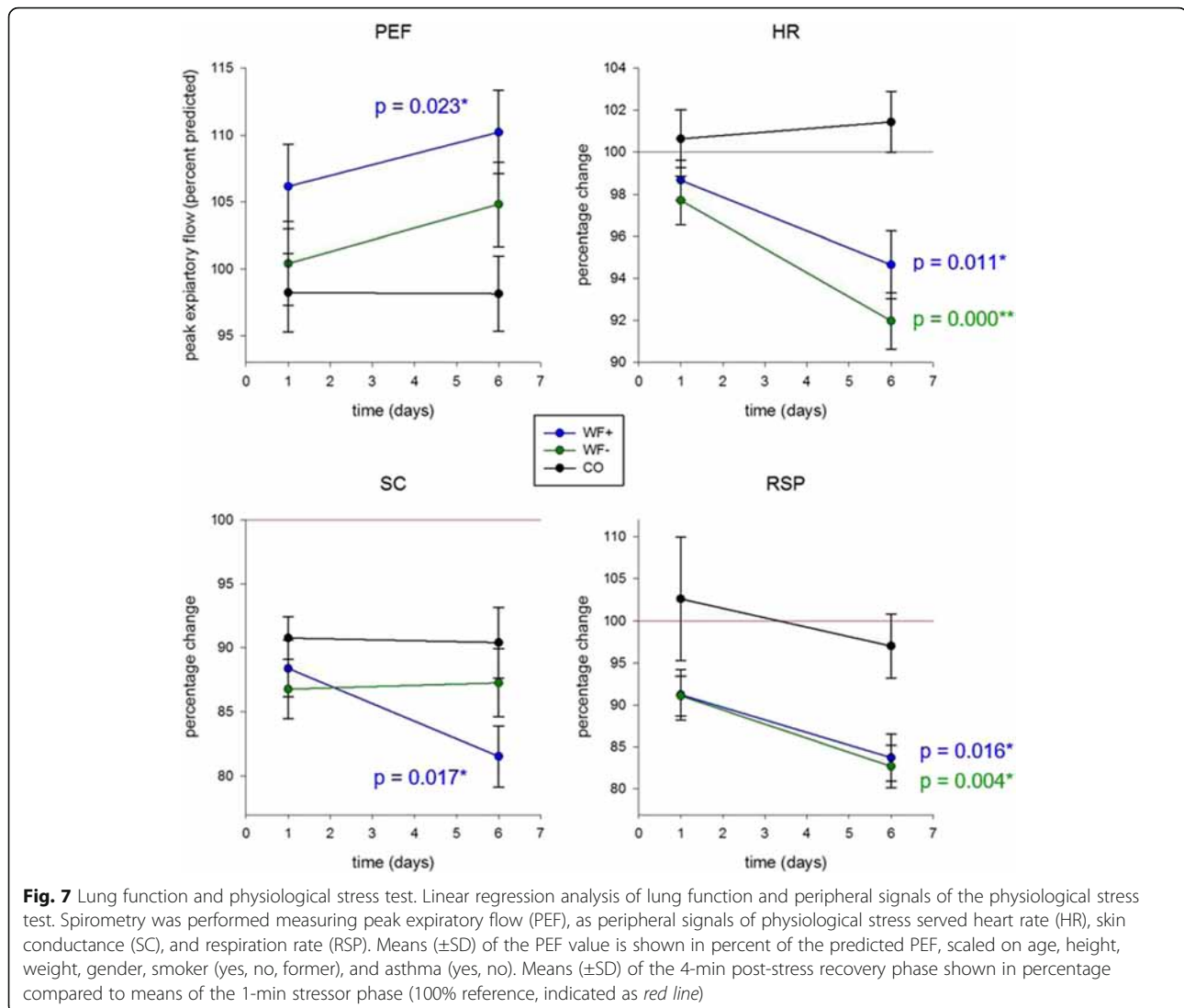
Discussion

The present controlled and randomized clinical study addressed the question whether the specific environment of a waterfall provides additional beneficial effects for prophylactic and therapeutic stress management when combined with high-altitude climate therapy and physical activity (mountain hiking in the protected area National Park Hohe Tauern in Austria). As stress represents a complex phenomenon including psychological, physiological, and immunological effects, we investigated selected parameters of all of these three aspects. For this purpose, two study groups with moderate to high stress levels spent an active 1-week sojourn in the National Park Hohe Tauern with identical parameters concerning daily mountain hiking, accommodation and food supply, except for 1 h/day. One group spent this time at the waterfall, the other at the same sea level but free from the waterfall-specific environment. A third study arm was recruited as a control group, keeping their normal daily life without any intervention.

Table 2 Means of evaluated physiological data (\pm SD)

		PEF (L/sec)	HR (%)	SC (%)	RSP (%)
WF+	Day 0	8.7 \pm 2.0	98.7 \pm 5.5	88.4 \pm 12.8	91.2 \pm 17.3
	Day 6	9.0 \pm 1.9	94.7 \pm 9.2	81.5 \pm 13.7	83.7 \pm 16.2
WF-	Day 0	8.5 \pm 1.5	97.7 \pm 6.0	86.8 \pm 12.4	91.1 \pm 12.3
	Day 6	8.9 \pm 1.7	92.0 \pm 6.9	87.3 \pm 14.3	82.7 \pm 13.0
CO	Day 0	8.6 \pm 2.1	100.6 \pm 7.0	90.8 \pm 8.2	96.1 \pm 17.3
	Day 6	8.6 \pm 1.8	101.4 \pm 7.3	90.4 \pm 13.6	97.4 \pm 19.6

Physiological data of the intervention groups (WF+ and WF-) and the control group on day 0 and day 6. Raw data of the peak expiratory flow (PEF) shown in means (\pm SD). Means (\pm SD) of the 4-min post-stress recovery phase of heart rate (HR), skin conductance (SC), and respiration rate (RSP) are shown in percentage (in relation to the 100% reference, means of the 1-min stressor phase)



The results of our study are in line with publications indicating positive health effects of green exercise and high-altitude climate therapy, which have been already proven to contribute to the improvement of respiratory and/or allergic diseases [3–5, 16]. Our data suggest to expand the applicability of this simple and cost-effective health provision for treatment of stress-related symptoms. Interestingly, several of the investigated parameters were significantly changed with a 1-h/day exposure to the environment of a waterfall. Most strikingly, beyond psychological and physiological stress-related symptoms, the specific humoral sIgA immune response after oral vaccination was significantly improved by the additional waterfall exposure. Secretory IgA is present in all mucosal surfaces; it is of crucial importance for the first line of defense of the immune system at mucosal barriers [33, 34].

Currently, we know that the immense power of the falling water cracks small water droplets in a specific way,

resulting in small nano particles carrying a negative charge, whereas the created bigger fragments are charged positively. The specific environment around waterfalls is characterized by these mainly negatively charged “Lenard’s ions” hovering in the air, while the positive-charged fragments sink to the ground [10, 60–62]. The airborne nano-aerosol is assumed to trigger a variety of biological effects, e.g., mild activation of the immune system, inducing a balance between TH1/TH2 immunity, stabilizing the autonomous nervous system, and improving blood flow [16, 63–65]. In a mouse model, water-generated negative ions have been shown to enhance cytotoxic activity of natural killer cells [66]. It is also conceivable that the high concentration of negative air ions near waterfalls could influence the human microbiota. Furthermore, the waterfall environment itself provides a specific microbiologic atmosphere, which may directly effect the microbiota of skin and mucosal surfaces [14]. This waterfall-altered

microbiome could act as an immunological adjuvant and thus be responsible for the observed effects on mucosal immunity.

Negative air ions have also been shown to influence psychological well-being by an increased serotonin level [18] and to enhance positive emotional processing in seasonal affective disorder [67] and have also been associated with lower depression scores [68]. An “added value” concerning the mood-raising effect may simply originate from the extraordinary beauty of the waterfall itself [69].

Conclusions

Numerous curing and healing effects are ascribed to waterfalls in ancient traditions and folk wisdom in many regions of the world. The present randomized, controlled clinical study provides evidence for an added value of a daily 1-h stay for 1 week in a waterfall environment in combination with green exercise and high-altitude climate therapy. Furthermore, the data point to an influence of the waterfall ionosols on complex “psychoneuroimmunological” regulatory circuits.

The results of this study also provides a rational basis for further research with an aim to develop schedules for new and effective prophylactic therapies for high-risk patients suffering from psychological and physiological stress symptoms.

Acknowledgements

We greatly appreciate all our study participants which enabled the implementation of the study. We want to thank Peter Suntinger, deputy mayor of Grosskirchheim, Austria, and Franziska Fellner, community of Grosskirchheim, for their important support. Many thanks to General Director Dr. Christian Heu, Grossglockner Hochalpenstrassen AG for his important input and discussion. We also want to thank Mag. Peter Rupitsch, director of the Hohe Tauern National Park, and the National Park Rangers Konrad Mariacher and Johanna Dullnig, for their help and guidance. We also want to thank Antonia Suntinger for her medical support, Veronika Granig for her input, and Mag. Brigitta Bernhard for the discussion of the psychological data. Also, many thanks to the Hotel Post, Hotel Schlosswirt, Hotel Marx, and Hotel Dorfwirt for their great hospitality.

Funding

This work was funded by the Oesterreichische Forschungsfoerderungsgesellschaft FFG, KNet Water Project 223.

Authors' contributions

CG carried out the statistical analysis, data analysis, visualization and interpretation, laboratory analysis, and preparation of the manuscript. MG participated in the study design and made operative involvement in conducting the study on site, laboratory analysis, data warehousing, and data analysis. JP participated in the statistical analysis. MR carried out the medical advising and proofreading of the manuscript. PK executed the physical characterization of the waterfall environment. CP made operative involvement in conducting the study on site and carried out the proofreading. JT participated in the preparation and proofreading of the manuscript. AH conceived of the study idea and the study design, made operative involvement in conducting the study on site, and participated in the laboratory analysis, data warehousing, data analysis, and interpretation of the data. All authors read and approved the final manuscript.

Competing interests

The authors declare that they have no competing interests.

Author details

¹Institute of Ecomedicine, Paracelsus Medical University, Strubergasse 22, 5020 Salzburg, Austria. ²Institute of Physiology and Pathophysiology, Paracelsus Medical University, Strubergasse 22, 5020 Salzburg, Austria. ³Gastein Research Institute, Paracelsus Medical University, Strubergasse 22, 5020 Salzburg, Austria. ⁴Department for Radon Therapy Research, Ludwig Boltzmann Cluster for Arthritis and Rehabilitation, Strubergasse 22, 5020 Salzburg, Austria. ⁵Institute of Physics, University of Belgrade, Pregrevaica 118, 11080 Belgrade, Serbia. ⁶Department of Molecular Biology, University of Salzburg, Hellbrunner Str. 34, 5020 Salzburg, Austria.

Received: 14 April 2016 Accepted: 7 November 2016

Published online: 13 January 2017

References

- Cepilova Z, Porubská M, Slamova J. Climate therapy of uveitis in a mountain environment. *Cesk Oftalmol*. 1993;49:90–4.
- Butykova L, Kolesar J, Turecekova A, Najvarova S. Changes in the elimination of histamine, noradrenaline, adrenaline and vanilmandelic acid during high-mountain climatic therapy at Strbske Pleso. *Fysiatr Revmatol Vestn*. 1973;51:103–7.
- Karagiannidis C, Hense G, Rueckert B, Mantel PY, Ichtters B, Blaser K, Menz G, Schmidt-Weber CB. High-altitude climate therapy reduces local airway inflammation and modulates lymphocyte activation. *Scand J Immunol*. 2006;63:304–10.
- Simon HU, Grotzer M, Nikolaizik WH, Blaser K, Schoni MH. High altitude climate therapy reduces peripheral blood T lymphocyte activation, eosinophilia, and bronchial obstruction in children with house-dust mite allergic asthma. *Pediatr Pulmonol*. 1994;17:304–11.
- van Leeuwen WS. Bronchial asthma in relation to climate. *Proc R Soc Med*. 1924;17:19–26.
- a Porta B, Barandun J, Wuthrich B. Atopic neurodermatitis—therapy in high altitude climate. *Praxis (Bern 1994)*. 2000;89:1147–53.
- Engst R, Vocks E. High-mountain climate therapy for skin diseases and allergies—mode of action, therapeutic results, and immunologic effects. *Rehabilitation (Stuttg)*. 2000;39:215–22.
- Rijssenbeek-Nouwens LH, Bel EH. High-altitude treatment: a therapeutic option for patients with severe, refractory asthma? *Clin Exp Allergy*. 2011;41:775–82.
- Kolarž P, Gaisberger M, Madl P, Hofmann W, Ritter M, Hartl A. Characterization of ions at Alpine waterfalls. *Atmos Chem Phys*. 2012;12:3687–97.
- Laakso L, Hirsikko A, Gronholm T, Kulmala M, Luts A, Parts TE. Waterfalls as sources of small charged aerosol particles. *Atmos Chem Phys*. 2007;7:2271–5.
- Wang XL, Li CR, Xu JW, Hu DM, Zhao ZL, Zhang LD. Air negative ion concentration in different modes of courtyard forests in southern mountainous areas of Jinan, Shandong Province of East China. *Ying Yong Sheng Tai Xue Bao*. 2013;24:373–8.
- Skromulis A, Noviks G. Atmospheric light air ion concentrations and related meteorologic factors in Rezekne city, Latvia. *J Environ Biol*. 2012;33:455–62.
- Mao GX, Cao YB, Lan XG, He ZH, Chen ZM, Wang YZ, Hu XL, Lv YD, Wang GF, Yan J. Therapeutic effect of forest bathing on human hypertension in the elderly. *J Cardiol*. 2012;60:495–502.
- Craig JM, Logan AC, Prescott SL. Natural environments, nature relatedness and the ecological theater: connecting satellites and sequencing to shinrin-yoku. *J Physiol Anthropol*. 2016;35:1.
- Li Q, Kawada T. Effect of forest environments on human natural killer (NK) activity. *Int J Immunopathol Pharmacol*. 2011;24:395–44.
- Gaisberger M, Sanovic R, Dobias H, Kolarž P, Moder A, Thalhamer J, Selimovic A, Huttegger I, Ritter M, Hartl A. Effects of ionized waterfall aerosol on pediatric allergic asthma. *J Asthma*. 2012;49:830–8.
- Hummelshoj L, Ryder LP, Poulsen LK. The role of the interleukin-10 subfamily members in immunoglobulin production by human B cells. *Scand J Immunol*. 2006;64:40–7.
- Wu CF, Lai CH, Chu HJ, Lin WH. Evaluating and mapping of spatial air ion quality patterns in a residential garden using a geostatistic method. *Int J Environ Res Public Health*. 2011;8:2304–19.
- Glaser R, Kiecolt-Glaser J. How stress damages immune system and health. *Discov Med*. 2005;5:165–9.
- Harbuz MS, Chover-Gonzalez AJ, Jessop DS. Hypothalamo-pituitary-adrenal axis and chronic immune activation. *Ann N Y Acad Sci*. 2003;992:99–106.
- Calcagni E, Elenkov I. Stress system activity, innate and T helper cytokines, and susceptibility to immune-related diseases. *Ann N Y Acad Sci*. 2006;1069:62–76.

22. Levy MM. Caring for the caregiver. *Crit Care Clin.* 2004;20:541–7. xi.
23. Lambert VA, Lambert CE, Ito M. Workplace stressors, ways of coping and demographic characteristics as predictors of physical and mental health of Japanese hospital nurses. *Int J Nurs Stud.* 2004;41:85–97.
24. Glaser R, MacCallum RC, Laskowski BF, Malarkey WB, Sheridan JF, Kiecolt-Glaser JK. Evidence for a shift in the Th-1 to Th-2 cytokine response associated with chronic stress and aging. *J Gerontol A Biol Sci Med Sci.* 2001;56:M477–82.
25. Trueba AF, Ritz T, Trueba G. The role of the microbiome in the relationship of asthma and affective disorders. *Adv Exp Med Biol.* 2016;874:263–88.
26. Deinzer R, Kleineidam C, Stiller-Winkler R, Idel H, Bachg D. Prolonged reduction of salivary immunoglobulin A (sIgA) after a major academic exam. *Int J Psychophysiol.* 2000;37:219–32.
27. Deinzer R, Schuller N. Dynamics of stress-related decrease of salivary immunoglobulin A (sIgA): relationship to symptoms of the common cold and studying behavior. *Behav Med.* 1998;23:161–9.
28. Jemmott 3rd JB, Magloire K. Academic stress, social support, and secretory immunoglobulin A. *J Pers Soc Psychol.* 1988;55:803–10.
29. Mouton C, Fillion L, Tawadros E, Tessier R. Salivary IgA is a weak stress marker. *Behav Med.* 1989;15:179–85.
30. Stone AA, Cox DS, Valdimarsdottir H, Jandorf L, Neale JM. Evidence that secretory IgA antibody is associated with daily mood. *J Pers Soc Psychol.* 1987;52:988–93.
31. Stone AA, Cox DS, Valdimarsdottir H, Neale JM. Secretory IgA as a measure of immunocompetence. *J Human Stress.* 1987;13:136–40.
32. Stone AA, Marco CA, Cruise CE, Cox DS, Neale JM. Are stress-induced immunological changes mediated by mood? A closer look at how both desirable and undesirable daily events influence sIgA antibody. *Int J Behav Med.* 1996;3:1–13.
33. Burns VE, Drayson M, Ring C, Carroll D. Perceived stress and psychological well-being are associated with antibody status after meningitis C conjugate vaccination. *Psychosom Med.* 2002;64:963–70.
34. Mestecky J, Russell MW, Jackson S, Brown TA. The human IgA system: a reassessment. *Clin Immunol Immunopathol.* 1986;40:105–14.
35. Kiecolt-Glaser JK, Glaser R, Gravenstein S, Malarkey WB, Sheridan J. Chronic stress alters the immune response to influenza virus vaccine in older adults. *Proc Natl Acad Sci U S A.* 1996;93:3043–7.
36. Miller GE, Cohen S, Pressman S, Barkin A, Rabin BS, Treanor JJ. Psychological stress and antibody response to influenza vaccination: when is the critical period for stress, and how does it get inside the body? *Psychosom Med.* 2004;66:215–23.
37. Vedhara K, Cox NK, Wilcock GK, Perks P, Hunt M, Anderson S, Lightman SL, Shanks NM. Chronic stress in elderly carers of dementia patients and antibody response to influenza vaccination. *Lancet.* 1999;353:627–31.
38. Glaser R, Kiecolt-Glaser JK, Bonneau RH, Malarkey W, Kennedy S, Hughes J. Stress-induced modulation of the immune response to recombinant hepatitis B vaccine. *Psychosom Med.* 1992;54:22–9.
39. Morag M, Morag A, Reichenberg A, Lerer B, Yirmiya R. Psychological variables as predictors of rubella antibody titers and fatigue—a prospective, double blind study. *J Psychiatr Res.* 1999;33:389–95.
40. Yumatov EA, Pertssov SS, Dudnik EN, Kramm MN, Strelkov NO. Monitoring of human physiological functions during the daily night sleep. *Patol Fiziol Eksp Ter.* 2015;3:47–54.
41. Azam MA, Katz J, Fashler SR, Changoor T, Azargive S, Ritvo P. Heart rate variability is enhanced in controls but not maladaptive perfectionists during brief mindfulness meditation following stress-induction: a stratified-randomized trial. *Int J Psychophysiol.* 2015;98:27–34.
42. Dieleman GC, Huizink AC, Tulen JH, Utens EM, Tiemeier H. Stress reactivity predicts symptom improvement in children with anxiety disorders. *J Affect Disord.* 2016;196:190–9.
43. Ritz T, Dahme B, Dubois AB, Folgering H, Fritz GK, Harver A, Kotses H, Lehrer PM, Ring C, Steptoe A, Van de Woestijne KP. Guidelines for mechanical lung function measurements in psychophysiology. *Psychophysiology.* 2002;39:546–67.
44. Hosseini SA, Khalilzadeh MA, Naghibi-Sistani MB, Homam SM. Emotional stress recognition using a new fusion link between electroencephalogram and peripheral signals. *Iran J Neurol.* 2015;14:142–51.
45. Del Rosso S, Abreu L, Webb HE, Zouhal H, Boulosa DA. Stress markers during a rally car competition. *J Strength Cond Res.* 2016;30:605–14.
46. Pusejnak N, Grad A, Tusak M, Leskovsek M, Schwarzlin R. Can biofeedback training of psychophysiological responses enhance athletes' sport performance? A practitioner's perspective. *Phys Sportsmed.* 2015;43:287–99.
47. Bejean S, Sultan-Taieb H. Modeling the economic burden of diseases imputable to stress at work. *Eur J Health Econ.* 2005;6:16–23.
48. Kalia M. Assessing the economic impact of stress—the modern day hidden epidemic. *Metabolism.* 2002;51:49–53.
49. Saghaei M. Random allocation software for parallel group randomized trials. *BMC Med Res Methodol.* 2004;4:26.
50. Cholera vaccines: WHO position paper. *Wkly Epidemiol Rec.* 2010; 85:117–128.
51. Rahman A, Rashu R, Bhuiyan TR, Chowdhury F, Khan AI, Islam K, LaRocque RC, Ryan ET, Wrammert J, Calderwood SB, et al. Antibody-secreting cell responses after *Vibrio cholerae* O1 infection and oral cholera vaccination in adults in Bangladesh. *Clin Vaccine Immunol.* 2013;20:1592–8.
52. Hucklebridge F, Clow A, Evans P. The relationship between salivary secretory immunoglobulin A and cortisol: neuroendocrine response to awakening and the diurnal cycle. *Int J Psychophysiol.* 1998;31:69–76.
53. Schulz PSW. The Trier Inventory for the Assessment of Chronic Stress (TICS): Scale construction, statistical testing, and validation of the scale work overload. In: *Diagnostica*, vol. 45. pp. 8–19. Goettingen: Hogrefe Verlag; 1999. p. 8–19.
54. Reips UD, Funke F. Interval-level measurement with visual analogue scales in Internet-based research: VAS Generator. *Behav Res Methods.* 2008;40:699–704.
55. Franke GH. SCL-90-R. Die Symptom-Checkliste von Derogatis, Deutsche Version (Manual). Göttingen: Beltz Test GmbH; 2002.
56. Büssing A, Perrar KM. Die Messung von Burnout. Untersuchung einer deutschen Fassung des Maslach Burnout Inventory (MBI-D). *Diagnostica.* 1992;38:328–53.
57. Zerssen DDB-LaT, 25, 1908 (1971). Die Beschwerden-Liste als Test. *Therapiewoche* 21. 1971; 25:1908–1914.
58. Dv Z, Koeller D-M, Rey E-R. Die Befindlichkeitskala (B-S)—ein einfaches Instrument zur Objektivierung von Befindlichkeits-Störungen, insbesondere im Rahmen von Längsschnitt-Untersuchungen. *Arzneim Forsch.* 1970;20: 915–8.
59. Kallus K. Der Erholungs-Belastungs-Fragebogen. Manual. Frankfurt/M: Swets Test Services; 1995.
60. Luts A, Parts TE, Laakso L, Hirsikko A, Gronholm T, Kulmala M. Some air electricity phenomena caused by waterfalls: correlative study of the spectra. *Atmos Res.* 2009;91:229–37.
61. Parts TE, Luts A, Laakso L, Hirsikko A, Gronholm T, Kulmala M. Chemical composition of waterfall-induced air ions: spectrometry vs. simulations. *Boreal Environ Res.* 2007;12:409–20.
62. Vostrikov AA, Drozdov SV, Rudnev VS, Kurkina LI. Molecular dynamics study of neutral and charged water clusters. *Comput Mater Sci.* 2006;35:254–60.
63. Krueger AP, Reed EJ. Biological impact of small air ions. *Science.* 1976;193: 1209–13.
64. Palti Y, De Nour E, Abrahamov A. The effect of atmospheric ions on the respiratory system of infants. *Pediatrics.* 1966;38:405–11.
65. Takahashi K, Otsuki T, Mase A, Kawado T, Kotani M, Ami K, Matsushima H, Nishimura Y, Miura Y, Murakami S, et al. Negatively-charged air conditions and responses of the human psycho-neuro-endocrino-immune network. *Environ Int.* 2008;34:765–72.
66. Yamada R, Yanoma S, Akaike M, Tsuburaya A, Sugimasa Y, Takemiya S, Motohashi H, Rino Y, Takanashi Y, Imada T. Water-generated negative air ions activate NK cell and inhibit carcinogenesis in mice. *Cancer Lett.* 2006; 239:190–7.
67. Harmer CJ, Charles M, McTavish S, Favaron E, Cowen PJ. Negative ion treatment increases positive emotional processing in seasonal affective disorder. *Psychol Med.* 2012;42:1605–12.
68. Perez V, Alexander DD, Bailey WH. Air ions and mood outcomes: a review and meta-analysis. *BMC Psychiatry.* 2013;13:29.
69. Joye Y, Bolderdijk JW. An exploratory study into the effects of extraordinary nature on emotions, mood, and prosociality. *Front Psychol.* 2014;5:1577.

See discussions, stats, and author profiles for this publication at: <https://www.researchgate.net/publication/317661236>

Prediction of long-term indoor radon concentration based on short-term measurements

Article in *Nuclear Technology and Radiation Protection* · January 2017

DOI: 10.2298/NTRP1701077S

CITATIONS

7

READS

98

10 authors, including:



[Zdenka Stojanovska](#)

Goce Delcev University of Štip

48 PUBLICATIONS 403 CITATIONS

[SEE PROFILE](#)



[Kremena Georgieva Ivanova](#)

National Centre of Radiobiology and Radiation Protection

23 PUBLICATIONS 143 CITATIONS

[SEE PROFILE](#)



[Blazo Boev](#)

Goce Delcev University of Štip

295 PUBLICATIONS 1,004 CITATIONS

[SEE PROFILE](#)



[Zora S. Zunic](#)

University of Belgrade

112 PUBLICATIONS 1,141 CITATIONS

[SEE PROFILE](#)

Some of the authors of this publication are also working on these related projects:



Study of Minerals by Vibrational (Infrared and Raman) Spectroscopy and X-ray Diffraction [View project](#)



Three sub-layer photoanodes: highly efficient PECs (Photoelectrochemical Cells) [View project](#)

PREDICTION OF LONG-TERM INDOOR RADON CONCENTRATION BASED ON SHORT-TERM MEASUREMENTS

by

**Zdenka STOJANOVSKA^{1*}, Kremena IVANOVA², Peter BOSSEW³,
Blazo BOEV⁴, Zora S. ŽUNIĆ⁵, Martina TSENOVA², Zoran ĆURGUZ⁶,
Predrag KOLARŽ⁷, Milka ZDRAVKOVSKA¹, and Mimoza RISTOVA⁸**

¹ Faculty of Medical Sciences, Goce Delcev University, Stip, Republic of Macedonia

² National Centre for Radiobiology Protection, Sofia, Bulgaria

³ German Federal Office for Radiation Protection, Berlin, Germany

⁴ Faculty of Natural and Technical Sciences, Goce Delcev University, Stip, Republic of Macedonia

⁵ Vinča Institute of Nuclear Science, University of Belgrade, Belgrade, Serbia

⁶ Faculty of Transport, Doboj, University of East Sarajevo, Republic of Srpska

⁷ Institute of Physics, University of Belgrade, Belgrade, Serbia

⁸ Institute of Physics, Faculty of Natural Sciences and Mathematic, Ss Cyril and Methodius University, Skopje, Republic of Macedonia

Scientific paper

<http://doi.org/10.2298/NTRP1701077S>

We present a method for the estimation of annual radon concentration based on short-term (three months) measurements. The study involves results from two independent sets of indoor radon concentration measurements performed in 16 cities of the Republic of Macedonia. The first data set contains winter and annual radon concentration obtained during the National survey in 2010 and the second, contains only the radon concentration measured during the winter of 2013. Both data sets pertain to radon concentration from the same cities and have been measured applying the same methodology in ground floor dwellings. The results appeared to be consistent and the dispersion of radon concentration was low. Linear regression analysis of the radon concentration measured in winter of 2010 and of the 2010 annual radon concentration revealed a high coefficient of determination $R^2 = 0.92$, with a relative uncertainty of 3%. Furthermore, this model was used to estimate the annual radon concentration solely from winter-term measurements performed in 2013.

The geometrical mean of the estimated annual radon concentration of the 2013: radon concentration (A-2013) = 98 Bqm⁻³ was almost equal to the geometrical mean of the annual radon concentration from the 2010, radon concentration (A-2010) = 99 Bqm⁻³. Analysis of the influence of building characteristics, such as presence/absence of a basement in the building, or the dominant building material on the estimated annual radon concentration is also reported. Our results show that a low number of relatively short-term radon measurements may produce a reasonable insight into a gross average obtained in a larger survey.

Key words: ground floor dwelling, indoor radon, linear regression analysis, uncertainty

INTRODUCTION

The majority of the urban population spends long periods indoors, where radon accumulates, which may lead to elevated indoor concentrations. Radon is known as the most significant contributor to the dose received by the population due to exposure to natural sources of ionizing radiation [1]. To reduce the risk from radon exposure, authorities of many countries prepared national radon programmes the overall designs of which are based on the experience gained from the national surveys. The programmes incorporated the knowledge about the temporal and spatial

variability of the radon concentrations (C_{Rn}) controlled by numerous natural and anthropogenic factors [2, 3]. A radon survey qualifies as being national when it involves simultaneously measuring the C_{Rn} in a representative sample of dwellings throughout the entire country during a year. In general, the measurements are performed with nuclear track detectors.

The detectors are usually deployed for the following periods of time:

- (a) quarterly, where the detectors are exposed in four successive periods of three months (one full season) [4-6],
- (b) semi-annually, two successive periods for a duration of six months, including two full seasons [7], or, and

* Corresponding author; e-mail: zdenka.stojanovska@ugd.edu.mk

(d) annually, for a period of one year [8, 9].

Regardless of the time of exposure, the results are expressed as an annual C_{Rn} . In cases (a) and (b) the annual C_{Rn} is presented as arithmetic mean of the measured concentrations in the successive periods. In the case under (c) the annual C_{Rn} is measured directly.

The radon problem became a serious concern throughout the Balkan region. Large amounts of regional data became available from recent surveys carried out in Serbia [10-14], the Republic of Srpska [15, 16], Bulgaria [17], Romania [18] and Greece [19]. Also, several campaigns of C_{Rn} measuring have been conducted in the Republic of Macedonia over the last decade. The greatest source of data was provided by the national surveys of radon and thoron in dwellings in the Republic of Macedonia from 2010 [20-22]. Further research of C_{Rn} was conducted in schools and dwellings [6, 8]. Moreover, some investigations were done for establishing a relationship between the indoor C_{Rn} and the activity of ^{226}Ra in surface soil [23]. As part of these activities, a supplementary survey was carried out in 47 dwellings from 16 cities during the winter months of 2013. The results are a subject of this study. We present the evaluation of annual C_{Rn} and its uncertainty comparing the variance of results with those of the national survey measured in the same cities in 2010. Variation related to building characteristic is also discussed.

MATERIALS AND METHODS

Design of survey

The radon detectors were distributed within a campaign that involved undergraduate students from the first year of the Faculty of Medical Sciences in Stip, class 2012/2013. Students originating from various cities throughout the country were instructed to deploy a radon track-detector at the ground floor of their homes in their home cities. They were asked to keep the detector deployed during a three-month winter period (January to March 2013). The 47 detectors were deployed at a distance greater than 50 cm away from a wall and away from a heating source in the most occupied room (either living room or bedroom). The students filled out a questionnaire, providing general information about the characteristics of the house or building: position (GPS co-ordinates), presence/absence of basement, smoking habits, and the type of dominant building material. Some of these factors were further considered as a grouping parameter in the statistical analysis of the results. Four of the detectors were lost during the campaign. Finally, we received results for 43 dwellings located in 16 cities, pertaining to winter 2013. The cities under observation are characterized by different geographical position through the country (fig. 1), and are located at altitudes between

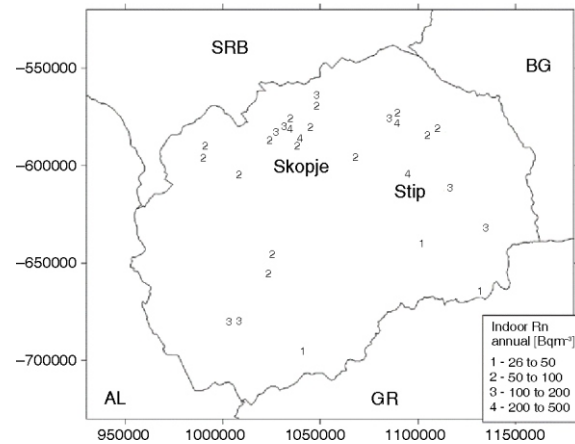


Figure 1. Spatial estimate of annual C_{Rn} in 43 dwellings; coordinates in m, GISCO Lambert azimuthal equal area projection

70 m to 650 m above sea level. They also belong to different geological zones categorised in different litho-stratigraphic units.

Using the list of the cities included in the 2013 survey we extracted the C_{Rn} results for the winter season in 2010, $C_{Rn}(W-2010)$, and for the entire year 2010, $C_{Rn}(A-2010)$. The 2010 dataset included C_{Rn} results from 186 different dwellings in 15 cities. One of the cities from the 2013 survey was not included in the list of the survey in 2010, but was kept for the study.

Measurements

The radon concentration in 2013 was measured using the same nuclear track detectors with commercial name RSKS, product of Radosys, Hungary, that were used for the survey in 2010. The track detectors consisted of a CR-39 detector placed in a cylindrical diffusion chamber with 25 mm × 40 mm. After being collected, the detectors were sent to the National Centre of Radiobiology and Radiation Protection in Sofia Bulgaria, for analysis.

The CR-39 detectors were detached from the diffusion chambers, and were chemically etched in 6.25 M solution of NaOH at a temperature of 95 °C for 3.4 hours. The track counting was performed by the optical transmission microscope using an automated image analysis system. The software identified the detector's ID code engraved onto the surface of the CR-39. Using an appropriate calibration factor, the software converted the detected number of tracks per unit area (track density) into radon concentration, expressed as

$$C_{Rn} = f_c \frac{\rho - \rho_b}{t} = f_c \frac{\rho_{net}}{t} \quad (1)$$

where C_{Rn} is radon concentration (in $kBq\ m^{-3}$), while ρ_b and ρ are the background and counted track density per mm^2 , respectively; f_c is a calibration factor, and t is

the exposure time in hours. The calibration factor for this series of detectors was provided by the manufacturer, $f_c = 44.47 \pm 3.53$ (in tracks per mm^2/KBqh per mm^{-2}). The background track density $\rho_b = 0.417 \pm 0.05$ (in tracks per mm^2) was determined from 10 blank detectors measurements.

To determine the annual radon concentrations by using short-term (winter) measurements one should first establish the relation between them. For this purpose we have provided a linear regression analysis of the measured C_{Rn} in the winter 2010, $C_{\text{Rn}}(\text{W-2010})$ and the annual $C_{\text{Rn}}(\text{A-2010})$. The analysis yielded the following eq.

$$C_{\text{Rn}}(A) = aC_{\text{Rn}}(W) + b = af_c \frac{\rho_{\text{net}}}{t} + b \quad (2)$$

where a and b are the constants of the linear dependence of the annual vs. the winter C_{Rn} .

The quantification of the uncertainty was done in accordance with the method, recommended in the EURACHEM Guide [24] and IAEA Tec doc 1401 [25]. The combined standard uncertainty was estimated by applying the law of uncertainty propagation for the independent variables

$$u_c(y) = y \sqrt{\frac{u(x_1)}{x_1}^2 + \frac{u(x_2)}{x_2}^2 + \dots + \frac{u(x_n)}{x_n}^2} \quad (3)$$

where the $u(x)/x$ are the uncertainties expressed as relative standard deviations.

The uncertainty of the annual radon concentration was estimated taking into account its probability distribution, converting each source of uncertainty into a standard uncertainty, and finally, combine them, as shown in eq. 4.

According to eqs. 2 and 3, the combined uncertainty of the estimated annual concentration $C_{\text{Rn}}(A)$ is given in eq. 4

$$u_c[C_{\text{Rn}}(A)] = C_{\text{Rn}}(A) \times \sqrt{\frac{u(f_c)}{f_c}^2 + \frac{u(\rho_{\text{net}})}{\rho_{\text{net}}}^2 + \frac{u(t)}{t}^2 + \frac{u(a)}{a}^2} \quad (4)$$

The uncertainty of the calibration factor $u(f_c)$ was provided by the manufacturer (Radosys). Its relative value was 7.9 %.

The uncertainty of the net track density is calculated as a combined uncertainty of the track density and the background track density of an unexposed (blank detector), as given with eq. 5

$$u(\rho_{\text{net}}) = \rho_{\text{net}} \sqrt{\frac{u(\rho)}{\rho}^2 + \frac{u(\rho_B)}{\rho_B}^2} \quad (5)$$

Both uncertainty components in eq. 5 were determined from multiple series of measurements. Repeated measurements of detectors for QA with low,

medium, and high track density gave the relative uncertainties of 8, 5, and 3 %, respectively. The relative uncertainty of 12.5 % for the background uncertainty was obtained from repeated measurements of 10 blank detectors.

It should be also noted that the exposure time in eqs. 1 and 2 is expressed in hours. On the other hand, the reported time of detector exposure is measured in days (24 h). Therefore, we assume a possible contribution of several hours' difference at the times of deployment of 46 track-detectors to the overall uncertainty. Lacking the knowledge about the shape of the data distribution, but knowing the time range of ± 2 day (1 day for deploying and 1 day for collecting detectors), we have estimated this type of uncertainty theoretically. Assuming a rectangular distribution of the exposure time, the uncertainty was calculated as $u(t) = 2/\sqrt{3}$ in days. For the detectors exposed during three months in winter 2013, the relative uncertainty for a time exposure was within the range: from 0.8 to 1.7 %.

The uncertainty of the constant a in eq. 4 was expressed with the uncertainty originating from the linear least squares fitting procedure. It was calculated as the root mean square (RMS) of the differences between the experimental and modelled values. It was found to be 3 %.

Finally, in this study, the relative combined uncertainty of annual C_{Rn} , that included the uncertainties of calibration factor, detector background, track counting, exposure time and seasonal correction was found to be between 10 % and 14 %.

RESULTS AND DISCUSSION

Table 1 shows the descriptive statistics of the indoor C_{Rn} . The last two columns refer to the results of the survey from 2010, whereas the second last column refers to winter quarterly measured $C_{\text{Rn}}(\text{W-2010})$ and the last one corresponding to the annual radon concentration $C_{\text{Rn}}(\text{A-2010})$, that was calculated as an average C_{Rn} from the measurements of the four seasons in 2010. The first and the second column pertain to the data from 2013, where $C_{\text{Rn}}(\text{W-2013})$ represents the measured values in the winter and $C_{\text{Rn}}(\text{A-2013})$ is the estimated annual value with applied seasonal correction, using the linear model from 2010. The measuring locations and the estimated annual $C_{\text{Rn}}(\text{A-2013})$ are mapped on fig. 1.

The results were fitted with a log-normal function. Kolmogorov-Smirnov and Chi-square tests were used for testing the hypothesis that the data follow a log-normal distribution. For all data sets, the assumption was confirmed at 95 % level of significance. Furthermore, normality was tested by using the Anderson-Darling and Shapiro-Wilk tests. The summary results of the tests are presented in tab. 2. The obtained values for the error probability (p) were greater than 0.05, and thus confirmed the hypothesis for log-normality and normality.

Table 1. Descriptive statistics of indoor radon concentrations covered in this work

Statistic	$C_{Rn}(W-2013)$ [Bqm ⁻³]	$C_{Rn}(A-2013)$ [Bqm ⁻³]	$C_{Rn}(W-2010)$ [Bqm ⁻³]	$C_{Rn}(A-2010)$ [Bqm ⁻³]
Number of observations	43	43	186	186
Minimum	30	26	17	18
Maximum	535	460	956	552
Median	110	95	135	96
Mean	140	120	179	123
Standard deviation	98	85	150	93
Variation coefficient (CV)	70 %	69 %	84 %	75 %
Geometric mean (GM)	114	98	137	99
Geometric standard deviation (GSD)	1.90	1.90	2.06	1.91

Table 2. The summary results of distribution fitting tests

Variable/test	Kolmogorov-Smirnov	Chi-square	Shapiro-Wilk	Anderson-Darling
	Log-normality testing original data		Normality testing ln transformed	
$C_{Rn}(W-2013)$	$p = 0.998$	$p = 0.454$	$p = 0.996$	$p = 0.992$
$C_{Rn}(A-2013)$	$p = 0.998$	$p = 0.421$	$p = 0.996$	$p = 0.992$
$C_{Rn}(W-2010)$	$p = 0.853$	$p = 0.033$	$p = 0.762$	$p = 0.553$
$C_{Rn}(A-2010)$	$p = 0.719$	$p = 0.150$	$p = 0.364$	$p = 0.317$

Linear model development

The model was developed with the parametric linear regression analysis applied to the results from 2010. It appeared that the dependence among the annual concentrations of radon can be very well described with a linear function. The results are shown graphically in fig. 2. The regression coefficients of the linear model, $C_{Rn}(A) = C_{Rn}(W) a + b$, are as follows: $a = 0.859$ and $b = 0.369$, with a high coefficient of determination $R^2 = 0.92$.

Comparison between C_{Rn} measured in 2010 and 2013

We compared the homogeneity of the $C_{Rn}(2010)$ and $C_{Rn}(2013)$ variances using the Bartlett test (BT). The null hypothesis assuming the variables have the same variance, was confirmed for $p = 0.05$. From here it follows that the variances of the measured $C_{Rn}(W-2010)$ and $C_{Rn}(W-2013)$ were practically equal (BT, $p = 0.978$). Likewise, it appeared that the variance of the

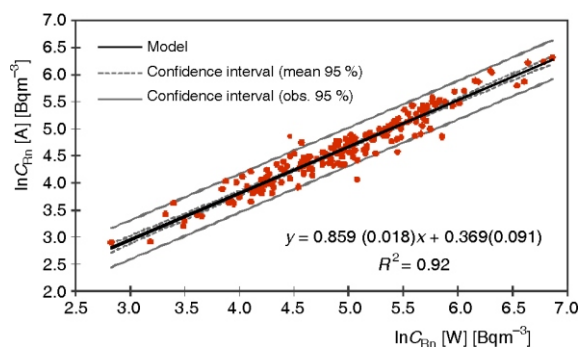


Figure 2. Result of the regression analysis of annual and C_{Rn} measured in the winter of 2010. Regression model: $y = ax + b$ (in brackets: uncertainty of coefficient)

annual concentrations $C_{Rn}(A-2010)$ and $C_{Rn}(A-2013)$ were also equal (BT, $p = 0.952$).

The differences between GM values were also tested. Since the data followed the normal distribution and the variances of the two data sets were equal, the Student's t -test for independent samples/two-tailed, was applied for the log-transformed values of the C_{Rn} . The differences between the GM values of the measured winter C_{Rn} for both surveys (2010 and 2013) were negligible (Student t -test, $p = 0.124$). It also applies to the differences between the estimated annual mean values (Student t -test, $p = 0.924$).

Impact of the building characteristics

We also compared the variances of C_{Rn} for two groups of data, classified according to either the presence or absence of a basement in a dwelling. Furthermore, we compared the variances between the groups of houses that were made of different dominant construction material. The results of the Bartlett test for all the groups are given in tab. 3. Because the datasets are homogeneous (BT, $p > 0.05$) and normal (AD, SW, $p > 0.05$), the influence of these factors was tested on the grouped C_{Rn} by ANOVA (analysis of variance) and Fisher LSD test.

ANOVA for winter and annual C_{Rn} from 2013, grouped according to the "presence of basement" and "building materials" showed significant differences between the mean values of the groups (ANOVA, $p < 0.0001$ in both cases). The 2010 data test also revealed significant differences. ANOVA gave a value $p = 0.006$ for the winter measurements and $p = 0.001$ for the annual values, respectively.

The Fisher LSD test for C_{Rn} winter measurements showed that its mean radon concentration values in houses without basements are higher than those

away” with only few samples. This illustrates that apart from the seasonal variations, the influence of some other factors related to characteristics such as age of the building [28, 29], type of windows [30], heating method [31], wall finishing [32], number of floors [33] and geology [34-36] should not be ignored.

CONCLUDING REMARKS

A student campaign was organized in the winter of 2013 for indoor C_{Rn} measurements in ground floor rooms of 43 dwellings in 16 randomly selected cities in the Republic of Macedonia.

To estimate the annual C_{Rn} for 2013, the winter data were adjusted to annual means by applying a linear model, derived from the results of the 2010 survey by regression of annual vs. winter. The obtained function in this way has a high coefficient of determination and a negligible contribution to the combined uncertainty of the annual radon concentration.

Analysis of the data shows that C_{Rn} measured in the winter as well as estimated annual C_{Rn} from the 2013 and 2010 survey:

- can be described with log-normal distributions,
- have the same variance and GM values (insignificant difference),
- have the same variances when grouped with respect to the presence of basement and the dominant building material,
- showed the same trend of the differences in GM values between C_{Rn} in houses with and with no basement, and
- showed the same trend of differences of GM values between the C_{Rn} values for houses built from concrete and stone.

The proposed method aims to provide time and cost effective measurements (three-month duration – single disposable detector) for estimation of the annual indoor radon concentrations $C_{Rn}(A)$. Similar models could be developed for estimation of the annual C_{Rn} using a different season of the year (summer, spring or fall). Actually, something very similar has been done already in Macedonia [22] and India [37] where the method was used to estimate missing seasons.

ACKNOWLEDGEMENTS

The authors gratefully acknowledge Dr. Eric Hulbert, from Radosys Company, Budapest, Hungary, for supporting this project with the RSKS detector donation.

The authors express their gratitude to the students of the Faculty of Medical Sciences in Stip who provided assistance for this survey. The work was supported by the research fund of the Goce Delcev University, Stip, Republic of Macedonia.

AUTHORS' CONTRIBUTIONS

The manuscript was written by Z. Stojanovska with contribution of all the authors. The figures were prepared by Z. Stojanovska and P. Bossew. The survey was organized by Z. Stojanovska and M. Zdravkovska and detector analysis were carried out by K. Ivanova and M. Tsenova. Theoretical investigation was carried out by Z. Stojanovska, K. Ivanova, P. Bossew, B. Boev, Z. S. Žunić, Z. Čurguz, P. Kolarž, M. Ristova. Results discussion and review of the manuscript involved all authors.

REFERENCES

- [1] ***, United Nations Scientific Committee on the Effects of Atomic Radiation, Effects of Ionizing Radiation, Report to the General Assembly with Scientific Annexes (Annex B), NY: UN, 2008
- [2] Yarmoshenko, I., et al., Variance of Indoor Radon Concentration: Major Influencing Factors, *Science of the Total Environment*, 541 (2016), Jan., pp. 155-160
- [3] Szabo, Z., et al., Radon and Thoron Levels, their Spatial and Seasonal Variations in Adobe Dwellings – a Case Study at the Great Hungarian Plain, *Isotopes in Environmental and Health Studies*, 50 (2014), 2, pp. 211-225
- [4] Quarto, M., et al., Indoor Radon Activity Concentrations Measurements in the Great Historical Museums of University of Naples, Italy, *Radiation Protection Dosimetry*, 168 (2015), 1, pp. 116-123
- [5] Smetanova, I., et al., The Results of integration Measurements of Indoor Radon Activity Concentration in Houses in Ruzomberok Town (Northern Slovakia), *Contributions to Geophysics and Geodesy*, 45 (2015), 1, pp. 41-51
- [6] Stojanovska, Z., et al., Results from Time Integrated Measurements of Indoor Radon, Thoron and Their Decay Product Concentrations in Schools in the Republic of Macedonia, *Radiation Protection Dosimetry*, 162 (2014), 1-2, pp. 152-156
- [7] Quarto, M., et al., Indoor Radon Concentration Measurements in Some Dwellings of the Penisola Sorrentina, South Italy, *Radiation Protection Dosimetry*, 156 (2013), 2, pp. 207-212
- [8] Stojanovska, Z., et al., Variation of Indoor Radon Concentration and Ambient Dose Equivalent Rate in Different Outdoor and Indoor Environments, *Radiation and Environmental Biophysics*, 55 (2016), 2, pp. 171-183
- [9] Kavasi, N., et al., Effect of Radon Measurement Methods on Dose Estimation, *Radiation Protection Dosimetry*, 145 (2011), 2-3, pp. 224-232
- [10] Žunić, Z. S., et al., High Variability of Indoor Radon Concentrations in Uraniferous Bedrock Areas in the Balkan Region, *Applied Radiation and Isotopes*, 94 (2014), Dec., pp. 328-337
- [11] Mishra, R., et al., An Evaluation of Thoron (and Radon) Equilibrium Factor Close to Walls Based on Long-Term Measurements in Dwellings, *Radiation Protection Dosimetry*, 160 (2014) 1-3, pp. 164-168
- [12] Žunić, Z. S., et al., Some Results of a Radon Survey in 207 Serbian Schools, *Romanian Journal of Physics*, 58 (2013), Suppl., pp. S320-S327
- [13] Gulan, L., et al., High Annual Radon Concentration in Dwellings and natural Radioactivity Content in Nearby

- Soil in Some Rural Areas of Kosovo and Metohija, *Nucl Technol Radiat*, 28 (2013), 1, pp. 60-67
- [14] Nafezi, G., et al., Radon Levels and Doses in Dwellings in Two Villages in Kosovo, Affected by Depleted Uranium, *Radiation Protection Dosimetry*, 158 (2013), 3, pp. 331-339
- [15] Ćurguz, Z., et al., Long-Term Measurements of Radon, Thoron and Their Airborne Progeny in 25 Schools in Republic of Srpska, *Journal of Environmental Radioactivity*, 148 (2015), Oct., pp. 163-169
- [16] Ćurguz, Z., et al., Active and Passive Radon Concentration Measurements and First-Step Mapping in Schools of Banja Luka, Republic of Srpska, *Romanian Journal of Physics*, 58 (2013), Suppl., pp. S90-98
- [17] Ivanova, K., et al., Pilot Survey of Indoor Radon in the Dwellings of Bulgaria, *Radiation Protection Dosimetry*, 157 (2013), 4, pp. 594-599
- [18] Muntean, L. E., et al., Assessment of Annual and Seasonal Variation of Indoor Radon Levels in Dwelling Houses from Alba County, Romania, *Romanian Journal of Physics*, 59 (2014), 1-2, pp. 163-171
- [19] Nikolopoulos, D., et al., Factors Affecting Indoor Radon Concentrations of Greek Dwellings through Multivariate Statistics – First Approach, *Journal of Physical Chemistry & Biophysics*, 4 (2014), 145, doi: 10.4172/2161-0398.1000145
- [20] Stojanovska, Z., et al., Indoor Exposure of Population to Radon in the FYR of Macedonia, *Radiation Protection Dosimetry*, 148 (2011), 2, pp. 162-167
- [21] Stojanovska, Z., et al., Seasonal Indoor Radon Concentration in FYR of Macedonia, *Radiation Measurements*, 46 (2011), 6-7, pp. 602-610
- [22] Stojanovska, Z., et al., National Survey of Indoor Thoron Concentration in FYR of Macedonia (Continental Europe, Balkan Region), *Radiation Measurements*, 49 (2013), Feb., pp. 57-66
- [23] Bossew, P., et al., Prediction of Indoor Radon Risk from Radium Concentration in Soil: Republic of Macedonia Case Study, *Romanian Journal of Physics*, 58 (2013), Suppl., pp. S29-S43
- [24] ***, EURACHEM/CITAC Guide CG 4, Quantifying Uncertainty in Analytical Measurement, Third Edition, QUAM, 2012
- [25] ***, IAEA-TECDOC-1401 Quantifying Uncertainty in Nuclear Analytical Measurements, IAEA, 2004
- [26] Valmari, T., et al., Radon in Finnish Apartment Buildings, *Radiation Protection Dosimetry*, 152 (2012), 1-3, pp. 146-149
- [27] Bossew, P., et al., Geographical Distribution of the Annual Mean Radon Concentrations in Primary Schools of Southern Serbia – Application of Geostatistical Methods, *Journal of Environmental Radioactivity*, 127 (2014), Jan., pp. 141-148
- [28] Branco, T. B. S. P., et al., Children's Exposure to Radon in Nursery and Primary Schools, *International Journal of Environmental Research and Public Health*, 13 (2016), 4, 386 doi:10.3390/ijerph13040386
- [29] Stajić, J., et al., Radon Concentrations in Schools and Kindergartens in Kragujevac City, Central Serbia, *Clean Soil Air Water*, 43 (2015), Sept., pp. 1361-1365
- [30] Ivanova, K., et al., Measurement of Indoor Radon Concentration in Kindergartens in Sofia, Bulgaria, *Radiation Protection Dosimetry*, 162 (2014), 1-2, pp. 163-166
- [31] Stojanovska, Z., et al., Annual and Seasonal Variations of Indoor Radon Concentration in Skopje, Republic of Macedonia, *Safety Engineering*, 4 (2012) 2, pp. 221-225
- [32] Karpinska, M., et al., Indoor Radon Concentrations in Concrete Slab Buildings Situated in Green Hills Housing Estate in Bialystok, *Polish Journal of Environmental Studies*, 17 (2008), 1, pp. 33-38
- [33] Chen, J., Estimate of Annual Average Radon Concentration in the Normal Living Area from Short-Term Tests, *Health Physics*, 85 (2003), 6, pp. 740-744
- [34] Kozak, K., et al., Correction Factors for Determination of Annual Average Radon Concentration in Dwellings of Poland Resulting from Seasonal Variability of Indoor Radon, *Applied Radiation and Isotopes*, 69 (2011), Jan., pp. 1459-1465
- [35] Gillmore, G. K., et al., The Effects of Geology and the Impact of Seasonal Correction Factors on Indoor Radon Levels: A Case Study Approach, *Journal of Environmental Radioactivity*, 84 (2005), June, pp. 469-479
- [36] Pinel, J., et al., Seasonal Correction Factors for Indoor Radon Measurements in the United Kingdom, *Radiation Protection Dosimetry*, 58 (1995), 2, pp. 127-132
- [37] Stojanovska, Z., et al., National Survey of Indoor Thoron Concentration in FYR of Macedonia (Continental Europe of Balcan region), *Radiation Measurements*, 49 (2013), Feb., pp. 57-66

Received on July 20, 2016

Accepted on January 19, 2017

**Зденка СТОЈАНОВСКА, Кремена ИВАНОВА, Питер БОСЕВ,
Блажо БОЕВ, Зора, С. ЖУНИЋ, Мартина ЦЕНОВА, Зоран ЂУРГУЗ,
Предраг М. КОЛАРЖ, Милка ЗДРАВКОВИЋ, Мимоза РИСТОВА**

ПРОЦЕНА ДУГОТРАЈНИХ КОНЦЕНТРАЦИЈА РАДОНА У ЗАТВОРЕНИМ ПРОСТОРИЈАМА НА ОСНОВУ КРАТКОРТАЈНИХ МЕРЕЊА

Представљена је метода процене годишње концентрације радона заснован на краткотрајним (тримесечним) мерењима. Студија обухвата резултате два независна скупа мерења концентрације радона у затвореним просторијама спроведених у 16 градова Републике Македоније. Први сет резултата садржи зимске и годишње концентрације радона добијене током националног мерења радона у 2010. години. Други сет података садржи само концентрације радона мерене током зиме 2013. године. Оба сета података односе се на концентрације радона из истих градова, где су мерења вршена у становама и приземљу истом методологијом. Добијени резултати били су увек са ниском дисперзијом концентрације радона. Линеарна регресиона анализа примењена на концентрације радона измерене у току зиме 2010. и годишње концентрације радона за 2010. годину показала је висок коефицијент детерминације $R^2 = 0.92$, са релативном несигурношћу од 3 %. Овај линеарни модел коришћен је за процену годишње концентрације радона за 2013. годину на основу зимских мерења изведених те године.

Геометријска средња вредност процењене годишње концентрације радона за 2013, $(A-2013) = 98 \text{ Bq m}^{-3}$, била је готово једнака вредности која се односи на концентрацију радона у 2010. години, $(A-2010) = 99 \text{ Bq m}^{-3}$. Анализа утицаја карактеристике зграда, одсуство подрума, односно доминантног грађевинског материјала, на процењене годишње концентрације радона, такође је приказана. Наши резултати показују да мали број релативно кратких мерења радона могу дати разуман увид у просечне резултате добијене у опсежнијем истраживању.

Кључне речи: ситан у приземљу, радон у затвореној просторији, линеарна регресиона анализа, несигурност

MERITS AND DEMERITS OF DIFFERENT METHODS FOR RADON EXHALATION MEASUREMENTS FOR BUILDING MATERIALS

A. Awhida¹, P. Ujić², P. Kolarž³, I. Čeliković², M. Milinčić⁴, A. Lončar⁴, B. Lončar^{1*}

¹Faculty of Technology and Metallurgy, University of Belgrade, Belgrade, Serbia

²Institute of Nuclear Sciences “Vinča”, University of Belgrade, Belgrade, Serbia

³Institute of Physics Belgrade, University of Belgrade, Belgrade, Serbia

⁴Faculty of Geography, University of Belgrade, Belgrade, Serbia

Abstract. *With an increase in the awareness of the need to save energy, residents tend to live in dwellings with increasingly tight windows and doors, thus reducing the ventilation rate of indoor air which leads to an increased accumulation of radon indoors. Having in mind that a dose from an exposure to inhaled radon and its progenies can be higher than a dose received from radium in building materials, it is suggested that radon exhalation measurements should receive due attention. In this contribution, the authors compare results gathered using a few methods for radon exhalation measurement and discuss its merits and demerits.*

Key words: Radon, building material, exhalation measurements

DOI: 10.21175/RadProc.2017.27

1. INTRODUCTION

It is well known that more than 50% of the radiation dose received by the general population is due to an exposure to radon and its decay products [1]. Recent surveys and pooled analysis of epidemiological studies conducted in Europe [2], Asia [3] and North America [4] have unambiguously showed a connection between the exposure to indoor radon and lung cancer. Based on these studies, the World Health Organization (WHO) has estimated that between 3% and 14% of all lung cancers originate from exposure to radon [5].

Among several possible sources of radon in buildings, the soil underneath the building is considered to be a dominant one. On the other hand, in the upper floors of multi-storey dwellings, building materials are the major contributors to indoor radon concentration. In the era of waste reduction policies, new kinds of building material are used, such as coal ash bricks and cellular concrete blocks. These materials are built from fly ash that has a higher concentration of uranium compared to coal before combustion [6]. In addition, with an increase in the awareness of the need for saving energy, residents tend to live in buildings with more and more tight windows and doors, thus reducing the average air exchange rate. All this leads to an increase of the indoor radon concentration in multi-storey buildings that is almost solely coming from the building materials [7], [8].

The technical guidance of the European Commission introduces the Activity concentration

index (colloquially known as “gamma index”) that takes into account that the annual effective dose received from the external exposure of inhabitants to radionuclides in building material should not be more than 1 mSv (or 0.3 mSv, depending on dose criteria) [9]. The same guidance estimates that the radon concentration is unlikely to exceed the Commission’s recommendation of 200 Bq m⁻³ as long as gamma doses from the building materials do not exceed 1 mSv a⁻¹ [9]. On the contrary, it is shown that it is possible that the concentration of ²²²Rn exceeds 200 Bq m⁻³ for building material with ²²⁶Ra concentrations larger than 200 Bq kg⁻¹ [10]. The assumption of proportionality between radium content and the exhalation rate is misleading to some extent since the exhalation rate strongly depends on the emanation coefficient, porosity, permeability, diffusion length and numerous other factors. Thus, the observation of poor correlation between the radium content in building material and the radon exhalation rate is not a surprise [11]. It was indicated that for a very low air exchange rate, of the order of 0.2 h⁻¹, the internal exposure of exhaling radon could exceed the external exposure coming from ²²⁶Ra [11]. Having in mind the abovementioned, it is not surprising that the issue of radon exhalation rate is becoming more relevant and that there are numerous recent publications on this matter that use various techniques.

Methods of radon exhalation measurements are divided by the way of enclosing sample about to be measured. Two main groups are distinguished: closed-chamber methods and open-chamber methods [12]. In

* bloncar@tmf.bg.ac.rs

the closed-chamber methods a sample is enclosed in a well sealed chamber. An increase of radon concentration in the chamber is then followed [12]. On the other hand, in the open-chamber methods measurements are performed in ventilated chambers. A gas in a chamber is continuously exchanged with a radon free or low-radon gas using a pump with a known and constant gas exchange rate. Exhalation is extracted from the measured radon concentration and known gas exchange rate [12]. This contribution compares several closed-chamber radon exhalation methods developed or used in our Laboratory for Nuclear and Plasma Physics of the "Vinča" Institute of Nuclear Sciences.

2. MATERIALS AND METHODS

Three different methods for radon exhalation measurements were compared in this paper. Two of them are well-established closed-chamber methods, also known as "sealed-can" methods [13]: one utilizes an active device, while the other uses solid state nuclear track detectors (SSNTD) to measure radon accumulated in the chamber. The dimensions of the chamber are $26.3 \times 26.3 \times 42.4 \text{ cm}^3$. The third method discussed in this paper is the recently developed "gamma method" [14].

The same sample used for all three measurements is of cylindrical shape with a diameter of 7.1 cm and a height of 12 cm. The 45% (of weight) of sample consist of travertine from "Niška Banja" known for high radium content. The travertine was smashed in the powdered form. Travertine was mixed with a 15% of sand and 40% of cement, homogenized and shaped into proper cylindrical form. Thus obtained density of the sample was 1750 kg m^{-3} and ^{226}Ra concentration was $174 \pm 2 \text{ Bq kg}^{-1}$. The sample was left to cure for about one month and afterwards was sealed by a bee-wax from all sides except for one base. Sample was then left for approximately 40 days in order to achieve equilibrium between ^{222}Rn and its progenies [14].

2.1. The closed-chamber method with an active device

In the closed-chamber method, the sample is enclosed in a preferably airtight chamber and the accumulation of radon exhaling from the sample is being measured. With the active device, radon growth in the chamber is being continuously measured.

In ideal cases, when the chambers are well-sealed there is no leakage of radon from them, and their volume V (m^3) is much larger than the sample volume, radon concentration C (Bq m^{-3}) in time t (s) can be expressed as [15]:

$$C(t) = \frac{EA}{V\lambda} (1 - e^{-\lambda t}) + C_0 e^{-\lambda t} \quad (1)$$

where E is the radon exhalation rate per unit of surface area ($\text{Bq s}^{-1} \text{ m}^{-2}$), A is the surface of the sample (m^2), V (m^3) is the total volume of the measurement system that includes volumes of the accumulation chamber, tubes and measurement chamber of the measuring device, and λ is the radon decay constant (s^{-1}). Initial radon concentration in the chamber at the time when

chamber is sealed is denoted as C_0 (Bq m^{-3}) and can be neglected since the chamber was sealed in a low-radon environment. From now on, radon exhalation rate per unit of surface area will be referred to as radon exhalation.

For sample pore volumes that are relatively large compared to the size of the chamber (more than 10%), there is a high probability that radon exhalation will decrease due to a decrease of the concentration gradient between the sample pores and inside air of accumulation chamber. In our case, the container free volume is more than 50 times larger than the sample pore volume, and therefore this effect can be neglected. Nevertheless, due to the leakage of radon, it was necessary to introduce an effective decay constant ($\lambda_{\text{eff}} = \lambda + \lambda_{\text{leak}}$) that corrects the decay constant for the removal of radon by leakage [12].

The measurement was performed using a RAD7 device from DurrIDGE Radon Instrumentation that was connected to the chamber through a drying tube. The measurement cycle was 4h, while duration of the measurement was 14 days. By fitting the experimental data with formula 1, one can obtain effective lifetime and knowing the radon decay constant, a correction to the leakage can be extracted. Detailed approach how to estimate different contributions to the effective decay constant can be found in [16].

2.1. The closed-chamber method with SSNTD

The only difference between this method and the one previously described is in the technique used to measure radon in the chamber. With the passive devices, such as SSNTD, it is not possible to perform continuous Rn measurements, but what is recorded is the track density ρ on the polycarbonate detector that is directly proportional to the exposure.

Therefore, by integrating equation (1), using the effective decay constant λ_{eff} and the relation between the radon concentration $C(t)$ and the track density ρ (m^{-2}):

$$\frac{d\rho(t)}{dt} = kC(t) \quad (2)$$

where k ($\text{m}^{-2}/(\text{Bq s m}^{-3})$) is the calibration coefficient of the detector,

one can obtain a general expression for the radon exhalation E :

$$E = \frac{V\lambda_{\text{eff}}}{A} \frac{1}{t - \frac{1}{\lambda_{\text{eff}}}} \left[\frac{\rho}{k} - \frac{C_0}{\lambda_{\text{eff}}} (1 - e^{-\lambda_{\text{eff}} t}) \right] \quad (3)$$

The sample was put into the chamber in the area with the small concentration of radon, so ambiguity coming from the second term can be neglected.

For this method, a single measurement with a Radtrak²® detector produced by Landauer Nordic was used and dose expressed by ρ/k was provided as a measurement result. In order to be able to compare the results between two closed-chamber methods, the Radtrak²® detector was exposed to the radon simultaneously with the measurement using RAD7. For the effective radon decay constant, a value extracted from the measurement with an active device was used.

2.3. The “Gamma method”

This method of radon exhalation measurement has been published recently [14]. Contrary to all existing models that directly measure the concentration of exhaled radon, in the “gamma method”, radon exhalation is deduced indirectly, by estimating the amount of non-exhaled radon. Non-exhaled radon is estimated by means of gamma spectrometric measurements, measuring the activity concentration of radon progenies ^{214}Bi and ^{214}Pb that did not escape from the building material. The whole procedure and the complicated mathematical apparatus of this model are given in the reference in detail [14].

A cylindrical sample was sealed from all sides but one base and left for forty days in order to achieve an equilibrium between ^{222}Rn and its progenies. Due to this asymmetrical sealing of the sample, a gradient in radon concentration is achieved, with the lowest concentration at the open base of the cylinder and highest ^{222}Rn concentration at the sealed base of the cylindrical sample.

The sample was measured by the Ortec HPGe detector with a relative efficiency of 37%, surrounded by passive lead shielding. The two-fold measurements, once with the sealed base of the sample placed on the HPGe detector and the other time with the open base of the sample placed on the HPGe detector were performed. Since the sample is open on one side, the concentration of radon progenies in the sample is not homogenous. Therefore in order to estimate the counting rate using a chosen γ -ray of radon progeny (609 keV, 1120 keV and 17645 keV for ^{214}Bi and 295 keV and 352 keV for ^{214}Pb) the next step is to estimate contribution of each layer of the sample to the counting rate (i.e. to estimate calibration coefficient of each layer) by using semi-empirical method, an EFFTRAN package [17] for example, to calculate efficiency transfer from a standard to a sample as described in details in [14]. Finally, solving the system of equations from [14], one can extract not only the exhalation rate, but the radon diffusion (and consequently radon diffusion length) and the emanation coefficient as well.

3. RESULTS AND DISCUSSION

Radon exhalation rate performed with a measurement with an active device was obtained by fitting experimental data on equation 1. Exhalation rate was found to be $33.2 \pm 1.8 \text{ mBq s}^{-1} \text{ m}^{-2}$ and $\lambda_{\text{eff}} = (2.25 \pm 0.03)10^{-6} \text{ s}^{-1}$. Measurement with RAD7 was performed with a drying tube. Operating with the drying tube can strongly decrease humidity in the chamber and consequently dry the sample. Since the change in humidity was not considered, uncertainty coming from a change in humidity is introduced into systematic error. The radon exhalation rate of slab changes by 30% from exhalation of the sample with an ambient humidity to dried sample [16]. Due to integrated nature of measurement with RAD7 the systematic uncertainty estimated to be 15%, (i.e. a half of the exhalation rate changes between completely dried and a sample at ambient humidity) should be taken into account.

The radon exhalation rate obtained from a measurement with a SSNTD was estimated using

equation 3. The effective decay constant extracted from the measurement with RAD7 was used. Obtained value of $34.0 \pm 2.0 \text{ mBq s}^{-1} \text{ m}^{-2}$ is from the single measurement.

Beside the estimated radon exhalation rate of $32.6 \pm 1.4 \text{ mBq s}^{-1} \text{ m}^{-2}$ shown in Figure 1 by using “gamma” method, the diffusion length of $0.31 \pm 0.03 \text{ m}$ and the radon emanation coefficient of 0.45 ± 0.02 were deduced at the same time.

Results of the radon exhalation of the same sample obtained by three different methods are presented in figure 1. The average, weighted by the variance is $33.2 \pm 0.8 \text{ mBq s}^{-1} \text{ m}^{-2}$ and is indicated by a dashed line.

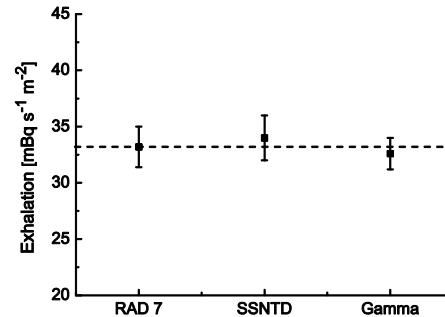


Figure 1. Results of the radon exhalation measurements from three different methods. A dashed line corresponds to the weighted average

Overall, a good agreement between the “gamma” method and the two other methods is observed. In general, the method with SSNTD is an integrating one, and thus the result cannot be corrected for any leakage of the accumulation chamber during the measurement period, while this correction can be done with an active device. For values of leakage that are small compared to the decay constant, a change of exhalation is not significant. Based on the extracted λ_{eff} leakage is deduced to be $\lambda_{\text{leak}} = 1.5 \cdot 10^{-7} \text{ s}^{-1}$, and therefore if it was not used to calculate exhalation rate with a passive device, exhalation rate would be underestimated by 6-7% of the measured one. On the other hand, leakage is not relevant for the “gamma” method.

For a method with SSNTD, the background radon concentration, present in a chamber at the moment of its sealing, is responsible for the overestimation of radon exhalation. For the method with an active device, the result can be corrected for the initial radon concentration. In order to eliminate this systematic error, the sample was put in a chamber in a very low radon environment. For the “gamma” method, background radon is not an issue.

The observed disagreement between the two methods could originate from the underestimation of measurement uncertainty.

With an active device, one can continuously measure ingrowth of the radon concentration and stop the measurements at a certain moment, when enough of statistics is provided. Using the method with SSNTD, it is not possible to obtain such feedback, so the duration of measurement should be longer to assure good statistics. This period can be shortened by using SSNTD with a larger sensitivity. With the

“gamma” method, it is also possible to continuously measure the number of counts under the peak.

The safe handling of numerous active devices requires the usage of a drying tube installed in a closed circuit with the accumulation chamber. This way, the sample used is constantly being dried and the moisture content is changing with time, which influences the radon exhalation. In our particular measurement, this influence additional systematic error of 15%. A good solution would be to use active devices that do not require the usage of a drying tube. On the contrary, in the closed chamber method with a passive device, there are no changes in the humidity. Regarding the gamma spectrometers, usually there are no changes in humidity as well, since these devices are usually working in an air-controlled environment.

As far as the time required for sample preparation is concerned, it is short for the two closed-chamber methods, while it is quite long for the “gamma” method since it is necessary to wait around 38 days to achieve an equilibrium between radon and its progenies. As far as the complexity of the analysis is concerned, the “gamma” method is the most difficult one due to rather complicated mathematical procedures and the necessity to calculate the relative counting efficiency for each infinitesimal layer of the sample [14], as opposed to the sealed-chamber method with a passive device, which requires only a single measurement.

4. CONCLUSION

This contribution compares three different methods for radon exhalation measurements: the closed-chamber method with an active device, the closed-chamber method with a passive device (SSNTD), and the recently developed “gamma” method. The results obtained are in the fair agreement.

The method with a SSNTD is the simplest one, but the least reliable. Due to the integrative nature of this method, it should be used in a well-controlled environment: radon leakage should be negligible, and a low Rn background area should be provided in the chamber.

The method with an active device is also simple to use. It is more reliable than the one with a SSNTD, since its continuous measurements enable correcting results for the radon leakage and radon background. The only drawback of this method, at least for certain devices, is the use of a drying tube disabling measurement in a moisture-controlled environment.

The “gamma” method is the most complicated one. In general, its only limitation is in a certain combination of geometry of a sample and emanation coefficient [14]. The method is not affected by the background radon concentration, the radon leakage is not an issue, and it can be performed in the moisture controlled environment. Besides, it is the only method that besides radon emanation provides values for the radon diffusion length and emanation coefficient, which would otherwise require additional equipment. These parameters are important characteristics of building materials, which are becoming an issue due to energy saving policies.

Acknowledgement: The authors acknowledge the support of the Ministry of Education, Science and Technological Development of the Republic of Serbia [P171018, P171007].

REFERENCES

1. “Sources and effects of ionizing radiation,” UNSCR, New York (NY), USA, Rep. Rep. 46 (A/55/46), 2000. Retrieved from: http://www.unscear.org/docs/publications/2000/UNSCAR_2000_Report_Vol.I.pdf Retrieved on: Jan. 9, 2017
2. S. Darby et al., “Radon in homes and risk of lung cancer: collaborative analysis of individual data from 13 European case-control studies,” *BMJ*, vol. 330, no. 7485, pp. 223-1 – 223-6, Jan. 2005. DOI: 10.1136/bmj.38308.477650.63
3. D. Krewski et al., “A combined analysis of North American case-control studies of residential radon and lung cancer,” *J. Toxicol. Environ. Health A*, vol. 69, no. 7-8, pp. 533 – 597, Apr. 2006. DOI: 10.1080/15287390500260945 PMID: 16608828
4. J. H. Lubin et al., “Risk of lung cancer and residential radon in China: pooled results of two studies,” *Int. J. Cancer*, vol. 109, no. 1, pp. 132 – 137, Mar. 2004. DOI: 10.1002/ijc.11683 PMID: 14735479
5. *WHO Handbook on Indoor Radon: a Public Health Perspective*, World Health Organization, Geneva, Switzerland, 2009. Retrieved from: http://apps.who.int/iris/bitstream/10665/44149/1/9789241547673_eng.pdf Retrieved on: Jan. 17, 2017
6. M. M. Janković, D. J. Todorović, J. D. Nikolić, “Analysis of natural radionuclides in coal, slag and ash in coal-fired power plants in Serbia,” *J. Min. Metall. Sect. B – Metall.* vol. 47, no. 2, pp. 149 – 155, May 2011. DOI: 10.2298/JMMB110208008J
7. “Effects of ionizing radiation Volume II,” United Nations Scientific Committee on Effects of Atomic Radiation, New York (NY), USA, Rep. A/61/46, 2006. Retrieved from: http://www.unscear.org/docs/publications/2006/UNSCAR_2006_Report_Vol.II.pdf Retrieved on: Jan. 9, 2017
8. I. V. Yarmoshenko, A. V. Vasilyev, A. D. Onishchenko, S. M. Kiselev, M. V. Zhukovsky, “Indoor radon problem in energy efficient multi-storey buildings,” *Radiat. Prot. Dosim.*, vol. 160 no. 1-3, pp. 53 – 56, Apr. 2014. DOI: 10.1093/rpd/ncu110 PMID: 24723188
9. EC Directorate General Environment, Nuclear Safety and Civil Protection. (Jun. 8, 1999). *Radiation protection 112 Radiological Protection Principles Concerning the Natural Radioactivity of Building Materials*. Retrieved from: https://ec.europa.eu/energy/sites/ener/files/document_s/112.pdf Retrieved on: Jan. 15, 2017
10. *Naturally Occurring Radioactivity in the Nordic Countries – Recommendations*, The Radiation Protection Authorities in Denmark, Finland, Iceland, Norway and Sweden, Stockholm, Sweden, 2000. Retrieved from: <https://www.sst.dk/~media/593F6353688A4B3BB8C8F88691248AB7.ashx> Retrieved on: Jan. 9, 2017
11. P. Ujčić, I. Čeliković, A. Kandić, I. Vukanac, M. Đurašević, D. Dragosavac, Z. S. Žunić, “Internal exposure from building materials exhaling 222 Rn and

- 220 Rn as compared to external exposure due to their natural radioactivity content," *Appl. Radiat. Isot.*, vol. 68, no. 1, pp. 201 – 206, Jan. 2010.
DOI: 10.1016/j.apradiso.2009.10.003
PMid: 19880324
12. N. P. Petropoulos, M. J. Anagnostakis, S. E. Simopoulos, "Building materials radon exhalation rate: ERRICCA intercomparison exercise results," *Science of The Total Environment*, vol. 272, no. 1-3, pp. 109 – 118, May 2001.
DOI: 10.1016/S0048-9697(01)00674-X
 13. F. A. Abu-Jarad, "Application of nuclear track detectors for radon related measurements," *Nucl. Tracks Radiat. Meas.*, vol. 15, no. 1-4, pp. 525-534, 1988.
DOI: 10.1016/1359-0189(88)90195-1
 14. A. Awhida, P. Ujić, I. Vukanac, M. Đurašević, A. Kandić, I. Čeliković, B. Lončar, P. Kolarž, "Novel method of measurement of radon exhalation from building materials," *Journal of Environmental Radioactivity*, vol. 164, pp. 337 – 343, Nov. 2016.
DOI: 10.1016/j.jenvrad.2016.08.009
PMid: 27552657
 15. P. Ujić, I. Čeliković, A. Kandić, Z. Žunić, "Standardization and difficulties of the thoron exhalation rate measurements using an accumulation chamber," *Radiat. Meas.*, vol. 43 no. 8, pp. 1396 – 1401, Sep. 2008.
DOI: 10.1016/j.radmeas.2008.03.003
 16. P. Tuccimei, M. Moroni, D. Norcia, "Simultaneous determination of ^{222}Rn and ^{220}Rn exhalation rates from building materials used in Central Italy with accumulation chambers and a continuous solid state alpha detector: influence of particle size, humidity and precursors concentration," *Appl. Radiat. Isot.*, vol. 64, no. 2, pp. 254 – 263, Feb. 2006.
DOI: 10.1016/j.apradiso.2005.07.016
PMid: 16154752
 17. T. Vidmar, "EFFTRAN – a Monte Carlo efficiency transfer code for gamma-ray spectrometry," *Nucl. Instrum. Methods A*, vol. 550, no. 3, pp. 603 – 608, Sep. 2005.
DOI: 10.1016/j.nima.2005.05.055

DIURNAL AND SPATIAL VARIATIONS OF RADON CONCENTRATION AND ITS INFLUENCE ON IONIZATION OF AIR

Predrag Kolarž^{1*}, Zdenka Stojanovska², Zoran Ćurguz³, Zora S. Žunić⁴

¹Institute of Physics Belgrade, Pregrevica 118, 11080 Zemun, Serbia

²Faculty of Medical Sciences, Goce Delčev University Stip,
Krste Misirkov No.10-A P.O. Box 201, Republic of Macedonia

³Faculty of Transport and Traffic Engineering, University of East Sarajevo,
Vojvode Mišića 52, 74 000 Dobojo, Republic of Srpska

⁴Vinca Institute of Nuclear Sciences, University of Belgrade,
Mike Petrovića Alasa 12-14, 11351 Vinča, Belgrade, Serbia

Abstract: The most abundant and efficient source of air ionization in the lower layer of the atmosphere is radon. As an alpha emitter, radon plays a crucial role in the earth's atmospheric electricity. Besides the physical, radon and ions have a significant biological role concerning human health: radon is a health hazard while the ions are beneficial ingredients of the air we breathe. In this study, we examined the dynamics of radon and air ions diurnal change in houses with different floor and windows insulations. Measurements were made using continual radon monitor Rad-7 and air ion counter CDI-06. Diurnal and spatial variations of both atmospheric constituents are mutually related and dependent mostly on radon exhalation potential, meteorological parameters, aerosol concentration and formation of the temperature inversion layer. Indoor concentrations are related to the potential for accumulation of radon that is coming from the ground beneath the foundation and also influenced by external radon concentration that is diffusing through the walls, doors, and windows. Level of diffusion is depending on insulation. The difference in the paths by which radon enters the home can be seen by analyzing changes during diurnal continuous measurements.

Keywords: radon, air ions, ionization, atmosphere, air, natural radioactivity.

1. INTRODUCTION

Radon (^{222}Rn) is radioactive noble gas generated in the decay chain of the primordial elements uranium and thorium which can be found in the soil worldwide. ^{222}Rn decays emitting α -particle with half-life 3.82 days and it is followed by a series of four further decays (2 α and 2 β) with much shorter half-lives. After its ancestor decay, ^{222}Rn penetrates through the ground and moves up by diffusion and convection toward the surface and into the air. ^{222}Rn exhalation rate, at the surface, is driven by weather conditions such as precipitation, air pressure, the temperature of air and also permeability, thermal gradient, and humidity of the soil [1]. Further movement of ^{222}Rn through the atmosphere is determined by thermal processes. Diurnal ^{222}Rn concentration change is driven by surface soil and air temperature ratio which is resulting in the highest concentrations during

temperature inversion during the night and lowest in the afternoon when upward gas diffusion is highest. When exhaling from the soil into the air ^{222}Rn can enter the house interior by pressure-driven flow of soil gas through openings through the floor and foundations. If there is no communication with the outside environment, then it accumulates and can reach concentrations up to a few of the tens of thousands of Bq m^{-3} . Indoor ^{222}Rn concentration is a consequence of ^{222}Rn exhalation from the soil and much less from certain building materials. The ratio of these two sources depends on underlying soil and building material. Indoor ^{222}Rn concentration is depending on floor insulation from underground gasses and also from diffusion coefficients of walls, doors, and windows. Measurements showed that houses with poor floor insulation and new doors and windows have very high potential for ^{222}Rn accumulation. On the other hand, during the night, near-ground air is rich with ^{222}Rn and as a

* Corresponding author: kolarz@ipb.ac.rs

consequence the inversion air layer is forming. If doors and windows insulation is poor than ^{222}Rn rich air can penetrate inside the house. Those two cases have different dynamics of diurnal ^{222}Rn change that is shown in this study.

^{222}Rn is 7.5 times heavier than air and when inhaled, short-lived ^{222}Rn progeny in the lungs results in the deposition of α -energy in the cells of the bronchial epithelium [2]. According to many epidemiological studies, long term inhalation of ^{222}Rn can be one of the causes of lung cancer [3]. Energy of ^{222}Rn and ^{224}Ra decays are 5.49 and 6.29 MeV, respectively. Both generate more than 10^5 ion pairs in the air per each α -particle. Those primary ions evolve within microseconds by process of hydration into complexes that are called small air ions, cluster ions or charged nano-aerosols (≥ 1 nm). They consist of one layer of water molecules (4–12) around central ion that is usually some inorganic molecule. Those are the smallest ions and the most important ones due to their mobility and relative long lifetime which is up to 5–60 s depending on air pollution [4]. The size categorization of air ions in small cluster ions 0.36–0.85 nm, big cluster ions 0.85–1.6 nm, intermediate 1.6–7.4 and large ions 7.4–79 nm are provided [4] and [5]. Small air ions are stable only when carrying only a single elementary charge that relates mobility with mass.

In the open atmosphere, air ions are generated by natural sources such as cosmic rays, the radioactive decay of ^{222}Rn and other radioactive minerals in the ground (most often ^{40}K). The average ionization rate in continental areas is approximately 10 ion pairs $\text{cm}^{-3}\text{s}^{-1}$ at height of 1m above the ground. The contribution of cosmic radiation to the air ion pair generation rate is approximately 20%, ^{222}Rn contributing 65% and residue is attributed to the decay of mentioned radioactive elements in the ground [6]. The near-ground ionization rate caused by background ionization in the open atmosphere on continental earth is about 10 ion pair's $\text{cm}^{-3}\text{s}^{-1}$ [7]. The atmospheric ion concentration (n^\pm) is determined by the following balance equation:

$$\frac{dn^\pm}{dt} = q - \alpha n^\pm n^\mp - n^\pm \beta Z \quad (1)$$

where q is the volumetric production rate, Z is the aerosol number concentration, α is an ion to ion recombination coefficient and β is an effective ion-aerosol attachment coefficient [8] and [9]. Measuring of air ions is very confident indicator of ^{222}Rn concentration and its short term changes [10], especially in indoor air when there are no other ionizing sources. Positive vs. negative ions ratio is known as „coefficient of unipolarity” with average value of $n^+/n^- = 1.12$ [11,12]. Imbalance between

positive and negative small air ion concentrations is the consequence of the atmospheric electric electrode effect in near ground layer and higher mobility of negative small air ions and thus higher probability for their removal.

2. MEASURING METHODS AND INSTRUMENTS

Cylindrical Gerdien condenser is the most common instrument for the air-ion concentration measurements. In this experiment Cylindrical Detector of Air-Ions (CDI-06, Figure 1) made in the Institute of Physics Belgrade, was used.



Figure 1. Cylindrical Detector of Air-Ions (CDI-06)

It is a fully automated portable instrument with the ability to alternatively measure concentrations of positive and negative air-ions, temperature (T), pressure (P) and relative humidity (RH). Instrument consists of sensor and power/control parts. The sensor part of the CDI-06 consists of 3 cylindrical and coaxially arranged stainless steel electrodes: measuring (central), polarizing and shielding electrode. Inter-electrode space is ventilated by a fan and air-ions of desired polarity and mobility are forced by an electric field to deflect to the central measuring electrode and deliver their charge which is then measured by the current amplifier. Polarizing voltage is set in a way that only small air-ions are collected on the central electrode. Larger ions fly through the electrodes since their kinetic energy is higher than the deflecting potential of polarizing electrode [12] and [13]. Concentration of air-ions (n_j) is:

$$n_j = \frac{I_j}{q_j Q} \quad (2)$$

where $q_j = \pm e = \pm 1.602 \times 10^{-19}$ C, Q is the air-flow I_j is current through the central electrode. Absolute

calibration of current (by electrometer) and airflow (by hot-wire anemometer) enables absolute measurements of the air-ion concentrations. Generated current is amplified, digitalized and zeroed [13]. Digitalization of CDI output signal enables programmed auto-zeroing and automatic long term measurements. Air ion concentrations are measured in real time and can be used as tracer for ^{222}Rn activity concentration. Since the results are instantaneous, it is possible to see a fine structure of changes in concentrations of ^{222}Rn their causes.



Figure 2. Radon continual monitor, Rad7- Durridge Co, USA

2.1. Rn detector

^{222}Rn activity concentration was measured using a commercial solid-state alpha detector Electronic Radon Detector - RAD7 (Durrigde Company, 2000).

Instrument was set to measure hour ^{222}Rn concentrations.

The uncertainty of this instrument depends on the measuring period and the level of ^{222}Rn activity. Longest measurement and higher concentration of ^{222}Rn resulting in lower uncertainty. Shortest ^{222}Rn concentration measurement is 5 minutes in so-called Sniff mode. This mode is with lowest accuracy but can be used as ^{222}Rn concentration indicator. Measurements that take an hour or longer are much more accurate.

2. MEASUREMENTS AND RESULTS

Measurements were carried out in 3 different measuring places: an open atmosphere, a house with poor floor and window insulation (no vapor membrane) and a house with good insulation of floor and windows. Aim was to demonstrate air ions and ^{222}Rn concentration variations depending on the quality of floor and windows insulation in dwellings.

First measurements (Fig. 3) were performed in the open atmosphere in the city of Belgrade, nearby other two measuring points. Diurnal variation of both, ^{222}Rn and air ions of both polarities, is obvious and ^{222}Rn concentration is relatively low with an average value of about 12 Bq m^{-3} . This value is near to world average for near ground ionization. Night maxima are caused by a temperature inversion in the near-ground atmospheric layer which is visible almost every night. Open atmosphere is subjected to the influence of various parameters, so changes in the concentrations of ions and ^{222}Rn are not always simultaneous and interdependent (Fig. 3) as they are in the indoor air (Figure 4,5).

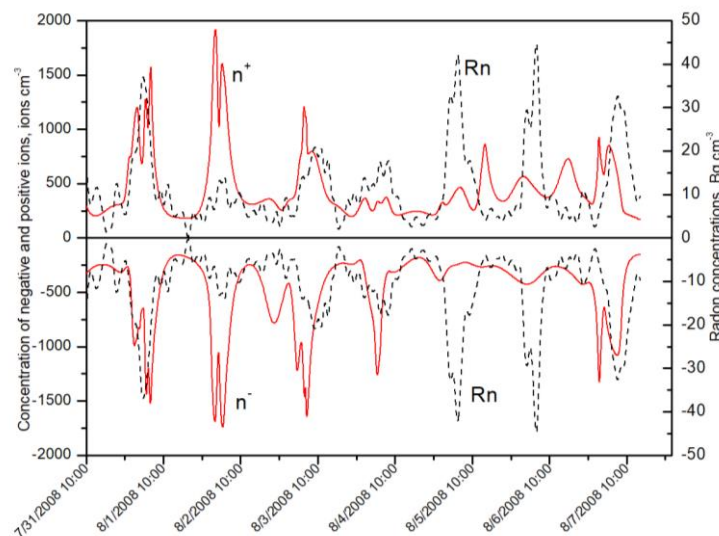


Figure 3. Typical daily outdoor ^{222}Rn and air ion variations

In the second part of the study, measurements were done in indoor air. First it was a ground floor house (Figure 4) which previously contained high concentrations of ^{222}Rn until remediation that was done 3 years ago. Remediation included concreting and floor insulation from water vapor which comprehends preventing of penetration of all other gases from under laying soil into the building. Also, all windows have been replaced with new ones (PVC) and walls were additionally insulated due to better thermal properties. All that provided better insulation from outdoor air. Since the house was occupied with inhabitants their activity can be seen on the graphs where short term changes during room ventilation are much clearer visible on air ion concentration lines on the graphs. Coefficient of unipolarity was 1.3, while during outdoor measurements it was 1.05. This implies on lower dust concentration outdoor since this coefficient is

influenced by higher coefficient of aerosol attachment of negative ions due to their higher mobility.

In Figure 5, measurements in the house with no floor insulation and poorly insulated windows are presented. Hence the assumption follows that the potential for ^{222}Rn exhalation in both houses is similar. Relatively high ^{222}Rn and air ion concentrations were measured with maxima at dawn and minima in the afternoon. Also, both measuring parameters are in high correlation. Except penetration of ^{222}Rn from the soil below the house, the influence of higher ^{222}Rn concentrations from the outside air is present. Weak insulation of the walls and windows is obvious due to low concentrations during the day. In well-insulated house, these differences are less pronounced. Coefficient of ion unipolarity was 1.2.

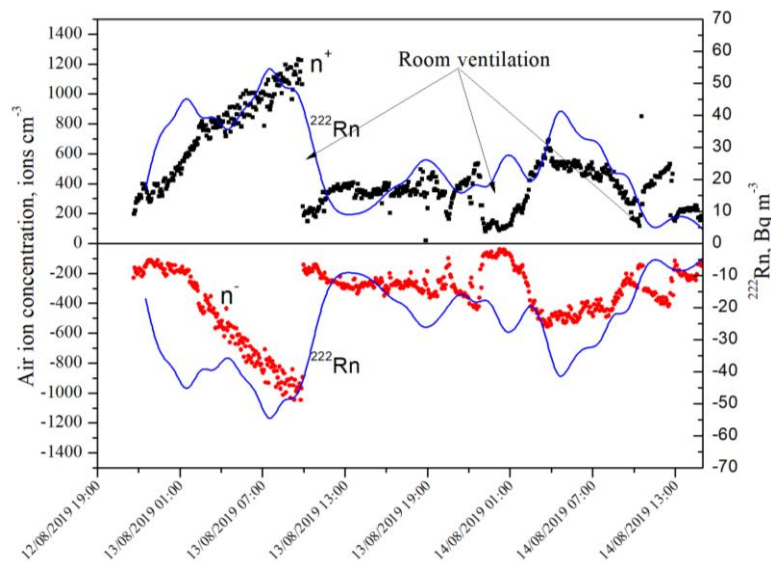


Figure 4. 2-day measurements in a ground floor house with insulated floor

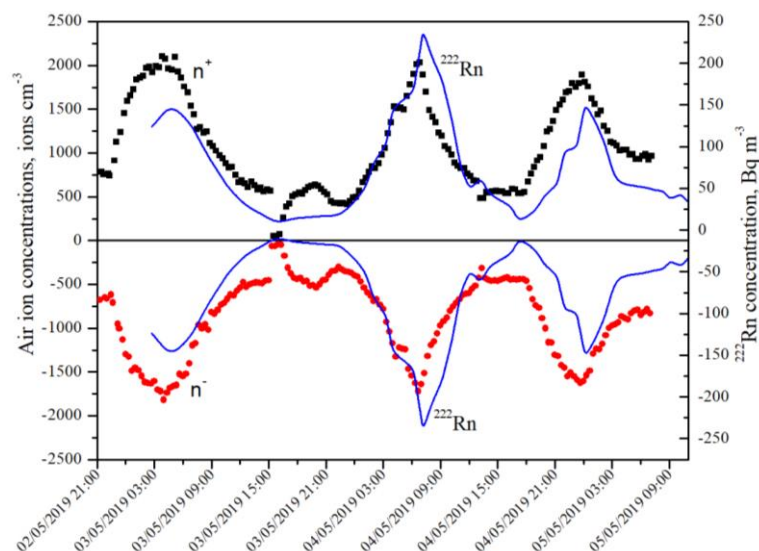


Figure 5. 3-day measurements in a ground floor house without floor insulation

Average concentrations of air ions in insulated house were 465 and 355 ions cm^{-3} , while ^{222}Rn concentration was 25 Bq m^{-3} . At the other hand, average ion concentrations in un-insulated house were 1004 and 836 ions cm^{-3} , while ^{222}Rn concentration was 79 Bq m^{-3} . ^{222}Rn concentration in both houses was relatively low and within acceptable limits, but ^{222}Rn less pronounced peaks and significantly higher concentration in un-insulated house is an obvious example of ^{222}Rn behavior in the indoor air.

4. CONCLUSION

Alpha particles from decay of ^{222}Rn and their descendants are the main source of the air ion generation in the lower atmosphere and thus the concentration of these two air constituents are highly correlated. This correlation is most visible in indoor air where the influence of interfering parameters is small. That way, using air ions as tracers, short term (order of a few seconds or more) changes of ^{222}Rn concentration can be detected. Diurnal and spatial variations of both values are mutually related with specific diurnal distribution in open atmosphere as well as in indoor air. House insulation from the gasses below the house and external air are crucial for lowering ^{222}Rn and air ion indoor concentrations. In insulated house ^{222}Rn concentration was lower and peaks were less pronounced. House with poor insulation from outdoor air was subjected to higher ^{222}Rn diffusion in and out, resulting in higher concentrations during the night and lower during the day. Old houses with typically bad floor insulation and new windows are prone to ^{222}Rn accumulation with small concentration amplitudes while same old houses with poorly insulating windows have high night ^{222}Rn concentration peaks.

5. REFERENCES

[1] C. Duenas, M. C. Fernandez, J. Carretero, E. Liger, M. Perez, *Release of ^{222}Rn from some soils*, Ann. Geophysicae, Vol. 15 (1997) 124–133.
[2] P. Hopke, B. Jensen, C. S. Li, N. Montassier, P. Wasiolek, A. J. Cavallo, K. Gatsby, R., Socolow, A. James, *Assessment of the Exposure to and Dose from Radon Decay Products in Normally Occupied Homes*, Environ. Sci. Technol., Vol. 29–5 (1995) 1359–1364.

[3] F. Bochicchio, *Radon epidemiology and nuclear track detectors: Methods, results and perspectives*, Radiat. Meas., Vol. 40 (2005) 177–190.
[4] U. Hõrrak, J. Salm, H. Tammet, *Statistical characterization of air ion mobility spectra at Tahkuse Observatory: Classification of air ions*, J. Geophys. Res., Vol. 105–D7 (2000) 9291–9302.
[5] U. Hõrrak, *Air Ion Mobility Spectrum at a Rural Area*, PhD Thesis, University of Tartu, Estonia, 2001.
[6] L. Laakso, A. Hirsikko, T. Gronholm, M. Kulmala, A. Luts, T. E. Parts, *Waterfalls as sources of small charged aerosol particles*, Atmos. Chem. Phys. Discuss., Vol. 6 (2006) 9297–9314.
[7] J. A. Chalmers, *Atmospheric Electricity*, Pergamon Press, Oxford, London, 1967.
[8] L. Laakso, A. Hirsikko, T. Gronholm, M. Kulmala, A. Luts, T. E. Parts, *Waterfalls as sources of small charged aerosol particles*, Atmos. Chem. Phys., Vol 7 (2007) 2271–2275.
[9] U. Hõrrak, P. P. Aalto, J. Salm, K. Komsaare, H. J. Tammet, M. Mäkelä, L. Laakso, M. Kulmala, *Variation and balance of positive air ion concentrations in a boreal forest*, Atmos. Chem. Phys., Vol. 8 (2008) 655–675.
[10] P. Kolarž, Z. Čurguz, *Air ions as indicators of short-term indoor radon variations*, Applied Radiation and Isotopes, Vol. 99 (2015) 179–185.
[11] W. A. Hoppel, R. V. Anderson, J. C. Willett, *Atmospheric electricity in the planetary boundary layer*, in *The Earth's Electrical Environment*, Electrical Environment, National Academy Press, Washington, USA, 1986, 149–165.
[12] U. Hõrrak, *Air ion mobility spectrum at a rural area*, Dissertationes Geophysicales Universitat Tartuensis, Tartu, Estonia, 2001.
[13] P. Kolarž, B. P. Marinković, D. M. Filipović, *Zeroing and testing units developed for Gerdien atmospheric ion detectors*, Review of Scientific Instruments, Vol. 76 (2005) 046107–046109.
[12] P. M. Kolarž, D. M. Filipović, B. P. Marinković, *Daily variations of indoor air ion and radon concentrations*, Applied Radiation and Isotopes, Vol. 67 (2009) 2062–2067.
[13] P. Kolarž, B. Miljković, Z. Čurguz, *Air-ion counter and mobility spectrometer*, Nuclear Instruments and Methods in Physics Research B, Vol. 279 (2012) 219–222.



ДНЕВНЕ И ПРОСТОРНЕ ПРОМЕНЕ КОНЦЕНТРАЦИЈЕ РАДОНА И ЊЕГОВ УТИЦАЈ НА ЈОНИЗАЦИЈУ ВАЗДУХА

Сажетак: Најприсутнији и најефикаснији извор јонизације ваздуха у приземном слоју атмосфере је радон. Као алфа емитер, радон игра пресудну улогу у атмосферском наелектрисању. Поред физичке, радон и јони имају значајну биолошку улогу по здравље људи: високе концентрације радона представљају опасност по здравље, док су јони као нуспродукт распада радона корисни састојак ваздуха који удишемо. Мерења су вршена коришћењем континуалног радон монитора “Rad7” и бројача јона у ваздуху CDI-06. Дневне и просторне варијације оба атмосферска састојка међусобно су повезане и углавном зависе од потенцијала распада радона, метеоролошких параметара, концентрације аеросола и стварања температурног инверзног слоја у приземном слоју атмосфере. Концентрације радона у затвореном простору повезане су са акумулацијом радона који долази из тла испод зграде као и са спољашњом концентрацијом радона који дифундује кроз зидове, врата и прозоре. Разлика путева на који радон улази у кућу може се видети анализом промена током дневних континуалних мерења.

Кључне речи: радон, атмосферски јони, јонизација, атмосфера, ваздух, природна радиоактивност.



Paper received: 14 October 2019
Paper accepted: 31 December 2019

LONG-TERM MEASUREMENTS OF EQUILIBRIUM EQUIVALENT RADON AND THORON PROGENY CONCENTRATIONS IN REPUBLIC OF SRPSKA DWELLINGS

Zoran Ćurguz^{1*}, Zdenka Stojanovska², Rosaline Mishra³, Balvindar K. Sapra³, Ilija V. Yarmoshenko⁴, Predrag Kolarž⁵, Dragoljub Lj. Mirjanić⁶, Aco Janićijević⁷, Zora S. Žunić⁸

¹ Faculty of Transport and Traffic Engineering, University of East Sarajevo,
Vojvode Mišića 52, 74 000 Dobojo, Republic of Srpska

² Faculty of Medical Sciences, Goce Delčev University Stip,
Krstes Misirkov No.10-A P.O. Box 201, Republic of Macedonia

³ Radiological Physics and Advisory Division, Bhabha Atomic Research Centre,
Trumbay, Mumbai – 400 085, India

⁴ Institute of Industrial Ecology Ural Branch of Russian Academy of Science, Ekaterinburg, Russia

⁵ Institute of Physics Belgrade, Pregrevica 118, 11080 Zemun, Serbia

⁶ University of Banja Luka, Faculty of Medicine, Sime Mrkalja 14, 78000 Banja Luka, Republic of Srpska
and Academy of Sciences and Arts of the Republic of Srpska, Str. Bana Lazarevića 1, 78000 Banja Luka,
Republic of Srpska, Bosnia and Herzegovina

⁷ Faculty of Technology and Metallurgy, University of Belgrade, Karnegijeva Street 4, Belgrade, Serbia

⁸ Vinča Institute of Nuclear Sciences, University of Belgrade,
Mike Petrovića Alasa 12-14, 11351 Vinča, Belgrade, Serbia

Abstract: The long-term measurements of radon and thoron equilibrium equivalent concentrations (*EERC* and *EETC*) were carried out the first time in Republic of Srpska in 25 schools of its capital Banja Luka and in its wider surroundings. After this successful survey, the measurements continued using the same type of the LR 115 nuclear track detectors, i.e., Direct Radon Progeny Sensors/Direct Thoron Progeny Sensors (DRPS/DTPS), and they were deployed in the 36 dwellings nearby the investigated schools. The detectors were exposed for one year period at 15–20 cm distance from the walls. The *EERC* and *EETC* were found to vary in the range from 6.3 to 14.4 Bq/m³ and from 0.10 to 1.1 Bq/m³, with geometric mean 9.3 and 0.36, respectively. The same variance of *EER* and *EET* concentrations, measured in living and bedrooms of buildings built with different construction materials as well at different floors have been obtained. The insignificant correlations between *EERC* and *EETC*, show that these concentrations appeared to be independent in investigated dwellings. The calculated ratio of *EETC* to *EERC* ranged from 0.01 to 0.16 with the geometric mean of 0.04. The aim of this study is to give possible scientific contribution considering the explanation of *EERC* and *EETC* behavior in an indoor environment.

Keywords: *EERC*, *EETC*, indoor, dwellings.

1. INTRODUCTION

Radon (²²²Rn) and thoron (²²⁰Rn) are naturally occurring radioactive gases with half-lives of 3.82d and 55.3 s, respectively. There are direct decay products of the respective isotopes of radium (²²⁶Ra and ²²⁴Ra) in ²³⁸U and ²³²Th chains. Radon and Thoron gases are generated in terrestrial materials, emanated from their surfaces, and then accumulated in the indoors. These processes are complex and

depend on a large number of geogenic and anthropogenic factors. Based on a large number of researches and results compounded in UNSCEAR reports, radon and thoron have been proven to be the major sources of public exposure [1].

Chronic exposure to high concentrations of radon and thoron can cause negative health effects [2]. Practically, the health risk due to radon and thoron is associated with inhalation of their short-lived decay products, which activities are reported as

* Corresponding author: curguzoran@yahoo.com

equilibrium equivalent concentration (*EEC*). The equilibrium equivalent concentration for radon *EERC* and for thoron *EETC* are the quantities relevant to the Potential Alpha Energy, concentration in air and therefore to the inhalation dose. *EERC* is a combination of radon short-lived decay products: ^{218}Po , ^{214}Pb and ^{214}Bi activity concentrations, denoted C_1 , C_2 and C_3 respectively, through the relation [1]:

$$EERC = 0.105(C_1) + 0.516(C_2) + 0.380(C_3), \quad (1)$$

and, *EETC* is compounded by the thoron short-lived decay products ^{212}Pb and ^{212}Bi activity concentrations, denoted C_1 and C_2 respectively, which is expressed by the relation:

$$EETC = 0.913(C_1) + 0.087(C_2). \quad (2)$$

For more precise dose estimation, accurate techniques to measure the concentration of radon and thoron decay products are important. As in the cases of radon and thoron gases, there are active and passive techniques. To measure radon and thoron progeny concentration in an indoor environment, time integrating passive technique is more appropriate in the assessment of human exposure than active techniques. For this purpose, a few years ago, low-cost time integrating passive detector for *EERC* and

EETC measurements have been [3,4], named DTSPS/DRPS detector.

As a result of international collaboration between scientists from the former Yugoslav Republics, during the past few years, several studies of the long-term equilibrium equivalent concentration for radon *EERC* and for thoron *EETC*s have been performed. The *EERC* and *EETC* were measured on 388 different locations [5], using the DTSPS/DRPS detectors. The surveys were performed in 122 dwellings in the region of Sokobanja, Serbia [6,7], 48 dwellings in Kosovo and Metohija [8], 44 schools in Republic of North Macedonia [9], 112 dwellings in Slovenia [10], as well as in the Republic of Srpska.

In the period 2011-2012, the first long-term measurements of *EERC* and *EETC* were carried out in 25 schools in Banja Luka city (the capital of Republic of Srpska) and in its wider surroundings [11]. Later these measurements of *EERC* and *EETC* were carried out in 37 individual dwellings in its the most frequently occupied room, nearby the investigated schools in Banja Luka, using the same type of direct progeny sensing detectors. This paper presents these results.



Figure 1. The geographical position of Banja Luka

2. MATERIALS AND METHODS

The direct progeny sensing detector system is based on the registration of alpha tracks originating from the deposited progeny activity on LR-115

detectors [4]. The energies of an alpha particle are selected by mounting absorbers of suitable thicknesses on the LR-115 detectors. The direct thoron progeny sensor (DTSPS) is made up of an LR-115 track detector mounted with an aluminized mylar

absorber of 50 mm thickness to selectively detect only the 8.78 MeV alpha particles emitted from ^{212}Po atoms (Mishra R. et al 2009). Similarly, the direct radon progeny sensor (DRPS) has an absorber thickness of 37 mm to detect mainly the alpha particles emitted from ^{214}Po (7.69 MeV). In a mixed radon and thoron progeny environment, this can have some interference from the alpha particles from ^{212}Po , which needs to be subtracted using the thoron sensor data. The LR-115 films were then removed and processed in the laboratory for measurements of

radon and thoron progeny concentrations. The measurements were made by DRPS/DTPS (Direct Radon Progeny Sensors/Direct Thoron Progeny Sensors) which were left exposed inside the house in the period of 12 months, from December 2011 to December 2012, in 37 houses inside rooms at 15-20 cm distance from walls or any available room surfaces. The houses were randomly chosen with an idea of surrounding a greater geographical part of Banja Luka city (Republic of Srpska-Balkan Region).



Figure 2a. Direct Radon Progeny Sensor

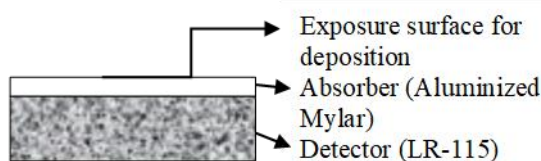


Figure 2b. Detector LR-115 structure

3. RESULTS AND DISCUSSION

Descriptive statistic and frequency distribution of indoor *EERC* and *EETC* are given in Table 2 and Figure 3. Both data sets were approximated with a log-normal function, the null hypothesis was confirmed at 5% error probability.

The *EERC* and *EETC* were found to vary in the range from 6.3 to 14.4 Bq/m³ and from 0.10 to 1.1 Bq/m³, with geometric mean 9.3 and 0.36 respectively. The same variance of *EER* and *EET* concentrations measured: in living rooms and bedrooms, buildings built with different construction materials as well at different floors were obtained.

In Figure 4 Geometric mean values of *EERC* and *EETC*, obtained in this study are compared with

values reported from some former Yugoslav Republics.

The geometric mean value GM and related (GSD) of 9.3 Bq/m³ (1.23) for *EERC* in this study is lower than the 11.2 Bq/m³ (1.26) previously reported for the schools in the Republic of Srpska [11]. It is also lower than those found in Serbian dwellings, 11 Bq/m³ (1.5) [6], and also in comparison with those in dwellings of Kosovo and Metohija 30 Bq/m³ (2.1) [8], in schools of North Macedonia 27 Bq/m³ (1.4) [9]. The value of 0.36 Bq/m³ (2.00) for *EETC* obtained for dwellings in this study is similar to 0.40 Bq/m³ (2.20) obtained for schools in Banja Luka but lower than those reported for dwellings in Serbia, 0.86 Bq/m³ (2.1) [6]; and Kosovo and Metohija, 1.9 Bq/m³ (1.9) [8]; as well as those reported in schools of North Macedonia, 0.75 Bq/m³ (2.5) [9].

Table 1. Descriptive statistic of measured *EERC* and *EETC*

Statistic	<i>EERC</i> (Bq/m ³)	<i>EETC</i> (Bq/m ³)
No. of observations	37	37
Minimum	6.3	0.10
Maximum	14.4	1.10
Median	9.5	0.38
Arithmetic mean	9.5	0.44
Standard deviation	2.0	0.28
Skewness	0.3	0.84
Kurtosis	-0.4	-0.03
Coefficient of variation	21%	64%
Geometric mean	9.3	0.36
Geometric standard deviation	1.23	2.00

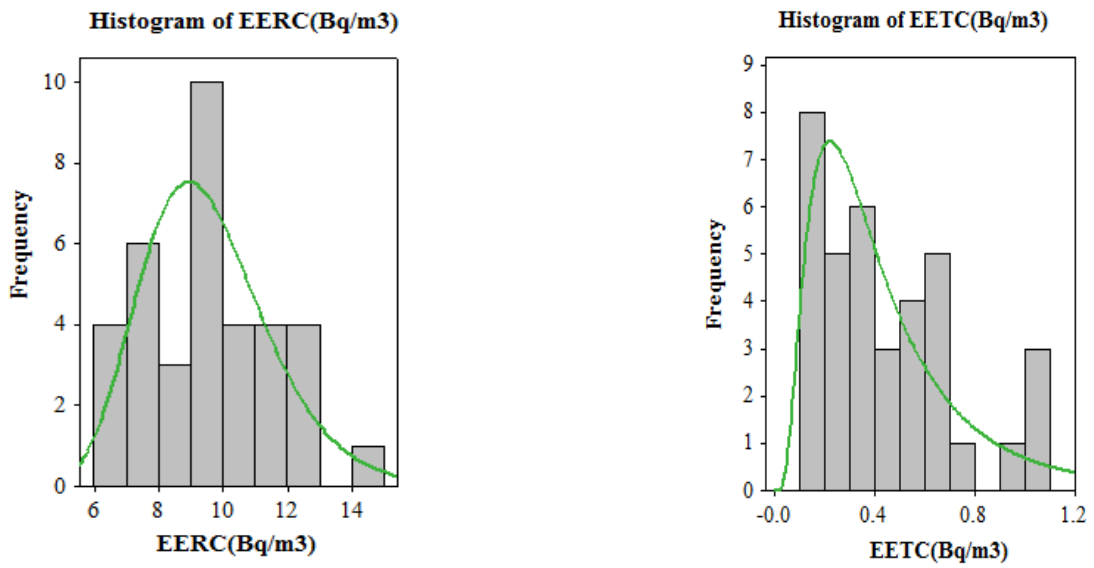
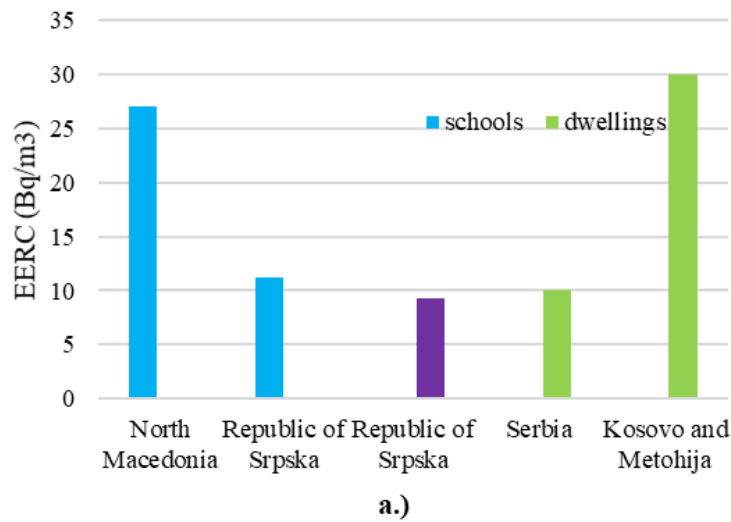
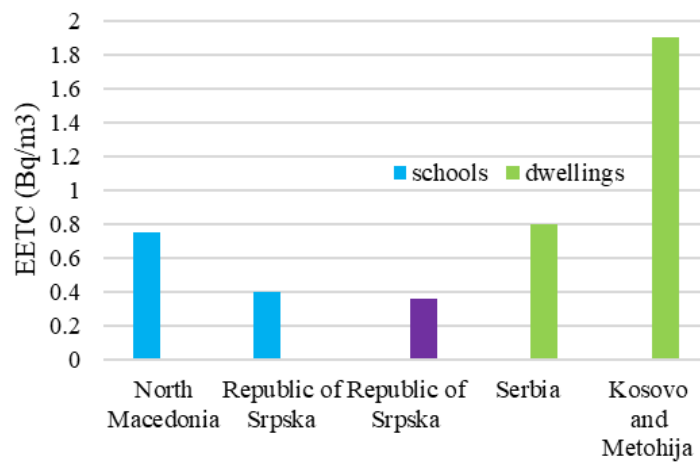


Figure 3. Histograms of EERC and EETC fitted by log-normal function



a.)



b.)

Figure 4. The geometric mean values of a.) EERC and b.) EETC obtained in this study and studies performed in some former Yugoslav Republics

The range of *EETC/EERC* ratio in dwellings considered in the present study was between 0.01 and 0.16, and GM of 0.039 (2.02). The results agree with Banja Luka schools [11-14] which were in a range from 0.01 to 0.12 and the same geometric mean as in the dwellings.

The correlation between *EERC* and *EETC* was tested. For this purpose, a model of parametric linear regression (LR) was applied on ln-transformed data in order to reduce the influence of extremes on the tests. The test results showed that the correlation between *EERC* and *EETC* was insignificant (Figure

5). It means that these concentrations appeared to be independent in investigated dwellings.

In the literature, different results from the correlations analysis between *EERC* and *EETC* have appeared. For example, the correlation in Banja Luka schools was not significant [11] as in the homes, neither it was significant in the schools of Northern Macedonia [9], while in the homes of Kosovo and Metohija the correlation was significant with a relatively high coefficient of determination ($R^2 = 0.56$) [8].

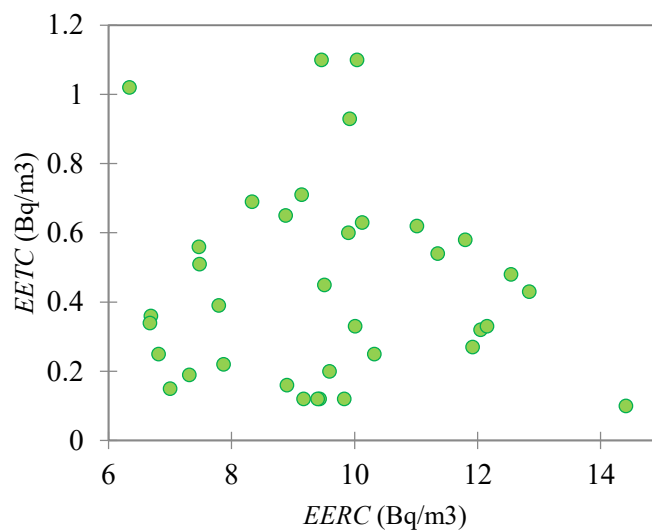


Figure 5. Scatter plot of *EETC* and *EERC*.

4. CONCLUSION

This work presents simultaneous long-term measurements of *EERC* and *EETC* in dwellings of Banja Luka with nuclear track detectors. *EERC* values were in the range from 6.3 to 0.1 Bq/m³, and *EETC* were in the range from 0.10 to 1.10 Bq/m³ while as the interval of the ratio *EETC/EERC* was between 0.01 and 0.16. The geometric mean and (geometric standard deviation) values of 9.3 Bq/m³ (1.23) for *EERC* and 0.36 Bq/m³ (2.00) for *EETC* obtained in this study are lower in comparison with GM values reported from the countries in that region.

Further investigation of the equilibrium factors in the dwellings of Banja Luka is planned.

5. REFERENCES

[1] United Nations Scientific Committee on the Effects of Atomic Radiation, *Effects of ionizing*

radiation. Report to the General Assembly with Scientific Annexes (Annex B), NY: UN,2000.

[2] S. Darby, D. Hill, A. Auvinen, et al., *Radon in homes and risk of lung cancer: Collaborative analysis of individual data from 13 European case-control studies*, (2005)*BMJ* 330.7485 223-0.

[3] W.Zhou and T. Iida, *Estimation of thoron progeny concentrations in dwellings with their deposition rate measurements*, *Health Phys*, Vol. 35 (2000) 365–370.

[4] R. Mishra and Y. S. Mayya, *Study of a deposition based direct thoron progeny sensor (DTPS) technique for estimating equilibrium equivalent thoron concentration (EETC) in indoor environment*, *Radiat. Meas*, Vol. 43(2008) 1408–1416.

[5] Z. S. Žunić, R. Mishra, I. Čeliković, et al., *Effective Doses Estimated from the Results of Direct Radon and Thoron Progeny Sensors (DRPS/DTPS) Exposed in selected Region of Balkans*, *Radiat Prot Dosim*, (2019) <https://doi.org/10.1093/rpd/ncz025>, online published 13 march 2019.

[6] Z. S. Žunić, et al., *Indoor radon, thoron and their progeny concentrations in high thoron rural serbia environments*, Radiat Prot Dosim, Vol. 177-1/2 (2017) 36-39.

[7] R. Mishra Z. S. Žunić, G. Venoso, et al., *An evaluation of thoron (and radon) equilibrium factor close to walls based on long-term measurements in dwellings*, Radiat Prot Dosim, Vol. 160 (2014) 164-168.

[8] L. Gulan, et al., *Field experience on indoor radon, thoron and their progenies with solid-state detectors in a survey of Kosovo and Metohija (Balkan region)*, Radiat Prot Dosim, Vol. 152-1/3 (2012) 189-197.

[9] Z. Stojanovska, et al., *Results from time integrated measurements of indoor radon, thoron and their decay product concentrations in schools in the Republic of Macedonia*, Radiat Prot Dosim, Vol. 162-1/2 (2014) 152-156.

[10] J. Vaupotic, A. Gregoric, M. Leban, et. al., *Radon survey within a regular grid in homes in Slovenia*, VII. Hungarian Radon Forum and Radon

and Environment Satellite Workshop (Veszprém, Hungary: Pannonian (2013) 195-200.

[11] Z. Ćurguz, et al., *Long-term measurements of radon, thoron and their airborne progeny in 25 schools in Republic of Srpska*, J. Environ. Radioact., Vol. 148 (2015) 163-169.

[12] Z. Ćurguz, D. Mirjanić, M. Popović, *Comparison of concentration of radon measurement short-term (active) and long-term (passive) method*, Contemporary materials, Vol. VII-2 (2017) 170-180.

[13] Z. Ćurguz, D. Mirjanić, *Determination of equilibrium equivalent of thoron and radon concentration in schools of the city of Banja Luka*, Contemporary materials, Vol. IX-1 (2018) 31-37.

[14] G. Venoso, Z. Ćurguz, Z. Žunic, D. Mirjanić, M. Ampollini, C. Carpentieri, D. C. Christian, M. Caprio, D. Alavantic, P. Kolarž, Z. Stojanovska, S. Antignani, F. Bochicchio, *Spatial patial variability of indoor radon concentration in schools: Implications on radon measurement*, 9th Conference on Protection against Radon at Home and at Work, 16-20 September 2019. Praha.



ДУГОРОЧНА МЈЕРЕЊА ЕКВИВАЛЕНТНИХ РАВНОТЕЖНИХ КОНЦЕНТРАЦИЈА РАДОНА И ТОРОНА У КУЋАМА РЕПУБЛИКЕ СРПСКЕ

Сажетак: Дугорочна мјерења еквивалентних равнотежних концентрација радона и торона (EERC and EETC) први су пут извршена у Републици Српској у 25 школа града Бањалуке и шире околине. Након овог успјешног истраживања, мјерења су настављена коришћењем истог типа нуклеарних траг детектора LR 115, тј. сензора директних потомака радона и торона (DRPS / DTPS) и распоређених у 36 домова у близини школа. Детектори су били изложени током једне године на удаљености 15-20 cm од зидова. Откривено је да се EERC и EETC разликују у опсегу од 6,3 до 14,4 Bq/m³ и од 0,10 до 1,1 Bq/m³, са геометријском средином 9,3 и 0,36, респективно. Добијена је иста разлика у концентрацији ЕЕР и ЕЕТ, измјерена у дневним и спаваћим собама зграда изграђених од различитих грађевинских материјала и на различитим подлогама. Незнатна повезаност између EERC-а и EETC-а показује да су ове концентрације биле независне у испитиваним становима. Прорачунати однос EETC-а и EERC-а кретао се у распону од 0,01 до 0,16 са геометријском средином 0,04. Циљ ове студије је анализа могућих објашњења понашања EERC и EETC у затвореном простору.

Кључне ријечи: EERC, EETC, затворен простор, куће.



Paper received: 23 December 2019

Paper accepted: 20 February 2020

THE INDOOR RADON AND THORON CONCENTRATIONS IN SCHOOLS OF SKOPJE (REPUBLIC OF NORTH MACEDONIA) AND BANJA LUKA (REPUBLIC OF SRPSKA) CITIES MEASURED BY RADUET DETECTORS

Zdenka Stojanovska^{1}, Zoran Ćurguz², Predrag Kolarž³, Zora S. Žunić⁴,
Ivan Boev⁵, Blazo Boev⁵*

¹ Faculty of Medical Sciences, Goce Delčev University Stip,
Krste Misirkov No.10-A P.O. Box 201, Republic of Macedonia

² Faculty of Transport and Traffic Engineering, University of East Sarajevo,
Vojvode Mišića 52, 74 000 Dobojo, Republic of Srpska

³ Institute of Physics, University of Belgrade, Serbia,

⁴ Institute of Physics Belgrade, Pregrevica 118, 11080 Zemun, Serbia

⁵ Faculty of Natural and Technical Sciences, Goce Delcev University, Stip,
Krste Misirkov10-A, P.O 201, Republic of Macedonia

Abstract: Radon (^{222}Rn) and thoron (^{220}Rn) are natural radioactive gases, generated in the terrestrial materials. They are the main sources of public exposure to ionising radiation in any of indoor environment worldwide. Differences in half-lives of ^{222}Rn ($T_{1/2} = 3.8$ d) and ^{220}Rn ($T_{1/2} = 55.6$ s) lead to its different indoor behavior. Several studies of indoor ^{222}Rn and ^{220}Rn in Northern Macedonia have been performed, starting with measurements in dwellings in 2008 and continuing with measurements in schools during 2012. The surveys in the Republic of Srpska began later (in 2011) with the simultaneous ^{222}Rn and ^{220}Rn measurements in the dwellings and schools of Banja Luka cities. This paper, as a result of our cooperation, summarizes the results and general conclusions obtained from ^{222}Rn and ^{220}Rn measurements in schools of capitals. In both cities, the measurements were made using Raduet - nuclear track detectors; deployed at distances: $>0.5\text{m}$ (Skopje) and 0.2m (Banja Luka); and exposed in a period: March 2012 - May 2012 (Skopje) and April 2011 - May 2012 (Banja Luka). Results for ^{222}Rn and ^{220}Rn concentrations in both cities have a log-normal distribution. The ^{222}Rn geometric mean value of 71 Bq/m^3 in Skopje is higher than in Banja Luka city ($\text{GM} = 50\text{ Bq/m}^3$). Among different radon potential in the cities, this difference could be related to the different exposure time of detectors. Furthermore, the dispersion of the ^{222}Rn results in each city expressed through geometric standard deviation is relatively low: $\text{GSD} = 2.13$ (Skopje) and $\text{GSD} = 2.11$ (Banja Luka) indicating relatively homogeneous data sets. The ^{220}Rn concentrations in Banja Luka ($\text{GM} = 51\text{ Bq/m}^3$) were higher than in Skopje ($\text{GM} = 11\text{ Bq/m}^3$). It is obvious that in the case of ^{220}Rn , the exposure period did not play a significant role. One of the reasons for this difference could be the position of the detectors as well as the different building materials in the schools. On the contrary, the dispersion of the ^{220}Rn results in Skopje ($\text{GSD} = 3.38$) was greater than in Banja Luka ($\text{GSD} = 2.07$).

Keywords: radon, thoron, gas, school.

1. INTRODUCTION

Radon (^{222}Rn) and thoron (^{220}Rn) are radioactive gases from the respective natural series of ^{238}U and ^{232}Th , which are present in the terrestrial materials from the earth formation to the present day. The existing trace concentrations of ^{238}U and ^{232}Th ,

and their corresponding decay products ^{226}Ra and ^{224}Ra in building materials and in the underlying rocks and soil are sources of radon and a thoron in a building. The generated gases move through enclosed spaces of the material, emanate from its surface and enter into other environments where they can be accumulated. The dynamics are complex and driven

* Corresponding author: zdenka.stojanovska@ugd.edu.mk

mainly by the processes of advection and diffusion. Amount of the accumulated radon or thoron indoors concentration, depends on many factors. In general, they are related to the concentration of the radionuclides in the terrestrial material together with its porosity (radon potential), building characteristics and mode of its use. Additionally, the advection process is in a direct function of the outdoor-indoor temperature gradient, after all, radon and thoron concentration variations strongly depend on the meteorological parameters (temperature, pressure, wind, etc.).

Radon has a relatively long half-life ($T_{1/2} = 3.8$ d), therefore the gas created in underlying soil in high depths can enter and accumulate in a building before it decayed. Contrary, due to short half-life ($T_{1/2} = 55.6$ s), thoron can travel only short distances before it decayed. The main consequences of this are the differences in the effect of the factors on the accumulation of these two gases in indoor environments. In general, according to a large number of studies [1-3], it can be said that the main source of radon is the underlying soil (rock) and to a lesser extent the building materials, while in the case of thoron: the building materials are the dominant source in a building. Also, the essential difference between these two gases is that the indoor radon concentrations are homogeneously distributed, unlike the indoor thoron, whose concentrations are at the maximum on the wall and decrease at distance from it. Moreover consequence of the differences in radon and thoron half-lives, are discrepancy in their temporal variations caused by the meteorological parameters. For example, they are more pronounced for radon than for thoron [4-9].

Based on a large number of studies, it has been shown that indoor radon and thoron, are dominant (over all) radioactive sources to public exposure [9-10]. The harmful health effects of chronic exposure to them, have been confirmed [11], so the indoor radon and indoor thoron are very important radiation protection issue in every country. Following world trends, numerous campaigns to measure indoor radon and thoron in the countries of the Balkan, have been performed in the last decade. Thus, many papers have been published, some of which are cited in this paper's references [12-22]. In most of them radon concentrations are measured while studies of indoor thoron concentrations are limited. Depending on the type of indoor environment, the studies were conducted mainly in dwellings, schools (kindergartens) or combined. In Republic of North Macedonia, the first indoor radon and thoron measurements were made in dwellings in 2008 [23] and only later (2012) in schools and kindergartens [24-26]. In Republika Srpska, an entity in Bosnia and Herzegovina, the first systematic survey indoor radon and thoron was launched in 2011, simultaneously measuring both dwellings and schools [27-28]. Most of the results of these studies are already published.

The main purpose of this paper is to show the extracted results of radon and thoron concentration measurements, previously performed as a part of the more complex survey. In this study, we considered, only measured concentrations with the same type of detector, in the schools of the capital cities Skopje and Banja Luka, The geographical positions of the two republics in Europe, as well as the position of the cities, are shown in the Figure 1.



Figure 1. Geographical position of Bosnia and Herzegovina and Macedonia in the European map (left). Sites of the Banja Luka municipality over municipalities of Republic of Srpska (coloured blue) (upper right) and of the Skopje municipalities in the Republic of North Macedonia (down right)

2. MATERIAL AND METHODS

The indoor radon and thoron concentrations were measured in the schools of Skopje and Banja Luka using a nuclear track detectors, with Raduet commercial name, manufactured in Radosys, Hungary (Figure 2). The operating principle of Raduet was explained precisely in our previous studies [6, 28].

In Skopje, the detectors were installed in a

classroom on the ground floor at a distance of 0.5 m from any wall surface and exposed in a period of three months, from March to May 2012. In Banja Luka, they were deployed in a shorter distance of 0.2 m from the wall surfaces and exposed for one year, from April 2011 to May 2012. Types of the rooms, the distances to the wall surfaces along with the detectors period of exposure in each of the surveys are specified in Table 1.



Figure 2. Raduet nuclear track detector produced in Radosys, Hungary

Table 1. Characteristic of the detector exposure in both surveys

City	Type of room	Distance from wall surface	Period of detectors exposure
Skopje	Classroom	>0.5m	March-May, 2012
Banja Luka	Assembly hall or hallway	0.2 m	April, 2011-May, 2012

3. RESULTS

The histograms of the measured indoor radon (^{222}Rn) and thoron (^{220}Rn) concentrations in both

cities are shown in Figure 3. The best fit for both gases data sets was the log-normal function whose parameters are also present on the graphs in Figure 3.

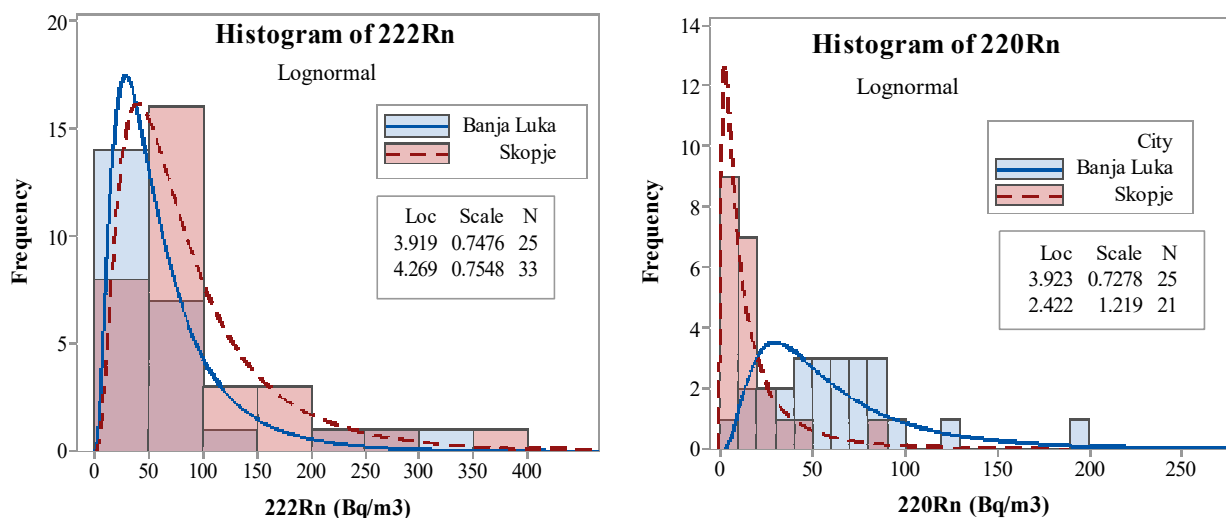


Figure 3. Histograms fitted with a log-normal function of ^{222}Rn and ^{220}Rn concentrations measured in schools of Skopje and Banja Luka

The number of schools under observation (N), number of schools with measured concentration below detection limit ($N_{<MDA}$), arithmetic mean (AM), standard deviation (SD), geometric mean (GM) and geometric standard deviation (GSD) of indoor radon (^{222}Rn) and thoron (^{220}Rn) concentration measured in the schools of Skopje and Banja Luka cities are given in Table 2. In schools of Skopje, radon values range from 9 to 379 Bq/m³ and those of thoron range from 1 to 80 Bq Bq/m³. The ranges in schools of Banja Luka are 25-341 Bq/m³ for radon and 7-198

Bq/m³ for thoron. In 12 schools of Skopje, thoron concentration was below the detection limit of 1 Bq/m³. Except in two schools, the radon concentrations in Skopje were higher in comparison to measured thoron concentrations. In Banjaluka, the thoron concentrations were higher than radon concentrations in most cases. The intervals of $^{220}\text{Rn}/^{222}\text{Rn}$ ratio in the schools considered in the present study were 0.01 - 4.72 for Skopje and 0.14-3.80 for Banja Luka (Figure 4) with geometric mean values of 0.19 and 1.00, respectively.

Table 2. Basic statistic of indoor radon and thoron concentrations considered in this study

	N	$N_{<MDA}$	AM Bq/m ³	SD Bq/m ³	GM Bq/m ³	GSD
^{222}Rn	58	0	85	81	61	2.15
^{222}Rn Skopje	33	0	94	78	71	2.13
^{222}Rn Banja Luka	25	0	72	85	50	2.11
^{220}Rn	58	12	42	39	25	3.42
^{220}Rn Skopje	33	12	18	18	11	3.38
^{220}Rn Banja Luka	25	0	63	40	51	2.07

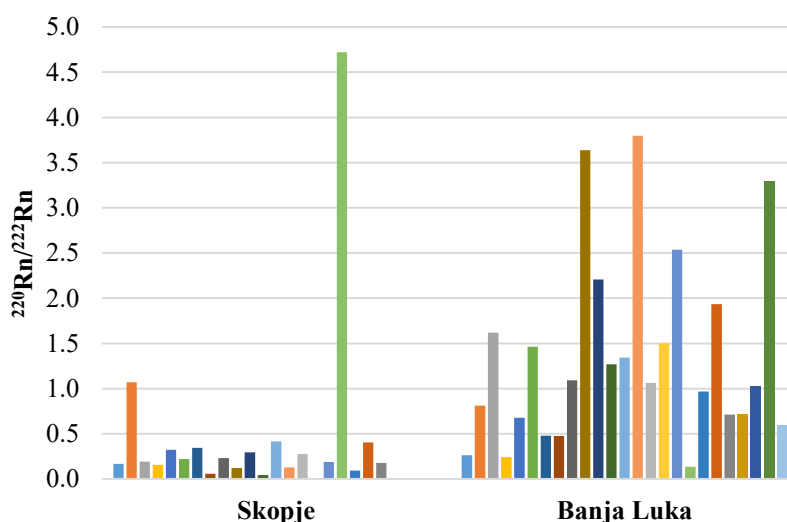


Figure 4. The $^{220}\text{Rn}/^{222}\text{Rn}$ ratio in schools of Skopje and Banja Luka

4. DISCUSSION AND CONCLUSION

This study presents the results for indoor radon (^{222}Rn) and thoron (^{220}Rn) concentrations measured in schools of Skopje and Banja Luka cities with Raduet detectors exposed in periods of 3 and 12 months, respectively (Table 1). Analysis of the distribution of radon and thoron concentration showed that the best fit of the data was log-normal function. Visually (from Figure 3) and further by testing, the differences between log-normal functions of the Skopje and Banja Luka data sets, was confirmed for radon as well for thoron. The reason for this may be the different contributions of the factors which are affecting radon and thoron concentrations variation in the cities.

The arithmetic and geometric mean values of radon concentrations measured in Skopje are higher than the mean concentrations obtained for Banja Luka (Table 2). We assumed that, among the different radon potentials, the different types of rooms where measurements were performed as well the different periods of detectors exposure, could be a reason for this. But, lower radon concentrations in the hall in comparison to the classroom in Skopje and assembly halls in Banja Luka schools, were not confirmed, so the assumptions about differences in exposure period and radon potential remain. In Banja Luka, the radon concentrations measured by Raduet (this study) in one room are lower than those reported previously, where the radon for each school was presented as a

mean value of measured results, with two different types of detectors in at least two different types of rooms. Furthermore, the geometric standard deviation values (GSD) obtained for radon data from Skopje and Banja Luka (Table 2), are relatively low which indicate relatively homogeneous factors effects on radon variation in each city.

Contrary to radon, the thoron concentrations measured in schools of Banja Luka city are higher in comparison to those of Skopje city (Table 2). It is obvious that in the case of thoron, a period of the detector exposure does not play a significant role. Some of the reasons for this difference could be the position of the detectors as well as the different building materials in the schools. The dispersion of the results in Skopje is greater than the result measured in Banja Luka.

For comparison, the geometric mean concentrations of radon in Banja Luka schools ($GM = 50 \text{ Bq/m}^3$) are lower than those reported by studies conducted in schools: in Skopje ($GM = 71 \text{ Bq/m}^3$), Eastern part of North Macedonia ($GM = 96 \text{ Bq/m}^3$) [25], ($GM = 87 \text{ Bq/m}^3$) [26], Southern Serbia ($GM = 97 \text{ Bq/m}^3$) [29], Osijek, Croatia ($GM = 70.6 \text{ Bq/m}^3$) [30], as well as lower than those published for kindergartens in Sofia, Bulgaria ($GM = 101 \text{ Bq/m}^3$) [31] and Kremikovtsi Municipality, Bulgaria ($GM = 542 \text{ Bq/m}^3$) [32]. The $GM = 51 \text{ Bq/m}^3$ for thoron measured in Banja Luka schools is not only higher than the $GM = 11 \text{ Bq/m}^3$ value obtained from measurements in Skopje, but also higher than the usual published values in the literature.

5. REFERENCES

- [1] K. Ivanova, Z. Stojanovska, M. Tsenova, B. Kunovska, *Building-specific factors affecting indoor radon concentration variations in different regions in Bulgaria*, Air Quality, Atmosphere & Health, Vol. 10-9 (2017) 1151–1161.
- [2] F. Bochicchio, Z. S. Žunić, C. Carpentieri, et al., *Radon in indoor air of primary schools: a systematic survey to evaluate factors affecting radon concentration levels and their variability*, Indoor Air, Vol. 24 (2014) 315–326.
- [3] P. Bossew, Z.S. Žunić, Z. Stojanovska, et al., *Geographical distribution of the mean radon concentrations in primary schools of Southern Serbia - application of geostatistical methods*, J Environ Radioact, Vol. 127 (2013) 141–148.
- [4] K. Ivanova, Z. Stojanovska, *Modelling of the temporal indoor radon variation in Bulgaria*, Radiat Environ Biophys, Vol. 58-3 (2019) 337–344.
- [5] Z. Stojanovska, J. Januseski, P. Bossew, et al., *Seasonal indoor radon concentration in FYR of Macedonia*, Radiat Meas., Vol. 46-(6-7) (2011) 602–610.
- [6] Z. Stojanovska, P. Bossew, S. Tokonami, et al., *National survey of indoor thoron concentration in FYR of Macedonia (continental Europe - Balkan region)*, Radiat Meas., Vol. 49-1 (2013) 57-66.
- [7] Z. Stojanovska, B. Boev, Z.S. Žunić, et al., *Results of radon CR-39 detectors exposed in schools due two different long-term periods*, Nukleonika, Vol. 61-3 (2016) 385–389.
- [8] Z. Stojanovska, K. Ivanova, P. Bossew, et al., *Prediction of long-term indoor radon concentration based on short-term measurements*, Nucl Technol Radiat, Vol. 32-1 (2017) 77–84.
- [9] United Nations Scientific Committee, *Effects of Atomic Radiation Effects of ionizing radiation. Report to the General Assembly with Scientific Annexes*, Annex B, NY: UN, 2000.
- [10] United Nations Scientific Committee, *Effects of Atomic Radiation Effects of ionizing radiation. Report to the General Assembly with Scientific Annexes*, Annex B, NY: UN, 2008.
- [11] S. Darby, D. Hill, A. Auvinen, et al., *Radon in homes and risk of lung cancer: Collaborative analysis of individual data from 13 European case-control studies*, (2005) *BMJ* 330.7485 223–0
- [12] Z. S. Žunić, Z. Stojanovska, B. Boev, et al., *Sjenica, a newly identified radon priority area in Serbia, and radon data correlated with geological parameters using the multiple linear regression model*, Carpathian Journal of Earth and Environmental Sciences, Vol. 14-1 (2019) 235–244.
- [13] Z. S. Žunić, R. Mishra, I. Čeliković, et al., *Effective Doses Estimated from the Results of Direct Radon and Thoron Progeny Sensors (DRPS/DTPS) Exposed in selected Region of Balkans*, Radiation Protection Dosimetry, Vol. 185-3 (2019) 387–390.
- [14] K. Ivanova, Z. Stojanovska, B. Kunovska, et al., *Analysis of the spatial variation of indoor radon concentrations (national survey in Bulgaria)*, Environmental Science and Pollution Research, Vol. 26-7 (2019) 6971–6979.
- [15] Z.S. Žunić, P. Bossew, F. Bochicchio, et al., *The relation between radon in schools and in dwellings: A case study in a rural region of Southern Serbia*, J Environ Radioact, Vol. 167-1 (2017) 188–200.
- [16] Z.S. Žunić, Z. Stojanovska, N. Veselinovic, et al., *Indoor radon, thoron and their progeny concentrations in high thoron rural Serbia environments*, Radiation Protection Dosimetry, Vol. 177-1-2 (2017) 36–39.
- [17] P. Kolarž, J. Vaupotič, I. Kobal, et al.,

Thoron, radon and air ions spatial distribution in indoor air, J Environ Radioact, Vol. 173 (2017) 70–74.

[18] Z.S. Žunić, P. Ujić, L. Nad, et al., *High variability of indoor radon concentrations in uraniumiferous bedrock areas in the Balkan region*, Appl radiat Isotop, Vol. 94 (2014) 328–337.

[19] R. Mishra R, Z. S. Žunić, G. Venoso, et al., *An evaluation of thoron (and radon) equilibrium factor close to walls based on long-term measurements in dwellings*, Radiat Prot Dosimetry, Vol. 160–1–3 (2014) 164–168.

[20] L. Gulan, F. Bochicchio, C. Carpentieri, et al., *High annual radon concentration in dwellings and natural radioactivity content in nearby soil in some rural areas of Kosovo and Metohija (Balkan region)*, Nucl Technol Radiat, Vol. 28–1 (2013) 60–67.

[21] K. Ivanova, Z. Stojanovska, V. Badulin, et al., *Pilot survey of indoor radon in the dwellings of Bulgaria*, Radiat Prot Dosimetry, Vol. 157–4 (2013) 594–599.

[22] L. Gulan, G. Milic, P. Bossew, et al., *Field experience on indoor radon, thoron and their progenies with solid-state detectors in a survey of Kosovo and Metohija (Balkan region)*, Radiat Prot Dosimetry, Vol. 152–(1–3) (2012) 189–197.

[23] Z. Stojanovska, J. Januseski, B. Boev, et al., *Indoor exposure of population to radon in the FYR of Macedonia*, Radiat Prot Dosimetry, Vol. 148–2 (2011) 162–167.

[24] Z. Stojanovska, Z. S. Žunić, P. Bossew, et al., *Results from time integrated measurements of indoor radon, thoron and their decay product concentrations in schools in the Republic of Macedonia*, Radiat Prot Dosimetry, Vol. 162–1–2

(2014) 152–156.

[25] Z. Stojanovska, Boev B, Z. S. Žunić, et al., *Variation of indoor radon concentration and ambient dose equivalent rate in different outdoor and indoor environments*. Radiat Environ Biophys, Vol. 55–2 (2016) 171–183.

[26] Z. Stojanovska, B. Boev, Z. S. Žunić, et al., *Factors Affecting Indoor Radon Variations: A Case Study in Schools of Eastern Macedonia*, Rom J Phys, Vol. 64 (2019) 801.

[27] Z. Čurguz, Z. S. Žunić, Tollefsen, et al., *Active and passive radon concentration measurements and first-step mapping in schools of Banja Luka, Republic of Srpska*, Rom J Phys, Vol. 58–S (2013) 90–98.

[28] Z. Čurguz, Z. Stojanovska, Z.S. Žunić, et al., *Long-term measurements of radon, thoron and their airborne progeny in 25 schools in Republic of Srpska*, J Environ Radioact, Vol. 148 (2015) 163–169.

[29] Z. S. Žunić, C. Carpentieri, Z. Stojanovska, et al., *Some results of a radon survey in 207 Serbian schools*. Rom J Phys, Vol. 58–S (2013) 320–327.

[30] J. Planinić, G. Šmit, Z. Faj, et al., *Radon in schools and dwellings of Osijek*, Journal of Radioanalytical and Nuclear Chemistry, Vol. 191–1 (1995) 45–51.

[31] K. Ivanova, Z. Stojanovska, M. Tsenova, et al., *Measurement of indoor radon concentration in kindergartens in Sofia, Bulgaria*, Radiat Prot Dosimetry, Vol. 162–(1–2) (2014) 163–166.

[32] Vuchkov D, K. Ivanova, Z. Stojanovska, et al., *Radon measurement in schools and kindergartens (Kremikovtsi Municipality, Bulgaria)*, Rom J Phys, Vol. 58–S (2013) 328–335.



КОНЦЕНТРАЦИЈЕ РАДОНА И ТОРОНА У ШКОЛАМА СКОПЉА
(РЕПУБЛИКА СЕВЕРНА МАКЕДОНИЈА) И БАЊЕ ЛУКЕ
(РЕПУБЛИКА СРПСКА) МЕРЕНЕ RADUET ДЕТЕКТОРИМА

Сажетак: Радон (^{222}Rn) и торон (^{220}Rn) су природни радиоактивни гасови који се генеришу у терестријалним материјалима. Они су главни извори излагања становништва јонизујућем зрачењу у затвореном простору широм света. Разлике у периоду полураспада ^{222}Rn ($T_{1/2} = 3,8$ д) и ^{220}Rn ($T_{1/2} = 55,6$ с) доводе до њиховог различитог понашања у просторијама. До сада је извршено неколико испитивања ^{222}Rn и ^{220}Rn у Северној Македонији, почевши од мерења у становима 2008. године и настављајући са мерењима у школама током 2012. Испитивања радона у Републици Српској започела су касније (у 2011. години) истовременим мерењима ^{222}Rn и ^{220}Rn у становима и школама града Бање Луке. Овај рад, као резултат заједничке сарадње, указује на резултате и опште закључке добијене мерењима ^{222}Rn и ^{220}Rn у главним градовима обе државе. У оба града мерења су извршена помоћу Raduet – нуклеарних траг детектора; распоређених на растојањима од зида: $> 0,5$ m (Скопље) и $0,2$ m (Бања Лука); и изложених у периоду: март 2012. – мај 2012. (Скопље) и април 2011. – мај

2012. (Бања Лука). Резултати концентрација ^{222}Rn и ^{220}Rn у оба града имају log-нормалну дистрибуцију. Средња геометријска вредност ^{222}Rn од 71 Bq/m^3 у Скопљу је већа него у Бањој Луци ($\text{ГС} = 50 \text{ Bq/m}^3$). Између разлике у потенцијалу радона који утичу на варијације ^{222}Rn , та се разлика може повезати са различитим временима излагања детектора. Даље, дисперзија резултата ^{222}Rn у сваком граду изражена геометријском стандардном девијацијом је релативно мала: ГСД = 2,13 (Скопље) и ГСД = 2,11 (Бања Лука) што указује на релативно хомогене скупове података. Концентрације ^{220}Rn у Бањој Луци ($\text{ГС} = 51 \text{ Bq/m}^3$) биле су веће него у Скопљу ($\text{ГС} = 11 \text{ Bq/m}^3$). Очигледно је да у случају ^{220}Rn , период изложености није играо значајну улогу. Један од разлога ове разлике могао би бити положај детектора као и различити грађевински материјали у школама. Супротно томе, дисперзија резултата ^{220}Rn у Скопљу (ГСД = 3,38) била је већа него у Бањој Луци (ГСД = 2,07).

Кључне речи: радон, торон, гас, школа.



Paper received: 16 August 2019
Paper accepted: 31 December 2019



THE HENRYK NIEWODNICZAŃSKI
INSTITUTE OF NUCLEAR PHYSICS
POLISH ACADEMY OF SCIENCES



BOOK of ABSTRACTS

2nd International Conference



Under the official patronage of the President of the National Atomic Energy Agency



III ERA WORKSHOP European Radon Association

GOLD SPONSOR:



SILVER SPONSOR:



SPONSORS:



ORGANIZING COMMITTEE

Institute of Nuclear Physics PAN, POLAND

Krzysztof KOZAK – chairman
Jadwiga MAZUR – co-chairman, scientific secretary
Dominik GRZĄDZIEL
Mariusz MROCZEK

SCIENTIFIC COMMITTEE:

Maciej BUDZANOWSKI	Institute of Nuclear Physics PAN (IFJ PAN), POLAND
Fernando P. CARVALHO	University of Lisbon (IST), PORTUGAL
Jing CHEN	Radiation Protection Bureau, Health Canada, CANADA
Werner HOFMANN	University of Salzburg, AUSTRIA
Karol HOLY	Comenius University, SLOVAKIA
Geraldine IELSCH	Institut de Radioprotection et de Sûreté Nucléaire (IRSN), FRANCE
Mirosław JANIK	National Institute of Radiological Sciences (NIRS), JAPAN
Tibor KOVACS	University of Panonnia, HUNGARY
Krzysztof KOZAK	Institute of Nuclear Physics PAN (IFJ PAN), POLAND
Beata KOZŁOWSKA	University of Silesia, POLAND
Jadwiga MAZUR	Institute of Nuclear Physics PAN (IFJ PAN), POLAND
Luis S. Quindós PONCELA	University of Cantabria, SPAIN
Tadeusz PRZYLIBSKI	Wroclaw University of Technology, POLAND
Vanja RADOLIČ	University of Osijek, CROATIA
Rakesh C. RAMOLA	H.N.B. Garhwal University, INDIA
Shinji TOKONAMI	Hirosaki University, JAPAN
Janja VAUPOTIČ	Jožef Stefan Institute, SLOVENIA
Małgorzata WYSOCKA	Central Mining Institute (GIG), POLAND
Michael ZHUKOVSKY	Institute of Industrial Ecology, RUSSIA
Weihai ZHUO	Fudan University, CHINA
Zora S. ZUNIČ	Vinča Institute of Nuclear Sciences, SERBIA

Book of abstracts edited by:

**Jadwiga Mazur (IFJ PAN, Poland)
Krzysztof Kozak (IFJ PAN, Poland)**

LONG-TERM MEASUREMENTS OF RADON, THORON AND THEIR AIRBORN PROGENY IN 25 SCHOOLS IN REPUBLIC OF SRPSKA

Z. Curguz¹, Z. Stojanovska², Z.S. Zunic³, P. Kolarž⁴, T. Ischikawa⁵, Y. Omori⁵, R. Mishra⁶,
B.K. Sapa⁶, J. Vaupotič⁷, P. Ujić³, P. Bossew⁸

¹ University of East Sarajevo, Faculty of Transport, Doboj, Republic of Srpska

² Goce Delcev University, Faculty of Medical Sciences, Stip, Republic of Macedonia

³ University of Belgrade, Institute of Nuclear Sciences “Vinča”, 11000 Belgrade, Serbia

⁴ University of Belgrade, Institute of Physics, Serbia

⁵ Fukushima Medical University, Department of Radiation Physics and Chemistry, Hikariga-oka 1, Fukushima, 960-1295, Japan

⁶ Bhabha Atomic Research Centre, Radiological Physics and Advisory Division, Mumbai, India

⁷ Institute Jozef Stefan, Radon Centre, Jamova 39, 1000 Ljubljana, Slovenia

⁸ German Federal Office for Radiation Protection, Köpenicker Allee 120-130, 10318 Berlin, Germany

E-mail: zdenka.stojanovska@ugd.edu.mk

This article reports results of the first investigations on indoor radon, thoron and their decay products concentration in 25 primary schools of Banja Luka, capital city of Republic Srpska. The radon and thoron measurements have been carried out in the period from May 2011 to April 2012 using 3 types of commercially available nuclear track detectors, named: long-term radon monitor (GAMMA 1), and radon-thoron discriminative monitor with nuclear track detectors (RADUET) while equilibrium equivalent radon concentration (*EERC*) and equilibrium equivalent thoron concentrations (*EETC*) measured by Direct Radon Progeny Sensors/Direct Thoron Progeny Sensors (DRPS/DTPS) were exposed in the period November 2011 to April 2012. In every school the detectors were positioned at 8-10 cm distance from the wall. The obtained geometric mean concentrations were 99 Bq m⁻³ for radon and 51 Bq m⁻³ for thoron. Those for equilibrium equivalent radon concentration (*EERC*) and equilibrium equivalent thoron concentrations (*EETC*) were 11.2 Bq m⁻³ and 0.4 Bq m⁻³, respectively. The correlation analyses showed weak relation only between radon and thoron concentrations as well as between thoron and *EETC*. The influence of the school geographical position and factors linked to buildings characteristic in relation to measured concentrations were tested. The geographical position and of floor significantly influence radon concentrations while thoron concentrations depend only from building materials (ANOVA, $p \leq 0.05$). The obtained geometric mean values of the equilibrium factors are 0.123 for radon and 0.008 for thoron.

Keywords: Indoor air, radon, thoron, primary schools, nuclear track detectors

V. TERRESTRIAL RADIOISOTOPES IN ENVIRONMENT

International Conference on Environmental Protection



VESZPRÉM

2016

Social Organization for Radioecological Cleanliness

Organizers:

University of Pannonia, Institute of Radiochemistry and Radioecology
Social Organization for Radioecological Cleanliness
Hungarian Biophysical Society, Section of Radioecology

Chair:

Tibor Kovács

Secretaries:

János Somlai, Edit Tóth-Bodrogi, Gergő Bátor, Erika Nagy, András Bednár

Edited by:

Tibor Kovács, Edit Tóth-Bodrogi, Gergő Bátor

SPACE DISTRIBUTION OF AIR IONS, THORON AND RADON IN INDOOR AIR

P. Kolarž¹, J. Vaupotič², I. Kobal², Z. S. Žunić³

¹*Institute of Physics, 11080 Belgrade, Serbia*

²*Jožef Stefan Institute, 1000 Ljubljana, Slovenia*

³*Institute of Nuclear Sciences Vinča, 11000, Belgrade, Serbia*

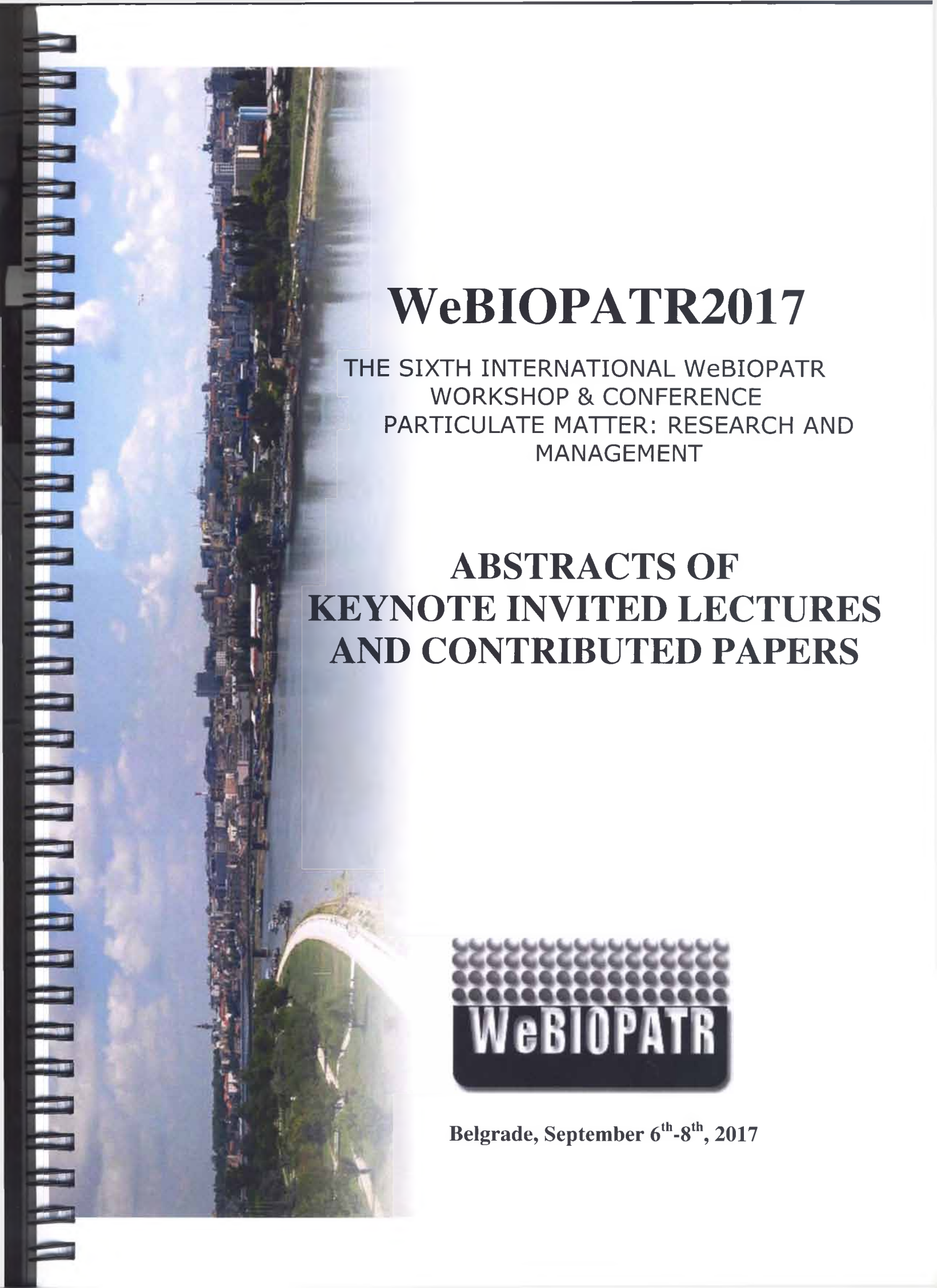
Air ions in indoor air are generated mostly by MeV-energy α -particles produced in radioactive transformations of radon (^{220}Rn and ^{222}Rn) and its short-lived descendants. Since the intensity of all other air ionizing sources is significantly lower and mostly constant in time, air ions may serve as confident indicator for spatial and temporal distribution ^{222}Rn and ^{220}Rn concentrations indoors. Example of vertical gradients of ^{220}Rn & ^{222}Rn activity concentrations measured above earthen floor in the basement at house in Sokobanja is presented.

Measurements were performed in Sokobanja region (Serbia), where ^{220}Rn concentration in soil and building materials is relatively high, and in Slovenia in villages Gorisnica and Rakitna, where ^{222}Rn concentrations are much higher than ^{220}Rn . Following equipment was used for the measurements: 2 x Rad7 (DurrIDGE company, USA), RTM 1688-2 Radon/Thoron Monitor (Sarad, Germany) and three Gerdien-type air-ion CDI-06 detectors.

During the $^{220,222}\text{Rn}$ measurements, inlets of measuring devices were fixed at 1 cm, 20 cm and 40 cm above the floor while air ion detectors were positioned at 10 and 85 cm above the floor. During measurements, switching of the air ion detectors places was performed in order to test their quality of operation.

Air ion concentration at the height of 85 cm was 37% lower than at 10 cm while in the case of thoron reduction was 75% after 40 cm. At the same time, moderate but still clearly measurable decrease of air ions concentration with height (gradient) was measured. Thoron and radon gasses are decaying with similar energy of α -particle and thus creating similar number of air ion pairs. Gradient of air ion concentrations from the floor would be probably much higher if it is not "diluted" with ions generated by radon and its decay products. Also, life time of air ions in relatively clean air is about 100 s which is twice as T_n so that ions can move for longer distances from point of origin than thoron.

During the survey, measurements of the mentioned parameters were also carried out at different distances from walls and have shown either linear or exponential pattern depending on microclimatic ambient. Many measurements of air ions were impossible to conduct due to electrostatic field of the walls that strongly influenced on ions.

An aerial photograph of a city, likely Belgrade, situated along a wide river. In the foreground, a large, modern stadium with a curved roof is visible. The city buildings and greenery extend along the riverbank under a blue sky with scattered clouds.

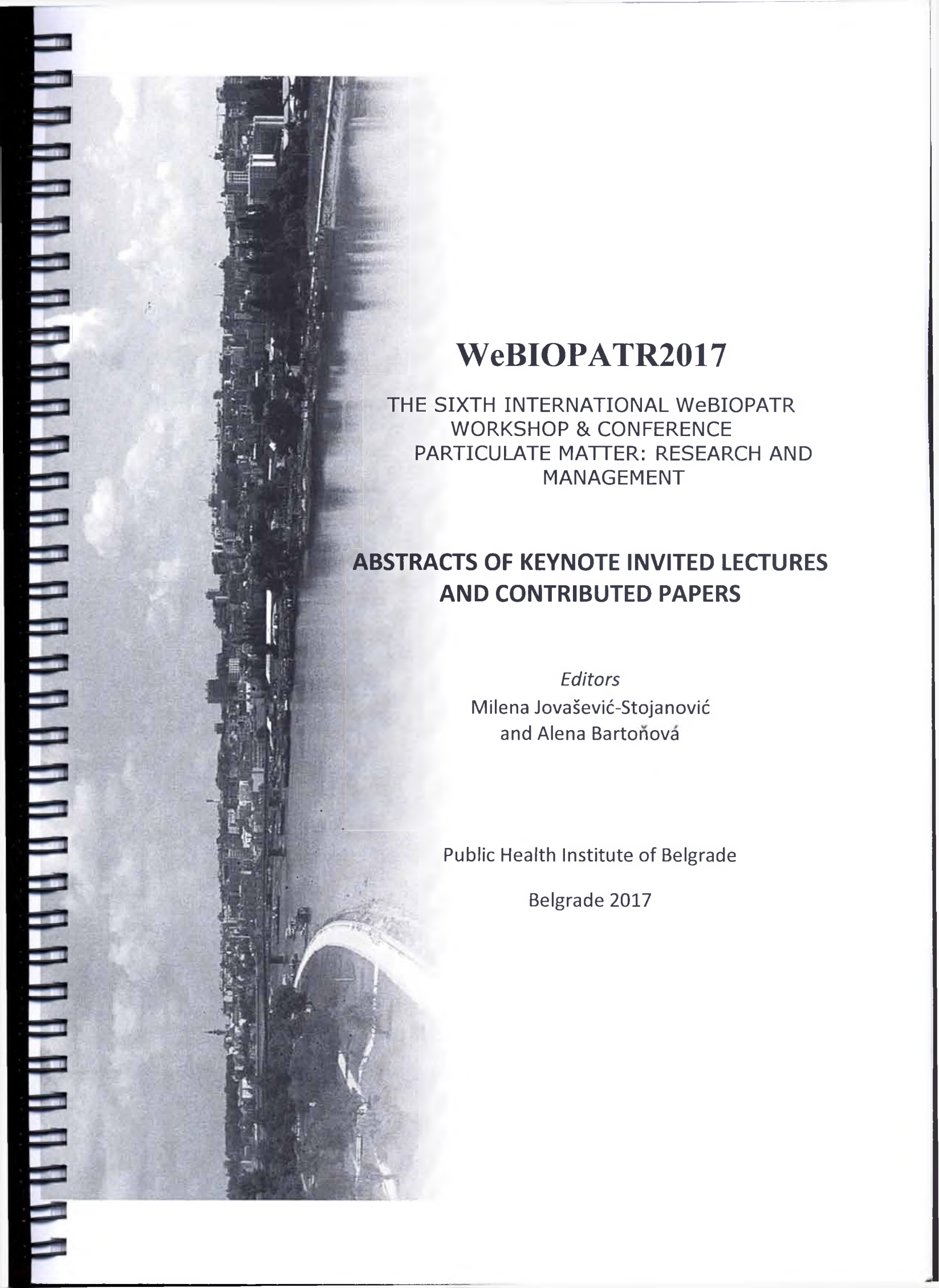
WeBIOPATR2017

THE SIXTH INTERNATIONAL WeBIOPATR
WORKSHOP & CONFERENCE
PARTICULATE MATTER: RESEARCH AND
MANAGEMENT

**ABSTRACTS OF
KEYNOTE INVITED LECTURES
AND CONTRIBUTED PAPERS**



Belgrade, September 6th-8th, 2017

An aerial photograph of a city, likely Belgrade, showing a river, a bridge, and buildings. The image is oriented vertically on the left side of the page.

WeBIOPATR2017

**THE SIXTH INTERNATIONAL WeBIOPATR
WORKSHOP & CONFERENCE
PARTICULATE MATTER: RESEARCH AND
MANAGEMENT**

**ABSTRACTS OF KEYNOTE INVITED LECTURES
AND CONTRIBUTED PAPERS**

Editors

**Milena Jovašević-Stojanović
and Alena Bartoňová**

Public Health Institute of Belgrade

Belgrade 2017

**ABSTRACTS OF KEYNOTE INVITED LECTURES AND
CONTRIBUTED PAPERS**

The Sixth International WeBIOPATR Workshop & Conference
Particulate Matter: Research and Management
WeBIOPATR2017

6 – 8 September 2017
Belgrade, Serbia

Editors

Milena Jovašević-Stojanović
Alena Bartoňová

Publisher

Public Health Institute of Belgrade
Prof. Dr Dušanka Matijević, Director
Boulevard Despota Stefana 54 a
Serbia, 11000 Belgrade

Printed by

Printing office of the Public Health Institute of Belgrade

Number of copies

200

978-86-83069-49-1

© Public Health Institute of Belgrade
www.zdravlje.org.rs

10.4 ANALYSIS OF PARTICULATE MATTER AND SMALL ION CONCENTRATIONS IN INDOOR ENVIRONMENT BASED ON BALANCE EQUATION

M. Davidović (1), D. B. Topalović (2,1), Predrag Kolarž (3), M. Jovašević-Stojanović (1)

(1) Institute Vinča, University of Belgrade, Belgrade, Serbia, (2) School of Electrical Engineering – University of Belgrade, Belgrade, Serbia, (3) Institute of Physics, University of Belgrade, Belgrade, Serbia
davidovic@vin.bg.ac.rs

Aim: Aim of this work was to explore a relation between particulate matter (PM) and small (cluster) air ions (SI) concentration in a typical indoor environment. Changes in SI concentration are due to several factors. First, SI are constantly created, in pairs, by ionizing radiation that exists in the environment. They are also continually destroyed in processes of recombination, attachment to aerosols (PM) and deposition on electrostatic surfaces. Because of this, a change in PM concentration directly results in a change in SI concentration. SI balance equation can be used to quantitatively describe above mentioned processes.

Method: Wide range of relevant air quality parameters were measured in indoor environment, occupied on work days, in March 2017. The measurements included negative SI measurements by Gerdien-type air ion detector (Kolarž, 2012), PM concentration in 10 nm to 10 μm diameter range using TSI NanoScan SMPS Model 3910 and TSI Optical particle sizer 3330, gravimetric measurements of particles in 3 fractions, and local temperature, pressure and humidity. In addition, hourly radon concentration was measured using Radon Scout. Collected data describes all relevant processes: 2 min. SI concentration measurements describe steady state, radon concentration gives insight into rate of volumetric ion pair generation and 1 minute PM measurements give insight into main loss mechanism for SI.

Results: Relation between negative SI concentration and PM concentration was derived using quasi steady state approximation of SI balance equation. Form of this relation suggests that the use of linear regression in modelling is sound and well justified approach, and that the regression coefficients can be interpreted as ion-particle attachment coefficients. Since there was a large number of individual channels (13 Nanoscan and 16 OPS channels), with significant cross correlation, ordinary least squares was not a reliable method, producing unphysical results. To ensure regression coefficients have physical meaning we used non-negative least squares solver (Lawson, 1995), and aggregation of channels into total counts and typical PM fractions. Results are shown in Fig. 1.

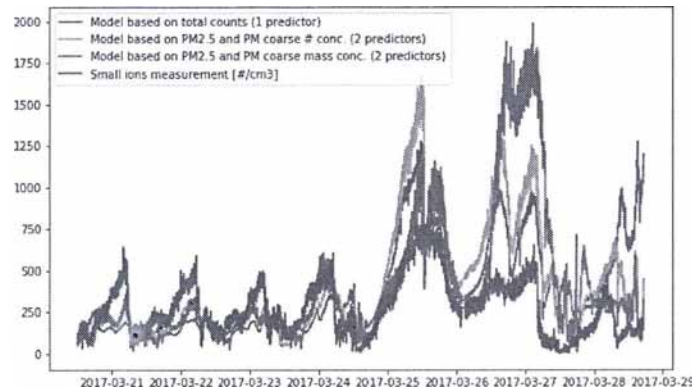


Figure 1. Comparison of negative small ion measurements and 3 models based on total counts and PM fractions

Conclusion: All models show daily variations of ion concentration, however, it seems that models are prone to overestimation, which occurs in periods of low particle counts, which are inherently less accurate. In the case of a model based on total counts, attachment coefficient is estimated to be $8.45\text{e-}06 \text{ cm}^3 \text{ s}^{-1}$. Note, however, that interpretation of regression coefficients as attachment constants is somewhat approximate, since there is a significant correlation between individual channels.

REFERENCES

1. Kolarž, P., Miljković, B., & Čurguz, Z. (2012). Air-ion counter and mobility spectrometer. *Nuclear Instruments and Methods in Physics Research Section B: Beam Interactions with Materials and Atoms*, 279, 219-222.
2. Lawson, Charles L., and Richard J. Hanson. *Solving least squares problems*. Society for Industrial and Applied Mathematics, 1995.

THE EFFECT OF INTENSE IONIZATION ON THE CHANGE IN THE CONCENTRATION OF TOBACCO SMOKE FINE PARTICLES

P. Kolarž (1), M. Živković (2), M. Davidović (2)

(1) Institute of Physics Belgrade, University of Belgrade, Serbia, (2) Vinča Institute of Nuclear Sciences, University of Belgrade, Serbia
kolarz@ipb.ac.rs

Background: Particulate matters (PM) generated by cigarette smoke is one of most harmful indoor air pollutants. It is unhealthy not only for smokers but also for non-smokers inhaling PM. There are several ways for reduction of number concentration of PMs, notable examples being ventilation and filtering. These approaches might be somewhat aided by ionization of the air in certain scenarios.

A preliminary study of influence of artificially generated ions on cigarette smoke particles size distribution is presented. In theory, bipolar ionizer generates primary electrified particles of both polarities. After ionization process, primary ions evolve within microseconds through process of hydration into charged nano-aerosols, known as small air ions (SI). SI are typically charged clusters with electric mobilities of $1\text{--}2\text{ cm}^2\text{V}^{-1}\text{s}^{-1}$, size range of $0.6\text{--}1\text{ nm}$ (Tamm et al., 2005) and typical lifetime of $5\text{--}60\text{ s}$. Processes of SI neutralization are by ion-aerosol attachment, ion-ion recombination and by the deposition on non-conductive (electrostatic) surfaces.

Methods: Bipolar barrier discharge ionizer (Bioclimatic GmbH) was used to generate up to $20\,000\text{ ions cm}^{-3}$ per each polarity, while single cigarette burning was generating PMs of different sizes. PMs was measured using TSI NanoScan SMPS 3910 (measuring range from $11.5\text{ to }365.2\text{ nm}$), while SI concentration was measured using Counter and spectrometer of air ions CDIS (Kolarž et al., 2012). Experiment was conducted in small office where PMs and SI was measured with and without ionization. During the measurements, there were no disturbances in the room. Ionization was switched on 3 minutes after the cigarette was burned (yellow line in Figure 1) and SI concentration was in the range $9000\text{ to }19000\text{ ions cm}^{-3}$ for positive and $7000\text{ to }14000\text{ ions cm}^{-3}$.

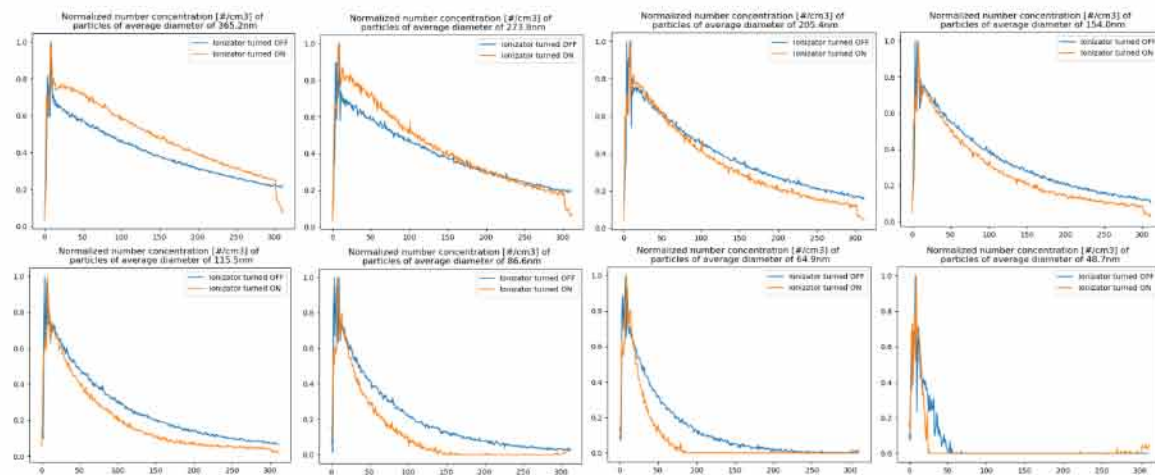


Figure 1. PM concentration reduction over time (min.) with (yellow line) and without (blue line) ionization.

Conclusion: The results (Figure 1) showed faster decrease in concentration of smaller PMs, up to 205 nm , as a consequence of SI to PM attachment mechanism. SI, as ions with higher mobility, quickly attaching on PMs and thus electrifying them. Electrified PMs are also attaching to other PMs and thereby significantly increasing mass and reducing mobility. According to our measurements, this process of aggregation of small PMs and ions takes place up to 200 nm of PMs diameter. After that PMs concentration during ionization is decreasing much slower than without ionization due to generation of new particles by ion induced aggregation process.

REFERENCES

- Tamm, H., Kulmala, M., 2005. Simulation tool for atmospheric aerosol nucleation bursts, *Aerosol Science* 36, 173–196.
Kolarž, P., Miljković, B., and Čurguz, Z. 2012. Air-ion counter and mobility spectrometer, *Nucl. Instr. Meth. B*, 279, 219–222.

KONTINUALNO MERENJE UV ZRAČENJA I OZONA U SRBIJI

Predrag KOLARŽ¹, Zoran MIJATOVIĆ², Aleksandar VLAJIĆ³

1) *Univerzitet u Beogradu, Institut za fiziku, Beograd, Srbija, kolarz@ipb.ac.rs*

2) *Univerzitet u Novom Sadu, Departman za fiziku, Prirodno matematički fakultet,*

Novi Sad, Srbija, mijat@uns.ac.rs

3) *NVO, GRES - Grupa za razvoj ekološke svesti, Beograd, Srbija,*

arborea.hyla@gmail.com

SADRŽAJ

UV zračenje se u Srbiji meri nezavisno u Beogradu i Novom sadu već duži niz godina. Radi bolje informisanosti stanovništva ova merenja su kroz projekat nevladinih organizacija pod nazivom „Ozonizacija“ objedinjena i uniformisana te su sada svima dostupna preko sajta <http://www.uv-srbija.rs> i aplikacije za android mobilne telefone „UV indeks Srbija“. Podaci Indeksa UV zračenja se obnavljaju na svakih pola sata dok se podaci za koncentraciju stratosferskog ozona iznad novog sada odnosno Srbije daju dnevno. Vrednosti UV indeksa se prikazuju grafički, a na sajtu je dato detaljno objašnjenje o tome šta UV indeks predstavlja, koje su vrednosti opasne, kako se zaštititi od preteranog izlaganja Sunčevom zračenju i kako se proračunava faktor zaštite (SPF) krema za sunčanje.

1. UVOD

Globalna svest o tome da su antropogeni uticaji na životnu sredinu izazvali poremećaje ekološke ravnoteže, izazivanjem i destabilizacijom dugoročnih procesa velikih razmera, razvijena je tek u drugoj polovini 20. veka. Danas su već identifikovane najznačajnije posledice globalnog (planetarnog) karaktera i među njima su dominantni procesi: slabljenje (stanjivanje) ozonskog omotača sa pojavljivanjem ozonskih rupa i promena klime – globalno zagrevanje atmosfere. Ova dva procesa su u stalnoj uzročno – posledičnoj interakciji i uzrokuju druge štetne efekte na sredinu i živi svet na Zemlji (kisele kiše, smanjivanje šumskih površina, širenje pustinja, smanjivanje biološke raznovrsnosti, uticaj na zdravstveno stanje ljudi, promene globalne epidemiološke slike, itd.). Stanjivanje stratosferskog sloja ozonskog omotača identifikovala je Svetska meteorološka organizacija (WMO) 1970. godine, a glavni krivac je proces katalitičke destrukcije hemijskim elementima pod nazivom halogeni. Glavni izvori halogena koji vrše fotodisocijaciju su rashladne tečnosti, rastvarači industrijski stvoreni raspršivač i sredstva za rasšrivanje pene (CFCs, HCFCs, freons, halons). Nakon ovoga sledi unapređenje čitavog sistema monitoringa ozona i sunčeve radijacije, posebno ultraljubičastog (UV) dela solarnog spektra čiji se intenzitet pojačava sa slabljenjem ukupnog ozona u atmosferi. Tada započinju i vrlo kompleksna i opsežna istraživanja uzroka i procesa vezanih za ovu pojavu, kao i posledica ove pojave po živi svet. Rezultat monitoringa i istraživanja je bio donošenje Međunarodne konvencije o zaštiti ozonskog omotača (UNEP- Beč, 1985) i Međunarodnog protokola o supstancama koje slabe ozonski omotač (UNEP- Monreal, 1987), koje je potpisala i naša država. Navedena međunarodna regulativa, naročito od 90-tih godina 20. veka, se uspešno sprovodi posebno u razvijenim zemljama, ali trend slabljenja ozonskog omotača nije u potpunosti zaustavljen do danas. U srazmeri sa slabljenjem ozonskog omotača povećava se intenzitet UV zračenja (kao posledica smanjene apsorpcije UV zraka od strane ozona) koji štetno

deluje na čitav živi svet, na zdravlje ljudi, a i na određene veštačke materijale. Iz ovih razloga, organizacije UN (Svetska zdravstvena organizacija – WHO, Svetska meteorološka organizacija – WMO, Program UN za životnu sredinu – UNEP i Međunarodna komisija za zaštitu od nejonizujućeg zračenja – ICBIRP), upućuju 1995. godine preporuku vladama svih zemalja da koriste UV indekse radijacije – UVI (koje su definisale ove četiri organizacije) u obeštavanju javnosti o stanju i potrebnim merama zaštite [1]. Ova preporuka, ponovljena je 1998. godine, kada je standardizovana formulacija ultravioletnog indeksa radijacije (UVI) na bazi referentnog spektra pojave eritema na koži čoveka u zavisnosti od talasne dužine UV, prema referenci Međunarodne komisije za iluminaciju – CIE [2].

2. OZONSKI OMOTAČ

Ozonski omotač, jedan je od slojeva zemljine atmosfere koji sadrži preko 91% ozona (O_3). Nastaje i nestaje fotohemijskim reakcijom UV zračenja i kiseonika. UV-A zračenje, opsega talasnih dužina od 315 do 400 nm, u potpunosti prolazi kroz ozonski omotač, dok sunčevu svetlost kraćih talasnih dužina UV-B opsega (280 - 315 nm) apsorbira u velikoj meri 93 - 99%, a u potpunosti apsorbira UV-C opseg (100 - 280 nm) deo UV Sunčevog spektra. Iz tog razloga je ozonski omotač od neprocenjivog značaja za živi svet na Zemlji. Naime, fotoni ovog dela spektra imaju dovoljnu energiju i sa velikom verovatnoćom razaraju DNK i druge organske molekule. Prisustvo ovog zračenja u Sunčevom zračenju bi potpuno promenilo oblike života na Zemlji. Ozonski omotač se prostire u donjem sloju stratosfere od 10 do 50 kilometara iznad Zemljine površine. Njegova debljina varira u zavisnosti od lokacije i godišnjeg doba (najdeblji u proleće, a najtanji u jesen). Osim "dobrog" stratosferskog postoji i "loš" troposferski ozon, u najnižim slojevima atmosfere u kojima se odvijaju sve životne aktivnosti. On nastaje kao posledica zagađenja atmosfere i sastavni je deo urbanog smoga.

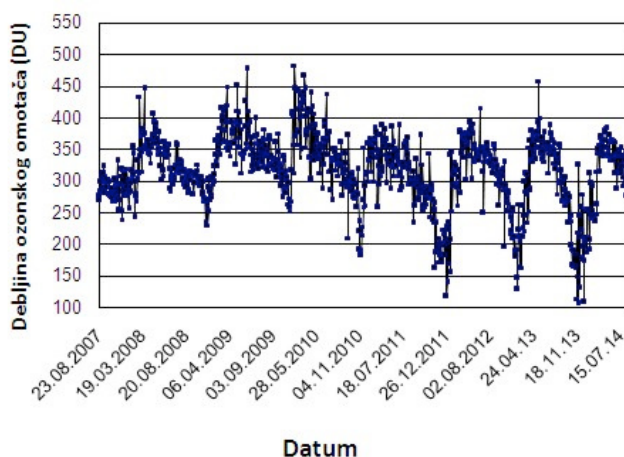
Dobson je jedinica za izražavanje količine atmosferskog ozona. Ukupna količina ozona u vertikalnom stubu vazduha se izražava kao debljina sloja ozona kada bi stub bio sabijen na standardni pritisak (1 atmosfera) pri temperaturi od $0^{\circ}C$. Sloj debljine 0.01 mm odgovara 1 Dobsonu. Prosečna vrednost debljine ozonskog omotača je oko 300 Dobsona, a iznad Evrope ta vrednost je oko 350, tj. debljina ozona je 3.5 mm. Vrednost od 220 Dobsona se smatra za kriterijum ozonske rupe, jer niža vrednost od nje nije zabeležena u posmatranjima pre 1979. godine. Reč "rupa" je zapravo metafora za deo atmosfere u kojem je koncentracija ozona ispod 220 Dobsonovih jedinica.

Ozon se u stratosferi kontinualno proizvodi i razlaže pod dejstvom UV zračenja. Ispuštanjem u atmosferu supstanci koje ovaj proces remete dolazi do stanjivanja ovog sloja i do povećavanja intenziteta UV-B zračenja na Zemlji. Supstance koje uništavaju ozon su: potpuno halogenovani ugljovodonici (CFC), hlorofluorouglijovodonici (HCFC), haloni, metil bromidi, karbon tetrahloridi, metil hloroformi i drugi. One su korišćene u rashladnim tečnostima, pesticidima, raspršivačima, sredstvima za gašenje požara i sl. Kada se jednom ispuste u atmosferu ove supstance se vrlo sporo degradiraju i kreću se kroz atmosferu dok ne stignu do stratosfere gde se pod dejstvom UV zračenja razlažu otpuštajući atome hlora i broma. Naučnici procenjuju da jedan atom hlora može da uništi oko 100 000 molekula ozona. U srazmeri sa stanjivanjem ozonskog omotača neprekidno se povećava intenzitet UV-B zračenja koji štetno deluje na čitav živi svet, na zdravlje ljudi i na određene veštačke materijale.

Osamdesetih godina prošlog veka je postalo jasno da se iznad Zemljinih polova stanjuje ozonski omotač i industrijsko загађење je označeno kao glavni krivac. U skladu sa time je u Montralu 1987. godine uz pomoć Programa UN za zaštitu životne sredine (United Nations Environment Programme) potpisan Montrealski protokol o supstancama koje oštećuju ozonski omotač. Ovaj protokol je potpisalo 197 zemalja među kojima i naša.

2.1 MONITORING DEBLJINE OZONSKOG OMOTAČA

Zahvaljujući međunarodnom FP-6 projektu, koji je dobio PMF u Novom Sadu, nabavljen je instrument Solar Light Microtops II za merenje debljine ozonskog omotača. Merenja su počela 23. avgusta 2007. godine. Merenja je moguće vršiti samo tokom vedrih dana i to je razlog zašto nedostaju vrednosti za neke dane. Na slici 1, prikazana je promena debljine ozonskog omotača iznad Novog Sada za period 23. avgust 2007. – 15. jula 2014. godine. S obzirom da se pod ozonskom rupom smatra oblast ozonskog omotača čija je debljina ispod 220 DU (dobsonove jedinice), sa slike se može zaključiti da je u ovom vremenskom periodu debljina ozonskog omotača uglavnom bila znatno iznad te vrednosti.



Slika 1. Promena debljine ozonskog omotača iznad Novog Sada. Merenja su vršena Departman za fiziku, PMF u Novom Sadu (GPS koordinate: 45.245, 19.853)

3. UV ZRAČENJE

UV zračenje je podeljeno na tri podopsega:

UV-A (315 - 400 nm), nije biološki aktivno, intenzitet se ne menja sa koncentracijom ozona. Prodire u dublje slojeve kože, vrši indirektna oštećenja, a prekomerno izlaganje je podjednako štetno kao i izlaganje UV-B zračenju.

UV-B (280 - 315 nm), biološki je aktivno, intenzitet zavisi od debljine ozonskog omotača. Oko 90% UV-B zračenja je apsorbovano od strane atmosfere. Apsorbuje se u površinskom sloju kože gde vrši direktna oštećenja.

UV-C (100 - 280 nm), kompletno se apsorbuje u atmosferi i praktično se ne opaža na površini Zemlje. Često se zove i sterilizujuće zračenje, jer se koristi u industrijskim pogonima.

3.1. DEJSTVO UV ZRAČENJA NA KOŽU

U ljudskoj koži se najveći deo zračenja apsorbuje u epidermu, tj. u površinskom sloju kože, stoga oštećenje koje je prouzrokovano UV zračenjem zavisi ne samo od intenziteta zračenja, nego i od propustljivosti epiderma. Dejstvo na kožu sastoji se u pojavi eritema (crvenilo kože) i edema (otok na koži), posle nekoliko sati od izlaganja. Izvesno vreme nakon početne upale kože ili pojave eritema, povećava se količina kožnog pigmenta melanina, kao prirodni odgovor organizma. Melanin služi kao zaštitni sloj od dejstva UV zračenja i uzrokuje tamnjenje kože.

Osetljivost kože na Sunčevo zračenje zavisi od njene pigmentacije, tj. od količine melanina u epidermu. Prema tome izvršena je podela na ukupno 6 fotobioloških tipova kože, a na našem podneblju on je uglavnom između 3 i 4. Za nastanak sunčevih opekotina presudna je dilatacija krvnih sudova koji se nalaze upravo ispod tog površinskog sloja i ta dilatacija se manifestuje kao crvenilo kože ili eritem. Da bi se na prosečnoj koži čoveka dobila minimalna primetna eritemna reakcija, potrebno je izložiti UV-B zračenju od 1 MED, što je u medicini poznato kao minimalna eritemalna doza (minimal Erythema Dose, MED). Ta vrednost zavisi od tipa kože i data je u tabeli 1, koja je bazirana na izlaganju od 3 MED-a ljudske kože koja ranije nije bila izlagana Sunčevom tj. UV zračenju.

Tabela 1. Opisi fototipova kože i njeno ponašanje pri osunčavanju

Fototip kože	Neizložena boja kože	MED opseg (mJ/cm ²)	Osetljivost na UV zračenje	Pregorevanje ili tamnjenje
I	bela	15 - 30	vrlo osetljiva	Uvek lako pregori, nikad ne potamni
II	bela	25 - 40	vrlo osetljiva	Uvek lako pregori, potamni malo uz teškoće
III	bela	30 - 50	osetljiva	Minimalno pregoreva, tamni postepeno i uniformno
IV	svetlo braon	40 - 60	umereno osetljiva	Minimalno pregoreva, uvek dobro potamni
V	braon	60 - 90	minimalno osetljiva	Retko pregoreva, obimno tamni (tamno braon)
VI	tamno braon ili crna	90 - 150	neosetljiva ili jedva osetljiva	Nikad ne pregoreva, obilno tamni (crna)

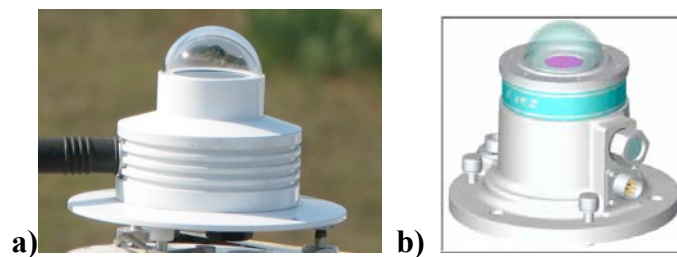
3.2. DEJSTVO UV ZRAČENJA NA OČI

Kod organa vida rožnjača i sočivo u velikoj meri apsorbuju UV zračenje. Pri tome rožnjača upija zračenje talasnih dužina do 300 nm, a sočivo talasne dužine od 295 do 400 nm. Očna tečnost je praktično prolazna za UV zračenje i ne štiti sočivo. Rožnjača je relativno otporna na UV zračenje i u prirodnim uslovima ne strada. Izuzetak predstavlja "snežno slepilo" (ophthalmia nivea), koje naročito nastaje u planinama prekrivenim snegom (visok albedo) gde je nivo zračenja izuzetno visok. Eksperimentalno je utvrđeno da prag traumatske doze za rožnjaču zavisi od talasne dužine. Najopasnije je oštećenje endotela rožnjače zbog toga što endotelijalne ćelije kod čoveka ne raspolažu regenerativnom sposobnošću (starenjem se njihov broj smanjuje). Profesionalno oštećenje sočiva izazvano višegodišnjom akumulacijom povreda UV zračenja kod lica koja se svakodnevno izlažu produženom dejstvu prirodnog ili veštačkog zračenja (mornari, zemljoradnici, radnici koji rade na planinama) nije teško sprečiti nošenjem naočara za sunce, koje upijaju ili odbijaju UV zrake.

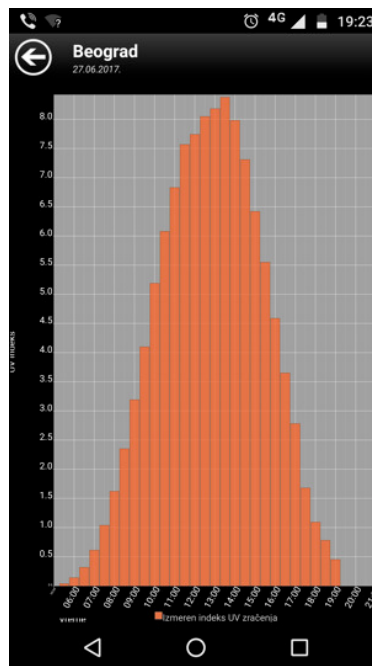
3.3. UV INDEKS

UV indeks, koji se koristi za obaveštavanje javnosti, je relativna jedinica (bezdimenzionalna) i vrednosti se kreću od 0 pa naviše [4]. Ovo daje mogućnost da osobe sa različitim fotobiološkim tipovima kože mogu da uspostave odnos UV-indeksa sa individualnom reakcijom svoje kože. Prognoza i objavljivanje UV-indeksa daje mogućnost da se individualno ponašanje prilagodi predviđenom i trenutnom UV-intenzitetu [3].

Na području grada Beograda i Novog Sada se duži niz godina unazad vrše merenja UV zračenja dok se u Novom Sadu (Priroidno-matematički fakultet) vrše i redovna merenja debljine ozonskog omotača. Merači UV zračenja su postavljeni na Institut za fiziku u Beogradu (Solar 501 UV biometer) i kampusu Univerziteta u Novom Sadu (Yankee Environmental System (YES) UVB-1 biometer) u Novom Sadu (slika 2). Za monitoring koristi se Solar Light Microtops II ozonemeter.



Slika 2. Instrumenti za merenje UV indeksa: a) Solar 501 UV biometer i b) Yankee Environmental System (YES) UVB-1 biometer



Slika 3. Grafički prikaz UV indeksa na dan 27.06.2017. godine adaptiran za android operativne sisteme

Treba napomenuti da su podaci koje se dobijaju spomenutim merenjima jedini relevantni podaci koji se mogu naći u Srbiji. Svi instrumenti koji se koriste i protokoli koji se primenjuju su standardizovani u skladu sa preporukama Svetske meteorološke organizacije (WMO).

Vrednost UV indeksa se menja tokom dana, ali i tokom godine. UV indeks počinje da raste izlaskom sunca da bi tokom tokom dana, oko 13 časova dostigao maksimalnu vrednost, a zatim opada. Na slici 3 je prikazana dnevna promena UV indeksa za vedar dan (27.06.2017). Sa ove slike se vidi da približno polovinu maksimalne dnevne vrednosti UV indeks dostiže oko 10 časove, a na tu vrednost opadne oko 16 časova. U tom periodu dana se emituje oko 80% ukupne dnevne doze UV zračenja. Doza zračenja se definiše kao proizvod snage zračenja po kvadratnom metru (W/m^2) i vremena (s). Jedinica doze zračenja je J/m^2 . Dnevna doza jako zavisi od oblačnosti tokom dana. Za dane koji su delimično ili potpuno oblačni, dnevna doza je manja nego što bi bila da je dan vedar.

Krajem zime i početkom proleća vrednost UV indeksa raste, da bi maksimum dostigla u periodu kraj juna - početak jula. Posle toga intenzitet UV zračenja opada, da bi od polovine novembra vrednost UV indeksa pala na vrednost ispod 1.

Merenja u koja se poslednjih godina vrše u Institutu za fiziku, Beograd i Departmanu za fiziku, Prirodno matematičkog fakulteta u Novom sadu, pokazuju da UV indeks na našem podneblju prelazi vrednost 9 tokom juna i jula. Organizacije pri UN su dale sledeću kategorizaciju UV-indeksa prikazanu u tabeli 2.

Tabela 2. Kategorizacija UV indeksa

INDEKS UV	KATEGORIJA	IZLAGANJE SUNCU
11 i više	Ekstremna	Ekstremna zaštita
8 do 10	Vrlo visoka	Ekstremna zaštita
6 do 7	Visoka	Potrebna zaštita
3 do 5	Srednja	Potrebna zaštita
1 i 2	Niska	Slobodno

Rezultati višegodisnjih merenja UV indeksa, slično kao vrednosti debljine ozonskog omotača tokom leta, ne pokazuju značajna odstupanja maksimalnih vrednosti iz godine u godinu. Maksimalne registrovane godišnje vrednosti UV indeksa se svake godine kreću između 8 i 9, doko su vrednosti debljine ozonskog omotača tokom leta u proseku nešto ispod 400 DU.

Zahvaljujući projektu "Ozonizacija" finansiranog od strane UNIDO (*United Nations Industrial Development Organization*), a povodom Međunarodnog dana zaštite ozonskog omotača (16. septembra 2014. godine), stanovnici Beograda i Novog Sada već 4 godine unazad mogu da prate trenutne vrednosti UV indeksa na sajtu: www.uv-srbija.rs kao i pomoću android aplikacije "UV Indeks Srbija" koja se na telefone instalira pomoću *Play store* aplikacije.

Osnovni cilj projekta je informisanje stanovništva o opasnostima od izlaganja UV zračenju i podizanje nivoa svesti o važnosti praćenja informacija o indeksu zračenja, izbegavanju nepotrebnog izlaganja ili izlaganja u vreme najjačeg zračenja i važnosti korišćenja zaštite za kožu i oči. Isto tako je važna i laka preglednost i dostupnost "on

line” podataka na mobilnim sredstvima komunikacije kao i izrada centralne baze podataka.

Podaci dobijeni mernjima na ova dva merna mesta su deo evropskih merenja i njihovi rezultati su zajedno sa rezultatima svih ostalih merenja UV zračenja u Evropi nedavno prihvaćeni za štampanje u časopisu Photochemical & Photobiological Sciences (M22) pod naslovom UV Index monitoring in Europe [5].

3.4. INFORMISANJE JAVNOSTI

Edukovanost stanovništva o važnosti zaštite od štetnog delovanja ovog dela Sunčevog spektra na ljudsku kožu i oči je u našoj zemlji na vrlo skromnom nivou. Stanovništvo zaštitu vrši po subjektivnom osećaju u želji da svoj ten učini tamnijim ne znajući da li to čini ispravno ili ne i nemajući nikakve podatke niti znanje o zdravstvenim posledicama. Posledica toga je da, prema nezvaničnim podacima dermatologa, broj malignih melanoma kože drastično raste iz godine u godinu.

Ova aktivnost je možda i najvažnija u procesu zaštite od štetnih dejstava UV zračenja, bez obzira na izvor iz kog ono dolazi. Informisanje mora biti kratko i jasno, putem svih raspoloživih medija – pisanih, elektronskih, panela i bilborda, ali i putem interneta gde stanovništvo može pristupiti trenutnim vrednostima UV indeksa. Osim toga, vrlo važnu ulogu ima i edukacija stanovništva, posebno mlade populacije i dece, koja bi se mogla sprovoditi u osnovnim i srednjim školama na časovima posvećenim zaštiti životne sredine. Na žalost, ta aktivnost kod nas nije razvijena.

Koža i oči su organi na ljudskom telu koji su najčešće izloženi UV zračenju stoga se najveća pažnja posvećuje njihovoj zaštiti. Ispitivanja su pokazala da adekvatna UV zaštita može u 70% slučajeva da predupredi rak kože. Smatra se da se koža najbolje štiti odećom, a delove tela koji nisu zaštićeni odećom treba mazati zaštitnim kremama. Međunarodne preporuke kažu da treba koristiti kremu sa zaštitnim faktorom 15 i primenjivati je na svaka 2 sata kao i svaki put posle plivanja. Posebnu pažnju treba obratiti na osetljive delove tela koji su više ili pod direktnijim uglom izloženi Sunčevom zračenju.

Najvažnija mera zaštite je izbegavanje izlaganja suncu onda kada je ono najopasnije (od 10 do 16 časova) i redovno praćenje i informisanje o intenzitetu UV zračenja i pridržavanje preporuka o prevenciji njegovog štetnog dejstva.

Vrednosti UV indeksa i preporuke za prevenciju štetnog dejstva tj. zaštite:

a) *Minimalan* - 0, 1, 2

Ova kategorija predstavlja minimalnu opasnost od UV zračenja. Većina ljudi može ostati na suncu i više od 1 sat, a da ne dobije opekotine. Pri dužim boravcima napolju preporučuje se upotreba naočara za sunce. Ljudi sa vrlo osetljivom kožom (tip 1) i novorođenčad treba da povedu računa o zaštiti od produženog boravka na suncu, sunčanim naočarima i zaštitinom kremom. Ne sme se zaboraviti na odbijeno (reflektovano) UV zračenje te se posebna opreznost preporučuje za skijaše i ljude koji borave u planinama, kao i one na moru koji trebaju posebno da zaštite područja ispod brade i nosa.

b) *Nizak* - 3, 4

UV indeks ovih vrednosti predstavlja malu opasnost od UV zračenja. Za većinu ljudi se preporučuje upotreba šešira sa širokim obodom, naočare za sunce i zaštitna krema. Osetljiva populacija još treba da doda i odeću s dugim rukavima, jer oni mogu dobiti

opekotine već posle 20 minuta izlaganja. Dobro je pratiti sopstvenu senku. Što je ona kraća, postoji veća opasnost od UV zračenja.

c) Srednji - 5, 6

Ove vrednosti predstavljaju već značajnu opasnost od UV zračenja. Za većinu ljudi se preporučuje upotreba šešira sa širokim obodom, naočara za sunce, zaštitne kreme i odeće sa dugim rukavima. Osjetljiva populacija može da dobije opekotine za manje od 20 minuta, pa se ne preporučuje izlaganje novorođenčadi suncu u vremenu od 10 do 16 sati. Ukoliko ovakve osobe borave ili rade na otvorenom treba da zaštitite vrlo osjetljiva područja kao što su nos, vrhovi ušiju i usne.

d) Visok - 7, 8, 9

Ove vrednosti UV indeksa predstavljaju visoku opasnost od UV zračenja. Treba smanjiti boravak na suncu između 10 i 16 sati, koristiti šešir sa širokim obodom, naočare za sunce, zaštitnu kremu i odeću dugih rukava. Ljudi sa vrlo osjetljivom kožom mogu dobiti opekotine za manje od 10 minuta. Preporuka je da novorođenčad i deca ne izlaze na sunce između 10 i 16 sati. Svakako je dobro potražiti senku, ali treba biti svestan da voda, pesak, beton, stene i sl. refleksijom mogu povećati nivo UV zračenja i na mestima koja nisu direktno izložena suncu, pa je i u senci potrebna zaštita. Dobro je koristiti odeću od gusto tkanog materijala, jer UV zraci mogu da prodru kroz tanku tkaninu.

e) Vrlo visok- 10 i više

Vrednosti UV indeksa 10 i više predstavljaju vrlo veliku opasnost od UV zračenja. Preporuka je da se maksimalno smanji boravak na otvorenom sredinom dana od 10 do 16 sati. Kao zaštita se svakako preporučuje upotreba šešira za širokim obodom, naočara za sunce, zaštitne kreme, odeće dugih rukava od gustog tkanja i izbegavanje boravka na direktnom suncu. Preporuka je da novorođenčad i deca nikako ne izlaze na sunce između 10 i 16 sati. Osjetljiva populacija može dobiti opekotine za manje od 5 minuta. Zaštitni faktor (Sun Protection Factor, SPF) je vrednost vidno istaknuta na ambalaži preparata za zaštitu od sunca koji pokazuje koliko se puta duže može boraviti na suncu uz primenu zaštitnog preparata nego bez njega, a da ne dođe do pojave crvenila (eritema) na koži.

Na primer: ukoliko je vaše lično vreme gorenja (pojavljivanja crvenila) 30 minuta i vi namažete telo zaštitnim preparatom za sunčanje sa SPF 8 to znači da možete ostati na suncu 8 puta duže tj. 4 sata, a da se ne pojavi crvenilo (eritem). Važno je napomenuti da nanošenje zaštite više puta zaredom ne povećava bezbedno vreme sunčanja tj. ne povećava SPF. Jedini način da se bezbedno vreme sunčanja produži je korišćenje kreme sa većim SPFom. Takođe, nanošenje zaštite se ne prenosi na sledeći dan već traje samo tog dana kada je nanoseno i to ukoliko nije mehanički skidano ili spirano.

4. ZAKLJUČAK

UV indeks je veličina koja omogućuje informisanje javnosti o intenzitetu Sunčevog UV zračenja u odnosu na fotobiološki tip kože. Ova veličina je oznančena od strane WHO pre više od 20 godina, dok se u Srbiji (Beogradu i Novom Sadu) meri već više od 10 godina i podaci se objavljuju na lokalnim internet stranicama. Svetska iskustva su pokazala da je prevencija odnosno pravovremeno izveštavanje javnosti o preteranom izlaganju Sunčevom UV zračenju kao i zaštiti najbolja prevencija raka kože i oštećenja oči. Obzirom da doskorašnja informisanost javnosti putem lokalnih internet stranica nije bila dovoljna, merenja u ova dva grada su objedinjena kroz projekat „Ozonizacija“ i

objavljaju se pomoću android aplikacije (UV indeks Srbija) i jedinstvene internet stranice (<http://www.uv-srbija.rs/>), a izmerene vrednosti se beleže na svakih 30 minuta. Uz podatke UV zračenja, objavljuju se i vrednosti debljine stratosferskog ozonskog omotača iznad Novog Sada kao i opširan tekst sa svim objašnjenjima vezanim za UV indeks, načine i sredstva zaštite od Sunčevog zračenja. Osim merenja i rezervne akvizicije podataka, vrši se i provera modela prognoze UV zračenja [6], godišnja interkomparacija instrumenata, kao i poređenja izmerenih vrednosti UV indeksa u ova dva grada. Poređenja vrednosti UV indeksa su pokazala veliku sličnost podataka čija disperzija zavisi uglavnom od lokalnih meteoroloških parametara (oblačnost i optička zamućenost atmosfere) kao i fizičke osobine UV zračenja, kao zračenja najkraće talasne dužine u atmosferi, da se rasejava.

5. LITERATURA

- [1] WMO-GAW, Report of the WMO Meeting of Experts on UV-B Measurements, Data Quality Control and Standardization of UV Indices, Rep. No. 95,1994.
- [2] F. McKinley and B.L. Diffey, CIE Journal 6,1987, 17.
- [3] Z. Mijatović, Lj. Čonkić, S. Miljković: UV zračenje, izvori, osobine, efekti i zaštita; Prirodno-matematički fakultet, Novi Sad, 2002.
- [4] WMO-GAW, Report of the WMO-WHO Meeting of Experts on Standardization of UV Indices and their Dissemination to the Public, July 1997.
- [5] Schmalwieser, A., Gröbner, J., Klotz, B., Blumthaler, M., De Backer, H., Bolsee, D., Werner, R., ... Kolarž, P., Mijatović, Z., et al., *UV Index monitoring in Europe*, Photochem. Photobiol. Sci., DOI: 10.1039/C7PP00178A, 2017.
- [6] S. Malinović, D.T. Mihailović, D. Kapor, Z. Mijatović, I.D. Arsenić, NEOPLANTA: a short description of the first Serbian UV index model. J Appl. Meteorol. Climatol. 45:1171–1177, 2006.

CONTINUAL MEASUREMENTS OF UV RADIATION AND OZONE I SERBIA

Predrag KOLARŽ¹, Zoran MIJATOVIĆ², Aleksandar VLAJIĆ³

1) Univerzitet u Beogradu, Institut za fiziku, Beograd, Srbija, kolarz@ipb.ac.rs

2) Univerzitet u Novom Sadu, Departman za fiziku, Prirodno matematički fakultet,
Novi Sad, Srbija, mijat@uns.ac.rs

3) NVO, GRES - Grupa za razvoj ekološke svesti, Beograd, Srbija,
arborea.hyla@gmail.com

ABSTRACT

UV radiation in Serbia is measured independently in Belgrade and Novi Sad for many years. For better public information, these measurements are unified and uniformed through the project of non-governmental organizations named "Ozonisation", and are now available on the website <http://www.uv-srbija.rs> and applications for Android mobile phones "UV index Serbia". Data of UV Index are updated every half hour, while the data for the concentration of stratospheric ozone above the Novi Sad, i.e. Serbia, are given daily. The UV index values are displayed graphically, and the site provides a detailed explanation of what the UV index represents, which index values are dangerous, how to protect against excessive exposure to sunlight, and how the sun protection factor (SPF) is calculated.

ИНДЕКС АУТОРА

**ДРУШТВО ЗА ЗАШТИТУ ОД ЗРАЧЕЊА
СРБИЈЕ И ЦРНЕ ГОРЕ**



**ЗБОРНИК
РАДОВА**

**XXIX СИМПОЗИЈУМ ДЗЗСЦГ
Сребрно језеро
27- 29. септембар 2017. године**

**Београд
2017. године**

ЗБОРНИК РАДОВА

XXIX СИМПОЗИЈУМ ДЗЗСЦГ
27-29.09.2017.

Издавачи:

Институт за нуклеарне науке „Винча“
Друштво за заштиту од зрачења Србије и Црне Горе

За извршног издавача:

Др Борислав Грубор

Уредници:

Др Јелена Станковић Петровић
Др Гордана Пантелић

ISBN 978-86-7306-144-3

© Institut za nuklearne nauke „Vinča“

Техничка обрада:

Јелена Станковић Петровић, Гордана Пантелић

Штампа:

Институт за нуклеарне науке ”Винча”, Мике Петровића Аласа 12-14, 11351
Винча, Београд, Србија

Тираж:

150 примерака

Година издања:

Септембар 2017.

**XXIX СИМПОЗИЈУМ ДРУШТВА
ЗА ЗАШТИТУ ОД ЗРАЧЕЊА
СРБИЈЕ И ЦРНЕ ГОРЕ**

Сребрно језеро, од 27.09. до 29.09.2017. године

Организатори:

ДРУШТВО ЗА ЗАШТИТУ ОД ЗРАЧЕЊА СРБИЈЕ И ЦРНЕ ГОРЕ

ИНСТИТУТ ЗА НУКЛЕАРНЕ НАУКЕ „ВИНЧА“

Лабораторија за заштиту од зрачења и заштиту животне средине „Заштита“

Организациони одбор:

Председник: Гордана Пантелић

Чланови:

Маја Еремић Савковић, Агенција за заштиту од јонизујућих зрачења и нуклеарну сигурност, Београд

Вера Спасојевић Тишма, Нуклеарни објекти Србије, Београд

Иван Кнежевић, Нуклеарни објекти Србије, Београд

Данијела Аранђић, Институт за нуклеарне науке „Винча“, Београд

Јелена Станковић Петровић, Институт за нуклеарне науке „Винча“, Београд

Милица Рајачић, Институт за нуклеарне науке „Винча“, Београд

Сандра Ђеклић, Институт за нуклеарне науке „Винча“, Београд

Наташа Сарап, Институт за нуклеарне науке „Винча“, Београд

Предраг Божовић, Институт за нуклеарне науке „Винча“, Београд

Никола Кржановић, Институт за нуклеарне науке „Винча“, Београд

Редакциони одбор:

др Невенка Антовић, Природно математички факултет, Подгорица

др Перко Вукотић, Природно математички факултет, Подгорица

др Софија Форкапић, Природно математички факултет, Нови Сад

др Душан Мрђа, Природно математички факултет, Нови Сад

др Миодраг Крмар, Природно математички факултет, Нови Сад

др Драгослав Никезић, Природно математички факултет, Крагујевац

др Ненад Стевановић, Природно математички факултет, Крагујевац

др Јелена Ајтић, Факултет ветеринарске медицине, Београд

др Владимир Удовичић, Институт за физику, Земун, Београд

др Драгана Тодоровић, Институт за нуклеарне науке „Винча“, Београд

др Ивана Вуканац, Институт за нуклеарне науке „Винча“, Београд

др Јелена Крнета Николић, Институт за нуклеарне науке „Винча“, Београд

др Марија Јанковић, Институт за нуклеарне науке „Винча“, Београд

др Милош Живановић, Институт за нуклеарне науке „Винча“, Београд

др Оливера Цирај-Бјелац, Институт за нуклеарне науке „Винча“, Београд

др Србољуб Станковић, Институт за нуклеарне науке „Винча“, Београд



РЕПУБЛИКА СРБИЈА
Завод за интелектуалну својину

Београд, Кнегиње Љубице 5

ИСПРАВА О МАЛОМ ПАТЕНТУ

Број 1202 U

Подносиоцу пријаве за признање малог патента

КОЛАРЖ, Предрагу, др,

Светогорска 30, 11000 Београд, RS,

признат је мали патент под називом

**ПОБОЉШАНА КОНСТРУКЦИЈА ВЕШАЊА МЕРНЕ ЕЛЕКТРОДЕ
КОД ЦИЛИНДРИЧНОГ ДЕТЕКТОРА АТМОСФЕРСКИХ ЈОНА**

по пријави МП -2010/0085, поднетој 30.11.2010. године,

са правом првенства од RS 30.11.2010. МП-2010/0085.

Мали патент је уписан у Регистар малих патената 07.03.2011. године,
и објављен у Гласнику интелектуалне својине 31.08.2011. године.

Мали патент важи до 30.11.2020. године, под условом
да се годишње таксе за његово одржавање редовно плаћају.

Ова исправа издата је на основу члана 49. Закона о патентима,
("Сл. лист СЦГ" бр. 32/2004, 35/2004 и "Сл. гл. РС", бр. 115/2006.).

Београд, 01.09.2011. године

Директор
Бранка Тотић



(19) REPUBLIKA SRBIJA (12) **Spis malog patenta** (11) **1776 U1**



ZAVOD ZA
INTELEKTUALNU SVOJINU
BEOGRAD

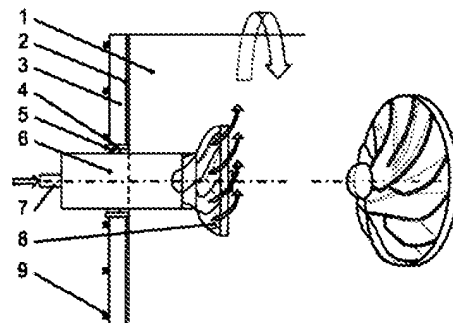
(51) Int. Cl.
B04C 5/00 (2006.01)

(21) Broj prijave:	MP-2022/0050	(73) Nosioци malog patenta:	INSTITUT ZA FIZIKU BEOGRAD Pregrevica 118, 11080 Zemun-Beograd, RS; MEDICINSKI FAKULTET, UNIVERZITET U BEOGRADU Dr Subotića starijeg 1, 11000 Beograd, RS
(22) Datum podnošenja prijave:	25.05.2022.	(72) Pronalazači:	KOLARŽ, Predrag; ILIĆ, Ž. Anđelija; TRBOVIĆ, M. Aleksandar; RISTIĆ, ĐUROVIĆ, Lj. Jasna; JOVANOVIĆ, Tanja; JANKOVIĆ, Marko
(45) Datum objavljivanja malog patenta:	30.12.2022.	(74) Zastupnik:	

(54) Naziv: **ROTIRAJUĆA KOMORA SA UNUTRAŠNJIM PASIVNIM IMPELEROM ZA POBOLJŠANO RASPRŠIVANJE ČESTICA I PRODUŽENO VREME IZLAGANJA**

(57) Apstrakt:

Predmetni pronalazak pripada oblasti biofizičkih ispitivanja interakcije jonizovanih čestica ili gasova sa bio-aerosolima u kontrolisanim uslovima eksperimentalne rotirajuće komore, a rešava problem konstrukcije elemenata za dovod čestica i jona, koji bi obezbedili što veću homogenost raspodele čestica po celoj zapremini tela komore (1), kao i dodatno produženo vreme izlaganja unutar tela komore (1), tokom eksperimenta. Problem se rešava centrifugalnim impelerom (8) koji aksijalni dovod čestica / jona prevodi u radijalno spiralni dovod u rotirajuće telo komore (1). Aerosoli preko creva uvodnika (7) ulaze u uvodnik (6) postavljen u centru ose rotacije. Uvodnik (6) je preko kotrljajućeg ležaja (5) i ležišta kotrljajućih ležaja (4) vezan za poklopac (3) komore, koji je vijcima (9) preko gumene zaptivke (2) poklopca pričvršćen za rotirajuće telo komore (1). Centrifugalni impeler (8) dovod čestica usmerava radijalno spiralno u odnosu na osu tela komore (1), u smeru suprotnom od smeru rotacije tela komore (1).



RS 1776 U1

Област технике на коју се проналазак односи

Предметни проналазак припада области експерименталне биофизике, односно спада у опрему и инструментацију који се користе при интеракцији јонизованих честица или гасова са био-аеросолима, тј. честицама распршеним у ваздуху.

Технички проблем

У сврху продуженог боравка честица у ваздуху унутар коморе, још 1958. је предложена употреба ротирајуће коморе, познате и као „Голдбергова ротирајућа комора“. Услед супротних ефеката гравитационих и центрифугалних сила, честице остају подржане у ваздуху коморе и до дан-два, односно, ротацијом се значајно продужава трајекторија честица (величина преко 0.6 μm) до коначног слегања уз зид коморе. Неравномерна расподела аеросола и јона по запремини коморе, као и релативно кратко време живота крупнијих честица значајно усложњавају и отежавају израду експеримената и доношење поузданих закључака.

Да би комора могла да ротира неопходно је уводник гасова буде у центру осе ротације. Уколико се јони или гасови убацују директно из уводника у комору они се не распоређују хомогено по целој запремини коморе него их има више у правцу осе с тим што честице веће од 0.6 μm релативно кратко бораве у ваздуху коморе док се под утицајем гравитације не депонују на њеном зиду. Технички проблем експерименталног уређаја је нехомогена расподела и кратко време излагања честица већих од 0.6 μm . Технички проблем који се решава предметним проналаском је како конструкцијски решити довод јона или гасова у комору да би се добила побољшана хомогена расподела истих и да би се продужило могуће време излагања. Предност предметног проналаска је и компактност и ниски трошкови уведеног додатка за решавање описаних проблема.

Стање технике

Уобичајени модел ротирајуће коморе користи директне уводнике аеросола у комору Л.Ј. Голдберга (Goldberg, L.J., Watkins, H.M.S. Boerke, E.E., Chatigny, M.A. (1958). *Am. J. Hyg.* **68**: 85-93; Goldberg, L.J. (1971). *Appl. Microbiol.* **21**: 244—252; Asgharian, B., Moss, O.R. (1992). Particle suspension in a rotating drum chamber when the influence of gravity and rotation are both significant. *Aerosol Sci. Technol.* **7**: 263-277). Решења сличне намене уз мање модификације, претежно у смислу довођења и одвођења аеросола, или контроле температуре, притиска и сл., су предлагана и у неким каснијим патентима и радовима, на пример (EP0357939A2 - Rotating drum; US3939065A - Screening device; Verreault, D., *et al.* (2014). Design of an environmentally controlled rotating chamber for bioaerosol aging studies. *Inhal. Toxicol.* **26**(9): 554—558; Santarpia, J.L., *et al.* (2012). Changes in fluorescence spectra of bioaerosols exposed to ozone in a laboratory reaction chamber to simulate atmospheric aging. *Opt. Express* **20**: 29867-29881; Huang, S.H., *et al.* (2019). Experimental characterization of aerosol suspension in a rotating drum. *Aerosol Air Qual. Res.* **19**: 688-697). Импелер, са друге стране, се користи у компресорима, гасним турбинама, и сл. Неке од примена везане за истовремено коришћење комора су дате у патентима US6372006B1 (Separator element for a centrifugal separator) и US8302779B2 (Separator drum and compressor impeller assembly).

У предметном проналаску, користимо нов начин примене импелера у ротирајућој Голдберговој комори (Goldberg rotating drum) чиме постижемо хомогену расподелу честица по целој запремини коморе као и њихов продужени боравак у ваздуху коморе. Импелер је причвршћен на уводник аеросола на страни која се налази у комори, док је сам уводник преко кугличног лежаја тесно причвршћен за страницу односно поклопац коморе у центру њене осе ротације. Притом, ток честица пролази између закривљених преграда импелера закренуто у смеру супротном од смера ротације коморе. Овакав начин усмеравања аеросола (радијално на осу ротације и под углом супротним од смера ротације коморе) доприноси већој хомогености расподеле честица по целој запремини коморе, као и додатно продуженом времену њиховог излагања.

Излагање суштине проналаска

Да би комора у којој се врше експерименти интеракције честица са гасовима или јонима могла да ротира око своје уздужне осе неопходно је да се улазни и излазни отвори за унос и узорковање честица налазе у центру те осе. Котрљајући лежајеви на улазном и излазном отвору поклопаца коморе омогућавају да уводна и излазна црева не ротирају

заједно са комором него остају статична. Најједноставнији начин убацивања гаса или честица у комору је кроз уводно црево директно у комору. Обзиром да се извлачење излаганих честица или гаса врши кроз излазни отвор на другој страници цилиндричне коморе, вероватноћа расподеле честица различитих величина при умереном протоку гаса (нпр. 121/min потребних за биосамплер филтер) није хомогена. Предметни проналазак је проистекао из потребе да се интеракција јонизованих честица или других гасова и био-аеросола, током експеримента, обавља при њиховој што више хомогеној расподели по целој запремини коморе као и да се притом омогући продужени боравак испитиваних честица у ваздуху у унутрашњости коморе.

Да би гас или аеросоли били хомогено распоређени по целој запремини коморе, и тако интераговали са јонима, који се због велике покретљивости много брже хомогено распоређују, потребно је усмерити их на излазу из уводника радијално у односу на осу.

Коришћење предметног проналазак, тј. центрифугалног импелера, омогућава не само радијално скретање доведених честица, већ и радијално спиралну ротацију у смеру закрилаца импелера, са циљем што више хомогене расподеле честица по целој комори. Услов да се честице депонују (таложе или налепе) на површини зидова коморе је да достигну исту угаону брзину као и површина зида коморе на који се депонују. На достизање ове угаоне брзине делују кретање зида коморе и гравитација. Да би се честице што спорије депоновале на зидовима, тј. да би биле што дуже присутне у ваздуху коморе, потребно је да је њихово почетно кретање усмерено супротно од смера ротације коморе. Тада је потребно много више времена да честице достигну брзину кретања једнаку брзини кретања зида коморе и да се депонују на њему. Увођењем импелера на излазу из уводника постиже се хомогенија расподела честица по целој запремини коморе и почетно кретање честица у супротном смеру од смера у коме се креће комора што обезбеђује дуже присуство честица величине веће од 0.6 μm у ваздуху.

Кратак опис слика нацрта

Слика 1 — шематски приказ основне структуре и делова улазне стране ротирајуће коморе за експерименте са аеросолима органског и неорганског порекла. Аеросоли који под притиском улазе у комору бивају скренути закрилцима импелера радијално на своју путању и у смеру супротном од смера ротирања коморе.

1 - тело коморе

2 - заптивка поклопца

- 3 - поклопац коморе
- 4 - лежиште котрљајућег лежаја
- 5 - котрљајући лежај
- 6 - уводник
- 7 - црево уводника
- 8 - импелер
- 9 - вијак

Слика 2 - на слици је приказан импелер који се пасивно монтира на непокретни уводник (Слика 1) који је у односу на комору причвршћен котрљајућим лежајем и налази се у оси коморе. Распршивање долазног млаза аеросола је пропорционално брзини честица и закривљености преграда импелера радијално у односу на осу и у смеру ротације супротном од смера ротирања коморе.

Детаљан опис проналаска

Експериментална комора цилиндричног облика ротира око уздужне осе уз помоћ постоља са ваљцима, који су са телом коморе 1 повезани силом трења, и помоћу спољашњег електромотора, што је све уобичајено за дизајн такозване Голдбергове ротирајуће коморе те систем за ротацију тела коморе 1 није предмет заштите патентом. Предмет заштите патентом је решење проблема како конструкцијски решити довод честица у тело коморе 1, тако да се већ приликом довода честице што хомогеније распореде по телу коморе 1 и да се правилним смером довода продужи време излагања. Бочне стране коморе су затворене поклопцима 3 коморе, који су помоћу вијака 9 причвршћени за тело коморе 1. Притом, између поклопаца 3 коморе и тела коморе 1 се налазе гумене заптивке 2 поклопаца. У средини округлих поклопаца 3 коморе, на оси тела коморе 1, са улазне као и са излазне стране тела коморе 1, налазе се отвори у којима су смештена лежишта котрљајућег лежаја 4 са котрљајућим лежајем 5, што омогућава да довод и одвод честица и гасова не ротирају са телом коморе 1 већ остају статични. Слика 1 приказује улазну страну ротирајуће коморе, на којој страни је, кроз котрљајући лежај 5, тесно углављен уводник 6 гаса (аеросола), а на страни уводника 6 која се налази унутар тела коморе 1, односно на излазном крају уводника 6, је пасивно причвршћен импелер 8, један од главних конструкцијских елемената предметног проналаска. Црево уводника 7 гаса (честица) и уводник 6 гаса (честица) не ротирају са ротацијом тела коморе 1, већ остају статични. Центрифугални импелер 8 има закривљене преграде,

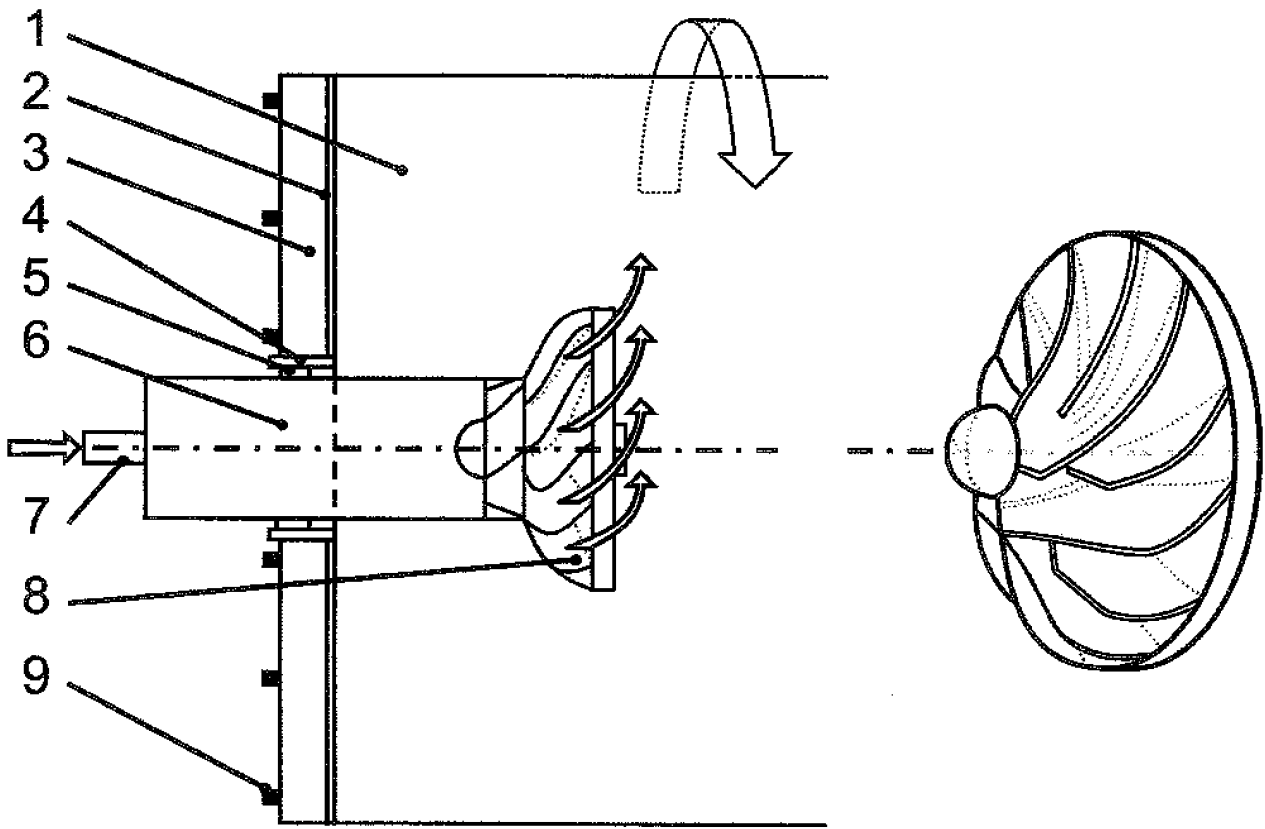
закрилца (Слика 2), између којих мора проћи гас (аеросол), након довода кроз уводник 6 гаса и цево уводника 7. Својим обликом односно закривљеношћу преграда, импелер 8 аксијални довод гаса (честица) из уводника 6 оријентише најпре радијално, а потом и спирално. Импелер 8 је тако оријентисан да долазеће честице скреће у смеру ротације супротном од смера ротирања тела коморе 1.

Начин индустријске или друге примене проналаска

Према је основна примена предметног проналаска за извођење експеримената из области биофизике, предметни проналазак се може користити за прецизно испитивање и спровођење процеса у индустрији. Увођење импелера у процесну/интеракциону комору на начин изнет у опису проналаска доприноси хомогености расподела и тиме повећава вероватноћу интеракције унетих честица и материјала, што може бити од интереса у процесима мешања гасовитих супстанци, филтрирања, глазирања наношењем слојева материјала и слично, осим основне изложене намене интеракције честица аеросола са јонизованим честицама или гасовима. У случају неке одређене индустријске примене, према задатој спецификацији проблема би се модификовао и дизајн коморе.

ПАТЕНТНИ ЗАХТЕВ

1. Ротирајућа комора са унутрашњим пасивним импелером (8), назначена тиме, што се састоји од цилиндричног тела коморе (1) са поклопцима 3 коморе на странама, постављеним преко заптивки 2 поклопаца и учвршћеним вијцима (9), са улазним и излазним отворима на оси коморе у којима се налазе лежишта котрљајућих лежаја (4) са котрљајућим лежајевима (5), кроз које је на улазу причвршћен уводник (6) са цревом уводника (7) за довод честица, а при чему је на крају уводника (6) у комори причвршћен импелер (8), који има преграде закривљене спирално супротно од смера ротирања тела коморе (1), које омогућавају довод честица из уводника (7) између преграда импелера (8) у тело коморе (1).



Слика 1.

Слика 2.

- [6] G. Pantelić, M. Eremić Savković, M. Živanović, J. Nikolić, M. Rajačić, D. Todorović. Uncertainty evaluation in radon concentration measurement using charcoal canister. *Applied Radiation and Isotopes*. 87, 2014, 452–455.

MEASUREMENT OF RADON EXHALATION FROM BUILDING MATERIALS

**Predrag UJIĆ¹, Igor ČELIKOVIĆ¹, Ahmed AWHIDA², Boris LONČAR²,
Gordana PANTELIC¹, Ivana VUKANAC¹, Predrag KOLARŽ³, Aleksandar
KANDIĆ¹, Mirjana ĐURAŠEVIĆ¹, Miloš ŽIVANOVIĆ¹**

- 1) *Institut za nuklearne nauke „Vinča“, Univerzitet u Beogradu, Beograd, Srbija,
ujic@vin.bg.ac.rs*
- 2) *Univerzitet Univerzitet u Beogradu, Tehnološko-metalurški fakultet, Beograd, Srbija*
- 3) *Univerzitet u Beogradu, Institut za fiziku, Beograd, Srbija*

ABSTRACT

A review of a new radon exhalation measurement method is presented. This method provides also a measurement of the radon diffusion length and the radon emanation coefficient, which is not possible by standard radon exhalation measurement methods. Besides, three standard radon exhalation measurements are presented: closed chamber with an active instrument, closed chamber with a solid state nuclear track detector and a charcoal canister method. An intercomparison of advantages and disadvantages is also given. A short review of previous measurements of radon exhalation from commercial building materials in Serbia will be given in the presentation.



РЕПУБЛИКА СРБИЈА
Завод за интелектуалну својину
Београд, Кнегиње Љубице 5

ИСПРАВА О МАЛОМ ПАТЕНТУ

Број **1597 U1**

Подносиоцима пријаве за признање малог патента
КОЛАРЖ, Предрагу, др, Светогорска 30, 11000 Београд, RS;
ЋУРЧИЋ, Милици, др, Слободана Перовића 4/1, 11000 Београд, RS;
ГИЛИЋ, Мартини, др, Бањалучка 2, 11000 Београд, RS;
ХАЦИЋ, Бранки, др, Гандијева 35А, 11000 Београд, RS,

признат је мали патент под називом

**МОДИФИКОВАНИ НОСАЧ ЗА ВЕРТИКАЛНО ПОЗИЦИОНИРАЊЕ
ТАБЛЕТНИХ УЗОРАКА ОД ПРАШКАСТИХ МАТЕРИЈАЛА КОЈИ ЈЕ ДЕО
КОМОРЕ ЗА ВАКУУМИРАЊЕ И ХЛАЂЕЊЕ КОЈА СЕ КОРИСТИ У
СПЕКТРОСКОПСКИМ МЕРЕЊИМА**

по пријави МП - 2018/0028, поднетој 19.06.2018. године.

Мали патент је уписан у Регистар малих патената 03.04.2019. године,
и објављен у Гласнику интелектуалне својине број 4/2019 дана 30.04.2019. године.

Мали патент важи до 19.06.2028. године, под условом
да се годишње таксе за његово одржавање редовно плаћају.

Ова исправа издата је на основу члана 110. Закона о патентима,
("Службени гласник РС", бр. 99/11).



Београд, 03.05.2019. године

Директор

Владимир Марић
Владимир Марић



ZAVOD ZA
INTELEKTUALNU SVOJINU
BEOGRAD

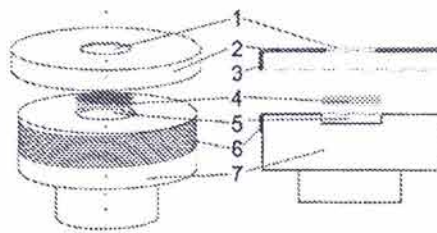
(51) Int. Cl.
G12B 9/08 (2006.01)

(21) Broj prijave:	MP-2018/0028	(73) Nosioci malog patenta:	KOLARŽ, Predrag, dr Svetogorska 30, 11000 Beograd, RS; ĆURČIĆ, Milica, dr Slobodana Perovića 4/1, 11000 Beograd, RS; GILIĆ, Martina, dr Banjalučka 2, 11000 Beograd, RS; HADŽIĆ, Branka, dr Gandijeva 35A, 11000 Beograd, RS
(22) Datum podnošenja prijave:	19.06.2018.	(72) Pronalazači:	KOLARŽ, Predrag, dr; ĆURČIĆ, Milica, dr; GILIĆ, Martina, dr; HADŽIĆ, Branka, dr
(45) Datum objavljivanja malog patenta:	30.04.2019.	(74) Zastupnik:	

(54) Naziv: **MODIFIKOVANI NOSAČ ZA VERTIKALNO POZICIONIRANJE TABLETNIH UZORAKA OD PRAŠKASTIH MATERIJALA KOJI JE DEO KOMORE ZA VAKUUMIRANJE I HLAĐENJE KOJA SE KORISTI U SPEKTROSKOPSKIM MERENJIMA**

(57) Apstrakt:

Pronalazak pripada oblasti eksperimentalne fizike, a odnosi se na rešavanje problema destrukcije tablete od praškastog materijala usled lepljenja na nosač za vertikalno pozicioniranje uzoraka u komori za vakumiranje i hlađenje pri spektroskopskim merenjima. Rešenje ovog problema je modifikacija nosača uzorka koja je suština ovog malog patenta. Modifikovani bakarni nosač ne razara uzorak i rešava problem homogene raspodele temperature po uzorku. Na bakarni nosač (7) pri vrhu bočne strane narezan je navoj (6) sitnog koraka tako da se bakarni poklopac (2) sa navojem (3) može naviti preko tablete (4) koja se nalazi u odgovarajućem udubljenju (5). Bakarni poklopac (2) je profilisan tako da je otvor (1), za 2 mm manji od prečnika tablete (4), koja je standardne veličine od 10 mm.



а) Област технике на коју се проналазак односи

Проналазак припада области експерименталне физике тј. опреми и инструментима који се користе при спектроскопским мерењима а конкретно се односи на носаче за коморе за вакуумирање и хлађење.

б) Технички проблем

Технички проблем који се решава предметним проналаском односи се на то како конструкционо решити носач за вертикално позиционирање таблетних узорака који ће спречити пуцање и распадање узорка након мерење и омогућити њихову даљу употребу.

ц) Стање технике

Према стању технике познате су различите конструкције носача за позиционирање узорака од прашкастих материјала као део коморе у спектроскопским мерењима. У објављеној пријави патента US6992759B2, описан је и приказан проналазак под називом “Држач узорка за мерење спектра и спектрофотометар”. Технички проблем који је решаван састојао се у томе да се овим држачем подешава положај и температура чврстих и течних узорака у току хемијске реакције а за добијање апсорпционих спектра. Познате су технике загревања чврстих узорака помоћу оптичких влакана, али скоро ништа није познато о метода хлађења течних узорака и снимања спектра на ниским температурама. За сада су откривене конфигурације које се инсталирају директно у апарат за снимање спектра, али не и оне које имају средства за подешавање положаја у различитим правцима као и за примену на различитим уређајима за снимање спектра. Овим патентним проналаском решен је и проблем снимања инфрацрвених спектра, код којих се узорак држи најчешће у вакууму при чему се загревање узорка врши специјалним грејним ћелијама.

Патентна пријава US2004/0263843 A1, под насловом “Специјални носач за Раманов спектроскопски систем” решава проблем позиционирања узорка у Рамановој спектроскопији, конструисањем оптичке сонде која смањује контаминацију узорка. Даљи циљ проналаска је конструисање такве оптичке сонде која је компактна и флексибилна. Таква сонда укључује фотонску кристалну светлосну водичу за пријем ласерског снопа из извора као и за усмеравање ласерског зрака према узорку изабраног материјала. Систем даље укључује и сочива за пријем оптичких зрака као и оптички анализатор који се користи за анализу рефлектованог спектра.

Међутим, сва горе назначена решења конструкције носача за постављање узорака у спектроскопским методама имају основни недостатак у сложености њихове конетрукције. Осим тога поставља се и питање њихове економичности. Горе наведени недостаци отклоњени су конструкцијом модификованог носача за вишенеменску примену у спектроскопским мерењима.

д) Излагање суштине проналаска

Да би се таблета од прашкастог материјала користала и за друге експерименте као и да би се обезбедило боље одвођење топлоте, бакарни носач је профилисан тако да се узорак таблете постави у удубљење које се налази у центру носача са горње стране. С обзиром да су све таблете истих димензија дубина профилисаног удубљења у телу бакарног носача је за 0,05 mm већа од дебљине таблете. На бакарни носач је са бочне стране нарезан навој финог корака (M25 x 0.75), тако да се бакарни поклопац са урезаним навојем истог корака може навити на носач преко узорка таблетног облика. Због мале разлике удубљења за позиционирање у бакарном носачу и дебљине таблете, поклопац се може завити до краја, а да притом не поломи узорак и да га држи чврсто у жељеном положају. Бакарни поклопац је профилисан тако да је пречник отвора за 2 mm мањи од пречника таблете, која је стандардне величине око 10 mm.

е) Кратак опис слике нацрта

Слика 1. Шематски приказ погледа са стране и попречног пресека бакарног тела носача са поклопцем и таблетом.

ф) Детаљан опис проналаска

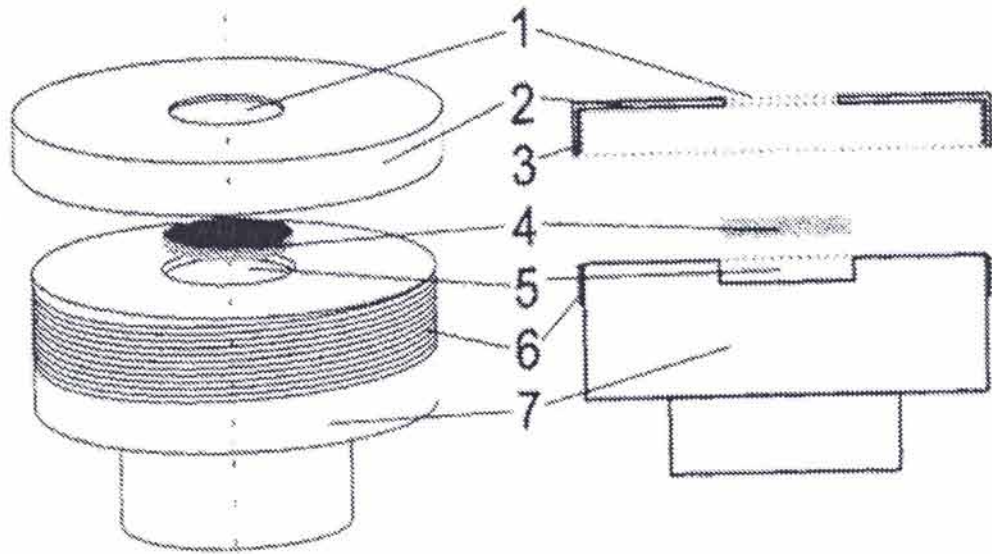
Бакарни носач 7 је профилисан тако да таблета 4 од прашкастог материјала у њега буде постављена у удубљење 5 које се налази у центру. На бакарни носач 7 је са бочне стране нарезан навој 6 финог корака (M25 x 0.75), тако да се бакарни поклопац 2 са отвором 1, на коме је урезан навој 3 истог корака, може навити преко таблете 4 од прашкастог материјала. Бакарни поклопац 2 је профилисан тако да је отвор 1 за 2 mm мањи од пречника таблете 4, која је стандардне величине око 10 mm. С обзиром да су све таблете 4 истих димензија, дубина профилисаног удубљења 5 у телу бакарног носача 7 је за 0,05 mm већа од дебљине таблете 4. Када се бакарни поклопац 2 до краја завије не оштећује таблету 4, а држи је чврсто у оси ласерског снопа.

г) Начин индустријске или друге примене проналаска

Проналазак је последица решавања проблема констуркције носача за вертикално позиционирање таблетних узорака од прашкастих материјала који је део коморе за вакумирање и хлађење која се користи у спектроскопским мерењима. Његова примена се односи на могућност коришћења истог узорка за различите експерименте, што отклања грешке које могу настати при упоређивању резултата добијених од различитог прашкастог материјала истог састава.

Патентни захтев

1. Модификовани носач за вертикално позиционирање таблетних узорака од прашкастих материјала, који је део коморе за вакуумирање и хлађење која се користи у спектроскопским мерењима, **назначен тиме**, састоји се од бакарног носача (7) у чијем центру је изведено удубљење (5) за смештање таблете (4), са изведеним навојем (6) са бочне стране чији корак одговара кораку навоја (3) изведеном на поклопцу (2) са отвором (1), у центру за 2 mm мањим од пречника таблете (4), изведеним тако да навијањем на носач (7) причвршћује таблету (4).



Слика 1а.

Слика 1б.



РЕПУБЛИКА СРБИЈА
Завод за интелектуалну својину
Београд, Кнегиње Љубице 5

ИСПРАВА О МАЛОМ ПАТЕНТУ

Број **1509 U1**

Подносиоцима пријаве за признање малог патента
КОЛАРЖ, Предрагу, др, Светогорска 30, 11000 Београд, RS;
ВЕЉОВИЋ, ЈОВАНОВИЋ, Соњи, др, Кнеза Вишеслава 76, 11000 Београд, RS;
МИЉКОВИЋ, Будимиру, Љубомира Стојановића 38, 11000 Београд, RS,
признат је мали патент под називом
ОПТИЧКИ ПОЈАЧАВАЧ МАЛИХ ИНТЕНЗИТЕТА UV-V ЗРАЧЕЊА
КАО ДЕО СИСТЕМА КОНТРОЛЕ ИЗЛАГАЊА ПЛАСТЕНИЧКИХ
САДНИЦА СУНЧЕВОМ ЗРАЧЕЊУ
по пријави МП -2017/0033, поднетој 19.05.2017. године.

Мали патент је уписан у Регистар малих патената 22.08.2017. године,
и објављен у Гласнику интелектуалне својине број 9/2017 дана 29.09.2017. године.

Мали патент важи до 19.05.2027. године, под условом
да се годишње таксе за његово одржавање редовно плаћају.

Ова исправа издата је на основу члана 110. Закона о патентима,
("Службени гласник РС", бр. 99/11).

Београд, 02.10.2017. године



В. д. директора
Владимир Марић
Владимир Марић



ZAVOD ZA
INTELEKTUALNU SVOJINU
BEOGRAD

(51) Int. Cl.
G02F 1/01 (2006.01)
G02F 1/29 (2006.01)

(21) Broj prijave: **MP-2017/0033**
(22) Datum podnošenja prijave: **19.05.2017.**
(45) Datum objavljivanja malog patenta: **29.09.2017.**

(73) Nosioци malog patenta:
KOLARŽ, Predrag, dr
Svetogorska 30, 11000 Beograd, RS;
VELJOVIĆ, JOVANOVIĆ, Sonja, dr
Kneza Višeslava 76, 11000 Beograd, RS;
MILJKOVIĆ, Budimir
Ljubomira Stojanovića 38, 11000 Beograd, RS

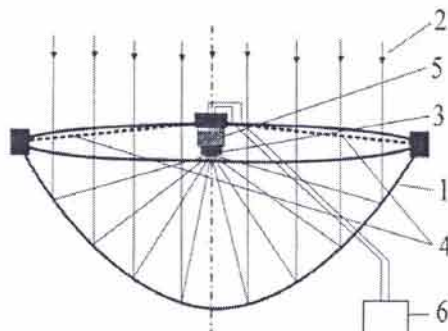
(72) Pronalazači:
KOLARŽ, Predrag, dr;
VELJOVIĆ, JOVANOVIĆ, Sonja, dr;
MILJKOVIĆ, Budimir

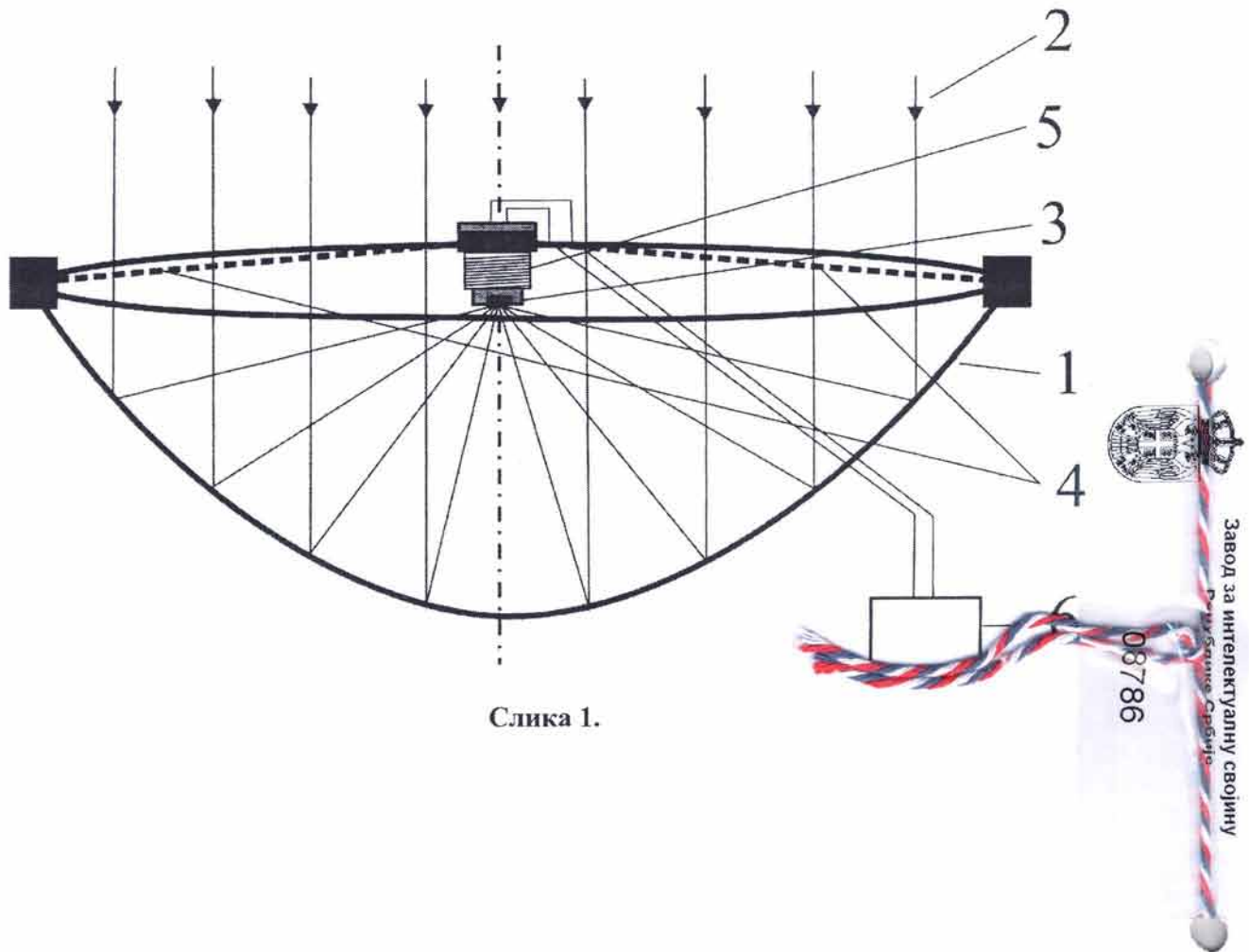
(74) Zastupnik:

(54) Naziv: **OPTIČKI POJAČAVAČ MALIH INTENZITETA UV-B ZRAČENJA KAO DEO SISTEMA KONTROLE IZLAGANJA PLASTENIČKIH SADNICA SUNČEVOM ZRAČENJU**

(57) Apstrakt:

Pronalazak pripada oblasti poboljšanja kvaliteta plasteničkih sadnica u poljoprivredi koje nisu u dovoljnoj meri izložene UV-B komponenti (2) Sunčevog zračenja. To izlaganje se omogućava dizanjem bočnih stranica plastenika. U uslovima smanjenog Sunčevog zračenja intenzitet UV-B komponente (2) je ispod praga osetljivosti UV-B fotodiode (3) i potrebno ga je pojačati. Korišćenjem paraboloidnog kvarcnog ogledala (1), na koje je centrično pričvršćen nosač (4) kućišta (5) UV-B fotodiode (3), UV-B komponenta (2) Sunčevog zračenja se prikuplja sa veće površine i projektuje u jednu tačku na kojoj se nalazi osetljiva površina UV-B fotodiode (3) koju na fokalnoj tački drži kućište (5) sa navojem. Navoj služi da bi se podesila fokalna tačka po osi paraboloidnog kvarcnog ogledala (1). Osetljiva površina fotodiode je $0,16 \text{ mm}^2$. Na taj način se zračenje prikuplja sa veće površine i projektovanjem na UV-B fotodiodu (3), optički pojačava iznad praga osetljivosti pri niskim intenzitetima UV-B komponente (2) Sunčevog zračenja. Analogni signal se potom pomoću pojačavača (6) pojačava i digitalizuje radi pretvaranja u snagu zračenja po jedinici površine.





Слика 1.